J. R. HOWELL
Associate Professor,
Department of Mechanical Engineering,
University of Houston,
Houston, Texas

R. E. DURKEE
Aerospace Engineer,
Structures and Mechanics Division,
NASA Manned Spacecraft Center,
Houston, Texas

Radiative Transfer Between Surfaces in a Cavity With Collimated Incident Radiation: A Comparison of Analysis and Experiment

Analysis and experiment are compared for the radiant exchange among three surfaces making up an infinitely long cavity Two of the cavity surfaces are specular-diffuse, while the third is bi directional The cavity is exposed to collimated incident energy to maximize the effect of the surface reflectivity characteristics on the radiation exchange

Introduction

INVESTIGATIONS of the importance of directional surface properties in radiative energy transfer have been limited to cases where the significant energy in the system originated over extended areas, references [1–4] [1] The energy sources were usually diffusely or nearly diffusely emitting surfaces or other diffuse sources The systems considered were composed of two or more such surfaces It has typically been found that the energy transfer in these systems is a weak function of the directional radiative properties of the individual surfaces Reference [1], for example, shows that in a triangular enclosure of two black sides and one gray side, the difference between the energy transfer for a diffusely or specularly reflecting gray surface is less than 10 percent In the simple geometry of an infinite parallel plate enclosure with one black surface, all directional characteristics of the other plate produce the same energy transfer so long as the hemispherical reflectivity of the surface is the same

Because directional characteristics have so little influence in these cases, it is difficult to determine the best analysis to use, best, that is, in the sense of how sophisticated a treatment must be given to the directional characteristics Schornhorst and Viskanta [2] found that an analysis based on diffuse radiative exchange was in better agreement with experiment than an analysis based on specular plus diffuse exchange for certain geometries, even though some of the surfaces in the system were highly specular Whether this discrepancy is due to certain assumptions present in the analysis or to experimental difficulties is not known

Similar conclusions are reached by Toor et al [3], and by Schornhorst and Viskanta [4]

Neu and Dummer [5] show a comparison of experiment with an analysis using bi-directional properties for the angular distribution of reflected energy from a model spacecraft exposed to collimated radiation Good agreement is obtained in this case where reflection effects are quite important

In the present paper, analysis and experiment are again compared Here, however, an open system is analyzed in which a directed external source of energy is brought into a cavity with an interior composed of directional surfaces In such a situation, as with the spacecraft modeling results of Neu and Dummer, the effects of directional surface characteristics are expected to be much larger than are found in enclosure problems This is because the interreflections of the strongly collimated incident radiation are a primary factor in determining the energy reaching certain surfaces of the cavity Results of experimental measurements are compared with an analysis of the energy exchange within the enclosure

Analysis

The system analyzed is shown schematically in Fig 1 It consists of an infinitely long (two-dimensional) three-sided cavity, with an open area at the top Surfaces 1 and 2 are fixed perpendicular to one another Surfaces 2 and 3 intersect at an angle φ Parallel incident radiation is entering the cavity at a known angle Surfaces 1 and 3 are taken to be specular-diffuse surfaces, while surface 2 has a directional absorptivity and bi-directional reflectivity

We use the definition of bi-directional reflectivity as presented by references [6, 7]

$$\rho''(\beta, \theta, \beta_r, \theta_r) = \frac{i''(\beta_r, \theta_r, \beta, \theta)}{i_i'(\beta, \theta) \cos \beta \, d\omega}$$

Here, β and θ are the cone and circumferential angles of incidence,

---

[1] Numbers in brackets designate References at end of paper

Contributed by the Heat Transfer Division and presented at the Space Technology and Heat Transfer Conference, Los Angeles Calif June 21–24 1970, of THE AMERICAN SOCIETY OF MECHANICAL ENGINEERS Manuscript received at ASME Headquarters March 19 1970 revised manuscript received October 5, 1970 Paper No 70-HT SpT-23

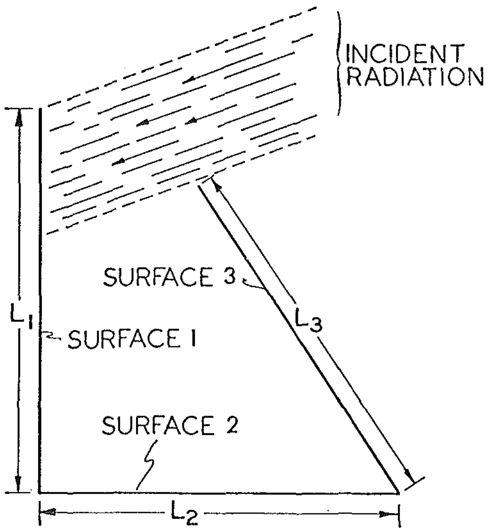

Fig. 1 Geometry of system analyzed; infinitely long cavity with three directional surfaces

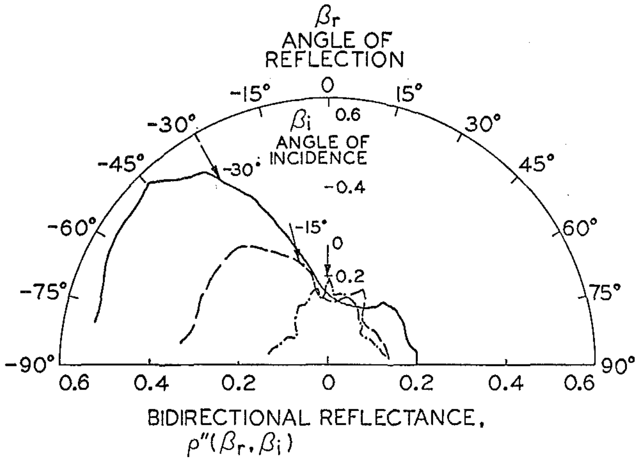

Fig. 3(a) Bi-directional reflectance of honeycomb surface in plane of incidence; incidence from 0, −15, and −30 deg

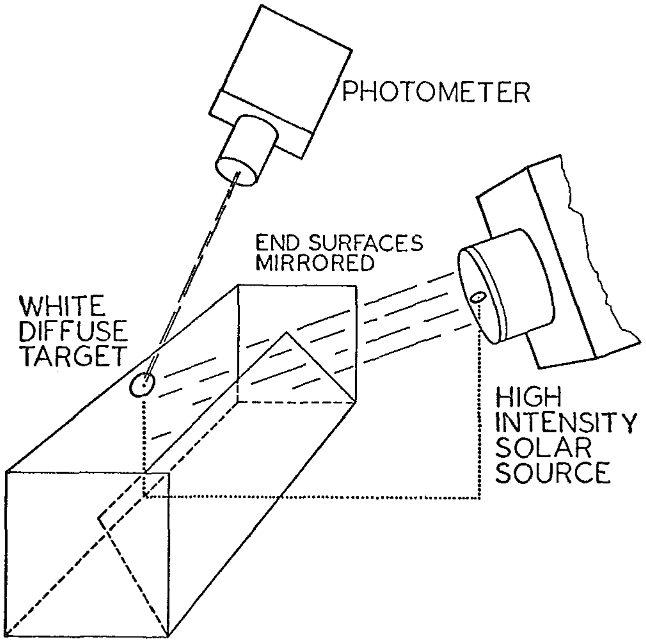

Fig. 2 Experimental apparatus

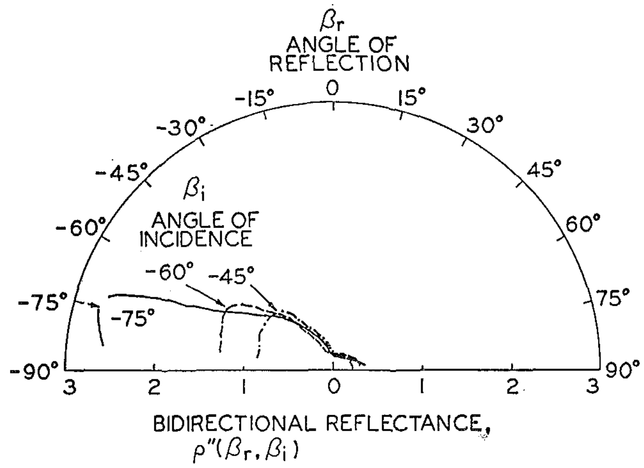

Fig. 3(b) Bi-directional reflectance of honeycomb surface in plane of incidence; incidence from −45, −60, and −75 deg

β_r and θ_r are the angles of reflection, i'' is the portion of the intensity reflected into the (β_r, θ_r) direction, and i_i' is the incident intensity. The $d\omega$ is the solid angle subtended by the source.

The bi-directional reflectivity of Surface 2 is assumed to be independent of θ_i. Circumferential angle of reflection θ_r is chosen randomly in the range of forward reflections or in the range of backward reflections, depending on the cone angle of reflection.

It is further assumed that all surfaces in the enclosure are at a sufficiently low temperature that emission for the surfaces can be neglected in comparison with the externally supplied energy. The surfaces are assumed to be gray.

Under these assumptions, the distribution of energy incident upon each of the internal surfaces of the enclosure is calculated. Because of the variety of directional properties present in the enclosure, a Monte Carlo procedure was used to obtain a solution. A detailed outline of the solution method will not be presented here; references [1, 8] give the formalism of the method along with example problems and programs. The method consists of dividing the incident energy into discrete bundles, and following the individual bundles through a series of events (reflection, absorption, etc.). The probability of the events is determined by the radiative properties of the surfaces. For example, a surface with absorptivity of 0.6 should have a 0.6 probability of absorbing a bundle and a 0.4 probability of reflecting it. For directional surfaces, determination of the probabilities becomes somewhat more difficult.

A tally is kept of the number of bundles that are incident upon each surface element. This number is then directly proportional to the energy incident upon the element, and this is the quantity we are after.

Experiment

An experimental system closely approaching the idealized system described in the analysis is required. In this way, a comparison of the results of experiment and analysis will give a measure of the adequacy of the analytical method. This can be done without clouding the comparison with questions of how well the assumptions in the analysis meet the realities of the experiment.

The general layout of the experimental equipment used in this investigation is shown in Fig. 2. The method of measurement is based upon that described by Bobco [9]. A source of parallel radiation is incident upon the entire cavity opening. A nearly

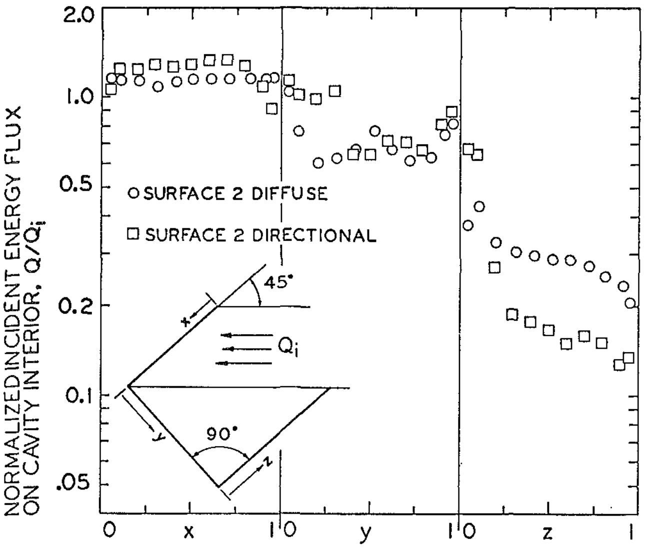

Fig. 4(a) Experimentally determined energy flux on interior of cavity; $\beta_s = 45$ deg; $\varphi = 90$ deg

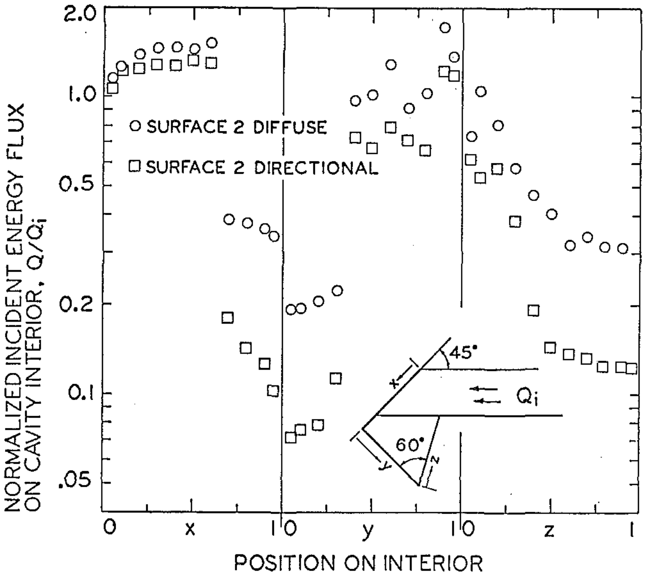

Fig. 4(c) Experimentally determined energy flux on interior of cavity; $\beta_s = 45$ deg; $\varphi = 60$ deg

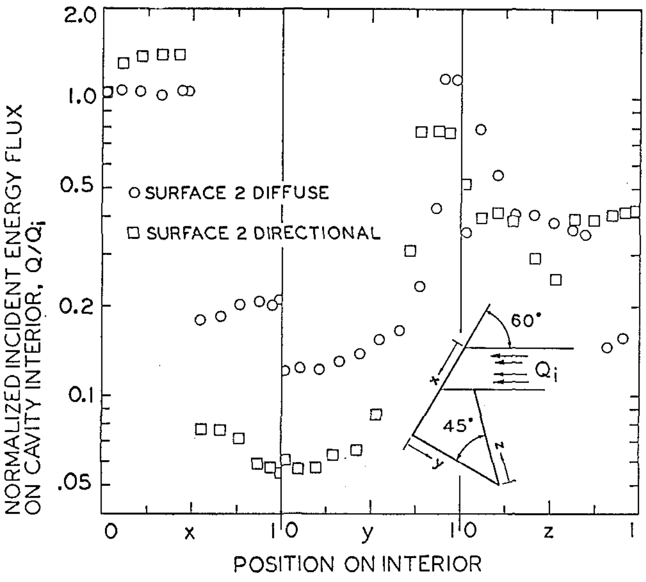

Fig. 4(b) Experimentally determined energy flux on interior of cavity; $\beta_s = 60$ deg; $\varphi = 45$ deg

diffuse white button is placed at the point where a measurement of incident energy is to be made. This button is carefully selected to be diffuse, so that the energy incident upon it is reflected equally into all directions. A photometer can then be focused upon the button, and the photometer reading will be in proportion to the energy incident upon the button. The orientation of the photometer with respect to the button is unimportant so long as the button is diffuse.

The cavity itself requires careful design. To approach the infinitely long cavity envisioned in the analysis is a practical impossibility because of two limiting difficulties: If the cavity dimensions are large enough to allow practical measurements, then end effects are probably extreme; if the cavity dimensions are small enough to allow illumination of a large length of cavity and thus minimize end effects near the point of measurement, then measurement of local incident radiant energy flux is imprecise. This occurs because the photometer reads the energy reflected from a finite area. If this area becomes of a size comparable to the dimensions of the surfaces, then the resolution of the measurements becomes unacceptable.

To eliminate these overlapping constraints on the experiment, the simple expedient was used of placing plane mirrors perpendicular to the cavity sides. Each elemental area on the interior of the cavity is then exposed to what appears to be an infinite extent of groove. The only error in this procedure is introduced by the non-zero absorptivity of the mirrors, and any misalignment that might occur. The cavity sides were 10 in. long, and are bounded by 10 × 10-in. flat mirrors.

The measurement of directional properties to be used in the analysis of the cavity is made directly on the experimental cavity surfaces. Two types of directional characteristics are used on Surface 2. The first is a diffuse highly reflective paint (see Appendix for details), and the second a highly directional surface made by attaching a black base to a hexagonal honeycomb structure coated with a diffuse highly reflective paint. The honeycomb is 0.25 in. flat-to-flat across the opening, and has a depth of 0.3 in. The bi-directional reflectivity in the plane of incidence for this surface is shown in Fig. 3 for three angles of incidence.

Bobco [9] has shown, with one exception, that for the coatings used in this study, the spectral effects of the surface properties can be ignored. The exception is the aluminized surface which was not considered in reference [7]. It is a fairly gray material over the region of response of the S-11 photomultiplier tube used in the detector, so that no spectral mismatch should be caused. More detailed consideration of the surfaces is given in the Appendix.

Results and Discussion

Fig. 4 shows the experimental data for the local incident radiative energy on the cavity surfaces observed for three combinations of cavity geometry and source orientation. The circles indicate data taken with the diffusely reflecting Surface 2, while the squares denote data for Surface 2 with the directional characteristics. The trends of the data can be explained by physical arguments based upon ray-tracing of the incident energy. The most obvious fact is that the experimental data shows deviations between the results for the diffuse and directional Surface 2 that are consequences of the directional characteristics of Surface 2. The differences in absorptivity in the two surfaces do not account for the observed changes in the experimental results. The data

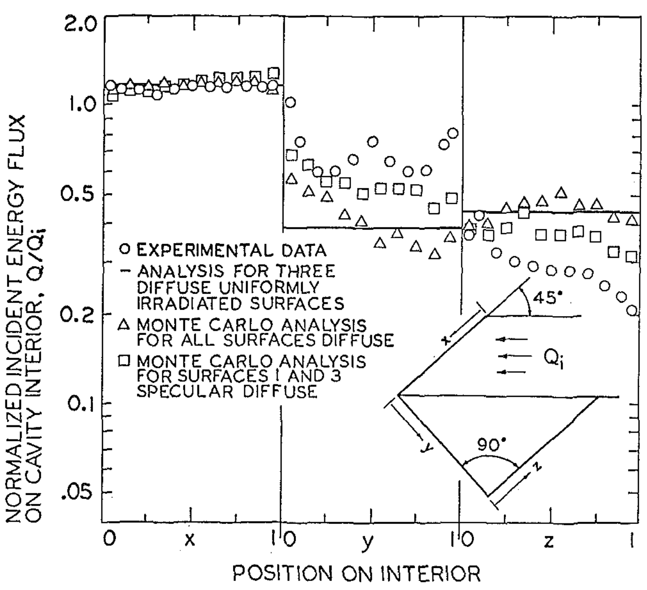

Fig. 5(a) Comparison of experiment and analysis for energy on cavity interior; $\beta_s = 45$ deg; $\varphi = 90$ deg; Surface 2 diffuse

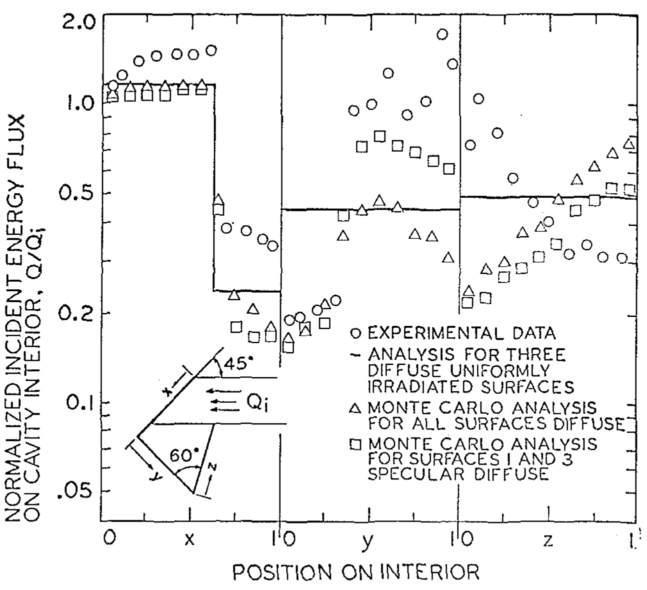

Fig. 5(c) Comparison of experiment and analysis for energy on cavity interior; $\beta_s = 45$ deg; $\varphi = 60$ deg; Surface 2 diffuse

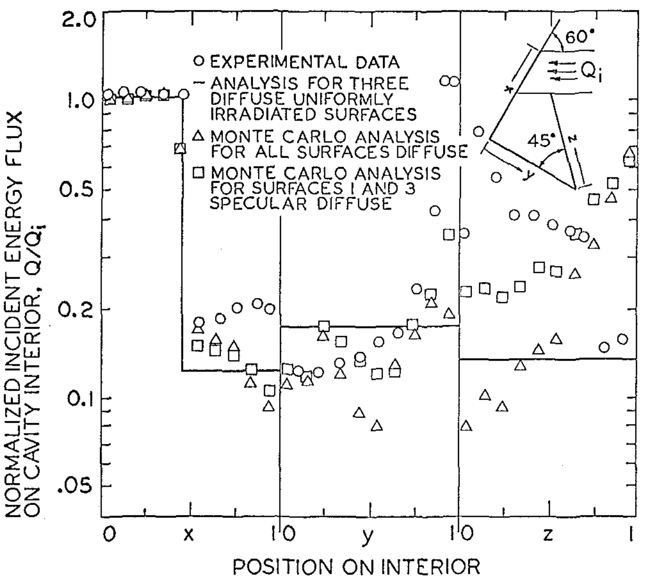

Fig. 5(b) Comparison of experiment and analysis for energy on cavity interior; $\beta_s = 60$ deg; $\varphi = 45$ deg; Surface 2 diffuse

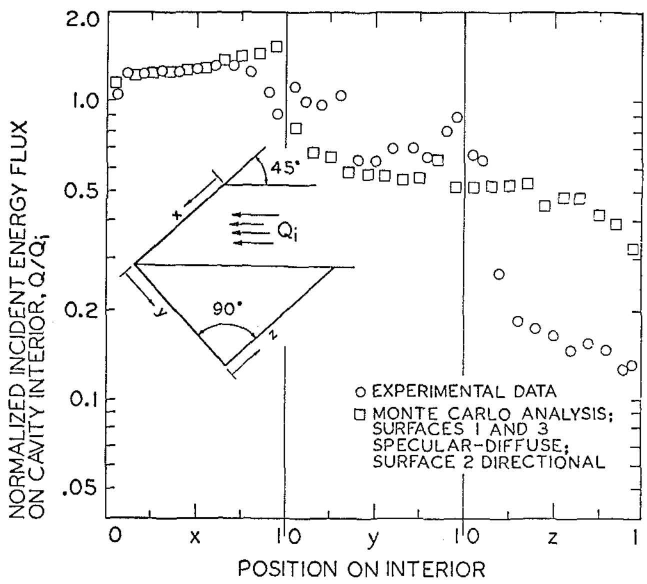

Fig. 5(d) Comparison of experiment and analysis for energy on cavity interior; $\beta_s = 45$ deg; $\varphi = 90$ deg; Surface 2 directional

shown in Fig. 4(*a*) for directional Surface 2 falls below a value of $Q/Q_i = 1$ near an x value of 1.0. This should not occur, because the Q is made up of Q_i plus energy reflected from other surfaces. The probable explanation is that the incident beam was nonuniform, leading to this observed deviation.

Figs. 5(*a*), 5(*b*), and 5(*c*) compare analytical results with the experimental data for Surface 2 diffuse. Various assumptions are used in the analyses to characterize the reflectivity of Surfaces 1 and 3. In general, the best comparison of analysis and experiment is found in all geometries if the specular-diffuse model is used for Surfaces 1 and 3. The experimentally determined values of the diffuse and specular components of reflectivity for Surfaces 1 and 3 were used in obtaining the analytical results. It appears by comparing the diffuse and diffuse-specular analytical results that better agreement with experiment could be found by allowing an even larger specular component on Surfaces 1 and 3. The measured value of specular reflectivity (0.22) may well be too small, because it was measured over a viewing angle of only 30 min at angles of incidence of 2, 5, and 9.5 deg. However, in thermal design only those values available to the analyst can be used: It didn't seem fair to make better agreement with experiment by putting new data into the analysis after the fact. The results do point up anew the necessity of obtaining reliable and accurate properties for use in any thermal analysis.

Figs. 5(*d*), 5(*e*), and 5(*f*) show a comparison of the experimental results for the directional honeycomb Surface 2 in the cavity and analytical results using measured bi-directional reflectivity data and directional absorptivity. Again, Surfaces 1 and 3 are taken to be specular-diffuse.

Fig. 5(*g*) shows a representative comparison of the diffuse, specular, and specular-diffuse assumptions on the analysis, and a comparison of these results with the experimental data. It appears that the pure specular and pure diffuse analyses bracket the data, and that choosing a certain ratio of specular-to-diffuse

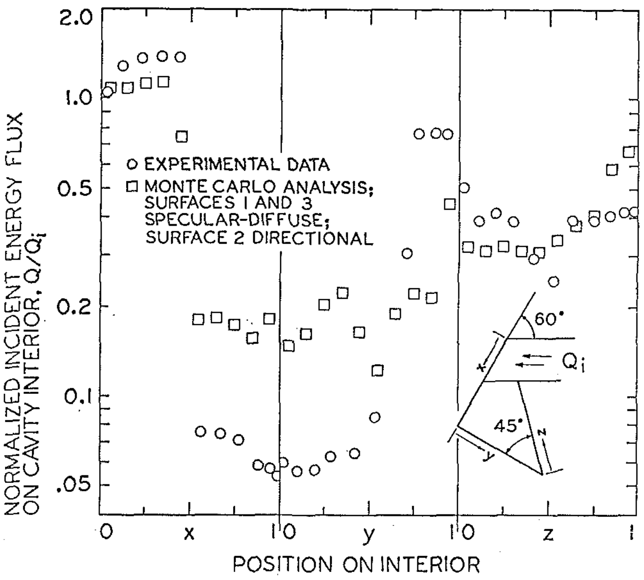

Fig. 5(e) Comparison of experiment and analysis for energy on cavity interior; $\beta_s = 60$ deg; $\varphi = 45$ deg; Surface 2 directional

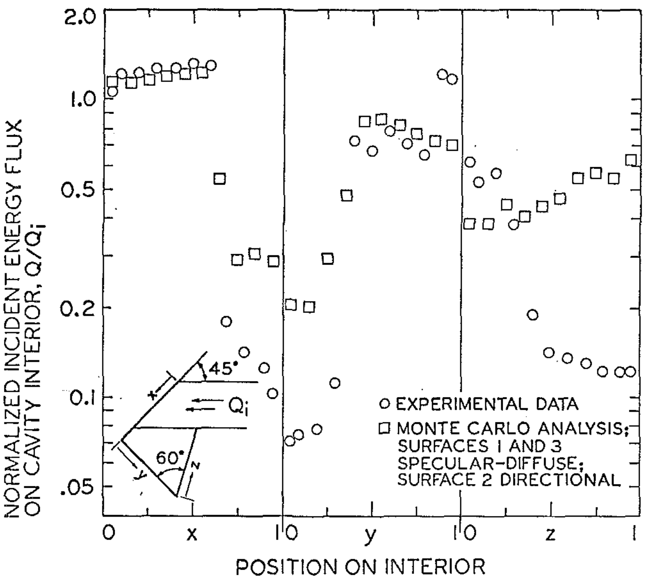

Fig. 5(f) Comparison of experiment and analysis for energy on cavity interior; $\beta_s = 45$ deg; $\varphi = 60$ deg; Surface 2 directional

components could give excellent agreement. The measured ratio, however, does not give as good agreement as the pure specular analysis.

Conclusions

It was found in the experiments reported here that: (*a*) The distribution of incident energy within a cavity exposed to a source of collimated incident energy can be strongly dependent upon the bi-directional reflectivities of the cavity surfaces, and (*b*) analyses that do not include directional effects in their formulation can lead to large errors in the predicted distribution of energy in such cases.

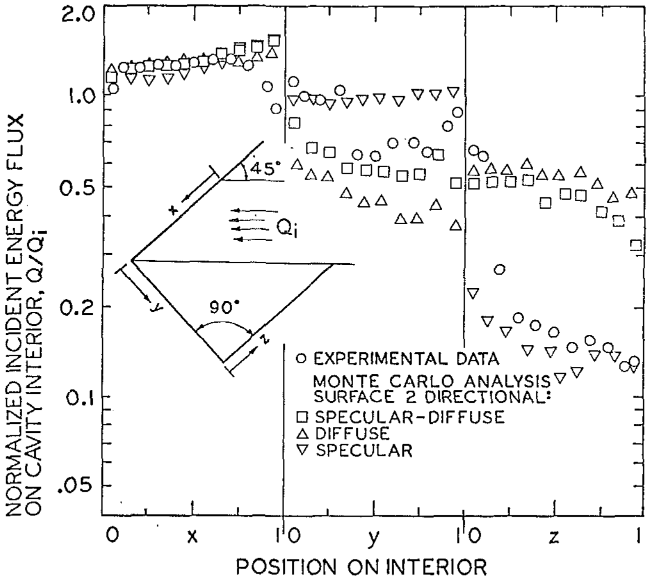

Fig. 5(g) Comparison of experiment and analysis for energy on cavity interior; $\beta_s = 45$ deg; $\varphi = 90$ deg; Surface 2 directional

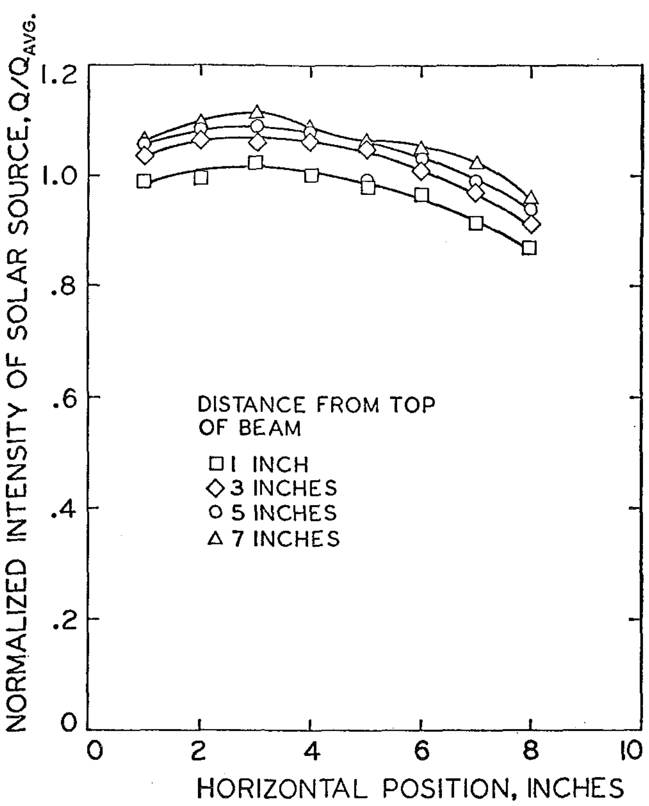

Fig. 6 Beam uniformity of 10 × 10-in. field

References

1 Howell, J. R., and Siegel, R., "Thermal Radiation Heat Transfer; II—Enclosure Theory," NASA SP-164, Vol. 2, 1969.

2 Schornhorst, J. R., and Viskanta, R., "An Experimental Examination of the Validity of the Commonly Used Methods of Radiant Heat Transfer Analysis," JOURNAL OF HEAT TRANSFER, TRANS. ASME, Series C, Vol. 90, No. 4, Nov. 1968, pp. 429–436.

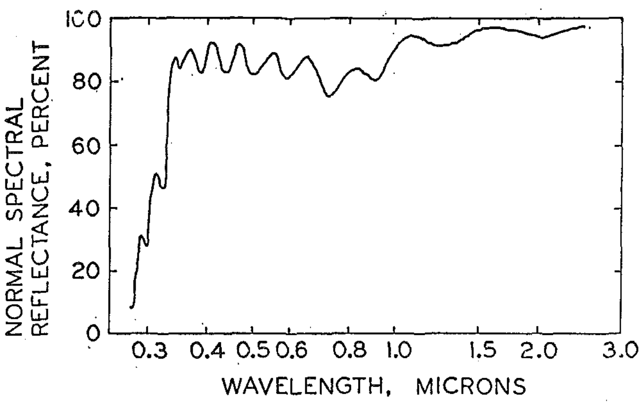

Fig. 7 Reflectance of Schjeldahl thermal control coating

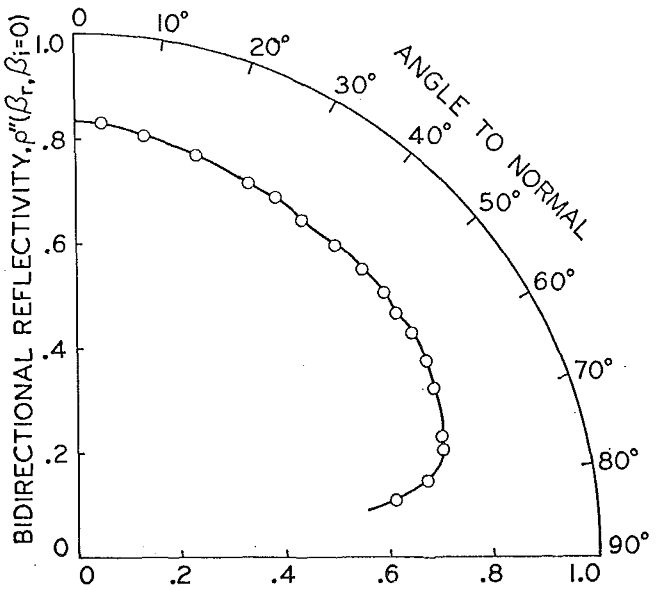

Fig. 8(a) Properties of white reflectors; bi-directional reflectivity of diffuse white buttons for normal incidence

3 Toor, J. S., Viskanta, R., and Winter, E. R. F., "Radiant Heat Transfer between Simply Arranged Surfaces with Direction Dependent Properties," AIAA paper 69-624, June 1969.

4 Schornhorst, J. R., and Viskanta, R., "Effect of Direction and Wavelength Dependent Surface Properties on Radiant Heat Transfer," *AIAA Journal*, Vol. 6, No. 8, 1968, p. 1458.

5 Neu, John T., and Dummer, R. S., "Theoretical and Practical Implication of the Bi-directional Reflectance of Spacecraft Surfaces," *AIAA Journal*, Vol. 7, No. 3, March 1969, pp. 484–491.

6 Siegel, R., and Howell, J. R., "Thermal Radiation Heat Transfer; I—The Blackbody, Electromagnetic Theory, and Material Properties," NASA SP-164, Vol. 1, 1968.

7 Sparrow, E. M., and Cess, R. P., *Radiation Heat Transfer*, Brooks/Cole, Belmont, Calif., 1966.

8 Howell, John R., "Application of Monte Carlo to Heat Transfer Problems," *Advances in Heat Transfer*, Vol. 5, T. F. Irvine, Jr., and J. P. Hartnett, eds., Academic Press, New York, 1968, pp. 1–54.

9 Bobco, R. P., "An Experimental Technique for Measuring Local Solar Irradiation with a Model Spacecraft," AIAA paper 68-770, June 1968.

APPENDIX

Details of Experiment

Radiation Source. The source of radiation in this study was an Aerospace Controls Corporation Type 302+ solar simulator. This device provides a 12 × 12-in. field of parallel radiation that is uniform, according to the manufacturer, to within ±3 percent across the field. Measured variations along the centerlines of the source are shown in Fig. 6. A flux of about 94 w/ft^2 exists within the illuminated area.

Photometer. The photometer is a Photo Research Corporation Pritchard photometer model 1970-PR. With the lens-aperture system used in these experiments, the photometer measured radiation from a field of about 0.07 × 0.07 in. when the photometer lens-to-object distance was 10 ft. The photomultiplier tube in this instrument has the S-11 type spectral response, with filters added to closely approximate the characteristics of the Standard Visual Response curve.

Surface Characteristics. Surfaces 1 and 3 in the cavity are covered with Schjeldahl tape, an aluminized polymer with a dielectric coating over the aluminized surface. This is a highly reflective coating (solar reflectivity 0.86) with a specular component of reflectivity measured over a 30-min viewing angle of 0.22. The spectral characteristics are shown in Fig. 7.

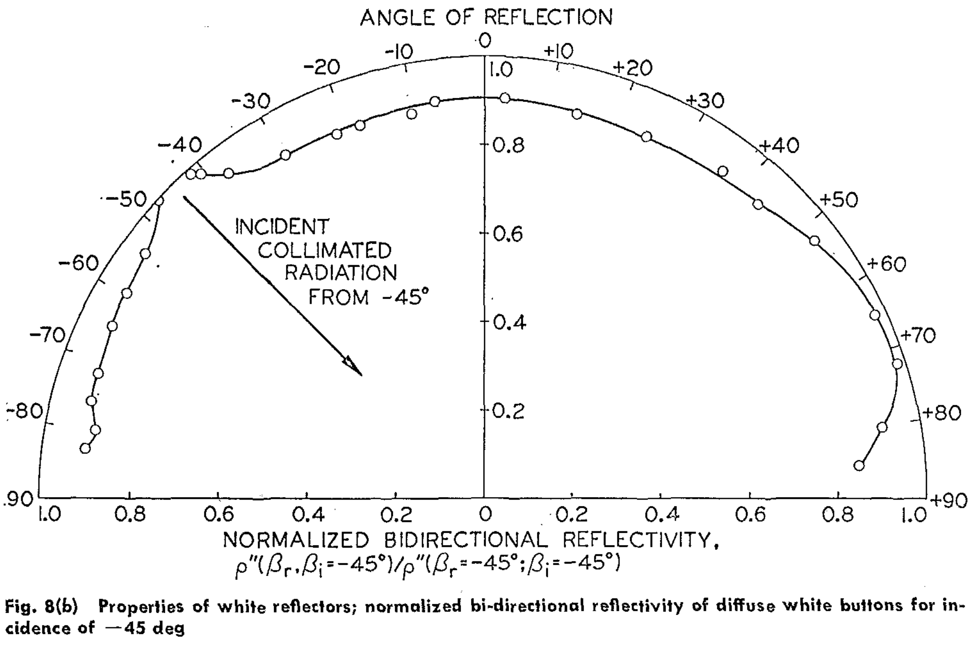

Fig. 8(b) Properties of white reflectors; normalized bi-directional reflectivity of diffuse white buttons for incidence of −45 deg

Surface 2 was first coated with 3M White Velvet paint. The spectral characteristics are given in reference [7]. After measurements were made with the flat white surface, a highly directional honeycomb surface was substituted for Surface 2. The honeycomb was painted with 3M White Velvet paint and then mounted on a black base coated with 3M Black Velvet paint. The directional characteristics of the honeycomb are shown in Fig. 3. The spectral characteristics of this composite surface were not measured, but probably vary with direction of incidence and reflection.

Diffuse Button. The button used for measurement of the incident radiation is nearly diffuse over an angular range of about ±70 deg measured from the normal to the button. The bi-directional reflectivity of the button is shown in Fig. 8 for 2 angles of incidence. The button is a magnetic disk coated with 3M White Velvet paint. The buttons are $\frac{1}{2}$ in. in diameter.

A. F. EMERY
Professor of Mechanical Engineering,
University of Washington, Seattle, Wash.;
Consultant,
Sandia Laboratories, Livermore, Calif.

W. W. CARSON
Research Mechanical Engineer,
Forest Engineering Research,
USDA Forest Service,
Seattle, Wash.

An Evaluation of the Use of the Finite-Element Method in the Computation of Temperature

A study is made of the accuracy and efficiency of the finite-element methods in comparison to the standard finite-difference algorithms used for the computation of temperature. Numerical tests of a linear, a quadratic, and two cubic elements indicate that the quadratic method is the most accurate and desirable of these finite-element models. It is demonstrated that for steady temperature distributions, with or without sources, the finite-element models are equivalent to the finite-difference method in execution time, inferior in core storage requirements, and may be superior in accuracy. The tests also indicate that the normal finite-difference method for variable-property steady-state problems and for constant-property transient problems may be as much as an order of magnitude faster in execution and may require an order of magnitude or more less machine core storage than the finite-element methods. The study suggests that the primary advantages of the finite-element methods are associated with the ease of inputting the required data and the capability of altering the basic accuracy of the method, and its major disadvantages are large core memory requirements and lengthy execution times, particularly for variable-property problems, and some possible inaccuracies associated with the source and transient coefficients.

Introduction

Recently the widespread use of the finite-element method (FEM) in the solution of material stress problems and the demonstration that the methods are applicable to any problem which can be formulated in a variational form has raised the possibility that the finite-element methods may be used for the computation of temperature. This interest is reinforced by the realization that many of the available finite-element stress programs may be directly converted to compute temperature and in a two-pass system can then be used to calculate thermal stresses without the necessity of using a special "thermal analyzer" for determining the required temperature distribution.

The primary characteristics of the usual finite-difference methods (FDM) and the finite-element methods (FEM) are listed in Table 1. From this table, four major differences are apparent: (*a*) the method of inputting the desired thermal conductances and capacitances; (*b*) the method of storing the matrix of coefficients; (*c*) the method of solution; and (*d*) variable accuracy.

In this paper we wish to examine the relative merits of the two methods in terms of items (*b*), (*c*), and (*d*) to determine the accuracy obtainable with the different finite-element models and their efficiencies, in terms of execution times and machine core storage, in comparison with the standard finite-difference algorithms (FDM). In this paper the basis of the finite-element method is discussed, several models are formulated, and their accuracy and efficiency numerically determined. It is also shown that although the finite-element method is not necessarily the best method to use, it can be used to create thermal analyzers which are significantly more useful than many present analyzers in terms of input efficiency and nodal-point placement.

The Finite-Element Formulation

Consider the two-dimensional transient heat-conduction equation

$$\rho c \frac{\partial T}{\partial t} = \frac{\partial}{\partial x}\left(k_x \frac{\partial T}{\partial x}\right) + \frac{\partial}{\partial y}\left(k_y \frac{\partial T}{\partial y}\right) + Q \qquad (1)$$

with the boundary conditions

Contributed by the Heat Transfer Division and presented at the Winter Annual Meeting, Los Angeles, Calif., November 16–20, 1969, of The American Society of Mechanical Engineers. Manuscript received by the Heat Transfer Division July 16, 1969; revised manuscript received August 25, 1970. Paper No. 69-WA/HT-38.

Table 1 General characteristics of the methods

	FDM	FEM
Conductances and capacitances	Usually input by hand unless special mesh generators and conductance-calculating routines are available	Internally computed
Boundary points	Usually treated as a standard internal point, but sometimes specially coded to maintain accuracy	Treated as a standard internal point
Matrix of conductances	Only non-zero elements are stored along with a matrix of node identification tags	Stored as a banded matrix in core or on disk
Method of solving steady-state problems	Either a direct Gauss elimination for small matrices or successive over-relaxation for large matrices	Direct Gauss elimination
Method of solving transient problems	Crank–Nicolson implicit method, solved by iteration	Crank–Nicolson implicit method
Method of solving variable-property problems	Successive over-relaxation for steady-state Crank–Nicolson method solved by iteration for transient	Direct Gauss elimination with iteration using different matrix coefficients
Accuracy of solution	Fixed at first order unless the entire problem is hand coded	Variable according to the element model chosen

$$\begin{aligned} T &= T_s \qquad \text{on} \qquad \Gamma_T \\ -k\frac{dT}{dn} &= q_n \qquad \text{on} \qquad \Gamma_q \\ h(T_\infty - T) &= k\frac{dT}{dn} \qquad \text{on} \qquad \Gamma_h \end{aligned} \tag{2}$$

Following Schechter [1][1] or Zienkiewicz [2], equations (1) and (2) may be cast in a variational form

$$\begin{aligned} I = \frac{1}{2}\int_A \left\{ k_x \left(\frac{\partial T}{\partial x}\right)^2 + k_y \left(\frac{\partial T}{\partial y}\right)^2 - 2QT + 2\rho c\,\frac{\partial T}{\partial t}\,T \right\} dA \\ + \int_{\Gamma_q} qTds + \int_{\Gamma_h} \left(\frac{1}{2}hT^2 - hT_\infty T\right) ds \end{aligned} \tag{3}$$

where the desired temperature distribution T is chosen to minimize the value of I for the region of interest. In performing the minimization the quantities dT/dt, q, T_∞ are to be considered as invariants. The solution to (3) can be easily shown to be an upper bound to the true temperature.

The integral which corresponds to I for the stress problem was originally derived by Turner et al. [3] on a physical basis, but it is now recognized that the variational derivation may be applied to any differential equation with its boundary conditions (2). It is this recognition which relieves us from a dependence upon a physical interpretation of the terms and permits the use of a number of models for the representation of T. The models are entirely mathematical and a large body of mathematical knowledge may be applied [4].

Consider the area A to be subdivided into a number of elements. Since the integral I can be represented as the sum of the integrals over the elements, we need only to examine a single element. Let the temperature in the element be given as a polynomial in x and y.

$$\begin{aligned} T = \alpha_1 + \alpha_2 x + \alpha_3 y + \alpha_4 x^2 + \alpha_5 xy + \alpha_6 y^2 + \alpha_7 x^3 \\ + \alpha_8 x^2 y + \alpha_9 xy^2 + \alpha_{10} y^3 \end{aligned} \tag{4a}$$

or more compactly as

$$T = \langle f\rangle \{\alpha\} \tag{4b}$$

where $\langle f\rangle$ is a row vector representing the spatial distribution and $\{\alpha\}$ is the column vector of coefficients.

If $\hat{T}$ denotes the values of the temperature at the selected nodal points which define the element, then by evaluating equation (4a) at these points we obtain the set of simultaneous equations for $\{\alpha\}$ of the form

$$\{\hat{T}\} = [A]\{\alpha\} \tag{5}$$

whose solution is

$$\{\alpha\} = [A]^{-1}\{\hat{T}\} \tag{6}$$

thus yielding the temperature profile

$$T = \langle f\rangle [A]^{-1}\{\hat{T}\} \tag{7a}$$

and

$$\frac{\partial T}{\partial t} = \langle f\rangle [A]^{-1}\left\{\frac{\partial \hat{T}}{\partial t}\right\} \tag{7b}$$

A similar consideration for the source strength Q in terms of the nodal-point values $\hat{Q}$ leads to

$$\hat{Q} = \langle fq\rangle [AQ]^{-1}\{\hat{Q}\} \tag{8}$$

where the source spatial distribution $\langle fq\rangle$ need not be identical to the temperature distribution $\langle f\rangle$. Substitution of the expressions for T and Q into I and performing the variation leads to the set of simultaneous equations

---

[1] Numbers in brackets designate References at end of paper.

Nomenclature

A = area of the body
B = matrix bandwidth
f, fq = polynomial distribution for temperature, for source strengths
h = surface film heat-transfer coefficient
H = surface convection matrix
I = number of elements in a row of packed matrix
k = thermal conductivity
n = number of unknowns per element or per body

Q = source strength
q_n = specified boundary heat flux
R = thermal boundary loads, equation (10)
S = thermal stiffness matrix
T, t = temperature, time
T_∞ = fluid temperature
x, y = rectangular cartesian coordinates
$\alpha, \alpha q$ = coefficients of f and fq
Γ, γ = bounding curve of body, of an element
σ = area of an element

ρc = heat capacity (density × specific heat capacity)
κ = thermal diffusivity
η, ξ = local rectangular cartesian coordinates for an element, Fig. 1
Δ = characteristic nodal spacing
$\langle\ \rangle$ = row vector
$\{\ \}$ = column vector
$[\ ]$ = matrix
$\hat{\ }$ = refers to nodal point values
$[\ ]^t$ = transpose

$$\int_\sigma [A^{-1}]^t \left\{k_x \left\langle \frac{\partial f}{\partial x}\right\rangle^t \left\langle \frac{\partial f}{\partial x}\right\rangle + k_y \left\langle \frac{\partial f}{\partial y}\right\rangle^t \left\langle \frac{\partial f}{\partial y}\right\rangle\right\}$$

$$\times\ [A^{-1}]\ \{\hat{T}\} d\sigma + \int_{\gamma_h} h[A^{-1}]^t \langle f\rangle^t \langle f\rangle [A^{-1}]\ \{\hat{T}\}\, d\gamma$$

$$= \int_\sigma [A^{-1}]^t \langle f\rangle^t \left\{\langle fq\rangle\ [AQ^{-1}]\ \{\hat{Q}\} - \rho c \langle f\rangle\ [A^{-1}]\right.$$

$$\left.\times \left\{\frac{\partial \hat{T}}{\partial t}\right\}\right\} d\sigma - \int_{\gamma_q} [A^{-1}]^t \langle f\rangle^t q_n\, d\gamma$$

$$+ \int_{\gamma_h} h[A^{-1}]^t \langle f\rangle^t T_\infty\, d\gamma \quad (9)$$

giving n equations for the n unknown nodal-point temperatures in the element. By taking these equations for each element and merging (i.e., combining) them for the assemblage of elements which constitutes the body, we obtain

$$[S]\ \{T\} + [H]\ \{T\} = [SQ]\ \{Q\} - [ST] \left\{\frac{\partial T}{\partial t}\right\} - \{R\} \quad (10)$$

It is important to note that since the merging can be accomplished simply and automatically within the program, the crucial step is the determination of the element influence matrices of equation (10). Inasmuch as these element matrices depend only upon the form of $\langle f\rangle$ and the spatial position of the nodes, the nucleus of the finite-element program is a subroutine which uses nodal-point positions, $\langle f\rangle$, and the physical properties k_x, k_y, and ρc. Once this subroutine is constructed, the user need only supply these values and the formulation becomes automatic. It is this feature upon which the usefulness of the finite-element method depends and which represents one of its major advantages over the finite-difference method.

Almost all thermal analyzers compute the temperature field by solving the finite-difference approximation to (1) of

$$\sum_{i=1}^{n} K_{ij}(T_i - T_j) + Q_j = (\rho c)_j \frac{\partial T_j}{\partial t} \quad (11a)$$

or

$$[K]\ \{T\} + \{Q\} = \rho c \left\{\frac{\partial T}{\partial t}\right\} \quad (11b)$$

which requires the conductance values K_{ij} and the thermal capacity $(\rho c)_j$ to be specified for each node. Most of the analyzers permit the above coefficients to vary with time and temperature, but because of the linear temperature distribution assumed in equation (11), the computations are accurate to $0(\Delta^2)$ only if all nodes are symmetrically located. If a nonuniform grid is used the accuracy of the computation is only $0(\Delta)$. Typical of these thermal analyzers are the Beta-2 analyzer of The Boeing Company, Chrysler's "Cinda," Honeywell's "Thermal Analyzer," and North American's "TAS." With the exception of some of the newer versions of these analyzers and the "HOT" analyzer of the University of Washington, few analyzers are constructed to compute K_{ij} and $(\rho c)_j$ from nodal-point data. There are some analyzers, typical of which is "HEATMESH" [5] of the Sandia Laboratory at Livermore, which will node the entire body based upon boundary information and the maximum Δx and Δy to be permitted. However, all of the presently used analyzers are linear temperature analyzers whose accuracy is significantly reduced for nonsymmetrical grids. It will be demonstrated later that these analyzers are equivalent to the linear finite-element method for steady, no-source problems, but are significantly different for transient problems or problems involving sources.

For the most accurate way of solving the transient thermal problems we follow Wilson and Clough [6] and use the Crank–Nicolson formulation, letting $\partial T/\partial t$ vary linearly with time over the interval of time Δt such that

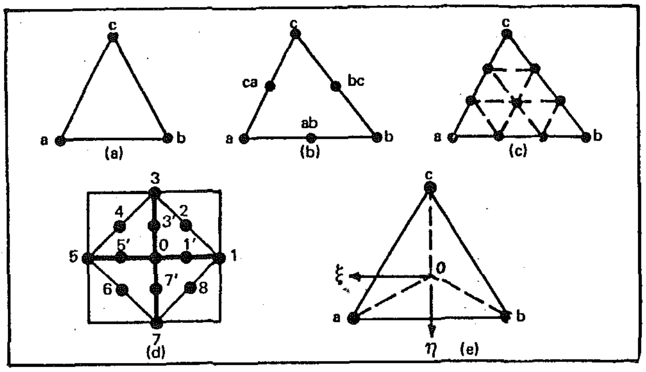

Fig. 1 Schematic of triangles

$$T(t + \Delta t) - T(t) = \frac{\Delta t}{2} \left\{\frac{\partial T(t + \Delta t)}{\partial t} + \frac{\partial T(t)}{\partial t}\right\} \quad (12)$$

The substitution of (12) into (10) yields the set of simultaneous equations

$$\left[S + \frac{2}{\Delta t} ST + H\right] \{T(t + \Delta t)\}$$

$$= [SQ]\ \{Q\} + \frac{2}{\Delta t} [ST]\ \{T(t)\} + [ST] \left\{\frac{\partial T}{\partial t}(t)\right\} - \{R\} \quad (13a)$$

with

$$\frac{\partial T}{\partial t}(t + \Delta t) = \frac{2}{\Delta t} \{T(t + \Delta t) - T(t)\} - \frac{\partial T}{\partial t}(t) \quad (13b)$$

for the temperature at time $t + \Delta t$.

Equations (13a) and (13b) applied consecutively constitute the necessary algorithm for the computation of the transient thermal field. It is important to note that because the procedure of the FEM is the simultaneous solution of all the n equations, one must store three $n \times n$ matrices. Furthermore each stage of the computation requires three $n \times n$ matrix multiplications (two if $Q = 0$) which for large n may be prohibitively expensive. (See the section on late time for further discussion of this point.)

The next requirement is to choose the shape of the element and the form of the approximating function f. Although a multiplicity of shapes is available, one of the most convenient is the triangle, which can be combined to yield squares, rectangles, etc., and which is best capable of representing arbitrary boundary shapes. In the following discussion only the triangular element will be used. The choice of the approximating function $\langle f\rangle$ is far more difficult because of the abundance of closed-form mathematical functions available. In general the function should be simple, should yield a well-conditioned matrix, and should be compatible. By compatible we mean that if the temperature and desired derivative in one element are specified, they must be so specified that an adjoining element with a common set of nodal points will yield the same values on the common side. (This point will be touched upon again in discussing the special cubic method.) Probably the most popular distributions are polynomials in x and y. Such polynomials may give rise to coefficient matrices $[A]$ (which in one dimension are principal minors of the infinite Hilbert matrix) which are difficult to accurately invert because of their ill-conditioning [7]. However, since the order is rarely greater than the third, the inversion is usually straightforward and furthermore the integration of $\langle f\rangle^t \langle f\rangle$ is simple to carry out. Accordingly we will discuss only the polynomial form of $\langle f\rangle$. (An excellent survey of polynomial distributions and triangular and quadrilateral elements is given by Felippa [8].)

The Linear Element. By taking the vertices of the triangle to be the nodal points, Fig. 1, and the temperature to be linear, we have

$$\langle f \rangle = \langle fq \rangle = \langle 1, x, y \rangle \tag{14}$$

Such a distribution is evidently compatible and represents the basis for nearly all thermal-inviscid-fluid and stress-finite-element programs. (See Zienkiewicz [2] for an excellent summary of the method.) The basic drawback to this distribution is that the heat flux, which is constant within each element, varies discontinuously from element to element and thus the heat flux is not compatible. Furthermore it is difficult to determine at which value of x and y the flux is to be ascribed. In fact a large body of literature exists as to the proper location of the gradient (or equivalently, the stresses), which is amply discussed by Zienkiewicz.

Since the assumption of a linear distribution is equivalent to the finite-difference method, a distribution of nodal points and triangles, such that a group of four yields the same grid pattern as the regular finite-difference method grid, Fig. 1(d), will be exactly equivalent to the finite-difference method. However, the source coefficients $[SQ]$ and the transient coefficients $[ST]$ are not equivalent. For a right triangle with sides a, a, and $a\sqrt{2}$ the element source term for node 0 is

$$\frac{a^2}{2}\left[\frac{1}{6}\,Q_0 + \frac{1}{12}\,Q_1 + \frac{1}{12}\,Q_3\right] \tag{15a}$$

and the combination of the four triangles, Fig. 1(d), will yield for node 0 the source contribution

$$\frac{a^2}{2}\left\{\frac{4}{6}\,Q_0 + \frac{1}{6}\,[Q_1 + Q_2 + Q_3 + Q_4]\right\} \tag{15b}$$

If all the source strengths are equal, node 0 only has a contribution of $^2/_3a^2Q$, with the remaining $^1/_3a^2Q$ being assigned to the other four nodes. Thus whereas the finite-difference method has a source contribution to node 0 of a^2Q_0, the finite-element method reduces the contribution of node 0 and includes a contribution from the surrounding nodes. (Note that it is often recommended [2] to assign to each node of a triangle a contribution of $\frac{a^2}{2}$ $(Q_0 + Q_1 + Q_2)/3$ although this is not consistent with the assumption that Q is linear.)

This incorporation of the source strengths at the neighboring nodes tends to pass information to node 0 about the spatial variation of Q and materially improves the calculated results. Since the $[SQ]$ and $[ST]$ matrices are alike (except for a multiplicative constant), the transient solution includes the effects of $\partial T/\partial t$ at the neighboring nodes. Consequently if $\partial T_0/\partial t$ is desired, a simultaneous solution of all $\partial T/\partial t$ in the body is needed with the attendant increase in storage and computation times.

One should note that if we follow Dusinberre [9] and subdivide the element area by perpendicular bisectors to the sides, we find that each node has a source contribution which varies with the shape of the element. However, each node still is affected by only its own source strength.

The Quadratic Element. By establishing nodal points at the midpoints of the side, Fig. 1(b), there will be six nodes per triangle, permitting the formulation

$$\langle f \rangle = \langle fq \rangle = \langle 1, x, y, x^2, xy, y^2 \rangle \tag{16}$$

Again since the temperature is quadratic and is uniquely determined on each side by the three nodal points on the side, adjoining triangles are compatible.

Furthermore since the temperature is quadratic in x and y, the heat flux will be linear and thus a value of the gradient may be associated with each nodal point. However the heat flux is not compatible and although the heat flux may be evaluated at each node, its value differs for each element and it is necessary to average all of the neighboring element values to determine a value at the node. Even if the nodal spacing is equal for the linear (3-point) and quadratic (6-point) elements, the size of the stiffness matrix is larger for the quadratic element because of the increased circle of influence. In essence the 6-point triangle may be regarded as being composed of four 3-point triangles and the 6-point bandwidth becomes accordingly larger. Thus the core storage requirement and the matrix-inversion computation times will be larger. Since these items are the principal drawbacks to the use of the finite-element method, it is essential that the accuracy inherent in the higher-order method be sufficiently greater in order to reduce the overall number of nodal points required and thus to reduce the core storage requirements and the execution time.

As will now be demonstrated, the apparent accuracy of the quadratic element is misleading. Consider the nest of triangles shown in Fig. 1(d). The nodal temperature T_0 is influenced by T_7, $T_{7'}$, $T_{3'}$, and T_3 in the y direction and thus the value of $\partial^2T_0/\partial y^2$ is accurate to $0(\Delta^4)$, which corresponds to the large-molecule finite-different elements of Bickley [10]. However, the temperature $T_{3'}$ is influenced in the y direction by only T_0 and T_3 and thus $\partial^2T_{3'}/\partial y^2$ is accurate only to $0(\Delta^2)$. Thus the corner temperatures of the quadratic element are significantly more accurate than the mid-side points. Consequently the overall accuracy is indeterminant and as will be demonstrated is more strongly dependent upon the respective values of Δx and Δy than one would desire.

The Cubic Distribution. The natural extension of the quadratic element is the cubic, and in fact one could continue to extend the method to higher-order distributions. However, the increased complexity of the formulations and the implementing difficulties presented by the cubic indicate that it is doubtful if higher-order distributions are efficient. For the cubic we let the distribution be

$$\langle f \rangle = \langle fq \rangle = \langle 1, x, y, x^2, xy, y^2, x^3, x^2y, xy^2, y^3 \rangle \tag{17}$$

To determine the 10 coefficients we may simply adjoin three 6-point triangles, thus yielding a maximum accuracy of $0(\Delta x^6)$ and temperature gradients which vary quadratically. The alternative is to place two equidistant nodal points on each side of the element triangle and then to place one node within the triangle (usually at the centroid). This formulation may be regarded as either the adjoining of three 6-point triangles or combining nine 3-point triangles. In either case the number of non-zero elements in the stiffness matrix increases proportionately.

As for the quadratic element, the temperature but not the heat flux is compatible and similar problems exist with the determination of the overall accuracy of the element. In fact, because the side points see an unequal number of nodal points to either side and are thus accurate only to $0(\Delta)$, we may anticipate that the overall accuracy may not be much greater than that of the linear element. For such a case, then, it is apparent that the quadratic element will be the most accurate polynomial element available.

The Special Cubic Element. Since increasing the order of the polynomial distribution cannot insure compatibility of the heat flux, it is worthwhile to consider the special element suggested by Tocher and Hartz [11] for the computation of torsional stress fields. This element is formulated by considering the triangular element subdivided into three sub-triangles, Fig. 1(c), and identifying the variables T, $\partial T/\partial x$, $\partial T/\partial y$ with each vertex of the main triangle. In doing so, we have 9 variables per element and consequently one term of (17) must be deleted. Suppose that equation (17) is applied to each sub-triangle with x and y replaced by the local variables ξ and η, Fig. 1(e). By deleting the term $\xi^2\eta$, the normal heat flux $\partial T/\partial\eta$ is at most linear on the exterior side $\overline{ab}$ and is thus determined uniquely by the values of $\partial T/\partial\eta$ at points a and b and is not a function of the values at point c. In this way the normal heat flux is compatible between triangles. Thus the special cubic is compatible in T, $\partial T/\partial x$, and $\partial T/\partial y$. Since there are 27 coefficients to evaluate (9 for each sub-triangle), we use the 15 conditions of matching T, $\partial T/\partial x$, and $\partial T/\partial y$ at each vertex (a, b, and c) and at the central point 0 in adjoining sub-triangles and the 9 conditions that the values of T, $\partial T/\partial x$, and $\partial T/\partial y$ at a, b, and c equal $\hat{T}$, $\partial \hat{T}/\partial x$, and $\partial \hat{T}/\partial y$. The remaining three conditions are found by requiring that the temperatures match at the midpoints of $\overline{a0}$, $\overline{b0}$, and $\overline{c0}$. The last three conditions insure that the sub-triangles are compatible in temperature, but not in the normal heat flux. This internal incompatibility is the price paid for large-triangle normal-heat-flux compatibility which is expected to yield an unusual degree of accuracy when computing systems with internal sources or transient systems, even though Felippa [8] has suggested that the element may be too stiff. Furthermore we now have at hand the temperature gradients as primitive variables. Since most heat-transfer problems incorporate boundary heat flux conditions, it is anticipated that with the gradients as variables such problems will be more accurately computed. On the other hand the evaluation of the coefficients requires the inversion of a 27 × 27 matrix and since the element stiffness matrix requires two 27 × 27 matrix multiplications, see equation (9), each element requires significant computation time. Furthermore, because of the presence of $\partial T/\partial x$ and $\partial T/\partial y$, a rotation of an element creates a new element, compounding the formulation time and storage requirements. This makes the special cubic distribution economical only if less than $1/3$ the number of linear nodes can give accuracy equivalent to the quadratic case.

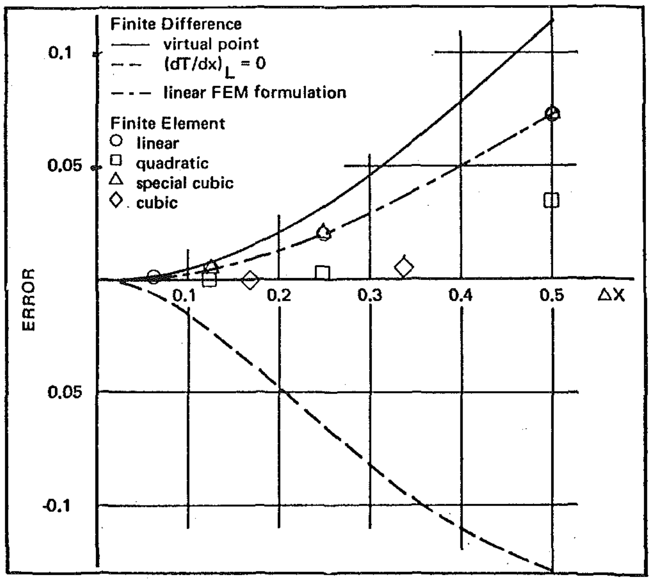

Fig. 2 Temperature error for source strength = X^5; $T_{\text{exact}} = 0.1429$

Evaluation of the Finite-Element Methods

To assess the value of the finite-element methods, three problems were treated. Two one-dimensional problems, one treating the source

$$T(0) = 0 \qquad \frac{dT(L)}{dx} = 0 \qquad Q = x^m \quad (m = 0, 1, \ldots, 5)$$

and a second treating the transient

$$T(x, 0) = 0 \qquad T(0, t) = 1 \qquad \frac{dT(L, t)}{dx} = 0$$

were computed especially to aid in the evaluation of the two cubic elements. Although the special cubic requires only three nodal points per triangle and is thus easiest to node, the difficulty of implementing suggested that it be applied to two-dimensional problems only if a successful one-dimensional evaluation could not be determined. Analogously, the cubic element with 10 nodes per triangle is excessively difficult to node in two dimensions and warrants an initial one-dimensional evaluation. Finally, a two-dimensional problem with a singularity in the heat flux was used to evaluate the linear, quadratic, and special cubic approaches.

The Source Problem. The source distribution problem was computed using all the element models and the standard finite-difference algorithm using equal nodal spacings and a nonuniform nodal mesh in which odd-numbered segments were Δx long and even-numbered segments were $2\Delta x$ long. The standard finite-difference algorithm

$$\frac{k[T(x + \Delta x) - T(x)]}{\Delta x} - \frac{k[T(x) - T(x - \Delta x)]}{\Delta x} + Q(x)\Delta x = 0 \tag{18}$$

(or a modification thereof for the unequal nodal spacing) was used.

The zero-heat-flux condition can be handled in a variety of ways when using the finite-difference method, but for simplicity we considered only two approaches. The first consisted of using the one-sided second-order-accurate expression (or its equivalent for the unequal spacing cases)

$$\frac{\partial T}{\partial x} = \frac{4T(L - \Delta x) - T(L - 2\Delta x) - 3T(L)}{2\Delta x} = 0 \tag{19}$$

to compute the value of $T(L)$. Because this method does not include a source contribution to the value of $T(L)$, this temperature was always less than the correct value. The second approach was to establish an image point at $L + \Delta x$ whose value was set equal to the value at $L - \Delta x$. In this approach, a source contribution to $T(L)$ exists. For this approach, the computed temperatures were always greater than the exact values. In formulating the finite-element methods the only difference noted between these methods and the finite-difference methods was the observation that the source contribution to any node was not restricted to values of Q at the specific node but also included contribution from the nodes on either side. These additional contributions in effect give each node some information about the spatial variation of Q, and therefore the finite-element method can be expected to yield better results. Because the source strengths were taken to be linear, quadratic, and cubic for the respective finite-element models, these distributions were treated exactly. The greatest errors were found for $m = 5$ and these errors, as shown in Fig. 2, were used as a measure of the accuracy of the methods.

The finite-difference method was found to treat only the constant source strength correctly ($m = 0$) and produced the greatest errors regardless of the formulation used to treat $dT(L)/dx = 0$. Of the finite-element models the quadratic and cubic elements were found to be of equal accuracy and to give results for $\Delta x/L = 0.33$ equal in accuracy to the linear finite-element method and the finite-difference methods for $\Delta x/L \sim 0.10$. Although the special cubic element can treat only the linear source exactly, surprisingly it gave no better results than the linear finite-element method, suggesting that the performance of a finite-element method is more dependent upon the number of nodal points contained within the element than upon the number of variables.

The accuracy of the finite-difference method can be significantly improved by using the finite-element-method formulation to determine the source contribution to the finite-difference-method algorithm and then programming as usual. In this way the accuracies are equal to those of the finite-element method. One point of particular importance is the treatment of nonuniform grid spacing. When a nonuniform spacing was used all the finite-element-method elements were exact to one order less in n

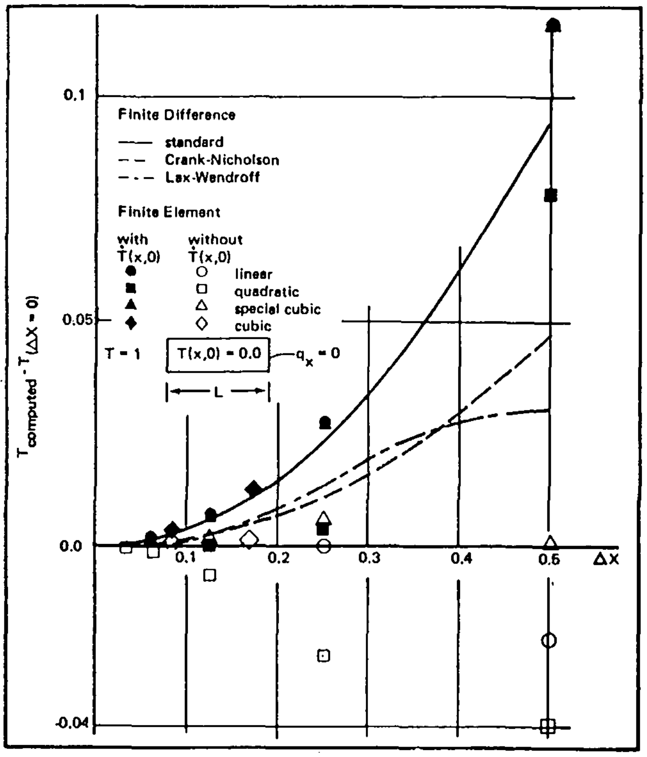

Fig. 3(a) Transient problem—$\tau = 0.0625$; $x/L = 0.5$; $T_{exact} = 0.1573$

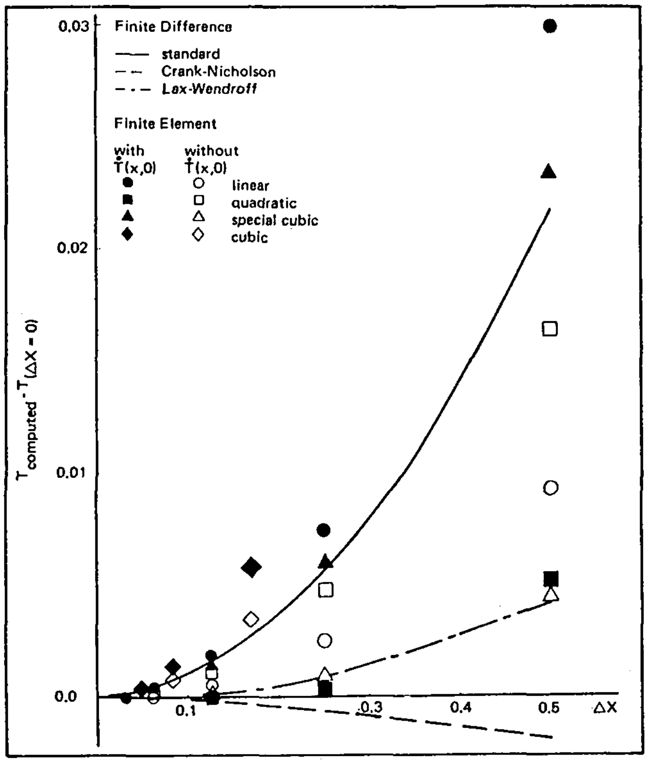

Fig. 3(b) Transient problem—$\tau = 0.500$; $x/L = 0.5$; $T_{exact} = 0.7378$

(i.e., linear $n = 0$, quadratic $n = 1$, cubic $n = 2$). Since it is unlikely that a typical problem will utilize symmetrical nodal patterns, it is apparent that the quadratic element is the minimum element which should be used if the source strength is to be permitted to vary spatially.

The Transient Problem. With the exception of thermal fields in which the heat flux is singular (i.e., unbounded) at points, probably no situation taxes the ability of a "thermal analyzer" as much as a transient problem with an impulsively changed boundary condition. Accordingly the transient problem of a one-dimensional bar with zero initial temperature and one face insulated and the other subjected to a temperature of unity at time zero was utilized. Prior to these tests, it was decided that inaccurate methods or those which were inconsistent in their behavior with increasing numbers of nodal points would not be used in creating two-dimensional algorithms. Figs. 3(a) and 3(b) show the errors in the temperatures computed at $x/L = 0.5$ for early and late times ($\kappa t/L^2 = 0.0625$ and 0.5).

Three finite-difference methods were used. The first was the standard explicit formula

$$T(x, t + \Delta t) = T(x, t) + \Delta t \frac{\partial T(x, t)}{\partial t} \tag{20}$$

with a maximum allowable time step of $\Delta t \leq \frac{\Delta x^2}{\kappa}$ and accurate to $0(\Delta t)$ and $0(\Delta x^2)$. The second method was the implicit method based upon the Crank–Nicolson formulation

$$T(x, t + \Delta t) = T(x, t) + \frac{\Delta t}{2}\left(\frac{\partial T(x, t + \Delta t)}{\partial t} + \frac{\partial T(x, t)}{\partial t}\right) \tag{21}$$

for which the maximum time step is unlimited [12] and has an accuracy of $0(\Delta t)$ and $0(\Delta x^2)$ and which requires an iterative solution for each time step. (All iterations were performed to an accuracy of 10^{-6}.) The third method was based upon the Lax–Wendroff approach [12]. Define

$$L(T) \equiv \frac{\partial^2 T}{\partial x^2} \tag{22a}$$

then let

$$T\left(x, t + \frac{\Delta t}{2}\right) = T(x, t) + \Delta t L[T(x, t)]$$

$$T(x, t + \Delta t) = T(x, t) + \frac{\Delta t}{2} L\left[T\left(x, t + \frac{\Delta t}{2}\right)\right] \tag{22b}$$

This two-step explicit method is accurate to $0(\Delta t^2)$ and $0(\Delta x^2)$ and admits of a maximum time step of $\Delta t \leq \Delta x^2/2\kappa$. Even though the C–N algorithm can use a large time step, all of the finite-difference methods and the finite-element-method computations (which are based on the C–N method) were made with a time step of $\Delta t = \Delta x^2/4\kappa$ to give a meaningful comparison of error and execution times. The finite-element methods may be computed either by assuming that $\partial T(x, 0)/\partial x$ is zero or by solving equation (10) for the initial values. In general it is best to assume that they are zero unless the element possesses considerable accuracy. The reason for this is that the finite-element method attempts to minimize an integral in which $\partial T/\partial t$ appears linearly. If $\partial T/\partial t$ at a given node is a large positive value, a neighboring point will have a large negative value. Consequently the initial $\partial T(x, 0)/\partial t$ profile will be distorted and unless the finite-element method has a high accuracy, the initial distorted time-derivative profile will affect the temperature profile for a long time. This is particularly true of the special cubic method which will have a poor profile not only of $\partial T/\partial t$ but also of $\partial T_x/\partial t$ and $\partial T_y/\partial t$.

Early Time. At the early time, which is presumed to represent the most critical performance of the methods, the C–N and the Lax–Wendroff methods are equivalent to and substantially

Table 2 Execution time (central processor) for the transient problem to achieve a value of $\kappa t/L^2 = 1.0$[a]

n	L–W	FDM explicit	FDM C–N	Linear	FEM quadratic	Cubic	Special cubic
3	0.100 sec		0.133	0.021 (0.133)	0.121 (0.237)		
5	0.180	0.206	0.261	0.146 (0.723)	0.292 (0.869)		0.584
7						0.729	
9	0.488	0.471	0.794	0.865 (4.19)	1.167 (4.751)		3.21
13						4.756	
17	2.284	1.632	3.230	6.545 (29.05)	8.492 (33.09)		24.30
19						16.630	
31						71.927	
33	14.25	8.56	15.613	47.718 (216.0)	66.359 (250.5)		199.08
61						579.106	
65	101.44	54.128	163.744	365.912 (1626.0)	534.894 (1959.0)		

[a] The numbers are times for constant-property problems with only one matrix inversion. The numbers in parentheses are execution times when the matrix is inverted at every time step.

better than the explicit finite-difference method. The linear and cubic finite-element methods are seen to perform excellently when no initial $\partial T/\partial t$ profile is used. However when the initial profile was used, all of these element methods were no better than the explicit finite difference method. The quadratic element gave poor values without $\partial T(x, 0)/\partial t$ but was the best when an initial time-derivative profile was utilized. Apparently the quadratic element possesses sufficient accuracy to override the perturbing influence of $\partial T(x, 0)/\partial t$. Probably the most encouraging feature of Fig. 3(*a*) is the excellent behavior of the special cubic element. It should be noted that both the C–N FDM and the linear FEM involve the simultaneous solution of the temperature field. However the FEM differs from the FDM in that the heat-storage term $\rho c(\partial T/\partial t)$ for each node is composed of the value of $\partial T/\partial t$ at the node under question and the values at the neighboring nodal points (see the source problem discussion, remembering that $[SQ] \equiv \rho c[ST]$). This effect accounts for the better results of the FEM.

Late Time. At the later time, the behavior is similar to the early-time values except that the C–N FDM underestimates the temperature, Fig. 3(*b*), and consequently this method does not yield an upper bound to the temperature. For both early and late time the cubic element is seen to be questionable in its results. Although no exact understanding of this method's behavior is presently known, it is felt that the inherently poor internal accuracy discussed in the formulation is the cause. Examination of both the early- and late-time results indicates that the cubic element is in fact no more accurate than the linear element for this transient problem, and based upon this finding this element was discarded. The execution times on a CDC 6400 are shown in Table 2.

In comparing the performance of the different methods several points should be noted: (*a*) the C–N FDM and the FEM's are implicit and may use larger time steps, thus reducing their execution times in comparison with the L–W and explicit methods; (*b*) the C–N FDM requires the storage of the 5 vectors, each N in length, $T(t)$, $\partial T(t)/\partial t$, $T(t + \Delta t)$, $\partial T(t + \Delta t)/\partial t$, and ρc, and a matrix of N rows each of which contains one term for each node which interconnects to any given node; (*c*) the solution of $T(t + \Delta t)$ requires $N(I + 1)$ multiplications and divisions per iteration (where I is the number of interconnected nodes) and while initially the method required 7–10 iterations per time step, after $\kappa t/L^2 > 0.05$ most time steps required only 1–2 iterations; (*d*) the FEM requires the storage of the 4 vectors, each N long, $T(t)$, $T(t + \Delta t)$, $\partial T(t)/\partial t$, and for the right-hand side of equation (13*a*), and 2 banded matrices of length N and width B where B is the maximum nodal-point number separation in any element; (*e*) each time step of the FEM required NB multiplications to establish the right-hand side, and NB to condition it, and NB to reduce it;[2] (*f*) for variable properties, the conductances and capacitances must be reevaluated, the FEM matrix reformed and reduced each time step. If we assume that the time to reevaluate the matrix and to reform it is equal for both the C–N FDM and the linear FEM, then the only difference will be the time necessary to reduce the matrix. The times listed in parentheses are for reducing the matrix and solving for $T(t + \Delta t)$ at each time step. It should be noted that in this one-dimensional problem the banded matrix contained no zeros and consequently the times listed for the FEM are the absolute minimum for the number of nodes noted, and for two-dimensional problems these times will be significantly increased while the C–N FDM times would be unchanged since zeros are not stored. (See the singular problem for further discussion of this point.)

From Table 2 it is readily apparent that the FEM's, particularly the quadratic, are of marginal value when compared to the C–N FDM for constant-property problems and decidedly inferior in terms of execution time and core memory requirements for variable-property transient problems.

Whereas the finite-difference method could be reformulated using the desired FEM source coefficients to give FEM accuracy at FDM execution times, this is not possible with the transient problem. The presence of $\partial T/\partial t$ contributions from the neighboring nodal points in the FEM requires a simultaneous solution for $\partial T(x, t)/\partial t$ for use in computing $T(t + \Delta t)$. Thus the FDM cannot be converted into a pseudo-FEM with reduced core storage and execution time. Fortunately both the C–N FDM and the L–W methods are rapid and very accurate.

The user should also be aware that the FEM's may not accurately treat either transient or source problems because of some inherent peculiarities. Consider the situation where either $\partial T/\partial t$ or Q is constant over an element of area A. The linear FEM will then assign $QA/3$ to each node of the triangle. Consequently if a node is common to n triangles, the source contribution to it will be $nQA/3$, while a node which is included in only one triangle will receive only $QA/3$. Thus if the geometric pattern of triangular elements is not symmetrical, the temperature distributions will not be symmetrical as expected and small errors will exist. For transient problems these errors will decay in time to minor values, but the user is forewarned to expect them. Similarly, for equal $\partial T/\partial t$ or Q, the quadratic-element model predicts no contribution to the vertex nodes and $QA/3$ to each of the side-point nodes. Unfortunately there is no way to order the ST or SQ matrix to eliminate these discrepancies other than a priori prescribing the matrix element values. Accordingly the attractiveness of the FEM as an internally consistent and wholly self-contained method is diminished.

The Singular Problem. As the final test of the methods, the two-dimensional problem schematically shown in Fig. 4(*a*) was used. Because of the insulated divider at $y/H = 0$, $0 < x/L < {}^1/_2$, the temperature gradient $\partial T/\partial y$ is infinite as $1/\sqrt{x}$ at $x/L = {}^1/_2$. This problem provides as severe a test of the methods as is practically attainable. Since no analytical solution is available we will use the methods of Motz [13] and Woods [14] to determine

---

[2] The reduction was done using the symmetric banded matrix solver of Wilson [15] in which the matrix is reduced to an upper triangular matrix.

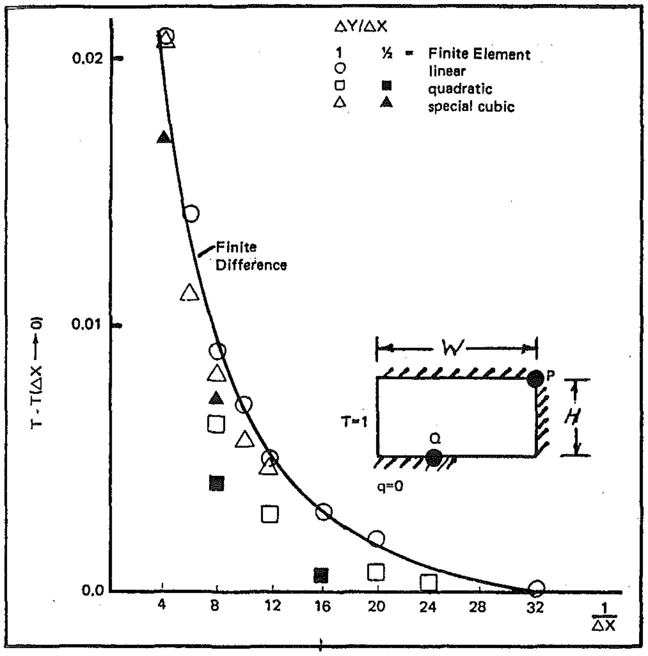

Fig. 4(a) Singular problem—T at point P; $T = 0.180$

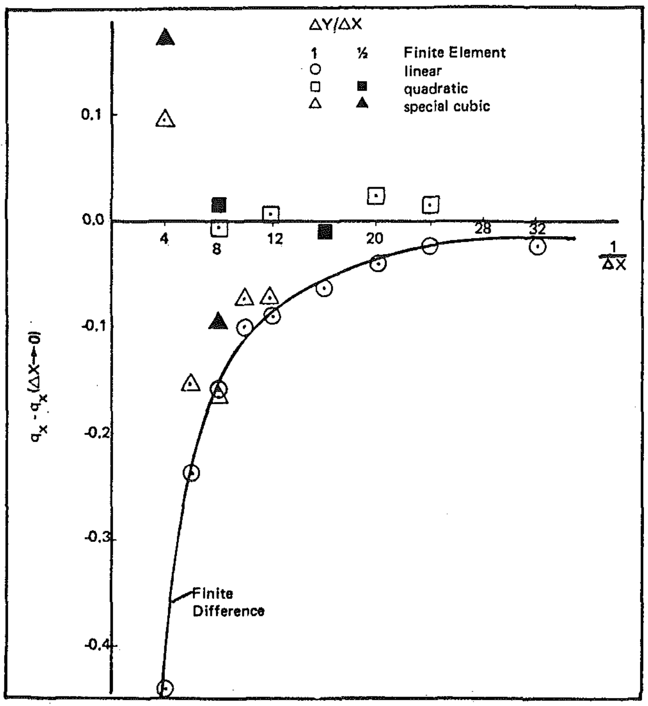

Fig. 4(b) Singular problem—q_x at point Q; $q_x = -1.560$

the solution. The numerical solutions indicated that the accuracies of the various methods were well typified by the temperature calculated at the point P, and the value of $\partial T/\partial x$ at the point Q. Figs. 4(a) and 4(b) present the results obtained with the different methods for equal numbers of nodal points. Inasmuch as a nonsymmetrical distribution of nodal points results in a reduction of accuracy (just as for the FDM), the results are restricted to the symmetrical nodal-point pattern developed by dividing the lengths L and H into 2, 4, 6, 8, 10, ... segments such that Δx and Δy are always equal or that $\Delta x = 2\Delta y$. The errors in $T(P)$ shown in Fig. 4(a) indicate that the linear element requires $\Delta x = \Delta y < {}^1/_{32}$ for an acceptable accuracy. The quadratic finite element is seen to be more accurate and to require only 60 percent of the total number of nodal points required by the linear method for equal accuracy. Since the computational times (for direct inversion of $[S]$) are nearly equal for both the linear and the quadratic elements, it is obvious that the quadratic element represents the best element treated. Of course this result was not unanticipated because of the high accuracy of the quadratic element. All elements show an improvement when $\Delta y = {}^1/_2\Delta x$, because of the closer nodal spacing.

The discouraging facet of Fig. 4(a) is the very poor behavior of the special cubic element. It is seen that this element is very slightly better than the linear method which has the same number of nodal points even though the special cubic element has three times the number of variables. Since the use of this more complicated method is justified only if it provides more accurate results, it appears that the special cubic method is unacceptable. A further reason to discard this method is given by the graph of the errors in the heat flux $q_x(Q)$, Fig. 4(b). In terms of the heat flux, the special cubic element is certainly no better than the linear element and its error does not monotonely decrease with an increase of nodal points. The behavior of this element may in part be due to its apparent stiffness [8] which prohibits rapid changes in T, $\partial T/\partial x$, and $\partial T/\partial y$ from element to element.

In terms of the heat flux, the discontinuous values of q_x and q_y of the linear element require that either the heat flux values in adjoining triangles be averaged and assigned to some preassigned point [2] or that the temperature be plotted to evaluate q, either method causing some problems. The quadratic element is not significantly better than the linear element and its errors are associated with two points: (a) the heat flux is not continuous and therefore one must compute $\partial T/\partial x$ at Q for all adjoining elements and then perform some individually chosen weighted averaging; (b) because the mid-side points are computed with a lower order of accuracy than the element vertex nodal points, values of $\partial T/\partial x$ and $\partial T/\partial y$ are often unusually strongly affected by neighboring nodal points, particularly if these influence the midpoints. For example, if $\Delta x = \Delta y = {}^1/_8$, q_x (left element) $= -1.5615 q_x$ (right element) $= -1.5622$, while if $\Delta x = {}^1/_8$, $\Delta y = {}^1/_{16}$ (left element) $= -1.5446$ (right element) $= -1.3006$.

The error in the last value is caused by the temperature at Q'

Table 3 Execution time for the singular problem; 2:1 rectangular nodal grid

Number of nodes	Δx (= Δy)	FEM linear	FEM quadratic	FEM cubic	FDM SØR	FDM SSØR
15	1/4	0.042/0.041^a sec	0.038		0.035	0.044/0.044
45	1/8	0.207/0.149	0.428	4.51	0.185	0.269/0.122
66	1/10	0.385/0.247			0.332	0.410/0.178
153	1/16	1.671/0.842	4.952	127.0	0.852	1.681/0.828
231	1/20	3.823/1.603	11.249		2.18	3.708/1.27
361	1/32	20.00/7.05	62.79		8.47	10.60/7.50

[a] The first times are for the maximum bandwidth and include the effect of large numbers of zeros and $B = 3 + 1/\Delta x$. The second times are for the minimum bandwidth, and contain minimum zeros and $B = 3 + 1/2\Delta y$.

maintaining $T(Q'')$ (the mid-side node) at a very high value and thus distorting the profile. Typical execution times on the CDC 6400 for this problem are given in Table 3.

In considering the core requirements of the methods, it must be recognized that the FDM's require a locator matrix to identify the conductances. However, a CDC 6400 word is 20 octal digits long and if each 4 digits are used to store a node number (yielding a maximum node number of 4095) we may store 5 locator tags in one core word, thus minimizing the storage. On the other hand the banded matrix of the FEM requires the storage of all elements from the diagonal element to the last non-zero element of every row, including all the zeros.

Now on a machine of the CDC 6000 series, a multiplication by zero takes as much as or more than one-half the time necessary to multiply two real numbers together. Consequently the execution time is significantly affected by the number of zeros in the band, as is well illustrated by the two times listed for the linear FEM. In general, the FEM requires NB^2 multiplications to triangularize the matrix, NB to condition the right-hand side, and NB to back-substitute.

The FDM's were solved by the successive over-relaxation method (SØR) of Young and Frank [16] and the symmetric successive over-relaxation method (SSØR) of Sheldon [17]. In the SØR the optimum over-relaxation factor and in the SSØR the number of iterations C which constitute one computational cycle must be determined for maximum computational efficiency. The times quoted in Table 3 include the times necessary to estimate these parameters. The second times listed for the SSØR were obtained when the number of iterations C was estimated according to the mesh spacing prior to the computation and do not reflect the minimum computing times possible when using the best value of C. Both the SØR and SSØR computations were continued until no nodal temperature changed by more than 10^{-6}, at which time no node differed by more than 10^{-5} from its exact value as found by direct inversion. For most cases, the use of an optimum over-relaxation parameter will require $\sqrt{N}$ iterations, each with NI multiplications, for a total of $N^{3/2}I$ multiplications.

As the number of nodes is increased in a rectangular grid, B is approximately $\sqrt{N}$, I remains at 5, and the ratio of the execution times becomes $t(\text{FEM})/t(\text{FDM}) \propto \sqrt{N}/I$ as $N \rightarrow \infty$. For three-dimensional problems, the banded matrix will be mainly zeros and the execution times will be larger by the ratio of B^2 and so will be significantly larger than the values quoted above.

For variable properties, a number of iterations will be required and the execution times (exclusive of reforming the matrices) will be multiples of the values quoted in Table 3. However, the SØR can easily incorporate matrix modifications without an undue increase in time. Several numerical experiments for variable properties have suggested that the SØR rarely requires more than twice the reported number of iterations. Thus if more than 2 or 3 property iterations are needed, the FDM easily exceeds the FEM in efficiency.

Conclusions and Comments

An inspection of the accuracy of the results for the three test problems and the computation times required indicates that the finite-element method is a viable alternative to the finite-difference methods except for transient problems or steady-state problems with variable thermal properties. For this latter type of problem, the necessary reevaluation of the thermal stiffness matrix and its triangularization result in computational time requirements for the linear FEM which may be an order of magnitude greater than the finite-difference method. For constant-property materials, the linear FEM and the FDM approaches require relatively equal core storage for optimum node-numbering schemes and equal execution time and appear to be of equal value. However, the consideration of a few non-simple geometries soon leads to the conclusion that the FEM is so easy to use and forms the necessary matrices so efficiently, with only the nodal-point locations and the material properties specified, that its limited disadvantages for the variable-material-property cases are not of importance and the FEM represents a useful general thermal analyzer. On the other hand, if the problem region is bounded by coordinate lines, or if the problem is one of variable properties and is to be solved for a large number of conditions, then it appears that the FDM is a more acceptable method, particularly if it is expressed as a pseudo-FEM. In the pseudo-FEM, a standard FEM of any element model (e.g., linear or quadratic) is used to form the $[S]$, $[H]$, and $[SQ]$ matrices for unit or constant thermal properties and only the non-zero elements are stored. The transient coefficient matrix is formed not by using $\partial T/\partial t = \langle f \rangle \, [A]^{-1}(\partial \hat{T}/\partial t)$, but by using Dusinberre's method [9] in which the coefficient for each node involves only the temperature of the node. The locator matrix, which specifies to which node the non-zero coefficients pertain, is then constructed to include both the mode of heat transfer (conduction, radiation, etc.) and a code to indicate the temperature-dependence of the coefficient. In this way, the pseudo-FEM possesses the accuracy of the FEM, the fast execution times of the C–N or L–W FDM's, requires the minimum core storage requirements, and permits an arbitrary node-numbering scheme. This latter point is of importance since the matrix bandwidth of the FEM is determined by the maximum difference in node numbers of nodal points which affect any specific nodal-point temperature. Consequently, most FEM's are restricted in one of the dimensions of the region, particularly when utilizing the quadratic or higher-order element models for which the bandwidth is intrinsically larger than that of the linear model.

Thus it appears that the finite-element method is the more attractive method for constant-property problems or for variable-property problems whose computation time is not excessive or which are not to be repeatedly computed. It should be noted that if only a linear finite-element method is to be employed for sourceless steady-state problems, both the FEM and FDM are identical except for the method of establishing and storing the conductance, and given equal mesh generators and sufficient core storage, both are of equal value. If, however, more-accurate difference methods are to be used, without hand coding the entire algorithm, the FEM is of greater value.

The results given here also show that there is no advantage gained by using element spatial distributions which are of higher order than the quadratic because of the loss of internal accuracy, and that attempts to guarantee heat flux compatibility are not to be recommended. It is the authors' opinion that the quadratic element is the best polynomial element and from the viewpoint of simplicity and ease of construction may well be the best of all elements.

Summary

1 Finite-element and ordinary thermal analyzers using iterative methods are comparable for constant-property steady-state and transient solutions only if the finite-element banded matrix has very few zeros.

2 Since the banded matrix bandwidths will become even larger for three-dimensional problems and execution times will rise accordingly, it appears unwise to consider replacing any working three-dimensional thermal analyzer with a finite-element direct-inverting program.

3 Variable-property steady-state problems should be treated by finite-element methods only if only 2 or 3 property iterations are needed and variable-property transient problems should never be treated by the finite-element method.

4 If a working thermal-analyzer program has a fairly easily used input system and a good-internal-conductance calculating routine, there is no reason for changing to the finite-element method.

5 The primary advantages of the finite-element method are associated with the ease of inputting data and the readiness with

which the form of the assumed temperature distribution in the element may be changed. It must be remembered that increasing the order of an approximating polynomial does not necessarily guarantee an equal increase in overall accuracy of the method and that the sources and heat-capacity matrices may not be consistent with physical observations.

References

1 Schechter, R. S., *The Variational Method in Engineering*, McGraw-Hill, New York, 1967.

2 Zienkiewicz, O. C., *The Finite Element Method in Structural and Continuum Mechanics*, McGraw-Hill, New York, 1967.

3 Turner, M. J., Clough, R. W., Martin, H. C., and Topp, L. J., "Stiffness and Deflection Analysis of Complex Structures," *Journal of Aerospace Science*, Vol. 23, 1956, pp. 805–823.

4 Visser, W., "A Finite Element Method for the Determination of Non-Stationary Temperature Distribution and Thermal Deformations," *Proceedings of Conference on Matrix Methods in Structural Mechanics*, Air Force Institute of Technology, Ohio, Oct. 1965.

5 Gabrielson, V., "HEATMESH—A Computer Code for Generating Geometrical Data Required for Studies of Heat Transfer in Axi-Symmetric Structures," Sandia Laboratory Rept. DR-67-30, Livermore, Calif.

6 Wilson, E. L., and Clough, R. W., "Dynamic Response by a Step by Step Analysis," *Proceedings of Symposium on the Use of Computers in Civil Engineering*, Lisbon, Oct. 1962.

7 Ralston, A., *A First Course in Numerical Analysis*, McGraw-Hill, New York, 1965.

8 Felippa, C. A., "Refined Finite Element Analysis of Linear and Non-Linear Two Dimensional Structures," Structures and Material Research Report 66-22, Dept. of Civil Engrg., Univ. of California, Berkeley, Calif., 1966.

9 Dusinberre, G. M., *Numerical Analysis of Heat Flow*, McGraw-Hill, New York, 1949.

10 Bickley, W. G., "Finite Difference Formulae for the Square Lattice," *Quarterly Journal of Mechanics and Applied Mathematics*, Vol. 1, 1948, pp. 35–42.

11 Tocher, J. L., and Hartz, B. J., "Higher Order Finite Element for Plane Stress," *Journal of the Engineering Mechanics Division*, ASCE, Vol. 93, No. EM4, Aug. 1967, pp. 149–172.

12 Richtmyer, R. D., and Morton, K. W., *Difference Methods for Initial Value Problems*, Interscience, New York, 1967.

13 Motz, H., "The Treatment of Singularities of Partial Differential Equations by Relaxation Methods," *Quarterly Journal of Applied Mathematics*, Vol. 4, 1946, pp. 371–377.

14 Woods, L. C., "The Relaxation Treatment of Singular Points in Poisson's Equation," *Quarterly Journal of Mechanics*, Vol. 6, 1953, pp. 163–185.

15 Wilson, E. L., "Finite Element Analysis of Two Dimensional Structures," Structural Engineering Lab. Rept. 63-2, Univ. of Calif., Berkeley, 1963.

16 Young, D. M., and Frank, T. G., "A Survey of Computer Methods for Solving Elliptic and Parabolic Differential Equations," *ICC Bulletin*, Vol. 2, No. 1, Jan. 1963, pp. 3–61.

17 Sheldon, J. W., "On the Numerical Solution of Elliptic Difference Equations," *Math Tables*, Vol. 9, No. 51, July 1955, pp. 101–111.

J. HEBERLEIN
Research Fellow.

E. PFENDER
Professor.

Department of Mechanical Engineering,
Heat Transfer Division,
University of Minnesota,
Minneapolis, Minn.

Transpiration Cooling of the Constrictor Walls of an Electric High-Intensity Arc[1]

In this paper transpiration cooling of a porous tube exposed to a high-temperature plasma is discussed. The plasma is generated by a high-intensity d-c arc which reaches a thermally and hydrodynamically fully developed state in the porous constrictor tube. From an energy balance over a tube cross section in this regime using a semiempirical relationship between pressure drop and mass flow rate across the porous wall, the temperature distribution in the porous material as well as local heat fluxes are determined. Properties of the porous material which are of particular importance for the performance of a transpiration-cooled arc are determined independently. The experiments provide a check on the reliability of these data. Analytical predictions of arc and constrictor performance are compared with experimental results. A large discrepancy exists in most of the results which is mainly attributed to turbulent-flow components in the tube which, in turn, can be confirmed by other diagnostic measurements. Finally, various sources for possible errors are discussed and the limitations imposed on the performance of a transpiration-cooled arc by imperfections of porous materials and the technology involved are indicated.

Introduction

Transpiration cooling represents an efficient method of protecting a porous surface from excessive heating by blowing gas through the porous material in counterflow to the imposed heat flux. The transpiring gas greatly increases the thickness of the thermal boundary layer and reduces the temperature gradient at the surface. The reduction of the heat flux to the surface results in a corresponding enthalpy increase of the transpiring gas in the boundary layer.

Transpiration cooling has attracted particular interest in applications associated with high heat-transfer rates as, for example, that experienced in rocket engines and gas turbines [1, 2].[2] More recently, attempts have been made to apply transpiration cooling to electric arcs confined in porous tubes [3–6]. In conventional arc devices the arc is confined and stabilized by a water-cooled constrictor tube. In this case, the maximum temperature attainable is limited by the highest permissible heat flux to the constrictor, which is approximately 20 kw/cm^2. By replacing the water-cooled wall with a porous transpiration-cooled constrictor, almost the entire heat flux to the wall may be intercepted by the radially oriented gas flow through the porous wall and redirected into the main gas stream. The temperature gradient at the wall is drastically reduced in this way and, therefore, appreciably higher power inputs per unit length of the arc and correspondingly higher axis temperatures should be feasible.

From numerical solutions of the conservation equations for an axis-symmetric, steady, laminar, fully developed transpiration-cooled arc [7, 8], temperature distributions and wall heat fluxes have been obtained as functions of the power input and the transpirant mass flow rate. Results for argon and nitrogen as coolant demonstrate the effectiveness of this cooling method. Experiments based on such theoretical predictions are reported in this paper. From basic considerations, equations are derived which relate main parameters, as for example inside wall temperature and wall heat flux, to easily measurable quantities. Because of the strong influence of the porous constrictor wall properties on the arc performance, these properties have been extensively investigated. Comparisons of theoretical predictions with experimental results show, in general, poor agreement which is mainly attributed to the existence of turbulent-flow components during experiments and to a lesser degree to the uncertainty of theoretical results due to uncertainties of thermodynamic and transport properties of high-temperature plasmas [9].

---

[1] This work was supported by the Aerospace Research Laboratories, USAF, under Contract F 33615-67-C-1353.

[2] Numbers in brackets designate References at end of paper.

Contributed by the Heat Transfer Division and presented at the Fluids Engineering, Heat Transfer, and Lubrication Conference, Detroit, Mich., May 24–27, 1970, of The American Society of Mechanical Engineers. Manuscript received by the Heat Transfer Division February 24, 1970; revised manuscript received August 20, 1970. Paper No. 70-HT-35.

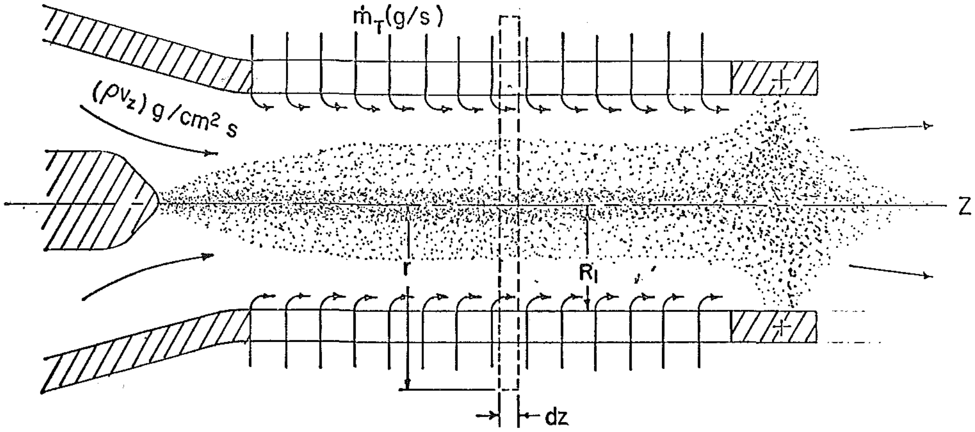

Fig. 1 Schematic of a transpiration-cooled constricted arc

Basic Considerations

A schematic of a transpiration-cooled constricted arc is shown in Fig. 1. The arc is confined by a porous cylinder through which the working gas is injected. The arc is termed "thermally fully developed" when the radial temperature profile in the transpiration-cooled constrictor becomes independent of the axial location, i.e., the energy dissipation rate exactly balances the heating of the injected gas so that the average enthalpy remains constant in various cross sections. The velocity field also becomes fully developed in the sense that the velocity profiles at various cross sections are similar to each other.

The inside wall temperature T_1, which determines the integrity of a transpiration-cooled arc, represents one of the most important parameters. Since a direct measurement of this temperature during arc operation is rather complicated, this temperature is conveniently derived from quantities which can be easily measured. These quantities are the pressure in the plenum chamber p_R, the pressure drop along the arc p_0, the total transpirant mass flow rate $\dot m_T$ through the constrictor tube, and the outside wall temperature T_2. With these quantities, the inside wall temperature can be calculated from an energy balance applied to unity length of the constrictor tube at any cross section. The following assumptions are made for this calculation:

1 The arc is steady and axis-symmetric, i.e., the wall heat flux is independent of time and circumferentially uniform.

2 The heat flux in the axial direction in the tube wall is negligible.

3 Compressibility effects are negligible.

4 The wall material properties are uniform throughout the constrictor.

5 The thermal conductivity k_w of the wall material is large compared to the conductivity k_g of the transpiring gas.

The validity of these assumptions will be discussed later on. With these assumptions, an energy balance over unity length of the constrictor tube may be written as:

$$\frac{1}{r}\frac{d}{dr}\left(k_w r\frac{dT_w}{dr}\right) + \frac{\dot m}{2\pi r}\frac{dc_pT_g}{dr} = 0 \qquad (1)$$

k_w may be factored out if an average value is taken which is independent of the radius. c_p may be considered as constant in the temperature range of interest. The wall temperature T_w and the

Nomenclature

c_1, c_2 = constants in equation (13)
c_p = specific heat at constant pressure
E = electric-field strength
h_v = volumetric heat-transfer coefficient
h_{vo} = constant describing volumetric heat transfer
I = arc current
k_w = thermal conductivity of the constrictor wall
L = length of constrictor tube
$\dot m$ = transpirant mass flow rate per unit length
$\dot m_T$ = total transpirant mass flow rate
$\dot m_0$ = axially introduced mass flow rate
n = $c_p/2\pi k_w$
P = porosity
p = pressure
p_i = static pressure in the flow duct
p_R = pressure in the plenum chamber
p_s = defined by equation (10*a*)
p_0 = pressure at cathode location
Q_L = heat loss from the outside constrictor wall surface per unit length and unit time
Q_w = heat flux per unit length to the inside constrictor wall surface
R_1, R_2 = inside and outside constrictor wall radius, respectively
$\tilde R$ = individual gas constant for argon
r = radial coordinate
T = temperature
T_1, T_2 = temperatures of inside and outside wall surface, respectively
T_∞ = gas-supply temperature
T_A = defined in equation (10*b*)
v = gas velocity
z = axial coordinate
α, β = parameters describing the flow through porous media
$\delta = \frac{\alpha}{\beta}$ = characteristic length
ϵ = total emissivity of solid
$\bar\epsilon$ = average emissivity of porous material
μ = viscosity
μ_1, μ_2 = constants describing the temperature dependence of the viscosity at moderate temperatures
ρ = gas density
σ_B = Stefan-Boltzmann constant

Subscripts

g = refers to the gas
w = refers to the wall
1 = at location of inside constrictor wall surface
2 = at location of outside constrictor wall surface
∞ = property of incoming gas

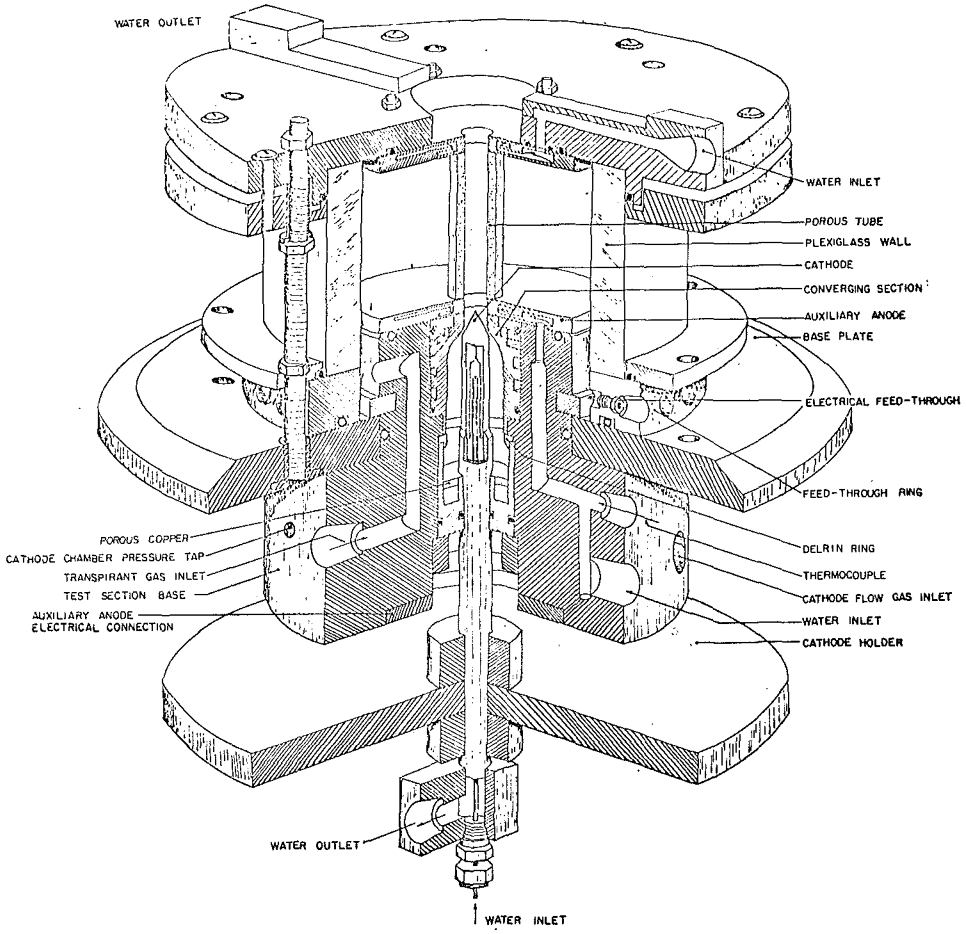

Fig. 2 Schematic of transpiration-cooled arc apparatus

gas temperature T_g are the remaining dependent variables in equation (1). Another relation between wall and gas temperature is obtained from the local heat transfer between wall and transpiring gas:

$$\frac{k_w}{r}\frac{d}{dr}\left(r\frac{dT_w}{dr}\right) = h_v(T_w - T_g) \tag{2}$$

In this equation, h_v is the volumetric heat-transfer coefficient. According to Druzhinin [10]

$$h_v \propto (\mathrm{Re}_\delta)^{1.84} = \left(\frac{\dot{m}\delta}{2\pi r\mu}\right)^{1.84}$$

where the Reynolds number is based on the characteristic length [11] $\delta = \frac{\beta}{\alpha}$. The parameters α and β appear in the equation describing the pressure drop of the flow through the porous wall and will be defined later on. With the approximation $h_v = \frac{h_{vo}}{r^2}$ equations (1) and (2) may be combined to a third-order differential equation for $T_w(r)$ [12]. An order-of-magnitude estimate based on typical values used in the experiment reveals that the volumetric heat-transfer coefficient is so large that the gas temperature approaches the wall temperature shortly after entering the porous wall [12, 13]. Therefore, the gas temperature T_g in equation (1) is replaced by the wall temperature $T_w = T$. With this assumption, the equation for the cross-sectional energy balance becomes

$$\frac{k_w}{r}\frac{d}{dr}\left(r\frac{dT}{dr}\right) + \frac{\dot{m}c_p}{2\pi r}\frac{dT}{dr} = 0 \tag{3}$$

Applying the boundary conditions for the outside wall surface $r = R_2$: $T = T_2$ and $-2\pi R_2 k_w \left.\frac{dT}{dr}\right|_{R_2} = \dot{m}c_p(T_2 - T_\infty) + Q_L$ the integration of this equation yields with $\frac{c_p}{2\pi k_w} = n$

$$\frac{T - T_\infty + \frac{Q_L}{\dot{m}c_p}}{T_2 - T_\infty + \frac{Q_L}{\dot{m}c_p}} = \left(\frac{R_2}{r}\right)^{n\dot{m}} \quad \text{for} \quad R_1 \le r \le R_2 \tag{4}$$

The heat flux Q_L which is not intercepted by the transpiring gas accounts for radiation from the outside wall. Heat transferred by free convection inside the thermal boundary layer to the water-cooled anode is negligible. The heat loss may be expressed by

$$Q_L = 2\pi R_2 \bar{\epsilon}\sigma_B(T_2^4 - T_\infty^4) \tag{5}$$

Thus, if the total emissivity $\bar{\epsilon}$ and the average thermal conductivity of the porous wall material are known and the outside wall temperature T_2 and the transpirant mass flow rate at a certain axial location are determined, the temperature distribution in the porous wall and, consequently, the inside wall temperature can be calculated. The transpirant mass flow rate can be obtained from the Forchheimer equation [14], which describes the relation between the pressure drop across and the flow velocity through a porous wall [15–17]:

$$-\mathrm{grad}\, p = (\alpha\mu v + \beta\rho v^2)\cdot\frac{\mathbf{v}}{v} \tag{6}$$

where **v** is the gas velocity in the porous medium. The two terms on the right-hand side represent viscous force and inertia force, respectively. The ratio of these two terms represents a Reynolds number $\mathrm{Re}_\delta = \frac{\rho\beta v}{\alpha\mu}$; $\delta = \frac{\beta}{\alpha}$ can, therefore, be interpreted as a characteristic length for the porous material.

With the continuity equation

$$2\pi \frac{d}{dr}(r\rho v) = \operatorname{div} \dot{m} = 0 \tag{7}$$

and the perfect gas law $p = \rho\bar{R}T$, one obtains the equation (again with the assumption of circumferential symmetry):

$$2pdp = \frac{\bar{R}}{\pi}\left[\alpha\mu T \frac{\dot{m}}{r} + \frac{\beta}{2\pi} T \frac{\dot{m}^2}{r^2}\right] dr \qquad (R_1 \le r \le R_2) \tag{8}$$

According to isothermal measurements, which will be discussed later on, α and β seem to be weak functions of the temperature and hence of the radius. The error introduced by considering these parameters as being constant is small compared to other errors. The viscosity of argon as a function of temperature is known and can be approximated in the temperature ranges of interest by $\mu = \mu_1 + \mu_2 T$. If equation (4) is introduced, equation (8) can be integrated with the boundary conditions $p = p_R$ for $r = R_2$ and $p = p_i$ for $r = R_1$

$$\begin{aligned}\frac{p_R{}^2 - p_i{}^2}{p_s{}^2} &= \left[\left(\frac{R_2}{R_1}\right)^{n\dot{m}} - 1\right]\left[1 + 2\frac{\mu_2}{\mu_1} T_A\right] \\ &+ \left[\left(\frac{R_2}{R_1}\right)^{2n\dot{m}} - 1\right]\frac{\mu_2}{2\mu_1}(T_2 - T_A) \\ &+ \left(1 + \frac{\mu_2}{\mu_1} T_A\right)\frac{n\dot{m}}{\frac{T_2}{T_A} - 1}\ln\frac{R_2}{R_1} \\ &+ \frac{1}{2\pi\mu_1}\frac{\delta}{R_1}\frac{n\dot{m}^2}{n\dot{m} + 1}\left[\left(\frac{R_2}{R_1}\right)^{n\dot{m}+1} - 1\right] \\ &+ \frac{1}{2\pi\mu_1}\frac{\delta}{R_1} n\dot{m}^2 \frac{\frac{R_2}{R_1} - 1}{\frac{T_2}{T_A} - 1}\end{aligned} \tag{9}$$

with

$$p_s{}^2 = \frac{\mu_1\alpha\bar{R}(T_2 - T_A)}{\pi n} \tag{10a}$$

$$T_A = T_\infty - \frac{Q_L}{\dot{m}c_p} \tag{10b}$$

p_i is the pressure inside of the tube at the chosen axial location. This pressure is calculated in [11] as a function of the axial location z and of the total pressure drop p_0 in the axial direction. Thus, if p_R, p_0, T_2, T_∞ are measured and the wall material properties are known, the mass flow rate $\dot{m}$ at a certain cross section can be calculated. This mass flow rate introduced into equation (4) yields the inside wall temperature. With these values an energy balance at $r = R_1$ yields

$$Q_w = \dot{m}c_p(T_1 - T_\infty) + Q_L \tag{11}$$

Thus, with the values obtained, the heat flux from the arc to the wall can be calculated.

Experimental Arrangement

The apparatus shown in Fig. 2 is described in detail in references [9, 11]. The porous tube is sealed between two water-cooled copper disks, one of which serves as anode. A concentric plexiglas or pyrex glass cylinder surrounds the constrictor tube and forms the outer wall of the plenum chamber for the transpiring gas. The cathode is located upstream of the constrictor tube. A certain fraction of the mass flow rate is introduced axially in order to stabilize the cathode arc attachment. Pressure taps are located in the plenum chamber and near the cathode.

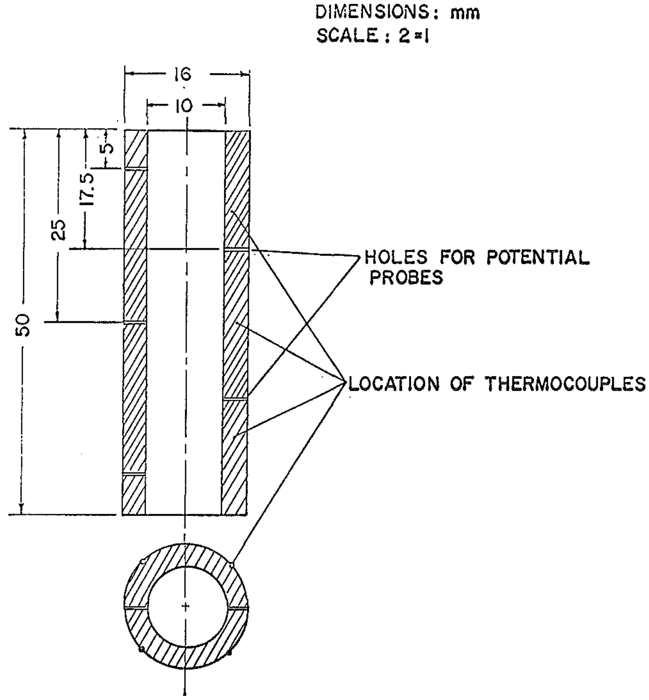

Fig. 3 Probe location on ALSIMAG 447 tubes

Constrictor tubes made of two different materials have been used: ALSIMAG 447 and porous tungsten tubes of two different porosities (30 and 55 percent).

ALSIMAG 447 is a porous ceramic material of the composition $2MgO \cdot 2Al_2O_3 \cdot 5SiO_2$. It has a porosity of approximately 15 percent. Its high electrical resistivity, small expansion coefficient (6×10^{-7} per deg K at room temperature), high compressive and tensile strengths (18,500 psi and 2500 psi, respectively) favor its use. Unfavorable are the melting temperature of about 1600 deg K and the low thermal conductivity of 1.0 w/m·deg K. As a consequence, any asymmetry of the arc may cause strong temperature gradients in axial and circumferential direction.

Most of the experiments have been performed with ALSIMAG 447 tubes of 5.0 cm length, 1.0 cm ID, and a constant OD of 1.6 cm.

In order to account for axially nonuniform transpirant mass flow rates due to significant axial pressure drops, constrictor tubes with axially varying wall thickness are utilized in this situation. The tube shape has been calculated with a method proposed in [11].

The outside wall temperature is measured by means of thermocouples at various locations along the outer tube surface, see Fig. 3. For potential measurements, tungsten wires are inserted through small holes in the constrictor wall, see Fig. 3.

Because of the high electrical conductivity, the tungsten constrictor tubes are built as a cascade consisting of several segments which are insulated against each other. Ten segments of 1.00 cm ID, 1.60 cm OD, and 0.48 cm height are assembled with Astroceram high-temperature cement.

The outside wall temperature of a ring, reaching a temperature sufficiently high to radiate in the wavelength range of visible light, is measured with an optical pyrometer. The wall temperature of the cooler rings is obtained by extrapolation.

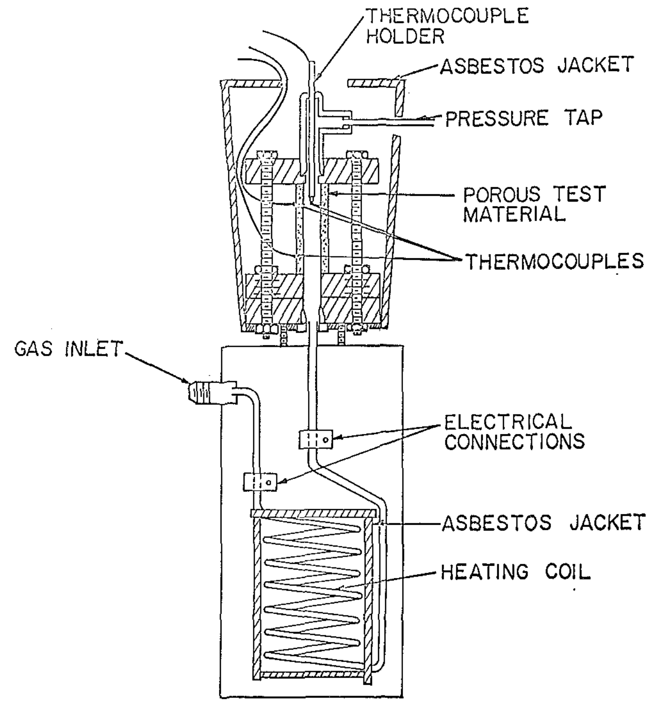

Fig. 4 Schematic of pressure-drop apparatus

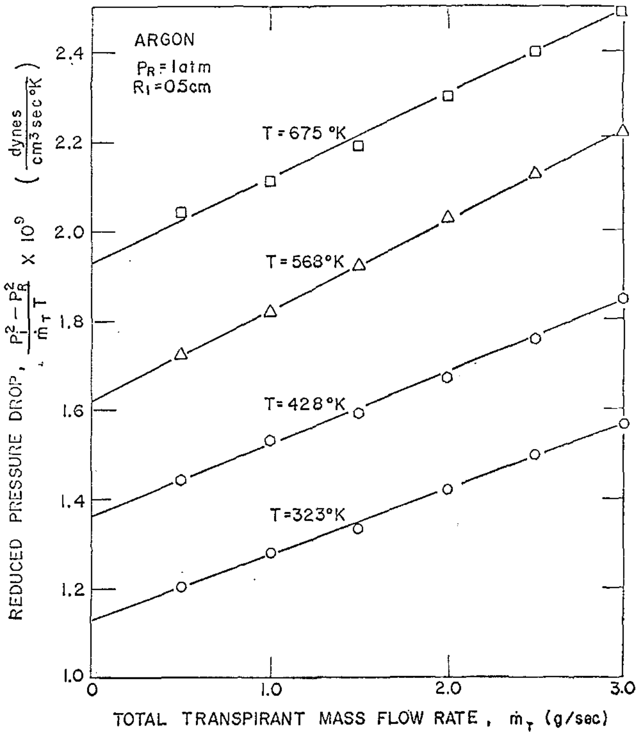

Fig. 6 Dependence of reduced pressure drop on mass flow rate for ALSIMAG 447 tube; $L = 5$ cm

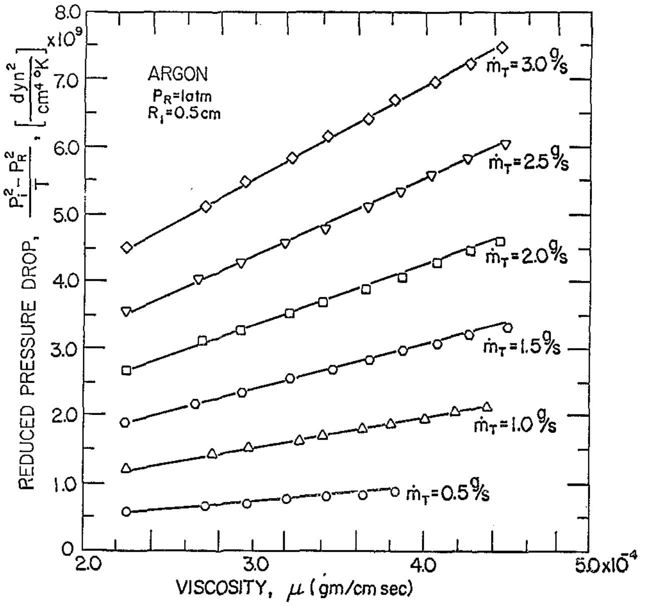

Fig. 5 Dependence of reduced pressure drop on viscosity for ALSIMAG 447 tube; $L = 5$ cm

Whereas an ALSIMAG tube is useless after local overheating, the tungsten tube can be reused many times, because damaged segments can be easily replaced. It turns out, however, that the axial distribution of the outside wall temperature becomes rather irregular after extended usage of segments, indicating that the permeability of the segments has changed, which is probably caused by changes in the grain size of tungsten.

Determination of Wall Properties. In order to solve equation (9), the wall material properties, thermal conductivity k_w, total emissivity $\bar{\epsilon}$, and the flow constants α and β must be known.

The thermal conductivity of ALSIMAG 447 is given by the manufacturer as approximately 1.25 w/m·deg K at room temperature. Because of the strong influence of the conductivity on the temperature profile in the wall at these low values of the conductivity, a more accurate value of this property for the temperature range of interest is needed. From equation (4) an average value for the thermal conductivity can be determined if the inside and outside wall temperatures and the mass flow rate are known. The inside wall temperature is determined by measuring the radiative flux emitted from the inside wall surface. This measurement is described in detail in [12]. Values are obtained for different wall heat fluxes and different mass flow rates and, therefore, different temperature distributions. The average value is 1.00 w/m·deg K with deviations of ±8 percent.

The large value for the thermal conductivity of tungsten makes the exponent in equation (4) so small that even 10 percent error has no significant influence on the calculated temperature profile.

The emissivity of ALSIMAG 447 is given by the manufacturer as $\bar{\epsilon} \approx 0.6$. The emissivity of porous tungsten has been calculated adopting a simplified model [9] which yields

$$\bar{\epsilon} = \epsilon \left[1 - P + 3P \frac{1 + \epsilon}{(1 - \epsilon)^2} + \frac{6P\epsilon}{(1 - \epsilon)^3} \ln \epsilon \right] \qquad (12)$$

where ϵ is the emissivity of a polished surface of the same material and P is the porosity, defined as the ratio of the density of the porous material to the density of the corresponding solid material. This model is valid for porosities below 55 percent.

For the determination of the flow constants α and β, again equation (6) is utilized. The Forchheimer equation integrated for isothermal conditions reads

$$\frac{p_R^2 - p_i^2}{T} = c_1 \dot{m} \mu \alpha + c_2 \dot{m}^2 \beta \qquad (13)$$

with the constants $c_1 = \frac{\bar{R}}{\pi} \ln \frac{R_2}{R_1}$ and $c_2 = \frac{\bar{R}}{2\pi^2} \frac{R_2 - R_1}{R_2 R_1}$. From this equation it follows that α and β can be determined either by measuring the pressure drop across the tube wall as a function

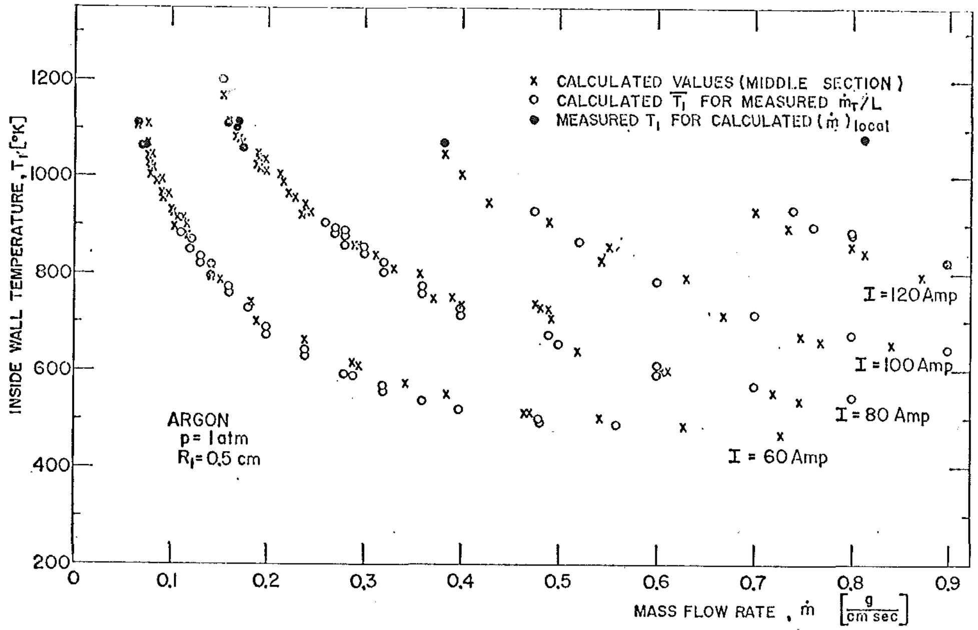

Fig. 7 Dependence of inside wall temperature on mass flow rate in a transpiration-cooled arc; tube length $L = 5$ cm

Table 1 Variations of the values of the flow constants for different methods of determination

Method of determination	ALSIMAG tube $\alpha(10^7\,\text{cm}^{-2})$	ALSIMAG tube $\beta(10^4\,\text{cm}^{-1})$	Tungsten tube $\alpha(10^7\,\text{cm}^{-2})$	Tungsten tube $\beta(10^4\,\text{cm}^{-1})$
Variation of mass flow at constant temperature				
T = 293 deg K	7.3	5.17	14.07	2.37
T = 723 deg K	6.78	6.62	12.45	3.63
Variation of temperature at constant mass flow				
$\dot{m}_T$ = 0.5 g/sec	6.11	18.23	9.93	40.51
$\dot{m}_T$ = 3.5 g/sec	7.37	4.92	11.72	5.10

of the temperature, keeping the mass flow rate constant, or by measuring the pressure drop as a function of the mass flow rate for a given temperature. In the first case $(p_R^2 - p_i^2)/T$ is plotted versus $\mu(T)$, whereas in the second case $(p_R^2 - p_i^2)/\dot{m}T$ is plotted versus $\dot{m}$.

For isothermal measurements the apparatus shown in Fig. 4 is utilized. The tube under investigation is sealed between two plates. The gas is heated in a stainless steel tube which is connected to a d-c power supply and blown axially into the inside of the tube. A pressure tap is located in the top plate. A thermocouple probe is inserted through the pressure tap into the inside of the tube and two thermocouples measure the outside wall temperature in order to detect deviations from isothermal conditions. The whole apparatus is insulated with asbestos to diminish radiative and convective heat losses which would disturb isothermal conditions. In spite of this precaution, a temperature drop across the tube wall of about 5 percent is observed at 800 deg K and increases strongly with increasing temperature. Therefore, the measurements are not extended to higher temperatures. The results for a particular ALSIMAG tube are shown in Figs. 5 and 6, and Table 1 shows the maximum variations of α and β for a particular ALSIMAG and porous tungsten tube. The flow constants determined at low but constant mass flow rates and varying temperatures deviate strongly from all the other measurements. These deviations are probably caused by a relatively large error in measuring small mass flow rates. At a total transpirant mass flow rate of 0.25 g/sec, an error of 10 percent changes β by 20 to 30 percent; if the mass flow rate, however, changes from 0.28 g/sec to 0.23 g/sec with increasing temperature, the curves in Fig. 5 are shifted and their slopes change, resulting in a change in β of several hundred percent. At higher mass flow rates, the relative error in the measurement of the flow rates is less significant. A slight variation of the flow constants with temperature can be observed: α seems to decrease and β to increase with increasing temperature, but these variations are within experimental accuracy. A decrease in α by 50 percent and an increase in $\frac{\beta}{\alpha}$ by 100 percent for a temperature increase of 45 deg C for a porous tungsten sample, as reported by Greenberg and Weger [18], has not been observed. It is therefore believed that the most accurate values for α and β are obtained from a variation in the mass flow rate at room temperature. It is found that the flow constants do change from tube to tube. Therefore, they are determined before every run after the tube is sealed in the arc apparatus.

Experimental Procedure and Results

The initial transpirant mass flow rate is chosen very high ($\approx$3 g/sec) in order to avoid damage of the tube by asymmetries during arc initiation. After adjusting the current and total transpirant mass flow rate, the system requires still some time to equilibrate as indicated by changes of the plenum chamber pressure. Data are taken after an equilibrium state is reached. The arc may be operated without interruption for several hours. Any local overheating of the tube is usually recognized first by a sudden increase of the plenum chamber pressure. The readings of the thermocouples at different circumferential positions but at the same axial location are averaged to yield an average outside wall temperature for this axial location. The pressure p_i at this location is obtained from the corresponding axial distribution of the normalized inside-tube pressure. The plenum-chamber

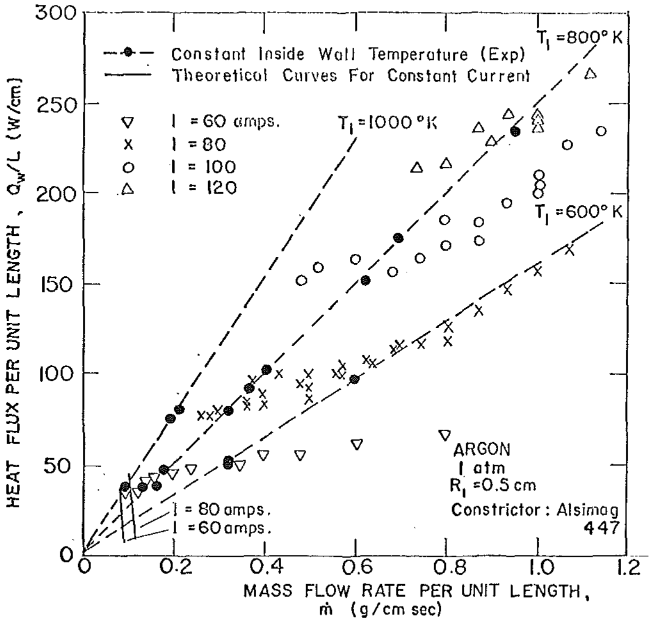

Fig. 8 Wall heat flux as a function of mass flow rate

pressure, the inside pressure p_i, and the outside wall temperature taken at a particular axial location, introduced into equation (9) yield the transpirant mass flow rates per unit length at this axial location. With this mass flow rate, equation (4) yields the inside wall temperature at that location. This is done for three different axial locations in the case of the ALSIMAG tube and for 10 different locations in the case of tungsten tubes. For the solution of these equations, a computer program has been developed for the CDC 6600 of the University of Minnesota Computer Center.

Fig. 7 shows values for inside wall temperatures of an ALSIMAG 447 tube for several transpirant mass flow rates and for currents ranging from 60 amp to 120 amp. Also shown in this figure are the values for the inside wall temperature which are obtained experimentally and which are used for the determination of the thermal conductivity. The agreement of these experimental points with the calculated curve for currents up to 100 amp justifies the utilization of an average value for the thermal conductivity.

The data points in Fig. 7 are, except for the filled circles which represent measured inside wall temperatures, not real experimental data. They are derived from experimentally measured quantities under certain assumptions as described before. A check for the validity of these assumptions can be obtained when the total transpirant mass flow rate is measured. The calculated mass flow rates for the different axial locations differ often considerably from each other, indicating that the wall heat flux is not uniform in the axial direction. The average value of these mass flow rates per unit length multiplied by the tube length gives a value for the total transpirant mass flow rate $\dot m_T$. Comparison of this value with the measured total transpirant mass flow rates shows good agreement for experiments with ALSIMAG tubes at currents below 120 amp.

Because of the strong influence of asymmetries at higher currents, the calculated inside wall temperatures cannot be considered reliable for such currents.

The mass flow rate through the porous tungsten tubes is calculated for each segment. In the runs with the tungsten tube the mass flow rate is kept low enough so that the tube assumes a temperature within the range of an optical pyrometer ($T_2 \geq 1000$ deg K). Under such conditions a high temperature gradient exists between constrictor tube and water-cooled auxiliary anode as well as between constrictor tube and anode, resulting in relatively large heat fluxes to these water-cooled components. The temperature of the segments bordering these components is considerably less than in the midsection of the tube and lies below the range of an optical pyrometer. Also, an additional heat-loss term enters the energy balance. An exact two-dimensional treatment of this heat loss is rather difficult because of the unknown outside wall temperature in the end regions of the tube and because of the unknown thermal properties of the insulating layers between the different segments. Therefore, only an estimated heat-loss term is introduced in the energy balance. With the tungsten tube of 55 percent porosity the temperature distribution is usually more uniform. This has, however, the consequence that the end seals of the tube bordering the copper disks are overheated.

In order to obtain information about the performance of the transpiration-cooled constrictor tube, the heat fluxes to the constrictor wall obtained from a theoretical treatment of the arc [7–9] are compared to those obtained from measured data using

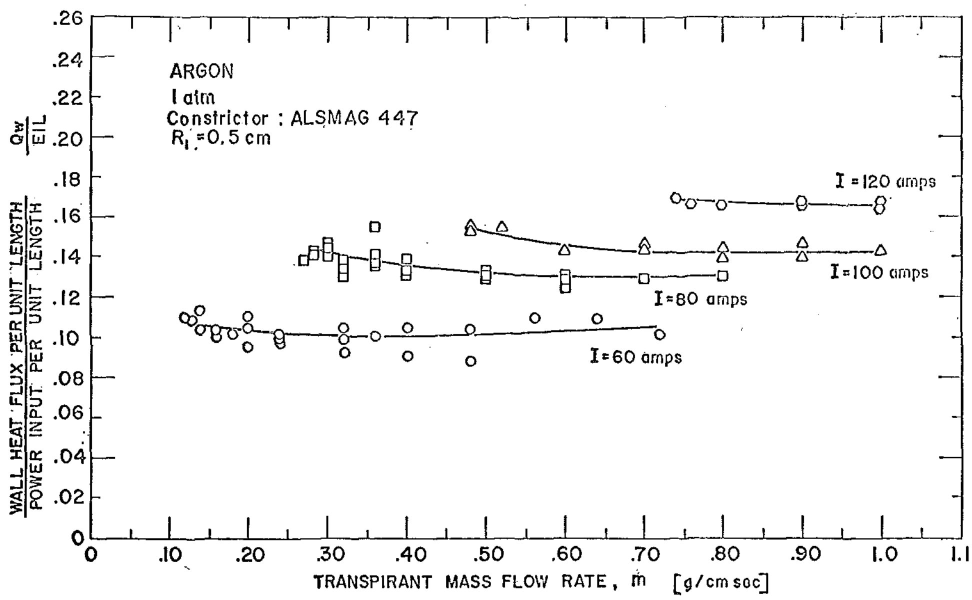

Fig. 9 Fraction of input power transferred to constrictor wall

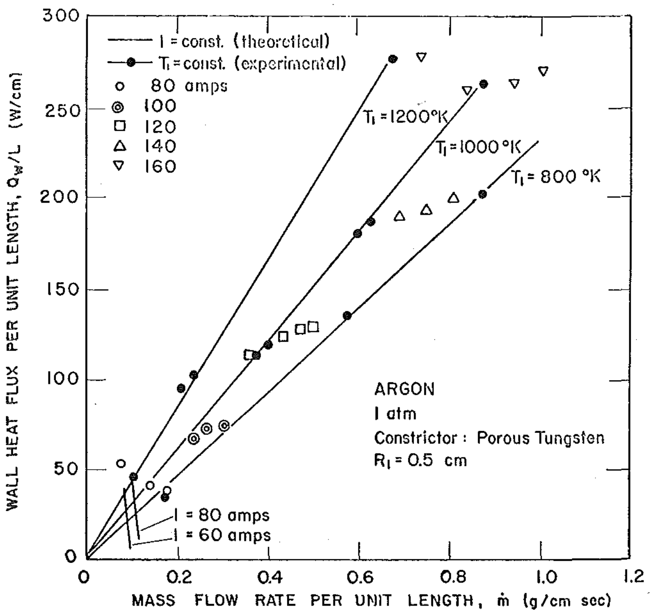

Fig. 10 Wall heat flux as a function of mass flow rate

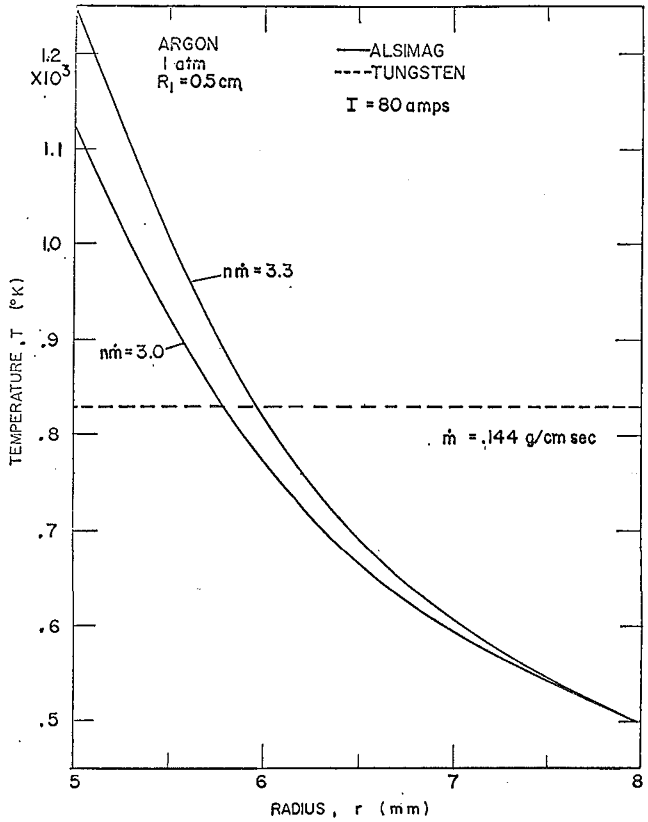

Fig. 11 Temperature profiles in the constrictor tube walls

equation (11). Theoretically, the wall heat flux for a certain arc current decreases strongly with increasing transpirant mass flow rate, see Fig. 8. The experimentally obtained values, however, show an increase of the wall heat flux with transpirant mass flow rate, in spite of a decreasing inside wall temperature. At the comparatively low peak temperatures of the plasma the radiative heat flux to the wall does not play an important role. It appears, therefore, that laminar flow cannot be assumed. Fig. 9 demonstrates that the fraction of the power transferred to the wall compared to that dissipated per unit length remains approximately constant with increasing mass flow rate. Since the dissipated power increases with transpirant mass flow rate, the cooling effect with increasing mass flow rate is obviously overbalanced by the heat transport through a turbulent boundary layer.

The higher wall temperatures permissible in experiments with porous tungsten constrictors allow a substantial reduction of the mass flow rate. As a consequence, the conditions for laminar flow inside the tube are approached, and for a current of 80 amp, the experimental curve indeed approaches the theoretical prediction, see Fig. 10.

Several diagnostic measurements have been performed, including a qualitative measurement of the degree of turbulence by tracing the current and potential fluctuations with an oscilloscope. In addition, the velocity and temperature distribution in the arc and in the jet have been measured using an enthalpy probe and/or by spectrometric methods. The results of these measurements corroborate the conclusions from the heat flux characteristics [9]

Errors and Limitations

Possible errors in the experimental results may be attributed to three sources:

1 Uncertainties of the constrictor wall properties.
2 Errors in the measurement.
3 Discrepancy between the assumptions made for the data reduction and the actual conditions in the experiment.

The discrepancy between the theory predicting the arc performance which is described elsewhere [7–9] and the experiment is not caused by experimental errors but rather by a fundamental discrepancy in the assumptions. The theoretical treatment is, for example, based on laminar flow, a condition which in general could not be met in the experiments.

The influence of an error in the thermal conductivity on the calculated temperature profile in the tube wall is displayed in Fig. 11. A difference of 10 percent in the value of the thermal conductivity changes the calculated value for the inside wall temperature for a specified outside wall temperature approximately by 10 percent, whereas the temperature change of the tungsten tube wall is negligible. The influence of erroneous flow constants is less strong in experiments with ALSIMAG tubes. Allowing an error of 10 percent in the value for α and 20 percent error in the value for β results in the most unfavorable case in an 8 percent error of the values for the inside wall temperature as well as for the mass flow rate. For tungsten tubes the error interval of the flow constants is much larger due to poor reproducibility of individual measurements of these constants using the same tube (10 to 15 percent) and due to occasional small leaks in the seals between the segments. In addition, the tungsten segments seem to "age" when utilized for several runs. These errors are transposed to considerable errors in the calculated mass flow rates and hence in the wall heat fluxes. The influence of these errors on the temperature profile is negligible.

From the experimental data which enter the calculation of the mass flow rate and the inside wall temperature, only the value of the outside wall temperature of the ALSIMAG tube may be burdened with a significant error. An absolute error of 1 deg results in considerable errors (>50 deg C) in the calculated values for the inside wall temperature when the difference between outside wall temperature and gas-supply temperature is 15 deg C or less. This difference is reached in experiments with high wall heat fluxes and correspondingly high mass flow rates, where temperature gradients of approximately 270 deg C/mm prevail in the tube wall.

It is easily verified that assumptions 3 and 5 in the section Basic Considerations hold in the temperature range of interest (< 1500 deg K for ALSIMAG tubes and < 2000 deg K for tungsten tubes). In the case of ALSIMAG tubes a variation of at least 8 percent in the thermal conductivity prevails according to the scatter of the data for various tubes. Nonuniformities of the permeability are negligible for the surface area over which the energy balance is taken. According to [11], an area of 0.5 cm^2 only reaches the average permeability of the entire tube. Deviations from the average thermal conductivity have very little influence in experiments with tungsten constrictors. However, frequent use of the same segments may cause strong variations between their permeabilities leading to erroneous numbers for the transpirant mass flow rate and the heat flux to the inside wall.

Deviations from axis-symmetry have been frequently experienced in the experiments with the ALSIMAG tube, mainly due to asymmetric electrode attachment of the arc. Utilization of a new anode design and proper experimental procedure eliminated its influence almost entirely.

Conclusions

The theoretically predicted performance of a transpiration-cooled arc hinges on the existence of laminar flow in the constrictor tube. This situation, however, has been approached experimentally for a rather restricted parameter range only, namely for relatively low input-power levels. There are two avenues along which a desirable extension of this parameter range appears promising:

1 Reduction of the transpirant mass flow rate is possible if a more uniform axial temperature distribution can be achieved and/or if higher wall temperatures are permissible.

2 Utilization of a working fluid with a higher specific heat producing less volumetric radiation. Nitrogen and hydrogen for example fulfill this requirement.

Although the utilization of ceramic constrictor tubes offers some technological advantages, the poor control of the inside wall temperature restricts their usefulness to lower input-power levels. With porous tungsten constrictor tubes this limitation does not exist, provided that axial heat losses can be reduced and that sufficient control of the local transpirant mass flow rate can be achieved. This requires a segmentation of the plenum chamber which, however, adds significantly to the complexity of the apparatus.

References

1 Oberth, H., *Methods of Space Travel*, Oldenberg, München, 1929.

2 Moore, N. P. W., and Grootenhuis, P., United Kingdom Patent 619634, 1946.

3 Pfender, E., Raithby, G. D., and Eckert, E. R. G., "An Anode Comparison Study in a Wall-Stabilized Argon Arc," ARL 65-232, Nov. 1965.

4 Tannen, P. D., "Experimental Study of a Transpiration-Cooled Wall-Stabilized D.C. Electric Arc," GA/ME/62-6, Air Force Institute of Technology, WPAFB, Ohio, Aug. 1962.

5 Baran, M. F., "An Experimental and Theoretical Study of the Wall-Stabilized, Transpiration-Cooled, D.C. Electric Arc," Air Force Institute of Technology, WPAFB, Ohio, Phys/63-2, Aug. 1963.

6 Jones, R. N., "An Investigation of the Wall-Stabilized, Transpiration-Cooled D.C. Electric Arc," Air Force Institute of Technology, WPAFB, Ohio, GAW/Mech 64-11, June 1964.

7 Anderson, J. E., "Transpiration Cooling of a Constricted Electric Arc Heater," ARL 66-0517, Aug. 1966.

8 Anderson, J. E., and Eckert, E. R. G., "Transpiration-Cooling of a Constricted Electric Arc Heater," *AIAA Journal*, Vol. 5, April 1967, p. 699.

9 Heberlein, J., Pfender, E., and Eckert, E. R. G., "Study of a Transpiration-Cooled, Constricted Arc," ARL 70-0007, Jan. 1970.

10 Druzhinin, S. A., "On the Calculation of Internal Heat Exchange During Porous Cooling," *Teploenergetika*, No. 9, Sept. 1961, p. 73.

11 Gruber, G. G., Pfender, E., and Eckert, E. R. G., "Experimental Study of a Transpiration-Cooled Constricted Arc," ARL 68-0023, Feb. 1968.

12 Willgohs, Ralph H., *The Temperature Distribution in the Porous Constrictor Wall of a Transpiration-Cooled Electric Arc*, MS thesis, University of Minnesota, June 1968.

13 Marschall, E., and Gauger, U., "Berechnung des Temperaturverlaufes in einer transpirationsgekühlten Rohrwand," *Wärme- und Stoffübertragung*, Vol. 2, 1968, p. 203.

14 Forchheimer, P., *Hydraulik*, Leipzig, 1914.

15 Scheidegger, A. E., *The Physics of Flow Through Porous Media*, Macmillan, New York, 1957.

16 Chiou, J. P., and El-Wakil, M. M., "Heat Transfer and Flow Characteristics of Porous Matrixes With Radiation as a Heat Source," JOURNAL OF HEAT TRANSFER, TRANS. ASME, Series C, Vol. 88, No. 1, Feb. 1966, pp. 69–76.

17 Green, L., and Duwez, P., "Fluid Flow Through Porous Metals," ASME Paper No. 50-SA-17, 1950.

18 Greenberg, D. B., and Weger, E., "An Investigation of Viscous and Inertia Coefficients for the Flow of Gases Through Porous Sintered Metals with High Pressure Gradients," *Chemical Engineering Science*, Vol. 12, 1960, p. 8.

H. TONG
Assistant Professor.

W. H. GIEDT
Professor.
Mem. ASME

Department of Mechanical Engineering,
University of California,
Davis, Calif.

Depth of Penetration During Electron Beam Welding[1]

An examination of available solutions for the penetration depth for electron beam welding revealed that they have been based on mathematical models which are not truly representative of the physical phenomena. The deposition of electron beam energy has been represented by a steady line source. Experimental evidence, however, shows that due to an oscillating flow of the molten material, the electron beam energy is deposited on a surface which varies from close to horizontal to the sides of a cone-shaped cavity. To account for this a cylindrical constant temperature boundary condition was proposed. Results based on this model were found to agree within 20 percent with available depth of penetration data.

Introduction

Electron beam welding has progressed from the specialty stage to where it is now a useful mass production technique [1].[2] This advance can be attributed to the development of electron beams with higher power levels and an acceptable degree of weld reproducibility. Electron beam parameters required to produce a given weld are generally determined empirically, although performance characteristics vary from machine to machine. One of the most important properties of a weld is the depth of penetration. Analytical methods used to predict this have been based on a line heat source [2, 3], which should be a reasonable procedure if a steady-state cavity is formed in the path of the electron beam. Experimental evidence [4], however, shows that the cavity under some conditions oscillates with time and that this oscillation accounts for welding defects such as spikes, base porosity, and cracks or cold shuts. The oscillation of the cavity causes the electron beam energy to be alternately deposited on the surface and along the cavity walls; as a consequence, the energy deposition alternates between essentially a surface-source representation and a line-source representation.

In reference [2], it was implicitly assumed that the heat conduction losses were the same in all directions from the source. To approximate the conduction loss, the temperature distribution was assumed to be given by a line source solution. As a boundary condition, the temperature at the cavity radius r_0 was taken to be the sublimation temperature of the material. Although the temperature distribution around a moving line source is not constant at a given radius, it was considered to be constant in order to simplify the analysis. This step eliminates the variation of temperature with angle around a moving line source. The temperature at r_0 is described as the sublimation temperature; values actually used, however, were above the triple point and should be referred to as the liquid metal temperature. The cavity radius

Nomenclature

a = cavity radius
A = parameter = $Ua/2\alpha$
c_p = specific heat capacity
$DV(\theta, A) = \dfrac{\partial}{\partial \bar{r}} \left(\dfrac{v}{V_0}\right)\Big|_{\bar{r}=1}$
E = beam voltage
g = gravitational constant
h = depth of penetration
H_{sf} = heat of fusion
I = beam current
I_n = modified Bessel function of the first kind
k = thermal conductivity
K_n = modified Bessel function of the second kind
p = pressure
p_v = vapor pressure
q = heat flux
Q = heat transfer rate
r = radial distance
$\bar{r}$ = r/a
t = time
T = temperature
T_m = equilibrium melting temperature
T_s = surface tension
T_n = melt surface temperature
U = welding speed
V = volume
$\dot{V}$ = volume flow rate
$V_0 = T_m - T_\infty$
x, y, z = coordinates
α = thermal diffusivity
ϵ = fraction of EB energy
θ = angle
ρ = density
ϕ = beam diameter defined in reference [3]

---

[1] The support of the Lawrence Radiation Laboratory at Livermore, Calif., is gratefully acknowledged.

[2] Numbers in brackets designate References at end of paper.

Contributed by the Heat Transfer Division and presented at the Winter Annual Meeting, New York, N. Y., November 29–December 3, 1970, of The American Society of Mechanical Engineers. Manuscript received by the Heat Transfer Division November 3, 1969; revised manuscript received April 2, 1970. Paper No. 70-WA/HT-2.

was determined from a semiempirical relation. The results of this analysis predict, at best, the correct order of magnitude for the penetration depth. However, the validity of some of the assumptions made is open to question, and the agreement achieved with observations may be due to compensating effects.

Reference [3] also used the implicit assumption that conduction losses were independent of direction but used a different source solution. The analysis is inconsistent in that a wedge-shaped weld profile is assumed for the energy balance, but the temperature gradient at the edge of the molten zone is evaluated at a distance from the source which is independent of depth. Even so, for some welding conditions this solution agrees well with data subsequently taken by the authors of reference [3].

A search for a more representative heat transfer model led to the investigation of a constant temperature boundary condition which would be applicable to both the steady and the oscillating cavity cases. The model which was formulated does not depend on the assumption of a heat source and includes the directional variation of heat flux.

Analytical Model

The two extreme states of an oscillating electron beam cavity are shown in Fig. 1: in (*a*) the cavity is at its maximum depth and in (*b*) the cavity is at its minimum depth. The observed oscillation rate of the cavity is of the order of 10–100 cycles per second. The times available per cycle are thus much too short for the molten metal to solidify. Therefore, although the cavity shape changes dramatically the melt–solid interface, as represented by Fig. 1, fluctuates only slightly. The analysis will be applied to welds with large depth-to-width ratios so that depthwise heat transfer will be negligibly small. In addition, earlier reported studies have shown that radiation and evaporation energy [2, 5] losses are small, so they will be omitted from the analysis.

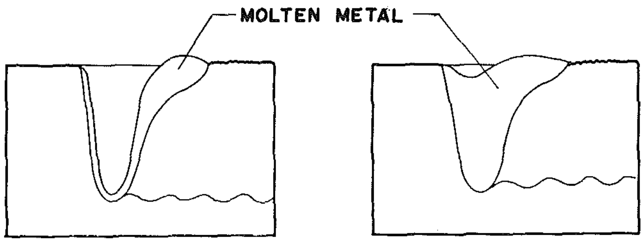

(a) (b)

Fig. 1 Oscillation of electron beam welding cavity

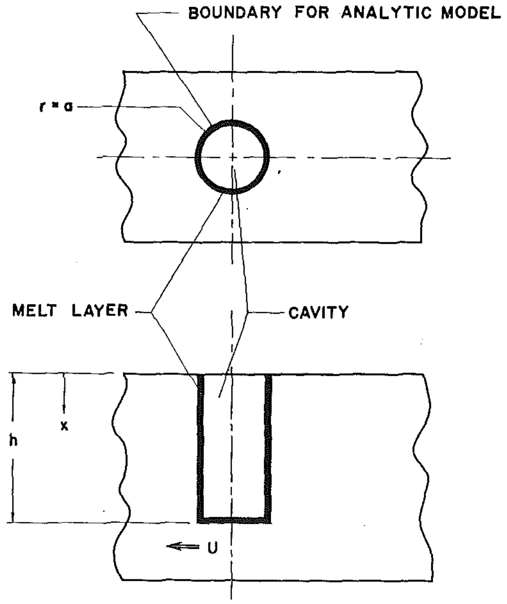

Fig. 2 Constant temperature boundary heat transfer model

To describe the model adopted for analysis, consider a constant temperature cylindrical boundary moving at a speed U as shown in Fig. 2. An actual weld zone will not have a circular boundary at its rear face but will instead contain an elongated molten zone. This rear-face boundary is rather ill-defined and depends to a large extent on the welding conditions. To circumvent this difficulty, only the forward half of the cylinder will be considered as a control volume and only a portion of the total electron beam energy will be incident on this control volume. Since the depthwise heat transfer will be very small, the problem is then reduced to a two-dimensional problem with energy transfer to and from a half-cylinder of radius a and depth h, as shown in Fig. 3. Then, since the thermal gradients at the rear face of this control volume will in general be very small, conservation of energy yields

$$E_{\text{in}} = Q_{\text{convection}} + Q_{\text{conduction}} \qquad (1)$$

The volume flow rate in the front face and out the back face is

$$\dot{V} = 2Uah$$

The enthalpy of the material will be taken to be c_pT, and the average temperature of the melt will be $(T_m + T_n)/2$. Then the net convected energy, per unit volume, out of the control volume is given by

$$\rho c_p\left(\frac{T_n - T_m}{2}\right) + \rho H_{sf}$$

The energy input will be some fraction ϵ of the electron beam power, that is

$$E_{\text{in}} = \epsilon\,\frac{EI}{4.186}$$

and ϵ will be shown to be approximately $^1/_2$. Equation (1) can then be written as

$$\frac{\epsilon}{4.186}\,EI = 2\rho Uah\left[\frac{c_p}{2}\,(T_n - T_m) + H_{sf}\right] + Q_{\text{conduction}} \qquad (2)$$

For two-dimensional radial heat conduction

$$\begin{aligned} Q_{\text{conduction}} &= h\left[2\int_0^{\frac{\pi}{2}} q(\theta)(a\,d\theta)\right] \\ &= -2ah\int_0^{\frac{\pi}{2}} k\left[\frac{\partial T}{\partial r}\,(\theta)\right]_{r=a} d\theta \end{aligned} \qquad (3)$$

A good approximation to the integral can be obtained by first solving the heat conduction problem for a constant temperature cylinder moving in a direction perpendicular to its axis. It can

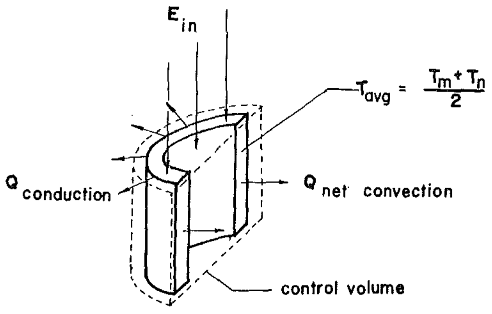

Fig. 3 Heat transfer model

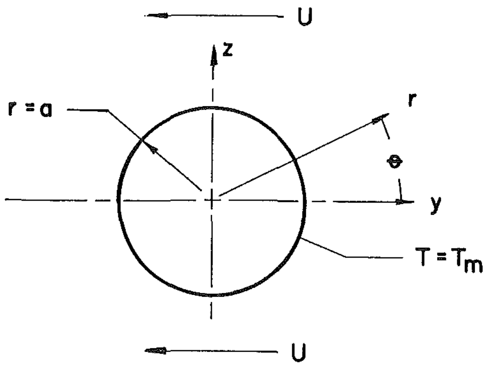

Fig. 4 Coordinate system

be imagined that material is being removed from the forward face of the cylinder and deposited at the rear face at a rate determined by the welding speed. The axis of the cylinder will be used as the origin of the coordinate system which is shown in Fig. 4. With $v = (T_m - T)$ and $V_0 = (T_m - T_\infty)$, the differential equation governing the conduction process becomes

$$\frac{\partial^2 v}{\partial y^2} + \frac{\partial^2 v}{\partial z^2} + \frac{U}{\alpha}\frac{\partial v}{\partial y} = \frac{1}{\alpha}\frac{\partial v}{\partial t}$$

The solution of the above time-dependent equation is obtained in reference [6] (p. 390) by the use of Laplace transform methods. For the steady-state case (i.e., for $t \to \infty$) the temperature distribution is given by the series solution

$$\frac{v(\theta, A)}{V_0} = 1 - e^{-A\bar{r}\cos\theta} \sum_{n=0}^{\infty} \xi_n \frac{I_n(A)}{K_n(A)} K_n(A\bar{r}) \cos n\theta \quad (4)$$

in which $A = Ua/2\alpha$.

The gradient at $\bar{r} = 1$ is given by

$$\begin{aligned} DV(\theta, A) &\equiv \left[\frac{\partial}{\partial \bar{r}}\left(\frac{v}{V_0}\right)\right]_{\bar{r}=1} \\ &= A\left\{\cos\theta + e^{-A\cos\theta}\left[\sum_{n=0}^{\infty} \xi_n \cos n\theta \right.\right. \\ &\quad \left.\left. \times \left(-\frac{I_{n-1}(A) + I_{n+1}(A)}{2} + \frac{1}{AK_n(A)}\right)\right]\right\} \quad (5) \end{aligned}$$

where $\xi_n = 1$ for $n = 0$ and $\xi_n = 2$ for $n \geq 1$.

Equation (2) can then be written as

$$\begin{aligned} Q_{\text{conduction}} &= 2ah \int_0^{\frac{\pi}{2}} -\frac{k(T_m - T_\infty)}{a} DV(\theta, A)d\theta \\ &= hk(T_m - T_\infty) \int_0^{\frac{\pi}{2}} 2DV(\theta, A)d\theta \end{aligned} \quad (6)$$

for constant or average properties. Substituting this into equation (2) and rearranging yields

$$\begin{aligned} \frac{4.186h}{\epsilon(EI)} = \Bigg\{ & A\left[2k(T_n - T_m) + 4\rho\alpha H_{sf}\right] \\ & + k(T_m - T_\infty)\left[\int_0^{\frac{\pi}{2}} 2DV(\theta, A)d\theta\right]\Bigg\}^{-1} \end{aligned} \quad (7)$$

The right-hand side is a function of the material properties and the parameter A, whereas the left-hand side is a ratio of the weld depth to the beam power. The definite integral can be evaluated numerically; the results are shown graphically in Fig. 5.

For any given material with known property values, equation (7) has the functional form

$$\frac{4.186h}{\epsilon(EI)} = f(A) = f(Ua) \quad (8)$$

From equation (7) it is apparent that the ratio of penetration depth to beam power is very dependent on the thermal properties of the material being welded. In addition, the surface temperature of the melt layer must be approximated. A first-order estimate would be to assume that the surface temperature is the same as the melting temperature of the material, i.e., $T_n = T_m$. Then equation (7) reduces to

$$\frac{4.186h}{\epsilon(EI)} \approx \left\{k(T_m - T_\infty)\left[\int_0^{\frac{\pi}{2}} 2DV(\theta, A)d\theta\right] + (4\rho\alpha H_{sf})A\right\}^{-1} \quad (9)$$

Because of the foregoing assumption, the penetration depth predicted by equation (9) will be greater than that predicted by equation (7).

An improved solution can be obtained by assuming that the melt surface temperature is constant and is represented by the temperature at the base of the cavity. This temperature can be calculated from a cavity oscillation analysis. However, this is a lengthy procedure and unnecessary for someone interested only in the depth of penetration.

A sufficient approximation for T_n can be obtained from the

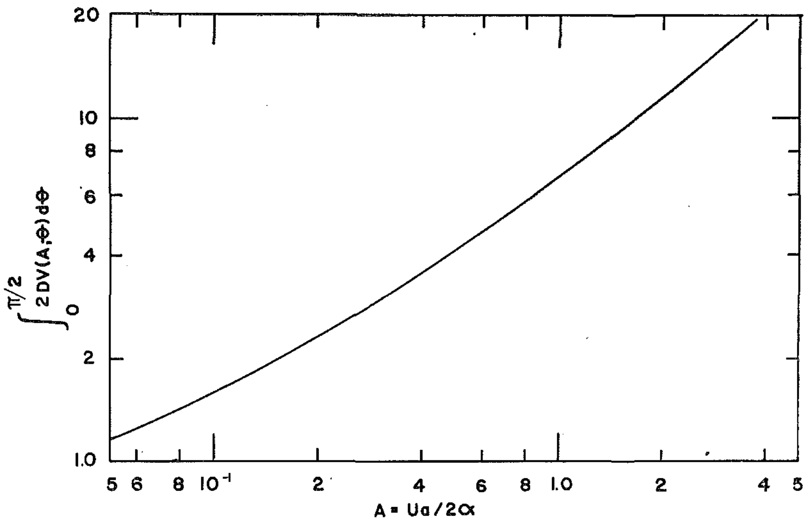

Fig. 5 Forward heat conduction parameter

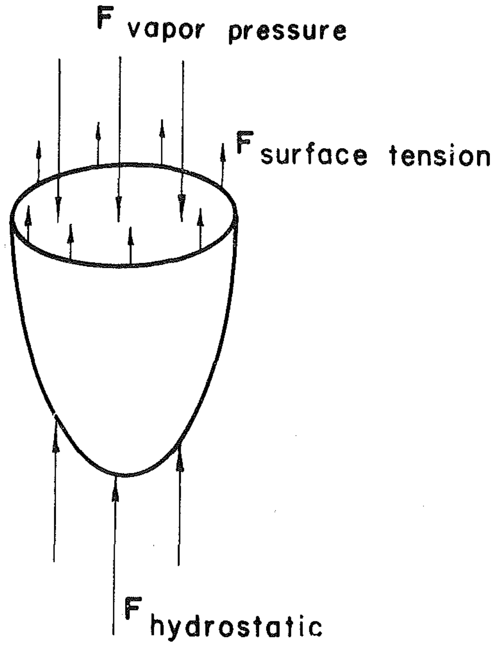

Fig. 6 Principle forces acting on cavity

forces on the molten fluid as shown in Fig. 6. For a cavity radius equal to a, the forces can be written as

$$F_{\text{vapor pressure}} = p_v(\pi a^2)$$

$$F_{\text{surface tension}} = T_s(2\pi a)$$

$$F_{\text{hydrostatic}} = \rho g h(\pi a^2)$$

In order for the cavity to have penetrated to a depth h, it must be true that

$$F_{\text{vapor pressure}} \geq F_{\text{surface tension}} + F_{\text{hydrostatic}}$$

or

$$p_v \geq \frac{2T_s}{a} + \rho g h \tag{10}$$

The surface tension is available from published literature [7, 8] so that the vapor pressure can be calculated from equation (10). Then the surface temperature can be obtained from published vapor pressure data, such as reference [9].

Since the vapor pressure is a very strong function of temperature, or conversely, temperature is a very weak function of the vapor pressure, only a rough approximation of p_v is required. This can be achieved by neglecting the hydrostatic term in equation (10) and using the approximation

$$p_v \approx \frac{2T_s}{a} \tag{11}$$

For example, with a cavity radius of 0.05 cm,

$$p_{v_{\text{iron}}} \simeq 54 \text{ torr}$$

$$p_{v_{\text{aluminum}}} \simeq 25 \text{ torr}$$

These pressures correspond to the approximate surface temperatures,

$$T_{n_{\text{iron}}} \simeq 2360 \text{ deg C}$$

$$T_{n_{\text{aluminum}}} \simeq 1890 \text{ deg C}$$

The radius a will generally vary for different electron gun designs and possibly even for different welding conditions. In any event, it can be approximated by visual observation of the incandescent spot on, say, a tungsten target or by measuring the weld width from a post-weld macrosection. The depth of penetration can then be calculated from equation (7) for any given power and welding speed if ϵ is known. The value to be used for ϵ can at best be approximated to be only $^1/_2$ as follows:

For a well-formed axisymmetric EB, the beam current is distributed in a near-gaussian manner about its axis so that the maximum power concentration is on the axis and falls off rapidly as the distance from the axis increases. Consider the case for which a steady cavity exists. (This is most likely for large values of Ua and small values of h.) The point or region at which the cavity is at its maximum depth will be that point at which the vapor pressure is greatest. Since vapor pressure is a direct function of the surface temperature and surface temperature for a thin melt layer is, to a first approximation, dependent on the power concentration, it is concluded that the maximum depth of the cavity is on the axis of the EB. Thus, half the EB energy must then be deposited on the forward half of the cavity wall and half on the rear half.

For very small values of Ua there will be a very efficient mixing of the fluid due to the oscillations of the cavity, and, hence, on a time-averaged basis, the distribution of energy in the fluid will be approximately uniform. For the cylindrical model, as Ua approaches zero the temperature gradient on the boundary becomes independent of θ (but now a function of time), so that the energy loss by conduction is equal in the forward and rearward directions. Thus, again the EB energy deposition can be considered as evenly divided between the front half and the rear half of the cylinder. Therefore, it will be assumed that ϵ is $^1/_2$. Then for any combination of beam and welding parameters, the depth of penetration can be calculated from equation (7) by using the method of equation (11). Or, an optimistic approximation can be obtained from equation (9).

The preceding analysis assumed that the constant temperature boundary had a radius that was independent of depth. In a post-weld macrosection, the fusion zone, in this case, would have a thickness that is almost constant. In many cases, the fusion zone is observed to be wedge-shaped as shown in Fig. 7. This would suggest that the constant temperature boundary would be conical rather than cylindrical. For an infinitesimal depth dx of a conical boundary model, equation (7) can be written as

$$d(EI) = \frac{4.186dx}{\epsilon}\{A[2k(T_n - T_m) + 4\rho\alpha H_{sf}] + k(T_m - T_\infty)(\text{HFAREA})\} \tag{12}$$

where

$$\text{HFAREA} = \int_0^{\frac{\pi}{2}} 2DV(\theta, A)d\theta$$

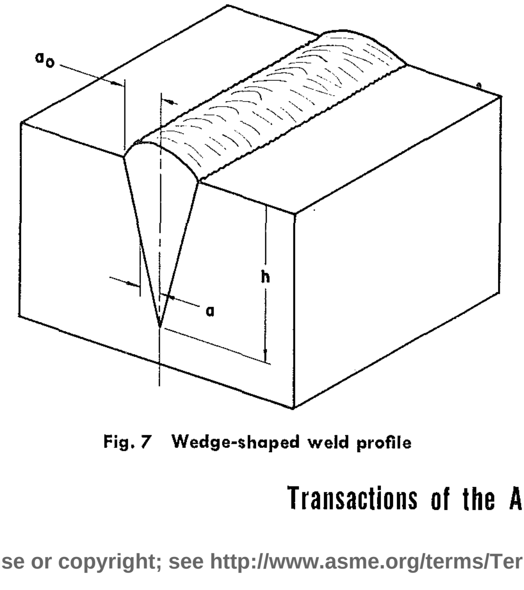

Fig. 7 Wedge-shaped weld profile

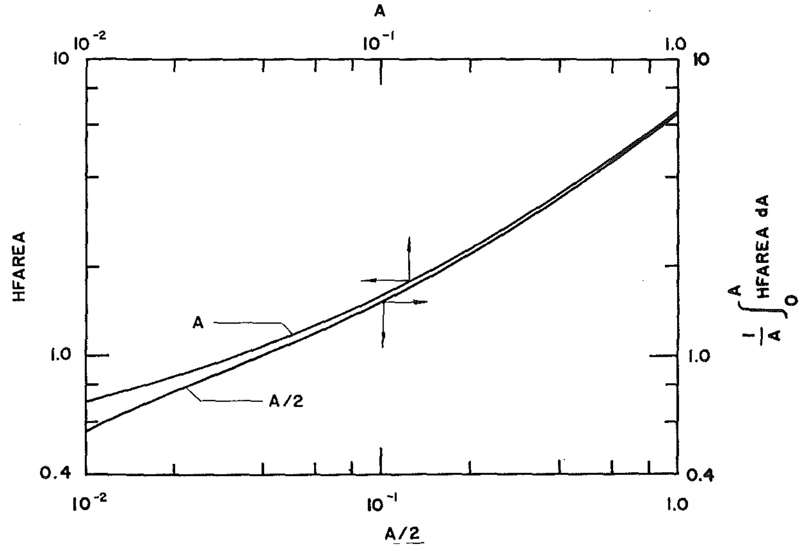

Fig. 8 Comparison of conduction loss for conical and uniform weld profiles

From Fig. 7, it is noted that

$$A = A_0\left(1 - \frac{x}{h}\right)$$

or

$$dx = -\frac{h}{A_0}\, dA$$

Then

$$d(EI) = \frac{4.186}{\epsilon}\left\{-\frac{h}{A_0}[2k(T_n - T_m) + 4\rho\alpha H_{sf}]A\,dA + k(T_m - T_\infty)\left(-\frac{h}{A_0}\right)(\text{HFAREA})dA\right\}$$

which after integration and some rearrangement yields

$$\left[\frac{4.186h}{\epsilon(EI)}\right]_w = \left\{\frac{A_0}{2}[2k(T_n - T_m) + 4\rho\alpha H_{sf}] + k(T_m - T_\infty)\left[\frac{1}{A_0}\int_0^{A_0}(\text{HFAREA})dA\right]\right\}^{-1} \quad (13)$$

To compare this with the result for a constant-thickness weld, equation (7) is expressed as

$$\left[\frac{4.186h}{\epsilon(EI)}\right]_c = \{A_c[2k(T_n - T_m) + 4\rho\alpha H_{sf}] + k(T_m - T_\infty)[\text{HFAREA}]\}^{-1} \quad (14)$$

Observation of equations (13) and (14) shows that if an average radius, $a_0/2$, is used for the thickness of the weld beam, the two equations are the same except for the last term in each. The error in calculating the depth of penetration of a conical-shaped weld using equation (14) can be assessed by comparing

$$(\text{HFAREA})|_{A_c} \text{ with } \frac{1}{A_0}\int_0^{A_0}(\text{HFAREA})dA\,|_{A_c=A_0/2}$$

where $A_c = Ua_c/2\alpha$ and a_c is an average constant weld thickness. The above integral was solved using a finite difference method; the solution is shown in Fig. 8 along with $(\text{HFAREA}|_{A_c}$.

$$(\text{HFAREA})|_{A_c} > \frac{1}{A_0}\int_0^{A_0}(\text{HFAREA})dA\,|_{A_c=A_0/2}$$

Equation (14) will predict a depth of penetration which is slightly less than would occur for a wedge-shaped weld profile. The relative percentage error between these two cases cannot be greater than the relative difference between the two curves shown in Fig. 8. This difference is observed to increase as A_c is decreased so that at $A_c = 0.01$, the difference is about 20 percent, whereas for $A = 0.1$, the difference is less than 6 percent. It is therefore concluded that, except for very small values of A_0, the error in calculating the depth of penetration for a wedge-shaped weld (using a constant cross section) is negligibly small if an average width is used for A_c.

Results

It is customary, in heat transfer calculations, to evaluate material properties at the mean temperature, which for this case is $(T_m - T_\infty)/2$. Using property values from references [7, 9, and 10], equation (7) was evaluated for a few representative materials, and the results are shown in Fig. 9. The surface tension and the vapor pressure–temperature relationship for the primary constituent was used since there is virtually no data for alloys. The curves were calculated for a uniform weld thickness of 0.10 cm and, as noted before, are also applicable for wedge-shaped weld profiles if the average thickness is used. For each of the materials in Fig. 9, calculations were also made for weld thickness between 0.06–0.20 cm. The greatest spread for these two thicknesses occurred for large values of Ua, which for the range shown in Fig. 10 was less than 5 percent. Thus for

$$0.03 \text{ cm} \leq a \leq 0.10 \text{ cm}$$

the use of equation (7) with $a = 0.05$ cm (or Fig. 10) will introduce a maximum error of about ±2 percent.

Comparison of Analyses With Experiments

A large amount of depth of penetration data along with ϕ, the EB spot diameter (as defined and measured in reference [5]), was presented in references [3 and 5]. In brief, the current distribution in the EB was measured and found to have a near-gaussian profile as represented in Fig. 10.

The dimension $2a$ used in the penetration analysis is more closely represented by a straight line extension of the steep sides of the distribution curve to the abscissa. From reference [3], $2a$ can be approximated as $\phi/2$.

The diameter $2a$ can also be approximated by visual measurements of the incandescent spot on, say, a slowly moving tungsten target. In general, $2a$ will depend on the electron beam gun design and focusing conditions (including gun-to-work distance) but can be readily approximated for any given machine.

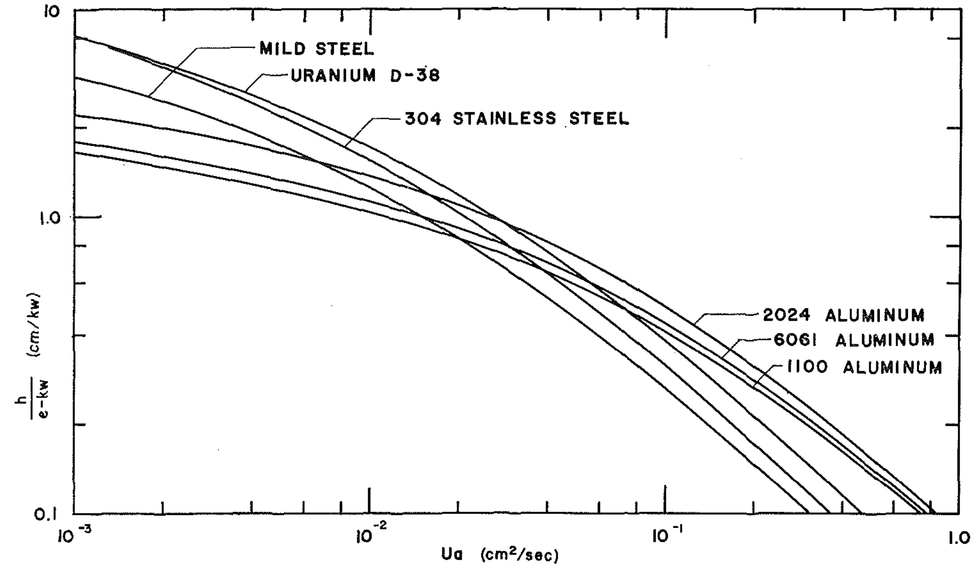

Fig. 9 Theoretical depth of penetration

In the reduction of the data from references [3 and 5] it was assumed that $2a = \phi/2$, and since deep welds or large depth-to-width ratios are a necessary part of the analysis leading to equation (7), all data with $\phi > 3$ mm were omitted. Further, for those tests in which ϕ was not given (reference [5]), it was assumed that $\phi = 2$ mm or $a = 0.05$ cm.

Comparisons of the foregoing experimental data with the theoretical curves from Fig. 10 are shown in Figs. 11–14 for type 304 stainless steel, low carbon steel, 1100 aluminum, and aluminum alloy. For the first three materials, the data are fairly consistent, and the bulk of the data lie in a ±20 percent band about the theoretical curve. For aluminum alloys, the data exhibit somewhat more scatter, but the theory still predicts the correct order of magnitude. The lack of consistency in the data and the inability of the theory to predict accurately may be due in part to the presence of alloying materials which have vapor pressure-temperature curves which are drastically different from the primary constituent. For instance, aluminum alloys 2024 and 6061 contain about 1 percent magnesium. At any given surface temperature magnesium has a vapor pressure which is about 5 orders of magnitude greater than aluminum. It is then very probable that small variation in the amount of magnesium present may have a very significant effect on the weld characteristics. In addition, the effect of an alloying agent on the surface tension is not known.

For stainless steels—chromium, iron, and nickel have vapor pressure-temperature relationships which are the same order of magnitude—and for low carbon steel and 1100 aluminum the impurities have vapor pressures which are substantially less than the primary component. Thus one might expect these three materials to behave more consistently.

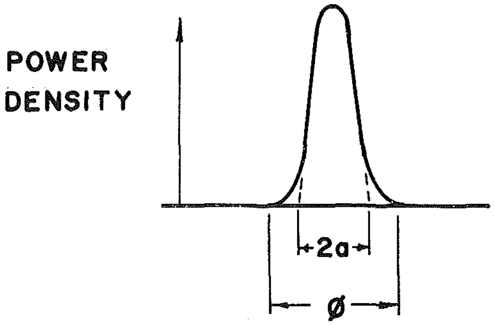

Fig. 10 Electron beam energy distribution

A direct comparison of the present analysis with that of references [3] or [5] can be made by noting that the latter solution can be written, in the present notation, as

$$h = \frac{1}{2.1}\,\frac{(EI)}{U\phi}\left[\frac{1}{\rho c_p T_m + \rho H_{sf}}\right]\left[\frac{1}{1 + 2.5k/\alpha + 5k/U\phi}\right] \quad (15)$$

Then for $\phi = 4a$, equation (15) can be expressed as

$$\frac{h}{(EI)} = \left\{2.1\left[\rho c_p T_m + \rho H_{sf}\right]\left[5k + 8(\alpha + 2.5k)\,\frac{Ua}{2\alpha}\right]\right\}^{-1} \quad (16)$$

Using the property values given on p. 32 of reference [5], equation (16) is plotted in Figs. 11–14 for comparison. For large values of Ua, the earlier solution and the present solution are in close agreement, but at smaller values of Ua, the present solution represents the data more closely.

From equation (16) it is noted that, as Ua approaches zero, $h/(EI)$ approaches a constant. Mathematically, this implies that if a and EI are held constant as U approaches zero (or U constant as a approaches zero), the depth h has a finite limit. This result is contrary to physical reasoning. Consequently, equation (16), although acceptable for values of Ua greater than, say, 0.1 cm²/sec, would be expected to be seriously in error for small values of Ua.

It will be stated without proof that as Ua approaches zero, equation (7) becomes

$$\frac{4.186h}{\epsilon(EI)} \approx \frac{\ln\left(\dfrac{4\alpha}{Ua}\right) - 0.577}{\pi k(T_m - T_\infty)} \quad (17)$$

which approaches infinity as Ua approaches zero. This is the trend that should be indicated for this limiting condition.

The penetration analysis was also compared with the experimental correlations reported by Engquist [11]. No information was given regarding the beam size, but a comparison of Engquist's results with Hashimoto's [5] data shows that for a given power, the penetrations reported by Engquist were greater than those of Hashimoto. Since both machines operated in the same voltage range, it can only be concluded that the effective beam size for Engquist's data must be smaller than for Hashimoto's data. Using an average beam radius of 0.035 cm, the present analysis was compared with typical correlation curves, and the

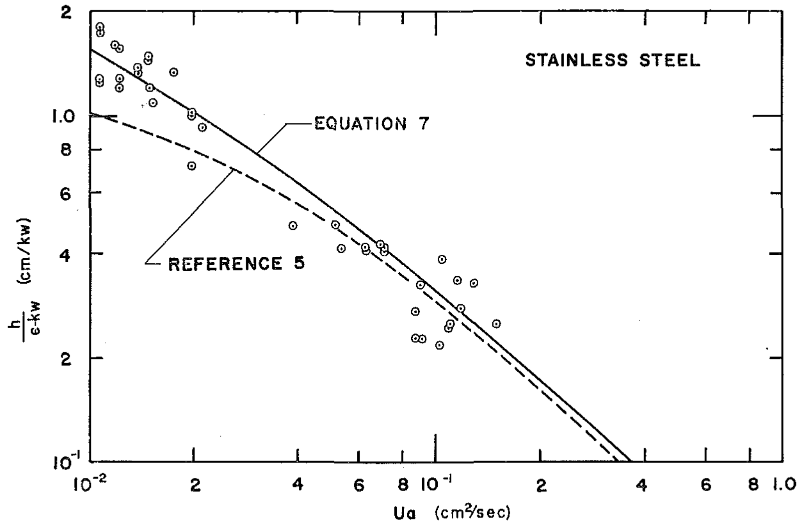

Fig. 11 Comparison of theory and experiment

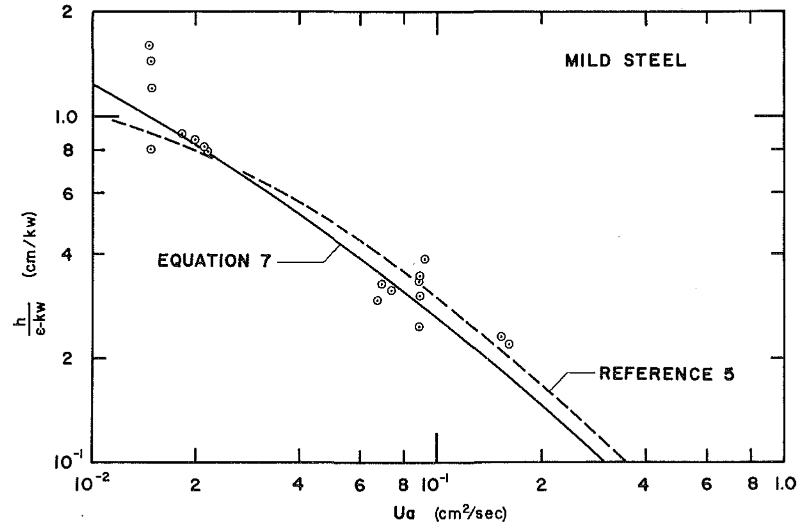

Fig. 12 Comparison of theory and experiment

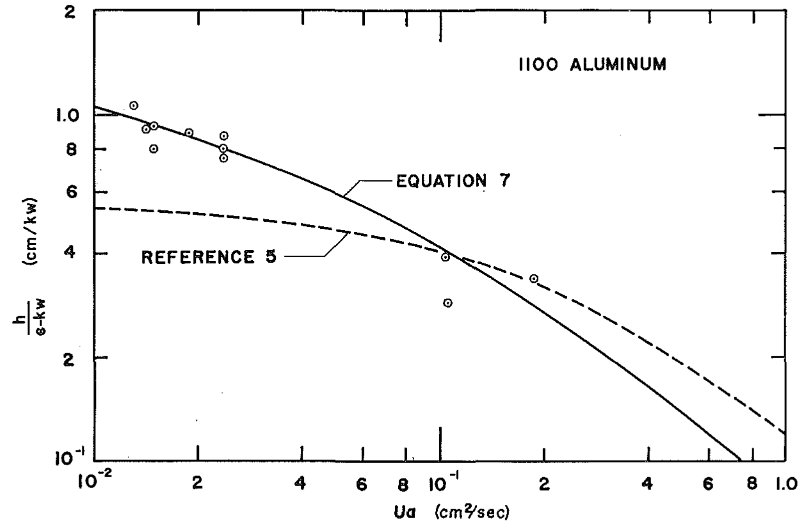

Fig. 13 Comparison of theory and experiment

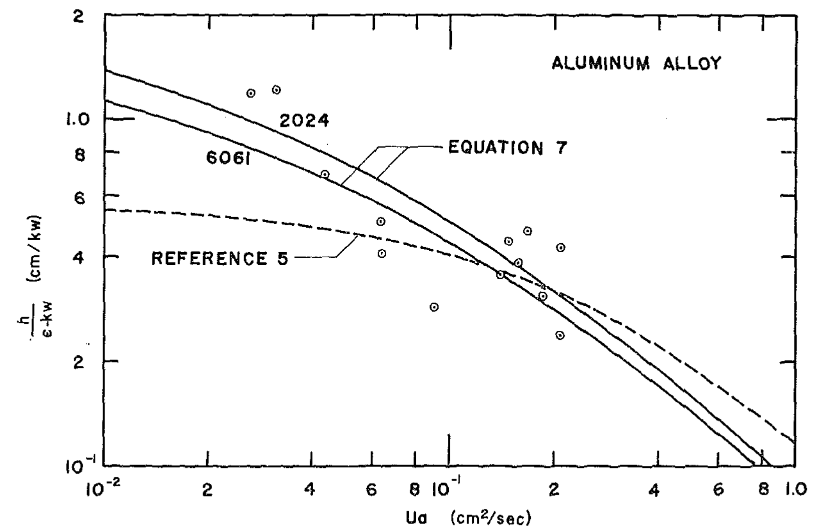

Fig. 14 Comparison of theory and experiment

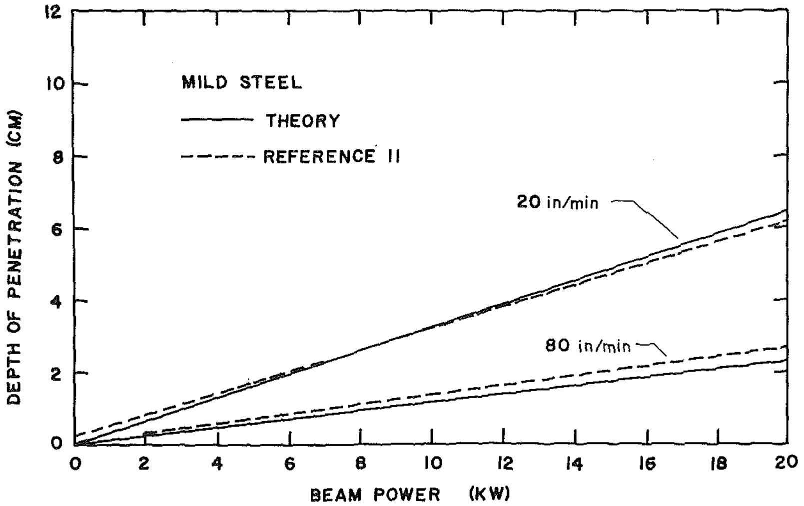

Fig. 15 Comparison of theory with correlation curves

results are shown in Figs. 15 and 16. For mild steels (Fig. 15) the theoretical curve lies within the 3σ error as given in reference [11]. For 6061 aluminum, the theoretical depth of penetration is about 25 percent less than the correlation curves as shown in Fig. 16.

It is apparent that any depth of penetration analysis must include a characteristic dimension such as ϕ or a. Accurate measurements of these characteristic dimensions are very difficult and time consuming. In general, for any given welding machine it is possible to approximate these dimensions after some experience and many trial welds, and in the main, one can be content with an average ϕ or a for all welding conditions. But at the extremes of very fast or very slow welding speeds, the effective value of the dimension might be expected to be quite different from the average value. Since changes in electron gun or welding distances may also have an influential effect on the characteristic dimensions, a simple, in situ, measurement would be highly desirable. A few approaches are being considered by independent investigators, and one would hope that this problem will be solved in the near future.

Conclusions

Due to the oscillation of the cavity, a representation of the electron beam energy as a line source was considered invalid. A new analytical solution for the depth of penetration was then developed using a constant melt-temperature interface as a boundary. This solution agrees within ±20 percent with available experimental data.

A comparison of the present solution with the line source solution of reference [5] shows good agreement except where the parameter Ua becomes very small. Under these conditions, the present analysis is in better agreement with available experimental data.

It is suggested that some of the inconsistencies associated with welds made with an electron beam are due to the presence of alloying materials which have vapor pressures which are many orders of magnitude greater than that of the primary constituent, for example, the presence of about 1 percent magnesium in 6061 and 2024 alloy aluminum.

References

1 Funk, E. R., *Electron Beam Welding Symposium*, Ohio State Univ., Columbus, Ohio, Nov. 1966, pp. 73–85, 119–133, 245–248.

2 Lupin, B. T., "A Correlation of Electron Beam Welding Parameters," ASME Paper 66-WA/MET-18.

3 Hashimoto, T., and Matsuda, F., "An Equation for Calculating Optimum Welding Conditions in Electron Beam Welding, "*Trans. National Research Institute for Metals*, Vol. 9, No. 1, Japan, 1967.

4 Tong, H., and Giedt, W. H., "Radiographs of the Electron

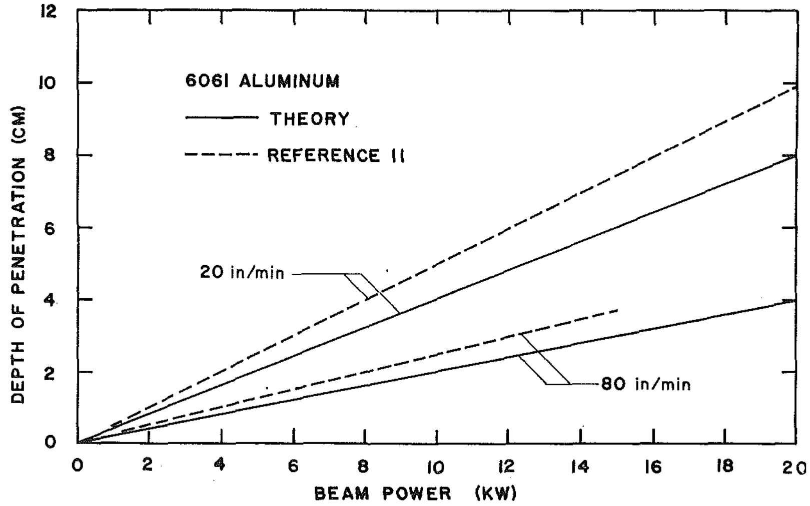

Fig. 16 Comparison of theory with correlation curves

Beam Welding Cavity," *Review of Scientific Instruments*, Vol. 40, No. 10, Oct. 1969, pp. 1283–1285.

5 Hashimoto, T., and Matsuda, F., "Effect of Welding Variables and Materials Upon Bead Shape in Electron-Beam Welding," *Trans. National Research Institute for Metals*, Vol. 7, No. 4, Japan, 1965.

6 Carslaw, H., and Jaeger, J. C., *Conduction of Heat in Solids*, Oxford Univ. Press, 1959.

7 Kohl, W. G., *Handbook of Materials and Techniques for Vacuum Devices*, Reinhold, New York, 1967.

8 Samsonov, G. V., *Handbook of the Physicochemical Properties of the Elements*, Plenum Press, New York, 1968.

9 Honig, R. E., "Vapor Pressure Data for the Solid and Liquid Elements," RCA Review, Vol. 23, Dec. 1962, pp. 567–586.

10 Goldsmith, A., et al., *Handbook of Thermophysical Properties of Solid Materials*, Macmillan, New York, 1961.

11 Engquist, R. D., "Parameters Affecting Electron Beam Welding," *Metals Engineering Quarterly*, Vol. 8, No. 4, Nov. 1968, pp. 56–63.

A. F. EMERY
Professor,
Department of Mechanical Engineering,
University of Washington,
Seattle, Wash.

H. W. CHI
Staff Scientist,
Gulf Atomic,
San Diego, Calif.

J. D. DALE[1]
Graduate Student,
Department of Mechanical Engineering,
University of Washington,
Seattle, Wash.

Free Convection Through Vertical Plane Layers of Non-Newtonian Power Law Fluids

Experimental measurements of the heat transferred from a constant heat flux hot wall across vertical plane layers of several pseudoplastic non-Newtonian fluids with generalized Prandtl numbers of 10–500 are reported for a range of Grashof moduli and layer height to width ratios. The rheological properties of the fluids are discussed and it is shown that the similarity analysis of free convection for constant-temperature vertical flat plates presented by Acrivos for infinite Prandtl numbers can be used to correlate the data. Several temperature profiles are given and compared to those measured in water.

Introduction

Recently, several investigators [1–5][2] presented measured data and numerically computed overall heat transfer and local field variables for the heat transferred from a vertical hot wall to a vertical cold wall through a two-dimensional layer of fluid, Fig. 1. These studies can now be said to define well the mode of heat transfer and to describe quantitatively the performance of both isothermal and constant heat flux hot walls for Newtonian fluids of Prandtl numbers from 1–20,000. Fig. 1 shows a compendium of recently reported data for both heated wall cases.

Although for practical purposes one might well state that this area of study is complete, there have yet been no reported studies which are concerned with a similar system filled with a non-Newtonian fluid. In fact the free convection from vertical heated surfaces to non-Newtonian fluids has been treated analytically in only a few papers [6–10] and experimentally in one work [11]. In this paper, we report some overall heat transfer measurements and local temperature and velocity field measurements for a vertical layer of pseudoplastic fluids. The study was prompted by the growing importance of non-Newtonian fluids in commercial applications and the desire to understand the effects of fluids which exhibit strong effective viscosity changes with changes in shear strain rates.

Description of Fluids Used

Fluids whose viscometric properties do not obey the linear shear stress-strain rate relationship for a two-dimensional flow

Nomenclature

c_p = specific heat capacity
C = constant of proportionality, equation (8b)
f = similarity variable
g = acceleration of gravity
Gr = Grashof modulus
h = film heat transfer coefficient
H = height
k = coefficient of thermal conductivity
L = length scale
m = fluid consistency
n = fluid flow index
Nu = Nusselt number
Pr = Prandtl number
q = wall heat flux
Ra = Rayleigh number
Re = Reynolds number
T = temperature
u, v = velocity components in the x, y directions
x, y = rectangular Cartesian coordinates, Fig. 1
β = coefficient of thermal expansion
$\dot{\gamma}$ = shear strain rate
ρ = density
θ = dimensionless temperature
τ, τ_y = shear stress, yield shear stress
μ = coefficient of dynamic viscosity
η = similarity variable

Subscripts

h = hot wall
c = cold wall
∞ = undisturbed fluid
H = based upon layer height
W = based upon layer width
y = yield

Superscripts

$\overline{}$ = average or nondimensional
$\wedge, *$ = generalized modulus

---

[1] Presently, Assistant Professor of Mechanical Engineering, University of Alberta, Edmonton, Alberta, Canada.

[2] Numbers in brackets designate References at end of paper.

Contributed by the Heat Transfer Division and presented at the Winter Annual Meeting, New York, N. Y., November 29–December 3, 1970 of The American Society of Mechanical Engineers. Manuscript received by the Heat Transfer Division May 12, 1969; final manuscript received January 21, 1970. Paper No. 70-WA/HT-1.

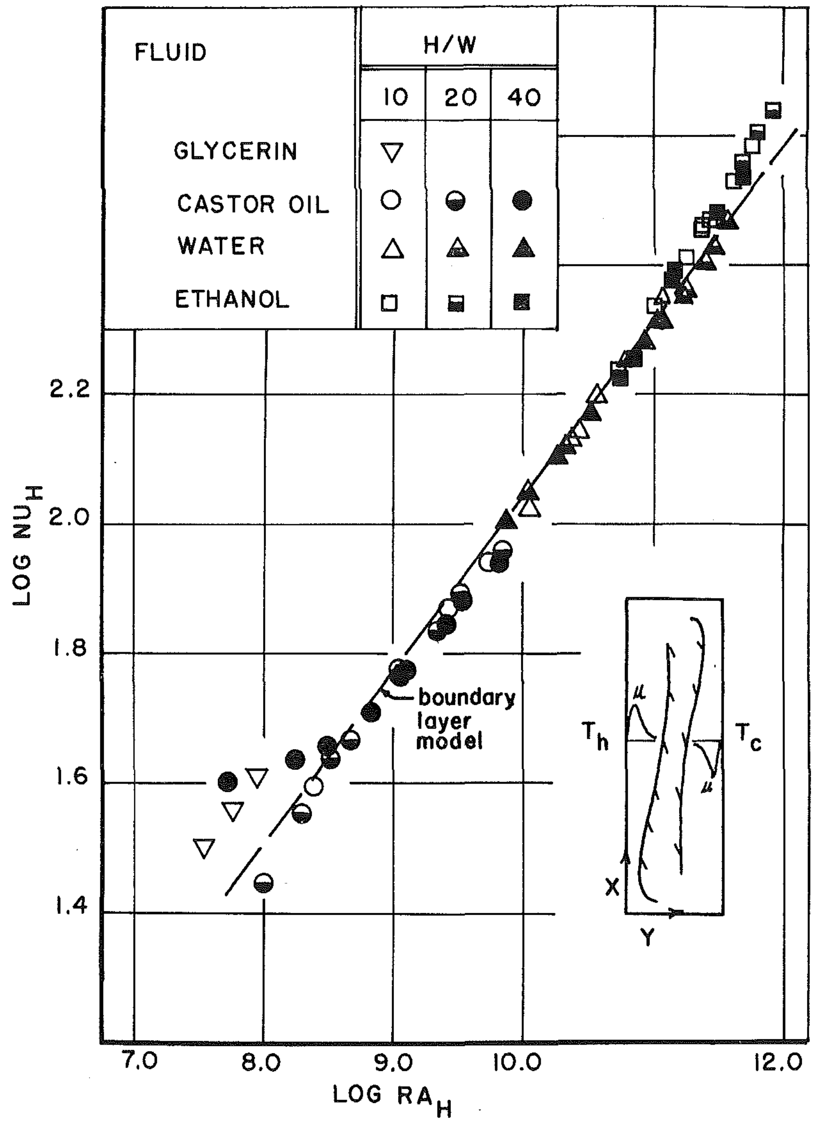

Fig. 1 Summary of Newtonian data and schematic of vertical enclosure (from reference [4])

$$\tau = \mu\dot{\gamma} \tag{1}$$

are usually classified as non-Newtonian fluids.

Although over long time periods, almost all non-Newtonian fluids are time-dependent and, for very short time scales, many are viscoelastic fluids, most commercially useful fluids can be described as time-independent over moderate time intervals. In addition, most of the time-independent fluids do not exhibit significant yield stresses (Bingham fluids) unless such a property is expressly desired (e.g., paint). Accordingly, this study was made using fluids with no yield stresses, except for one fluid tested. These so-called "pseudoplastic" and "dilatant" fluids can be described by the constitutive relationship

$$\tau = m(\dot{\gamma})^n = m|\dot{\gamma}|^{n-1}\dot{\gamma} \tag{2}$$

over a limited range of shear strain rates. The quantity $m|\dot{\gamma}|^{n-1}$ is called the apparent viscosity, m the fluid consistency, and n the fluid flow index. Pseudoplastic fluids exhibit decreasing apparent viscosity with increasing shear strain rates ($n < 1$) and dilatant fluids show increasing effective viscosities ($n > 1$). For this study, the fluids chosen were pseudoplastic in nature. Of course it must be recognized that the behavior characterized by equation (2) applies only over a limited range of $\dot{\gamma}$, and almost all non-Newtonian fluids tend toward Newtonian behavior as $\dot{\gamma}$ decreases to very small values (order of 0.01 $\sec^{-1}$), and in the non-Newtonian range, both m and n may be defined differently over different ranges of $\dot{\gamma}$. In fact, the power law fluids (those obeying equation (2)) are never really truly power law fluids, but if one is to characterize these fluids in order to establish flow and heat transfer correlations, some form of a rheological constitutive relationship must be assumed. Although a number of constitutive relationships have been introduced [12, 13], the most practical is that of Ostwald-deWaele [14]—the power law—and this is the only one to which we shall refer the fluid behavior exclusive of any yield stress.

The fluids used in these experiments were dilute aqueous solutions of sodium carboxymethylcellulose[3] (CMC) and carboxypolymethylene[4] (carbopol). The densities and specific heat capacity of the dilute solutions were assumed to be that of water in accordance with the work of Reilly [15] and St. Pierre [16]. However, since the molecular thermal conductivity is delicately related to the type and orientation of the high polymer macro molecules, the thermal conductivity was measured by the use of a comparative thermal conductivity bridge referenced to water of the type described by Grassman and Straumann [17]. The

---

[3] Hercules Incorporated, Type 7H35, Lot No. 59753.

[4] B. F. Goodrich Chemical Company, Type 934, Lot 4217, and Type 940, Lot No. 43965.

measured values agreed with those of St. Pierre and Reilly to within 5 percent. The viscometric behavior of the fluids was determined by using a Brookfield coaxial cylinder viscometer which was especially modified to yield accurate measurements over the range of shear straining rates of 0.08 sec^{-1} to 74 sec^{-1}. The temperature-dependent flow indexes (n) and fluid consistencies (m) for the two fluids are given in Figs. 2, 3, and 4, with some data reported by Reilly [15] and St. Pierre [16]. Because CMC and carbopol solutions are mixed from powders, and because they are sensitive to the mixing process, it is important that the rheological properties be determined for each sample. Fig. 3, which shows the carbopol results for 1.0 and 0.5 percent solutions (unneutralized), emphasizes this point. St. Pierre and Reilly, working with the same viscometer and at the same institution, but with different powder mixing techniques, show significantly different behaviors for both m and n, in magnitudes and in temperature dependencies. Whether the differences are due to the mixing processes or to possible differences in powder batches (the work encompassed a two-year period) is not known, but the differences do strongly emphasize the necessity for continual viscometric measurements.

The importance of careful mixing to answer a definite concentration is well illustrated by noting that the consistency of carbopol 934 increases an order of magnitude with a change of 0.05 percent in concentration and that a concentration of 0.05 percent carbopol 940 is an order of magnitude more viscous than 0.05 percent carbopol 934.

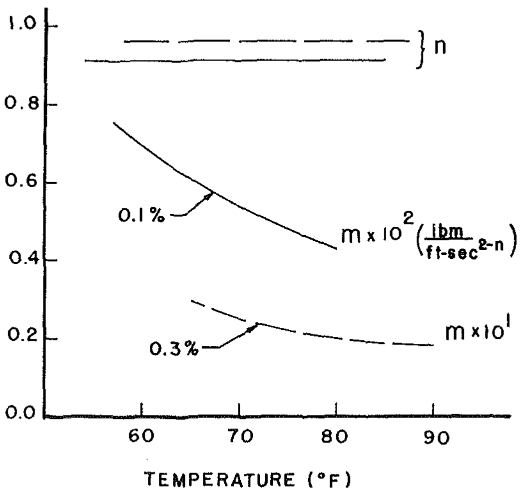

Fig. 4 Fluid consistency and flow index of CMC

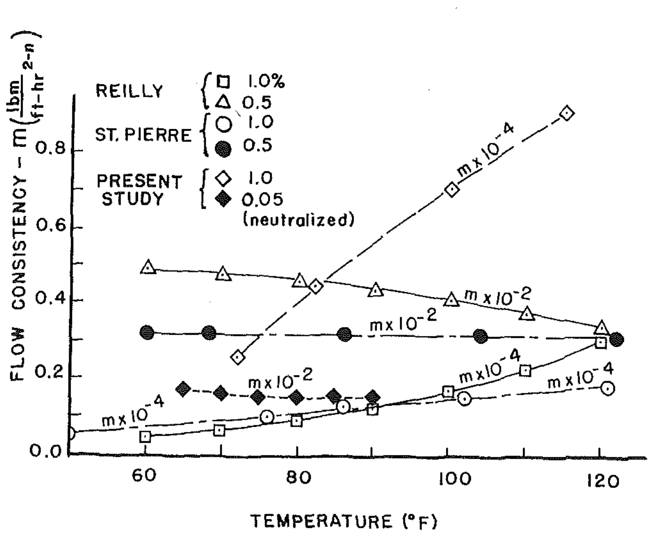

Fig. 2 Fluid consistency of carbopol 934

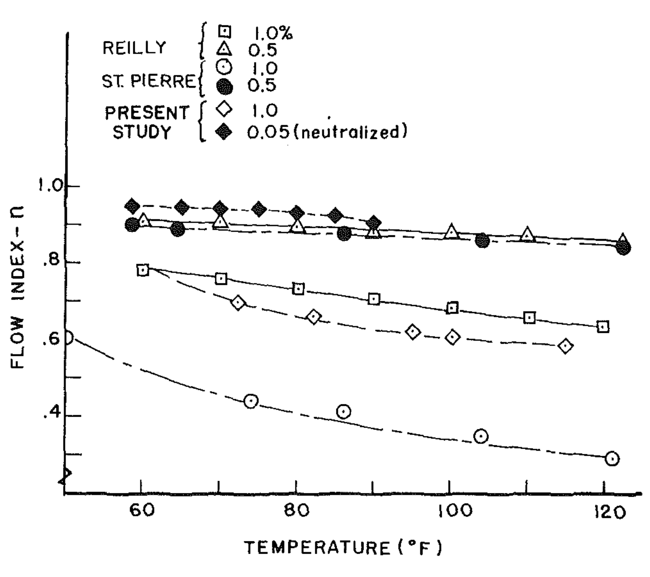

Fig. 3 Fluid-flow index of carbopol 934

Care must be exercised in interpreting flow consistency data because of the dependency of the shear stress upon the flow index n. For example, the curve for the 0.05 percent neutralized solution shows an increasing value of m with temperature, but because of the simultaneous decrease of n with temperature, the torque necessary to shear the fluid actually decreases and the fluid thins upon heating.

The unexpected increase of the consistency of the 1.0 percent carbopol solution with temperature found in this study occurred every time the sample was measured and was repeatable to within 5 percent over more than 10 tests. The consistency increased with temperature according to

$$m = m_0 e^{E/RT} \qquad E/R = -3530 \text{ deg K}$$

although the flow index, n, was quite constant with temperature. In contrast, the 0.05 and 0.07 percent carbopol solutions behaved as "normal pseudoplastic" fluid with E equal to the heat of evaporation of water [20].

The 0.06 percent neutralized carbopol was found to exhibit a yield stress although its value was so low ($\tau_y \simeq 0.02$ dynes/cm^2, $\dot{\gamma} \simeq 0.03$ sec^{-1}) that a precise resolution with the present viscometer was not possible. However, velocity profiles measured for free convection over a single flat plate showed no shear stresses which were less than this yield value in the outer portion of the fluid, thus substantiating this value. The 1.0 percent carbopol (934) unneutralized solution was observed to have a yield stress when aged and increased with both time and heating until jelling occurred.

Rheological Properties Changes

Both the CMC and the carbopol aqueous solutions showed significant aging effects which limited the experiments. Fig. 5 illustrates typical torque-time cures for CMC. Since the vertical layer requires 12–24 hr to achieve steady state, it is apparent that no tests can be confidently made within 20 days after mixing without considerable uncertainty about the fluid properties. (The carpobol time scale was of the order of five days.) Only by aging all solutions until their properties were invariant with time could reproducible data be secured.

One must be careful to distinguish between the properties of the original fluids and fluids which have experienced a history of heating and cooling. After the test cell had come to equilibrium with 0.06 percent carbopol 940, three 25-cc fluid samples were

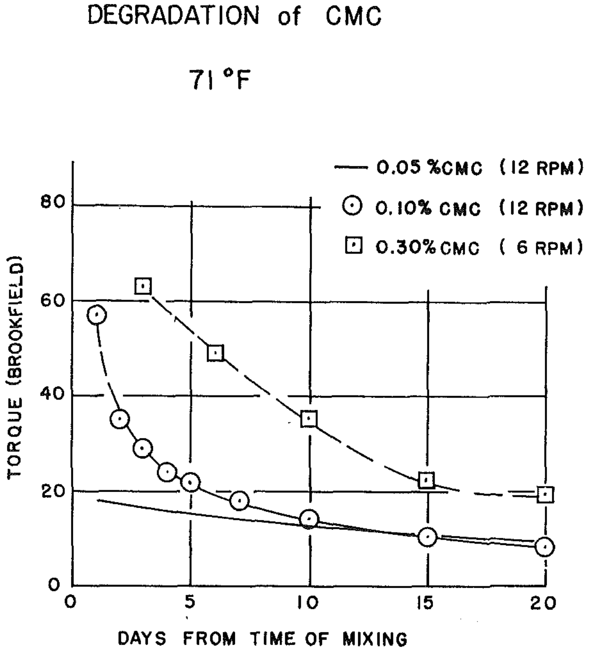

Fig. 5 Degradation of unused CMC with time after mixing

withdrawn: the first slowly, the second after a fast collection of 325 cc, and the third after the fast drawing of an additional 525 cc. Visual observations indicated that the first sample came from the quiescent fluid at the bottom of the layer, the second from a region near the edge of the boundary layer, and the third from the central core of fluid. Fig. 6 gives the viscometric characteristics of the sample and of the original fluid. Another sample of original fluid was heated to 80 deg F (the average fluid layer temperature) and continuously sheared for 24 hr at a shear rate approximately equal to the maximum in the layer, and no changes were observed. Apparently the changes illustrated in Fig. 6 are history-dependent effects. No correlation of the heat transfer data was possible unless the rheological properties of the core fluid were used in evaluating the Grashof and Prandtl moduli. This suggests that it is the shearing of the core fluid which determines the heat transfer performance of the fluid layer.

As noted previously, the 1.0 percent carbopol (940) would eventually jell regardless of its thermal-mechanical history. A series of exploratory tests revealed that (*a*) for all temperatures, jelling would always occur after sufficient time; (*b*) elevated temperatures accelerated the thickening; (*c*) mechanical stirring would partially reverse the jelling process; (*d*) the free convection motion in the fluid layer also retarded the jelling. Unfortunately we do not now know enough about the effects of the thermal-mechanical history to be able to predict the behavior of this fluid.

Heat Transfer Correlation

It has been previously shown by Emery and Chu [1] and MacGregor and Emery [4] that the overall heat transfer coefficient for fluids with $\mathrm{Pr} \geq 1.0$ in the vertical plane layer can be accurately predicted by considering that the flow resembles two boundary layers, one rising up the heated surface and the other falling down the cold surface. The thermal energy is assumed to be transported by the boundary layers and none is assumed to be conducted across the nearly quiescent fluid which fills the central core of the layer. The resulting correlation, using the single vertical flat plate heat transfer equations and taking T_∞ for both layers to be $(T_h + T_c)/2.0$, is for laminar flow

$$\mathrm{Nu}_w = \frac{hW}{k} = \frac{q}{(T_h - T_c)}\,\frac{W}{k} = 0.280\left(\frac{H}{W}\right)^{-1/4}\mathrm{Ra}_w{}^{1/4}$$

or (3)

$$\mathrm{Nu}_H = \frac{hH}{k} = 0.280(\mathrm{Ra}_H)^{1/4}$$

Because of the success of this correlation for Newtonian fluids, as illustrated in Fig. 1, it can be hypothesized that the behavior of non-Newtonian fluids in the layers might be based upon the single flat plate results of Acrivos [10]. However, because Acrivos' solution is valid for only constant-temperature surfaces, for fluids whose Prandtl number approaches infinity, and for fluids whose flow indexes and fluid consistencies are independent

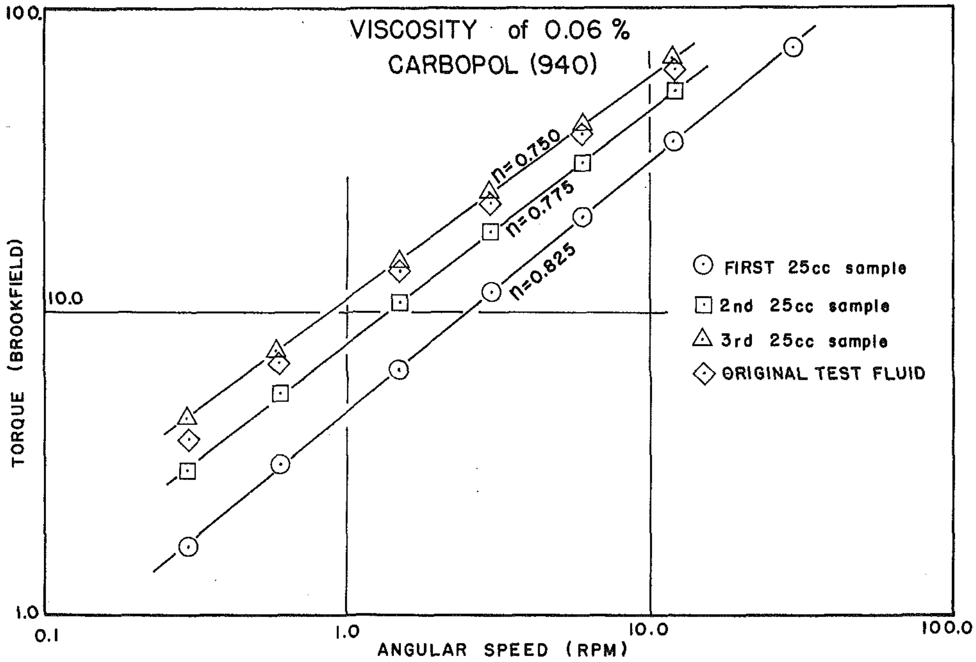

Fig. 6 Fluid characteristics of 0.06 percent carbopol in vertical enclosure

of temperature, the hypothesis must be tested experimentally.

The laminar boundary-layer equations for incompressible non-Newtonian power law fluids with constant properties and no viscous dissipation can be written by using the Boussinesq assumption as [10]

$$u\frac{\partial u}{\partial x} + v\frac{\partial u}{\partial y} = g\beta(T - T_\infty) + \frac{m}{\rho}\frac{\partial}{\partial y}\left\{\left|\frac{\partial u}{\partial y}\right|^{n-1}\frac{\partial u}{\partial y}\right\}$$

$$\frac{\partial u}{\partial x} + \frac{\partial v}{\partial y} = 0 \tag{4}$$

$$u\frac{\partial \theta}{\partial x} + v\frac{\partial \theta}{\partial y} = \frac{k}{\rho c_p}\frac{\partial^2 \theta}{\partial y^2}$$

where

$$\beta = \left(\frac{\rho_\infty}{\rho} - 1\right)\Big/(T - T_\infty)$$

By defining generalized Grashof and Prandtl numbers as

$$\hat{\mathrm{Gr}} = \left(\frac{\rho}{m}\right)^2 L^{n+2}\,[g\beta(T - T_\infty)]^{2-n}$$

$$\hat{\mathrm{Pr}} = \frac{\rho c_p}{k}\left(\frac{m}{\rho}\right)^{2/(1+n)} L^{(1-n)/(1+n)}[g\beta(T - T_\infty)]^{3(n-1)/2(1+n)} \tag{5}$$

and nondimensional coordinates and velocities as

$$\bar{y} = \frac{y}{L}\,\hat{\mathrm{Gr}}^{\frac{1}{2n+2}}\,\hat{\mathrm{Pr}}^{\frac{n}{3n+1}}$$

$$\bar{x} = x/L$$

$$\bar{u} = u\,\hat{\mathrm{Pr}}^{\frac{n+1}{3n+1}}\sqrt{g\beta L(T_w - T_\infty)} \tag{6}$$

$$\bar{v} = v\,\hat{\mathrm{Gr}}^{\frac{1}{2n+2}}\,\hat{\mathrm{Pr}}^{\frac{2n+1}{3n+1}}\sqrt{g\beta L(T_w - T_\infty)}$$

The boundary-layer equations reduce to

$$\frac{\partial}{\partial y}\left\{\frac{\partial \bar{u}}{\partial y}\left|\frac{\partial \bar{u}}{\partial y}\right|^{n-1}\right\} + \theta = \hat{\mathrm{Pr}}^{-\frac{2n+2}{3n+1}}\left\{\bar{u}\frac{\partial \bar{u}}{\partial x} + \bar{v}\frac{\partial \bar{u}}{\partial y}\right\}$$

$$\frac{\partial \bar{u}}{\partial x} + \frac{\partial \bar{v}}{\partial y} = 0 \tag{7}$$

$$\frac{\partial^2 \theta}{\partial y^2} = \bar{u}\frac{\partial \theta}{\partial x} + \bar{v}\frac{\partial \theta}{\partial y}$$

Both Acrivos [10] and Na and Hansen [8] have shown that no similar solutions exist for non-Newtonian power law fluids ($n \neq 1$) in free convection over vertical flat plates regardless of the wall thermal conditions unless the Prandtl number is infinite and then only for constant wall temperatures. Allowing $\hat{\mathrm{Pr}}$ to approach infinity, the following similar solution was given by Acrivos

$$\overline{\mathrm{Nu}} = C\,\hat{\mathrm{Gr}}^{\frac{1}{2n+2}}\,\hat{\mathrm{Pr}}^{\frac{n}{3n+1}} \tag{8a}$$

where

$$C = -\left(\frac{d\theta}{d\eta}\right)_{\eta=0}\cdot\left(\frac{3n+1}{2n+1}\right)^{\frac{2n+1}{3n+1}} \tag{8b}$$

and where θ is the solution to

$$\frac{d}{d\eta}(f'')^n + \theta = 0$$

$$\theta'' + f\theta' = 0 \tag{9}$$

with

$$\bar{u} = \left[\frac{3n+1}{2n+1}\,\bar{x}\right]^{\frac{n+1}{3n+1}} f'(n)$$

and the boundary conditions

$$\theta(0) = 1 \qquad \theta(\infty) = 0; \quad f'(0) = 0 \qquad f''(\infty) = 0$$

The numerical solution of equations (9) suggests that the average Nusselt number passes through a minimum near $n = 0.3$, although no experimental substantiation of the minimum has yet been reported. If the generalized Grashof and Prandtl moduli are rewritten in the forms which arise from the natural nondimensionalization of the governing equations, we find

$$\mathrm{Gr}^* = \frac{g\beta(T_w - T_\infty)L^{\frac{n+2}{2-n}}}{(m/\rho)^{2/2-n}}$$

$$\mathrm{Pr}^* = \rho\,\frac{c_p}{k}\left(\frac{m}{\rho}\right)^{\frac{1}{2-n}} L^{\frac{2n-2}{n-2}} \tag{10a}$$

which were suggested by Reilly, Tien, and Adelman [11]. Equation (8*a*) may then be written as

$$\overline{\mathrm{Nu}} = C(\mathrm{Gr}^*\,\mathrm{Pr}^{*n})^{\frac{1}{3n+1}} \tag{10b}$$

Following Emery and Chu [1] we assume that the temperature at the edge of both the hot and cold boundary layers can be approximated by

$$T = \frac{T_h + T_c}{2} \tag{11a}$$

and noting that

$$q_w = h_H(T_H - T) = h_w(T_H - T_c) \tag{11b}$$

we may rearrange equation (10*b*) to obtain

$$\mathrm{Nu}_H = \frac{C}{2}\,(\mathrm{Gr}_H^*\,\mathrm{Pr}_H^{*n})^{\frac{1}{3n+1}}$$

$$\overline{\mathrm{Nu}_w} = \frac{C}{2}\,(\mathrm{Gr}_w^*\,\mathrm{Pr}_w^{*n})^{\frac{1}{3n+1}}\left(\frac{H}{W}\right)^{\frac{-n}{3n+1}} \tag{12a}$$

It is worth noting that while the correlation reduces to the normal one for Newtonian fluids ($n = 1$), the results obtained by Acrivos and for the layer by using Acrivos' method are strictly valid only for fluids for which $\mathrm{Pr}^* = \infty$, constant fluid properties, and constant wall temperatures. Furthermore, although the length dimension appears in the product $\mathrm{Gr}^*\,\mathrm{Pr}^{*n}$, it also appears separately in each modulus, thus leading to a situation where the velocities and temperature depend upon a fluid parameter which is size-dependent. Since we report here only overall heat transfer measurements which depend upon the product, the correctness of the inclusion of a length scale and the precise nature of this scale is not determinable. Because these analytical results apply only to fluids whose Prandtl numbers approach infinity and because of the basic tenets of the boundary-layer model, this correlation form must be tested experimentally.

Experimental Measurements

Fluid layers with aspect ratios of 10, 20, and 40 were cooled by an isothermal vertical surface and heated by an electrically heated hot wall. The heat losses of the unit were determined by placing the layer in a horizontal position with the hot surface uppermost, measuring the difference between the heat supplied and the heat conducted across the layer for a cold wall tempera-

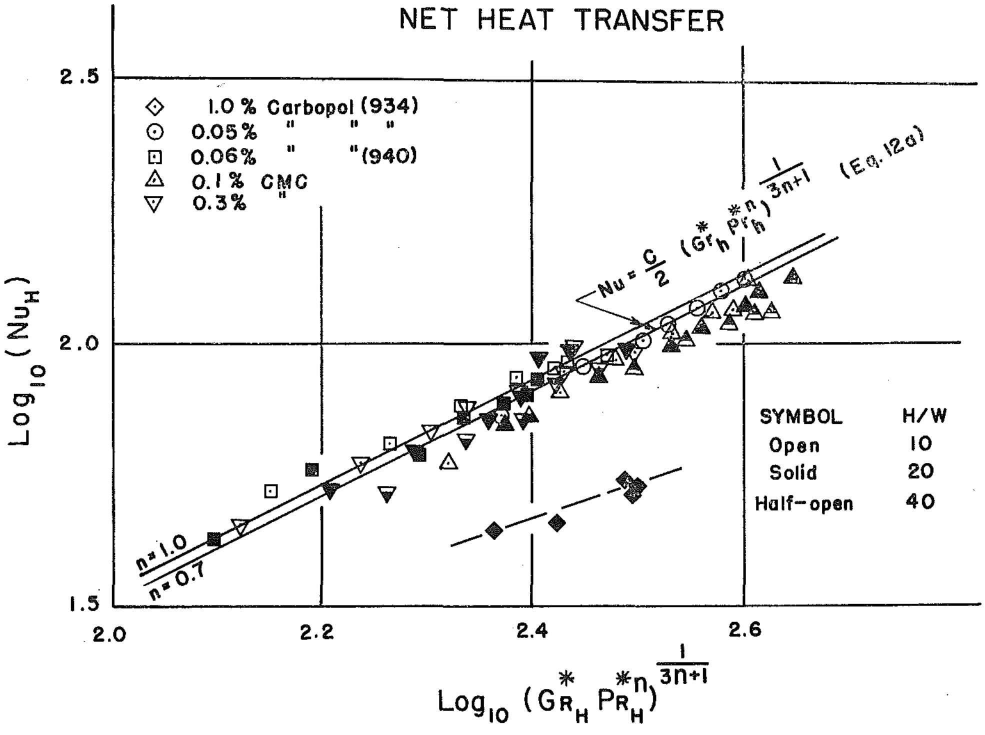

Fig. 7 Net heat transfer data for vertical enclosure—non-Newtonian fluids

ture equal to that used in the tests. The layer was then placed in an upright position, and the average hot wall temperature measured for a number of different heating rates. Fig. 7 represents the resulting data expressed in terms of the generalized Rayleigh number ($Ra^* = Gr^* Pr^{*n}$) and compared to the boundary-layer model correlation. With the exception of the 1.0 percent carbopol (934) data, all of the fluids are seen to agree well with the correlation and with the Newtonian fluids shown in Fig. 1.

A least-squares fitting of the data biased to have a slope of unity yields

$$\overline{Nu}_H = 0.331 \, (Gr_H^* \, Pr_H^{*n})^{\frac{1}{3n+1}}$$

with a standard deviation of the log $\overline{Nu}_H$ of 0.09. A least-squares fitting of the data in the form

$$\log \overline{Nu}_H = \log C + b \log (Gr_H^* \, Pr_H^{*n})^{\frac{1}{3n+1}}$$

showed that the slope was unity with a 99.9 percent confidence. The constants computed from Acrivos' solution and experimentally determined are shown in Table 1.

Although Acrivos' numerical solution for $d\theta/d\eta$ varies from 0.65 to 0.52 as n decreases from 1.0 to 0.3, the inclusion of the function of n into the constant C gives a Nusselt-Rayleigh correlation which is almost totally insensitive to the flow index except for its inclusion in the exponent of Ra*, which is in excellent agreement with the measured constants.

When the data are plotted versus Gr* Pr*, no simple correlation can be obtained with respect to either the aspect ratio (H/W) or the Prandtl number Pr*, however, the presentation illustrated in Fig. 7 (Nu versus Gr^*Pr^{*n}) is relatively insensitive to the aspect ratio and does conform to the Newtonian behavior of a slightly increased Nusselt number with increased Prandtl number. From Fig. 7, we may conclude that the generalized Rayleigh number is best related to the Grashof and Prandtl numbers in the form

$$Ra^* = Gr^* \, Pr^{*n}$$

rather than the normal form

$$Ra^* = Gr^* \, Pr^*.$$

The reduced heat transfer performance of the 1.0 percent carbopol 940 was inferred to be a result of a monotonely increasing thickening and yield stress. This assumption is reinforced by two observations:

Table 1

Fluid	n	Pr_H^*	C	$C/2$	Experimental C ($b = 1.0$)	Experimental b
0.1 percent CMC	0.91	20–65	0.667	0.333	0.331 ± 0.039	1.0
0.3 percent CMC	0.96	85–500	0.672	0.336	0.331 ± 0.029	1.0
0.05 percent carbopol 934 (neutralized)	0.95	65–90	0.671	0.335	0.331 ± 0.029	1.0
0.06 percent carbopol 940 (neutralized)	0.75 $\left(\frac{H}{W} = 10\right)$	1800–2700	0.652	0.329	0.331 ± 0.029	1.0
	0.64 $\left(\frac{H}{W} = 20\right)$	4800–8000				
1.0 percent carbopol 934 (unneutralized)	0.7	170–310	0.645	0.322	0.16 (b = 0.65)	0.6

1 The tests were sequential in time, and the curve shows that for long enough times the heat transfer performance diminished even though the generalized Rayleigh number increased (the Nusselt number was a maximum near $Gr^* Pr^{*n} = 10^7$ and further increases in heat flux reduced the Nusselt number and increased the $Gr^* Pr^{*n}$ modulus minutely).

2 A study of a single flat plate [19] indicated that the velocities in the boundary layer of 0.06 percent carbopol, which has a low yield stress, were significantly lower than those of the nonyielding fluid, 0.05 percent carbopol, and the CMC computed values [19].

Since the yield stress of 0.06 percent carbopol is significantly lower than that of 1.0 percent carbopol and shows a minimal increase with time, we infer that as the 1.0 percent carbopol was heated over long periods of time and the yield stress increased, the fluid velocities diminished and the heat transfer performance was degraded.

Local Profiles

Some velocity profiles were taken in CMC by photographically recording the movement of small neutrally buoyant spheres [4, 18] or the movement of the CMC macro molecules as they passed through an intense beam of light. Because of the opacity of even very dilute CMC and carbopol solutions, such measurements are very difficult to make if the magnification is to be sufficiently high enough to give the shallow depth of field (0.001 in.) which is necessary to define accurately the plane of motion. The velocity profiles were found to agree with those extrapolated from water data according to the Prandtl numbers of the two fluids.

Fig. 8 is a composite of several temperature profiles measured at the half height of the layer at equal heat transfer rates. All of the profiles except the 1.0 percent carbopol possess the temperature inversion points (the negative temperature gradient in the center portion of the cell) which have been observed by others in Newtonian fluids at high Rayleigh moduli.

The most striking feature of the graphs is the similarity of shape and the agreement of values of the temperatures of all of the fluids, whether they be Newtonian or strongly pseudoplastic. The only exception is the 1.0 percent carbopol, and its lack of the inversion and unusually high temperatures can be attributed to its peculiar rheological characteristics. Because of the strong increase of m and the relative constancy of n with temperature, the fluid in the upper portion of the layer becomes stiffer, decreases in velocity, and increases in temperature in a self-aggravating cycle. Thus, even though the shear characteristics at room temperature of the 1.0 percent carbopol and the 0.3 percent CMC are nearly equal, the carbopol tends to stagnate, not to develop the temperature inversion which is characteristic of a fully developed boundary-layer-like velocity profile, and to create such a high temperature zone that as much as half of the electrical heat input is conducted in the hot wall to the cooler region at the base of the layer as evidenced by the reduced wall temperature gradient. Since, as noted earlier, some motion is necessary to prevent jelling, the increased consistency tends to promote jelling and to further aggravate the situation. Examination of the fluid layer after several weeks of operation showed the presence of jelled carbopol in the upper portion of the layer.

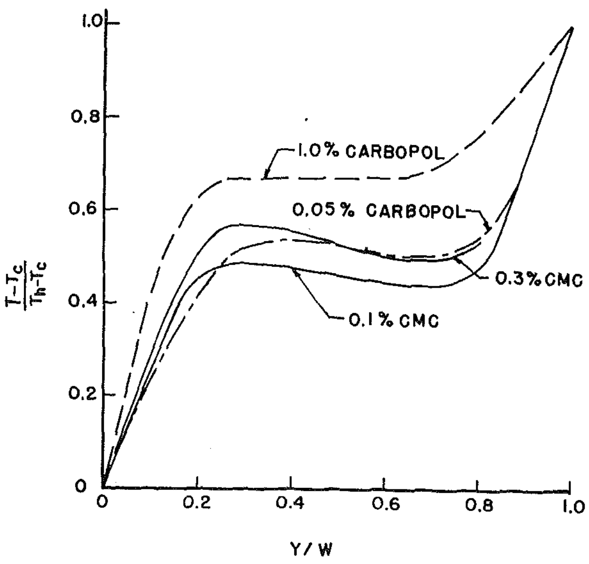

Fig. 8 Temperature profiles

Conclusions

Overall heat transfer data for a constant heat flux hot wall and an isothermal cold wall system demonstrate that Acrivos' boundary-layer solution may be combined with the boundary-layer model of Emery and Chu to predict accurately the thermal characteristics of a vertical layer of those non-Newtonian pseudoplastic fluids which do not exhibit strong yield stresses. The agreement is shown to be within 5 percent even though Acrivos' similarity solution can be strictly applied to only infinite Prandtl number fluids with constant properties heated by an isothermal hot wall.

The experiments have also shown that unneutralized 1.0 percent carbopol 934, which possesses a yield stress and has a fluid consistency which increases with temperature, behaves anomalously and has a heat transfer behavior which cannot be predicted through the boundary-layer model. It is possible that other fluids will also behave similarly to 1.0 percent carbopol. For any non-Newtonian fluid, the experiments described have conclusively shown that no steady-state heat transfer results are meaningful unless careful viscometric measurements are made not only concurrently with the heat transfer tests but upon a sample of the fluid which is contained within the layer.

Acknowledgments

The results presented here were obtained under the sponsorship of the National Science Foundation through Grant GK-567.

References

1 Dropkin, D., and Somerscales, E., "Heat Transfer by Natural Convection in Liquids Confined by Two Parallel Plates Which Are Inclined at Various Angles With Respect to Horizontal," Journal of Heat Transfer, Trans. ASME, Series C, Vol. 87, 1965, pp. 77–84.

2 Landis, F., and Yanowitz, H., "Transient Natural Convection in a Narrow Vertical Cell," *Proceedings, 3rd International Heat Transfer Conference*, 1966, pp. 139–151.

3 deVahl Davis, G., "Laminar Natural Convection in a Rectangular Cavity," New York University Report No. F-67-2, 1967.

4 MacGregor, R. K., and Emery, A. F., "Free Convection Through Vertical Plane Layers—Moderate and High Prandtl Number Fluids," Journal of Heat Transfer, Trans. ASME, Series C, Vol. 91, No. 3, Aug. 1969, pp. 391–404.

5 Elder, J. W., "Laminar Free Convection in a Vertical Slot," *Journal of Fluid Mechanics*, Vol. 23, 1965, pp. 77–111.

6 Schowalter, W. R., "The Application of Boundary-Layer Theory to Power Law Pseudoplastic Fluids: Similarity Solution," *AIChE Journal*, Vol. 6, No. 1, 1960, p. 24.

7 Lee, S. Y., and Ames, W. F., "Similarity Solutions for Non-Newtonian Fluids," *AIChE Journal*, Vol. 12, No. 4, 1966, p. 700.

8 Hansen, A. G., and Na, T. Y., "Possible Similarity Solutions of the Laminar Natural Convection Flow of Non-Newtonian Fluids," *International Journal of Heat and Mass Transfer*, Vol. 9, No. 3, 1966, p. 261.

9 Kubair, V. G., and Pei, D. C. T., "Combined Laminar Free and Forced Convection Heat Transfer to Non-Newtonian Fluids," *International Journal of Heat and Mass Transfer*, Vol. 11, 1968, pp. 855–869.

10 Acrivos, A., "A Theoretical Analysis of Laminar Natural Convection Heat Transfer to Non-Newtonian Fluids," *AIChE Journal*, Vol. 6, No. 4, 1960, p. 584.

11 Reilly, I. G., Tien, C., and Adelman, M., "Experimental

Study of Natural Convective Heat Transfer From a Vertical Plate in a Non-Newtonian Fluid," *Canadian Journal of Chemical Engineering*, Vol. 43, No. 4, 1965, p. 157.

12 Reiner, M., *Deformation and Flow*, Lewis, London, 1949.

13 Frederickson, A. G., *Principles and Applications of Rheology*, Prentice-Hall, Englewood Cliffs, N. J., 1964.

14 Ostwald, W., *Kolloid-Zeitschrift*, Vol. 38, 1926, p. 261.

15 Reilly, I. G., "Experimental Study of Natural Convection Heat Transfer From Vertical and Horizontal Flat Plates," MS thesis, University of Windsor, Windsor, Ontario, 1964.

16 St. Pierre, C., "Experimental Investigation of Natural Convection Heat Transfer in a Confined Space for Non-Newtonian Fluids," MS thesis, University of Windsor, Windsor, Ontario, 1962.

17 Grassman, P., and Straumann, W., "Ein Instationäres Verfahren zur Messung der Warmeleitfähigkeit von Flüssigkeiten und Gasen," *International Journal of Heat and Mass Transfer*, Vol. 1, 1960, pp. 50–54.

18 Eichhorn, R., "Measurement of Low Speed Gas Flows by Particle Trajectories: A New Determination of Free Convection Velocity Profiles," *International Journal of Heat and Mass Transfer*, Vol. 5, 1962, p. 915.

19 Dale, J. D., and Emery, A. F., "The Free Convection of Non-Newtonian Fluids on Vertical Flat Plates," in preparation.

20 Bird, R. B., Stewart, W. E., and Lightfoot, E. N., *Transport Phenomena*, Wiley, New York, 1960.

S. H. CHAN
Assistant Professor of Mechanical Engineering,
New York University,
Bronx, N. Y.

C. L. TIEN
Professor of Mechanical Engineering,
University of California,
Berkeley, Calif. Mem. ASME

Infrared Radiation Properties of Sulfur Dioxide

The low resolution measurements of infrared absorption are presented for ν_1, ν_3, $2\nu_1$, and $\nu_1 + \nu_3$ bands of sulfur dioxide. These measurements were performed at room temperature and at the optical pathlengths such that the data cover the transition and strong absorption regions. The spectral data were correlated in terms of the line-strength and the line-shape parameters by use of the Elsasser model while the Edwards exponential wide-band model was employed to correlate the total band absorptance data. The total emissivity was then calculated from these total band absorptance correlations to compare with Hottel's result. It is found that Hottel's result is much higher than the present calculations. Possible causes for such a large discrepancy in Hottel's result are discussed.

Introduction

Furnace designs, combustion chamber studies, and recent problems in meteorology, rocketry, and space technology have increased the demand of information regarding the thermal radiation properties of gases. Many common gases have repeatedly received extensive consideration [1–4].[1] However, the radiation property of sulfur dioxide, which is of particular interest to engineers due to its common presence and its comparatively high emissivity in the infrared, remains little known.

In 1905, Coblentz [5], by use of a fairly crude prism apparatus, measured the absorption spectrum of sulfur dioxide at room temperature and at a particular optical pathlength. Based on this work, Hottel and his co-workers [3, 6] presented a total emissivity chart for quantitative calculations. Later, Bailey, Cassie, and Angus [7] performed another measurement but they were more interested in identifying the infrared bands and determining three different moments of inertia than studying the absorption characteristics of SO_2. More recent works including those of Morcillo and Herranz [8], Mayhood [9], as well as Eggers and Schmid [10], are all confined to the measurement of integrated band intensities of the three fundamental bands of SO_2. For high-temperature measurements, Giguere and Savoie [11] measured the spectrum of SO_2 up to 700 deg C but provided no detailed absorption or emission information that can be utilized for radiative transfer analyses. It appears that Coblentz's measurement in 1905 is still the only available source that can provide some information for practical applications. In view of the modern instrumentation and recent progress in the study of band models [1–4], a new experimental study of SO_2 should be made.

It is the purpose of the present study to measure the detailed infrared absorption of SO_2 and to present results useful in radiative transport calculations. Results of the spectral absorption measurements of SO_2 at room temperature are first presented. On the basis of the established narrow-band models, the narrow-band properties are correlated in terms of the two basic spectroscopic parameters, namely, the line-strength parameter and the line-shape parameter. For the wide-band properties, a semi-empirical correlation for the total band absorptance is obtained on the basis of the Edwards exponential model [12]. From this wide-band correlation, the total emissivity is presented as a function of the optical pathlength and is compared with Hottel's result [3].

Experimental Apparatus and Measurements

The apparatus used for the experimental study consists of three basic units: the source unit, the absorption cell, and a monochromator with the sodium chloride prism. Details of construction and gas supply and exhaust circuits are basically the same as described previously [13]. The test pathlength is defined by the distance between two Irtran 2 (manufactured by Eastman Kodak Company, Rochester, N. Y.) windows. These windows are held in two stainless steel window holders by means of inside threads and a ring-shaped nut. The windows are sealed in the holders by a Teflon O-ring. Provision is made to balance the pressures on both sides of the windows to prevent possible leakage through the O-ring.

Sulfur dioxide was purchased from the Mathieson Company, which specifies the purity of the gas as 99.98 percent. Therefore no attempts were made to remove other possible impurities. The nitrogen used in mixing with the test gas has a 99.7 percent

---

[1] Numbers in brackets designate References at end of paper.

Contributed by the Heat Transfer Division and presented at the Winter Annual Meeting, New York, N. Y., November 29–December 3, 1970, of THE AMERICAN SOCIETY OF MECHANICAL ENGINEERS. Manuscript received by the Heat Transfer Division September 22, 1969; revised manuscript received February, 1970. Paper No. 70-WA/HT-4.

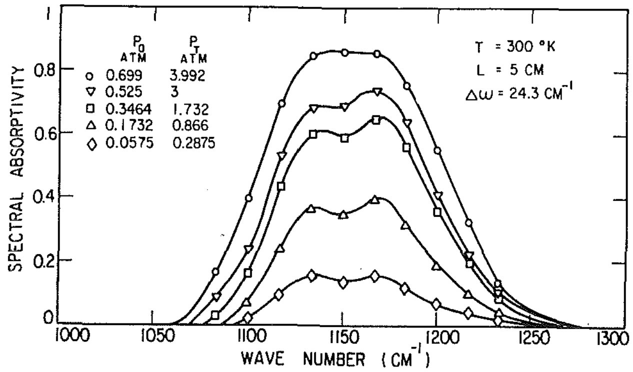

Fig. 1 The spectral absorptivity of ν_1 band

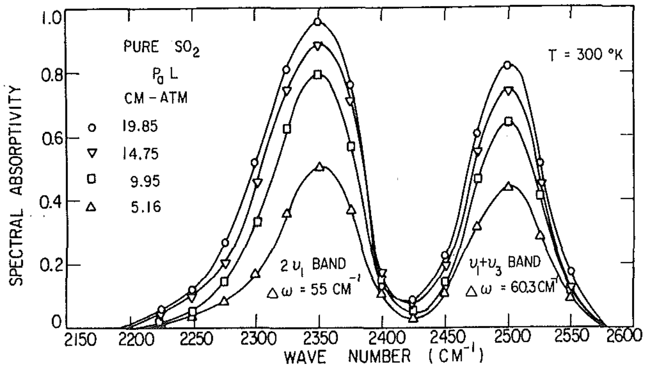

Fig. 3 The spectral absorptivity of $2\nu_1$ and $\nu_1 + \nu_3$ bands

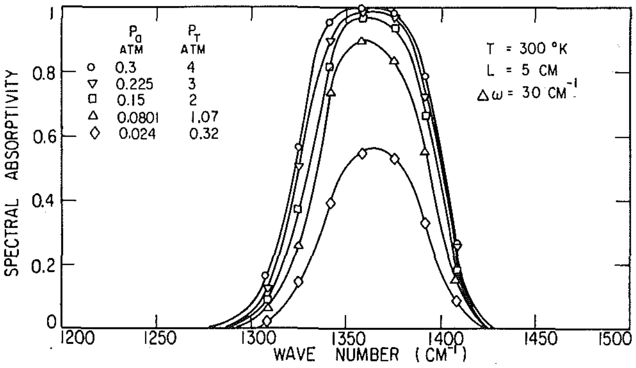

Fig. 2 The spectral absorptivity of ν_3 band

purity, with only traces of oxygen and water vapor remaining. Thus the nitrogen is passed through a dessicant before entering the test cell.

After warming up the electronics and rechecking the prism calibration, a "reference transmission" scan is taken by purging dry nitrogen into the test cell, source box, and monochromator. Then the test gas is admitted into the test cell and the dry nitrogen is further mixed with the test gas. Measurements of the test-cell pressure before and after introducing the dry nitrogen enable the determination of the test-gas partial pressure and the total pressure of the mixture. When the detected signal shown in the recorder reaches steady state, it is assumed that the test gas and nitrogen have properly mixed and the "absorbing transmission" scan is then recorded. The ratio of the value of the "absorbing transmission" scan to that of the "reference transmission" scan will give the spectral absorptivity of the test gas.

In general, the infrared absorption is a function of temperature, optical pathlength, test gas pressure, and the total pressure of the mixture if the absorbing gas is mixed with another nonabsorbing gas. In the present measurements, spectral absorptivities were obtained for the following important infrared bands: ν_1, ν_3, $2\nu_1$ and $\nu_1 + \nu_3$. For the absorption measurements of the ν_1 and ν_3 fundamentals, nitrogen was introduced into the absorption cell to broaden the bands while pure SO$_2$ was used for the measurements of $2\nu_1$ and $\nu_1 + \nu_3$ bands. Representative spectral absorptivity measurements are shown in Figs. 1–3.

It should be noted that, because it is extremely difficult to remove completely the atmospheric CO$_2$ from the source unit and monochromator, the present absorption measurement of $2\nu_1$ band may be interfered by the strong 4.3μ band of CO$_2$. Consequently, the spectral absorption of $2\nu_1$ band shown in Fig. 3 may not be as accurate as others. The possible error involved is expected to be very small. Moreover, in the calculation of the total emissivity of SO$_2$, the contribution of $2\nu_1$ band is less than 1 percent.

Correlation of Spectral and Total Band Absorption Data

Correlation of Spectral Absorption Data of ν_1 and ν_3 Fundamentals

Different narrow-band models were tried to correlate the spectral absorption data. It is found that the Elsasser model gives the best correlation. According to the Elsasser model, the mean spectral absorptivity for the Lorentz line profile is given by [4]

$$A_\omega = 1 - \frac{1}{2\pi}\int_{-\pi}^{\pi} \exp\left(\frac{-\beta_\omega x_\omega \sinh \beta_\omega}{\cosh \beta_\omega - \cos z}\right) dz \qquad (1)$$

where

$$\beta_\omega = \frac{2\pi b}{d}, \qquad x_\omega = \frac{SX}{2\pi b}$$

Nomenclature

A = total band absorptance of isothermal gas
A_0 = band width parameter
B = self-broadening coefficient
b/d = line-shape parameter
C_1 = band intensity parameter in the wide-band model
C_2 = line-shape parameter in the wide-band model
C_3 = band width parameter in the wide-band model
d = line spacing
e_{ω_i} = Planck's function evaluated at wave number ω_i
$f(x_\omega)$ = Reiche function
k = absorption coefficient
L = geometrical pathlength
L_0 = mean beam length
n = a constant in defining effective pressure p_e
p_a = pressure of absorbing gas
p_e = effective pressure
p_N = pressure of inert gas
p_T = total pressure of mixture
S = integrated line intensity
S/d = line-strength parameter
T = temperature
t = wide-band model pressure-broadening parameter
X = optical pathlength
x_ω = band model spectroscopic parameter
α = integrated band intensity
β_ω = band model spectroscopic parameter
ϵ_T = total emissivity
ϵ_ω = spectral emissivity
ω = wave number
ω_i = band center of i-th band

Subscripts

g = refers to gas temperature
0 = refers to reference condition
ω = refers to wave number

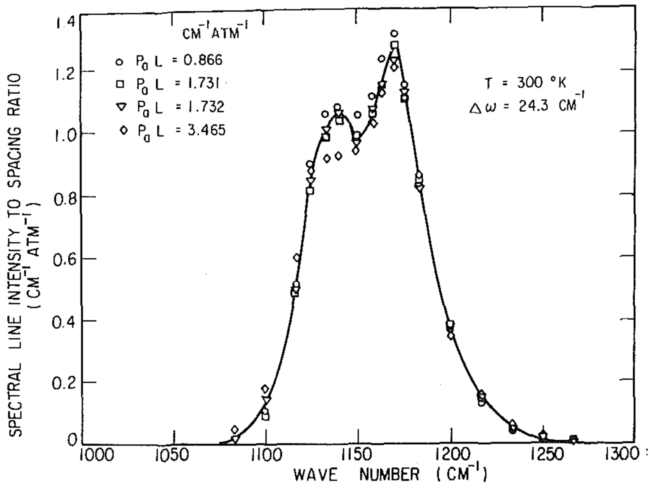

Fig. 4 Spectral data correlation of ν_1 band

b is the line half-width, d the line spacing, S the spectral line intensity, and X the optical pathlength. The integral can be represented accurately by the Godson approximation [2]

$$A_\omega = \operatorname{erf}\left[\tfrac{1}{2}\pi^{1/2}\beta_\omega f(x_\omega)\right] \tag{2}$$

where the Reiche function

$$f(x_\omega) = x_\omega e^{-x_\omega}[J_0(ix_\omega) - iJ_1(ix_\omega)]. \tag{3}$$

which can be further approximated by [4]

$$f(x_\omega) = x_\omega \left[1 + \frac{\pi x_\omega}{2}\right]^{-1/2} \tag{4}$$

By substituting (4) into (2), (S/d) can be expressed in terms of (b/d) and A_ω. Thus, the correlation can be carried out in a similar manner as described by Ferriso and his co-workers [14]. Since (b/d) is generally a weak function of wave number [15], a band-averaged value of (b/d) is assumed throughout the band. With this band-averaged (b/d) and experimental A_ω's, it is possible to solve (S/d) as a function of wave number. The resulting curve of (S/d) is then integrated with respect to wave number over the whole band to check whether the integrated result is identical to the known value of the integrated band intensity. The procedure is repeated until the integrated result agrees with the known value.

The values of the integrated band intensity have been measured by several investigations [8–10]. Their results at STP are summarized in Table 1. Due to the slight deviations in the reported values, the mean values as shown in the last column were used here. These values at STP can be extrapolated to the values corresponding to the actual experimental conditions by the following relationship:

$$\alpha(T) = \alpha(T_0)\left(\frac{T_0}{T}\right)\frac{\Phi(T)}{\Phi(T_0)} \tag{5}$$

For fundamental vibration-rotation bands, $\Phi = 1$ [16].

To correlate b in a more useful way, it is noted that the temperature and pressure dependence of (b/d) is given by [2]

$$\left(\frac{b}{d}\right) = \left(\frac{b_0}{d}\right) p_e \left(\frac{T_0}{T}\right)^{1/2} \tag{6}$$

where p_e is the effective pressure and b_0 is the line width at temperature T_0 and the effective pressure of unity. Since b_0 is a constant independent of temperature and pressure, it is advantageous here to convert all correlated b's into b_0's according to (6).

For a binary gas mixture, p_e is defined by

$$p_e = p_T + (B - 1)p_a \tag{7}$$

where p_T is the total pressure of the mixture, p_a the partial pressure of the absorbing gas, and B the self-broadening coefficient. Because the value of B has not been reported in the literature for SO_2-N_2 mixture, it must be determined experimentally in order to correlate (b_0/d).

To determine B, two different absorption measurements were performed. In one measurement, the test cell consisted of pure SO_2 with the geometrical path $L = 2$ cm and the optical pathlength $X = 0.875$ cm-atm while in the other measurement N_2 was allowed to mix with SO_2 and the geometrical path was increased to $L = 5$ cm but X still remained the same. It is found that when the total pressure in the second measurement is 0.509 atm, the total band absorptances in both measurements are identical. Since the total band absorptance is only a function of X and p_e at a given temperature, this implies the effective pressures in both experiments must be the same. From the definition of p_e the self-broadening coefficient is then found to be 1.28. Similar procedures were used by other investigators for measuring the self-broadening coefficients of other gases [17, 18]. Since the total band absorptance depends only weakly on the nitrogen pressure p_N, the present setup cannot detect accurately such a minor change of the absorption due to the different amount of P_N. Thus some error may involve in the present value of B. However, in view of the fact that the value of B will solely be employed to correlate other parameters, this possible error in B will be partially compensated by adjusting those correlation parameters such that calculated values agree well with experimental data.

Results of correlations of (S/d) for the ν_1 and ν_3 fundamentals at room temperature are presented in Figs. 4 and 5 while their corresponding (b_0/d)'s are found to be 0.0409 and 0.0589 at $T_0 = 273$ deg K.

Correlation of Total Band Absorptance. The total band absorptance defined by

Table 1 Integrated band intensity measurements for the fundamental bands of sulfur dioxide

band	frequency (cm^{-1})	wavelength (μ)	band intensity (cm^{-2} atm^{-1} at STP) reference [8]	reference [9]	reference [10]	average
ν_1	1151	8.68	117.0	105.7	92.7	105.0
ν_2	519	19.28	120.0	125.3	116.0	120.4
ν_3	1361	7.35	880.0	853.3	840.0	857.8

Table 2 Results of correlation parameters at 300 deg K

band	wavelength (μ)	C_1 (cm^{-2} atm^{-1})	C_2 ($cm^{-3/2}$ $atm^{-1/2}$)	C_3 (cm^{-1})	n
ν_1	8.68	95.6	35.5	43	0.70
ν_3	7.35	780.0	171.5	15.2	0.65
$2\nu_1$	4.34	11.0	28.3	28.5	0.60
$\nu_1 + \nu_3$	4.00	9.0	23.0	18.9	0.60
ν_2	19.27	109.8	43.9	57.3	0.70

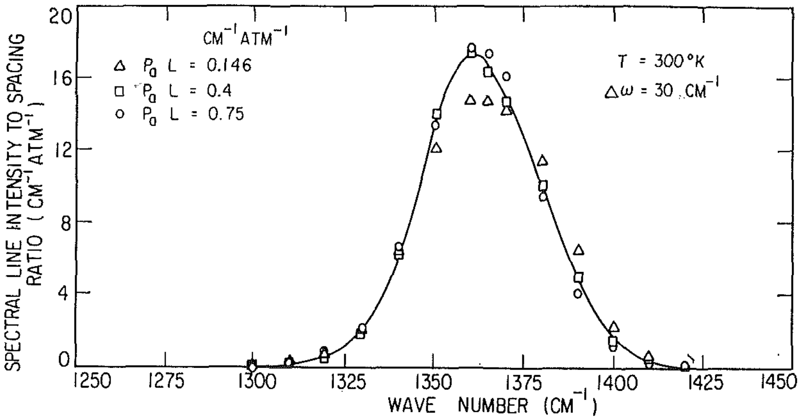

Fig. 5 Spectral data correlation of ν_3 band

Table 3 Comparison of total band absorptance of ν_1 band

optical pathlength cm-atm	partial pressure atm	total pressure atm	Edwards correlation cm^{-1}	Tien-Lowder correlation cm^{-1}	experimental data cm^{-1}
6.930	0.700	4.00	127.32	127.74	119.2
5.160	0.521	2.98	107.45	110.19	107.4
3.465	0.350	2.00	80.11	87.59	83.2
1.731	0.175	1.00	44.09	53.78	49.4
3.495	0.699	3.99	97.84	99.60	94.6
2.625	0.525	3.00	78.56	84.11	73.5
1.732	0.346	2.00	55.00	63.81	62.2
0.866	0.173	1.00	30.19	37.10	34.9
0.287	0.057	0.32	11.47	13.82	13.6
1.360	0.698	4.00	59.39	63.82	58.9
1.035	0.521	3.00	46.59	52.20	43.3
0.677	0.347	2.00	32.33	37.45	28.5

Table 4 Comparison of total band absorptance of ν_3 band

optical pathlength cm-atm	partial pressure atm	total pressure atm	Edwards correlation cm^{-1}	Tien-Lowder correlation cm^{-1}	experimental data cm^{-1}
2.970	0.300	4.02	89.89	92.19	88.56
2.210	0.224	2.98	86.67	87.38	85.12
1.500	0.150	2.00	81.22	80.63	79.36
0.750	0.075	1.00	69.27	67.76	68.64
0.267	0.027	0.35	48.03	47.00	50.48
1.500	0.300	4.00	79.58	81.49	79.72
1.125	0.225	3.00	76.33	76.68	74.88
0.750	0.150	2.00	70.68	69.58	68.32
0.400	0.080	1.07	59.95	57.83	57.88
0.120	0.024	0.32	35.16	34.32	34.04
0.056	0.011	0.15	19.40	21.41	19.04
0.600	0.300	4.00	65.61	66.74	72.92
0.450	0.225	3.00	62.40	61.75	65.60
0.292	0.150	2.00	56.34	53.97	59.40
0.146	0.075	1.00	44.40	40.92	37.32
0.051	0.026	0.35	23.01	22.53	20.12
0.021	0.011	0.15	10.77	11.51	10.16

Table 5 Comparison of total band absorptance of $\nu_1 + \nu_3$ and $2\nu_1$ bands

			$\nu_1 + \nu_3$ band			$2\nu_1$ band	
optical pathlength cm-atm	total pressure atm	Edwards correlation cm^{-1}	Tien-Lowder correlation cm^{-1}	experimental data cm^{-1}	Edwards correlation cm^{-1}	Tien-Lowder correlation cm^{-1}	experimental data cm^{-1}
56.90	3.02	77.84	80.63	72.2	114.41	114.48	113.6
38.10	2.02	72.98	71.98	62.0	104.90	101.11	102.6
18.85	1.00	60.38	56.05	56.0	83.89	76.76	73.8
19.85	1.96	60.52	57.97	60.5	86.37	79.99	89.5
14.75	1.46	55.69	51.28	52.7	77.99	69.89	82.0
9.95	0.98	48.26	42.46	45.5	65.61	56.84	68.1
5.16	0.51	33.86	28.80	31.3	42.50	37.35	41.1
1.95	0.97	17.55	14.53	15.2	21.45	18.30	20.6
0.99	0.50	8.93	8.04	8.6	10.91	9.96	9.8

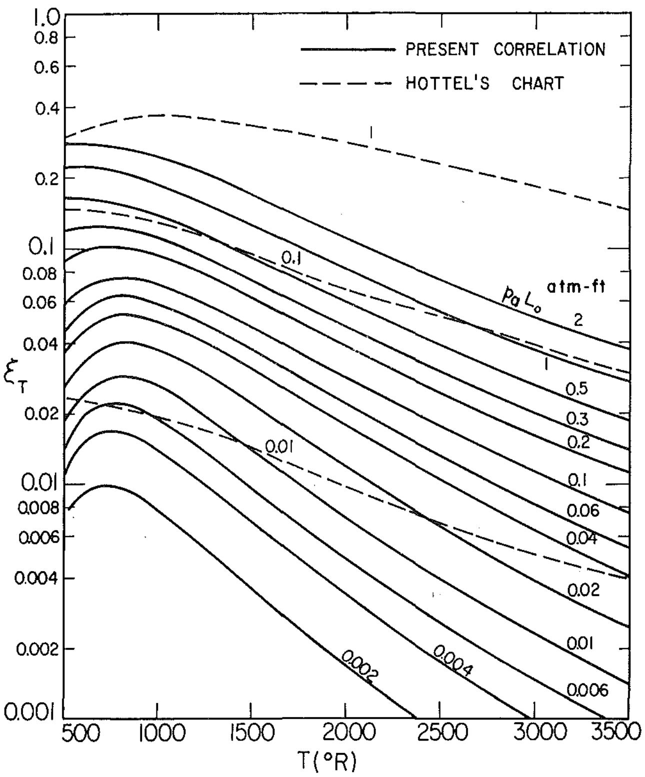

Fig. 6 Total emissivity of sulfur dioxide

$$A = \int_{\text{band}} A_\omega d\omega \tag{8}$$

can be obtained by measuring the area under the spectral absorption curve. In general, it is a function of temperature, optical pathlength, and effective pressure.

The band absorptance data are correlated according to the Edwards exponential wide-band model [12]. The values of the correlation parameters for ν_1, ν_3, $2\nu_1$, and $\nu_1 + \nu_3$ bands are presented in Table 2. The comparison of total band absorptance between the measured data and the calculated values of these four bands based on these correlation parameters is presented in Tables 3 to 5. Also included in Tables 3 to 5 is the total band absorptance calculated according to the Tien-Lowder correlation [19]. The Tien-Lowder correlation is based on the Edwards model such that the total band absorptance is expressed in a single continuous function

$$\bar{A} = \ln\left\{uf_2(t)\left[\frac{u + 2}{u + 2f_2(t)}\right] + 1\right\} \tag{9}$$

where

$$\bar{A} = A/C_3, \qquad u = C_1X/C_3,$$

and

$$f_2(t) = 2.94[1 - \exp(-2.6t)]$$

As shown in Tables 3 to 5 the general agreement is good between the measured and calculated total band absorptance based on either correlation.

For ν_2 band, attempts to measure the absorption spectrum have failed since the ν_2 band is located at such a long wavelength region (around 19.3μ) that the low transmittance of optical windows and prism as well as low source intensity prevents any accurate measurements by the present setup. Therefore the corresponding parameters cannot be correlated. However, C_1 of the ν_2 band is already known (see Table 1) and C_2, C_3, and n can also be estimated for the purpose of quantitative analysis. Physically C_3 characterizes the band width and, thus, can be estimated by inspecting the spectra taken by Barker [20]. In addition, the ν_2 and ν_1 fundamental bands have a similar contour (i.e., no Q-branch), it is appropriate to assume that both bands have identical values of b/d and n. Accordingly, C_2 can be easily determined by noting that [12]

$$\frac{b}{d} = \frac{C_2^2}{16C_1C_3} p_e^n \tag{10}$$

All these values are also listed in Table 2.

Total Emissivity. The total emissivity can be calculated from total band absorptance correlations by the following relation [4]

$$\epsilon_T(T_g, X, p_T) = \sum_i \frac{e_{\omega_i}}{\sigma T_g^4} A_i(T_g, X, p_e) \tag{11}$$

where T_g is the gas temperature, e_{ω_i} the Planck radiance evaluated at T_g and at center of band i, and A_i the total band absorptance of the i-th band.

The only available information in the literature that can be compared with the present study is Hottel's total emissivity chart [3]. This chart is based on the work of Coblentz [5] who measured the absorption spectrum of SO$_2$ up to 15μ wavelength at room temperature. The absorption coefficient was then evaluated from this room temperature spectrum and assumed to be independent of temperature to construct the total emissivity chart up to 3500 deg R. In order to compare with his result, the present total band absorptance correlations will be extrapolated to higher temperature. To the harmonic-oscillator approximation, the integrated band intensity C_1 ($\equiv \alpha$) is given by equation (5) with [16]

$$\Phi(T) = \left[1 - \exp\left(-\frac{hc}{kT}\omega_a\right)\right]^{-n_a} \times \left[1 - \exp\left(-\frac{hc}{kT}\omega_b\right)\right]^{-n_b} \ldots X \left\{1 - \exp\left[-\frac{hc}{kT}(n_a\omega_a + n_b\omega_b + \ldots)\right]\right\} \tag{12}$$

and the temperature dependence of C_3 is given by

$$C_3(T) = C_3(T_0)\left(\frac{T}{T_0}\right)^{1/2} \tag{13}$$

according to the vibrating rigid rotator model [12]. As to C_2, combining equations (6), (10), and (13) yields

$$C_2(T) = C_2(T_0)\left[\frac{C_1(T)}{C_1(T_0)}\right]^{1/2} \tag{14}$$

With equations (12) to (14) and Table 2, it is possible to calculate the total band absorptance at elevated temperatures. The total emissivity is evaluated on the basis of the above five infrared bands with the total band absorptance given by the Edwards correlation, and is presented in Fig. 6 as a function of the mean beam length [3]. Also shown in Fig. 6 are some representative results from Hottel's chart. It is indicated that, except at lower temperatures and smaller mean beam lengths, Hottel's results are much higher than the present result. This large discrepancy is largely due to the crude measurements of Coblentz and the neglect of the temperature dependence of the absorption coefficient. As was pointed out by Bailey, Cassie, and Angus [7], in Coblentz' original absorption curve the two bands at 3.18μ and 10.37μ do not belong to the spectrum of SO$_2$ [21, 22] and the band at 5.68μ is not clear since it looks like the $\nu_2 + \nu_3$ band at 5.35μ yet it exhibits much too strong absorption than what the $\nu_2 + \nu_3$ band should have. Also Coblentz showed the two fundamentals ν_1 and ν_3 as having the same intensities while, in reality, the ν_1 band is much less powerful [8–10]. Thus the absorption characteristic of ν_1 band may be overestimated. Also, the use of the particular room temperature absorption coefficient in calculating the total band absorptance at higher temperature will overpredict the corresponding result. Since ν_2 band was not detected by Coblentz, the total emissivity in Hottel's chart neglects the contribution due to the ν_2 band. Even though this fortuitous factor may underestimate the total emissivity, it does not seem to compensate all other factors which result in a higher estimate of the total emissivity.

References

1 Penner, S. S., *Quantitative Molecular Spectroscopy and Gas Emissivities*, Addison-Wesley, Massachusetts, 1959.

2 Goody, R. M., *Atmospheric Radiation*, Clarendon Press, Oxford, 1964.

3 Hottel, H. C., and Sarofim, A. F., *Radiation Transfer*, McGraw-Hill Book Co., Inc., New York, 1967.

4 Tien, C. L., "Thermal Radiation Properties of Gases," in *Advances in Heat Transfer*, (eds. Hartnett, J. P., and Irvine, T. F.), Vol. 5, Academic Press, New York, 1968.

5 Coblentz, W. W., *Investigations of Infrared Spectra*, Part I, Carnegie Institute, Washington, D. C., 1905, p. 52, 177.

6 Guerrieri, S. A., S. M. thesis in Chem. Engr., M.I.T., Cambridge, Mass., 1932.

7 Bailey, C. R., Cassie, A. B. D., and Angus, W. R., "Investigations of Infrared Region of the Spectrum, Part II.—The Absorption Spectrum of Sulfur Dioxide," *Proceedings of the Royal Society* (London), Vol. 145, 1934, p. 336.

8 Morcillo, J., and Herranz, J., "Antonio de Gregoria Rocasolano," Pulds. inst. quim. fis, Vol. 10, 1956, p. 162.

9 Mayhood, J. E., "Infrared Intensities and Bond Moments in Sulfur Dioxide," *Canadian Journal of Physics*, Vol. 35, 1957, p. 954.

10 Eggers, D. F., Jr., and Schmid, E. D., "Infrared Intensities of Sulfur Dioxide: A Re-determination," *Journal of Physical Chemistry*, Vol. 64, 1960, p. 279.

11 Giguere, P. A., and Savoie, R., "Infrared Spectrum of SO_2 at High Temperature," *Canadian Journal of Chemistry*, Vol. 43, No. 8, 1965, p. 2357.

12 Edwards, D. K., and Menard, W. A., "Comparison of Models for Correlation of Total Band Absorption," *Applied Optics*, Vol. 3, 1964, p. 621.

13 Tien, C. L., and Giedt, W. H., "Experimental Determination of Infrared Absorption of High Temperature Gases," in *Advances in Thermophysical Properties at Extreme Temperatures and Pressure* (ed. Gratch, S.), ASME, New York, 1965.

14 Ferriso, C. C., Ludwig, C. B., and Thomson, A. L., "Empirically Determined Infrared Absorption Coefficients of H_2O from 300 to 3000°K," *Journal of Quantitative Spectroscopy and Radiative Transfer*, Vol. 6, 1966, p. 241.

15 Oppenheim, U. P., and Ben-Aryeh, Y., "A General Method for the Use of Band Models with Application to Infrared Atmospheric Absorption," *Journal of Quantitative Spectroscopy and Radiative Transfer*, Vol. 4, 1964, p. 599.

16 Breeze, J. C., Ferriso, C. C., Ludwig, C. B., and Malkmus, W., "Temperature Dependence of the Total Integrated Intensity of Vibrational-Rotational Band Systems," *Journal of Chemical Physics*, Vol. 42, 1965, p. 402.

17 Edwards, D. K., "Absorption by Infrared Bands of Carbon Dioxide Gas at Elevated Pressures and Temperatures," *Journal of the Optical Society of America*, Vol. 50, 1960, p. 617.

18 Burch, D. E., Singleton, E. G., and Williams, D., "Absorption Line Broadening in the Infrared," *Applied Optics*, Vol. 1, 1962, p. 359.

19 Tien, C. L., and Lowder, J. E., "A Correlation for Total Band Absorptance of Radiative Gases," *International Journal of Heat and Mass Transfer*, Vol. 9, 1966, p. 698.

20 Barker, E. F., "VII. Spectra of Simple Molecules, the Infrared Spectra of Triatomic Molecules," *Review of Modern Physics*, Vol. 14, 1942, p. 198.

21 Herzberg, G., *Infrared and Raman Spectra*, D. Van Nostrand Co., Inc., New York, 1945, p. 285.

22 Sheton, R. D., Nielsen, A. H., and Fletcher, W. H., "The Infrared Spectrum and Molecular Constants of SO_2," *Journal of Chemical Physics*, Vol. 21, 1953, p. 2178.

the ν_1 band is much less powerful [8–10]. Thus the absorption characteristic of ν_1 band may be overestimated. Also, the use of the particular room temperature absorption coefficient in calculating the total band absorptance at higher temperature will overpredict the corresponding result. Since ν_2 band was not detected by Coblentz, the total emissivity in Hottel's chart neglects the contribution due to the ν_2 band. Even though this fortuitous factor may underestimate the total emissivity, it does not seem to compensate all other factors which result in a higher estimate of the total emissivity.

References

1 Penner, S. S., *Quantitative Molecular Spectroscopy and Gas Emissivities*, Addison-Wesley, Massachusetts, 1959.

2 Goody, R. M., *Atmospheric Radiation*, Clarendon Press, Oxford, 1964.

3 Hottel, H. C., and Sarofim, A. F., *Radiation Transfer*, McGraw-Hill Book Co., Inc., New York, 1967.

4 Tien, C. L., "Thermal Radiation Properties of Gases," in *Advances in Heat Transfer*, (eds. Hartnett, J. P., and Irvine, T. F.), Vol. 5, Academic Press, New York, 1968.

5 Coblentz, W. W., *Investigations of Infrared Spectra*, Part I, Carnegie Institute, Washington, D. C., 1905, p. 52, 177.

6 Guerrieri, S. A., S. M. thesis in Chem. Engr., M.I.T., Cambridge, Mass., 1932.

7 Bailey, C. R., Cassie, A. B. D., and Angus, W. R., "Investigations of Infrared Region of the Spectrum, Part II.—The Absorption Spectrum of Sulfur Dioxide," *Proceedings of the Royal Society* (London), Vol. 145, 1934, p. 336.

8 Morcillo, J., and Herranz, J., "Antonio de Gregoria Rocasolano," Pulds. inst. quim. fis, Vol. 10, 1956, p. 162.

9 Mayhood, J. E., "Infrared Intensities and Bond Moments in Sulfur Dioxide," *Canadian Journal of Physics*, Vol. 35, 1957, p. 954.

10 Eggers, D. F., Jr., and Schmid, E. D., "Infrared Intensities of Sulfur Dioxide: A Re-determination," *Journal of Physical Chemistry*, Vol. 64, 1960, p. 279.

11 Giguere, P. A., and Savoie, R., "Infrared Spectrum of SO_2 at High Temperature," *Canadian Journal of Chemistry*, Vol. 43, No. 8, 1965, p. 2357.

12 Edwards, D. K., and Menard, W. A., "Comparison of Models for Correlation of Total Band Absorption," *Applied Optics*, Vol. 3, 1964, p. 621.

13 Tien, C. L., and Giedt, W. H., "Experimental Determination of Infrared Absorption of High Temperature Gases," in *Advances in Thermophysical Properties at Extreme Temperatures and Pressure* (ed. Gratch, S.), ASME, New York, 1965.

14 Ferriso, C. C., Ludwig, C. B., and Thomson, A. L., "Empirically Determined Infrared Absorption Coefficients of H_2O from 300 to 3000°K," *Journal of Quantitative Spectroscopy and Radiative Transfer*, Vol. 6, 1966, p. 241.

15 Oppenheim, U. P., and Ben-Aryeh, Y., "A General Method for the Use of Band Models with Application to Infrared Atmospheric Absorption," *Journal of Quantitative Spectroscopy and Radiative Transfer*, Vol. 4, 1964, p. 599.

16 Breeze, J. C., Ferriso, C. C., Ludwig, C. B., and Malkmus, W., "Temperature Dependence of the Total Integrated Intensity of Vibrational-Rotational Band Systems," *Journal of Chemical Physics*, Vol. 42, 1965, p. 402.

17 Edwards, D. K., "Absorption by Infrared Bands of Carbon Dioxide Gas at Elevated Pressures and Temperatures," *Journal of the Optical Society of America*, Vol. 50, 1960, p. 617.

18 Burch, D. E., Singleton, E. G., and Williams, D., "Absorption Line Broadening in the Infrared," *Applied Optics*, Vol. 1, 1962, p. 359.

19 Tien, C. L., and Lowder, J. E., "A Correlation for Total Band Absorptance of Radiative Gases," *International Journal of Heat and Mass Transfer*, Vol. 9, 1966, p. 698.

20 Barker, E. F., "VII. Spectra of Simple Molecules, the Infrared Spectra of Triatomic Molecules," *Review of Modern Physics*, Vol. 14, 1942, p. 198.

21 Herzberg, G., *Infrared and Raman Spectra*, D. Van Nostrand Co., Inc., New York, 1945, p. 285.

22 Sheton, R. D., Nielsen, A. H., and Fletcher, W. H., "The Infrared Spectrum and Molecular Constants of SO_2," *Journal of Chemical Physics*, Vol. 21, 1953, p. 2178.

DISCUSSION

A. Balakrishnan[2] and D. K. Edwards[3]

The authors have used room-temperature measurements to obtain correlations for the band absorption of sulfur dioxide gas. The room-temperature correlations are interesting and useful. Sulfur dioxide is an important gas in the food-processing industry and is present in small amount in combustion gases. To give such correlations at room temperature is thus an important contribution by the authors, and they are to be congratulated.

---

[2] Postgraduate Research Engineer, Energy and Kinetics Department, School of Engineering and Applied Science, University of California, Los Angeles, Calif.

[3] Professor, Energy and Kinetics Department, School of Engineering and Applied Science, University of California, Los Angeles, Calif.

Table 6 Comparison of C_2 values

temperature deg R	ν_1 band old value*	ν_1 band new value*	ν_3 band old value	ν_3 band new value	$2\nu_1$ band old value	$2\nu_1$ band new value	$\nu_1 + \nu_3$ band old value	$\nu_1 + \nu_3$ band new value	ν_2 band old value	ν_2 band new value
300	6.96	5.14	33.6	25.0	5.53	4.01	4.50	3.27	8.61	6.12
400		5.76		28.0	5.53	4.53	4.50	3.69		7.01
500		6.58		31.8	5.54	5.22	4.50	4.25		8.11
540		6.96		33.6	5.55	5.55	4.51	4.51		8.61
600		7.58		36.5	5.56	6.09	4.52	4.95		9.40
800		10.00		48.1	5.66	8.35	4.58	6.77		12.40
1000		13.00		62.3	5.81	11.30	4.68	9.17		16.00
1500		22.30		107.0	6.34	21.70	5.06	17.70		26.40
2000		33.70		162.0	6.95	36.40	5.50	30.00		37.60
2500		46.70		226.0	7.56	55.00	5.96	45.80		48.40
3000		60.80		296.0	8.15	77.00	6.41	64.60		58.50
3500	6.96	75.40	33.6	371.0	8.72	101.00	6.85	85.80	8.61	67.70

* C_2 is in $\text{cm}^{-1}/(\text{gm}\cdot\text{m}^{-2})^{1/2}$ units.

Table 7 Comparison of total emissivity

temperature deg R	pL = 0.01 atm-ft old C_2	pL = 0.01 atm-ft new C_2	pL = 0.1 atm-ft old C_2	pL = 0.1 atm-ft new C_2	pL = 1.0 atm-ft old C_2	pL = 1.0 atm-ft new C_2
500	0.0352	0.0341	0.106	0.102	0.245	0.238
600	0.0359	0.0375	0.104	0.110	0.239	0.250
800	0.0337	0.0393	0.0963	0.115	0.218	0.258
1000	0.0283	0.0355	0.0830	0.108	0.191	0.248
1500	0.0153	0.0209	0.0505	0.0726	0.127	0.189
2000	0.0083	0.0115	0.0302	0.0451	0.0833	0.133
2500	0.0048	0.0066	0.0189	0.0285	0.0560	0.0921
3000	0.0029	0.0039	0.0124	0.0188	0.0388	0.0652
3500	0.0018	0.0025	0.0084	0.0128	0.0278	0.0473

The authors have also extrapolated the room-temperature correlations to temperatures as high as 3500 deg R. Their theoretical extrapolations for the integrated intensity C_1 are the best that can currently be made and for other gases have been successful. The authors' extrapolations of C_3 are also the best that can be made and have again resulted in good agreement with data for other gases, but they are on somewhat less firm theoretical ground, because of shifting of "hot bands." In the case of the square-root coefficient C_2, however, the authors have used an equation suitable only at low temperatures and have thus obtained results which underpredict by an order of magnitude the increase of C_2 at high temperature.

Weiner and Edwards[4] have shown that the ratio of line width to line spacing increases rapidly at high temperatures, despite the fact that the line width decreases, because hot bands become superposed on the bands resulting from molecules which are in the ground state. A better extrapolation of the line-width-to-spacing ratio can be made as follows:

$$b/d = (b_0/d)p_e(T_0/T)^{1/2}F(T)/F(T_0)$$

where

$$F(T) = \prod_{i=1}^{3} \phi^2(u_i, \delta_{ij})[1 - \exp(-u_i)]^{\delta_{ij}+1}$$

$$\phi(u, \delta) = \sum_{n=0}^{\infty} \left\{ \frac{(n+\delta)!}{n!\delta!} \exp(-nu) \right\}^{1/2}$$

$$u_i = hc\nu_i/kT$$

Replacing the authors' equation (6) with the above and combining it with their equations (10) and (13) gives a physically more reasonable estimate,

$$C_2(T) = C_2(T_0) \left\{ \frac{C_1(T)\,F(T)}{C_1(T_0)\,F(T_0)} \right\}^{1/2}$$

Table 6 below shows the new values. For the fundamental bands, instead of remaining constant, C_2 increases by an order of magnitude as T increases from 300 deg R to 3500 deg R.

Comparison of new values of total emissivity in Table 7 below with the authors' Fig. 6 shows that this more reasonable extrapolation of C_2 reconciles to some degree the band-absorption relations and the curves of Hottel. Hottel's values do remain somewhat high.

In general it is hazardous to calculate total emittance at 3500 deg R from data obtained at 500 deg R. High-temperature data are very much needed. In addition to a lack of knowledge of the shifting locations of the hot bands, there is, without good data, a lack of knowledge of the C_1 band intensities for the difference bands whose origins lie in upper states. For example, one would not predict correctly the absorption by the 9.4 and 10.4μ CO_2 bands ($\nu_3 - 2\nu_2$ and $\nu_3 - \nu_1$ bands) from 300 deg R data. The inclusion of such bands would, of course, raise the present predictions of total emissivity and could make Hottel's chart look prophetic indeed.

The discussers would close by reiterating that the room-temperature correlations given by the authors are quite valuable in themselves. The extrapolated values of C_1 and C_3 are probably reasonable, and the estimates of C_2 given in this discussion complete the extrapolation. However, there may be bands excited at high temperatures which do not manifest themselves significantly at room temperature.

Authors' Closure

We appreciate very much the valuable suggestion made in the above discussion concerning the extrapolation of C_2. The use of the suggested formula for C_2 and our formula for C_1 and C_3 probably will yield better high-temperature results. The indicated slightly better agreement between the calculation based on the suggested formula and Hottel's high-temperature results, however, does not necessarily lend support to the contention that Hottel's results should be more prophetic than ours. This is not only because the way we extrapolated from room-temperature measurements to calculate the high-temperature quantities is much more rigorous than that of Hottel but also because the room-temperature data on which Hottel's result was based are off by as much as 100 percent as compared to the more reliable measurement made by us, as was explained in the paper.

---

[4] Weiner, M. M., and Edwards, D. K., "Theoretical Expression of Water Vapor Spectral Emissivity with Allowance for Line Structure," *International Journal of Heat and Mass Transfer*, Vol. 11, 1968, pp. 55–65. Note that the general expression equation (25) is correct, but an example, equation (35), is in error in this reference.

ROBERT E. HENRY[1]
HANS K. FAUSKE
Argonne National Laboratory,
Argonne, Ill.

The Two-Phase Critical Flow of One-Component Mixtures in Nozzles, Orifices, and Short Tubes

The critical flow of one-component, two-phase mixtures through convergent nozzles is investigated and discussed including considerations of the interphase heat, mass, and momentum transfer rates. Based on the experimental results of previous investigators, credible assumptions are made to approximate these interphase processes which lead to a transcendental expression for the critical pressure ratio as a function of the stagnation pressure and quality. A solution to this expression also yields a prediction for the critical flow rate. Based on the experimental results of single-phase compressible flow through orifices and short tubes, the two-phase model is extended to include such geometries. The models are compared with steam-water, cryogenic, and alkali-metal experimental data.

Introduction

THE TWO-PHASE critical flow of one-component mixtures has been the subject of many analytical and experimental investigations because of its importance in (1) safety analyses of pressurized water, boiling water, and liquid-metal-cooled nuclear reactors [1–15],[2] (2) the flow of refrigerants and cryogens [16–19], and (3) the operation of turbines within the two-phase region [20]. With the exception of reference [1], the analytical models which resulted from these studies were either thermodynamic equilibrium or frozen (no mass transfer) models. In addition, most of these models require a knowledge of the throat pressure which is generally unknown. Those which can be based on stagnation conditions, such as the equilibrium model proposed by Moody [13], considerably overestimate the flow rates in nozzles [19, 21]. Therefore, the purpose of this paper is to develop a model which requires only a knowledge of the stagnation conditions and at the same time accounts for the nonequilibrium nature of the flow.

Nomenclature

A = cross-sectional area
C = discharge coefficient
c = specific heat
F = viscous forces
f = function
G = flow rate per unit area
H = enthalpy
h = enthalpy
k = velocity ratio, u_g/u_l
N = experimental parameter
n = polytropic exponent
P = pressure
s = entropy
T = temperature
u = velocity
v = specific volume
W = flow rate
x = quality, $W_g/(W_g + W_l)$
z = axial length
α = void fraction, A_g/A_l
γ = isentropic exponent
η = critical pressure ratio, P_t/P_0
τ = time

Subscripts

B = back pressure
c = critical condition
E = equilibrium (corresponding to local static pressure)
F = frozen
g = vapor phase
H = homogeneous (equal phase velocities)
l = liquid phase
0 = stagnation
p = constant pressure
R = reduced pressure
TP = two-phase
t = throat
v = constant volume
w = wall

---

[1] Formerly, Lewis Research Center, Cleveland, Ohio.

Contributed by the Heat Transfer Division and presented at the Winter Annual Meeting, New York, N. Y., November 29–December 3, 1970, of THE AMERICAN SOCIETY OF MECHANICAL ENGINEERS. Manuscript received by the Heat Transfer Division April 28, 1969; revised manuscript received June 12, 1970. Paper No. 70-WA/HT-5.

[2] Numbers in brackets designate References at end of paper.

Analysis

The steady-state, one-dimensional continuity and momentum equations for one-component, two-phase flow can be written as

Liquid Continuity

$$W_l v_l = A_l u_l \tag{1}$$

Vapor Continuity

$$W_g v_g = A_g u_g \tag{2}$$

Momentum

$$-A dP = d(W_g u_g + W_l u_l) + dF_w \tag{3}$$

For the high-velocity flows in a converging nozzle, such as that shown in Fig. 1, the wall shear forces are negligible compared to the momentum and pressure gradient terms. Therefore, equation (3) can be approximated by

$$-dP = G d[x u_g + (1 - x) u_l] \tag{4}$$

It is assumed that, for fixed stagnation conditions, x, v_g, v_l, u_g, and u_l are either constant or composite functions of P and z ($f[P(z)]$) for fixed upstream conditions. Hence, equation (4) shows that

$$G_t^{-1} = -\left\{\frac{d[x u_g + (1 - x) u_l]}{dP}\right\}_t \tag{5}$$

(The subscript t indicates that all the enclosed quantities are evaluated at the throat.) At critical flow, the mass flow rate exhibits a maximum with respect to the throat pressure.

$$\left.\frac{dG_c}{dP}\right|_t = 0 \tag{6}$$

Equation (6) can be applied to equation (5) to give an expression for the critical flow rate

$$G_c^2 = \left\{-\frac{d}{dP}\left[\frac{xk + (1 - x)}{k}\,[(1 - x)k v_l + x v_g]\right]\right\}_t^{-1} \tag{7}$$

where k is defined by $k = u_g/u_l$. Equation (7) can be expanded to

$$G_c^2 = -\left\{k\left[[1 + x(k - 1)]x\frac{dv_g}{dP} + [v_g\{1 + 2x(k - 1) + k v_l 2(x - 1) + k(1 - 2x)\}]\frac{dx}{dP} + k[1 + x(k - 2) - x^2(k - 1)]\frac{dv_l}{dP} + x(1 - x)\left(k v_l - \frac{v_g}{k}\right)\frac{dk}{dP}\right]^{-1}\right\}_t \tag{8}$$

The rapid expansion of a one-component mixture through a converging nozzle is not expected to follow a thermodynamic equilibrium path, and, since the phases have different densities, the pressure gradient will also tend to accelerate the lighter vapor phase more than the liquid. These resulting temperature, free energy, and velocity differences cause the interphase transfer of heat, mass, and momentum. These interphase processes determine the thermodynamic paths followed by each phase in the expansion; thus, the variables v_g, v_l, x, and k are functions of the stagnation conditions and the path traced by the expansion. The local values of these quantities at the throat are indicative of the *amounts* of interphase heat, mass, and momentum transfer occurring in the expansion between the stagnation and throat regions. The derivatives $\left.\frac{dv_g}{dP}\right|_t$, $\left.\frac{dv_l}{dP}\right|_t$, $\left.\frac{dx}{dP}\right|_t$, and $\left.\frac{dk}{dP}\right|_t$, which are assumed to be functions of P and z, can be expressed as

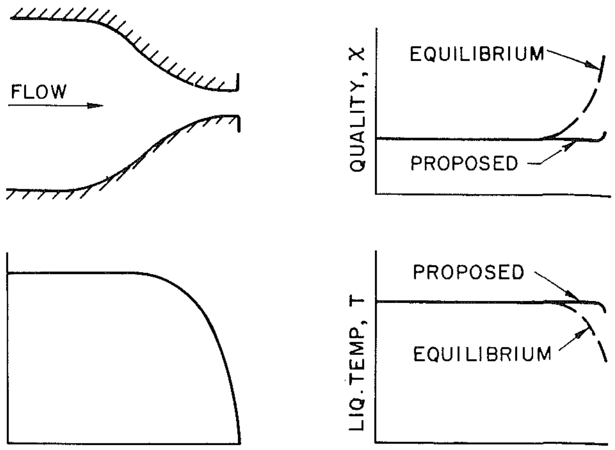

Fig. 1 Comparison of equilibrium and proposed heat and mass transfer processes for critical flow in a nozzle

$$\left.\frac{dL}{dP}\right|_t = \left.\frac{dL}{dz}\right|_t \Big/ \left.\frac{dP}{dz}\right|_t \tag{9}$$

where L_t denotes v_{gt}, v_{lt}, x_t, or k_t. If the above derivatives are viewed from a Lagrangian system, such that $z = u_t\tau$ and $\frac{dz}{d\tau} = u_t$, equation (9) shows that

$$\left.\frac{dL}{dP}\right|_t = \left.\frac{dL}{d\tau}\right|_t \Big/ \left.\frac{dP}{d\tau}\right|_t \tag{10}$$

Hence, these quantities describe the local *rates* of interphase heat, mass, and momentum transfer occurring at the throat.

In a converging nozzle, the acceleration and the accompanying steep pressure gradients essentially occur between the upstream location which has a diameter twice that of the throat and the throat itself as shown in Fig. 1. Therefore, in normal nozzle configurations, there is little time for mass transfer to take place, and it is reasonable to assume that the amount of mass transferred in the expansion is negligible.

$$x_t \approx x_0 \tag{11}$$

This is illustrated by the solid line in Fig. 1 as compared to the dotted line which is representative of the thermodynamic equilibrium behavior commensurate with the pressure profile.

An analogous argument can be applied to the transfer of heat between the phases, which is illustrated by the essentially constant liquid temperature shown in Fig. 1.

$$T_{lt} \approx T_{l0} \tag{12}$$

This is in agreement with the two-component measurements of Smith et al. [22].

There is little experimental data available to evaluate the velocity ratios in nozzles as a function of pressure. The measured void fractions in reference [1] indicate that for a throat pressure of 50 psia, the velocity ratios in long constant-area ducts are between 1.0 and 1.5. The interphase velocity differences result from density differences and are thus suppressed by increased pressures. Since many of the above applications involve rather high levels of reduced pressure $P_R > 0.05$, it is assumed that the phase velocities are equal.

$$u_g = u_l = u \tag{13}$$

The validity of this approximation increases with increased pressure.

The lack of interphase heat and mass transfer during the expansion generates temperature and free energy differences within the mixture. To evaluate such conditions it is assumed equilibrium thermodynamic relations can be used to approximate the behavior of each phase.

Since wall shear, heat exchange with the environment, and interfacial viscous terms are neglected, the system entropy during the expansion can be assumed constant

$$ds_0 = d[(1 - x)s_l + xs_g] = 0 \tag{14}$$

This result along with the assumptions stating negligible amounts of interphase heat and mass transfer imply that each phase expands isentropically.

$$s_{g0} = s_{gt} \quad \text{and} \quad s_{l0} = s_{lt} \tag{15}$$

$$P_0 v_{g0}^{\gamma} = P_t v_{gt}^{\gamma} \tag{16}$$

$$v_{l0} = v_{lt} \tag{17}$$

The negligible interphase heat transfer during the expansion results in a large temperature difference between the phases at the throat, which in turn indicates that the local rate of heat transfer can be large. The temperature data reported by Smith et al. [22] for two-phase, air-water critical flow in a venturi show that large heat transfer *rates* are in evidence at the throat. Due to these large heat transfer rates, it is not reasonable to evaluate the derivative $\left.\frac{dv_g}{dP}\right|_t$ in an adiabatic manner. A description of the actual heat transfer process requires a detailed knowledge of the flow configuration which is unknown. Therefore, as a compromise between simplicity and the real process, it is assumed that the vapor behavior at the throat can be described by a polytropic process such that

$$\left.\frac{dv_g}{dP}\right|_t = \left.\frac{v_g}{nP}\right|_t \tag{18}$$

where n is the thermal equilibrium polytropic exponent derived by Tangren et al. [23] and given by

$$n = \frac{(1 - x)c_l/c_{pg} + 1}{(1 - x)c_l/c_{pg} + 1/\gamma} \tag{19}$$

This exponent reflects a significant heat transfer rate at the throat.

The liquid compressibility is generally a very small part of that characterizing the two-phase system. Hence, it is assumed herein that the liquid phase can be considered incompressible.

$$\frac{dv_l}{dP} = 0 \tag{20}$$

The term $\left.\frac{dk}{dP}\right|_t$, which is indicative of the momentum transfer rate, is difficult to evaluate and appears to be significant [1, 24]. According to the approximation of equation (11), a one-component mixture essentially expands in a two-component manner. Vogrin [25] determined axial velocity ratio profiles for low-quality, air-water critical flows in a converging-diverging nozzle. Since k was assumed to be $f[P(z)]$,

$$\left.\frac{dk}{dP}\right|_t = \frac{dk/dz|_t}{dP/dz|_t} \tag{21}$$

Several of the axial pressure and velocity ratio profiles reported in reference [25] are shown in Fig. 2. Under critical flow conditions the velocity ratio appears to exhibit a minimum at the throat, but the pressure gradient is not zero. Thus,

$$\left.\frac{dk}{dP}\right|_t = 0 \tag{22}$$

It is assumed that this expression also applies to one-component critical flows in converging nozzles.

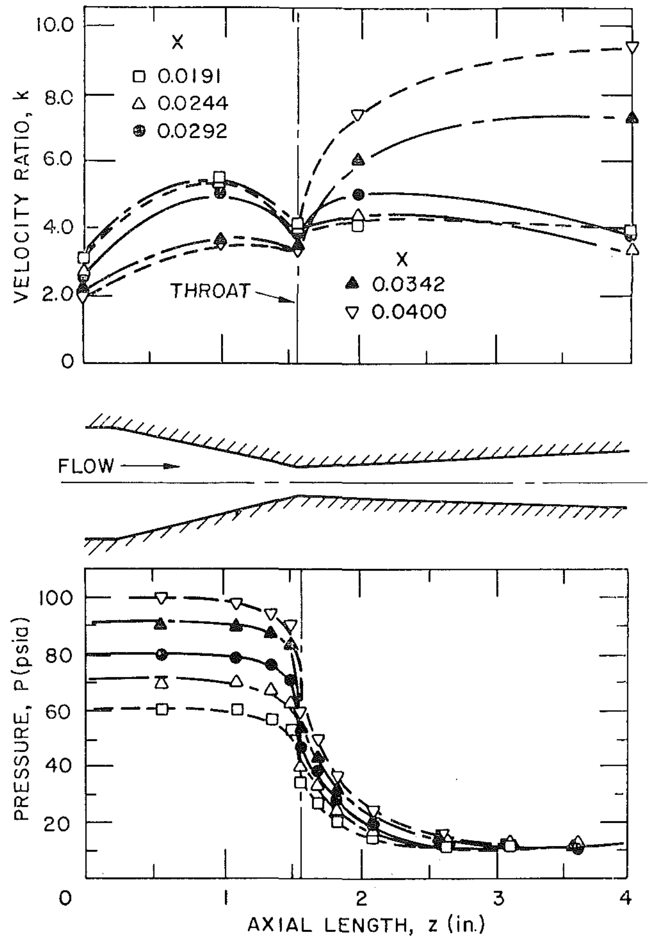

Fig. 2 Axial velocity ratio and pressure profiles for converging-diverging nozzle as reported in reference [25]

Like the local heat transfer rate, the rate of mass transfer at the throat can be appreciable. In reference [1] it was shown that, if an equilibrium quality is defined as

$$x_E = \frac{s_0 - s_{lE}}{s_{gE} - s_{lE}} \tag{23}$$

the exit plane mass transfer rate for steam-water critical flows in constant-area ducts can be correlated by

$$\left.\frac{dx}{dP}\right|_t = -\left[\frac{(1 - x_0)\frac{ds_l}{dP} + x_0\frac{ds_g}{dP}}{s_{g0} - s_{l0}}\right]_t = N\left.\frac{dx_E}{dP}\right|_t \tag{24}$$

where

$$N = N(x_E) \tag{25}$$

In the low-quality region for which this formulation was intended, it can be shown numerically that the mass transfer is dominated by the behavior of the liquid phase. Therefore, the correlation essentially describes the flashing of the liquid, or since $(1 - x_0) \approx 1$ at low qualities,

$$\left[\frac{1}{s_{g0} - s_{l0}}\frac{ds_l}{dP}\right]_t = N\left[\frac{1}{s_{gE} - s_{lE}}\frac{ds_{lE}}{dP}\right]_t \tag{26}$$

The experimental measurements of reference [1] show that N can be represented by $N = 20x_{Et}$. However, for the nozzle flows considered herein, the flow regimes and throat pressure gradients will differ from those of constant-area ducts. Therefore, it is assumed that the formulation of equation (26) is ap-

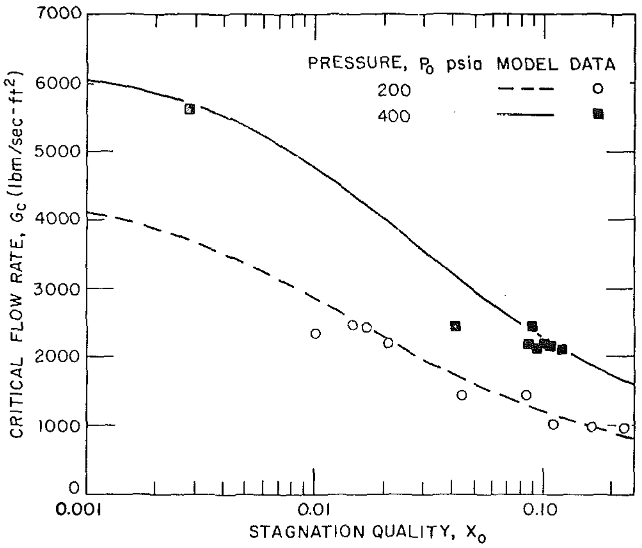

Fig. 3 Comparison between proposed model and experimental data of references [26, 27]

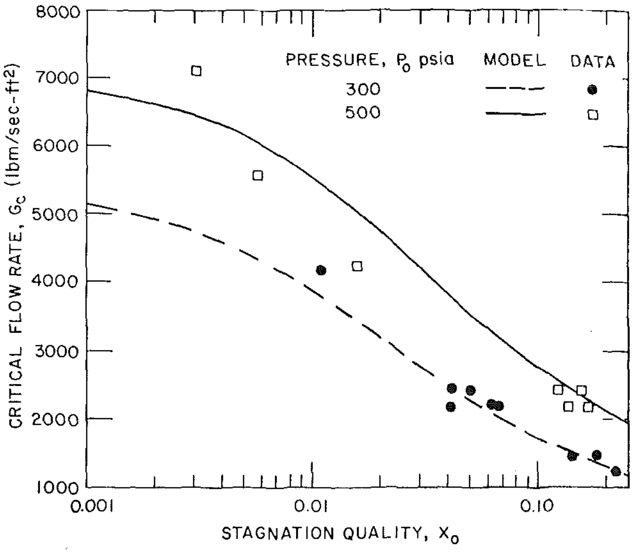

Fig. 4 Comparison between proposed model and experimental data of references [26, 27]

plicable to nozzle flows and that N can be represented by $N = C_1 x_{Et}$, but the constant C_1 will have a value other than 20.

The derivative $\left.\frac{ds_g}{dP}\right|_t$ can be determined from the expression

$$T_g ds_g = dh_g - v_g dP \qquad (27)$$

If it is assumed that the vapor behaves as a real gas following the polytropic process described in equation (18), it can be shown that

$$\left.\frac{ds_g}{dP}\right|_t = -\frac{c_{pg}}{P_t}\left[\frac{1}{n} - \frac{1}{\gamma}\right] \qquad (28)$$

The above approximations for x_t, $\left.\frac{dx}{dP}\right|_t$, k_t, and $\left.\frac{dk}{dP}\right|_t$ simplify the critical flow rate expression to

$$G_c^2 = \left[\frac{x_0 v_g}{nP} + (v_g - v_{l0})\left\{\frac{(1 - x_0)N}{s_{gE} - s_{lE}}\frac{ds_{lE}}{dP} - \frac{x_0 c_{pg}(1/n - 1/\gamma)}{P(s_{g0} - s_{l0})}\right\}\right]_t^{-1} \qquad (29)$$

If N equals unity, the prediction of equation (29) is close to that of the homogeneous equilibrium model, and if N equals zero the solution is approximately the homogeneous frozen model. (These two solutions are discussed later in the paper.) Therefore, the quantity N describes the partial phase change occurring at the throat. The experimental results of reference [11] indicate that the critical flow rates are in relatively good agreement with the homogeneous equilibrium model for stagnation qualities greater than 0.10. For qualities less than this value, the equilibrium model underestimates the data. Hence, since N describes the deviation from equilibrium mass transfer, N is set equal to unity when $x_0 = 0.10$. As was discussed earlier, the term N is correlated as a function of throat equilibrium quality, x_{Et}. For the operating conditions reported in reference [11], a stagnation quality of 0.10 corresponds to throat equilibrium qualities ranging from 0.125 to 0.155 depending on the pressure level. For the evaluations given herein, an average value of 0.14 was chosen, thus

$$N = x_{Et}/0.14 \qquad (30)$$

For throat equilibrium qualities greater than 0.14, N is set equal to unity. This numerical evaluation for N is common to all fluids and geometries considered herein.

The equation for the critical flow rate is coupled with the momentum equation describing the overall pressure history to obtain a solution in terms of the stagnation conditions. The two-phase momentum equation (4), under the restrictions listed above, can be written as

$$-[(1 - x_0)v_{l0} + x_0 v_g]dP = d\left(\frac{u^2}{2}\right) \qquad (31)$$

This expression can be integrated between the stagnation and throat locations to give

$$(1 - x_0)v_{l0}(P_0 - P_t) + \frac{x_0\gamma}{\gamma - 1}[P_0 v_{g0} - P_t v_{gt}] = \frac{[(1 - x_0)v_{l0} + x_0 v_{gt}]^2}{2} G_c^2 \qquad (32)$$

Substitution of equation (29) for the critical flow rate enables one to rearrange equation (32) and express it more compactly as

$$\eta = \left\{\frac{\frac{1 - \alpha_0}{\alpha_0}(1 - \eta) + \frac{\gamma}{\gamma - 1}}{\frac{1}{2\beta\alpha_t^2} + \frac{\gamma}{\gamma - 1}}\right\}^{\frac{\gamma}{\gamma - 1}} \qquad (33)$$

where

$$\eta = P_t/P_0 \qquad (34)$$

$$\beta = \left[\frac{1}{n} + \left(1 - \frac{v_{l0}}{v_{gt}}\right)\left(\frac{(1 - x_0)NP_t}{x_0(s_{gE} - s_{lE})_t}\frac{ds_{lE}}{dP}\right)_t - \frac{c_{pg}(1/n - 1/\gamma)}{(s_{g0} - s_{l0})}\right] \qquad (35)$$

$$\alpha_0 = \frac{x_0 v_{g0}}{(1 - x_0)v_{l0} + x_0 v_{g0}} \qquad (36)$$

$$\alpha_t = \frac{x_0 v_{gt}}{(1 - x_0)v_{l0} + x_0 v_{gt}} \qquad (37)$$

and

$$v_{gt} = v_{g0}\left(\eta^{-\frac{1}{\gamma}}\right) \qquad (38)$$

For given stagnation conditions of P_0 and x_0, the transcen-

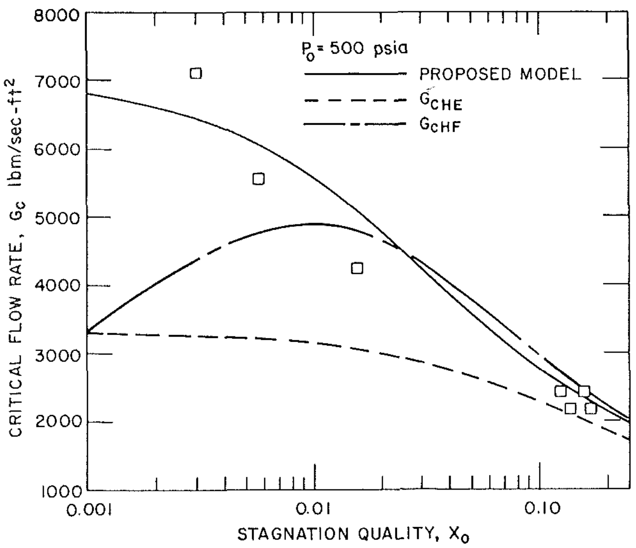

Fig. 5 Comparison of critical flow predictions and experimental data of references [26, 27]

dental expression for the critical pressure ratio, equation (33), can be solved. This solution implicitly involves the critical flow rate as shown by equation (32). Therefore, a solution of equation (33) yields predictions of both the critical pressure ratio and flow rate.

In summary, a model is presented to describe the two-phase critical flow of one-component, liquid-vapor mixtures through convergent nozzles. The salient feature of the model is that it requires only a knowledge of the stagnation conditions. The model was formulated by examining pertinent high-velocity, two-phase flow data and extracting from these results reasonable approximations for the amounts and rates of interphase heat, mass, and momentum transfer. These approximations were used to generate a nonequilibrium critical flow model which was then combined with the overall momentum equation to yield a solution in terms of the stagnation properties.

Comparison With Experimental Results

The proposed model is compared with the experimental steam-water results of references [26, 27] in Figs. 3 and 4 for a range of stagnation pressures. The good agreement between the theory and the data throughout the quality range investigated is apparent.

One of the standard approaches used in the literature is the homogeneous equilibrium model. This model is described in reference [11] and is based on the following assumptions:

1 The average velocities for the phases are equal.

2 Thermodynamic equilibrium exists between the phases.

3 The expansion is isentropic.

4 Properties correspond to those presented in the steam tables, reference [28]. The flow rate prediction resulting from these assumptions is

$$G_{cHE} = \frac{\{2[H_0 - (1 - x_E)h_{lE} - x_E h_{gE}]\}^{1/2}}{(1 - x_E)v_{lE} + x_E v_{gE}} \qquad (39)$$

The critical flow rate prediction of this model is computed by choosing successively lower downstream pressures until the flow rate exhibits a maximum.

Another model which has appeared frequently in the literature is the homogeneous frozen model which is based on the following assumptions:

1 The average velocities of the phase are equal.

2 No heat or mass transfer occurs between the phases.

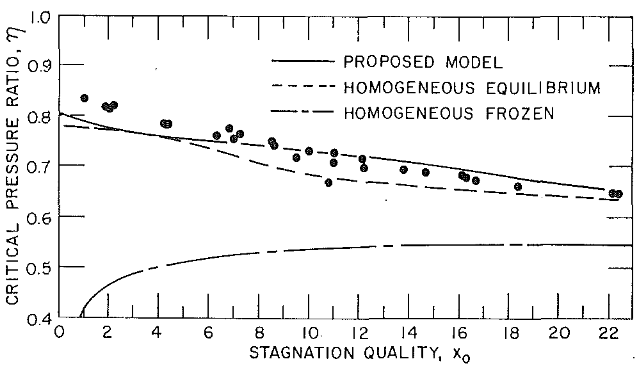

Fig. 6 Comparison of critical pressure ratio predictions for P_0 = 500 psia and experimental data of reference [27]

3 The vapor expands isentropically as a perfect gas, i.e., $Pv_g{}^\gamma$ is constant.

4 The kinetic energy is due solely to the vapor expansion.

5 The critical flow rate is defined by gas-dynamic principles.

These assumptions lead to an expression for the critical pressure ratio which is given by the following transcendental equation:

$$\frac{(1 - x_0)v_{l0}}{x_0 v_{g0}}(1 - \eta) + \frac{\gamma}{\gamma - 1}\left[1 - \eta^{\frac{\gamma-1}{\gamma}}\right] = \left[\frac{(1 - x_0)v_{l0}}{x_0 v_{g0}} + \eta^{-\frac{1}{\gamma}}\right]^2 \frac{\gamma}{2}\,\eta^{\frac{\gamma+1}{\gamma}} \qquad (40)$$

When $\frac{(1 - x_0)v_{l0}}{x_0 v_{g0}} \ll 1$, equation (40) can be simplified to

$$\eta = \left[\frac{2}{\gamma + 1}\right]^{\frac{\gamma}{\gamma-1}} \qquad (41)$$

Under the assumptions outlined above, the energy equation and the two-phase specific volume can be expressed as

$$H_0 - h_t = x_0 v_{g0} P_0 \left(\frac{\gamma}{\gamma - 1}\right)\left[1 - \eta^{\frac{\gamma-1}{\gamma}}\right] \qquad (42)$$

$$v = (1 - x_0)v_{l0} + x_0 v_{g0} \eta^{\frac{1}{\gamma}} \qquad (43)$$

respectively, and the critical flow rate is given by

$$G_{cHF} = \frac{1}{v}\left\{2x_0 v_{g0} P_0 \left(\frac{\gamma}{\gamma - 1}\right)\left[1 - \eta^{\frac{\gamma-1}{\gamma}}\right]\right\}^{1/2} \qquad (44)$$

The predictions of the three models are compared to the experimental data in Fig. 5 for a stagnation pressure of 500 psia. The model proposed in this study exhibits the best agreement throughout the quality range of interest.

The critical pressure ratio predictions of the three models discussed above are compared to the experimental data in Fig. 6. Again, it is seen that the formulation developed herein is the best solution throughout the range. It should be noted here that there were discrepancies in the critical pressure ratio data reported in reference [27]. The two nozzles employed gave two different characteristic curves for the critical pressure ratio as a function of stagnation quality. As was discussed in reference [11], this difference could easily be a result of a small difference in the relative locations of the throat taps. In Fig. 6 the data of nozzle no. 2 was not used because it was found that these results gave critical pressure ratios which were less than those reported for two-component, air-water systems (reference [29]), which is not realistic. Therefore, the data shown were generated solely by nozzle no. 1.

By considering Figs. 5 and 6 together, the reader can discern

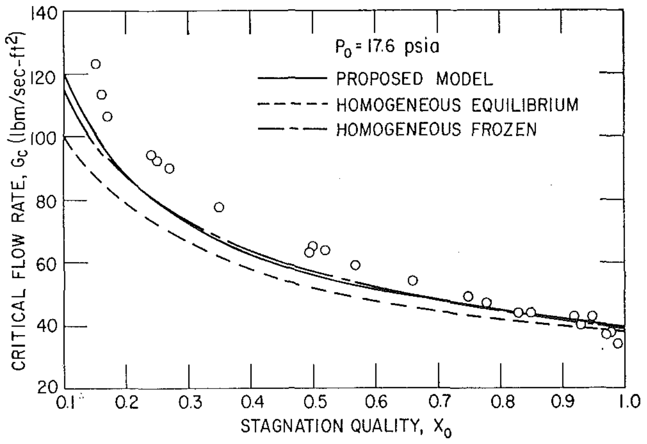

Fig. 7 Comparison of critical flow predictions and experimental data of reference [30]

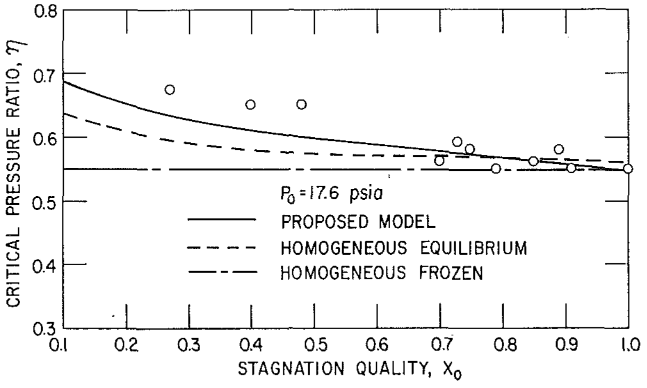

Fig. 8 Comparison of critical pressure ratio predictions and experimental data of reference [30]

the merits of the proposed model. The homogeneous frozen model yields a good prediction for the critical flow rate but considerably underestimates the critical pressure ratio. On the other hand, the homogeneous equilibrium model gives a good estimate of the critical pressure ratio but underestimates the flow rate. Therefore, neither of these solutions correctly describes the complete physical phenomenon. The proposed formulation gives accurate predictions for both the critical pressure ratio and flow rate and, thus, is more characteristic of the actual behavior. This is further verified by the recent low-pressure, steam-water data of Deich et al. [30] shown in Figs. 7 and 8. The stagnation pressure is so low that the applicability of the approximation given in equation (13) is weakened considerably. However, these results confirm the above discussion regarding various models.

Fig. 9 compares the proposed solution to the high-temperature, high-quality potassium data [31]. The tabular properties of Weatherford [32] were used in calculating the predictions. Table 1 shows the good agreement between the predictions of the proposed model and the recent high-quality, steam-water nozzle data of Carofano and McManus [33]. Figs. 10 and 11 compare the present analysis with the two-phase carbon dioxide nozzle reported by Hesson and Peck [16] and detailed in reference [17].

Saturated and Subcooled Conditions

The proposed solution applies to a saturated-vapor stagnation condition when $x_0 = 1$. The model can also be applied to cases where the stagnation condition is either saturated or subcooled liquid. For such cases $x_0 = 0$ and the critical flow expression is simplified to

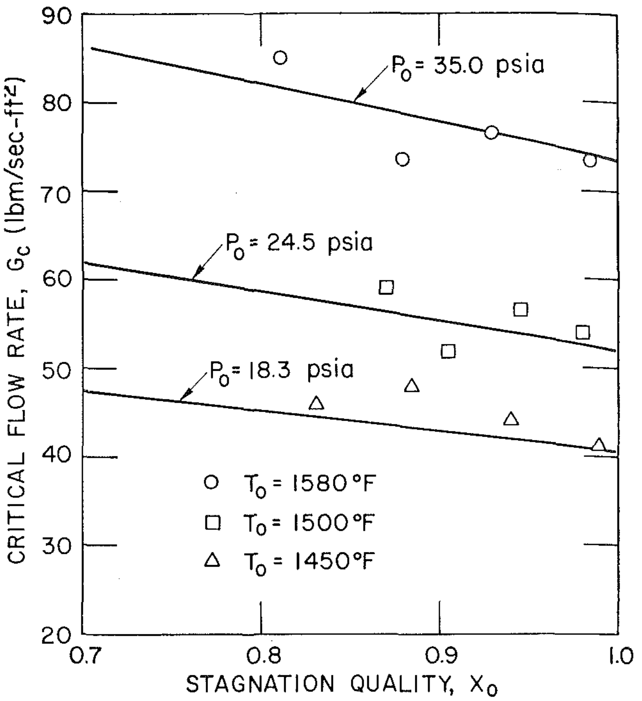

Fig. 9 Comparison between proposed model and potassium data of reference [31]

Table 1 Comparison between the proposed model and data of reference [33]

Run	P_0(psia)	X_0	Flow rate (lbm/sec-ft^2) Experimental	Predicted
1	21.1	0.788	54.8	53.7
2	19.6	0.727	54.7	52.2
3	26.9	0.871	64.1	64.7
4	26.3	0.890	61.4	62.7
5	27.5	0.834	68.1	67.5
6	26.0	0.873	61.3	62.6
7	26.8	0.795	67.4	67.4
8	23.0	0.680	66.0	62.7
9	19.5	0.641	59.1	55.2

$$G_c^2 = \left[(v_{gE} - v_{l0}) \frac{N}{s_{gE} - s_{lE}} \frac{ds_{lE}}{dP} \right]_t^{-1} \tag{45}$$

where N is given by equation (30). Since no vapor is formed until the throat is reached, an additional assumption is necessary to estimate the vapor specific volume at the throat. As shown in equation (45), it is assumed that the vapor which is formed is saturated at the local pressure.

The critical pressure ratio relationship for such flows is greatly simplified.

$$\eta = 1 - \frac{v_{l0} G_c^2}{2P_0} \tag{46}$$

Equation (45) can be substituted into equation (46) to give a transcendental expression for the critical pressure ratio. A solution to this expression gives predictions for both the critical pressure ratio and flow rate.

In Fig. 12 the predictions for initially saturated and subcooled water are compared to the data of references [8, 34, 35, 36, 37, 38]. The model describes the general behavior of the experimental results. The agreement is better for higher pressures and subcoolings. The model is also compared to recent subcooled liquid nitrogen data [39] in Fig. 13. The agreement is excellent throughout the reported ranges of pressures and sub-

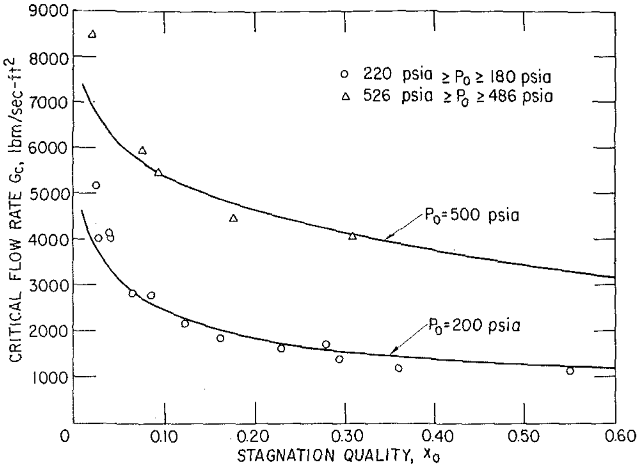

FIG. 10

Fig. 10 Comparison between proposed model and carbon dioxide data of reference [17]

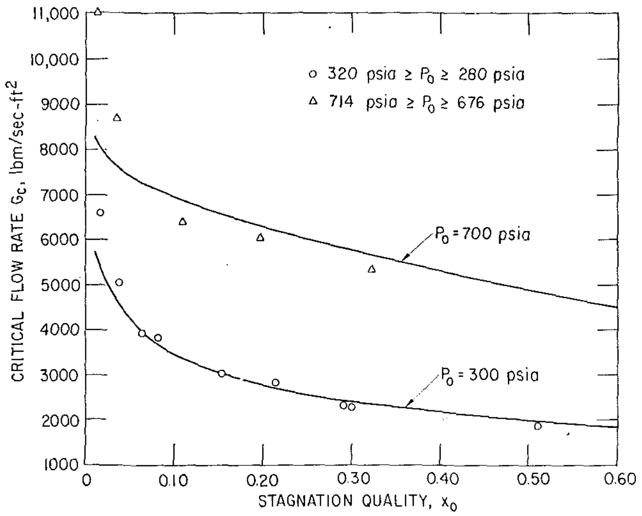

Fig. 11 Comparison between proposed model and carbon dioxide data of reference [17]

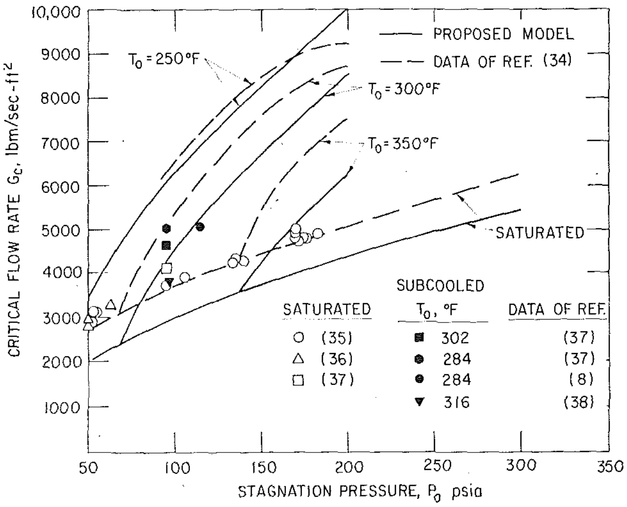

Fig. 12 Comparison between proposed model and saturated and subcooled water data of references [8, 34–38]

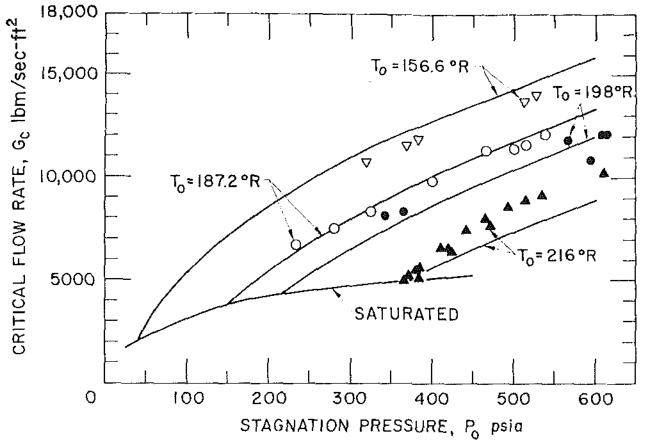

Fig. 13 Comparison between proposed model and subcooled liquid nitrogen data of reference [39]

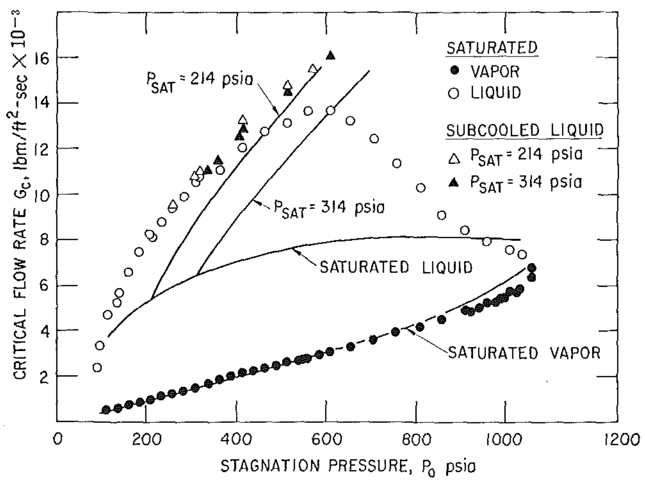

Fig. 14 Comparison between proposed model and subcooled and saturated liquid and saturated vapor data of reference [17]

coolings. Finally, Fig. 14 compares the model with the data of Hesson [17] for stagnation conditions of subcooled and saturated liquid and saturated vapor.

Orifices and Short Tubes

The model derived above, and in particular the mass transfer correlation given in equation (26), is for a thoroughly dispersed mixture. It has been shown by numerous investigators [3, 8, 16, 40–43] that the discharge of initially subcooled or saturated liquid through an orifice or short tube (short, constant-area duct with a sharp-edged entrance) has a unique separated flow pattern. However, if the upstream stagnation condition is a thoroughly dispersed mixture, the flow will remain dispersed throughout the expansion. Thus, the model can be extended to such flows.

As shown by Perry [44], compressible flows through sharp-edged orifices do not choke; however, they do asymptotically approach a maximum flow rate. For flows operating well into the compressible range ($P_B/P_0 < 0.3$ where P_B is the downstream receiver pressure), a compressible discharge coefficient for fixed stagnation conditions can be defined as

$$C = \frac{\text{actual flow rate}}{\text{critical flow rate in ideal nozzle}}$$

This definition can be incorporated into equation (32) to give a

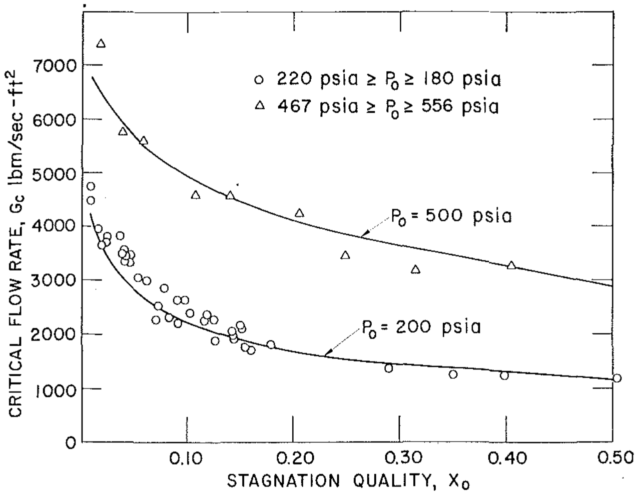

Fig. 15 Comparison between proposed model and two-phase orifice data of reference [17]

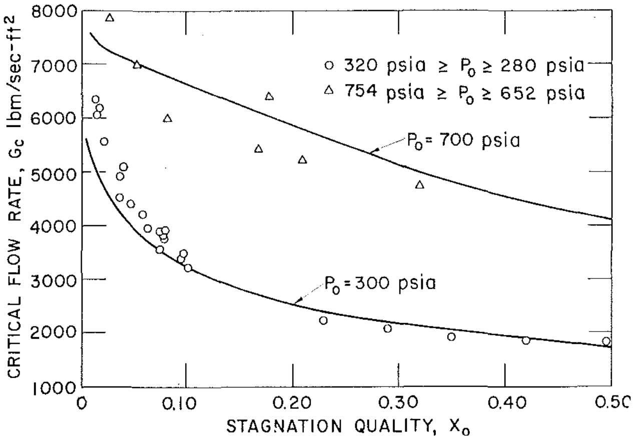

Fig. 16 Comparison between proposed model and two-phase orifice data of reference [17]

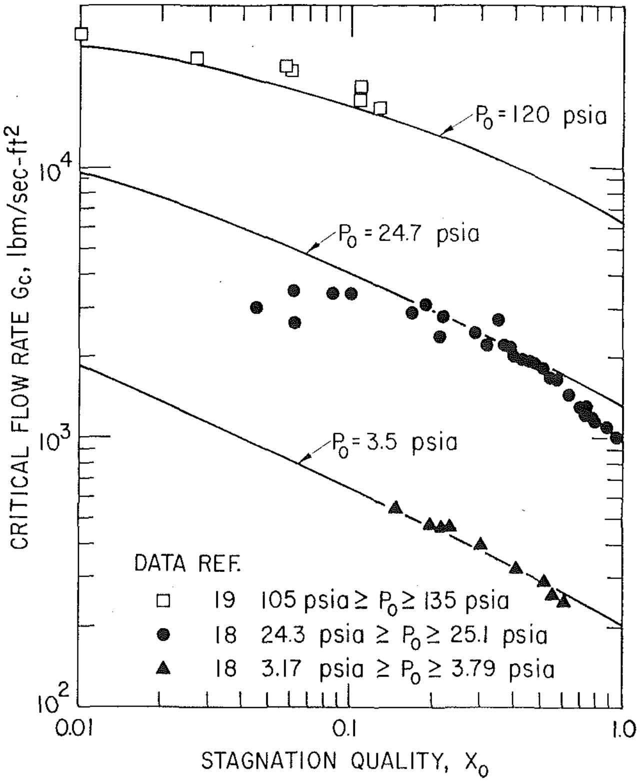

Fig. 17 Comparison between proposed model and two-phase nitrogen orifice data of references [18, 19]

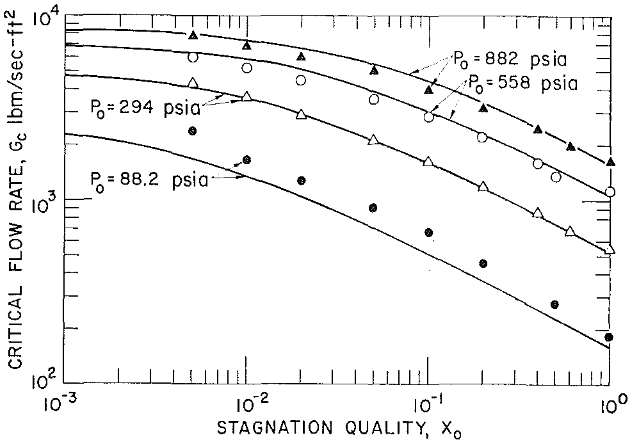

Fig. 18 Comparison between proposed model and short-tube, steam-water data of reference [49]

formulation for two-phase compressible flows through orifices. Equation (33) is then written as

$$\eta = \left\{ \frac{\dfrac{1-\alpha_0}{\alpha_0}(1-\eta)+\dfrac{\gamma}{\gamma-1}}{\dfrac{1}{2C^2\beta\alpha_{t}^{2}}+\dfrac{\gamma}{\gamma-1}} \right\}^{\frac{\gamma}{\gamma-1}} \tag{47}$$

As before, this transcendental expression for the critical pressure ratio can be solved to give a prediction for the maximum flow rate.

The single-phase experiments of Perry show the compressible discharge coefficient for sharp-edged orifices is 0.84. This value is also representative of single-phase critical flows through short tubes [45]. It is assumed that this discharge coefficient is also applicable to one-component, two-phase flows through similar geometries. (As stated above, this only applies to systems which are two-phase mixtures in the upstream stagnation chamber.)

The predictions for compressible two-phase flow of carbon dioxide through a sharp-edged orifice are compared to the data of Hesson [17] in Figs. 15 and 16. The saturation properties of carbon dioxide were assembled from references [46, 47]. Fig. 17 compares the model to the two-phase nitrogen data of Bonnet [19] and Campbell and Overcamp [18]. To effect a common basis for comparison, the model and the data from both references were all evaluated from the saturation properties of Strobridge [48]. In Fig. 18, the model is also compared to the short-tube, steam-water results of Friedrich [49]. The model is in good agreement for all the mixtures considered.

Summary and Conclusions

A model is developed for the two-phase critical discharge of one-component mixtures through convergent nozzles. The salient features of the model are:

1 The proposed solution is based on and requires a knowledge of only the geometry and the upstream stagnation conditions.

2 The stagnation conditions covered by the model include subcooled liquid, saturated liquid, two-phase mixtures, and saturated vapor.

3 The model assumes neither completely frozen nor complete equilibrium heat and mass transfer processes. Instead, the model uses the best available data to determine reasonable approximations for the heat transfer process and the best available correlation for the rate of interphase mass transfer at the throat.

Comparisons between the theoretical predictions and the available experimental results, which include water, nitrogen, potassium and carbon dioxide data, show that the model is in good agreement with the data over a wide range of stagnation conditions.

For the cases where the mixture is in a two-phase condition in the stagnation chamber, the compressible flow through orifices and short tubes can be related to nozzle flow in the same manner as single-phase flow. The predictions show good agreement with the experimental data for such geometries.

References

1 Henry, R. E., "A Study of One- and Two-Component, Two-Phase Critical Flows at Low Qualities," ANL-7430, Argonne National Laboratory, 1968.

2 Fauske, H. K., "Contribution to the Theory of Two-Phase, One-Component Critical Flow," ANL-6633, Argonne National Laboratory, 1962.

3 Fauske, H. K., "The Discharge of Saturated Water Through Tubes," *Chem. Eng. Prog. Symp. Ser.*, Vol. 61, 1965, p. 210.

4 Fauske, H. K., "Two-Phase, Two- and One-Component Critical Flow," *Proc. of Symp. on Two-Phase Flow*, University of Exeter, Devon, England, Vol. 3, SG101, 1965.

5 Isbin, H. S., Moy, J. E., and Cruz, A. J. R., "Two-Phase, Steam-Water Critical Flow," *AIChE Journal*, Vol. 3, 1957, p. 361.

6 Faletti, D. W., and Moulton, R. W., "Two-Phase Critical Flow of Steam-Water Mixtures," *AIChE Journal*, Vol. 9, 1963, p. 247.

7 Zaloudek, F. R., "The Low-Pressure Critical Discharge of Steam-Water Mixtures from Pipes," HW-68936, Hanford Works, 1961.

8 Zaloudek, F. R., "The Critical Flow of Hot Water Through Short Tubes," HW-77594, Hanford Works, 1963.

9 Zaloudek, F. R., "Steam-Water Critical Flow From High Pressure Systems," Interim Report, HW-80535, Hanford Works, 1964.

10 Zaloudek, F. R., "The Low Pressure Critical Discharge of Steam-Water Mixtures From Pipe Elbows and Tees," BNWL-34, Pacific Northwest Laboratory, 1965.

11 Starkman, E. S., Schrock, V. E., Neusen, K. F., and Maneely, D. J., "Expansion of a Very Low Quality Two-Phase Fluid Through a Convergent-Divergent Nozzle," *Journal of Basic Engineering*, TRANS. ASME, Series D, Vol. 86, No. 2, June 1964, pp. 247–256.

12 Levy, S., "Prediction of Two-Phase Critical Flow Rate," JOURNAL OF HEAT TRANSFER, TRANS. ASME, Series C, Vol. 87, No. 1, Feb. 1965, pp. 53–58.

13 Moody, F. J., "Maximum Flow Rate of a Single Component, Two-Phase Mixture," JOURNAL OF HEAT TRANSFER, TRANS. ASME, Series C, Vol. 87, No. 1, Feb. 1965, pp. 134–142.

14 Cruver, J. E., "Metastable Critical Flow of Steam-Water Mixtures," PhD thesis, University of Washington, 1963.

15 Klingebiel, W. J., "Critical Flow Slip Ratios of Steam-Water Mixtures," PhD thesis, University of Washington, 1964.

16 Hesson, J. C., and Peck, R. E., "Flow of Two-Phase Carbon Dioxide Through Orifices," *AIChE Journal*, Vol. 4, 1958, p. 207.

17 Hesson, J. C., "Flow of Two-Phase Carbon Dioxide Through Orifices," PhD thesis, Illinois Institute of Technology, 1957.

18 Campbell, H. M., and Overcamp, T. J., "Critical Flowrate of Two-Phase Nitrogen," NASA TM X-53492, 1966.

19 Bonnet, F. W., "Critical Two-Phase Flow of Nitrogen and Oxygen Through Orifices," *Advances in Cryogenic Engineering*, Vol. 12, 1966, p. 427.

20 Ryley, D. J., and Parker, G. J., "Two-Phase Critical Flow Through Suction Slots in Low Pressure Steam Turbine Blades," *Journal of Mechanical Engineering Science*, Vol. 10, 1968, p. 337.

21 Neusen, K. F., discussion of reference [13], JOURNAL OF HEAT TRANSFER, TRANS. ASME, Series C, Vol. 87, No. 1, Feb. 1965, pp. 141–142.

22 Smith, R. V., Cousins, L. B., and Hewitt, G. F., "Two-Phase Two-Component Critical Flow in a Venturi," AERE-R5736, 1968.

23 Tangren, R. F., Dodge, C. H., and Seifert, H. S., "Compressibility Effects in Two-Phase Flow," *Journal of Applied Physics*, Vol. 20, 1949, p. 736.

24 Henry, R. E., Grolmes, M. A., and Fauske, H. K., "Propagation Velocity of Pressure Waves in Gas-Liquid Mixtures," *Cocurrent Gas-Liquid Flow*, Vol. 1, Plenum Press, 1969.

25 Vogrin, J. A., "An Experimental Investigation of Two-Phase, Two-Component Flow in a Horizontal Converging-Diverging Nozzle," ANL-6754, Argonne National Laboratory, 1963.

26 Maneely, D. J., "A Study of the Expansion Process of Low Quality Steam Through a de Laval Nozzle," UCRL-6230, University of California Radiation Laboratory, 1962.

27 Neusen, K. F., "Optimizing of Flow Parameters for the Expansion of Very Low Quality Steam," UCRL-6152, University of California Radiation Laboratory, 1962.

28 Keenan, J. H., and Keyes, F. G., *Thermodynamic Properties of Steam*, John Wiley and Sons, N. Y., 1959.

29 Netzer, D. W., "Calculations of Flow Characteristics for Two-Phase Flow in Annular Converging-Diverging Nozzles," TM-62-3, Jet Prop. Center, Purdue University, Lafayette, Ind., 1962.

30 Deich, M. E., Danilin, V. S., Tsiklauri, G. V., and Shanin, U. K., "Investigation of the Flow of Wet Steam in Axisymmetric de Laval Nozzles Over a Wide Range of Moisture Content," *High Temperature*, Vol. 7, 1969, p. 294.

31 Rossbach, R. J., "Critical Flow of Potassium Vapor Through Instrumented Convergent-Diverging Nozzle," ASME Paper No. 65-GTP-22.

32 Weatherford, W. D., Jr., Tyler, J. C., and Ku, P. M., "Properties of Inorganic Energy-Conversion and Heat Transfer Fluids for Space Applications," WADD TR-61-96, Southwest Research Institute, 1961.

33 Carofano, G. C., and McManus, H. N., Jr., "An Analytical and Experimental Study of Air-Water and Steam-Water Mixtures in a Converging-Diverging Nozzle," *Progress in Heat and Mass Transfer*, ed. by Irvine et al., Vol. 2, 1969, p. 395.

34 Yarnall, D. R., discussion of "The Flow of Saturated Water Through Throttling Orifices," TRANS. ASME, Vol. 63, 1941, p. 428.

35 Burnell, J. G., "Flow of Boiling Water Through Nozzles, Orifices, and Pipes," *Engineering*, Vol. 164, 1948, p. 572.

36 Bottomley, W. T., "The Flow of Boiling Water Through Orifices and Pipes," *Trans. of North East Coast Inst. of Engrs and Shipbuilders*, Vol. 43, 1936, p. 65.

37 Friedrich, H., and Vetter, G , "Influence of Nozzle Shape on the Through Flow Behavior of Jets for Water at Various Thermodynamic States," *Energie*, Vol. 14, 1962, p. 3.

38 Danforth, J. L., "Flow of Hot Water Through A Rounded Orifice," MS thesis, M.I.T., 1941.

39 Henry, R. E., Henricks, R. C., Simoneau, R. J., and Watterson, R., "Two-Phase Critical Flow of Initially Subcooled Liquid Nitrogen," to be published as an NASA Technical Note.

40 Fauske, H. K., and Min, T. C., "A Study of the Flow of Saturated Freon-11 Through Apertures and Short Tubes," ANL-6667, Argonne National Laboratory, 1963.

41 Pasqua, P. F., "Metastable Flow of Freon-12," *Refrigerating Eng.*, Vol. 61, 1953, p. 1084A.

42 Uchida, H., and Nariai, H., "Discharge of Saturated Water Through Pipes and Orifices," *Proceedings of the Third International Heat Transfer Conference*, Vol. 5, 1966, p. 1.

43 Benjamin, M. W., and Miller, J. G., "The Flow of Saturated Water Through Throttling Orifices," TRANS. ASME, Vol. 63, 1941, p. 419.

44 Perry, J. A., Jr., "Critical Flow Through Sharp-Edged Orifices," TRANS. ASME, Vol. 71, 1949, p. 757.

45 Arnberg, B. T., "Review of Critical Flowmeters for Gas Flow Measurements," *Journal of Basic Engineering*, TRANS. ASME, Series D, Vol. 84, No. 4, Dec. 1962, pp. 447–460.

46 *Handbook of Chemistry and Physics*, 45th ed., The Chemical Rubber Co., Cleveland, Ohio, 1964.

47 Perry, J. H., *Chemical Engineers Handbook*, 3rd ed., McGraw-Hill, New York, 1950.

48 Strobridge, T. R., "The Thermodynamic Properties of Nitrogen from 64 to 300°K Between 0.1 and 200 Atmospheres," TN-129, U. S. Dept. of Commerce, National Bureau of Standards, 1962.

49 Friedrich, H., "Flow Through Single-Stage Nozzles with Different Thermodynamic States," *Energie*, Vol. 12, 1960, p. 3.

Critical Rayleigh Numbers for Natural Convection of Water Confined in Square Cells With L/D From 0.5 to 8

W. L. HEITZ
Shell Development Company,
Emeryville, Calif.

J. W. WESTWATER
Professor of Chemical Engineering,
University of Illinois,
Urbana, Ill.
Mem. ASME

An experimental study of heat transfer modes in water heated from below was conducted using test cells of square cross section, 0.5 × 0.5 in., and heights of 1.25 to 4 in. Heat transfer was unidirectional and parallel to gravity. Tests both included and excluded the maximum density region of 4 deg C. Ice was present above the liquid during certain runs. The three modes of heat transfer, conduction and laminar and turbulent natural convection, were characterized by temperature profiles, fusion-front velocities and positions, and fluid flow patterns. Transitions between modes occur at well-defined critical Rayleigh numbers which are distinct functions of the L/D of the liquid. The critical values are not affected by the presence of ice, motion of the fusion front, or the temperatures of the warm and cold boundaries, if the Rayleigh number is calculated as described. The L/D was varied from 0.5 to 8 and the critical Rayleigh numbers varied from about 1700 to 10^8.

Introduction

THE EFFECT of boundary geometry, boundary temperature, and boundary motion on the modes of heat transfer in confined liquids is of wide interest. Possible applications include heat storage in space vehicles, the solidification of castings, crystal growth, and the circulation of liquids in tanks. Bénard [1][1] and Rayleigh [2], working with unbounded systems, were the first to study natural convection.

Studies of the effect of boundary dimensions on the transition between modes of heat transfer have been limited principally to the transition from pure conduction to laminar natural convection. This occurs under conditions which are defined herein as the first critical Rayleigh number, Ra_{c1}.

A mathematical model predicting Ra_{c1} for particular boundary configurations was presented by Ostrach and Pnueli [3]. Sherman and Ostrach [4] mathematically determined that for an arbitrary region $\mathrm{Ra}_{c1} > 1558\ (L/d)$ where L is the vertical liquid dimension and d is the diameter of an equal-volume sphere. Finite-difference methods were used by Samuels and Churchill [5] to show that $\mathrm{Ra}_{c1} = f\ (\mathrm{Pr}, L/D)$, for $^1/_3 \leq L/D \leq 2$, where D is the horizontal liquid dimension. Edwards and Catton [6] and Edwards [7] presented mathematical models to predict Ra_{c1} with respect to L/D and cell-wall conductance.

---

[1] Numbers in brackets designate References at end of paper.

Contributed by the Heat Transfer Division and presented at the Winter Annual Meeting, New York, N. Y., November 29–December 3, 1970, of THE AMERICAN SOCIETY OF MECHANICAL ENGINEERS. Manuscript received by the Heat Transfer Division March 23, 1970; revised manuscript received July 8, 1970. Paper No. 70-WA/HT-7.

Nomenclature

C = liquid heat capacity, (cal)(gm)$^{-1}$ (deg C)$^{-1}$
D = horizontal dimension of square test cell, cm
E = vertical dimension of test cell, cm
Gr = Grashof number, dimensionless
g = acceleration of gravity, (cm)(sec)$^{-2}$
k = thermal conductivity, (cal)(sec)$^{-1}$ (cm)$^{-1}$(deg C)$^{-1}$
L = vertical dimension of liquid, cm
Pr = Prandtl number, dimensionless
Ra = Rayleigh number, dimensionless
T = temperature, deg C
ΔT = temperature difference, deg C
Δx = significant vertical length, cm
β = liquid coefficient of expansion, (deg C)$^{-1}$
ϵ = ice thickness, cm
μ = liquid viscosity, (gm)(cm)$^{-1}$ (sec)$^{-1}$
ρ = liquid density, (gm)(cm)$^{-3}$

Subscripts

a = lower boundary
b = upper boundary
$c1$ = critical value between pure conduction and laminar natural convection
$c2$ = critical value between laminar and turbulent natural convection
1 = solid phase
2 = liquid phase

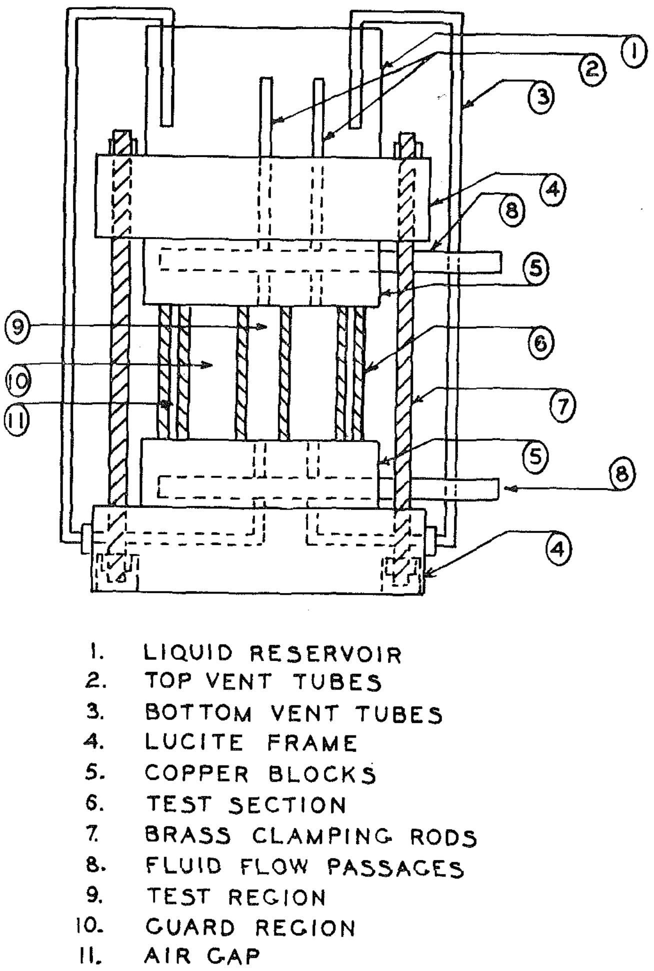

Fig. 1 Front view of test cell

The model of Davis [8] appears to be the most rigorous. Linear stability theory is used to predict Ra_{c1} as a function of L/D for enclosed fluids with both square and rectangular horizontal cross section, for conducting walls, and for $1/6 \leq L/D \leq 4$.

Experimental Ra_{c1} were presented by Schmidt and Silveston [9] for $L/D < 0.1$ and by Catton and Edwards [10] for $0 < L/D \leq 2.5$.

There have been no models presented which will predict the transition between laminar and turbulent natural convection. In this paper, this second crisis is defined by means of a second critical Rayleigh number, Ra_{c2}. Schmidt and Silveston presented an experimental value for test conditions with $L/D < 0.1$.

The object of the present study was to define the three modes of heat transfer, in terms of experimental measurements, and to determine values of the Rayleigh numbers at the transition points. Variables included the liquid depth, boundary temperatures, and motion of one boundary.

Apparatus and Procedure

The test assembly is illustrated in Fig. 1. All test measurements were taken in the center chamber of three concentric square tubes having inside dimensions in the horizontal plane of 0.5 × 0.5 in., 2.25 × 2.25 in., and 2.875 × 2.875 in. Three nominal heights were used: 1.25, 2.0, and 4.0 in. The walls were of 0.125-in-thick polymethylmethacrylate transparent plastic. The test liquid, distilled deaerated water, was present in the center chamber and in the first surrounding guard region. This water-filled guard region, the next surrounding guard region (filled with air), and 3 in. of glass wool surrounding the test assembly insured one-dimensional heat transfer in the center chamber (to within a maximum error of 5 percent). For certain tests described later, for which the error would have exceeded 5 percent with the above arrangement, the two outer plastic tubes were removed and replaced with 6 in. of glass wool. This resulted in one-dimensional heat transfer again within 5 percent.

Heat sources and sinks were located at the top and bottom of the test assembly. These were constructed of 3.44 × 3.44 × 1.00 in. copper blocks. Grooves of 0.156-in. depth were milled in one surface of each copper block to accommodate the test section. The test section was sealed in the grooves with silicone rubber and held by tie rods.

The temperature of each copper block was controlled by passing methanol at various temperatures through the fluid flow passages. A series of constant-temperature baths (dry ice–Freon-11, ice water–salt, ice water, tap water, and tap water–steam) and pumps and heating tapes controlled by Variacs allowed temperatures in either copper block to be maintained at from -50 to $+50$ deg C and to within 0.1 deg C for over 2 hr.

To accommodate volume changes and eliminate the resultant destructive pressures which occur during phase change, the top and bottom of the test and guard regions were connected to a liquid reservoir by $1/8$-in-dia vent tubes. An excess of water was maintained in the liquid reservoir during all runs. The actual intake or outflow of water during a run was small and had no important effect on heat transfer inside the test region.

Thermocouples (three or five, depending on the cell height) of 0.005-in. duplex copper–constantan wires were inserted horizontally into the test region. The thermocouples were approximately equally spaced in a vertical direction and were located 0.06 in. from the back wall of the test region to minimize their possible influence on interfacial and fluid motion. The exact thermocouple spacings were determined with a cathetometer after each test cell had been assembled. Two additional thermocouples were located in the copper blocks near the top and bottom of the test region. Their temperatures were defined as the boundary temperatures of the test material. Temperatures were recorded using a 2-sec multi-point recorder and three single-point continuous recorders.

The test cell was mounted in one of three optical systems. The first, similar to one used by Thomas and Westwater [11], consisted of the test cell, a microscope, a camera, and a light source mounted on an optical bench. Time-lapse photography of motion of the fusion front, at 1 frame every 1 or 2 sec and with a magnification on the negative of from 4.5 to 50×, was obtained using this system. The second and third optical systems were used to observe fluid flow patterns. The Schlieren system consisted of a light source, a slit, a knife edge, two 6-in-dia parabolic mirrors, and a camera. It was used to observe laminar and turbulent convective fluid motion and the transition between the two modes. The suspension system consisted of a light source, a slit, a 6-in-dia parabolic mirror, and a camera. It was used to view a suspension of polystyrene dust in water. The particles, of diameter less than 0.003 in., were present in a concentration of about 20 per cu cm of water. This third system was used to observe laminar convection, or the lack of motion (conduction), and the transition between the two modes. In the latter two systems, the two guard regions of the test assembly were replaced by 6 in. of glass wool. Motion pictures of the Schlieren patterns and suspended particles were obtained at 12 frames per sec with a 0.3× magnification on the negative. During photography or direct visual observations, a plug of insulation was removed from each side of the cell to provide an optical path. The time during which the insulation was open was short (about 15 sec) and had negligible effect on the heat transfer as indicated by temperature profiles.

The procedure consisted of loading and mounting the test cell, obtaining the desired boundary temperatures, and then recording

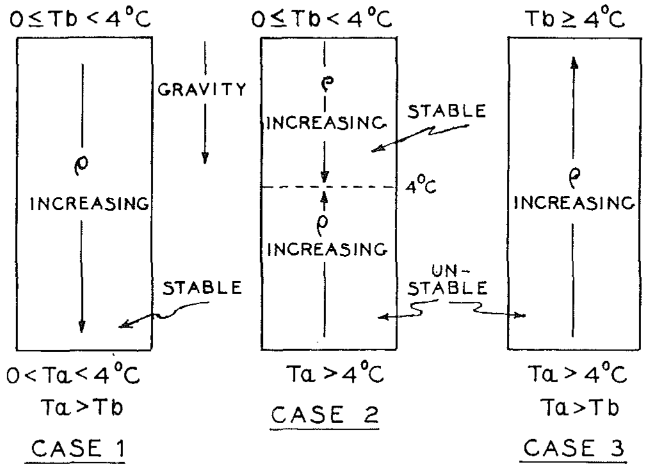

Fig. 2 Stability configurations for water heated from below

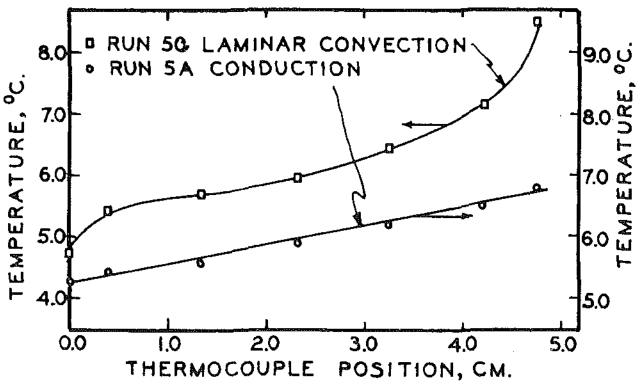

Fig. 3 Comparison of typical temperature profiles for conduction and for laminar natural convection in the liquid heated from below

temperatures, fusion-front motion, and liquid motion for both transient and steady-state conditions. Complete details of the apparatus and procedure are available [12].

Results and Discussion

Modes of Heat Transfer in the Liquid. When water, confined between parallel horizontal plates, is heated from below, three density configurations are possible as indicated in Fig. 2. The first two configurations are possible also with ice at the top, in which case $T_b < 0$ deg C. Case 1 is stable and heat transfer is by conduction only. If the density inversions in Cases 2 and 3 are very small, conduction is the mode of heat transfer. However, as the buoyancy forces are increased, laminar convection will arise. If the buoyancy driving force becomes sufficiently large, turbulent convection occurs.

Conduction. At steady state, the pure conduction region is characterized by a linear temperature profile along the vertical axis, as shown by the lower curve in Fig. 3. Deviations from linearity were less than 4 percent, and these were due to the recording accuracy. When both solid and liquid are present during conduction in the liquid, the Nusselt number is unity and

$$\frac{k_1 \Delta T_1 (E - \epsilon)}{k_2 \Delta T_2 \epsilon} = 1 \qquad (1)$$

During steady-state conduction, equation (1) was obeyed to within 5 percent. No motion could be detected when suspended particles were added. When ice was present, its interface was flat. If phase change was occurring (unsteady-state heat transfer), the interface was flat and its motion was continuous.

Laminar Natural Convection. Laminar natural-convection heat transfer is characterized by a smooth, nonlinear temperature profile along the vertical direction. The fluid motion is in the form of steady, cellular convection. A typical temperature profile is shown as the upper curve in Fig. 3.

The laminar region includes a multiple number of flow patterns. Fig. 4 shows the four patterns detected in the present tests. These were identified by examination of suspended particles. A selection of the motion pictures is available for loan [13]. The single-roll cell was always observed at the onset of convection and thus at low Rayleigh numbers. As the Rayleigh number was increased, this configuration was replaced by one of the three remaining configurations. For any particular value of L/D, configurations *b* and *c* were usually observed at lower Ra than was configuration *d*. The multiple-cell patterns occurred always as a vertical array. Presumably, the test cell was too narrow to permit a horizontal array of circulation cells.

In a small number of cases repetitive temperature oscillations were observed during laminar convection. Oscillations similar to those in Fig. 5*a* had amplitudes usually less than 0.5 deg C, existed for less than 10 min, and were recorded near steady-state conditions. The use of suspensions and also the use of Schlieren

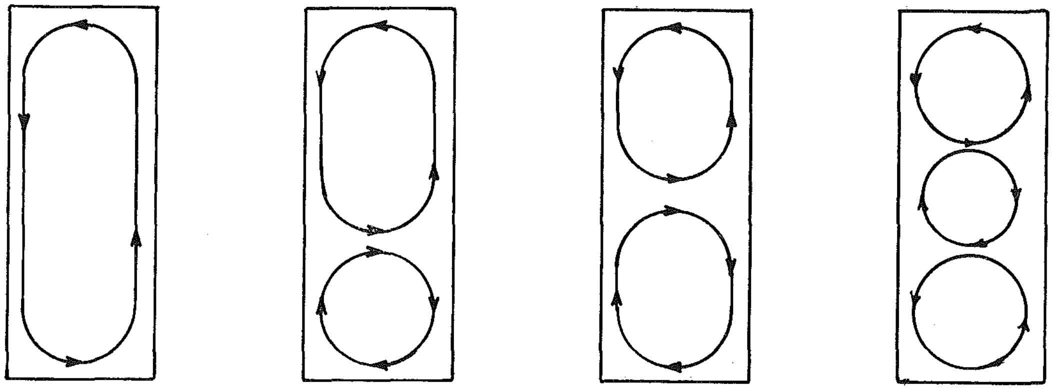

a
RUN 10Q, L/D=2.35
Ra=4.1 X 10^6

b
RUN 12L, L/D=2.35
Ra=5.9 X 10^6

c
RUN 10A, L/D=3.83
Ra=2.4 X 10^7

d
RUN 14C, L/D=7.88
Ra=5.3 X 10^7

Fig. 4 Observed laminar natural convection flow patterns

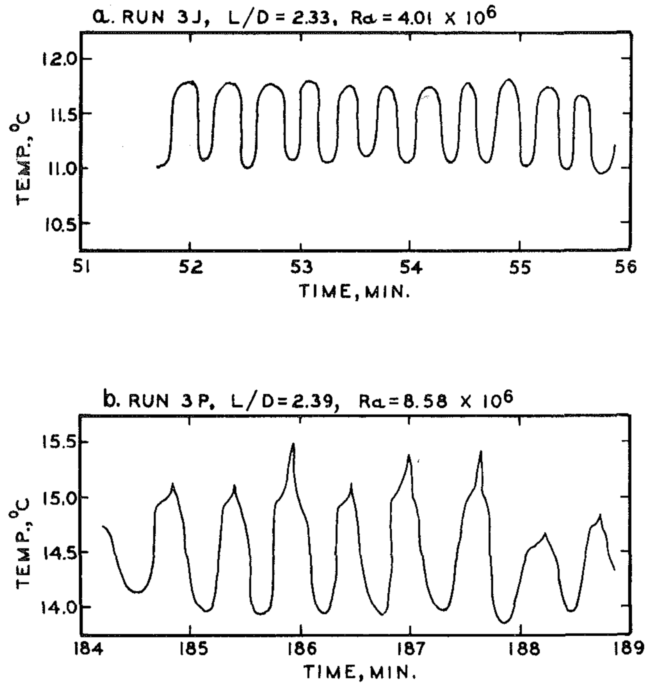

Fig. 5 Typical temperature oscillations recorded during laminar natural convection under certain conditions

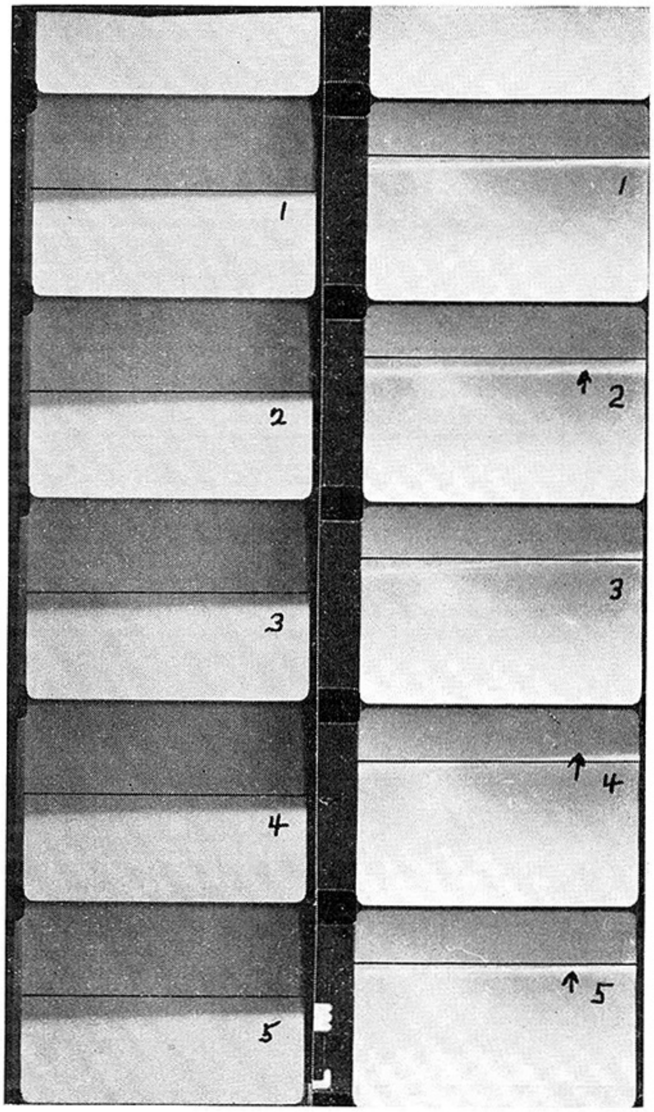

Fig. 6 Time-lapse motion pictures at 1 frame per 2 sec taken through a microscope showing motion of the fusion front during freezing; the width of the view is 0.090 in.; during laminar natural convection (left) the interface moves continuously away from the drawn reference line; during turbulent natural convection (right) the interface oscillates below (frame 2), above (frame 4), and below (frame 5) the reference line

illumination showed that these oscillations occurred during a transition from one flow configuration (in Fig. 4) to another, when the edge of a roll cell was at or near a thermocouple. During transition, the boundaries of the roll cells fluctuated up and down, passing the thermocouple. Similarly, oscillations shown in Fig. 5*b* occurred near the transition from laminar to turbulent convection. These lasted as long as an hour.

Phase change occurred during some tests with laminar convection. The motion of the fusion front was continuous as shown in Fig. 6. However, the interface was concave into the ice, in contrast to the conduction case. This is the result of the liquid flow pattern, such as in Fig. 4. The curvature of the interface was obvious in photographs at low magnification. It is not obvious at high magnification such as in Fig. 6.

Turbulent Natural Convection. A significant feature of turbulent natural convection is that the temperature at every thermocouple in the liquid becomes randomly oscillatory. This is illustrated in Fig. 7. The transition in the temperature profile was simultaneous with the transition from turbulent to laminar convective flow. Also shown in Fig. 7 is the temperature history of a thermocouple in the ice for the same run. The fact that the thermocouple in ice gave a flat temperature record indicates that the temperature oscillations observed with water are not caused by any equipment or background "noise."

Fig. 8 illustrates Schlieren photographs for both laminar and turbulent liquid convection. The laminar convective patterns are stationary. Their images are not as sharp as for the turbulent patterns since the density gradients are not as large. During turbulent convection the patterns are no longer stationary; random plumes of warm fluid rise and random plumes of cold liquid plunge in the bulk liquid. These plumes can be seen in the motion pictures [13].

During turbulence, boundary layers develop at both the top and bottom of the liquid. Viewed by Schlieren illumination, the upper cool layer is dark and is not as easily seen as the warm layer at the bottom. Plumes of warm liquid were observed to rise both from the surface of the copper block and from the interface between the bulk fluid and the warm boundary layer. The intermittent, irregular plumes caused the observed temperature oscillations and variations in the thickness of the boundary layers. Although the point temperatures in the liquid fluctuated, the time-average and space-average temperature in the liquid was constant.

Phase change occurred during some tests with turbulent convection. The motion of the water–ice interface frequently reversed direction. Thus, both melting and freezing occurred during a run having net melting (or net freezing). This erratic behavior is a result of the erratic fluid motion. The distance traveled during each reversal in the motion of the fusion front is microscopic. This is illustrated in Fig. 6. Oscillations of the water–ice interface were reported also by Boger and Westwater [14]. Oscillations of the interface cause an apparent large scatter in data for the fusion-front velocity. The magnitude of the scatter depends on the time increments selected for measurements of the position of the fusion front. The scatter seen in Fig. 9 is arbitrary in that sense. However, the scatter is a result of the physical phenomenon and is not due to experimental error.

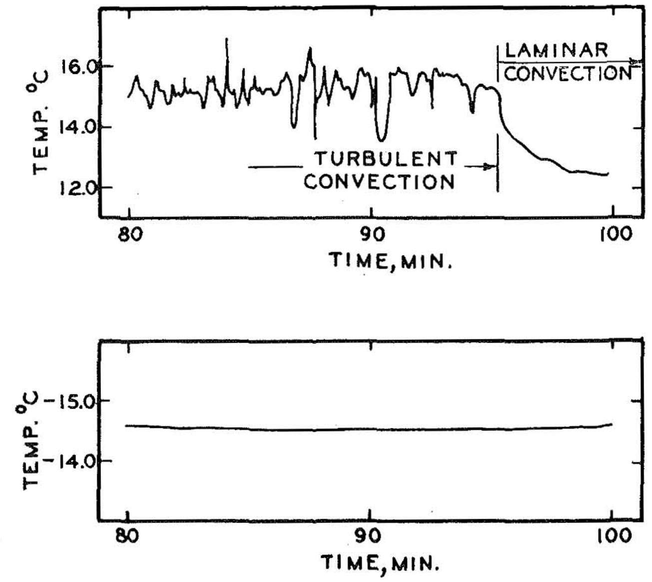

Fig. 7 Random temperature oscillations during turbulent natural convection followed by transition to laminar natural convection; the upper record is for a thermocouple in the liquid; the lower is for the solid; run 8E, $T_b = -36.4$ deg C, $T_a = 11.5$ deg C

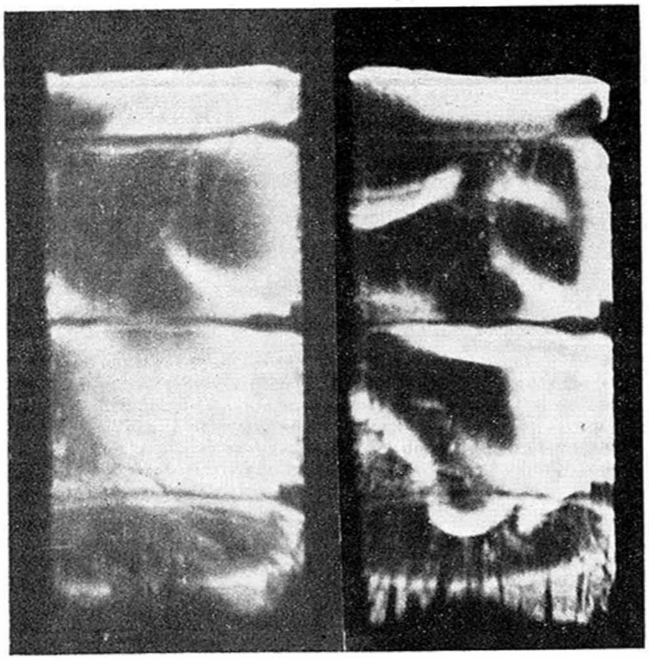

Fig. 8 Schlieren photographs of laminar (left) and turbulent (right) natural convection; the width of the view is 0.5 in.; the 3 horizontal wires are the thermocouples

In Fig. 9 velocity data during turbulent and during laminar natural convection may be compared. The velocity of the fusion front increases at 50 min as the transition to laminar convection occurs. It is a general observation that an increase in convection reduces the rate of freezing and increases the rate of melting. A decrease in convection causes the opposite effects.

The magnitudes of the oscillations in the liquid temperature at a point and in the fusion-front velocity during turbulent convection are shown in Fig. 10. The amplitudes of the oscillations and their frequencies increase as the Rayleigh number increases. The largest temperature oscillation shown is about 3 deg C with

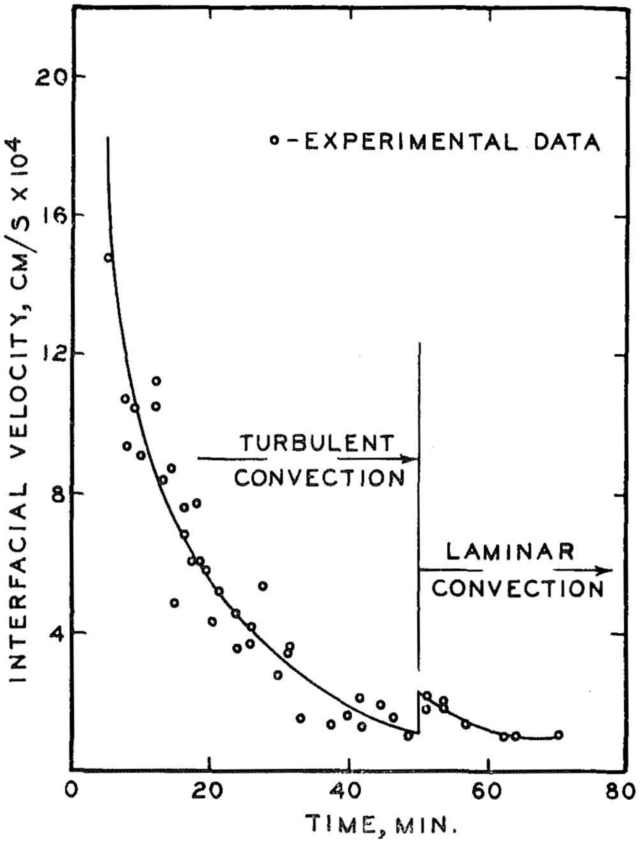

Fig. 9 Fusion-front velocity during transition from turbulent to laminar natural convection; run 3F, freezing of water at 24 deg C from the top by reducing the top temperature to -44 deg C

a period of about 8 sec. The largest velocity oscillation was about 10^{-3} cm/sec and the period was about 14 sec.

Transitions Between Heat-Transfer Modes. Transitions from one heat-transfer mode to another were determined and the corresponding Rayleigh numbers were computed.

$$\mathrm{Ra} = \frac{\rho^2 g C \beta \Delta T \Delta x^3}{\mu k_2} \propto \frac{\text{buoyancy forces}}{\text{viscous forces}} \qquad (2)$$

When water is used, the density maximum at 4 deg C complicates the selection of the physical properties, the liquid depth, and the temperature driving force. Boger and Westwater used empirical means to show the best selection, and their recommendations are used herein. Thus, when $T_a > T_b > 4$ deg C, water behaves as a normal fluid and one uses

$\Delta x = E - \epsilon$
$\Delta T = T_a - T_b$
ρ, C, μ, and k_2 are evaluated at $(T_a + T_b)/2$
β is evaluated at T_a

When the liquid contains the maximum-density region one uses

$\Delta x = E - \epsilon$
$\Delta T = T_a - 4$, deg C
ρ, C, μ, and k_2 are evaluated at $(T_a + 4)/2$, deg C
β is evaluated at T_a

The first critical Rayleigh number (onset of laminar convection) was identified by the temperature profiles, the water ice interface position, and the motion of suspended particles. The second critical Rayleigh number (onset of turbulent convection) was identified by temperature profiles, fusion-front velocity data as in Fig. 9, the motion of suspended particles, and the motion

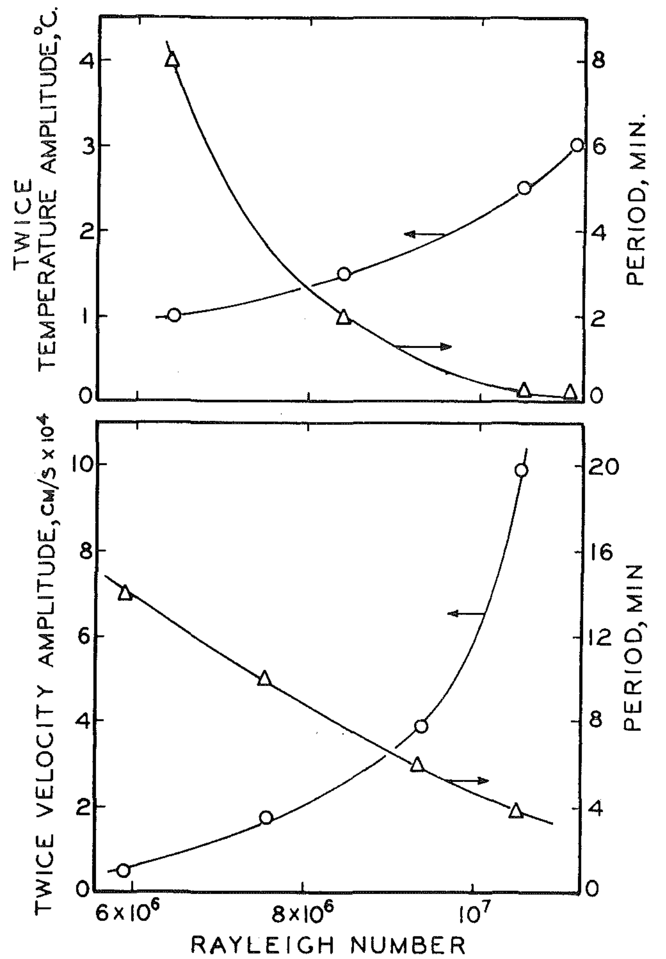

Fig. 10 Dependence of liquid temperature oscillations and fusion-front velocity oscillations on Rayleigh number

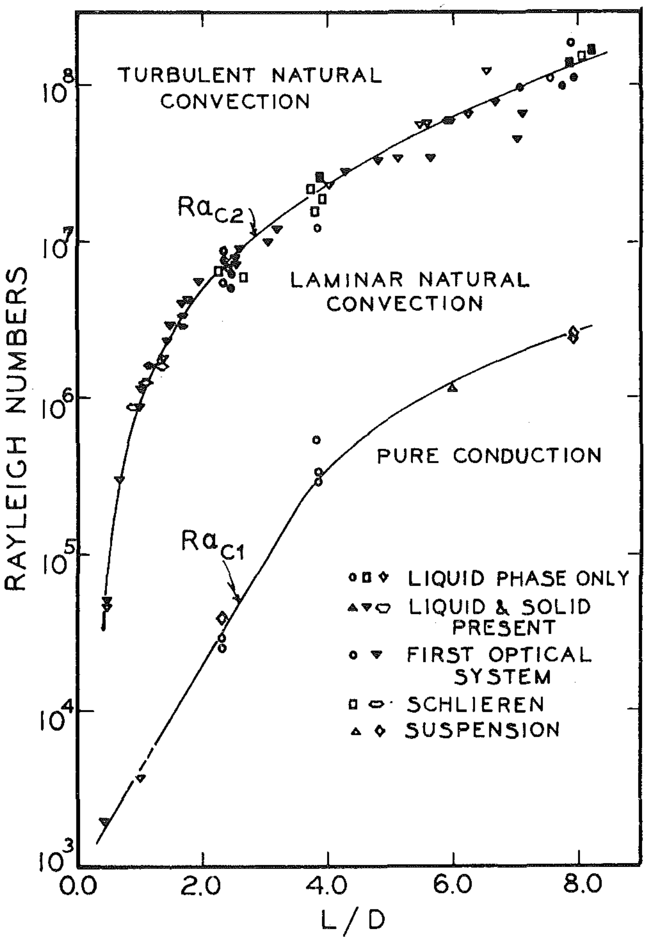

Fig. 11 Effect of L/D on the critical Rayleigh numbers for transitions between three modes of heat transfer; D = 0.5 in.; open symbols for Ra_{c2} are for transitions from laminar to turbulent convection; solid symbols are the reverse

visible by Schlieren illumination. Thus, three and four checks were used and the likelihood of a false judgment is remote.

Fig. 11 shows that the two critical Rayleigh numbers are functions of the liquid depth/width ratio, L/D. The lower curve (Ra_{c1}) separates the region of pure conduction from that of laminar convection, whereas the upper curve (Ra_{c2}) separates laminar convection from turbulent convection. Each point on the lower curve is the result of several steady-state runs approaching the transition from each side. The time to achieve steady state was 2 to 5 hr. The upper curve was determined at both steady-state and transient conditions, and again the approach was from both sides. For a given L/D, the range of the Rayleigh number over which a transition occurs is roughly 50 percent of the Rayleigh number. This bandwidth is a small magnitude for natural convective processes.

Also designated in Fig. 11 is the optical system used to obtain each data point. Scatter in the data obtained using the first optical system arose because liquid was present in both the test region and guard region of the test cell. Since the L/D in the guard region was less than the L/D in the test region, convection in the guard region may have been greater than in the test region. This could result in some horizontal temperature gradients. In the Schlieren and suspension studies, this possibility was eliminated, and the data scatter was small.

Although the moving boundary during phase change causes the L/D ratio to change, the results show that for any particular value of L/D, the values of the critical Rayleigh numbers are not affected by the presence of the solid phase nor by the presence of a moving boundary with a velocity of the order of 10^{-4} cm/sec.

The Rayleigh number, equation (2), is proportional to the ratio of buoyancy to viscous forces. Drag forces introduced at the boundaries are a function of the size and shape of the boundaries. Thus the effect of cell size may be expected to be a function of the ratio of total wetted area to liquid volume. For a cell of square cross section, this ratio is

$$M = \frac{\text{area}}{\text{volume}} = \frac{2}{D}\left[\frac{1}{L/D} + 2\right] \qquad (3)$$

For small values of L/D, M is very sensitive to changes in L/D. For large values of L/D, M approaches the limit $4/D$ asymptotically and Ra_c should show less dependence on L/D. The data of Fig. 11 illustrate this relationship. For the largest L/D used in this work, 8.0, M was within about 6 percent of its limiting value. Note that $D = 0.5$ in. for all data in Fig. 11. The curves could be different for other values of D. Cases for which the maximum density region was both present and absent are included in Figs. 11 and 12. The results are consistent for both cases.

The results of this work are compared with those of other investigators in Fig. 13. The experimental data of Catton and Edwards [10] were obtained using silicone oil (Dow Corning, 50 and 100 cp) confined in cells of hexagonal cross section. Good agreement suggests that the Ra_c versus L/D correlations may be applicable to a wide range of liquids confined in cells of various cross sections. The results of Schmidt and Silveston [9] were obtained in thin fluid layers where $3 \leq Pr \leq 4 \times 10^3$, $10^{-1} \leq Gr \leq 8 \times 10^4$; the effect of L/D was not considered.

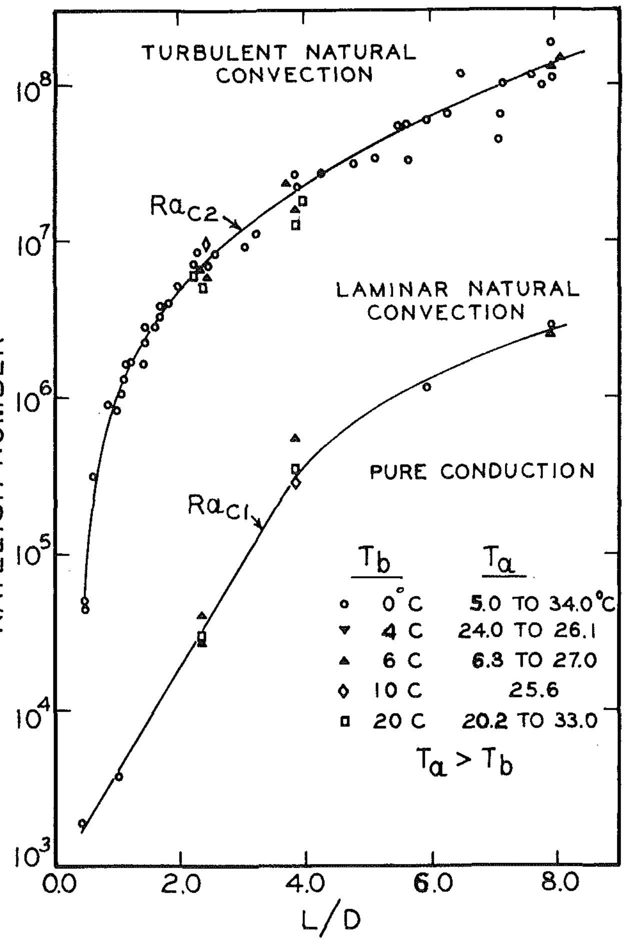

Fig. 12 Test for possible effect of boundary temperatures on the critical Rayleigh numbers; no effect is apparent

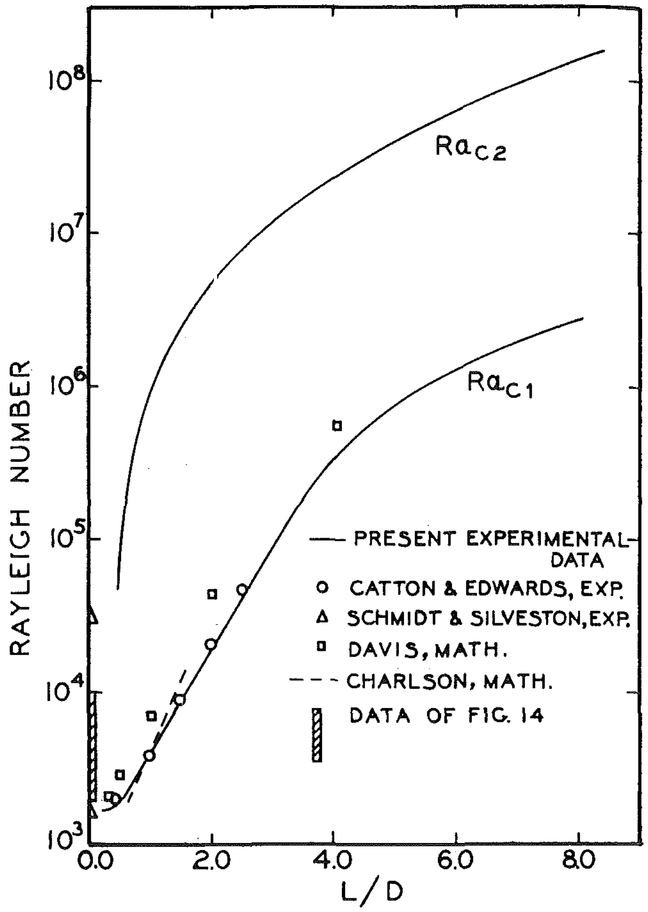

Fig. 13 Comparison of new data with results of other investigators

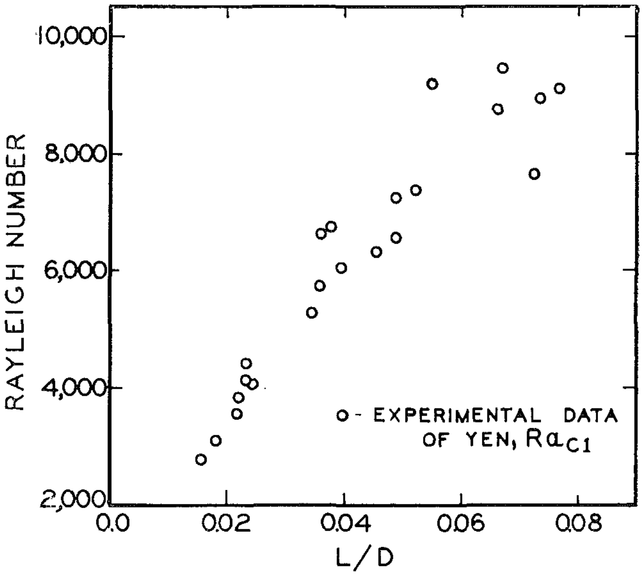

Fig. 14 Effect of *L/D* on Ra_{c1}; data of Yen

The mathematical results of Davis [8] were obtained for the same boundary conditions as used in this work except that Davis assumed the boundaries to be perfect conductors. The results lie above but parallel to those of this work. This is expected, because conducting walls transfer part of the energy and thereby reduce buoyancy forces. The results of Charlson and Sani for cylindrical cells [15] are in good agreement with the data; insulating boundaries were assumed in their mathematical model.

Yen [16] obtained the following experimental relationship:

$$\mathrm{Ra}_{c1} = 1.42 \times 10^4 \exp(-6.64 \times 10^{-2}T_s) \quad (4)$$

where T_s is the lower surface temperature ($6.72 \leq T_s \leq 25.5$ deg C). This result indicates that the onset of convection is dependent only on T_s and is independent of L/D. The results of the present work do not agree with this conclusion. Yen's data replotted actually show a dependence of L/D on Ra_{c1} as shown in Fig. 14. In addition, the data do not agree with those of other investigators (see Fig. 13).

Tien [17] presents a mathematical model for Ra_{c1} also based on boundary temperatures only. His predicted results were shown to be in agreement with the data of Boger and Westwater. Unfortunately, the cell length in reference [14] had been rounded off to 2 in. (5.08 cm); the correct values varied from 4.75 to 5.07 cm. When correct values are used, the model of Tien fails to predict the transition. If the predicted results of Tien are plotted versus L/D as shown in Fig. 15, they disagree with the present data.

Tien and Yen state that the critical Rayleigh number for the onset of convection varies with the temperature of the heated boundary. This possibility was examined also in the present study. The results, Fig. 12, show no effect, nor does the temperature of the cold boundary affect the critical Rayleigh number. Note that four independent methods were used to detect the critical Rayleigh numbers in the present tests. Tien and Yen used one method only, the identification of a change in the slope of a graph.

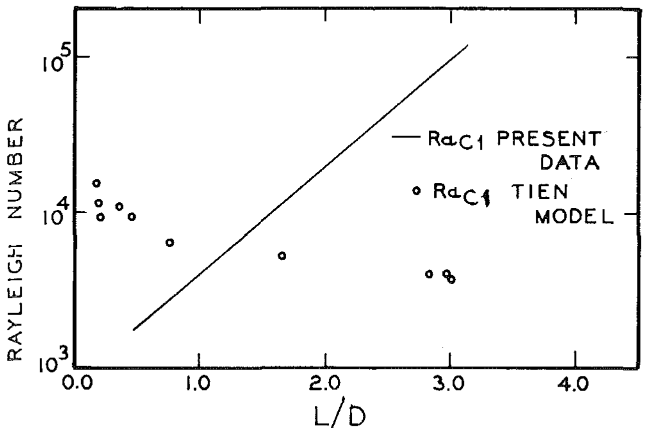

Fig. 15 Comparison of new data with results of Tien

Conclusions

1 An apparatus was developed which permitted the use of four independent methods to detect the three modes of one-dimensional heat transfer in water confined in a cell.

2 Transitions between heat-transfer modes were studied and the corresponding Rayleigh numbers were determined in the range 1700 to 10^8.

3 The critical Rayleigh numbers are strongly dependent on L/D in the range $0.5 < L/D < 8.0$.

4 The bandwidth of the transition region corresponds to a Rayleigh-number variation of about 50 percent.

5 The presence of ice at the top or a moving fusion front has negligible effect on the critical Rayleigh numbers.

6 The presence of the maximum density region does not affect the critical values, provided the physical properties and the temperature difference are selected as described.

7 The data agree with mathematical predictions by Davis, and by Charlson and Sani; they agree with data of Catton and Edwards, and Schmidt and Silveston; they disagree with the mathematical predictions by Tien and the experimental results of Yen.

Acknowledgment

A NASA Traineeship, a Dow Chemical Company Fellowship, and a National Science Foundation Grant supported this research.

References

1 Bénard, H., "Les tourbillons cellulaires dans une nappe liquide transport—aut de la chaleur par convection en régime permanent," *Ann. Chem. Phys.*, Vol. 23, 1901, pp. 62–144.

2 Lord Rayleigh, "On Convective Currents in a Horizontal Layer of Fluid When the High Temperature is on the Underside," *Philosophical Magazine*, Vol. 32, 1916, pp. 529–546.

3 Ostrach, S., and Pnueli, D., "The Thermal Instability of Completely Confined Fluids Inside Some Particular Configurations," JOURNAL OF HEAT TRANSFER, TRANS. ASME, Series C, Vol. 85, No. 4, Nov. 1963, pp. 346–354.

4 Sherman, M., and Ostrach, S., "Lower Bounds to the Critical Rayleigh Number in Completely Confined Regions," *Journal of Applied Mechanics*, Vol. 34, TRANS. ASME, Series E, Vol. 89, No. 2, June 1967, pp. 308–312.

5 Samuels, M. R., and Churchill, S. W., "Stability of a Fluid in a Rectangular Region Heated from Below," *AIChE Journal*, Vol. 13, No. 1, 1967, pp. 77–85.

6 Edwards, D. K., and Catton, I., "Prediction of Heat Transfer by Natural Convection in Closed Cylinders Heated from Below," *International Journal of Heat and Mass Transfer*, Vol. 12, 1969, pp. 23–30.

7 Edwards, D. K., "Suppression of Cellular Convection by Lateral Walls," JOURNAL OF HEAT TRANSFER, TRANS. ASME, Series C, Vol. 91, No. 1, Feb. 1969, pp. 145–150.

8 Davis, S. H., "Convection in a Box: Linear Theory," *Journal of Fluid Mechanics*, Vol. 30, Part 3, 1967, pp. 465–478.

9 Schmidt, E., and Silveston, P. L., "Natural Convection in Horizontal Liquid Layers," *Chem. Engr. Prog. Symp. Series*, Vol. 55, No. 29, 1959, pp. 163–169.

10 Catton, I., and Edwards, D. K., "Effect of Side Walls on Natural Convection Between Horizontal Plates Heated from Below," JOURNAL OF HEAT TRANSFER, TRANS. ASME, Series C, Vol. 89, No. 4, Nov. 1967, pp. 295–299.

11 Thomas, L. J., and Westwater, J. W., "Microscopic Study of Solid-Liquid Interfaces During Melting and Freezing," *Chem. Engr. Prog. Symp. Series*, Vol. 59, No. 41, 1963, pp. 155–164.

12 Heitz, W. L., "Hydrodynamic Stability of Water and Its Effect on Melting and Freezing," PhD thesis, Univ. of Illinois, Urbana, Ill., 1970.

13 Westwater, J. W., and Heitz, W. L., "Heat Transfer Modes to Confined Water Heated from Below," motion picture, Univ. of Illinois, Urbana, Ill., 1970.

14 Boger, D. V., and Westwater, J. W., "Effect of Buoyancy on the Melting and Freezing Process," JOURNAL OF HEAT TRANSFER, TRANS. ASME, Series C, Vol. 89, No. 1, Feb. 1967, pp. 81–89.

15 Charlson, G. S., "Thermoconvective Instability in a Bounded Cylindrical Fluid Layer," MS thesis, directed by R. L. Sani, Univ. of Illinois, Urbana, Ill., 1969.

16 Yen, Y. C., "Onset of Convection in a Layer of Water Formed by Melting Ice from Below," *Phys. Fluids*, Vol. 11, No. 6, 1968, pp. 1263–1270.

17 Tien, C., "Thermal Instability of a Horizontal Layer of Water Near 4°C," *AIChE Journal*, Vol. 14, No. 4, 1968, pp. 652–653.

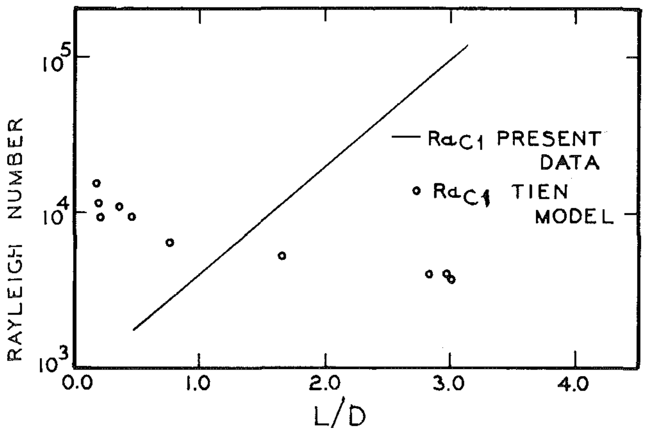

Fig. 15 Comparison of new data with results of Tien

Conclusions

1 An apparatus was developed which permitted the use of four independent methods to detect the three modes of one-dimensional heat transfer in water confined in a cell.

2 Transitions between heat-transfer modes were studied and the corresponding Rayleigh numbers were determined in the range 1700 to 10^8.

3 The critical Rayleigh numbers are strongly dependent on L/D in the range $0.5 < L/D < 8.0$.

4 The bandwidth of the transition region corresponds to a Rayleigh-number variation of about 50 percent.

5 The presence of ice at the top or a moving fusion front has negligible effect on the critical Rayleigh numbers.

6 The presence of the maximum density region does not affect the critical values, provided the physical properties and the temperature difference are selected as described.

7 The data agree with mathematical predictions by Davis, and by Charlson and Sani; they agree with data of Catton and Edwards, and Schmidt and Silveston; they disagree with the mathematical predictions by Tien and the experimental results of Yen.

Acknowledgment

A NASA Traineeship, a Dow Chemical Company Fellowship, and a National Science Foundation Grant supported this research.

References

1 Bénard, H., "Les tourbillons cellulaires dans une nappe liquide transport—aut de la chaleur par convection en régime permanent," *Ann. Chem. Phys.*, Vol. 23, 1901, pp. 62–144.

2 Lord Rayleigh, "On Convective Currents in a Horizontal Layer of Fluid When the High Temperature is on the Underside," *Philosophical Magazine*, Vol. 32, 1916, pp. 529–546.

3 Ostrach, S., and Pnueli, D., "The Thermal Instability of Completely Confined Fluids Inside Some Particular Configurations," JOURNAL OF HEAT TRANSFER, TRANS. ASME, Series C, Vol. 85, No. 4, Nov. 1963, pp. 346–354.

4 Sherman, M., and Ostrach, S., "Lower Bounds to the Critical Rayleigh Number in Completely Confined Regions," *Journal of Applied Mechanics*, Vol. 34, TRANS. ASME, Series E, Vol. 89, No. 2, June 1967, pp. 308–312.

5 Samuels, M. R., and Churchill, S. W., "Stability of a Fluid in a Rectangular Region Heated from Below," *AIChE Journal*, Vol. 13, No. 1, 1967, pp. 77–85.

6 Edwards, D. K., and Catton, I., "Prediction of Heat Transfer by Natural Convection in Closed Cylinders Heated from Below," *International Journal of Heat and Mass Transfer*, Vol. 12, 1969, pp. 23–30.

7 Edwards, D. K., "Suppression of Cellular Convection by Lateral Walls," JOURNAL OF HEAT TRANSFER, TRANS. ASME, Series C, Vol. 91, No. 1, Feb. 1969, pp. 145–150.

8 Davis, S. H., "Convection in a Box: Linear Theory," *Journal of Fluid Mechanics*, Vol. 30, Part 3, 1967, pp. 465–478.

9 Schmidt, E., and Silveston, P. L., "Natural Convection in Horizontal Liquid Layers," *Chem. Engr. Prog. Symp. Series*, Vol. 55, No. 29, 1959, pp. 163–169.

10 Catton, I., and Edwards, D. K., "Effect of Side Walls on Natural Convection Between Horizontal Plates Heated from Below," JOURNAL OF HEAT TRANSFER, TRANS. ASME, Series C, Vol. 89, No. 4, Nov. 1967, pp. 295–299.

11 Thomas, L. J., and Westwater, J. W., "Microscopic Study of Solid-Liquid Interfaces During Melting and Freezing," *Chem. Engr. Prog. Symp. Series*, Vol. 59, No. 41, 1963, pp. 155–164.

12 Heitz, W. L., "Hydrodynamic Stability of Water and Its Effect on Melting and Freezing," PhD thesis, Univ. of Illinois, Urbana, Ill., 1970.

13 Westwater, J. W., and Heitz, W. L., "Heat Transfer Modes to Confined Water Heated from Below," motion picture, Univ. of Illinois, Urbana, Ill., 1970.

14 Boger, D. V., and Westwater, J. W., "Effect of Buoyancy on the Melting and Freezing Process," JOURNAL OF HEAT TRANSFER, TRANS. ASME, Series C, Vol. 89, No. 1, Feb. 1967, pp. 81–89.

15 Charlson, G. S., "Thermoconvective Instability in a Bounded Cylindrical Fluid Layer," MS thesis, directed by R. L. Sani, Univ. of Illinois, Urbana, Ill., 1969.

16 Yen, Y. C., "Onset of Convection in a Layer of Water Formed by Melting Ice from Below," *Phys. Fluids*, Vol. 11, No. 6, 1968, pp. 1263–1270.

17 Tien, C., "Thermal Instability of a Horizontal Layer of Water Near 4°C," *AIChE Journal*, Vol. 14, No. 4, 1968, pp. 652–653.

DISCUSSION

D. K. Edwards[2]

The authors are to be congratulated for a valuable experimental work. The authors' Fig. 4 is especially noteworthy, for it adds direct support for the Stuart-Malkus-Veronis discrete transition theory which is the foundation of the power integral method used in the authors' reference [6] to predict the Nusselt number versus Rayleigh number relationship. It is hoped that the authors can supply Nu versus Ra from their data so that further comparisons with the power integral method can be made.

If one uses the method pieced together from various theoretical asymptotic solutions summarized in the authors' reference [6] to compute Ra_{c1} versus L/D, one obtains the following calculated values (rounded off to two significant figures):

L/D	Ra_{c1}	L/D	Ra_{c1}
0	1700	4	2.3×10^5
1	3800	6	1.1×10^6
2	21000	8	3.3×10^6

These values may be compared with the authors' Fig. 11. They will be found to be in good agreement. The slope of the authors' curve for Ra_{c1} is somewhat flat in the range of L/D from 4.0 to 8.0, as theory shows that Ra_{c1} based on height should go like $(L/D)^4$ when L/D is large. To what would the authors attribute this deviation from the $(L/D)^4$ law?

In comparing their results with the predictions of Davis for perfectly conducting walls, the authors perhaps give the impression that the side-wall boundary conditions are not important. In fact they are very important. At an L/D of 8 the value of Ra_{c1} for conducting walls would be 1.0×10^7 instead of 3.3×10^6 for nonconducting walls. It is therefore inappropriate to compare the present results with those of Davis. The authors' apparatus with $\frac{1}{8}$-in-thick plastic walls had an appreciable conduction effect, but it may be estimated[3] to result in not more than a 20 percent increase in Ra_{c1} over the value for adiabatic walls at large L/D. The authors' side walls were therefore much closer to being nonconducting than perfectly conducting.

The authors twice refer to Rayleigh number as proportional to buoyancy forces over viscous forces. They are, of course, correct, but not complete in so describing Rayleigh number. It is suggested that more insight into Rayleigh number can be gained by

---

[2] Professor, Energy and Kinetics Department, School of Engineering and Applied Science, University of California, Los Angeles, Calif.

[3] Sun, W. M., and Edwards, D. K., "Natural Convection in Cells with Finite Conducting Side Walls Heated from Below," *Heat Transfer 1970*, reprints of papers presented at the Fourth International Heat Transfer Conference, Vol. 4, Paper NC2.3, pp. 1–11, Elsevier Publ. Co., Amsterdam, 1970.

viewing it as the product of two ratios: One ratio is the mechanical power supplied by the action of buoyant forces on a velocity perturbation to the mechanical work dissipated through viscosity; the second ratio is the thermal power supplied by convection in the velocity perturbation to that dissipated through conduction.

$$\mathrm{Ra} = \frac{\text{buoyant power supply}}{\text{power loss by viscosity}} \times \frac{\text{heat convection supply}}{\text{heat loss by conduction}}$$

In a cube of side L one would write

$$\mathrm{Ra} = \frac{\Delta\rho g L^3 V}{\mu \dfrac{V}{L} L^2 V} \times \frac{\rho c_p V \Delta T L^2}{\dfrac{k}{L} \Delta T L^2} = \frac{(\Delta\rho/\rho) g L^3}{(\mu/\rho)(k/\rho c_p)}$$

In a very long square passage one would prefer to write

$$\mathrm{Ra}_D = \frac{\Delta\rho g D^2 L V}{\mu \dfrac{V}{D} LDV} \times \frac{\rho c_p V \Delta T D^2}{\dfrac{k}{D} \Delta T L D} = \frac{(\Delta\rho/\rho L) g D^4}{(\mu/\rho)(k/\rho c_p)}$$

When the Rayleigh number is viewed in this way, the importance of lateral wall conduction is clear. A conducting or radiating wall will help increase the heat loss by conduction from a velocity perturbation. In order to make convection occur one would then have to increase the buoyant power supply above that needed for a cell with nonconducting walls.

Authors' Closure

Concerning the fourth power of L/D predicted by Cotton and Edwards, the horizontal shear at the top and bottom boundaries was neglected in their derivation. Perhaps that causes the prediction to differ from the data. Fig. 1 of their paper also shows a curvature inconsistent with the fourth power.

It was not the goal of the present study to obtain the functionality of Nu vs. Ra. The critical Rayleigh numbers were desired, and 158 observations of these are recorded in reference [12].

We welcome the other comments; the proposed meaning of the Rayleigh number is particularly useful.

R. T. LAHEY, JR.
Technical Leader,
Core Development.
Assoc. Mem. ASME

B. S. SHIRALKAR
Engineer,
Core Development.
Assoc. Mem. ASME

D. W. RADCLIFFE
Engineer,
Core Development.

General Electric Company,
Atomic Power Equipment
Department,
San Jose, Calif.

Mass Flux and Enthalpy Distribution in a Rod Bundle for Single- and Two-Phase Flow Conditions

Diabatic multirod subchannel data have been obtained in a 9-rod bundle for operating conditions typical of a boiling water reactor. These data have been used to obtain both the natural flow and enthalpy distribution in a rod bundle and information on the flow diversion enthalpy and the effective flow diversion length.

Introduction

In recent years there has been considerable interest in the area of ventilated subchannel analysis. This interest is reflected in the rather large bibliographies to be found in the recent state-of-the-art summary papers on mixing in rod bundles [1, 2].[1] Virtually all of this experimental and analytical work has been motivated by the desire of designers of both pressurized water and boiling water nuclear reactors to better understand the critical heat flux (CHF) phenomenon. It has been known for some time that CHF is a local phenomenon rather than a "bundle average" phenomenon, and since subchannel analysis provides a method of CHF predictions on a local basis, it is highly useful to industry.

The present paper is concerned with the presentation and discussion of subchannel flow and enthalpy distribution data taken in a "clean" (i.e., without grid spacers) 9-rod (3 × 3) bundle with uniform heat flux. All the representative subchannels

---

Contributed by the Heat Transfer Division and presented at the Winter Annual Meeting, New York, N. Y., November 29–December 3, 1970, of The American Society of Mechanical Engineers. Manuscript received by the Heat Transfer Division February 23, 1970; revised manuscript received July 10, 1970. Paper No. 70-WA/HT-8.

[1] Numbers in brackets designate References at end of paper.

Nomenclature

De = equivalent subchannel diameter (ft)
A_{CH} = subchannel flow area (ft^2)
G = mass flux (lbm/hr-ft^2)
$\langle G \rangle$ = average mass flux for adjacent subchannels (lbm/hr-ft^2)
g = acceleration due to gravity (ft/hr^2)
g_c = conversion factor (lbm/hr-ft^2/lbf)
H = enthalpy (Btu/lb)
H_x = cross-flow enthalpy (Btu/lb)
$j_f{}^*$ = dimensionless superficial liquid velocity = $G(1 - x)\rho_f{}^{-1/2}/[gDe(\rho_f - \rho_g)]^{1/2}$
$j_g{}^*$ = dimensionless superficial vapor velocity = $Gx\rho_g{}^{-1/2}/[gDe(\rho_f - \rho_g)]^{1/2}$
P = pressure (lbf/ft^2)
P_{CH} = subchannel friction perimeter (ft)
P_H = subchannel heated perimeter (ft)
S = rod-to-rod spacing (ft)
$\tilde{V}$ = average linear velocity in adjacent subchannels (ft/hr)
x = equilibrium quality
β = mixing parameter
δP = transverse pressure differential between subchannels (lbf/ft^2)
ρ = density (lbm/ft^3)
$\rho_{2\phi}$ = two-phase density (lbm/ft^3)
τ = shear stress (lbf/ft^2)
$\tilde{w}$ = fluctuating flow rate per axial foot (lbm/hr-ft)

Subscripts and Superscripts

$\bar{q}$ = bundle average value of q
$\hat{q}$ = average value of q obtained by summing up subchannels
CH = refers to subchannel quantity
$'$ = refers to non-isokinetic quantity
f = refers to liquid
g = refers to gas

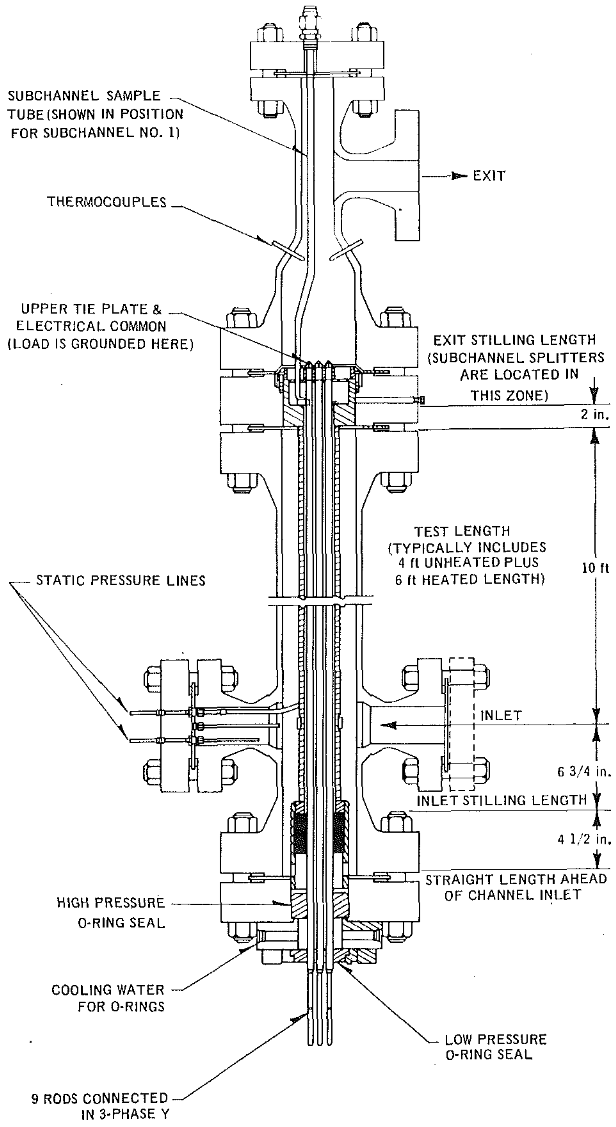

Fig. 1 9-rod subchannel test section

were sampled for both isokinetic (natural flow split) and non-isokinetic conditions; hence, much valuable information on single- and two-phase "mixing" can be obtained. Actual multi-rod data of this type provide not only insight into subchannel analysis but the final check for any effective subchannel computer code, of which there are many [1]. A relatively large number of experimental programs [1, 2] have been directed toward obtaining single- and two-phase data in two adjacent subchannels. In contrast, very little effort has been directed toward actual measurements in rod bundles. The present subchannel data are the only two-phase multirod subchannel data of a non-proprietary nature available for square arrays (typical of U. S. reactors) apart from measurements made at Columbia University [3]. The data discussed in this paper have the advantage that they can be checked for consistency as all representative subchannels were sampled. Also, since the Columbia study concentrated on average exit qualities between −5 and +5 percent, this investigation complements it by providing information at higher qualities.

Test Technique and Equipment

The test section and pressure vessel used for this test are shown in Fig. 1. The heater rods used were of the indirect cal-rod type. The salient geometrical features are:

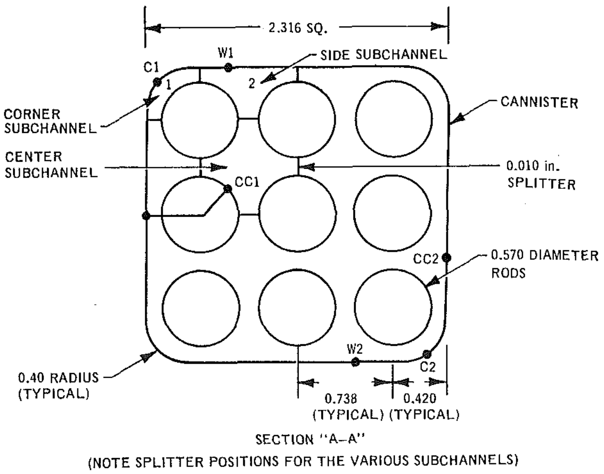

Fig. 2 Subchannel division and pressure taps

number of rods	nine (3 × 3 square array)
rod diameter	0.570 in.
radius of canister (corner)	0.40 in.
rod/rod clearance	0.168 in.
rod/wall clearance	0.135 in.
hydraulic diameter	0.474 in.
heated length	6.0 ft
unheated length	4.0 ft
power supply	3-phase a-c

The relative radial position of the rods was maintained with $^1/_8$-in-dia stainless steel pins which were located every 12 in. in the axial direction (the last set being 10 in. before the end of the heated length to minimize flow disturbance).

The method used to sample the flow in a particular subchannel can be best described with reference to Fig. 2. This figure is an axial section of the test assembly at a location just beyond the end of the heated length. The three representative subchannels are shown with all the 0.010-in-thick stainless steel splitters in place. During actual test operation only one subchannel was sampled at a time, and thus only one set of splitters was installed. These splitters were slid into grooves in the heater rods and channel walls to seal off a given subchannel. If, for example, the corner subchannel was to be sampled, the flow tube formed by the corner rod, canister wall, and two splitters would be sealed at the top and the sample led via a sample tube out through the top of the pressure vessel as shown in Fig. 1. Since the mixture surrounding the tube is in general at saturated conditions there are no heat-loss problems from the sample tube to the surrounding fluid associated with operation during bulk boiling. The isokinetic flow split was obtained by adjusting the pressure differential between the static pressure taps C1 and C2. Both these taps were located at the same axial position, and thus when the differential was adjusted to the same value it had when no splitters were installed, the isokinetic condition was achieved and the bundle flow split was presumably the same as when no sample was being withdrawn (i.e., the natural flow split). Similarly, if the side subchannel were being sampled, static wall taps W1 and W2 would be used to establish the isokinetic setting, while for the center subchannel, taps CC1 and CC2 would be used. At the onset of this program it was discovered that these pressure differentials, though small, were not exactly zero under conditions of no sampling. Care was taken to assure that this was not due to leakage into the test section from the annular region between the pressure vessel and test section by repeating some tests using thin copper strips as gaskets along the length of the channel walls during its assembly. This was not found to make appreciable difference to the sampling measurements, since previous measurements could be satisfactorily repeated.

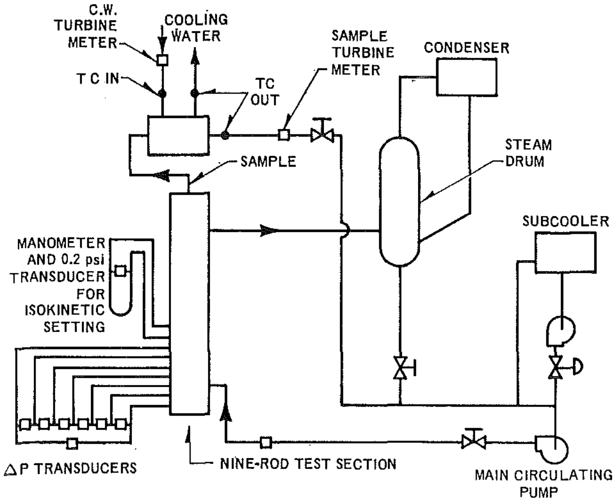

Fig. 3 Schematic of loop showing sampling circuit

Table 1 Nominal test conditions

$P = 1000$ psia

Test point	$\bar{G}/10^6$ (lb/ft²-hr)	Power (kw)	Heat flux (Btu/ft²-hr)	Subcooling (Btu/lb)	$\bar{X}_e$
1B	0.480	0	0	504.6	...
1C	0.990	0	0	504.6	...
1D	1.510	0	0	504.6	...
1E	1.970	0	0	504.6	...
2B2	0.530	532	225,000	149.9	0.029
2B3	0.535	532	225,000	108.7	0.090
2B4	0.535	532	225,000	52.8	0.176
2C1	1.060	532	225,000	57.2	0.042
2C2	1.068	532	225,000	35.1	0.075
2D1	0.540	1064	450,000	259.2	0.110
2D3	0.540	1064	450,000	124.4	0.318
2E1	1.080	1064	450,000	142.9	0.035
2E2	1.080	1064	450,000	96.7	0.106
2E3	1.060	1064	450,000	29.1	0.215
2G1	1.070	1596	675,000	225.9	0.038
2G2	1.080	1596	675,000	189.8	0.090
2G3	1.070	1596	675,000	146.7	0.160

Leak checks made by pressurizing the channel with air in a bench test were also satisfactory. It was concluded that these small measured transverse pressure differentials (δP) associated with the natural flow split were due to slight impacting at some of the static pressure ports. This phenomenon can easily be evaluated by plotting the measured differential versus the dynamic head. A monotonic increase of δP was found with $G^2/2g_c\rho_{2\phi}$ indicating impacting, and thus the isokinetic settings were determined from calibration runs made prior to splitter installation.

Once the subchannel sample has been removed from the pressure vessel, its flow rate and enthalpy must be determined. This was done in a manner shown in Fig. 3. The sample was passed through a Heliflow heat exchanger where it was condensed and subcooled. The temperature of the subcooled sample was then measured with several chromel-alumel thermocouples and its flow rate measured with a Potter turbine flow meter having the appropriate flow range. The sample was then passed via a throttle valve to the suction side of the main circulating pump in the existing 1500-psi loop at APED. The cooling water which was used to condense the sample was metered with another Potter flow meter and its temperature difference across the heat exchanger was measured with several chromel-alumel thermocouples. All these thermocouples were later checked against a Hewlett Packard crystal thermometer with an accuracy over an order of magnitude better than the thermocouples (0.001 deg C) and found to be within ±1 deg F of the true temperature. An accuracy of ±1 deg F has been assumed for these thermocouples in subsequent error analysis of the data. The sample enthalpy can then be calculated from a heat balance on the heat exchanger if the heat loss term is known. Since the calorimetry equipment was well insulated, the actual heat loss to the ambient was small. Nevertheless, hot single-phase calibration runs were made at the start of each day to determine the "heat loss" which was used in the heat balance equation for the two-phase runs.

The transverse pressure differential (δP) measurements were made using both inclined manometers and 0.2-psi (full-scale) Pace cell transducers. Finally, a permanent record of all the data measured was accumulated by a DYMEC data acquisition system and Sanborn recorders, the data reduction being performed on a G.E.-635 time-share computer terminal.

Isokinetic Subchannel Data and Analysis

Diabatic subchannel flow and enthalpy data have been taken in the various representative subchannels of a 9-rod array. Most of these data were taken at isokinetic conditions in a "clean" test section (i.e., one using $^1/_8$-in. pins rather than grid-type spacers to maintain the proper radial clearances between rods) having a uniform axial and radial heat flux distribution.

Tabulated summaries of the test conditions and the data are given in Tables 1 and 2, respectively. One important check on the validity of the data is that mass and energy must be conserved. That is, the net total mass and energy flow from the test section must be the same as the sum of the mass and energy flow out of the various subchannels. Since the subchannels were sampled one at a time and the "exact" operating conditions could not always be duplicated, the data from the various subchannels were corrected to the nominal in the following manner:

Table 2 Summary of uniform data

Test point	$\bar{G}/10^6$	$\bar{X}$	$G_1/10^6$	X_1	$G_2/10^6$	X_2	$G_3/10^6$	X_3	$\hat{G}/10^6 = \frac{\Sigma A_i G_i/10^6}{A_T}$	$\hat{X} = \frac{\Sigma G_i X_i A_i}{\bar{G} A_T}$
1B	0.480	...	0.311	...	0.462	...	0.526	...	0.472	...
1C	0.990	...	0.701	...	0.939	...	1.150	...	0.997	...
1D	1.510	...	1.095	...	1.441	...	1.690	...	1.517	...
1E	1.970	...	1.620	...	1.910	...	2.190	...	1.991	...
2B2	0.530	0.029	0.372	0.003	0.521	0.014	0.540	0.030	0.522	0.019
2B3	0.535	0.090	0.550	0.072	0.530	0.076	0.521	0.104	0.529	0.085
2B4	0.535	0.176	0.524	0.133	0.517	0.180	0.560	0.220	0.535	0.191
2C1	1.060	0.042	0.965	0.029	1.066	0.018	1.077	0.059	1.060	0.036
2C2	1.068	0.075	0.968	0.063	1.028	0.075	1.144	0.100	1.068	0.084
2D1	0.540	0.110	0.425	0.083	0.560	0.105	0.556	0.117	0.544	0.108
2D3	0.540	0.318	0.490	0.260	0.532	0.330	0.563	0.364	0.540	0.337
2E1	1.080	0.035	0.950	0.004	1.102	0.026	1.162	0.051	1.110	0.035
2E2	1.080	0.106	1.046	0.049	1.078	0.097	1.180	0.105	1.115	0.099
2E3	1.060	0.215	0.965	0.160	1.081	0.185	1.126	0.249	1.087	0.214
2G1	1.070	0.038	0.882	0.032	0.968	0.044	1.142	0.043	1.018	0.041
2G2	1.080	0.090	1.000	0.020	1.111	0.068	1.130	0.110	1.107	0.082
2G3	1.070	0.160	0.865	0.074	1.132	0.127	1.160	0.176	1.114	0.151

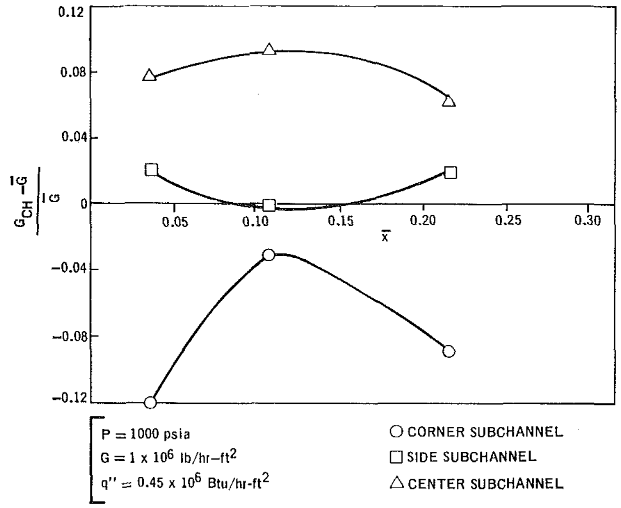

Fig. 4 Comparison of subchannel flows for the three subchannels

$$G_{CH} = G_{CH\ \text{experimental}} \times \frac{\bar{G}_{\text{nominal}}}{\bar{G}_{\text{experimental}}}$$

$$x_{CH} = x_{CH\ \text{experimental}} + (\bar{x}_{\text{nominal}} - \bar{x}_{\text{experimental}})$$

These corrections are based on isokinetic sampling tests that were conducted for that purpose involving small changes in the total flow rate and average exit quality. The changes in the subchannel quantities due to these small changes can be expressed as:

$$\Delta G_{CH} = \frac{\partial G_{CH}}{\partial \bar{G}}\, d\bar{G} + \frac{\partial G_{CH}}{\partial \bar{x}}\, d\bar{x}$$

$$\Delta x_{CH} = \frac{\partial x_{CH}}{\partial \bar{x}}\, d\bar{x} + \frac{\partial x_{CH}}{\partial \bar{G}}\, d\bar{G}$$

where ΔG_{CH} and Δx_{CH} are changes in subchannel conditions due to $d\bar{G}$ and $d\bar{x}$. The tests showed that the second term on the right-hand side of both equations was of a smaller order of magnitude than the first term. Also, the derivatives $\partial G_{CH}/\partial \bar{G}$ and $\partial x_{CH}/\partial \bar{x}$ were of the order $G_{CH}/\bar{G}$ and 1, respectively. Therefore

$$\Delta G_{CH} \simeq \frac{\partial G_{CH}}{\partial \bar{G}}\, d\bar{G} \cong \frac{G_{CH}}{\bar{G}}\, d\bar{G}$$

or

$$G_{CH} - G_{CH\ \text{experimental}} \simeq \frac{G_{CH\ \text{experimental}}}{\bar{G}_{\text{experimental}}} \times (\bar{G}_{\text{nominal}} - \bar{G}_{\text{experimental}})$$

so that

$$\frac{G_{CH} - G_{CH\ \text{experimental}}}{G_{CH\ \text{experimental}}} \simeq \frac{\bar{G}_{\text{nominal}} - \bar{G}_{\text{experimental}}}{\bar{G}_{\text{experimental}}}$$

or

$$\frac{G_{CH}}{G_{CH\ \text{experimental}}} \simeq \frac{\bar{G}_{\text{nominal}}}{\bar{G}_{\text{experimental}}}$$

and similarly,

$$\Delta x_{CH} \simeq \frac{\partial x_{CH}}{\partial \bar{x}}\, d\bar{x}$$

or

$$\Delta x_{CH} \simeq d\bar{x}$$

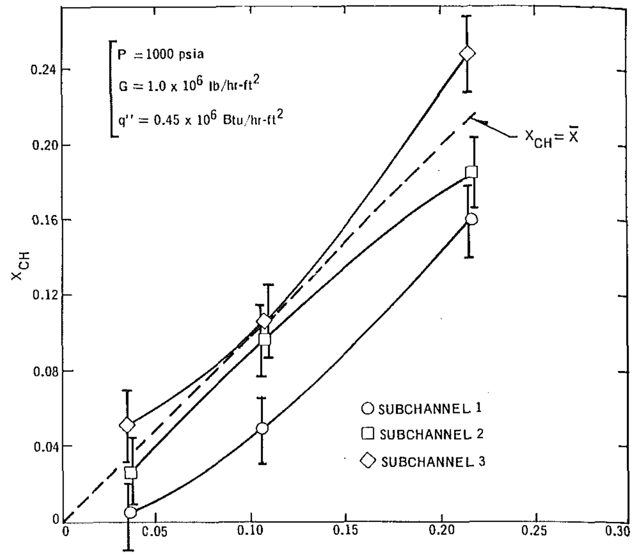

Fig. 5 Variation of subchannel qualities with average quality

so that finally,

$$x_{CH} - x_{CH\ \text{experimental}} \simeq \bar{x}_{\text{nominal}} - \bar{x}_{\text{experimental}}$$

The maximum variations in the test conditions between the different subchannels were of the order of 4 percent in the average mass flux $\bar{G}$ and 0.026 in average quality $\bar{x}$. (This largest correction in $\bar{x}$ was for point 2E3 where $\bar{x} \simeq 0.215$.) The mean variations in $\bar{G}$ and $\bar{x}$ were 1.3 percent and 0.008, respectively. In order to check the present data the bundle average quantities $\bar{G}$ and $\bar{x}$ were compared with the subchannel averaged quantities $\hat{G}$ and $\hat{x}$. It can be seen in Table 2 that continuity checks within ±5 percent with only three runs deviating by more than ±3 percent. In addition, the energy balance is within the ±2 percent error in quality that can be predicted from a detailed error analysis of the calorimetry equipment [4]. The error analysis, based on the Kline and McClintock method [5] for independent errors also predicts ±3 percent error limits for the subchannel mass fluxes. Other investigators [3, 6] have made subchannel measurements in rod bundles, but these data are of somewhat limited value since either not all the subchannels were sampled [3] or the required mass and energy balances are not met [6]. In short, it appears that the present data are the only valid data available to date in which the complete flow and enthalpy distribution has been measured in a rod bundle.

The trends indicated by the data for two-phase conditions at the exit can be seen more clearly by plotting a typical run. Fig. 4 shows the mass flux in the various subchannels normalized to the bundle average mass flux versus the bundle average equilibrium quality. It can be seen that the corner subchannel is always at lower than average mass flux, the center subchannel is always higher than average, and the side subchannel is about average. It is seen that there is a significant flow split in the bundle with the central regions of the bundle having the most flow. It can also be seen that there appears to be enhanced mixing in the region of quality associated with the slug-annular flow regime transition (at approximately 10 percent quality for 1000 psig based on the Wallis [7] criterion, $j_g^* = 0.4 + 0.6 j_f^*$). This dependence of mixing on flow regime has been observed by other investigators [8–10], but it appears to be less pronounced in multirod geometries with typical BWR clearances than in two-subchannel test sections.

The distribution of subchannel enthalpies can be seen for the same run by plotting subchannel equilibrium quality versus bundle average equilibrium quality, shown in Fig. 5. It can

Table 3 Single-phase data (cold)

Test point		$\bar{G}/10^6$ lb/hr-ft²	$G_1/10^6$ lb/hr-ft²	$G_2/10^6$ lb/hr-ft²	$G_3/10^6$ lb/hr-ft²
1B	Data	0.480	0.311	0.462	0.526
	"$D_H^{2/3}$ prediction"*	0.480	0.322	0.447	0.562
	COBRA β = 0.01	0.480	0.352	0.451	0.551
	COBRA β = 0.005	0.480	0.336	0.447	0.560
1C	Data	0.990	0.701	0.939	1.150
	"$D_H^{2/3}$ prediction"	0.990	0.664	0.922	1.159
	COBRA β = 0.01	0.990	0.740	0.934	1.128
	COBRA β = 0.005	0.990	0.704	0.925	1.149
1D	Data	1.510	1.095	1.441	1.690
	"$D_H^{2/3}$ prediction"	1.510	1.013	1.406	1.768
	COBRA β = 0.01	1.510	1.143	1.427	1.713
	COBRA β = 0.005	1.510	1.085	1.414	1.746
1E	Data	1.970	1.620	1.910	2.190
	"$D_H^{2/3}$ prediction"	1.970	1.321	1.834	2.306
	COBRA β = 0.01	1.970	1.502	1.865	2.229
	COBRA β = 0.005	1.970	1.424	1.847	2.273

* This assumes no mixing or transverse momentum.

Table 4 Two-phase data

Test point	$\bar{G}/10^6$	$\bar{X}$		$G_1/10^6$	X_1	$G_2/10^6$	X_2	$G_3/10^6$	X_3
2B2	0.530	0.029	Data	0.372	0.003	0.521	0.014	0.540	0.030
			COBRA (β = 0.04)	0.482	0.030	0.523	0.026	0.552	0.031
			COBRA (β = 0.01)	0.491	0.046	0.516	0.025	0.558	0.029
2B3	0.535	0.090	Data	0.550	0.072	0.530	0.076	0.521	0.104
			COBRA (β = 0.04)	0.478	0.090	0.528	0.086	0.560	0.092
			COBRA (β = 0.01)	0.454	0.104	0.524	0.084	0.571	0.092
2B4	0.535	0.176	Data	0.524	0.133	0.517	0.180	0.560	0.220
			COBRA (β = 0.04)	0.469	0.177	0.526	0.172	0.565	0.178
			COBRA (β = 0.01)	0.417	0.194	0.524	0.169	0.581	0.179
2E1	1.080	0.035	Data	0.950	0.004	1.102	0.026	1.162	0.051
			COBRA (β = 0.04)	0.990	0.035	1.082	0.031	1.102	0.038
			COBRA (β = 0.01)	0.874	0.057	1.068	0.030	1.151	0.034
2E2	1.080	0.106	Data	1.046	0.049	1.078	0.097	1.180	0.105
			COBRA (β = 0.04)	0.979	0.106	1.073	0.102	1.117	0.109
			COBRA (β = 0.01)	0.878	0.125	1.073	0.099	1.143	0.109
2E3	1.060	0.215	Data	0.965	0.160	1.081	0.185	1.126	0.249
			COBRA (β = 0.04)	0.938	0.215	1.044	0.211	1.113	0.217
			COBRA (β = 0.01)	0.826	0.234	1.046	0.206	1.140	0.220

be noted the center subchannel is "hotter" than average (i.e., the center subchannel is at a higher quality than the bundle average quality), the side subchannel is at about average conditions (or slightly below average), and the corner subchannel is "colder" than bundle average conditions. The flow regime effect on turbulent mixing can again be seen in this figure. It should be noted that, within the error bands shown, an energy balance is maintained in the slug-annular transition region since most of the flow and energy flux is in the center subchannel. Probably the most important observation that can be made from this figure is that the subchannel with the highest mass flux (the center subchannel) has the highest quality and that with the lowest mass flux (the corner subchannel) has the lowest quality, even though the corner subchannel has a higher power-to-flow ratio than the center subchannel. In fact, as has been previously discussed [2], this is a general trend which has been seen in both air-water and diabatic steam-water experiments in rod bundles and is not associated with leakage or heat-loss problems with the peripheral subchannels. It is apparent that even if small errors of this kind occurred during the tests, they could not explain the higher than expected qualities in the center subchannel.

This trend is evidently strongly related to the affinity of the vapor phase for the less-obstructed high-velocity regions, such that, at least for conditions of annular flow, there appears to be a relatively thick liquid film on the unheated canister which surrounds the rod array. This rather large amount of liquid necessarily lowers the subchannel average quality in the corner subchannel. These data have very important implications when considered in conjunction with existing subchannel prediction schemes, since all the computer codes presently in the open literature deal with node average enthalpies rather than keeping a liquid inventory as in a film flow model.

Comparison with other data also indicates that rod bundles tend to behave qualitatively like heated pipes in annular flow with the highest quality in the central regions. Multirod radial void fraction measurements in a 16-rod square-pitch heated assembly by Kangas and Neusen [11] as well as gamma scan void profile measurement made by Nylund, et al. [12, 13] in triangular-pitch 6- and 36-rod bundles illustrate this trend. Quality contours plotted by Schraub, et al. [14] for an adiabatic 9-rod assembly based on isokinetic sampling also show the air concentrations were the highest in the central region, while the corner subchannels had a higher water fraction than average. Flow regime maps obtained by Bergles [15] in a 4-rod assembly show transitions occurring earlier in the center subchannel which indicates higher qualities in this region.

Isokinetic sampling tests were also made at Columbia University [3] for a 16-rod square-pitch array, in which two center subchannels were sampled. One of these comprised the subchannel formed by 4 heater rods with higher than average power ("hot subchannel") whereas the other was surrounded by 4 rods with less than average power ("cold subchannel"). It was found that both "cold" and "hot" center subchannels ran hotter than average, in agreement with the trends seen in the present data. A direct comparison of the present data with that obtained at Columbia University is not possible since the latter were taken under different operating conditions, i.e., non-uniform radial heat flux and subcooled or very low exit qualities. The present data show little effect of heat flux on the center subchannel flow rate or of bundle average flow rate on the subchannel quality for bulk boiling exit conditions, whereas marked changes were noted in [3] during subcooled boiling. However, the center subchannel quality was found to increase at constant average quality when the heat flux was raised, a trend also seen in [3].

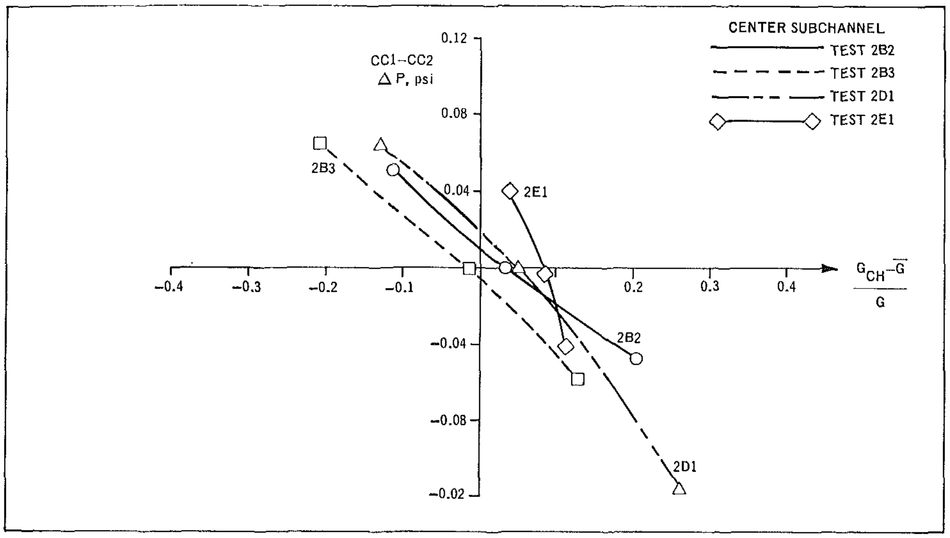

Fig. 6 Variation of differential pressure with subchannel flow

The multirod subchannel sampling data previously discussed are of considerable value in that they provide the data base on which to assess the accuracy of prediction of existing subchannel computer codes.

There are several ventilated subchannel computer codes in the open literature, for instance, HAMBO [16], SASS [17], and COBRA-I [18], all of which predict the flow and enthalpy distribution in a rod bundle. COBRA was chosen to compare with the present data since it is known that in principle all these codes are similar and that their predictions compare favorably with each other. Two values of Rowe's [18] mixing parameter β (the mixing Stanton number), defined implicitly by the relation

$$\tilde{W} = \beta S \langle G \rangle$$

were chosen which bracketed those recommended by Rowe [8]. In addition, the theoretical flow split of $D_H{}^{2/3}$ was calculated for the single-phase cases. A more detailed discussion of this analysis is given in reference [4]; however, the important results can be seen in Tables 3 and 4. Table 3 indicates that the best overall agreement with single-phase data is obtained for $\beta = 0.005$; however, for the highest flow case, it appears $\beta > 0.01$ would produce better agreement with the data. It is also interesting that the simple hand calculation of $G \sim D_H{}^{2/3}$ gives fair agreement, particularly at the lower flow rates. This indicates a fully developed flow split, which might be expected since 10 ft of heater rod (4 ft unheated followed by 6 ft of heater section) is ahead of the sampling point.

For the two-phase runs the mixing parameter would most likely be different in the single-phase region, subcooled region, and bulk boiling region and thus would vary in the axial direction. Nevertheless, previous practice has been to assume that a single value of β is valid at every axial node. Thus, in order to be consistent with previous comparisons and, since the present version of COBRA [18] has no subcooled voids, two bracketing values of β were again assumed. Table 4 indicates that a somewhat better comparison between the predicted results and the data was obtained for the larger β ($\beta = 0.04$). However, it is seen that even with the higher mixing, COBRA cannot predict the trends in the data for the corner subchannel. In fact, if the mixing were made infinite, this would bring all the subchannels to the bundle average enthalpy and thus mixing alone cannot explain the trend of lower than average quality in the corner subchannel and the substantially higher than average quality in the center subchannel. It is evident that without modification of the thermal-hydraulic physics in these codes, agreement with actual multirod data cannot be achieved. It appears that this modification must take into account the drift of the lighter phase into the more-open, higher-velocity regions of the bundle.

Non-Isokinetic Data and Analysis

Introduction. Some data were taken under non-isokinetic conditions, i.e., with a non-isokinetic pressure differential imposed between the subchannel being sampled and a diametrically opposite subchannel. These results with a forced flow split between subchannels yield information about the flow diversion cross flow between subchannels and the enthalpy associated with this cross flow.

Fig. 6 shows some typical non-isokinetic data plotted in terms of the non-dimensionalized subchannel flow against the pressure differential with respect to the isokinetic setting. The intersections of the curves with the horizontal axis represent isokinetic conditions. The difference between the slope of test series 2B2, 2B3, 2D1, and that of 2E1 is due to the fact that the first three runs were made at a mass flux of 0.5 × 10^6 lb/hr-ft^2 while the last one was at a mass flux of 1 × 10^6 lb/hr-ft^2. Fig. 7 shows the variation in subchannel enthalpy as the flow in the center subchannel is varied for constant average test conditions. It can be seen that the enthalpy increases as the subchannel mass flux is increased.

Prediction of Non-Isokinetic Results. For single-phase adiabatic runs, the theoretical pressure differential can be readily calculated assuming that the pressure is uniform across the channel at a small distance upstream from the flow splitters. The pressure differential has components of acceleration and friction pressure drop. Under isokinetic conditions the pressure differential is almost zero and there is very little flow redistribution over a short length near the exit. For non-isokinetic conditions, there is a measurable change in the axial acceleration component of pressure drop due to a sizeable change in subchannel flow; also some change in the friction pressure drop over the axial length of flow diversion would be expected. Fig. 8 shows the non-isokinetic cold data for the center subchannel for two mass fluxes together with the theoretical acceleration pressure differential. The good agreement between the two indicates that the frictional component, and thus the diversion length, are relatively small, an observation in agreement with other investigators [6].

For two-phase exit conditions a similar procedure can be applied, but it is rather sensitive to the accuracy of the measured exit conditions. Fig. 9 shows representative comparisons be-

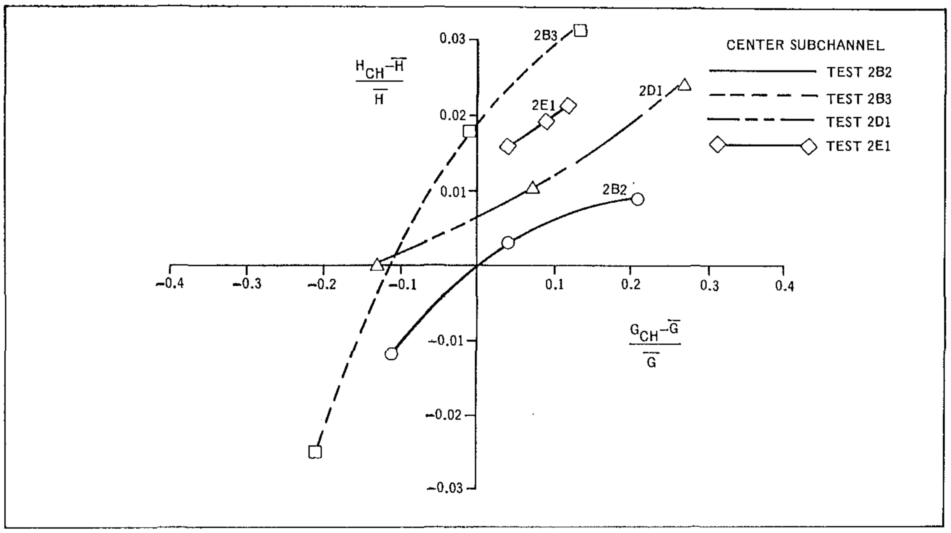

Fig. 7 Variation of subchannel enthalpy with subchannel flow

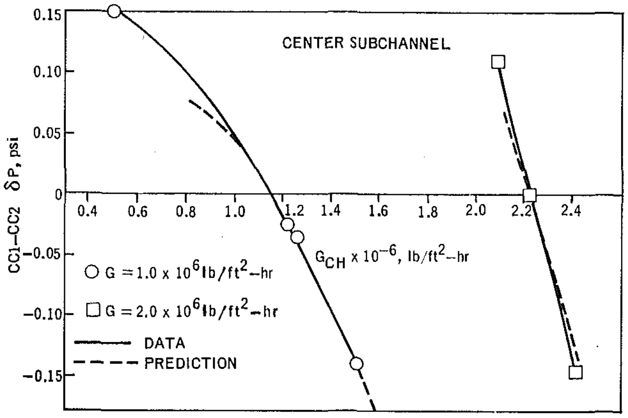

Fig. 8 Non-isokinetic cold data and predictions

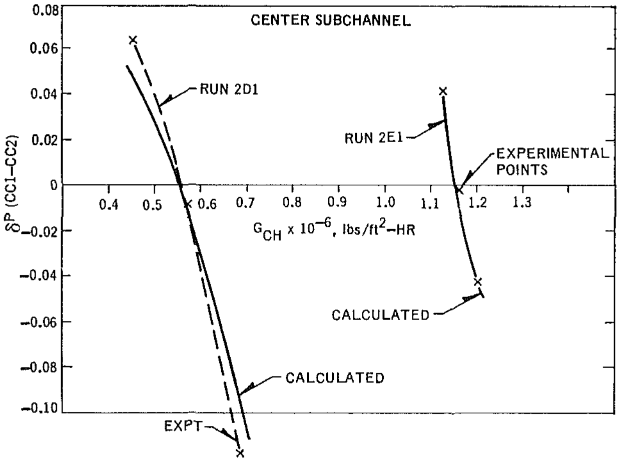

Fig. 9 Non-isokinetic two-phase data and predictions

tween the experimental and calculated values for the center subchannels. The agreement is good for both values of mass flux considered, again indicating that the flow diversion length (*dl*) is small as assumed.

The details of the single- and two-phase calculational procedure are given in Appendix 1.

Cross-Flow Enthalpy. The enthalpy associated with the cross flow into or out of a subchannel is an important parameter in ventilated subchannel analysis of multirod bundles. The cross-flow enthalpy under non-isokinetic conditions can be defined as:

$$H_X = \frac{\Delta(G_{CH}H_{CH})}{\Delta G_{CH}} \qquad \text{(Appendix 2)}$$

and in particular, in the vicinity of the isokinetic condition:

$$H_X\Big|_{\text{iso}} = \frac{d(G_{CH}H_{CH})}{dG_{CH}}\Big|_{\text{iso}}$$

Values of the cross-flow enthalpy were estimated from the slopes of $G_{CH}H_{CH}$ versus G_{CH} plots as shown in Fig. 10. It is particularly interesting to obtain the value of cross-flow enthalpy from the lower portion of the plot since under these conditions the flow rate in the subchannel is less than isokinetic, and the enthalpy is associated with cross flow from that subchannel as opposed to cross flow into the subchannel. This can be compared with the average enthalpy of the subchannel, as shown in Fig. 11 for the corner subchannel. It can be seen that the cross-flow enthalpy from the corner subchannel is generally higher than the enthalpy of the donor subchannel.

Also, if the data are grouped by flow regime as determined using the Wallis criterion [7], it is found that there is a drop in the cross-flow enthalpy near the bubbly-annular transition, probably due to liquid slugging in this flow regime. Beyond this region, the cross-flow enthalpy increases monotonically with subchannel quality. An identical trend has been observed with the center subchannel [4].

It should be noted that these data were taken in a bundle having nominal rod/wall and rod/rod clearances of 0.135 in. and 0.168 in., respectively. There is some evidence [19] which indicates that the same trends may not hold for smaller gap sizes.

Summary and Conclusions

Adiabatic and diabatic subchannel data have been taken in a 3 × 3 rod array having geometry typical of a boiling water reactor (BWR) and operating at typical BWR conditions. The flow and enthalpy distribution trends seen in these data are consistent with the data of previous investigators [2]; however, the present data is more detailed and more applicable to the needs of subchannel analysis. The salient conclusions to be drawn from this data are:

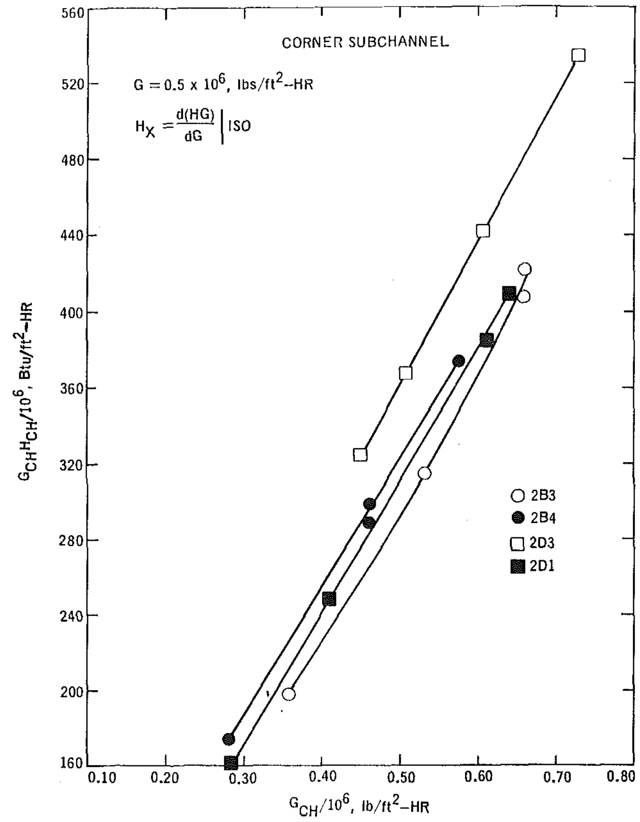

Fig. 10 Graphical determination of cross-flow enthalpy

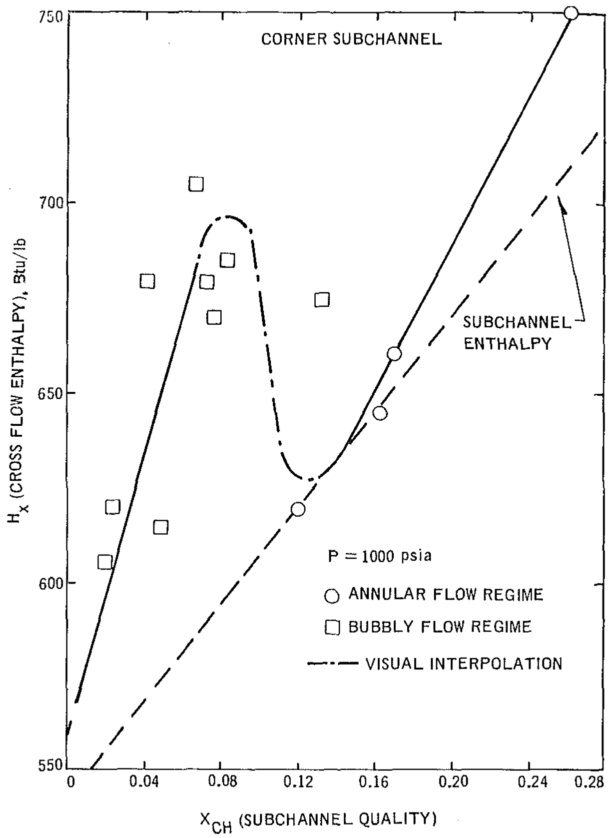

Fig. 11 Cross-flow enthalpy versus quality of donor subchannel

1 There is a significant flow and enthalpy variation in the various subchannels of a rod bundle.

2 The corner subchannel of the subject rod bundle was at lower than bundle average quality even though its power-to-flow ratio was greater than average.

3 The cross-flow enthalpy was higher than the enthalpy of the donor subchannel and appeared to be a function of flow regime.

4 The effective length for flow diversion is apparently quite small.

It has also been shown that a subchannel code typical of the present generation codes (COBRA) is unable to predict the trends in the two-phase data regardless of the magnitude of eddy diffusivity mixing, thus indicating a fundamental problem in the thermal-hydraulic modeling. It is hoped that this data will thus provide a reliable basis to further the understanding of subchannel analysis.

Acknowledgments

The authors wish to gratefully acknowledge the assistance of all those who participated in this program. Specifically, we wish to thank Dr. E. Janssen who is responsible for the AEC program under which this work was done, and AEC Contract AT(04-3)-189, PA-44, for making funds available to support this study. In addition, we wish to thank Dr. F. A. Schraub for his technical assistance and encouragement during the course of this program.

References

1 Rogers, J. H., Todreas, N. E., "Coolant Interchannel Mixing in Reactor Fuel Bundles Single Phase Coolants," *Heat Transfer in Rod Bundles*, ASME, Dec. 1968.

2 Lahey, R. T., Schraub, F. A., "Mixing, Flow Regimes, and Void Fraction for Two-Phase Flow in Rod Bundles," *Two-Phase Flow and Heat Transfer in Rod Bundles*, ASME, Nov. 1969.

3 Casterline, J. E., Castellana, F. A., "Flow and Enthalpy Measurements in a Simulated Nuclear Fuel Assembly," CU-187-2, Feb. 1969.

4 Lahey, R. T., Shiralkar, B. S., Radcliffe, D. W., "Subchannel and Pressure Drop Measurements in a Nine-Rod Bundle for Diabatic and Adiabatic Conditions," GEAP-13049, March 1970.

5 Kline, S. J., McClintock, F. A., "Describing Uncertainties in Single-Sample Experiments," *Mechanical Engineering*, Vol. 75, Jan. 1953, p. 3.

6 Bowring, R. W., Levy, J., "Freon 7-Rod Cluster Subchannel Mixing Experiments," AEEW-M-906, May 1969.

7 Collier, J. G., Wallis, G. B., *Two-Phase Flow and Heat Transfer*, Vol. 2, Stanford University Press, Aug. 1967.

8 Rowe, D. S., Angle, C. W., "Crossflow Mixing Between Parallel Flow Channels During Boiling—Part III," BNWL-371, Pt. 3, Jan. 1969.

9 Walton, F. W., Petrunik, K. J., St. Pierre, C. C., "Two-Phase Air-Water Turbulent Mixing Between Parallel Open Flow Channels," Paper No. 5F, National Meeting AIChE, Aug. 1969.

10 Spigt, C. L., et al., "Final Report on the Research Program on the Heat Transfer and Fluid Flow Characteristics of a Pressurized Water Reactor," Technological University of Eindhoven, WW-015-R128, Dec. 1967.

11 Kangas, G., Neusen, K., "Pressure Drop and Void Fraction Experiments in Simulated Pathfinder Boiler Fuel Elements," ACNP-63002, March 1963.

12 Nylund, O., Becker, K. M., et al., "Measurements of Hydrodynamic Characteristics, Instability Thresholds, and Burnout Limits for 6-Rod Clusters in Natural and Forced Circulation," FRIGG-I, R4-422/RTL-914, Sweden, 1967.

13 Nylund, O., Becker, K. M., et al., "Hydrodynamic and Heat Transfer Measurements on a Full Scale Simulated 36-Rod Marviken Fuel Element with Uniform Heat Flux Distribution," FRIGG-II, R4-447/RTL-1007, Sweden, 1968.

14 Schraub, F. A., Simpson, R. L., Janssen, E., "Two-Phase Flow and Heat Transfer in Multirod Geometries: Air-Water Flow Structure Data for a Round Tube Concentric and Eccentric Annulus, and Nine-Rod Bundle," GE-AEC Research and Development Report, GEAP-5739, Jan. 1969.

15 Bergles, A. E., "Two-Phase Flow Structure Observations for High Pressure Water in a Rod Bundle," *Two-Phase Flow and Heat Transfer in Rod Bundles*, ASME, Nov. 1969.

16 Bowring, R. W., "HAMBO, A Computer Programme for the

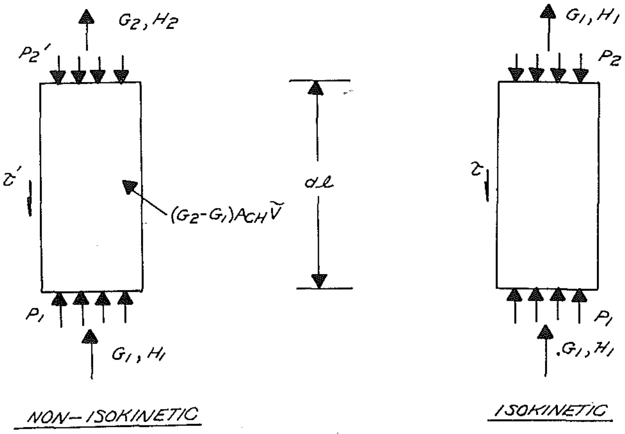

Fig. 12 Calculation of non-isokinetic pressure differential

Subchannel Analysis of the Hydraulic and Burnout Characteristics of Rod Clusters—Part 2, The Equations," AEEW-R-582, Jan. 1968.

17 St. Pierre, Carl C., "SASS Code-I, Subchannel Analysis for the Steady-State," APPE-41, Sept. 1966.

18 Rowe, D. S., "Crossflow Mixing Between Parallel Flow Channels During Boiling," BNWL-371, Pt. 1, March 1967.

19 Madden, J. M., and St. Pierre, C. C., "Two-Phase Air-Water Flow in a Slot-Type Distributor," University of Leeds (Great Britain), *Symposium on Fluid Mechanics and Measurements in Two-Phase Systems*, Sept. 1967.

APPENDIX 1

The simple model in Fig. 12 can be used to estimate the pressure differential due to flow diversion. It is assumed that for non-isokinetic conditions, the flow diversion occurs over a small length dl, and upstream of this point there is no difference between the two cases. It is also assumed that the length dl is small enough so that negligible flow diversion occurs over this length under isokinetic conditions. With the notation used in the figure, the momentum equations can be written as follows:

Cold Runs

Non-Iso:

$$(P_1 - P_2')A_{CH} - \tau' P_{CH} dl - \rho \frac{g}{g_c}\, dl\, A_{CH} = \frac{G_2^2}{\rho g_c} A_{CH} - \frac{G_1^2}{\rho g_c} A_{CH} - A_{CH}(G_2 - G_1)\tilde{V}/g_c \quad (1)$$

Iso:

$$(P_1 - P_2)A_{CH} - \tau P_{CH} dl - \rho \frac{g}{g_c}\, dl\, A_{CH} = 0 \quad (2)$$

where

G_2 = non-isokinetic mass flux (lb/hr-ft^2)
G_1 = isokinetic mass flux (lb/hr-ft^2)
A_{CH}, P_{CH} = flow area and friction perimeter of subchannel
$\tilde{V}$ = average axial velocity of the crossflow.

Subtracting equation (2) from (1) and dividing through by A_{CH},

$$\delta P \triangleq (P_2 - P_2') = \text{non-isokinetic pressure differential}$$
$$= \frac{G_2^2}{\rho g_c} - \frac{G_1^2}{\rho g_c} - (G_2 - G_1)\frac{\tilde{V}}{g_c} + (\tau' - \tau)\frac{P_{CH} dl}{A_{CH}} \quad (3)$$

$\tilde{V}$ was assumed to be the mean linear velocity in the two adjacent subchannels during the calculation and the friction term can be neglected if dl is small.

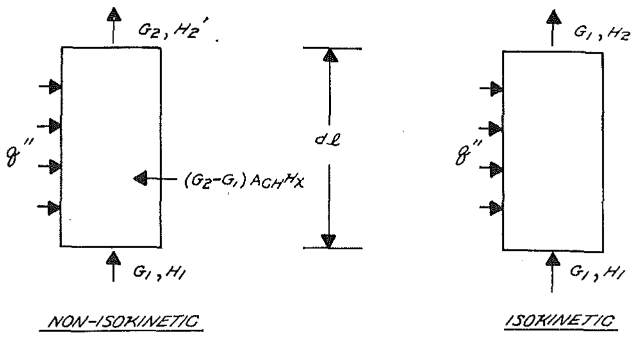

Fig. 13 Cross-flow enthalpy

Two-Phase Exit Conditions

Non-Iso:

$$(P_1 - P_2')A_{CH} - \tau' P_{CH} dl - \bar{\rho}' \frac{g}{g_c}\, dl A_{CH}$$
$$= \frac{G_2^2}{g_c}\left[\frac{x_2'^2}{\alpha_2'\rho_g} + \frac{(1-x_2')^2}{(1-\alpha_2')\rho_f}\right] A_{CH}$$
$$- \frac{G_1^2}{g_c}\left[\frac{x_1^2}{\alpha_1\rho_g} + \frac{(1-x_1)^2}{(1-\alpha_1)\rho_f}\right] A_{CH} - (G_2 - G_1)\frac{\tilde{V}}{g_c} A_{CH} \quad (4)$$

Iso:

$$(P_1 - P_2)A_{CH} - \tau P_{CH} dl - \bar{\rho} \frac{g}{g_c}\, dl A_{CH}$$
$$= \frac{G_1^2}{g_c}\left[\frac{x_2^2}{\alpha_2\rho_g} + \frac{(1-x_2)^2}{(1-\alpha_2)\rho_f}\right] A_{CH}$$
$$- \frac{G_1^2}{g_c}\left[\frac{x_1^2}{\alpha_1\rho_g} + \frac{(1-x_1)^2}{(1-\alpha_1)\rho_f}\right] A_{CH} \quad (5)$$

Subtracting equation (5) from (4) and dividing through by A_{CH},

$$\delta P \triangleq (P_2 - P_2') = \frac{G_2^2}{g_c}\left[\frac{x_2'^2}{\alpha_2'\rho_g} + \frac{(1-x_2')^2}{(1-\alpha_2')\rho_f}\right]$$
$$- \frac{G_1^2}{g_c}\left[\frac{x_2^2}{\alpha_2\rho_g} + \frac{(1-x_2)^2}{(1-\alpha_2)\rho_f}\right] - (G_2 - G_1)\frac{\tilde{V}}{g_c}$$
$$+ (\tau' - \tau)\frac{P_{CH} dl}{A_{CH}} + (\bar{\rho}' - \bar{\rho})\frac{g}{g_c} dl \quad (6)$$

For fairly small cross flow over a short diversion length,

$$\delta P \triangleq (P_2 - P_2') \simeq \frac{G_2^2}{g_c\rho_f}\left[\frac{x_2'^2}{\alpha_2'}\left(\frac{\rho_f}{\rho_g}\right) + \frac{(1-x_2')^2}{(1-\alpha_2')}\right]$$
$$- \frac{G_1^2}{g_c\rho_f}\left[\frac{x_2^2}{\alpha_2}\left(\frac{\rho_f}{\rho_g}\right) + \frac{(1-x_2)^2}{(1-\alpha_2)}\right] - (G_2 - G_1)\frac{\tilde{V}}{g_c} \quad (7)$$

$\tilde{V}$ was taken to be the average of the linear velocities in the adjacent subchannels, calculated as

$$\tilde{V} \triangleq \frac{1}{2}\left[\frac{G_1}{\rho_{1M}} + \frac{G_2}{\rho_{2M}}\right]$$

where ρ_{1M}, ρ_{2M} are the "momentum densities" in the two subchannels:

$$\frac{1}{\rho_{iM}} \triangleq \left[\frac{x_i^2}{\alpha_i\rho_g} + \frac{(1-x_i)^2}{(1-\alpha_i)\rho_f}\right]$$

APPENDIX 2

With the same assumptions as in Appendix 1, the energy balance for the node of length dl (neglecting mechanical energy terms) gives:

Non-Iso:

$$A_{CH}G_2H_2' - A_{CH}G_1H_1 - (G_2 - G_1)A_{CH}H_X = q''P_H dl \qquad (8)$$

Iso:

$$A_{CH}G_1H_2 - A_{CH}G_1H_1 = q''P_H dl \qquad (9)$$

where

H_X = cross-flow enthalpy
P_H = subchannel heated perimeter.

Subtracting equation (9) from (8) and dividing by A_{CH},

$$G_2H_2' - G_1H_2 - (G_2 - G_1)H_X = 0$$

or

$$H_X = \frac{G_2H_2' - G_1H_2}{G_2 - G_1} = \frac{\Delta(GH)_{CH}}{\Delta G_{CH}}$$

APPENDIX 2

With the same assumptions as in Appendix 1, the energy balance for the node of length dl (neglecting mechanical energy terms) gives:

Non-Iso:

$$A_{CH}G_2H_2' - A_{CH}G_1H_1 - (G_2 - G_1)A_{CH}H_X = q''P_Hdl \quad (8)$$

Iso:

$$A_{CH}G_1H_2 - A_{CH}G_1H_1 = q''P_Hdl \quad (9)$$

where

H_X = cross-flow enthalpy
P_H = subchannel heated perimeter.

Subtracting equation (9) from (8) and dividing by A_{CH},

$$G_2H_2' - G_1H_2 - (G_2 - G_1)H_X = 0$$

or

$$H_X = \frac{G_2H_2' - G_1H_2}{G_2 - G_1} = \frac{\Delta(GH)_{CH}}{\Delta G_{CH}}$$

DISCUSSION

J. E. Casterline[2]

The purpose of the experimental study described in this paper was to provide subchannel flow and enthalpy data that could be used to evaluate and improve existing rod bundle thermal-hydraulic analysis codes. While the results obtained for the wall channel and the center channel are consistent with previous studies, the results for the corner channel C1 were unexpected and would not have been predicted by computer codes generally in use. This review will concentrate on determining the confidence limits that can be placed on data taken from the corner channel.

1 The authors state that the data may be checked for consistency since all representative subchannels were sampled. It is important to note, however, that since the flow area of the four corner channels was only 11 percent of the total flow area, significant measurement errors in channel 1 flow could occur without being detected from continuity considerations. Table 5 gives an indication of the possible magnitude of this error based on observed differences between total flow and summed flow measurements. In some cases the error can be as much as 55 percent of the experimental value.

2 This experimental program was reported in detail in a series of GEAP Quarterly Progress Reports. Unfortunately, there are some disturbing differences in the description of the experiment in these Q.P.R.'s and in this paper. The principal differences are:

(*a*) From Q.P.R. April 1–June 30, 1969, p. 2, it is stated: "Preliminary tests were performed to determine the isokinetic setting, following a procedure similar to that for the corner subchannel. The pressure difference between taps W1 and W2 was measured for different conditions of single-phase and two-phase flow, with the sample tube removed. This was done with the splitters in place, but with the top of the box formed by the splitters being open so flow could pass through with little resistance." In the paper under review, the procedure is described as follows: "The isokinetic settings were determined from calibration runs made prior to splitter installation." Were the splitters in place or were they not, during the calibration runs? If they were in place, it will be difficult to prove that their presence caused no effect on the small corner channel.

(*b*) The philosophy of this experiment is to balance static pressure measurements in geometrically and thermally equivalent subchannels, i.e., C1 and C2 or W1 and W2. In the Q.P.R. Jan. 1–March 31, 1969, p. 4, the statement is made "When sampling the corner subchannel, C1 and C2 or W2 can be used." The plot for the cold flow in the same report, shown below as Fig. 14, indicates that W2 was used. Why was the basic philosophy of the experiment abandoned? Were the runs with power balanced against C2 or W2? In the paper being reviewed, it is implied that only taps in equivalent channels were used for all runs.

3 Referring to Fig. 14, it is seen that the change in subchannel flow with differential pressure was very great at the low mass velocities (0.5 and 1.0 × 10^6 lb/hr-ft^2). Unfortunately, all the two-phase data were obtained at these flow rates. When dealing with extremely low differential pressures at high temperatures it is very difficult to obtain measurements better than ±0.01 psi. Slight differences in the temperature of the water in the tubing line to the manometer or transducer or almost undetectable leaks in these lines can easily cause errors of this magnitude. Lines at ±0.01 psi are drawn on the figure showing the variation in flow that would occur with a measurement error of this magnitude.

4 The cold flow data for the corner channel raise additional questions about all the measurements made in this channel, especially when viewed in the light of Fig. 15 which shows a plot of $G_{\text{channel}}/G_{\text{av}}$ versus G_{av}. As indicated above, the measurements at 1.5 and 2.0 × 10^6 lb/hr-ft^2 are expected to be the most accurate of the cold flow data, for all channels. These show essentially no change for channels W1 and CC1 as expected, however there is a sharp increase in percentage of flow to the corner channel, the magnitude of which would not be anticipated by any of the usual hydraulic analysis techniques. It is unfortunate that the experimenters did not continue their cold flow runs to a G_{av} of 3.0 ×

Table 5 Channel 1 flow errors based on considerations of continuity

RUN	GAVEXP	GAVSUM	DG	WERROR	W1	WERROR/W1
2B2	0.530	0.522	0.008	165	822	0.20
2B3	0.535	0.529	0.006	124	1216	0.10
2B4	0.535	0.535	...	...	...	...
2C1	1.060	1.060	...	...	...	...
2C2	1.068	1.068	...	...	...	...
2D1	0.540	0.544	0.004	83	940	0.09
2D3	0.540	0.540	...	...	...	...
2E1	1.080	1.110	0.030	620	2100	0.29
2E2	1.080	1.115	0.035	724	2313	0.31
2E3	1.060	1.087	0.027	558	2134	0.26
2G1	1.070	1.018	0.052	1075	1950	0.55
2G2	1.080	1.107	0.027	558	2211	0.25
2G3	1.070	1.114	0.044	910	1913	0.48

RUN = run number.
GAVEXP = average mass velocity × 10^{-6} (lb/hr-ft^2)—experimental value.
GAVSUM = average mass velocity × 10^{-6} (lb/hr-ft^2)—as defined in paper.
DG = GAVEXP − GAVSUM (× 10^{-6} lb/hr-ft^2).
WERROR = DG × A_T.
W1 = subchannel 1 flow rate (lb/hr) × 4.

---

[2] Senior Research Associate, Chemical Engineering Research Laboratories, School of Engineering and Applied Science, Columbia University, New York, N. Y.

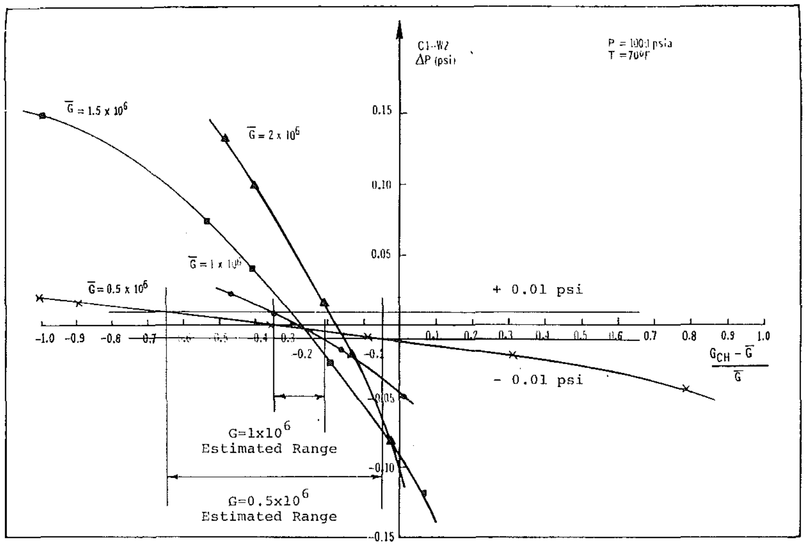

Fig. 14 Corner channel flow as a function of the balancing ΔP

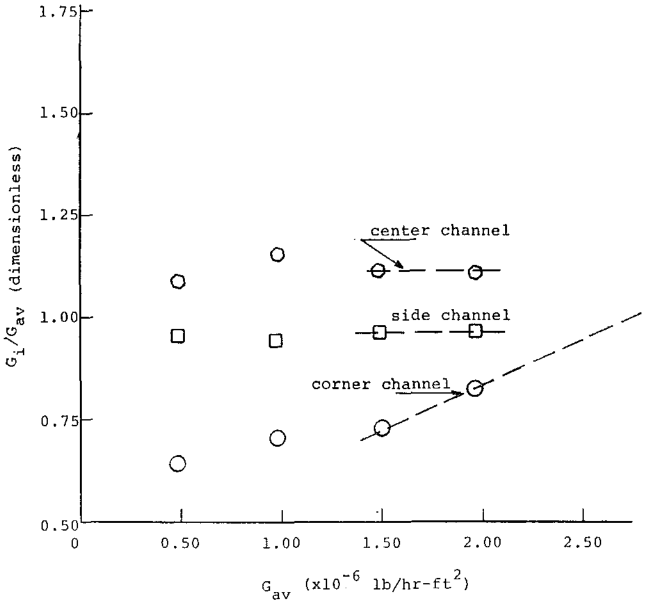

Fig. 15 Subchannel mass velocity as a function of average mass velocity

10^6 lb/hr-ft^2, at which point, if the observed trends had continued, the mass velocity in the corner channel would have been greater than the average mass velocity, an obviously impossible situation. If this behavior was not due to test-section leakage, as the authors seem convinced, do they have an explanation?

In conclusion it is recommended that the data for the corner channel be viewed with some skepticism until confirmed by additional studies that have also been carefully reviewed.

R. W. Bowring[3]

The paper represents a valuable contribution to our knowledge of the behaviour of subchannels in rod clusters and the authors are to be congratulated upon the successful conclusion of a very difficult experiment.

One of the most interesting features of the experimental data is the observation that both exit mass velocity and quality in the corner subchannel were lower than the cluster average values under two-phase conditions. This was contrary to the predictions using the subchannel code COBRA (Table 4). The data have subsequently been analysed (Table 6) using the British code HAMBO, reference [12], which substantially predicts similar

---

[3] U.K.A.E.A., Winfrith, England.

Table 6 Two-phase data comparison using HAMBO (cf. Table 2)

Test point	$\bar{G}/10^6$	$\bar{X}$		$G_1/10^6$	X_1	$G_2/10^6$	X_2	$G_3/10^6$	X_3
2B2	0.530	0.029	Data	0.372	0.003	0.521	0.014	0.540	0.030
			HAMBO ($F_m = 30$)	0.476	0.037*	0.524	0.036*	0.552	0.037*
			HAMBO ($F_m = 3$)	0.425	0.057	0.516	0.035*	0.576	0.036*
2B3	0.535	0.090	Data	0.550	0.072	0.530	0.076	0.521	0.104
			HAMBO ($F_m = 30$)	0.472	0.091	0.528	0.088	0.561	0.091
			HAMBO ($F_m = 3$)	0.403	0.122	0.523	0.082	0.585	0.092
2B4	0.535	0.176	Data	0.524	0.133	0.517	0.180	0.560	0.220
			HAMBO ($F_m = 30$)	0.464	0.178	0.526	0.175	0.565	0.177
			HAMBO ($F_m = 3$)	0.382	0.215	0.518	0.168	0.598	0.177
2E1	1.080	0.035	Data	0.950	0.004	1.102	0.026	1.162	0.051
			HAMBO ($F_m = 30$)	0.974	0.039*	1.070	0.038*	1.121	0.039*
			HAMBO ($F_m = 3$)	0.700	0.086	1.067	0.037*	1.199	0.036*
2E2	1.080	0.106	Data	1.046	0.049	1.078	0.097	1.180	0.105
			HAMBO ($F_m = 30$)	0.954	0.107	1.068	0.104	1.129	0.107
			HAMBO ($F_m = 3$)	0.752	0.157	1.069	0.098	1.183	0.106
2E3	1.060	0.215	Data	0.965	0.160	1.081	0.185	1.126	0.249
			HAMBO ($F_m = 30$)	0.941	0.212	1.063	0.209	1.140	0.211
			HAMBO ($F_m = 3$)	0.756	0.257	1.051	0.202	1.205	0.211

* Indicates "subcooled void quality," i.e., thermodynamic non-equilibrium values whereas the "Data" values are in equilibrium. A nominal value of F_m would be about 5.

trends to those of COBRA. However, it is considered that the authors may be unduly pessimistic in concluding that present-generation subchannel codes would be unable to predict their results. It may be possible to do so with comparatively minor modifications to the hydraulic model and this is the value of the present and other experiments in that they show where changes are necessary.

The authors indicate three complementary changes to the hydraulic model which may be necessary. These are to allow for (*a*) enhanced mixing in the slug-annular flow regime, (*b*) a "drift of the lighter phase into the more open, higher velocity regions of the bundle," and (*c*) "a relatively thick liquid film on the unheated canister which surrounds the rod array." Of these, the first is probably the most important. The second, as typified by Fig. 11, may not be a separate effect but due to subcooled boiling occurring early in the corner subchannel; alternatively it might be satisfactorily accounted for by the enthalpy of the cross flow being somewhat higher than that of the donor subchannel as observed in reference [6]. The third does imply a new generation of subchannel codes in which a film flow model is incorporated and this cannot be attempted until a model for simpler geometries has been made to work. However, the effect is already partially allowed for in existing subchannel codes as the film thickness would affect the pressure drop, through the wetted diameter, and thus the cross flow.

An indication of the sort of modification necessary may be obtained from an analysis of the experimental data without recourse to a code. For example, the data from Runs 1C and 2E3 may be combined, normalising to the channel average values to allow for the difference in mass velocity. Assuming little change in the mass velocity along the subchannel under single-phase conditions, the normalised exit velocity for Run 1C would be that at inlet for Run 2E3. Hence in the latter run, the corner subchannel experiences a net gain in flow (from 0.71 to 0.91 of the channel-average mass velocity) but loses 31 percent of the electrical heat it receives (calculated from the exit velocity and quality). The heat could only have been lost near the inlet where the rate of enthalpy rise was greater than in the adjacent side-channel as, at exit, the quality was less than in the side-channel. Thus, one pictures boiling occurring early in the corner subchannel with a large heat loss due to a peak in mixing. The side-channel boils and there is a large cross flow into the corner which regains some of the heat it lost but ends up at a net quality less than the average value.

Although there is a scarcity of experimental data on the mixing peak at low quality, a crude model (e.g., very high or even infinite mixing during subcooled boiling) could be programmed to test whether it is possible to predict the observed behaviour of the cluster without invoking a film flow model. Subcooled boiling and an adjusted enthalpy of the cross flow would also be required in the model. The standard HAMBO model, reference [12], which contains subcooled boiling but with the other modifications unprogrammed, gives a sequence of events similar to that pictured above but the effects are not large enough to predict the experimental results. Do the authors plan to continue their analysis using a modified version of their subchannel code?

The authors comment that the experimental accuracy of the Freon tests described in reference [6] was inadequate. In fact, the errors in mass and heat balance were not very different from those in the present work; the standard deviation from the mean of the error in heat balance was about 5 percent in reference [6] compared to 3.9 percent for the present work, deduced from the data given in Table 2. The main uncertainty in the Freon tests was in the determination of the natural flow split between subchannels. Reference [6] gave only a brief account of the work as it was written for a conference; the determination of the accuracy is described more fully in AEEW–R 663, a report with the same authors and title.

Authors' Closure

The authors appreciate the careful review given their paper by Mr. Casterline and are indeed heartened that someone apparently follows their Quarterly Progress Reports so carefully.

It is quite true that a satisfactory total mass and energy balance is a necessary but not sufficient test for the accuracy of the corner subchannel data, since these balances are not very sensitive to variations in the relatively small corner subchannel. However, these particular data were carefully repeated many times throughout the test program in order to better appraise the observed trends. In all cases the corner subchannel quality was significantly lower than the bundle average quality and the corner subchannel mass flux was lower than the bundle average mass flux. We believe that the repeatability of the data trends from assembly to assembly does much to strengthen our case. Moreover, since the same type of calorimetry and flow metering system was used for each subchannel it is quite unfair to assign all the error to the corner subchannel, as Mr. Casterline has done, and thus calculate the unreasonably high mass defects tabulated in Table 5. A detailed error analysis presented in reference [4] has indicated that the uncertainty in mass flux of each subchannel is approximately ±3 percent, which agrees with the overall mass defect.

Regarding question number 2, we strongly feel that a good journal paper should be the distilled knowledge gained in a successful study. The gory details which are not necessary to understand the essential contribution should be referenced rather than presented. In our case, the AEC topical report cited in reference [4] is where the interested reader can find a more detailed account of the subject study. Nevertheless, since certain specific questions have been asked we feel obligated to supply the answers.

The first test which was run was a calibration test in which the 9-rod bundle was operated at various single- and two-phase conditions and the various isokinetic pressure differentials were measured. Specifically, referring to Fig. 2, the δP from C1–C2, W1–W2, CC1–CC2, C1–W1, and C2–W2 were measured. Subsequent to these runs, the rod bundle was removed and corner subchannel splitters were installed. In order to try and determine the effect of the added friction surface of these splitters on the natural flow split, the previous calibration runs were repeated with the splitters in place and the sample tube removed. It was found that the splitters had little effect on the corner subchannel isokinetic calibration curve. A similar result was found for the side subchannel, thus it appears that one can generate the calibration curves either with or without splitters.

During some of the earlier subchannel tests it was found that the pressure tap C2 was defective. Rather than perform a long and costly reassembly we chose to switch to tap W2. Since we already had δP (C2–W2) calibration data, we were able to do this with no loss of accuracy to the experiment.

Mr. Casterline's comment number 3 about the uncertainty of the low mass flux data (i.e., $G \leq 0.5 \times 10^6$) is quite valid. Indeed this concern is the reason that we originally constructed Fig. 14 in reference [4]. Unfortunately, this is a fact of life and aside from careful isokinetic setting one can not avoid this problem. However, this potential error was included in the uncertainty analysis presented in reference [4], which indicated a ±3 percent uncertainty in the mass flux measurements of each subchannel.

Mr. Casterline's final comment (number 4) brings out an interesting point. The observed trends in the normalized subchannel mass flux data indicate that eddy diffusivity increases as the bundle average mass flux increases, causing the $G_i/\bar{G}$ to tend towards unity. In fact, a more careful plot of these and subsequent data which we have obtained indicates that as bundle average mass flux increases this is apparently the case.

The authors wish to thank Dr. Bowring for his comments and observations. We agree with Dr. Bowring that modifications to the present-generation subchannel computer codes are possible which may allow one to predict the observed trends seen in the subject data without having to go to a detailed film flow model.

A mechanism which we feel can explain the observed trends is one which accounts for the affinity of the vapor phase for the more open, higher velocity regions. We have called this mechanism "void drift" although it may be the redistribution of the liquid phase which actually controls the process. We have recently run several basic experiments in San Jose to better appraise this mechanism. A low-pressure air–water experiment was conducted in a triangular test section in which air bubbles were introduced into the narrow region of the isosceles triangle. It was found that as the void fraction increased the vapor moved strongly into the more open region of the triangle. That is, there was a "void drift." Similarly, a diabatic experiment was performed in an eccentric annulus, in which a hot-wire probe was used to measure the local void fraction in boiling Freon-114. It was found that while the void fraction was the highest in the narrow gap during subcooling boiling, for bulk boiling in the annular flow regime, the void fraction was highest in the more open gap. This again suggests a "void drift" mechanism which could easily explain the trends seen in the corner subchannel. Unfortunately, the precise physical mechanisms involved are not known at this time and it is hoped that future work in this area will help illuminate these points.

Our reference to the "errors" in Dr. Bowring's Freon subchannel experiment [6] was not meant to discredit his investigation. Indeed much of the data analysis he suggested was used in the reduction of our non-isokinetic subchannel data. The point to be made is that since Freon has a latent heat (h_{fg}) which is an order of magnitude smaller than that of water, for the same error in heat balance the errors in quality determination are much larger in Freon than in water. This is undesirable since subchannel CHF correlations, flow regime transitions, etc., are normally based on the local qualities.

In closure, we feel that it is fair to say that our first reaction to the data presented in this paper was much the same as Mr. Casterline's. This is due to the fact that we were used to looking at the output of subchannel computer codes which yield predictions in accordance with postulated thermal-hydraulic models. Naturally these predictions are only as good as the programmed models, which may or may not capture the actual physics involved.

It is our contention that if an accurate "void drift" model were included in the physics of existing subchannel codes, the corner subchannel data trends could well be predicted. Hence, one should be very wary of discarding data which do not agree with the predictions of existing analytical techniques.

R. E. POWE
Assistant Professor,
Department of Aerospace and
Mechanical Engineering,
Montana State University,
Bozeman, Mont.
Assoc. Mem. ASME

C. T. CARLEY
Professor and Head,
Department of Mechanical Engineering,
Mississippi State University,
State College, Miss.
Mem. ASME

S. L. CARRUTH
Sales Engineer,
The Trane Company,
Houston, Texas

A Numerical Solution for Natural Convection in Cylindrical Annuli

The results of a finite-difference solution for natural convection within horizontal cylindrical annuli for Prandtl numbers near 0.7 (air) are presented. The ranges of Rayleigh number and inverse relative gap width over which such a solution yields valid results are investigated. It is shown that this solution, though formulated for steady flow, can be used to obtain an indication of the Rayleigh number at which transition from a steady to an unsteady flow will occur for a wide range of inverse relative gap widths (2.8–12.5). A recent experimental investigation has shown that steady secondary cellular flows occur immediately prior to transition for this range of inverse relative gap widths, and the Rayleigh number at which these secondary flows occur is accurately predicted by the numerical solution, thereby yielding a good indication of the Rayleigh number at which transition to an unsteady flow occurs. Flow patterns predicted by the numerical solution near transition are compared with photographs of the flow, and excellent qualitative agreement is noted. It is thus shown that this numerical technique gives, at least qualitatively, valid results for all Rayleigh numbers at which the flow is steady for the range of inverse relative gap widths under consideration. Heretofore unavailable data on temperature profiles, radial and angular velocity components, and local Nusselt numbers for Rayleigh numbers near the transition value are presented. It is found that the foregoing parameters (velocity, temperature, and Nusselt number) are little affected by the appearance of the secondary flow for the smaller inverse relative gap widths considered, whereas for the larger inverse relative gap widths a pronounced increase in magnitude of temperatures and velocity components is noted. The overall or mean Nusselt number is not affected by the appearance of these secondary flows for any of the inverse relative gap widths considered.

Introduction

The problem of accurately predicting the heat transfer due to natural convection within enclosed spaces has recently received increased attention in the literature, but knowledge in this area is still rather limited. This paper presents a finite-difference solution to the Navier-Stokes equations and the energy equation, without boundary layer approximations, for steady laminar natural convection in the horizontal concentric cylindrical annulus geometry. A similar solution has previously been presented by Crawford and Lemlich [1],[1] but only one case considered by them falls within the range of available experimental data. Thus, their solution yields little information about the range of values of the various parameters (Rayleigh number, diameter ratio, Prandtl number) over which a finite-difference solution will yield valid results.

A second numerical method of solution for this problem is presented by Abbott [2], and it provides a convenient check on the results of the current analysis, even though it is limited to very small diameter ratios. Mack and Bishop [3] have presented an analytical solution for the stream function and temperature in terms of power-series expansions of the Rayleigh number. They found that it was only feasible to utilize the first three terms in each of these series in their calculations, and thus the solution is restricted to low Rayleigh numbers. For inverse relative gap widths $\left(\frac{2}{R-1}\right)$ greater than about 8.5, the maximum Rayleigh number at which they estimated that their solution would yield valid results was somewhat smaller than that at which the flow has been found experimentally to be steady. The numerical technique presented here enables prediction of the flow patterns and temperature profiles within this region.

---

[1] Numbers in brackets designate References at end of paper.

Contributed by the Heat Transfer Division and presented at the Winter Annual Meeting, New York, N. Y., November 29–December 3, 1970, of The American Society of Mechanical Engineers. Manuscript received by the Heat Transfer Division January 9, 1970; revised manuscript received July 22, 1970. Paper No. 70-WA/HT-9.

Several experimental investigations are also available for comparison with the results of the numerical solution. Liu, Mueller, and Landis [4] present sketches of both steady and unsteady flow patterns observed in five different cylinder combinations. Photographic studies and qualitative descriptions of the convective flow patterns are presented by Bishop and Carley [5], by Grigull and Hauf [6], and by Lis [7]. A detailed study of one type of unsteady flow, an oscillatory flow, is given by Bishop, Carley, and Powe [8]. This study gives the Rayleigh number at which the flow will change from a steady to an unsteady condition for certain diameter ratios.

In a recent experimental study by Powe, Carley, and Bishop [9] the maximum Rayleigh number for which the flow is actually steady and laminar for a wide range of diameter ratios is given. They found that, for inverse relative gap widths greater than about 2.8, stable secondary cellular flows, consisting of counter-rotating eddy pairs, occurred in the upper portion of the annulus for Rayleigh numbers slightly below that at which the flow became unsteady. The numerical solution presented here was utilized in an attempt to predict the onset of these secondary flows, thereby indicating the inception of the unsteady flow. For inverse relative gap widths less than about 2.8, Powe et al. [9] found the unsteady flow to first appear as oscillations in the basic steady flow pattern. Thus, the numerical technique would not be expected to indicate the onset of the unsteady flow for these inverse relative gap widths.

Although the numerical technique was formulated for an arbitrary Prandtl number, the results actually calculated were restricted to Prandtl numbers near 0.7 (air) since the majority of experimental data is for this case. The results of this solution are compared with the currently available numerical and analytical results and with experimental data.

Analysis

The problem under consideration is that of two-dimensional steady laminar convection between horizontal isothermal concentric cylinders. Utilizing cylindrical coordinates, let the angular coordinate θ be measured from the downward vertical, $\theta = 0$. For steady-state conditions the flow must be symmetric about a vertical plane through the axis of the cylinders. Even if secondary flows exist they must necessarily appear as counter-rotating eddy pairs and therefore be symmetrical. Thus, attention is restricted to $0 < \theta < \pi$. All fluid properties (evaluated at the arithmetic mean temperature of the two cylinders) except the specific weight are taken to be constant. A discussion of allowing a variation in specific weight while allowing no variation in density is given by Mack and Bishop [3]. Viscous and compressional heating are taken to be negligible.

The following development of the governing differential equations for the problem described above follows that of Mack and Bishop [3]. The fundamental differential equations which must be satisfied by the solution to this problem are the two-dimensional conservation equations of mass, momentum, and energy. By taking the curl of the Navier-Stokes (momentum) equation, the pressure gradient term is eliminated, and the introduction of the stream function ψ'[2] in place of the velocity components V_r' and V_θ' yields the vorticity equation. By using the stream function ψ', the continuity equation is automatically satisfied.

Thus, the two governing differential equations for this problem are the vorticity equation and the energy equation. These equations were nondimensionalized by Mack and Bishop [3] to yield

$$\nabla^4\psi = (\mathrm{Ra})\left(\sin\theta\,\frac{\partial T}{\partial r} + \frac{1}{r}\cos\theta\,\frac{\partial T}{\partial \theta}\right) + \frac{1}{r}\,\frac{1}{(\mathrm{Pr})}\,\frac{\partial(\nabla^2\psi, \psi)}{\partial(r, \theta)} \tag{1}$$

$$\nabla^2 T = \frac{1}{r}\,\frac{\partial(T, \psi)}{\partial(r, \theta)} \tag{2}$$

The Jacobians in these expressions are given by

$$\frac{\partial(f, g)}{\partial(r, \theta)} = \frac{\partial f}{\partial r}\frac{\partial g}{\partial \theta} - \frac{\partial f}{\partial \theta}\frac{\partial g}{\partial r}$$

and the operators ∇^2 and ∇^4 are given by

$$\nabla^4 = \nabla^2(\nabla^2)$$

$$\nabla^2 = \frac{\partial^2}{\partial r^2} + \frac{1}{r}\frac{\partial}{\partial r} + \frac{1}{r^2}\frac{\partial^2}{\partial \theta^2}$$

The boundary conditions to be satisfied by a solution to equations (1) and (2) are

$$\psi = \frac{\partial \psi}{\partial r} = 0 \quad \text{at} \quad r = 1, R \tag{3}$$

$$\psi = \frac{\partial^2 \psi}{\partial \theta^2} = 0 \quad \text{at} \quad \theta = 0, \pi \tag{4}$$

$$T = 1 \quad \text{at} \quad r = 1 \tag{5}$$

$$T = 0 \quad \text{at} \quad r = R \tag{6}$$

$$\frac{\partial T}{\partial \theta} = 0 \quad \text{at} \quad \theta = 0, \pi \tag{7}$$

The differential equations (1) and (2) together with the boundary conditions (3) through (7) comprise the mathematical model utilized for this problem. Equations (1) and (2) were con-

---

[2] All primed quantities are dimensional while unprimed quantities are dimensionless.

Nomenclature

f = any dependent variable
g' = acceleration of gravity
g = any dependent variable
Gr = Grashof number, $g'\beta'(r_o' - r_i')^3 \times (T_i' - T_o')/\nu'^2$
N = Nusselt number, $\mathrm{N}_{i,o} = -\ln R \times \left[r\frac{\partial T}{\partial r}\right]_{r=1,R}$
$\overline{\mathrm{N}}$ = mean Nusselt number, $\overline{\mathrm{N}}_{i,o} = \frac{-\ln R}{\pi}\int_0^\pi \left[r\frac{\partial T}{\partial r}\right]_{r=1,R} d\theta$
$\overline{\mathrm{N}}_T$ = overall Nusselt number, $(\overline{\mathrm{N}}_i + \overline{\mathrm{N}}_o)/2$
Pr = Prandtl number
r' = radial coordinate
r = dimensionless radial coordinate, r'/r_i'
R = diameter ratio, r_o'/r_i'
Ra = Rayleigh number, $g'\beta'(T_i' - T_o')r_i'^3/\nu'\alpha'$
T' = temperature
T = dimensionless temperature, $(T' - T_o')/(T_i' - T_o')$
V_r' = radial velocity component
V_θ' = angular velocity component
V_r = dimensionless radial velocity, $r_i'V_r'/\alpha'$
V_θ = dimensionless angular velocity, $r_i'V_\theta'/\alpha'$
x = any independent variable
Δx = grid spacing in x direction
y = any independent variable
Δy = grid spacing in y direction
α' = thermal diffusivity
β' = thermal expansion coefficient
ψ' = stream function
ψ = dimensionless stream function, ψ'/α'
θ = angular coordinate measured from downward vertical
ν' = kinematic viscosity

Subscripts

i = refers to inner cylinder
o = refers to outer cylinder

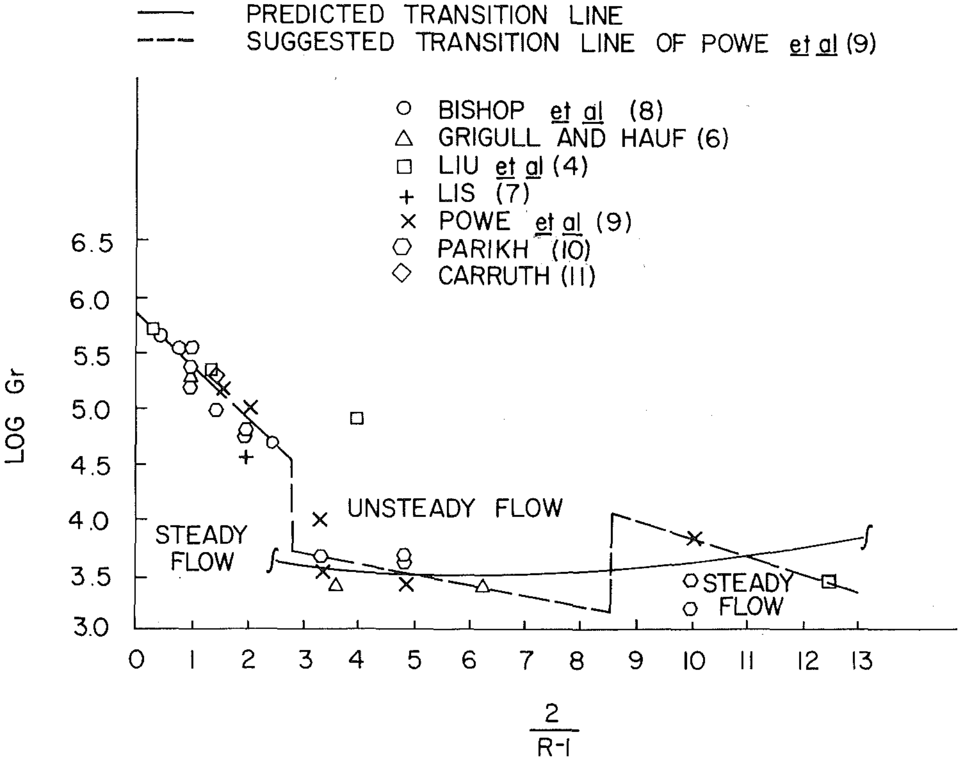

Fig. 1 Transition from steady to unsteady flow

verted from differential equations to difference equations following conventional "central difference" techniques. In particular let x or y represent either r or θ, and let f represent either ψ or T. Then the various derivatives appearing in equations (1) and (2) can be approximated by

$$\frac{\partial f_{00}}{\partial x} \simeq (f_{10} - f_{-10})/2\Delta x \tag{8a}$$

$$\frac{\partial^2 f_{00}}{\partial x^2} \simeq (f_{10} - 2f_{00} + f_{-10})/\Delta x^2 \tag{8b}$$

$$\frac{\partial^3 f_{00}}{\partial x^3} \simeq (f_{20} - 2f_{10} + 2f_{-10} - f_{-20})/2\Delta x^3 \tag{8c}$$

$$\frac{\partial^4 f_{00}}{\partial x^4} \simeq (f_{20} - 4f_{10} + 6f_{00} - 4f_{-10} + f_{-20})/\Delta x^4 \tag{8d}$$

$$\frac{\partial^2 f_{00}}{\partial y \partial x} \simeq (f_{11} - f_{1-1} - f_{-11} + f_{-1-1})/4\Delta x \Delta y \tag{8e}$$

$$\frac{\partial^3 f_{00}}{\partial y \partial x^2} \simeq (f_{11} - 2f_{01} + f_{-11} - f_{1-1} + 2f_{0-1} - f_{-1-1})/2\Delta x^2 \Delta y \tag{8f}$$

$$\frac{\partial^4 f_{00}}{\partial y^2 \partial x^2} \simeq (f_{11} - 2f_{10} + f_{1-1} - 2f_{01} + 4f_{00} - 2f_{0-1} + f_{-11} - 2f_{-10} + f_{-1-1})/\Delta x^2 \Delta y^2 \tag{8g}$$

In these expressions f_{ij} is written for

$$f_{ij} = f(x + i\Delta x, y + j\Delta y)$$

and Δx and Δy denote the grid spacings in the x and y directions, respectively. Both Δx and Δy were taken as constant throughout the flow field, and this technique proved satisfactory for the ranges of inverse relative gap widths and Rayleigh numbers of interest.

By introducing the approximations for the derivatives, equations (8), into equations (1) and (2), these differential equations were transformed into a pair of coupled difference equations. These equations were programmed for solution on an IBM 360/40 digital computer using a stepwise Gauss-Seidel procedure, always moving from point to point in an orderly fashion and calculating ψ and T at a particular grid point using the most recent values at surrounding grid points. This process was continued until the difference between ψ from the current iteration and that from the previous iteration and the difference between T from the current iteration and that from the previous iteration were both less than a specified limit at several selected grid points. This technique, in conjunction with the Gauss-Seidel process, eliminated the necessity of storing two complete T and ψ matrices within the computer. The boundary conditions were conveniently satisfied by defining values of T and ψ on the boundary and at imaginary grid points outside the boundary after each iteration. In general, 36 grid spacings in the angular direction and 15 in the radial direction were utilized, although these numbers were decreased slightly for very small diameter ratios and increased slightly for large diameter ratios. The Gauss-Seidel technique was selected as being rather straightforward and simple to apply. However, it should be noted that other methods, such as that proposed by de Vahl Davis [13], might be more advantageous from the standpoint of computational time required.

Once the iteration process had converged to yield specific values of T and ψ at each grid point, the radial and angular components of velocity at the grid point were calculated using the definition of the stream function

$$V_r = \frac{1}{r}\frac{\partial \psi}{\partial \theta}, \qquad V_\theta = -\frac{\partial \psi}{\partial r} \tag{9}$$

The derivatives in these expressions were evaluated using the relations specified by equations (8). Local Nusselt numbers, representing the ratio of the effective thermal conductivity to the actual thermal conductivity, are defined for the inner and outer cylinder surfaces respectively by

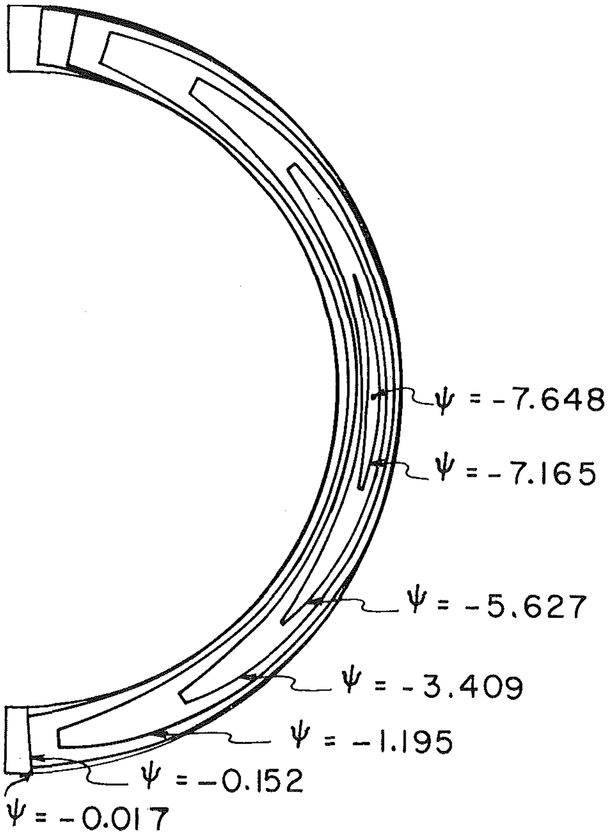

Fig. 2 Flow pattern for Rayleigh number below transition; R = 1.2, Ra = 345,920

$$\mathrm{N}_i = -\ln(R)\left[\frac{\partial T}{\partial r}\right]_{r=1} \tag{10}$$

$$\mathrm{N}_o = -R\ln(R)\left[\frac{\partial T}{\partial r}\right]_{r=R} \tag{11}$$

Values of N_i or N_o were calculated at each grid point on the cylinder surfaces using either "forward" or "backward" difference techniques to find the temperature gradient. Mean or average values of the Nusselt number at each surface were then defined as

$$\overline{\mathrm{N}}_i = -\frac{\ln(R)}{\pi}\int_0^{\pi}\left[\frac{\partial T}{\partial r}\right]_{r=1} d\theta \tag{12}$$

$$\overline{\mathrm{N}}_o = -\frac{R\ln(R)}{\pi}\int_0^{\pi}\left[\frac{\partial T}{\partial r}\right]_{r=R} d\theta \tag{13}$$

The indicated integrations were performed numerically using Simpson's rule to determine the values of $\overline{\mathrm{N}}_i$ and $\overline{\mathrm{N}}_o$. Of course a simple energy balance will immediately show that these two values should be equal, but due to the numerical techniques involved, the values actually obtained differed slightly. Thus, a total Nusselt number $\overline{\mathrm{N}}_T$ was defined simply as the arithmetic mean of $\overline{\mathrm{N}}_i$ and $\overline{\mathrm{N}}_o$.

Calculated values of stream functions, dimensionless temperatures, radial and angular velocity components, inner and outer surface local Nusselt numbers, and the total Nusselt numbers were plotted by a numerically controlled Stromberg-Carlson 4020 electronic plotter.

Results

In order to verify that reasonable results would be obtained by application of the technique described in the previous section, the first cases considered were those for which results have previously been published by other investigators. Crawford and Lemlich [1] present plots of the stream function and temperature profiles for a diameter ratio of 2, a Rayleigh number, based on inner radius, of 8940, and a Prandtl number of 0.714. The temperature profiles from the current analysis were found to be almost identical with those of Crawford and Lemlich [1] as were the flow patterns, although numerical values of the stream function could not be compared since an unspecified scaling velocity was used in their analysis. Abbott [2] also presents plots of the stream function and temperature profiles for a diameter ratio of 1.0256, a Rayleigh number, based on inner radius, of -3.57×10^9 (the negative sign indicating that the outer cylinder is at a higher temperature than the inner), and a Prandtl number of 0.714. The current analysis again predicted essentially identical results for the flow patterns and temperature profiles.

Mack and Bishop [3] present plots of the stream functions, temperature profiles, angular velocity components, and local Nusselt numbers for a diameter ratio of 1.85, a Rayleigh number of 3000, and a Prandtl number of 0.7. Again very close agreement was found between these results and those of the current analysis for the flow patterns, temperature profiles, and velocities. The local Nusselt numbers were also in good agreement except near the $\theta = 0$ and $\theta = \pi$ positions where deviations of less than 10 percent occurred.

Having thus gained confidence that the numerical solution indeed yielded valid results for these cases, the solution was utilized in an attempt to predict the Rayleigh number at which transition from a steady to an unsteady flow would occur as a function of the diameter ratio for a Prandtl number of 0.7 (air). Recent experimental measurements of this transition Rayleigh

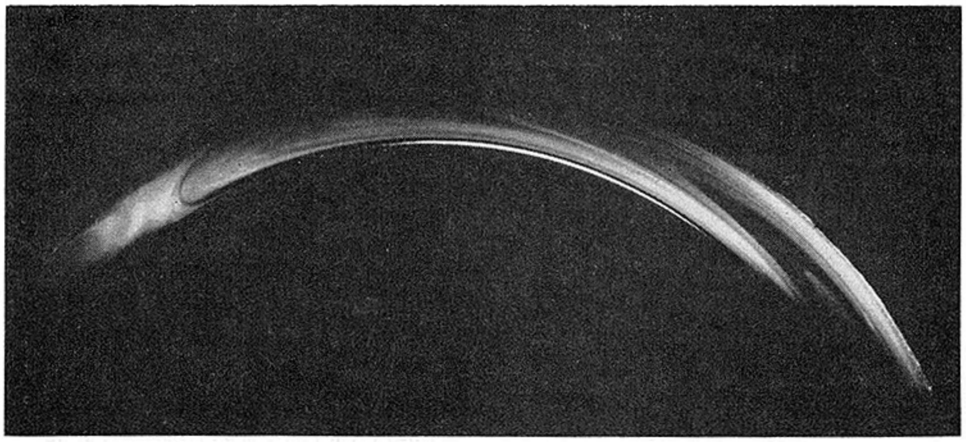

Fig. 3 Flow photograph for Rayleigh number below transition (from Powe [12]); R = 1.2, Ra = 500,000

number by Powe, Carley, and Bishop [9] were available for comparison. Although it would seem basically unsound to attempt to use a solution formulated for steady flow to predict the inception of an unsteady flow, the measurements of Powe, et al. [9] indicated that the onset of the unsteady flow was initially characterized by the appearance, in the upper portion of the annulus, of small stable cell pairs superimposed on the basic "crescent eddy" type flow pattern for inverse relative gap widths greater than about 2.8. Then for slightly higher Rayleigh numbers this cellular flow would become unsteady. Thus it was hoped that the numerical solution would predict the appearance of these secondary cells, thereby giving an indication of the inception of unsteady flow. Of course no information as to the type of unsteady flow which would occur above the transition Rayleigh number could be expected from the numerical solution.

The computer program for conducting the finite-difference solution was modified in the following manner to determine the transition Rayleigh number. The stream function for the basic "crescent eddy" flow pattern was negative at all points in the flow field, and the appearance of any positive value thus signaled the onset of a secondary counter-rotating flow or cell. For a given diameter ratio, a Rayleigh number near the experimentally determined transition value was selected and values of the stream function and temperature at each grid point were determined by the stepwise Gauss-Seidel process. If no positive values of the stream function appeared anywhere within the flow field, the Rayleigh number was increased and the calculations for the stream function and temperature were repeated. This process was carried out successively until positive values of the stream function appeared in the flow field. The Rayleigh number was then decreased, but by a much smaller increment than that used in the foregoing increases. This entire process was repeated until the Rayleigh number converged to the transition value, within specified limits.

It was recognized in the early stages of the investigation that the positive values of the stream function which were obtained were very small compared with the maximum negative values, and as noted by Rubel and Landis [14], such positive values of

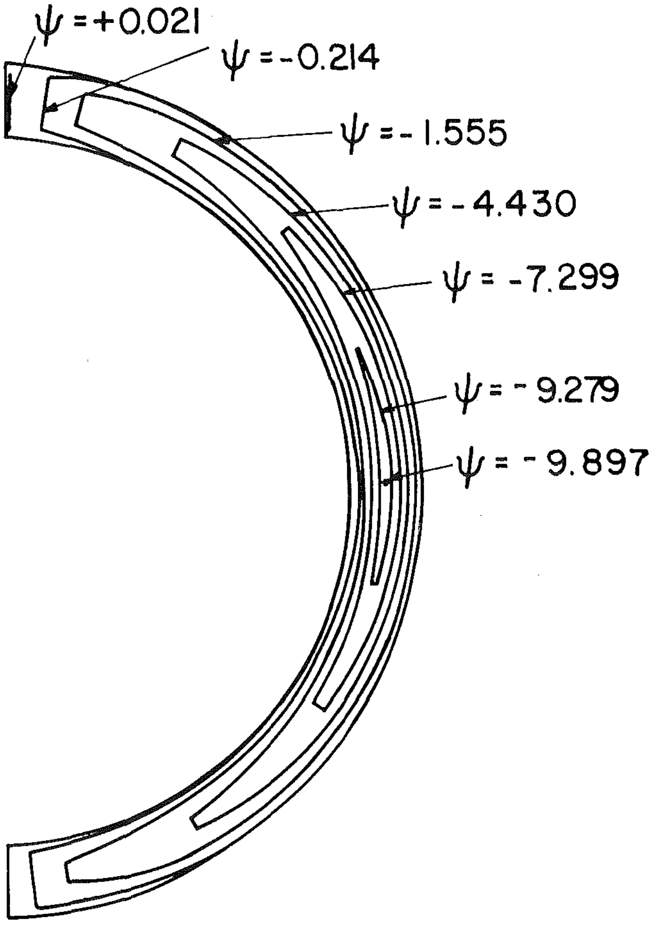

Fig. 4 Flow pattern for Rayleigh number above transition; $R = 1.2$ $Ra = 452{,}000$

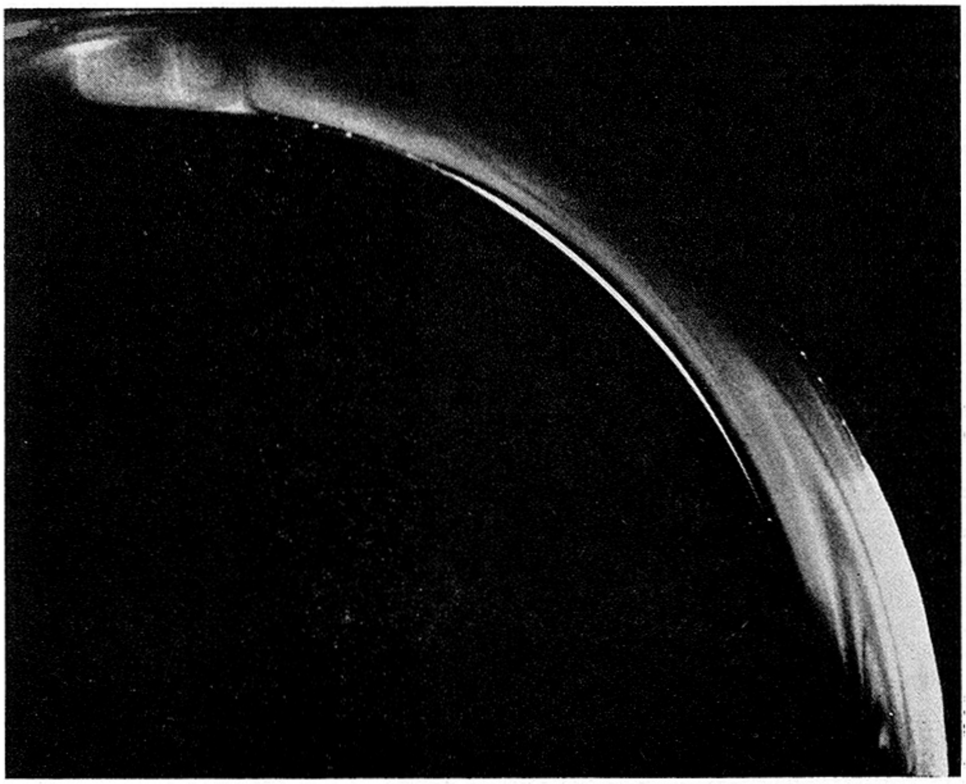

Fig. 5 Flow photograph for Rayleigh number above transition (from Powe, et al. [9]); $R = 1.2$, $Ra = 1{,}053{,}000$

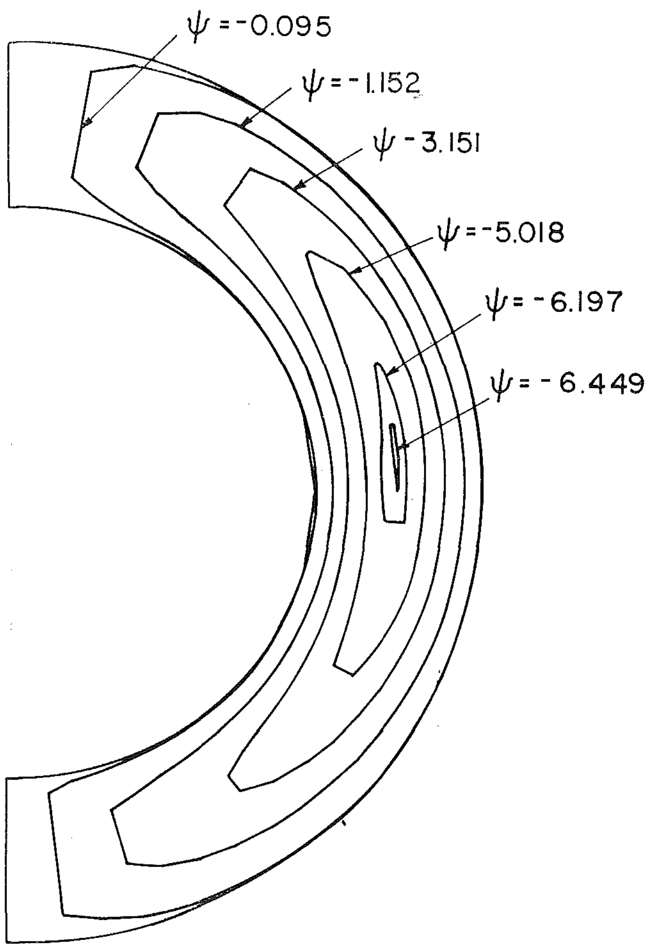

Fig. 6 Flow pattern for Rayleigh number below transition; $R = 1.57$, Ra $= 13,348$

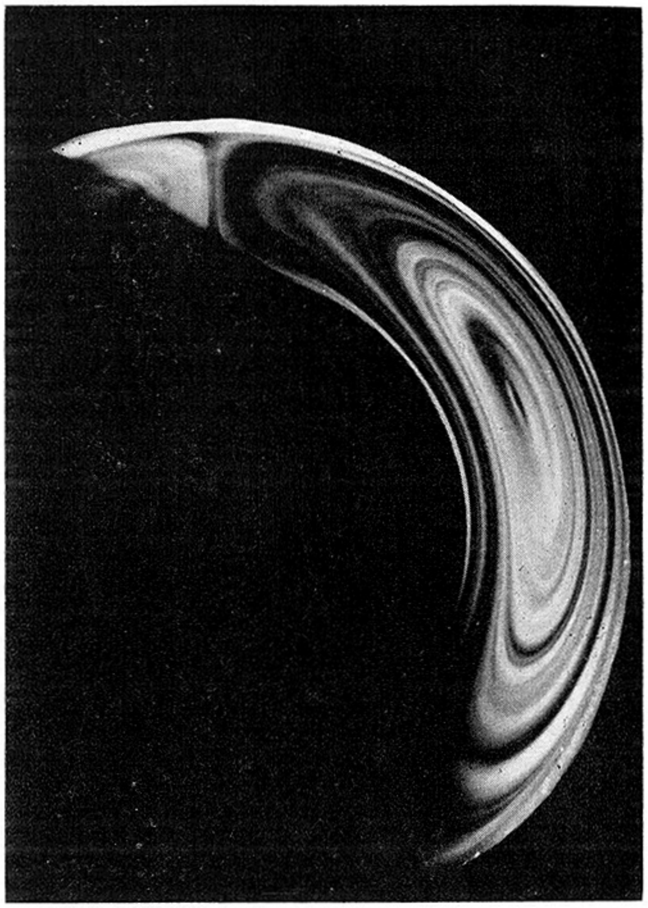

Fig. 7 Flow photograph for Rayleigh number below transition (from Powe [12]); $R = 1.6$, Ra $= 12,400$

the stream function may appear spuriously if too coarse a grid size is utilized. In order to eliminate this possibility, the initial calculations of the stream function for Rayleigh numbers slightly above the transition value were repeated utilizing various grid sizes for inverse relative gap widths at the extremes of the range under consideration. In each case as many as 72 angular and 30 radial grid spacings were utilized, but no noticeable change in the results was observed for grid spacings as small as about 30 angular by 10 radial. Thus a grid size of 36 angular by 15 radial was arbitrarily selected for use in the calculations, although these numbers were decreased slightly for very small diameter ratios and increased slightly for large diameter ratios.

The results of the iteration process for determining the transition Rayleigh number are shown with the available experimental data in Fig. 1. This curve is shown in the form of the transition Grashof number, Gr, versus the inverse relative gap width, $\frac{2}{R-1}$. The transition curve obtained from the numerical solution shows excellent agreement with the experimental data for inverse relative gap widths greater than about 2.8, and it was for these inverse relative gap widths that Powe et al. [9] found the inception of the unsteady flow to be preceded by pairs of steady secondary cellular flows.

In contrast to the grid size problems discussed previously which may lead to a spurious instability, Torrance [15] has pointed out that the nature of the truncation error inherent in any finite-difference approximation may lead to a false sense of stability. However, in view of the agreement with experimental results, truncation errors apparently do not present a problem in the current application.

For inverse relative gap widths less than about 2.8, the onset of the unsteady flow is not signaled by any definite change in the basic steady flow pattern, but instead the unsteady flow is oscillatory in nature from origination. Thus the numerical solution could not be expected to yield any information about this particular unsteady flow. It should be noted however, that excellent agreement with the analytical solution of Mack and Bishop [3] was obtained for an inverse relative gap width within this region, 2.36 ($R = 1.85$), at a Grashof number of 2610 (Ra = 3000), and also with the numerical solution of Crawford and Lemlich [1] at an inverse relative gap width of 2.0 ($R = 2.0$) and a Grashof number of 12,500 (Ra = 8750).

Also shown in Fig. 1 is the transition curve suggested by Powe et al. [9] from a consideration of the available experimental data. Sharp dividing lines between the different types of unsteady flow are indicated on this curve. These dividing lines are somewhat arbitrary due to the lack of experimental data in these areas, and such a discontinuity would not be expected to occur physically. The transition curve obtained from the finite-difference solution expectedly shows no distinction between the different types of unsteady flow as does the experimental curve. This must be the case, however, because a formulation of the problem for steady flow could not yield information as to the nature of unsteady flows. Except for distinction between the different types of unsteady flow, good agreement between the two aforementioned curves is noted.

Once the transition curve had been numerically determined, the computer program was utilized for calculating stream functions, temperatures, velocities, and Nusselt numbers for Rayleigh numbers both slightly above and slightly below the transition value for diameter ratios less than about 1.72 $\left(\frac{2}{R-1} \gtrsim 2.8\right)$. Qualita-

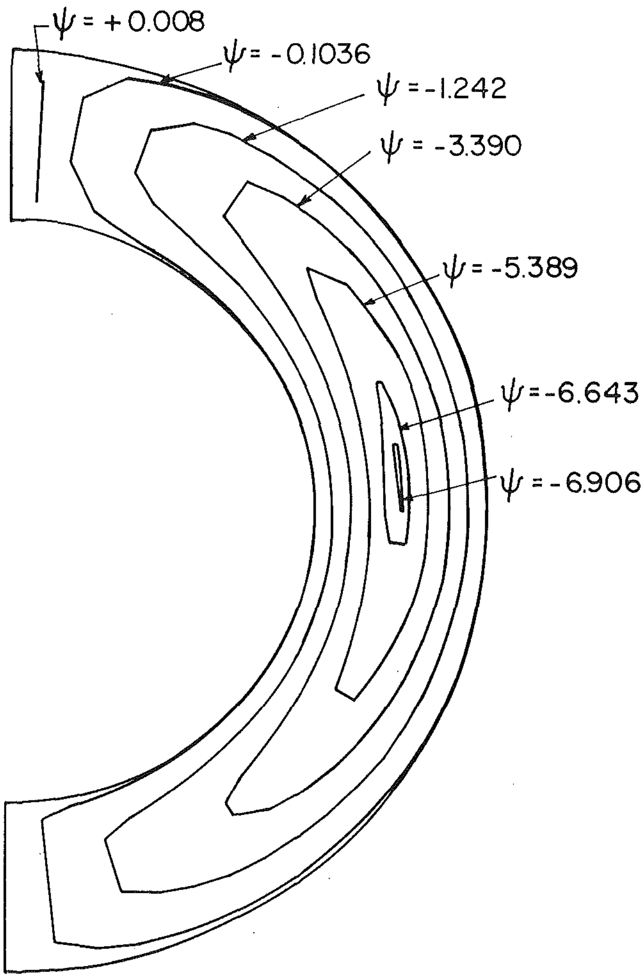

Fig. 8 Flow pattern for Rayleigh number above transition; $R = 1.57$, $Ra = 14{,}420$

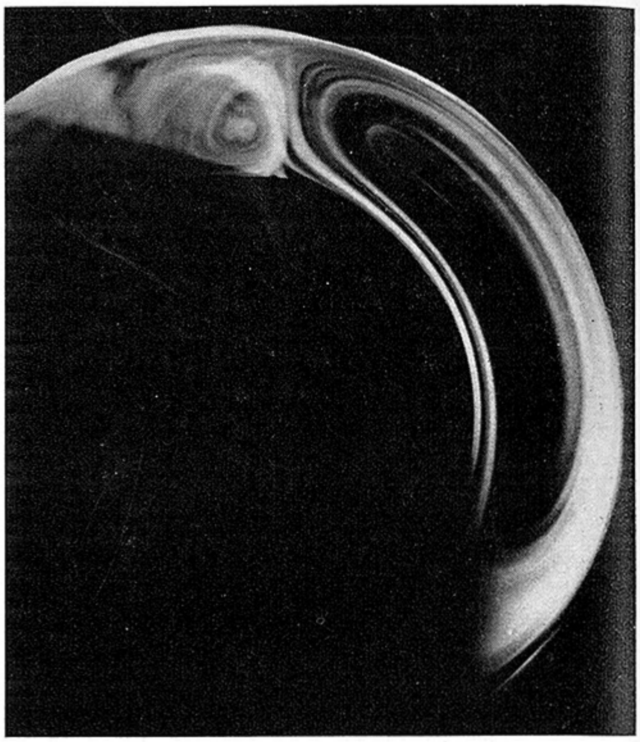

Fig. 9 Flow photograph for Rayleigh number above transition (from Powe [12]); $R = 1.6$, $Ra = 128{,}600$

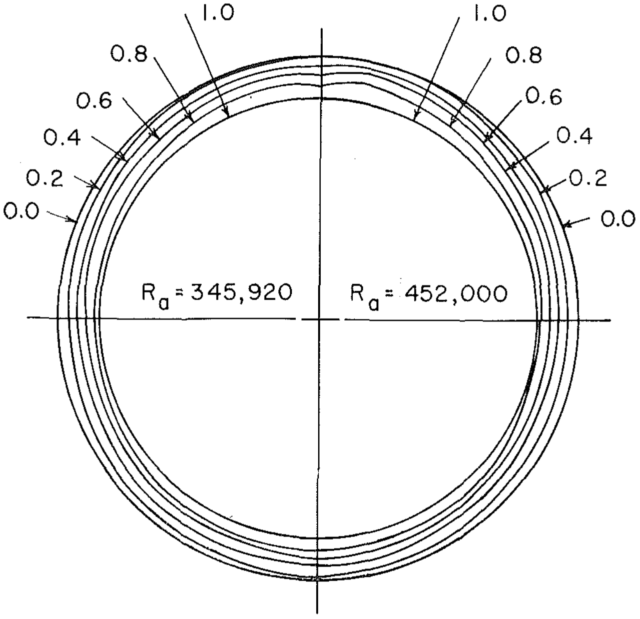

Fig. 10 Predicted isotherms for $R = 1.2$

tive comparisons between typical samples of these results and previous experimental results follow.

In Fig. 2 the stream function obtained from the numerical solution is shown for an inverse relative gap width of 10 ($R = 1.2$) and a Rayleigh number of 345,920, which is slightly below the transition value. This flow pattern is compared with the photograph of the "crescent eddy" flow shown in Fig. 3, and good qualitative agreement is noted. In a similar manner, Figs. 4 and 5 respectively show good qualitative agreement between the flow pattern obtained from the numerical solution and a photograph of the secondary cellular flow for a Rayleigh number slightly above the transition value at the same inverse relative gap width. Likewise for an inverse relative gap width of about 3.5, Figs. 6 and 7 show striking similarity between numerically and experimentally determined flows for a Rayleigh number slightly below the transition value while Figs. 8 and 9 show such a similarity for a Rayleigh number above the transition value.

Although the Rayleigh number for Fig. 9 is considerably larger than the transition value, it was indicated by Powe [12] that this same type of flow pattern occurred for Rayleigh numbers only slightly above the transition value. Photographs of the flow at smaller Rayleigh numbers for this inverse relative gap width are not available.

In Fig. 10 the isotherms obtained for Rayleigh numbers above and below the transition value for an inverse relative gap width of 10 are indicated. These two sets of isotherms are nearly identical except in the upper portion of the annulus where a distinct dip is observed for the Rayleigh number yielding the secondary cellular flow. Such a dip would probably be expected since the fluid in the large eddy to the side of the inner cylinder remains adjacent to the heated inner cylinder for a much longer period of time than does the fluid in the secondary cellular flow. Thus it would be expected that, near the interface of the main eddy and the secondary cell, a given isotherm would be displaced further from the inner cylinder in the main eddy than it would in the region of the secondary flow. For the smaller inverse relative gap width, 3.5, Fig. 11 indicates essentially no change in the isotherms as the Rayleigh number is increased above the transition value. Although a dip would probably be expected near the $\theta = \pi$ position as in the above case, such a dip would be much

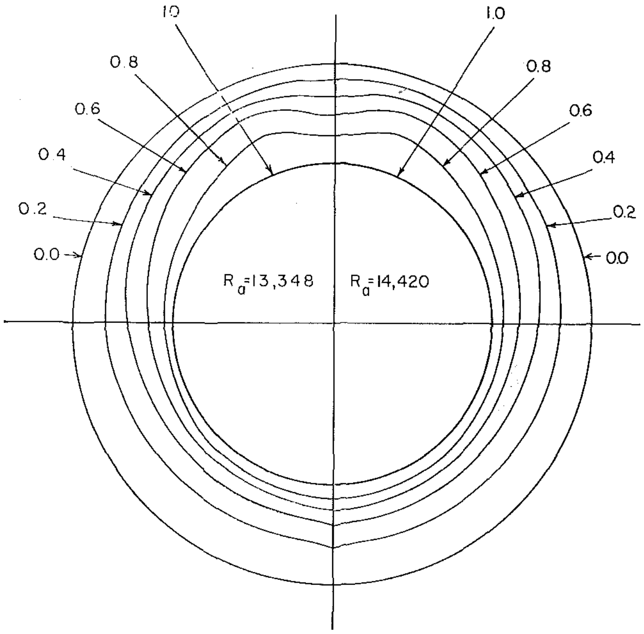

Fig. 11 Predicted isotherms for $R = 1.57$

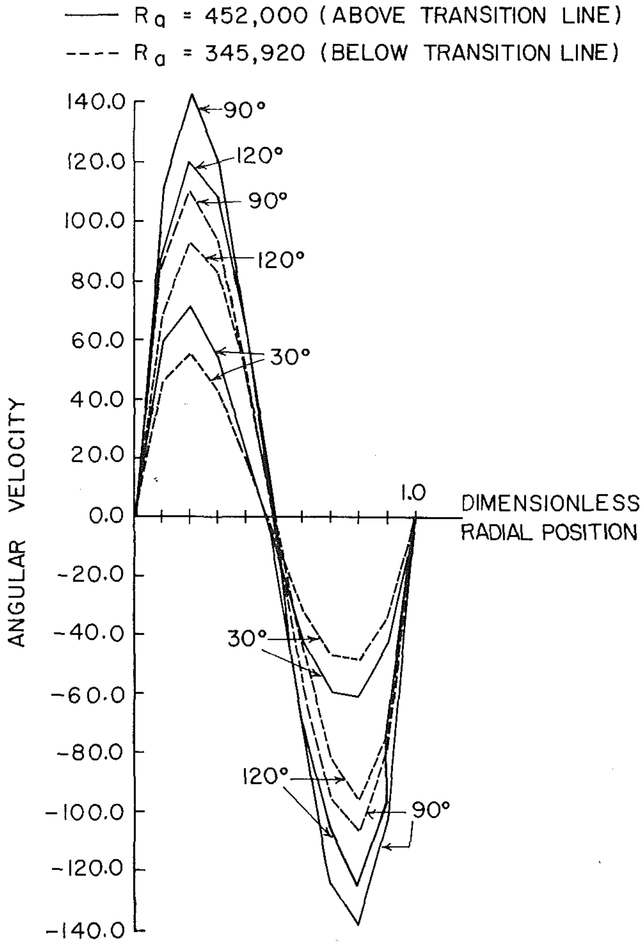

Fig. 12 Predicted angular velocity for $R = 1.2$

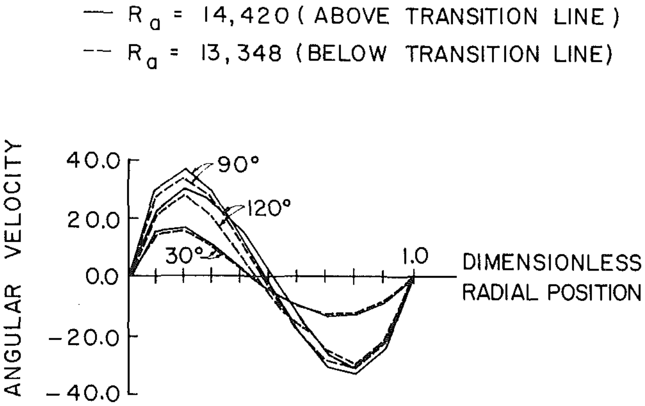

Fig. 13 Predicted angular velocity for $R = 1.57$

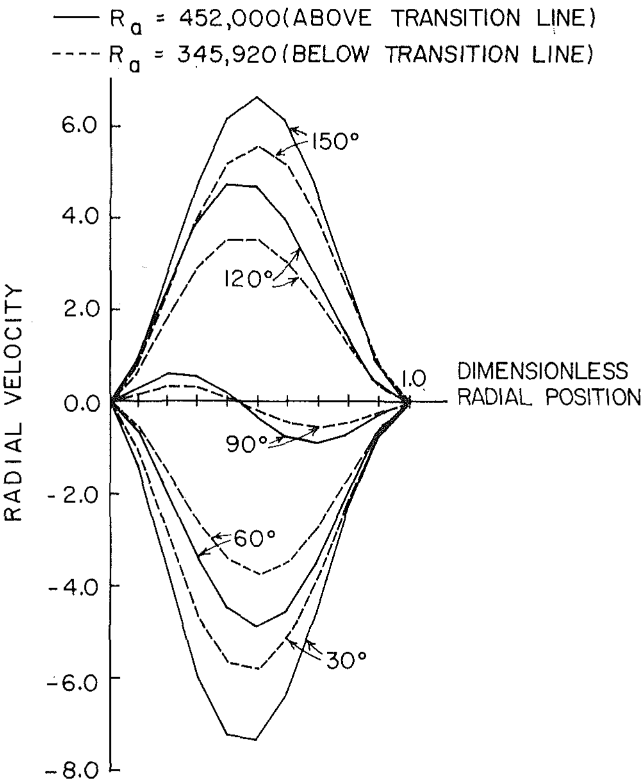

Fig. 14 Predicted radial velocity for $R = 1.2$

less pronounced because of the increased relative gap width (decreased inverse relative gap width).

The change in angular velocity as the Rayleigh number is increased above the transition value is shown in Figs. 12 and 13 for these same two inverse relative gap widths, 3.5 and 10.0. Fig. 13 indicates almost no change in this velocity component for the smaller inverse relative gap width, while for the larger, Fig. 12 illustrates a very pronounced increase in magnitude for the larger Rayleigh number. Essentially this same trend is indicated for the radial velocity components in Figs. 14 and 15, although in this case at the smaller inverse relative gap width, the radial velocity components for the higher Rayleigh number are slightly larger than those for the smaller Rayleigh number.

Similar comparisons for the local Nusselt number are shown in Figs. 16 and 17, and the trends in these quantities appear identical

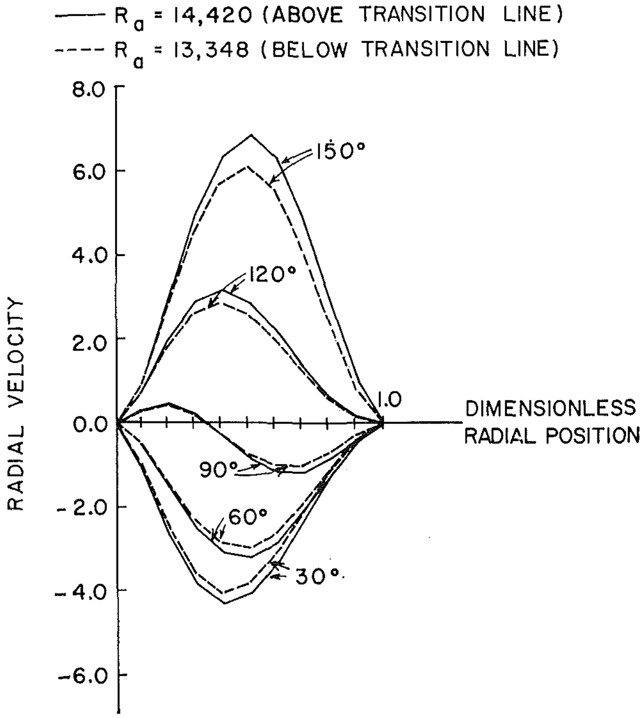

Fig. 15 Predicted radial velocity for $R = 1.57$

to those stated above, i.e., little change is observed in the local Nusselt number with increasing Rayleigh number for the small inverse relative gap width while a more pronounced change is observed for the large inverse relative gap width. For all the inverse relative gap widths considered, no abrupt change in the total Nusselt number $\overline{N}_T$ was observed as the Rayleigh number was increased above the transition value. Instead, the total Nusselt number was found to increase in a continuous fashion through transition. Thus for the range of inverse relative gap widths investigated, it appears that the variation in the total Nusselt number is independent of the type of flow, so long as the flow is steady and laminar. For a change in the type of flow, the local Nusselt numbers appear simply to be redistributed over the cylinders in a manner such that the total Nusselt number is not affected.

Numerical results were obtained for many inverse relative gap widths between those reported above $\left(3.5 < \frac{2}{R - 1} < 10\right)$, but in order to conserve space only the two sets of results are presented here. The remaining results do indicate, however, the same trends as described previously.

Conclusion

The results of a numerical investigation, utilizing finite-difference techniques, of natural convection within horizontal isothermal cylindrical annuli are presented in this paper. The problem is formulated for steady laminar flow, and all results presented are for a Prandtl number near 0.7 (air). The dimensionless forms of the governing differential equations suggested by Mack and Bishop [3] are used as a starting point for deriving the governing difference equations. These difference equations were programmed for solution on an IBM 360/40 digital computer using Fortran IV-E. The results of the current numerical solution, as plotted by a Stromberg-Carlson 4020 electronic plotter, are compared with the limited numerical and analytical data available in the literature and excellent agreement is found.

Even though the problem is formulated in terms of steady laminar flow it was found that the present numerical solution can be used to predict the Rayleigh number at which transition from a steady to an unsteady flow would occur for inverse relative gap widths between about 2.8 and 12.5. This is due to the fortunate occurrence of small areas of steady counter-rotating secondary flows immediately preceding the unsteady flow, and the Rayleigh number at which these secondary flows is predicted by the numerical solution is found to be in excellent agreement with experimental measurements of this value. The flow patterns predicted by this solution are compared with photographs of the flow patterns for Rayleigh numbers both slightly above and below the transition value and very good qualitative agreement is noted.

As the curvature of the annular space becomes small the configuration of the upper annulus approaches that of a fluid con-

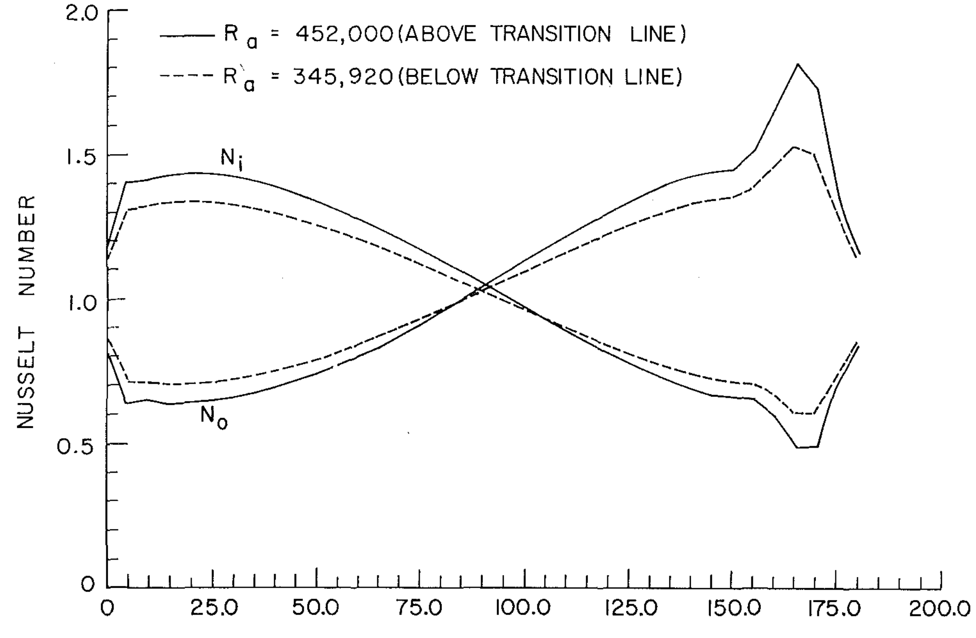

Fig. 16 Predicted Nusselt numbers for $R = 1.2$

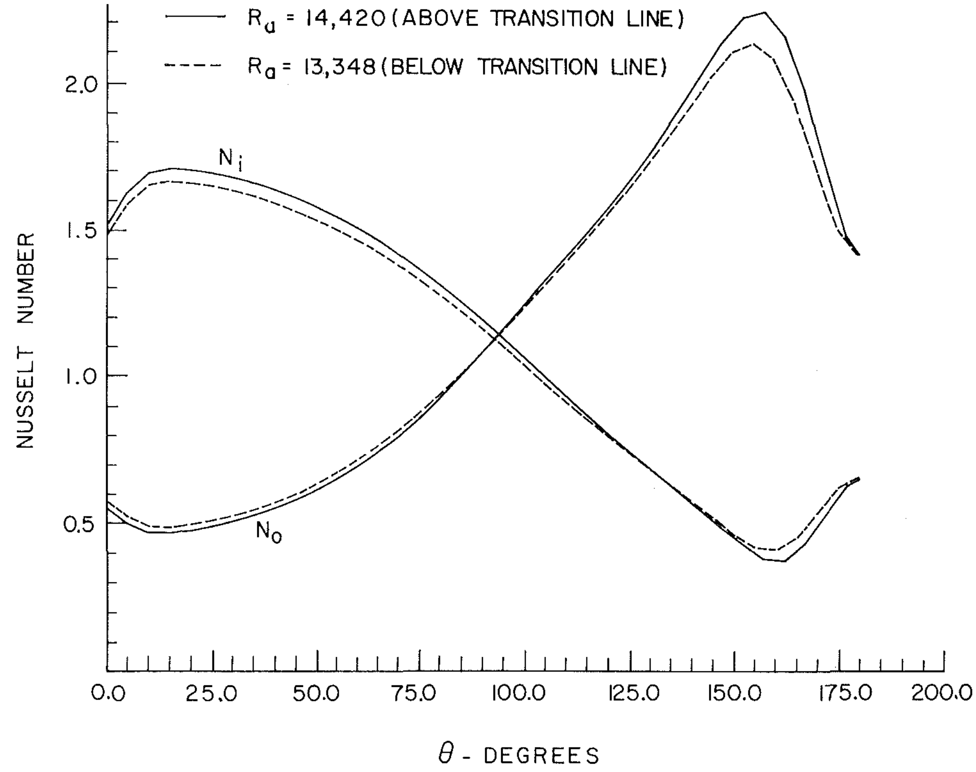

Fig. 17 Predicted Nusselt numbers for R = 1.57

tained between infinite horizontal planes. It is therefore natural to ask if the counter-rotating cell pairs are a type of Bénard instability. If considered in this light these cell pairs when viewed from above appear as a single long cell with fluid moving down in the center and up on the two edges. This is not typical of Bénard cells. The critical Rayleigh number for the Bénard problem is approximately 1700. If the minimum transition Grashof number from Fig. 1 is converted to a Rayleigh number (Pr = 0.71) this yields a Rayleigh number of 2300. It may be speculated that the counter-rotating cell pairs are the result of a Bénard type instability initiated by the basic steady flow in the central part of the annulus. It appears that a stability analysis of this configuration would yield interesting results.

Typical results of temperature profiles, radial and angular components of velocity, and local Nusselt numbers from the numerical solution are presented for Rayleigh numbers above and below the transition value at inverse relative gap widths near the ends of the range under consideration $\left(2.8 < \frac{2}{R-1} < 12.5\right)$. It is found that there is little change in any of the above parameters as the Rayleigh number is increased above the transition value for the smaller inverse relative gap widths, but a pronounced increase in magnitude of the velocity components and a distortion in the temperature profile is noted for the larger inverse relative gap widths.

In summary, it has been shown that a relatively simple numerical technique using conventional "central differences" can be utilized for natural convection calculations in the cylindrical annulus geometry throughout the range of Rayleigh numbers for which the flow is actually steady and over a wide range of inverse relative gap widths. The experimentally determined transition curve of Powe et al. [9] from steady to unsteady flow has been confirmed numerically for those inverse relative gap widths where the unsteady flow is preceded by a secondary cellular flow. Previously unavailable temperature profiles, velocity components, and local Nusselt numbers for Rayleigh numbers near the transition value are presented for a wide range of inverse relative gap widths.

Acknowledgments

Fig. 5 is reproduced from reference [9] by permission of J. J. Jaklitsch, Jr., editor of the JOURNAL OF HEAT TRANSFER. The authors are grateful for the assistance of the computing center of Mississippi State University and the Data Processing Center of the General Electric Company at the National Aeronautics and Space Administration's Mississippi Test Facility.

References

1 Crawford, L., and Lemlich, R., "Natural Convection in Horizontal Concentric Cylindrical Annuli," *Industrial and Engineering Chemistry Fundamentals*, Vol. 1, No. 4, Nov. 1962, pp. 260–264.

2 Abbott, M. R., "A Numerical Method for Solving the Equations of Natural Convection in a Narrow Concentric Cylindrical Annulus with a Horizontal Axis," *Quarterly Journal of Mechanics and Applied Mathematics*, Vol. 17, 1964, pp. 471–481.

3 Mack, L. R., and Bishop, E. H., "Natural Convection Between Horizontal Concentric Cylinders For Low Rayleigh Numbers," *Quarterly Journal of Mechanics and Applied Mathematics*, Vol. 21, No. 2, May 1968, pp. 223–241.

4 Liu, C. Y., Mueller, W. K., and Landis, F., "Natural Convection Heat Transfer in Long Horizontal Cylindrical Annuli," *International Developments in Heat Transfer*, Paper No. 117, Part V, 1961, pp. 976–984.

5 Bishop, E. H., and Carley, C. T., "Photographic Studies of Natural Convection Between Concentric Cylinders," *Proceedings of the 1966 Heat Transfer and Fluid Mechanics Institute*, Stanford University Press, 1966, pp. 63–78.

6 Grigull, U., and Hauf, W., "Natural Convection in Horizontal Cylindrical Annuli," *Proceedings of the Third International Heat Transfer Conference*, Paper No. 60, Vol. 2, 1966, pp. 182–195.

7 Lis, J., "Experimental Investigation of Natural Convection Heat Transfer in Simple and Obstructed Horizontal Annuli," *Proceedings of the Third International Heat Transfer Conference*, Paper No. 61, Vol. 2, 1966, pp. 196–204.

8 Bishop, E. H., Carley, C. T., and Powe, R. E., "Natural Convective Oscillatory Flow in Cylindrical Annuli," *International Journal of Heat and Mass Transfer*, Vol. 11, 1968, pp. 1741–1752.

9 Powe, R. E., Carley, C. T., and Bishop, E. H., "Free Convective Flow Patterns in Cylindrical Annuli," JOURNAL OF HEAT TRANSFER, TRANS. ASME, Series C, Vol. 91, No. 3, Aug. 1969, pp. 310–314.

10 Parikh, D. C., *Free Convective Flows in Horizontal Cylindrical Annuli*, MS thesis, Mississippi State University, State College, Miss., Jan. 1969.

11 Carruth, S. L., *Analytical Prediction of Natural Convective Flow Patterns in Cylindrical Annuli*, MS thesis, Mississippi State University, State College, Miss., July, 1969.

12 Powe, R. E., *Free Convective Flows in Horizontal Cylindrical Annuli*, MS thesis, Mississippi State University, State College, Miss., Jan. 1968.

13 de Vahl Davis, G., "Laminar Natural Convection in an Enclosed Rectangular Cavity," *International Journal of Heat and Mass Transfer*, Vol. 11, No. 11, 1968, pp. 1675–1693.

14 Rubel, A., and Landis, F., "Numerical Study of Natural Convection in a Vertical Rectangular Enclosure," *High Speed Computing in Fluid Dynamics, The Physics of Fluids, Supplement II*, Vol. 12, No. 12, Part 2, 1969, pp. 208–213.

15 Torrance, K. E., "Comparison of Finite-Difference Computations of Natural Convection," *Journal of Research of the National Bureau of Standards*, Series B, Vol. 72B, No. 4, 1968, pp. 281–301.

J. B. YASINSKY
Fellow Scientist,
Bettis Atomic Power Laboratory,
West Mifflin, Pa.

The Solution of Three-Dimensional, Composite Media Heat Conduction Problems by Synthesis Methods[1]

A method, known as synthesis, is applied to the task of obtaining approximate solutions to the static heat conduction equation for three-dimensional, composite media problems with mixed boundary conditions. The method is based upon an expansion in terms of known two-dimensional solutions of the problem of interest. These known two-dimensional solutions (trial functions) are blended over the remaining dimension by unknown mixing coefficients which are defined by means of variational techniques. A modified canonical variational principle is derived which permits the use of discontinuous trial functions, which expands the class of problems to which the synthesis method can be applied. The equations defining the mixing coefficients are derived in some detail, and the results of several test problems display the potential of this method for analyzing realistic heat conducting systems.

Introduction

The problem of solving the equilibrium heat conduction equation in three dimensions for composite media is indeed very difficult. Such problems usually arise in designing any heat producing mechanism, and when accurately solved permit the designer to describe the removal of heat from the device in an optimum fashion. In addition an accurate temperature distribution yields a detailed description of thermal stress sources in the device. Hence it is very desirable to know as much as possible about the spatial temperature distribution when designing realistic heat producing devices.

For three-dimensional composite media problems, such classical solution techniques as expansions in terms of orthogonal functions are not, in general, feasible; and since exact analytical solutions are certainly not attainable, one must resort to some approximation method. Quite often a designer obtains some knowledge of the three-dimensional temperature distribution by solving more tractable equivalent two-dimensional problems. However, this is not often possible or desirable if accurate tem-

Nomenclature

T = temperature
k = thermal conductivity
S = heat source
$\mathcal{R}$ = volume of interest
$\mathcal{S}$ = external surface of $\mathcal{R}$
$\mathcal{S}_1, \mathcal{S}_2, \mathcal{S}_3, \mathcal{S}_4$ = connected segments of $\mathcal{S}$
H = trial function
Z = mixing coefficient
$\hat{n}$ = unit normal surface vector
T_s = surface temperature
∇ = gradient operator
h = convective surface coefficient
q_n = normal surface heat flow
N = number of trial functions
δ = variation operator
V_1, V_2 = variational functionals
V_1', V_2' = reduced functionals
$\mathcal{S}_i$ = internal surfaces on which k is discontinuous
Σ = summation symbol
$(+), (-)$ = denotes one-sided evaluation of a discontinuous function
$\langle , \rangle$ = volume integration symbol
$\{ , \}$ = surface integration symbol

a = x-y cross sectional area
c = contour of a
$\bar{z}$ = denotes axial dimension of system
$\mathfrak{z}_i$ = axial regions where k is continuous
L = axial size of test problem
R = radial size of test problem
deg F = degrees Fahrenheit
$\mathcal{L}$ = Lagrangian density
$\mathcal{U}$ = integral of surface term in functional
$\mathbf{p}$ = vector valued generalized momenta
p_x, p_y, p_z = components of $\mathbf{p}$
$\mathcal{H}$ = Hamiltonian density
$\bar{\mathcal{S}}_j$ = internal surfaces on which trial functions are discontinuous
$\mathcal{R}_j$ = volume regions in which trial functions are continuous
z_i = axial mesh points
Δ_i = axial mesh spacing
s_i, t_i = unit step functions
I = number of axial mesh points

M = number of discontinuous trial functions used
P^x, P^y, P^z = heat flow mixing coefficients
$(\tilde{\ })_i$ = denotes quantity averaged about mesh point z_1
$\delta_{i,0}; \delta_{i,I}$ = Kronecker delta function
B_i, C_i = terms in synthesis equations (see equation (40))

Subscripts

n = index of summation in synthesis expansion
i = axial mesh point indicator; internal surface and volume indicator
z = 0, $\bar{z}$ = evaluation on surface $z = 0$ on $z = \bar{z}$
j, k = components of matrix
$m(i)$ = index of summation about mesh point z_i

Superscripts

T = transpose of a matrix
-1 = inverse of a matrix
x, y, z = x, y, or z component

---

[1] Work performed under the auspices of the U. S. Atomic Energy Commission.

Contributed by the Heat Transfer Division of The American Society of Mechanical Engineers for presentation at the AIChE-ASME Heat Transfer Conference, Philadelphia, Pa., August 11–14, 1968. Manuscript received by Heat Transfer Division May 19, 1967; revised manuscript received March 11, 1968. Paper No. 68-HT-40.

perature shapes are required. An obvious remedy is to superimpose a finite mesh structure on the domain of interest and obtain numerical solutions. This may be feasible if only a crude approximation is desired, but if an accurate temperature distribution is required, then a detailed mesh must be used. This can be a prohibitively expensive task even with today's fast digital computers.

This paper describes a method of constructing accurate numerical solutions for equilibrium composite media heat conduction problems in three dimensions. This method, which constructs three-dimensional solutions from known lesser dimension solutions of the problem of interest, is known as the synthesis approximation [1].[2] Synthesis techniques have been applied with much success to the solution of the neutron group diffusion problem and other problems arising in reactor theory [2].

The Synthesis Concept

The synthesis method is based on a "bracket-blend" idea which we now proceed to describe. Consider, for example, the problem of solving the heat conduction equation,

$$\begin{aligned} -\nabla \cdot k \nabla T &= S \qquad \text{in } R \\ T &= 0 \qquad \text{on } \mathcal{S} \end{aligned} \tag{1}$$

for the heat conducting device shown in Fig. 1. In equation (1) $T = T(x, y, z)$ is the temperature, $k = k(x, y, z)$ is the thermal conductivity, and $S = S(x, y, z)$ is the heat source. R is the volume enclosing the device which is bounded by the surface $\mathcal{S}$. Let $H_1(x, y)$ and $H_2(x, y)$ be two-dimensional temperature distributions obtained for x-y slices through axial compositions 1 and 2, respectively. Now it is reasonable to assume that H_1 and H_2 are good approximations to the true x-y temperature shape in the central portion of axial compositions 1 and 2, respectively. In addition a linear combination of H_1 and H_2 should yield a good approximation to the x-y temperature shape near the interface $z = z'$. Then for this problem, we see that the trial functions H_1 and H_2 in some sense "bracket" the true x-y shape of the temperature. The three-dimensional temperature distribution is then synthesized as

$$T(x, y, z) \cong H_1(x, y)Z_1(z) + H_2(x, y)Z_2(z) \tag{2}$$

where the unknown mixing coefficients "blend" the trial functions H_1 and H_2. The basic difference between the synthesis approximation and usual expansion type approximations is that the synthesis trial functions are found directly from the problem of interest. Since these trial functions are so tailored to the specific problem to be solved, an accurate solution can be obtained by using only a few such functions. In general, the procedure to be followed is to subdivide the geometry of interest into "axial compositions," within which k and S are either independent of, or only slowly varying functions of z. Then we obtain an x-y temperature trial function for each different axial composition by solving the two-dimensional heat conduction equation for slices through each of these axial compositions. If there are N such axial compositions in the problem of interest we use the approximate form

$$T(x, y, z) \cong \sum_{n=1}^{N} H_n(x, y)Z_n(z) \tag{3}$$

where $H_n(x, y)$ is the known trial function found from axial composition n. For problems in which there is a drastic change in material in going from one axial composition to the next, one can include additional trial functions in the form (3) which may help in approximating the temperature shape near this interface. Such functions will be referred to as "transition trial functions." The unknown mixing coefficients, $Z_n(z)$, can be obtained by either of two methods. The first is the method of weighted residuals [3], for which the equations defining the mixing coefficients are found by substituting the approximate form (3) into the heat conduction equation (1), multiplying the resulting equation in turn by each of the trial functions and then integrating these N equations over the x-y cross section of the heat conducting system. This results in N coupled ordinary second order differential equations which define the mixing functions, $Z_n(z)$. The second way of finding the functions $Z_n(z)$ is to use the form (3) with an appropriate variational principle. The variational formulation will be used in this presentation since it is the most systematic method and because it will lead to certain generalizations which will extend the usefulness of the synthesis procedure. We shall refer to the approximation based on the expansion (3) as "continuous synthesis" since both the trial functions $H_n(x, y)$ and the mixing coefficients $Z_n(z)$ are required to be spatially continuous functions throughout the domain of interest.

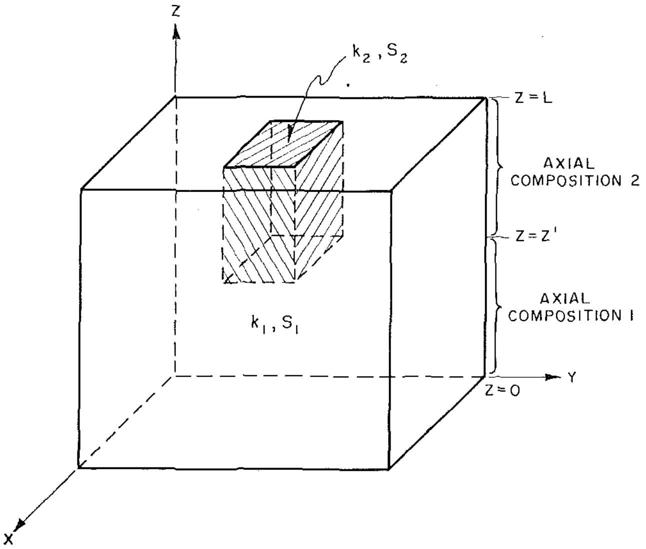

Fig. 1 Heat conducting geometry to illustrate the synthesis method

The Continuous Synthesis Method

We now focus our attention on obtaining approximate solutions to the heat conduction problem

$$\nabla \cdot k \nabla T + S = 0 \qquad \text{in } \mathcal{R} \tag{4}$$

subject to the boundary conditions

$$k \nabla T \cdot \hat{n} = 0 \qquad \text{on } \mathcal{S}_1, \tag{5a}$$

$$T = T_S \qquad \text{on } \mathcal{S}_2, \tag{5b}$$

$$k \nabla T \cdot \hat{n} + h(T - T_S) = 0 \qquad \text{on } \mathcal{S}_3, \tag{5c}$$

$$k \nabla T \cdot \hat{n} = q_n \qquad \text{on } \mathcal{S}_4 \tag{5d}$$

where $\mathcal{R}$ is the volume enclosing the heat conducting system of interest, which is bounded by the external surface $\mathcal{S} = \mathcal{S}_1 + \mathcal{S}_2 + \mathcal{S}_3 + \mathcal{S}_4$.

Within the framework of the continuous synthesis approximation, the temperature is approximated as

$$T(x, y, z) \cong \sum_{n=1}^{N} H_n(x, y)Z_n(z) \tag{6}$$

where the $H_n(x, y)$ are the predetermined trial functions which bracket the true solution in the sense that they are two-dimensional solutions representative of x-y slices through the heat conducting medium of interest at several z elevations where k and S are independent of, or only slowly varying functions of z. The $Z_n(z)$ are the unknown mixing coefficients which blend the trial functions in such a way as to obtain the best (in a variational sense) solution of the form (6). The variational principle to be used is

---

[2] Numbers in brackets designate References at end of paper.

$$\delta V_1[T] = 0 \tag{7}$$

$$V_1[T] = \iiint\limits_{\mathcal{R}} (\nabla T\cdot k\nabla T - 2TS)d\mathbf{r} + \oint\!\!\!\!\oint\limits_{\mathcal{S}} [h(T - T_S)^2 - 2q_nT]d\mathcal{S}. \tag{8}$$

This principle admits functions $T(\mathbf{r})$, which are continuous with at least piecewise continuous first derivatives in $\mathcal{R}$, and has as its stationary conditions equations (4) and (5).

In order to simplify the algebra we define the matrix notation

$$Z(z) \equiv \begin{bmatrix} Z_1(z) \\ \cdot \\ \cdot \\ \cdot \\ Z_N(z) \end{bmatrix} \quad \text{and} \quad H(x, y) \equiv \begin{bmatrix} H_1(x, y) \\ \cdot \\ \cdot \\ \cdot \\ H_N(x, y) \end{bmatrix}.$$

Then if superscript T denotes a transpose of a matrix we may replace the synthesis expansion (6) by

$$T(x, y, z) \cong Z^T(z)H(x, y). \tag{9}$$

In addition we define the following integration notation

$$\langle A, OB\rangle \equiv \iint\limits_a AOBdxdy$$

$$\langle OB\rangle \equiv \iint\limits_a OBdxdy$$

where a is the x-y cross-sectional area of the system of interest, and

$$\{A, OB\} = \oint\limits_c AOBdc$$

where c is the closed line contour bounding the x-y area a. The z dimension of the system of interest is defined by $0 \le z \le \bar{z}$.

We now substitute the synthesis form (9) into the functional (8) and perform the x-y integrations. This results in a reduced functional of Z, which when its first variation is required to vanish yields the stationary conditions

$$-\frac{d}{dz}\langle H, kH^T\rangle \frac{d}{dz} Z + [\langle\nabla H, k\nabla H^T\rangle + \{H, hH^T\}]Z = \langle SH\rangle + \{(hT_S + q_n)H\} \qquad \text{for } z \text{ in } \mathfrak{z}_i \tag{10}$$

subject to the boundary conditions

$$\begin{aligned} -\langle H, kH^T\rangle_{z=0} \frac{d}{dz} Z(0) + \langle H, hH^T\rangle_{z=0}Z(0) &= \langle(hT_S + q_n), H\rangle_{z=0} \\ \langle H, kH^T\rangle_{z=\bar{z}} \frac{d}{dz} Z(\bar{z}) + \langle H, hH^T\rangle_{z=\bar{z}}Z(\bar{z}) &= \langle(hT_S + q_n), H\rangle_{z=\bar{z}} \end{aligned} \tag{11}$$

and the continuity conditions

$$\left.\begin{aligned} \langle H, k(-)H^T\rangle \frac{d}{dz} Z(-) &= \langle H, k(+)H^T\rangle \frac{d}{dz} Z(+) \\ Z(-) &= Z(+) \end{aligned}\right\} \text{ at } \quad z = z_1, \tag{12}$$

where the z_i are those axial positions where k is discontinuous, and the $\mathfrak{z}_i$ denote the axial regions wherein k varies continuously with z.

Equation (10) is a set of $N \times N$ coupled differential equations, subject to the boundary conditions (11) and continuity conditions (12), which completely define the synthesis mixing coefficients, $Z_n(z)$.

In equation (10), $Z(z)$ is the column matrix of unknown mixing coefficients

$$Z(z) = \begin{bmatrix} Z_1(z) \\ Z_2(z) \\ \cdot \\ \cdot \\ \cdot \\ Z_N(z) \end{bmatrix}, \tag{13}$$

$\langle H, kH^T\rangle$ is a $N \times N$ matrix whose j, kth element is

$$\langle H, kH^T\rangle_{j,k} = \iint\limits_a H_j(x, y)k(x, y, z)H_k(x, y)dxdy, \tag{14}$$

$\langle\nabla H, k\nabla H^T\rangle$ is a $N \times N$ matrix whose j, kth element is

$$\langle\nabla H, k\nabla H^T\rangle_{j,k} = \iint\limits_a \nabla H_j(x, y)\cdot k(x, y, z)\nabla H_k(x, y)dxdy, \tag{15}$$

$\langle SH\rangle$ is an N element column matrix whose jth element is

$$\langle SH\rangle_j = \iint\limits_a H_j(x, y)S(x, y, z)dxdy, \tag{16}$$

$\{H, hH^T\}$ is an $N \times N$ matrix whose j, kth element is

$$\{H, hH^T\}_{j,k} = \oint\limits_c H_j(x, y)h(x, y, z)H_k(x, y)dc, \tag{17}$$

and $\{(hT_S + q_n)H\}$ is an N element column matrix whose jth element is

$$\{(hT_S + q_n)H\}_j = \oint\limits_c H_j(x, y)[h(x, y, z)T_S(x, y, z) + q_n(x, y, z)]dc. \tag{18}$$

Continuous Synthesis Test Problems

In order to display the utility of the continuous synthesis method for obtaining accurate numerical solutions to multidimensional, composite media, heat conduction problems, we describe the results of two two-dimensional test problems. Both problems used the axially symmetric cylindrical heat conducting system described in Fig. 2. For these problems equations (10)–(12), in cylindrical geometry, were solved numerically, using a modified neutron diffusion theory synthesis program [4]. For purposes of comparison, an r-z finite difference solution [5] of the heat conduction equation was obtained for each test problem, utilizing the same mesh structure as was used for the solution of the synthesis equations (10)–(12). These pointwise temperatures were accurate to 0.001 deg F.

In all, six radial trial functions were considered in the synthesis solutions of test problems 1 and 2. Trial functions $H_1(r)$, $H_2(r)$ and $H_3(r)$ were one-dimensional finite difference solutions [6] of the heat conduction equation representing radial slices through axial compositions 1, 2, and 3, respectively. Trial functions $H_4(r)$ and $H_5(r)$ were transition type functions, which were one-dimensional finite difference solutions using material properties which are averages for axial compositions 1–2 and 2–3, respectively. These first five trial functions vanished at the radial boundary $r = R$. The final trial function, $H_6(r) = 1$ for $0 \le r \le R$.

Test Problem 1. This problem was concerned with approximating the temperature distribution for the system in Fig. 2, subject to the boundary conditions

$$\frac{\partial}{\partial z} T(r, z) = 0 \qquad \text{at} \quad z = 0, L,$$

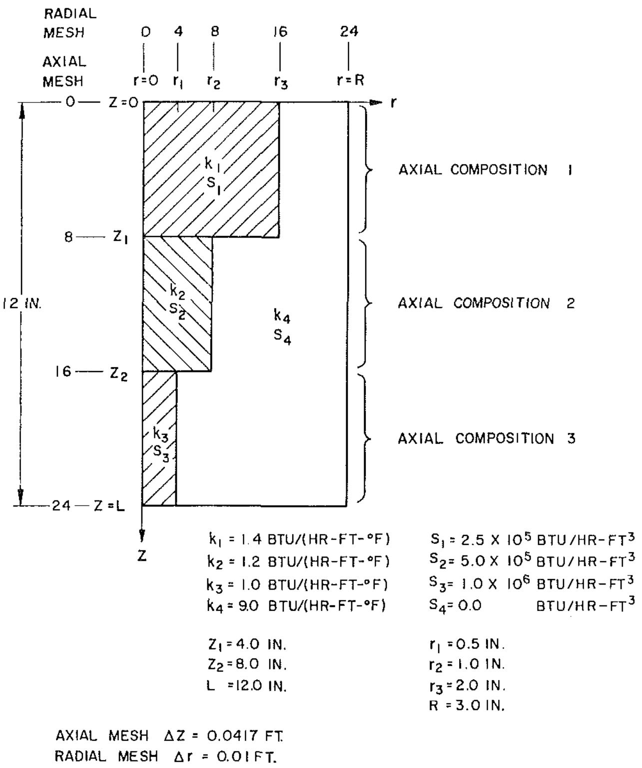

Fig. 2 Axially symmetric cylindrical conducting medium

$$T(R, z) = 80 \text{ deg F} \quad \text{for} \quad 0 < z < z_1,$$

$$T(R, z) = 100 \text{ deg F} \quad \text{for} \quad z_1 < z < z_2,$$

$$T(R, z) = 80 \text{ deg F} \quad \text{for} \quad z_2 < z < L.$$

The synthesis expansion was then constructed as

$$T(r, z) \cong \sum_{n=1}^{6} Z_n(z) H_n(r), \tag{19}$$

with $\frac{d}{dz} Z_n(z) = 0$, at $z = 0, L$. Note that the unit trial function, $H_6(r)$, was included to accommodate the nonzero boundary conditions at $r = R$. Fig. 3 presents a comparison of the synthesis solution (19) and the r-z finite difference solution for this problem.

Test Problem 2. The second test problem again considered the heat conducting system of Fig. 2. The boundary conditions for this problem included convective conditions over a portion of the external surface. Specifically the boundary conditions were

$$\frac{\partial}{\partial z} T(r, z) = 0 \qquad \text{at} \quad z = 0, L,$$

$$T(R, z) = 80 \text{ deg F} \quad \text{for} \quad 0 < z < z_1,$$

$$k \frac{\partial}{\partial r} T(R, z) + h[T(R, z) - T_S] = 0 \qquad \text{for} \quad z_1 < z < z_2,$$

where $h = T_S = 100$

$$T(R, z) = 80 \text{ deg F} \quad \text{for} \quad z_2 < z < L.$$

The synthesis solution was obtained using all six trial functions, as in (19). The resulting synthesized temperature distribution is shown in Fig. 4, along with the r-z finite difference solution of this problem at several radial points.

The preceding test problems show that the continuous synthesis method can yield very accurate approximate temperature distributions. However, this method does have some deficiencies. Consider the application of the continuous synthesis approximation to a heat conduction problem involving a material system with a great deal of complexity in the axial direction (i.e., a heat conducting system with many different axial compositions). In order to obtain an accurate solution for such a problem it may be necessary to use a large number of trial functions which, in turn, would result in a large, expensive computation effort. One would like to be able to switch sets of trial functions for problems of this type. That is, for z near the bottom of the system one would like to use only those trial functions relevant to the lower axial compositions. Then, as z increases, one would like, in stages, to discard the lower region trial functions and replace them with middle and upper region trial functions. Another way to say this is that we would like to make the trial functions $H_n(x, y)$ in equation (6) be discontinuous functions of z. Hence, if we can use trial functions which have a discontinuous z behavior, then we can synthesize heat conduction problems involving many axial material discontinuities by using only a few relevant trial functions at any specific axial position.

Another deficiency of the continuous heat conduction synthesis (which can be remedied by the use of axially discontinuous trial functions)[3] is that it cannot be applied to problems involving nonregular geometries for which the x-y boundaries change with z.

We have seen that the continuous synthesis procedure has certain deficiencies which can be circumvented if the synthesis expansion (6) is modified as

$$T(x, y, z) \cong \sum_{n=1}^{N} Z_n(z) H_n^{z}(x, y) \tag{20}$$

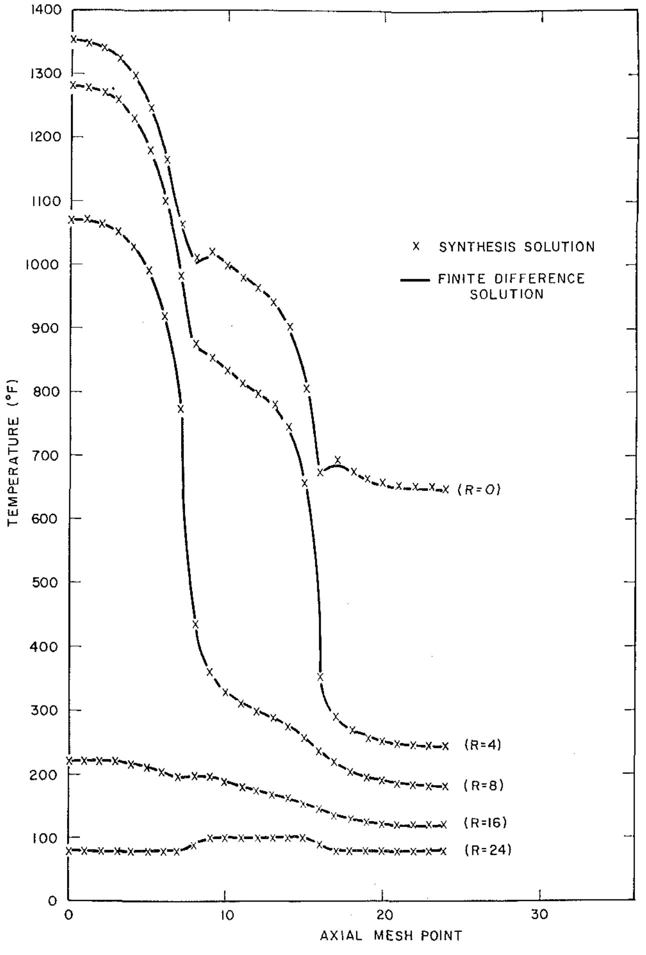

Fig. 3 Heat conduction synthesis test problem I—axial temperature distributions

---

[3] Synthesis approximations, using x-y trial functions which are discontinuous functions of z, for a nonregular reactor geometry treated by two-group diffusion theory, have yielded very accurate results [1].

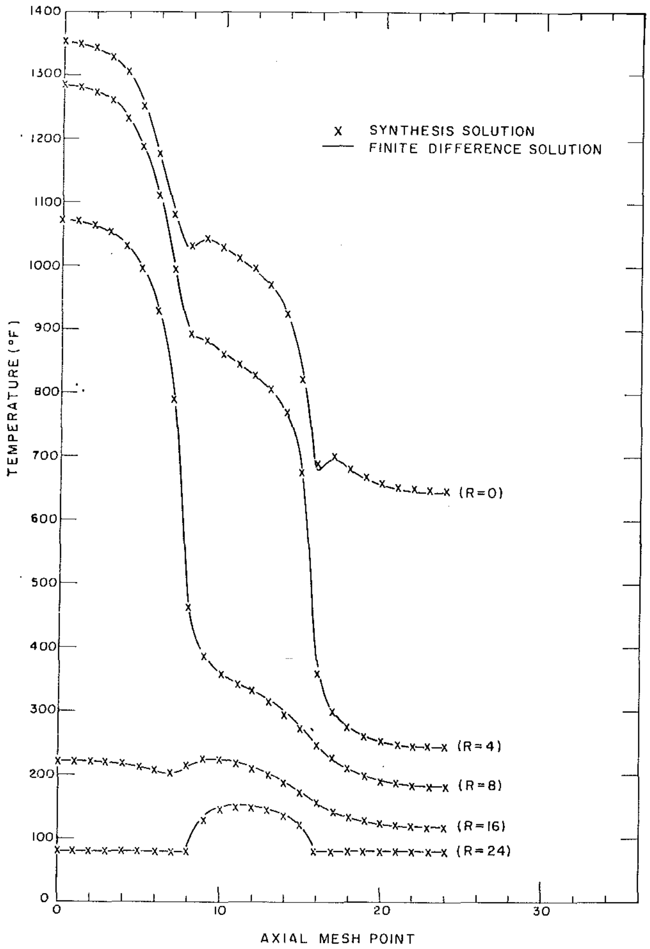

Fig. 4 Heat conduction synthesis test problem 2—axial temperature distributions

where the trial functions $H_n^z(x, y)$ are known x-y temperature distributions which apply only over specified regions of the z axis. That is, the H_n^z are to be discontinuous functions of z. As was previously mentioned, the variational principle, equations (7) and (8), admits only continuous approximating functions. Hence this principle cannot be used to develop a "discontinuous" heat conduction synthesis procedure using the axially discontinuous form (20). We now proceed to develop a discontinuous synthesis approximation for static heat conduction problems.

The Discontinuous Synthesis Method

We now concern ourselves with formulating a temperature synthesis approximation of the form

$$T(x, y, z) \cong \sum_{n=1}^{N} Z_n(z) H_n^z(x, y) \tag{21}$$

where the $H_n^z(x, y)$ are known x-y trial functions which are axially discontinuous. The discontinuous form (21) will permit one to synthesize a much larger class of static heat conduction problems than was possible within the continuous synthesis framework. However, using discontinuous trial functions complicates the problem of defining the mixing coefficients $Z_n(z)$. In order to develop a discontinuous heat conduction synthesis approximation, a variational functional must be used which admits discontinuous approximating functions. Such a functional may be obtained by transforming the functional $V_1[T]$, equation (8), into canonical form [8], and interpreting contributions due to the spatial discontinuities of the approximating functions. We now proceed to derive such a functional.

Let us write equation (8) as

$$V_1[T] = \iiint_{\mathcal{R}} \mathcal{L}(T, \nabla T, \mathbf{r})d\mathbf{r} + \oint_{\mathcal{S}} U(T)d\mathcal{S}. \tag{22}$$

In analogy with classical mechanics we may look upon (22) as the functional of Hamilton's principle. Then we can identify $\mathcal{L}$ as the Lagrangian density

$$\mathcal{L}(T, \nabla T, \mathbf{r}) \equiv \nabla T \cdot k \nabla T - 2TS \tag{23}$$

and proceed to define generalized momenta as

$$\mathbf{p} = \frac{\partial \mathcal{L}}{\partial(\nabla T)} \equiv 2k\nabla T. \tag{24}$$

Next we define a Hamiltonian density

$$\mathcal{H}(T, \mathbf{p}, \mathbf{r}) \equiv \mathbf{p} \cdot \nabla T - \mathcal{L}(T, \nabla T, \mathbf{r}) \tag{25}$$

where it is assumed that ∇T can be eliminated from (25) using (24). Such a substitution yields

$$\mathcal{H}(T, \mathbf{p}, \mathbf{r}) = \mathbf{p} \cdot \mathbf{p}/4k + 2TS. \tag{26}$$

From equations (25) and (26) we have

$$\mathcal{L} = \mathbf{p} \cdot \nabla T - \mathbf{p} \cdot \mathbf{p}/4k - 2TS \tag{27}$$

which, when used in (22), results in the canonical functional

$$V_2[\mathbf{p}, t] = \iiint_{\mathcal{R}} (\mathbf{p} \cdot \nabla T - \mathbf{p} \cdot \mathbf{p}/4k - 2TS)d\mathbf{r} + \oint_{\mathcal{S}} [h(T - T_S)^2 - 2q_n T]d\mathcal{S} \tag{28}$$

where we have set $U(T) = [h(T - T_S)^2 - 2q_n T]$. This functional does not admit the use of discontinuous functions, but it is of such a form that it can be augmented to permit $\mathbf{p}$ and T to possess a countable number of discontinuities. Such an extension requires an interpretation of the term $\iiint_{\mathcal{R}} \mathbf{p} \cdot \nabla T d\mathbf{r}$ at internal surfaces $\mathcal{S}_j$, on which T is discontinuous. Following the reasoning of Selengut and Wachspress [9] we interpret this term as

$$\iiint_{\mathcal{R}} \mathbf{p} \cdot \nabla T d\mathbf{r} = \sum_j \iiint_{\mathcal{R}_j} \mathbf{p} \cdot \nabla T d\mathbf{r} + \sum_j \oint_{\mathcal{S}_j} \left[\frac{\mathbf{p}(+) + \mathbf{p}(-)}{2}\right] [T(+) - T(-)] \cdot \hat{n} d\mathcal{S}_j \tag{29}$$

where the $\mathcal{R}_j$ are those regions within which T and $\mathbf{p}$ are continuous. $\hat{n}$ is a unit outward normal, and $(+)$ denotes quantities evaluated on the side of $\mathcal{S}_j$ toward which $\hat{n}$ points and $(-)$ denotes evaluation on the other side. Using the interpretation (29) in the functional (28) we arrive at

$$V_2[\mathbf{p}, T] = \sum_j \iiint_{\mathcal{R}_j} (\mathbf{p} \cdot \nabla T - \mathbf{p} \cdot \mathbf{p}/4k - 2TS)d\mathbf{r} + \oint_{\mathcal{S}} [h(T - T_S)^2 - 2q_n T]d\mathcal{S} + \sum_j \oint_{\mathcal{S}_j} \left[\frac{\mathbf{p}(+) + \mathbf{p}(-)}{2}\right] [T(+) - T(-)] \cdot \hat{n} d\mathcal{S}_j. \tag{30}$$

This functional now admits functions T and $\mathbf{p}$ which possess a countable number of discontinuities on the internal surfaces $\mathcal{S}_j$.

Those functions $T(x, y, z)$ and $\mathbf{p}(x, y, z)$ which make (30) stationary must satisfy

$$\delta V_2 \equiv V_2[\mathbf{p} + \delta\mathbf{p}, T + \delta T] - V_2[\mathbf{p}, T] = 0, \tag{31}$$

neglecting second order terms in δT and $\delta\mathbf{p}$. Using (30) and (31) we find that $V_2[\mathbf{p}, T]$ is stationary for those functions T and $\mathbf{p}$ which satisfy

$$\left.\begin{aligned}\frac{1}{2}\nabla\cdot\mathbf{p}+S&=0\\ \mathbf{p}&=2k\nabla T\end{aligned}\right\}\text{ in }\mathcal{R}_j, \qquad (32)$$

$$\frac{1}{2}\,\mathbf{p}\cdot\hat{n}+h(T-T_S)=q_n\text{ on }\mathcal{S}, \qquad (33)$$

$$\left.\begin{aligned}T(+)&=T(-)\\ \mathbf{p}(+)\cdot\hat{n}&=\mathbf{p}(-)\cdot\hat{n}\end{aligned}\right\}\text{ on }\tilde{\mathcal{S}}_j. \qquad (34)$$

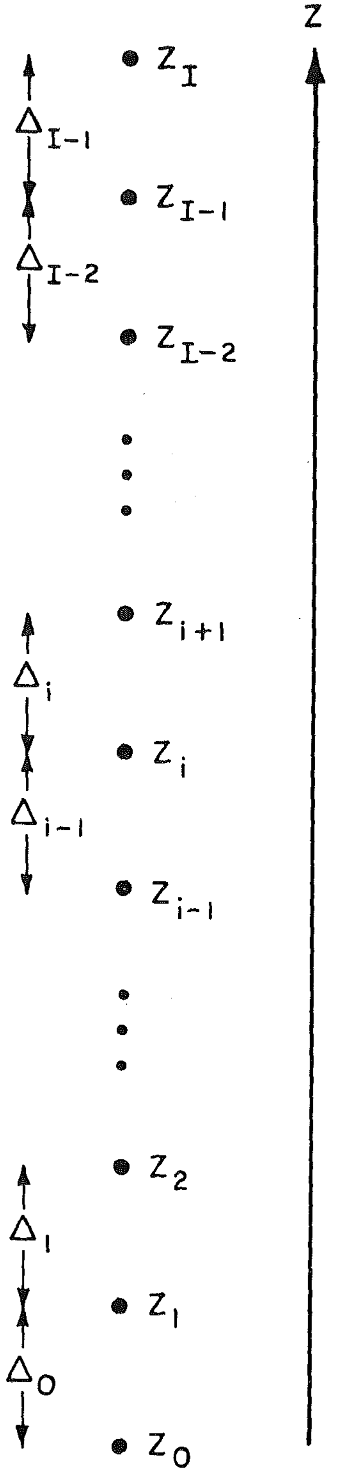

Fig. 5

Hence we see that the Euler equations (32) are just the heat conduction equation in first order form. Equation (33) is the general type boundary condition (5), and equations (34) require continuity of temperature and heat flux on all internal surfaces. Hence the functional (30) does have the desired stationary conditions to permit its use for developing a discontinuous synthesis approximation for static heat conduction problems. We now proceed to develop a synthesis approximation which permits the switching of sets of x-y trial functions at specified z locations.

We begin by superimposing a mesh structure on the z axis as is shown in Fig. 5. Material properties and surface functions are assumed constant between axial mesh points and denoted as $k(z) = k_i$, $S(z) = S_i$, $h(z) = h_i$ and $T_S(z) = T_{S_i}$, for $z_i < z < z_{i+1}$. Next we introduce unit step functions

$$s_i(z)=\begin{cases}1, & \text{for}\quad z_i-\dfrac{\Delta_{i-1}}{2}<z<z_i+\dfrac{\Delta_i}{2}\\ 0, & \text{otherwise}\end{cases} \qquad (35)$$

where Δ_i is the mesh spacing between z_i and z_{i+1},

$$t_i(z)=\begin{cases}1, & \text{for}\quad z_i<z<z_{i+1}\\ 0, & \text{otherwise}\end{cases} \qquad (36)$$

Let $H_{m(i)}(x, y)$ denote a set of continuous functions of x, y which we think may approximate the actual x-y temperature distribution in the vicinity of axial elevation z_i. Using the step functions $s_i(t)$ and $t_i(t)$, we proceed to expand the temperature and components of heat flow as

$$\begin{aligned}
T(x, y, z) &\cong \sum_{i=0}^{I}\sum_{m(i)=1}^{M} s_i(z)Z_{m(i)}H_{m(i)}(x, y)\\
p_x(x, y, z) &\cong \sum_{i=0}^{I}\sum_{m(i)=1}^{M} s_i(z)[t_{i-1}(z)k_{i-1}\\
&\qquad + t_i(z)k_i]P_{m(i)}{}^{x}\frac{\partial}{\partial x}H_{m(i)}(x, y)\\
p_y(x, y, z) &\cong \sum_{i=0}^{I}\sum_{m(i)=1}^{M} s_i(z)[t_{i-1}(z)k_{i-1}\\
&\qquad + t_i(z)k_i]P_{m(i)}{}^{y}\frac{\partial}{\partial y}H_{m(i)}(x, y)\\
p_z(x, y, z) &\cong \sum_{i=0}^{I-1}\sum_{m(i)=1}^{M} t_i(z)k_iP_{m(i)}{}^{z}H_{m(i)}(x, y)
\end{aligned} \qquad (37)$$

where $t_{-1}(z) = 0$. Note here that we are free to choose different sets of trial functions, $H_{m(i)}$, to be used about any particular mesh point z_i. For simplicity we have restricted our approximation to use the same number, M, of trial functions for each mesh indicator i. In general we could specify different numbers of trial functions for different i. To simplify the algebra, we again introduce matrix notation. Let

$$\left.\begin{aligned}
&H_i\equiv\begin{bmatrix}H_{1(i)}(x, y)\\ H_{2(i)}(x, y)\\ \vdots\\ H_{M(i)}(x, y)\end{bmatrix},\quad Z_i\equiv\begin{bmatrix}Z_{1(i)}\\ Z_{2(i)}\\ \vdots\\ Z_{M(i)}\end{bmatrix},\quad P_i{}^{x}\equiv\begin{bmatrix}P_{1(i)}{}^{x}\\ P_{2(i)}{}^{x}\\ \vdots\\ P_{M(i)}{}^{x}\end{bmatrix}\\
&\qquad P_i{}^{y}\equiv\begin{bmatrix}P_{1(i)}{}^{y}\\ P_{2(i)}{}^{y}\\ \vdots\\ P_{M(i^y)}\end{bmatrix},\quad P_i{}^{z}\equiv\begin{bmatrix}P_{1(i)}{}^{z}\\ P_{2(i)}{}^{z}\\ \vdots\\ P_{M(i)}{}^{z}\end{bmatrix}.
\end{aligned}\right\}$$

Then we may write (37) as

$$\begin{aligned}
T(x, y, z) &\cong \sum_{i=0}^{I} s_iZ_i{}^{T}H_i\\
p_x(x, y, z) &\cong \sum_{i=0}^{I} s_i[t_{i-1}k_{i-1}+t_ik_i]P_i{}^{x^T}\frac{\partial}{\partial x}H_i
\end{aligned} \qquad (38)$$

$$p_y(x, y, z) \cong \sum_{i=0}^{I} s_i[t_{i-1}k_{i-1} + t_ik_i]P_i^{y^T} \frac{\partial}{\partial y} H_i$$

$$p_z(x, y, z) \cong \sum_{i=0}^{I-1} t_ik_iP_i^{z^T}H_i$$

where superscript T denotes transpose of a matrix. We also invoke the integration notation used earlier. However, the cross-sectional area a and the contour c may now change with z if the x-y boundaries of the system of interest are functions of z. With this notation, we may substitute the approximation expansions (38) into the functional (30), observing that the $\tilde{\mathrm{S}}_j$ consists only of horizontal surfaces midway between the mesh points z_i, and performing the x-y integrations we obtain the reduced functional $V'[Z_i, P_i^x, P_i^y, P_i^z]$. The stationary conditions for the reduced functional are found by requiring

$$\frac{\partial V_2'}{\partial Z_i} = \frac{\partial V_2'}{\partial P_i^x} = \frac{\partial V_2'}{\partial P_i^y} = \frac{\partial V_2'}{\partial P_i^z} = 0 \qquad (39)$$

for all i.

When we apply these stationary conditions, and eliminate the heat flow mixing coefficients P_i^x, P_i^y and P_i^z, we obtain the following set of three point difference equations which define the temperature mixing coefficients Z_i.

$$\begin{aligned}\langle\nabla H_i, \tilde{k}_i\nabla H_i^T\rangle Z_i &- \left\langle H_i, \frac{k_{i-1}}{\Delta_{i-1}} H_{i-1}^T \right\rangle Z_{i-1} \\ &- \left\langle H_i, \frac{k_i}{\Delta_i} H_{i+1}^T \right\rangle Z_{i+1} + \left[\left\langle H_i, \frac{k_i}{\Delta_i} H_i^T \right\rangle\right. \\ &+ \left.\left\langle H_i, \frac{k_{i-1}}{\Delta_{i-1}} H_{i-1}^T \right\rangle \langle H_{i-1}, k_{i-1}H_{i-1}^T\rangle^{-1}\langle H_{i-1}, k_{i-1}H_i^T\rangle\right] Z_i \\ &+ B_iZ_i - C_i = \langle\tilde{S}_iH_i\rangle \quad \text{for} \quad i = 1, 2, \ldots, I \qquad (40)\end{aligned}$$

where

$$B_i = \{H_i, \tilde{h}_iH_i^T\} + \langle H_0, h_0H_0^T\rangle\delta_{i,0} + \langle H_I, h_IH_I^T\rangle\delta_{i,I}$$

$$\begin{aligned}C_i = \{\tilde{h}T_{S_i}H_i\} + \{\tilde{q}_{n_i}H_i\} &+ [\langle T_{S_0}H_0\rangle + \langle q_{n_0}H_0\rangle]\delta_{i,0} \\ &+ [\langle T_{S_I}H_I\rangle + \langle q_{n_I}H_I\rangle]\delta_{i,I},\end{aligned}$$

$$\delta_{i,0} = \begin{cases}1, & \text{if} \quad i = 0 \\ 0, & \text{otherwise}\end{cases}; \quad \delta_{i,I} = \begin{cases}1, & \text{if} \quad i = I \\ 0, & \text{otherwise}\end{cases}$$

and

$$\tilde{k}_i = \frac{1}{2} (k_{i-1}\Delta_{i-1} + k_i\Delta_i)$$

$$\tilde{S}_i = \frac{1}{2} (S_{i-1}\Delta_{i-1} + S_i\Delta_i)$$

$$\tilde{h} = \frac{1}{2} (h_{i-1}\Delta_{i-1} + h_i\Delta_i)$$

$$\tilde{h}_iT_{S_i} = \frac{1}{2} (h_{i-1}T_{i-1}\Delta_{i-1} + h_iT_i\Delta_i).$$

It is interesting to note that if the same set of trial functions is used about mesh point z_{i-1} as is used about mesh point z_i, then the term $\langle H_{i-1}, k_{i-1}H_{i-1}^T\rangle^{-1}\langle H_{i-1}, k_{i-1}H_i^T\rangle$ is just the identity matrix, since $H_i = H_{i-1}$. In addition if the same set of trial functions is used for $0 \leq z_i \leq z_I$, then the equations (40) are just a finite difference form of the continuous synthesis equations (10)–(12). An ALGOL computer program was written to solve the synthesis equations (40). We now proceed to describe a test problem using axially discontinuous trial functions.

Discontinuous Synthesis Test Problem

The symmetric cylindrical heat conducting system considered for this problem is described in Fig. 6. Zero temperature boundary conditions were applied on all external surfaces. Four one-dimensional trial functions were considered for this problem, although only two functions were used at any z_i elevation. The computer program, WANDA [6], was used to calculate these trial functions and all necessary matrix elements. The trial functions; $H_1(r)$, $H_2(r)$, $H_3(r)$, $H_4(r)$ are one-dimensional solutions for radial slices through axial compositions 1, 2, 3, and 4, respectively, of the geometry depicted in Fig. 6. Table 1 describes the axial mesh regions over which each of these trial functions were used. We see that the trial functions used were discontinuous between axial mesh points 9–10, 24–25, and 37–38. Using these trial functions, the difference equations (40) were solved and the synthesized r-z temperature distribution was constructed. This synthesized solution is compared with an r-z finite difference solution [5] (accurate to 0.001 deg F) of this same problem in Fig. 7. From this figure we see that the synthesis solution is quite accurate, and most impressively, smoothly varying near the axial points where the trial functions are discontinuous.

Table 1 Axial dependence of discontinuous trial functions

Trial function	Used over z-Mesh points
$H_1(r)$, $H_2(r)$	$i = 0$ to $i = 9$
$H_2(r)$, $H_3(r)$	$i = 10$ to $i = 24$
$H_3(r)$, $H_4(r)$	$i = 25$ to $i = 37$
$H_4(r)$, $H_1(r)$	$i = 38$ to $i = 48$

Conclusion

In this paper variational techniques have been applied to develop continuous and discontinuous synthesis approximations for static composite media heat conduction problems. The basic idea behind these methods is that of using known two-dimensional trial functions representative of asymptotic solutions for axial regions of constant material properties. These trial functions, tailored to the problem of interest, are blended axially by means of z dependent mixing coefficients to yield the synthesized three-dimensional temperature distribution.

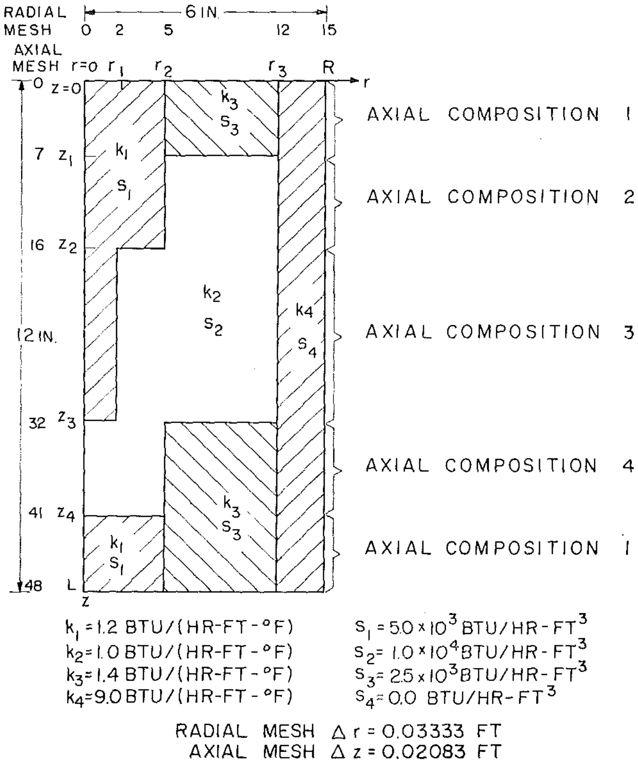

Fig. 6 Cylindrical conducting medium for discontinuous synthesis test problem

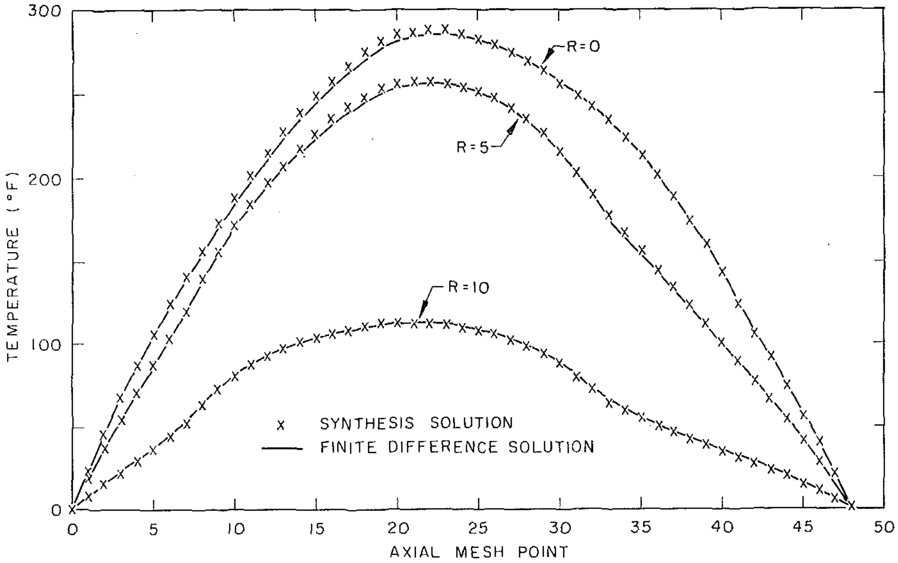

Fig. 7 **Discontinuous heat conduction synthesis test problem—axial temperature distributions**

The results of several two-dimensional test problems indicate the accuracy that can be obtained with the method. However, the advantage of using the synthesis methods, as opposed to finite difference methods, manifests itself when detailed three-dimensional problems must be solved. For such problems (possibly involving millions of spatial mesh points) the solution of the three-dimensional finite difference equations would be extremely expensive even on today's fast digital computers, while the synthesis method requires the solution of two-dimensional problems (to obtain the trial functions) and one one-dimensional solution (for the mixing coefficients). One- and two-dimensional numerical solutions are very inexpensive.

The ability to use axially discontinuous trial functions (switch sets of trial functions along the z axis) permits one to solve heat conduction problems involving irregular geometries. Hence synthesis methods can prove to be powerful tools for analyzing realistic heat conducting designs.

Acknowledgment

The author wishes to thank Dr. S. Kaplan for many helpful discussions throughout the course of this work.

References

1 Kaplan, S., *Nuclear Science and Engineering*, Vol. 13, 1962, pp. 22–31.

2 Kaplan, S., "Synthesis Methods in Reactor Analysis," *Advances in Nuclear Science and Technology*, Greebler, P. R., ed., Vol. III, Academic Press, 1965.

3 Crandall, S. H., *Engineering Analysis*, McGraw-Hill, New York, 1956.

4 Kaplan, S., Marlowe, O. J., and Cadwell, W. R., "Equations and Programs for Solutions of the Neutron Group Diffusion Equations by Synthesis Approximations," WAPD-TM-377, 1963.

5 Smith, R. B., and Spanier, J., "HOT-1: A Two-Dimensional Steady-State Heat Conduction Program for the Philco-2000," WAPD-TM-465, 1964.

6 Marlowe, O. J., and Suggs, M. C., "WANDA-5: A One-Dimensional Neutron Diffusion Equation Program for the Philco-2000 Computer," WAPD-TM-241, 1960.

7 Yasinsky, J. B., and Kaplan, S., "Synthesis of Three-Dimensional Flux Shapes Using Discontinuous Sets of Trial Functions," *Nuclear Science and Engineering*, Vol. 28, 1967, pp. 426–437.

8 Courant, R., and Hilbert, D., *Methods of Mathematical Physics*, Vol. I, Interscience Publishers, 1953.

9 Wachspress, E. L., and Becker, M., "Variational Multichannel Synthesis With Discontinuous Trial Functions," KAPL-3095, 1965.

technical briefs

This section consists of contributions of 1500 words or less (about $2^1/_2$ double-spaced typewritten pages, including figures). Technical Briefs will be reviewed and approved by the specific division's reviewing committee prior to publication. After approval such contributions will be published as soon as possible, normally in the next issue of the Journal.

A Comparison of Transient and Steady-State Pool-Boiling Data Obtained Using the Same Heating Surface

D. R. VERES[1] **and L. W. FLORSCHUETZ**[2]

Nomenclature

A = heat-transfer surface area, ft^2
$c_p(T)$ = specific heat of copper, Btu/lbm·deg F
M = mass of copper sphere, lbm
q/A, $(q/A)_{\min}$ = heat flux, minimum stable-film-boiling heat flux
T = sphere temperature
$T_s - T_{\text{sat}}$, $(T_s - T_{\text{sat}})_{\min}$ = surface temperature minus saturation temperature, value corresponding to $(q/A)_{\min}$
t = time

Introduction

The use of the transient calorimeter technique for generating pool-boiling data has been increasingly exploited during the last few years. It has been used in a number of investigations for the expressed purpose of constructing characteristic pool-boiling curves or portions of such curves. For example, the technique was used by Merte and Clark [1],[3] by Adams [2], by Bradfield [3], by Rhea and Nevins [4], and by Fischer [5]. A recently reported study by Bergles and Thompson [6] had as its objective an investigation of the relationship of quench data to steady-state pool-boiling data. However, the same heating surfaces used in the steady-state tests were not used for the transient tests. Discrepancies appearing in the comparison of the results were attributed mainly to differences in surface conditions. The purpose of this note is to report the results of an investigation performed preliminary to Fischer's work [5], with the object of comparing transient and steady-state saturated-pool-boiling data obtained using the same heating surface.

Experimental Apparatus and Procedures

For the purpose of conducting both transient and steady-state tests with a single system, it was decided to use induction heating of a solid copper sphere. The spherical geometry was selected to eliminate end effects. Copper was selected because of its high thermal conductivity, which would allow adequate data analysis based on just one thermocouple mounted at the center of the sphere. Two test assemblies were constructed using 0.938-in-dia spheres. Assembly No. 1 contained a commercially manufactured 24-gage chromel–alumel thermocouple, insulated with magnesium oxide, and grounded to the hemispherical end of a $\frac{1}{8}$-in-OD stainless steel sheath. The thermocouple assembly was soldered in place in an argon-atmosphere furnace and served also to suspend the sphere inside the boiling vessel. Assembly No. 2 contained a 30-gage copper–constantan thermocouple held in place by fine aluminum powder packed into the 0.040-in-dia hole provided. It was suspended from the thermocouple lead wires which were fitted inside a rigid brass tube to prevent a pendulum motion of the sphere.

The boiling vessel was a vertical glass tube 15 in. high by $1\frac{7}{8}$ in. ID, with a reflux condenser positioned at the top, and an auxiliary immersion heater at the bottom to maintain the Freon-113 test liquid at saturation conditions. The induction heating coil was positioned concentrically outside the vessel with a small clearance allowed. The particular sphere assembly in use was centered both with respect to the vessel and the induction coil. The operating frequency was 280 kHz. All tests were conducted at atmospheric pressure, with the liquid level maintained at $2\frac{1}{2}$ in. above the sphere.

No mechanical processes were applied to the surface finishes of the copper spheres as received from the manufacturer. Acetone was used as a cleaning agent prior to those runs labeled "cleaned," and prior to run 112TC the oxide layer was chemically removed. Prior to each run the system was degassed by vigorous boiling.

Transient Tests. With power to the coil turned on, the liquid level was decreased, thus exposing the sphere to the Freon vapor. The sphere was then heated to a temperature high enough so that when the original liquid level was restored stable film boiling was immediately achieved. Power to the coil was then cut off, allowing the sphere to cool while recording its transient temperature response. Reduction of the data was based on the assumption that the copper sphere could be thermally lumped. The heat flux was calculated from

$$q/A = -\frac{Mc_p(T)}{A}\frac{dT}{dt} \cong -\frac{Mc_p(T)}{A}\frac{\Delta T}{\Delta t}, \tag{1}$$

using discrete points selected from the strip-chart record at appropriate time intervals. To verify the accuracy of the piecewise-linear approximation implied by the right-most term in equation (1), the initially selected intervals were cut in half and the calculation repeated. The two sets of time intervals yielded essentially identical boiling curves.

Steady-State Tests. Here, careful calibration for the power input from the induction coil to the sphere was necessary. With the test fluid removed, inert gas was bled through the vessel at a constant rate just sufficient to keep the vessel purged during the entire calibration procedure in order to prevent unnecessary oxidation of the copper surface. For each given power setting, the transient temperature rise of the sphere was monitored. From this record, the power input to the sphere (neglecting heat loss to the environment) as a function of sphere temperature, could be computed using equation (1). The heat loss from the sphere to the environment as a function of sphere temperature was also determined from equation (1) based on the transient temperature response of the sphere as it cooled to the same environment after cutting off power immediately following a calibration run.

Additional details may be found in reference [7].

---

[1] Formerly Graduate Assistant, Department of Mechanical Engineering, Arizona State University, Tempe, Ariz.; currently with Motorola, Inc., Phoenix, Ariz.

[2] Associate Professor, Department of Mechanical Engineering, Arizona State University, Tempe, Ariz.

[3] Numbers in brackets designate References at end of technical brief.

Contributed by the Heat Transfer Division of THE AMERICAN SOCIETY OF MECHANICAL ENGINEERS. Manuscript received by the Heat Transfer Division July 6, 1970.

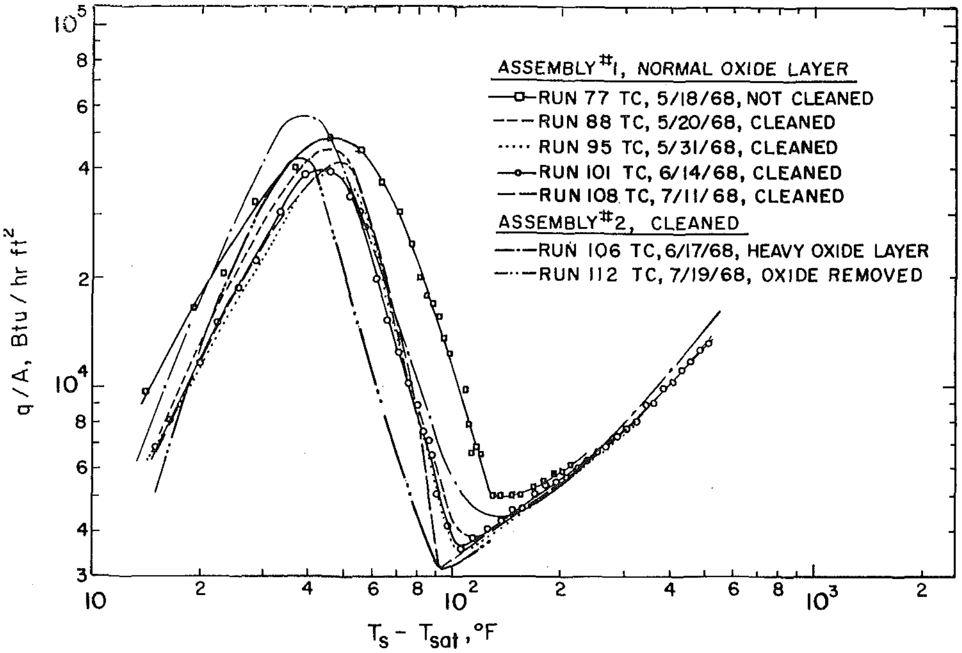

Fig. 1 Transient test results showing effect of surface condition; pool boiling of Freon-113

Results and Discussion

The reduced data from the transient tests are displayed in Fig. 1 as smooth curves which were faired through the calculated data points. For comparison, the calculated data points are shown for runs 77TC and 101TC.[4] The smoothing is deemed appropriate since most of the small scatter that does exist arises from uncertainties associated with the reading of the millivolt levels at discrete points from the strip-chart record. Runs 88TC, 95TC, 101TC, and 108TC spaced over a period of almost two months show the reproducibility of the data when the sphere surface is carefully cleaned with acetone prior to the run. When the sphere was not cleaned prior to the test, transition from stable film boiling occurred much sooner and significantly higher heat fluxes resulted in all regions except stable film boiling, as shown by run 77TC. Based on visual inspection, the surface of assembly No. 2 appeared to be more heavily oxidized than that of assembly No. 1. Even when cleaned with acetone prior to a run, assembly No. 2 gave a boiling curve, run 106TC, with an earlier transition similar to that of run 77TC. For run 112TC the oxide layer was chemically removed. This resulted in a transition point in excellent agreement with that of run 108TC. The effects of surface cleanliness and oxidation on the transition from stable film boiling as observed here are in agreement with previous observations and have been explained in terms of surface wettability [8]. Fin effects due to the thermocouple assemblies would be expected to be minimal for assembly No. 2. Comparison of the stable-film-boiling data for the two assemblies indicates that the fin effect of assembly No. 1 was also very small.

In Fig. 2 sets of transient and steady-state runs performed on the same day with presumably the same surface conditions are compared for both the nucleate and film-boiling regions. The steady-state nucleate-boiling heat fluxes were larger than those for the transient tests. Since the characteristic time for the transient cooling process was clearly much larger than the characteristic time associated with the bubble growth and departure phenomena, reasonable agreement might be expected. Two possible causes for the discrepancy were postulated: (1) error introduced by the thermal lumping of the sphere assembly and (2) a possible direct effect of the electromagnetic field of the induction coil on the nucleate-boiling process itself during steady-state runs. This induction field was not present during the transient runs. The first possibility was eliminated based on finite-difference calculations performed on a digital computer.

Electric-field effects on pool-boiling heat transfer have been reported in the literature, for example, by Markels and Durfee [9]. The nucleate-boiling data for assembly No. 1 as compared to assembly No. 2 are in good agreement for the steady-state tests, but a discrepancy exists for the transient test results. This discrepancy can be attributed to differences in detailed surface condition for the two assemblies. A possible explanation for the good agreement of the steady-state results for both assemblies is, then, that the field effects present during these tests overshadowed the effect of surface condition. A final argument in support of this interpretation is that subsequent results reported by Owens [10], who used electric-resistance heating of a copper disk to boil Freon-113, showed that to within experimental uncertainties transient nucleate-boiling test data were in agreement with the steady-state data for the same system.

The transient and steady-state film-boiling results are in excellent agreement, Fig. 2. Runs 107SS and 108TC are particularly definitive. The surface was carefully cleaned with acetone prior to each run and the steady-state test, run 107SS, was conducted with decreasing power levels so that the last data point represents a measured value for the minimum film-boiling flux and is in good agreement with the minimum point obtained from the corresponding transient test, run 108TC. This minimum flux is also in good agreement with Berenson's theoretical result for film boiling from a horizontal surface [11]. The $(T_s - T_{sat})_{min}$, however, is somewhat smaller than the prediction based on Berenson's theory. The occurrence of an earlier transition for run 77TC was a result of the intentional omission of surface cleaning prior to the test. Although the data of run 77TC do not cover as large a region in film boiling as the data of run 79SS, the data do overlap nicely, and an extrapolation of run 77TC would be in excellent agreement wirh run 79SS. Since run 79SS was made using increasing power levels the corresponding minimum film-boiling point was not obtained.

The steady-state stable-film-boiling data is also in excellent agreement with that of several other investigators, Fig. 3, and further verifies that stable film boiling is not strongly dependent on geometry.

---

[4] Run numbers with a suffix "TC" refer to transient cooling runs, while those with suffix "SS" are steady-state.

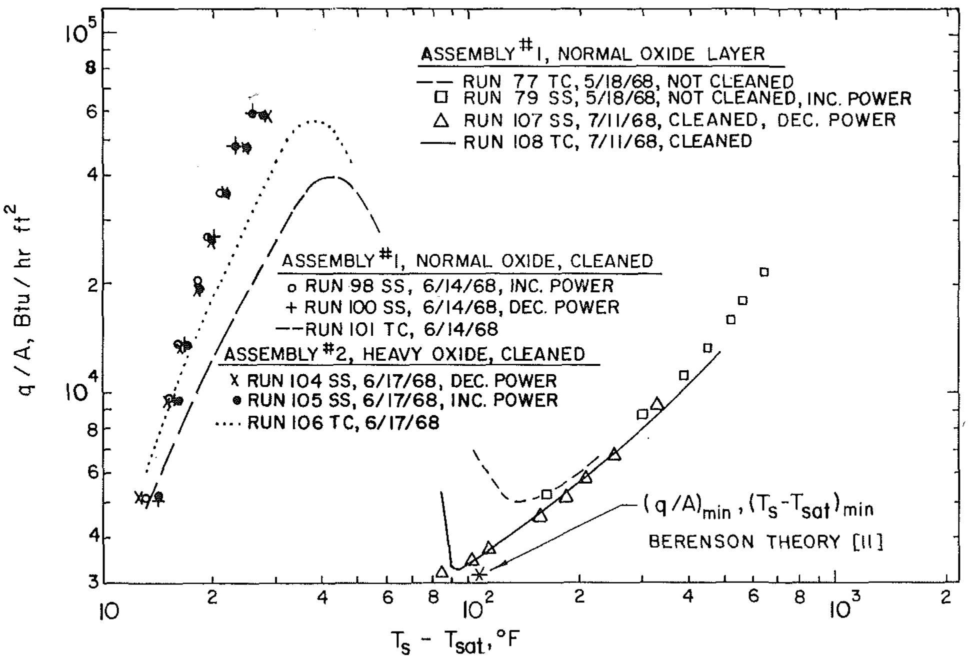

Fig. 2 Steady-state and transient test results compared for the same surface and surface condition; pool boiling of Freon-113

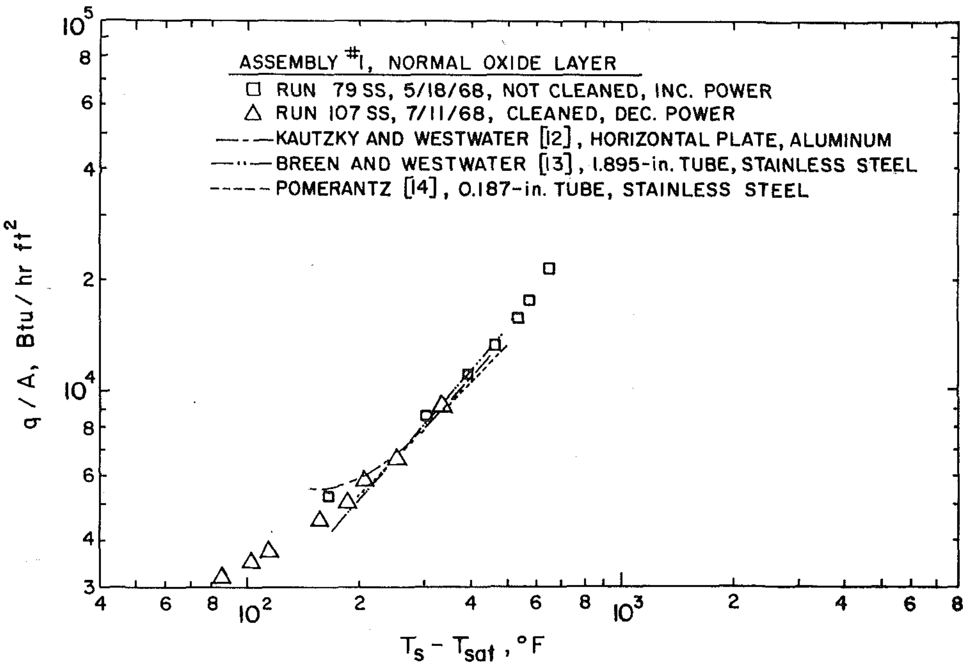

Fig. 3 Steady-state film-boiling test results compared to those of previous investigators; pool boiling of Freon-113

Concluding Remarks

It is reasonable to expect that transient film and nucleate-boiling processes occurring during the cooling of systems of sufficient thermal capacity can be assumed to be quasi-steady. Therefore, boiling curves constructed from transient test data for such systems would be expected to represent the correct steady-state boiling characteristic for the same or an exactly identical system. The results reported here provide direct experimental verification of this expectation for both the stable-film-boiling region and the minimum film-boiling point. The results for the nucleate-boiling region were not conclusive due to effects attributed to the presence of the induction field during the steady-state tests. However, conclusive results for the nucleate-boiling region were obtained in subsequent tests by Owens [10] using a different apparatus with direct electric-resistance heating.

References

1 Merte, H., Jr. and Clark, J. A., "Boiling Heat Transfer With Cryogenic Fluids at Standard, Fractional, and Near-Zero Gravity," Journal of Heat Transfer, Trans. ASME, Series C, Vol. 86, No. 3, Aug. 1964, pp. 351–359.

2 Adams, J. M., "An Investigation of Heat Transfer to Pool-Boiling Magnesium," ASME Paper No. 65-HT-49.

3 Bradfield, W. S., "On the Effect of Subcooling on Wall Superheat in Pool Boiling," Journal of Heat Transfer, Trans. ASME, Series C, Vol. 89, No. 3, Aug. 1967, pp. 269–270.

4 Rhea, L. G. and Nevins, R. G., "Film Boiling Heat Transfer From an Oscillating Sphere," Journal of Heat Transfer, Trans. ASME, Series C, Vol. 91, No. 2, May 1969, pp. 267–272.

5 Fischer, S. R., "Measurements of Complete Pool Boiling Heat Transfer Characteristics for Binary Mixtures with Emphasis on Parametric Effects of Concentration," PhD dissertation, Arizona State University, Tempe, Ariz., 1970.

6 Bergles, A. E. and Thompson, W. G., Jr., "The Relationship of Quench Data to Steady-State Pool Boiling Data," *International Journal of Heat and Mass Transfer*, Vol. 13, 1970, pp. 55–68.

7 Veres, David R., "A Comparison of the Transient and Steady State Methods of Obtaining Boiling Heat Transfer Data," MS thesis, Arizona State University, Tempe, Ariz., 1969.

8 Berenson, P. J., "Experiments on Pool Boiling Heat Transfer," *International Journal of Heat and Mass Transfer*, Vol. 5, 1962, pp. 985–999.

9 Markels, M., Jr. and Durfee, R. L., "Studies of Boiling Heat Transfer with Electrical Fields," *AIChE Journal*, July 1965, pp. 716–723.

10 Owens, F. L., Jr., "Measurements of Nucleate Pool Boiling from a Horizontal Surface Comparing Transient and Steady State Techniques," MS thesis, Arizona State University, Tempe, Ariz., 1969.

11 Berenson, P. J., "Film-Boiling Heat Transfer From a Horizontal Surface," JOURNAL OF HEAT TRANSFER, TRANS. ASME, Series C, Vol. 83, No. 3, Aug. 1961, pp. 351–358.

12 Kautzky, D. E. and Westwater, J. W., "Film Boiling of a Mixture on a Horizontal Plate," *International Journal of Heat and Mass Transfer*, Vol. 10, 1967, pp. 253–256.

13 Breen, B. P. and Westwater, J. W., "Effect of Diameter of Horizontal Tubes on Film Boiling Heat Transfer," *Chemical Engineering Progress*, Vol. 58, No. 7, 1962, pp. 67–72.

14 Pomerantz, M. L., "Film Boiling on a Horizontal Tube in Increased Gravity Fields," JOURNAL OF HEAT TRANSFER, TRANS. ASME, Series C, Vol. 86, No. 2, May 1964, pp. 213–219.

On the Rohsenow Pool-Boiling Correlation

C. W. FROST[1] and K. W. LI[2]

IN THE past, most of the experimental work used for the evaluation of constants in the Rohsenow pool-boiling correlation was conducted at atmospheric pressure or higher [1,2].[3] The purpose of this technical brief is to report the variation of these constants with vacuum pressure. Fig. 1 shows the schematic diagram of the apparatus used in this investigation. The vacuum tank was a Pyrex, cross-shaped container. All accessories and measuring devices were attached to the tank through blind flanges. A heater in the bottom of the tank was used to heat the water to the saturation temperature. A condenser on the top of the tank cooled the water vapor exhausted by the vacuum pump. The water temperature in the tank was measured with a thermometer calibrated to within 0.2 deg F. The pressure was measured with a Bourdon-tube vacuum gauge calibrated to within 0.5 in. Hg for pressure from atmospheric to 2 psia and a mercury manometer calibrated to within 1.0 mm Hg for pressures less than 2 psia. The heating surface on which the heat-transfer rates were measured consisted of a piece of platinum wire 0.008 in. in diameter and approximately 3 in. in length. The noncorrosive clamping device for the platinum wire supplied electrical power to the wire with no noticeable voltage drop across the wire support. Measurement of the voltage drop across the platinum wire of the test section and the current through the wire provided the data to determine the temperature of the heating surface and the heat-transfer rate.

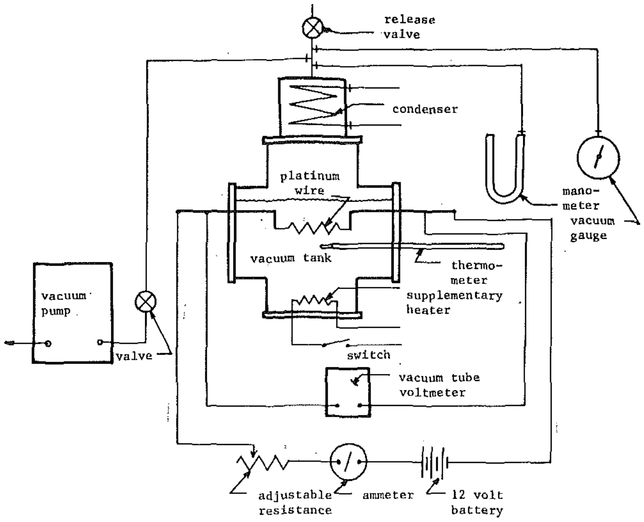

Fig. 1 Schematic diagram of apparatus

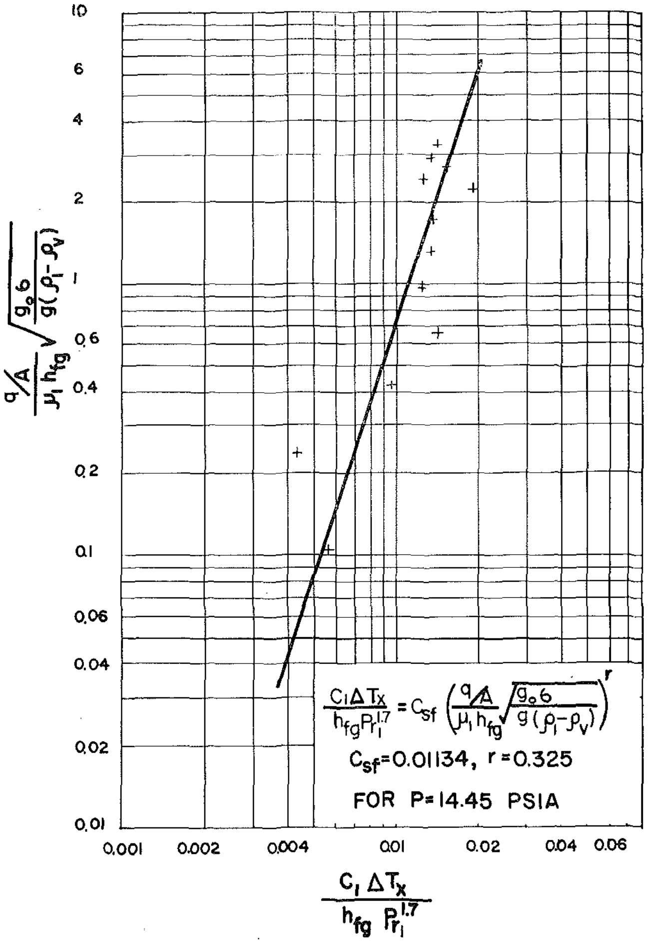

Fig. 2 Correlation of data at 14.45 psia

During all experiments the vacuum tank was filled with distilled water. The water was heated and maintained at the saturation temperature by submerged heater. To prevent induced convective currents around the platinum wire, two fine protective screens were installed just above the submerged heater (not shown in Fig. 1). The power to the platinum wire of the test section was increased by small increments while the vacuum in the tank was maintained at the desired level. All heat-transfer measurements were taken and recorded under equilibrium condi-

---

[1] Graduate Assistant, Department of Mechanical Engineering, North Dakota State University, Fargo, N. D.

[2] Associate Professor, Department of Mechanical Engineering, North Dakota State University, Fargo, N. D.

[3] Numbers in brackets designate References at end of technical brief.

Contributed by the Heat Transfer Division of THE AMERICAN SOCIETY OF MECHANICAL ENGINEERS. Manuscript received by the Heat Transfer Division December 29, 1970.

5 Fischer, S. R., "Measurements of Complete Pool Boiling Heat Transfer Characteristics for Binary Mixtures with Emphasis on Parametric Effects of Concentration," PhD dissertation, Arizona State University, Tempe, Ariz., 1970.

6 Bergles, A. E. and Thompson, W. G., Jr., "The Relationship of Quench Data to Steady-State Pool Boiling Data," *International Journal of Heat and Mass Transfer*, Vol. 13, 1970, pp. 55–68.

7 Veres, David R., "A Comparison of the Transient and Steady State Methods of Obtaining Boiling Heat Transfer Data," MS thesis, Arizona State University, Tempe, Ariz., 1969.

8 Berenson, P. J., "Experiments on Pool Boiling Heat Transfer," *International Journal of Heat and Mass Transfer*, Vol. 5, 1962, pp. 985–999.

9 Markels, M., Jr. and Durfee, R. L., "Studies of Boiling Heat Transfer with Electrical Fields," *AIChE Journal*, July 1965, pp. 716–723.

10 Owens, F. L., Jr., "Measurements of Nucleate Pool Boiling from a Horizontal Surface Comparing Transient and Steady State Techniques," MS thesis, Arizona State University, Tempe, Ariz., 1969.

11 Berenson, P. J., "Film-Boiling Heat Transfer From a Horizontal Surface," JOURNAL OF HEAT TRANSFER, TRANS. ASME, Series C, Vol. 83, No. 3, Aug. 1961, pp. 351–358.

12 Kautzky, D. E. and Westwater, J. W., "Film Boiling of a Mixture on a Horizontal Plate," *International Journal of Heat and Mass Transfer*, Vol. 10, 1967, pp. 253–256.

13 Breen, B. P. and Westwater, J. W., "Effect of Diameter of Horizontal Tubes on Film Boiling Heat Transfer," *Chemical Engineering Progress*, Vol. 58, No. 7, 1962, pp. 67–72.

14 Pomerantz, M. L., "Film Boiling on a Horizontal Tube in Increased Gravity Fields," JOURNAL OF HEAT TRANSFER, TRANS. ASME, Series C, Vol. 86, No. 2, May 1964, pp. 213–219.

On the Rohsenow Pool-Boiling Correlation

C. W. FROST[1] **and K. W. LI**[2]

IN THE past, most of the experimental work used for the evaluation of constants in the Rohsenow pool-boiling correlation was conducted at atmospheric pressure or higher [1,2].[3] The purpose of this technical brief is to report the variation of these constants with vacuum pressure. Fig. 1 shows the schematic diagram of the apparatus used in this investigation. The vacuum tank was a Pyrex, cross-shaped container. All accessories and measuring devices were attached to the tank through blind flanges. A heater in the bottom of the tank was used to heat the water to the saturation temperature. A condenser on the top of the tank cooled the water vapor exhausted by the vacuum pump. The water temperature in the tank was measured with a thermometer calibrated to within 0.2 deg F. The pressure was measured with a Bourdon-tube vacuum gauge calibrated to within 0.5 in. Hg for pressure from atmospheric to 2 psia and a mercury manometer calibrated to within 1.0 mm Hg for pressures less than 2 psia. The heating surface on which the heat-transfer rates were measured consisted of a piece of platinum wire 0.008 in. in diameter and approximately 3 in. in length. The noncorrosive clamping device for the platinum wire supplied electrical power to the wire with no noticeable voltage drop across the wire support. Measurement of the voltage drop across the platinum wire of the test section and the current through the wire provided the data to determine the temperature of the heating surface and the heat-transfer rate.

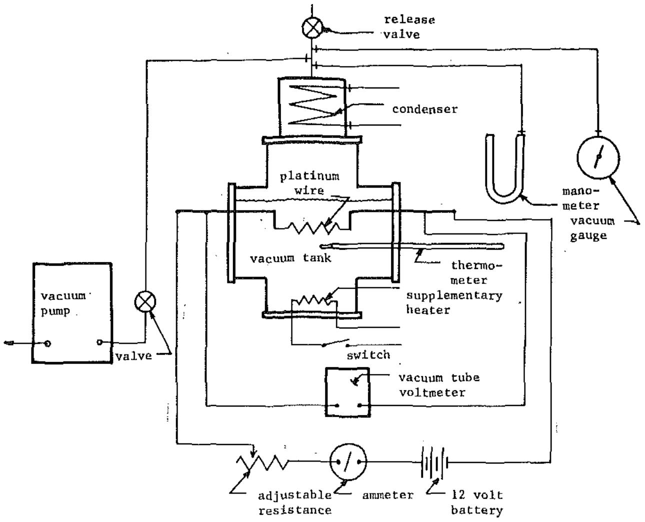

Fig. 1 Schematic diagram of apparatus

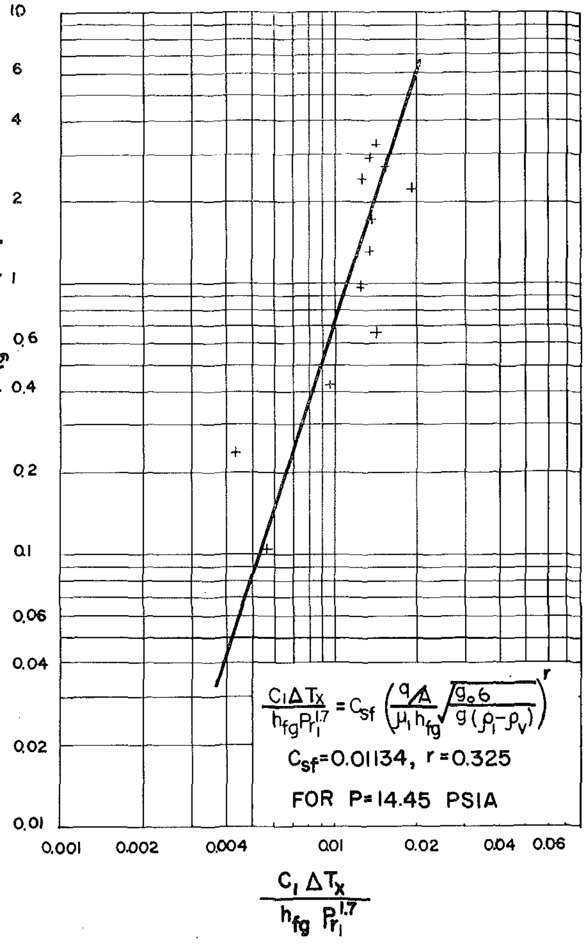

Fig. 2 Correlation of data at 14.45 psia

During all experiments the vacuum tank was filled with distilled water. The water was heated and maintained at the saturation temperature by submerged heater. To prevent induced convective currents around the platinum wire, two fine protective screens were installed just above the submerged heater (not shown in Fig. 1). The power to the platinum wire of the test section was increased by small increments while the vacuum in the tank was maintained at the desired level. All heat-transfer measurements were taken and recorded under equilibrium condi-

---

[1] Graduate Assistant, Department of Mechanical Engineering, North Dakota State University, Fargo, N. D.

[2] Associate Professor, Department of Mechanical Engineering, North Dakota State University, Fargo, N. D.

[3] Numbers in brackets designate References at end of technical brief.

Contributed by the Heat Transfer Division of THE AMERICAN SOCIETY OF MECHANICAL ENGINEERS. Manuscript received by the Heat Transfer Division December 29, 1970.

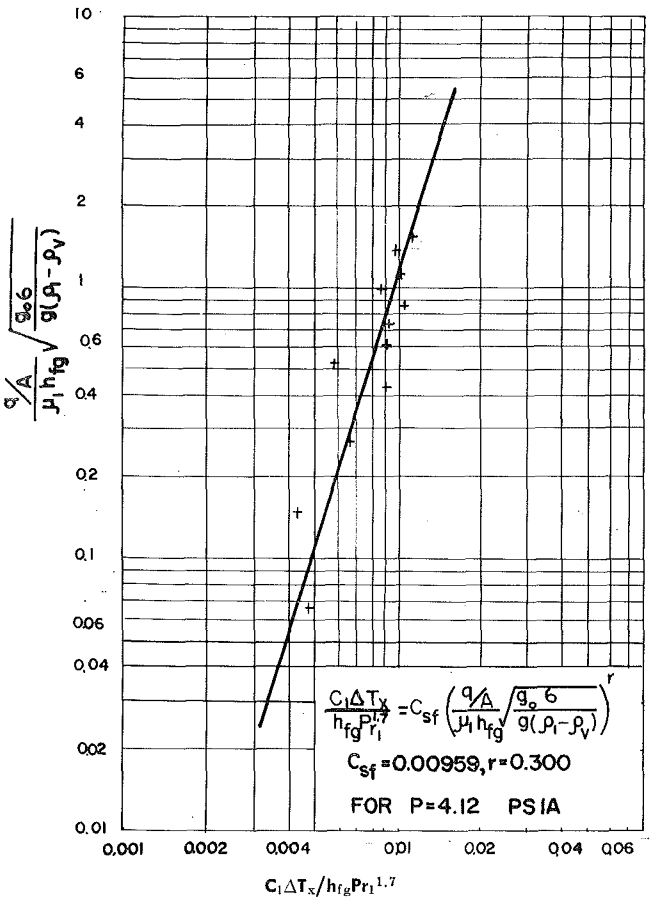

Fig. 3 Correlation of data at 4.12 psia

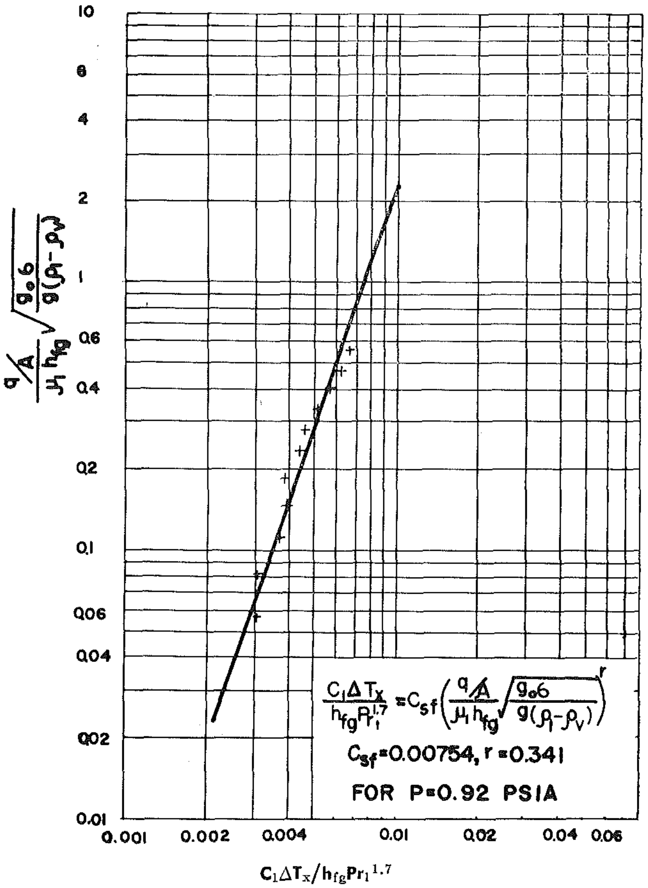

Fig. 5 Correlation of data at 0.92 psia

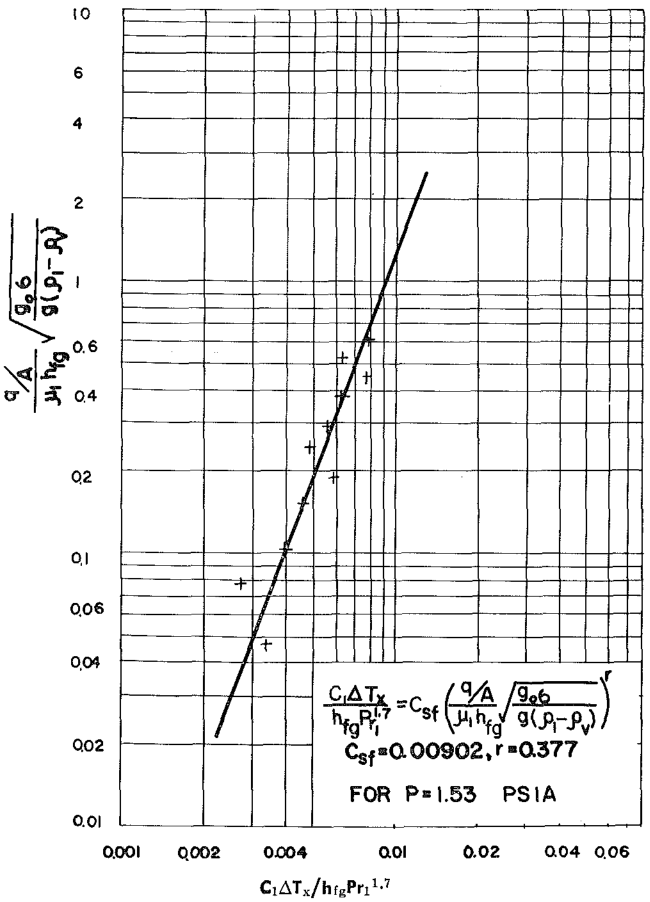

Fig. 4 Correlation of data at 1.53 psia

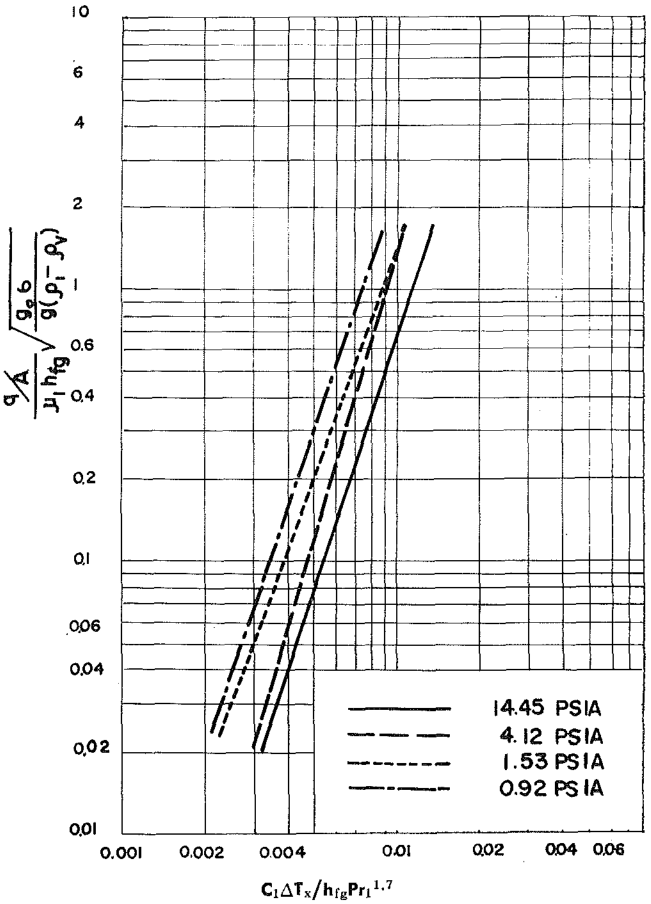

Fig. 6 Comparison of the Rohsenow correlations

Table 1

Pressure	Constant C_{sf}
14.45 psia	0.01134
4.12 psia	0.00959
1.53 psia	0.00902
0.92 psia	0.00754

tions. When the maximum power attainable was reached, the power was disconnected and the platinum wire of the test section was replaced. The same procedures were repeated with different pressures in the vacuum tank. In this investigation 21 runs were carried out. It was indicated that the reproducibility of the data was quite satisfactory.

The typical results which had been correlated by the Rohsenow equation are shown in Figs. 2, 3, 4, and 5. The method of least-squares was used to obtain these curves. It was found that the exponents (r) varied from a minimum of 0.300 to a maximum of 0.377. These values compared very favorably with the value of 0.33 obtained by Rohsenow [2]. The value of the constant of proportionality (C_{sf}) obtained in this work was 0.01134 for a pressure of 14.45 psia. This value compared well with the value of 0.013 obtained by Rohsenow at atmospheric and higher pressures. However, the present experimental results indicated a significant effect of vacuum pressure on this constant as shown in Table 1. Fig. 6 indicates the shifting of the correlation curves over the present pressure range. For example, for the same value of the dimensionless superheat temperature, say equal to 0.005, the dimensionless heat flux had a value of 0.08 at a pressure of 14.45 psia, whereas at a pressure of 0.92 psia it had a value of 0.3. This was almost a fourfold increase in the rate of heat transfer. These findings should be of interest to designers and researchers.

In summary, this experimental work showed that while the vacuum pressure has little influence on the exponent (r), it has a significant effect on the constant (C_{sf}) in the Rohsenow pool-boiling correlation.

References

1 Rohsenow, W. M., "A Method of Correlating Heat-Transfer Data for Surface Boiling of Liquids," TRANS. ASME, Vol. 74, No. 6, Aug. 1952, pp. 969–976.

2 Vachon, R. I., Nix, G. H., and Tanger, G. E., "Evaluation of Constants for the Rohsenow Pool-Boiling Correlation," JOURNAL OF HEAT TRANSFER, TRANS. ASME, Series C, Vol. 90, No. 2, May 1968, pp. 239–247.

Coefficients for Calculation of Freezing in a Semi-Infinite Region

S. W. CHURCHILL[1] **and L. B. EVANS**[2]

CONDUCTION to (or from) a surface at constant temperature, T_W, from (or to) a semi-infinite region at a uniform, initial temperature, T_0, with freezing at an intermediate temperature, T_F, can be described as follows:

$$\frac{\partial T}{\partial t} = K_S \frac{\partial^2 T}{\partial x^2} \qquad x_F > x > 0 \tag{1}$$

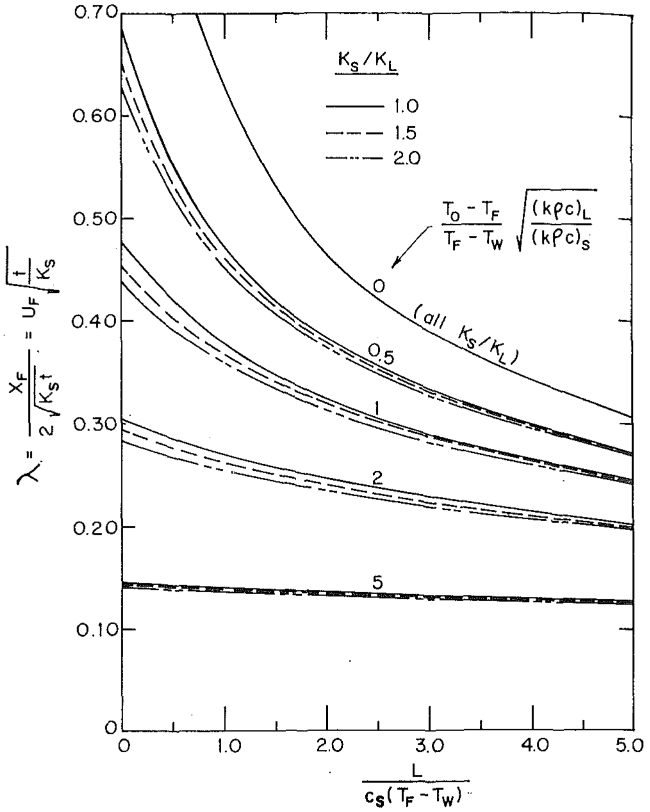

Fig. 1 Freezing front velocity and location as a function of $L/c_S(T_F - T_W)$

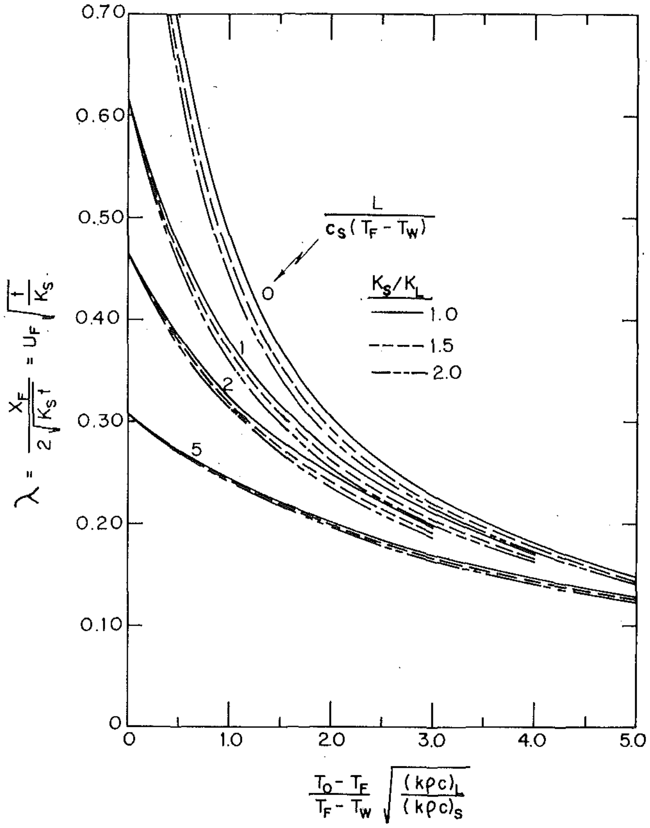

Fig. 2 Freezing front velocity and location as a function of $(T_0 - T_F)\sqrt{(k\rho c)_L}/(T_F - T_W)\sqrt{(k\rho c)_S}$

---

[1] Carl V. S. Patterson Professor of Chemical Engineering, University of Pennsylvania, Philadelphia, Pa.

[2] Associate Professor, Department of Chemical Engineering, Massachusetts Institute of Technology, Cambridge, Mass.

Contributed by the Heat Transfer Division of THE AMERICAN SOCIETY OF MECHANICAL ENGINEERS. Manuscript received by the Heat Transfer Division March 4, 1969; revised manuscript received July 13, 1970.

Table 1

Pressure	Constant C_{sf}
14.45 psia	0.01134
4.12 psia	0.00959
1.53 psia	0.00902
0.92 psia	0.00754

tions. When the maximum power attainable was reached, the power was disconnected and the platinum wire of the test section was replaced. The same procedures were repeated with different pressures in the vacuum tank. In this investigation 21 runs were carried out. It was indicated that the reproducibility of the data was quite satisfactory.

The typical results which had been correlated by the Rohsenow equation are shown in Figs. 2, 3, 4, and 5. The method of least-squares was used to obtain these curves. It was found that the exponents (r) varied from a minimum of 0.300 to a maximum of 0.377. These values compared very favorably with the value of 0.33 obtained by Rohsenow [2]. The value of the constant of proportionality (C_{sf}) obtained in this work was 0.01134 for a pressure of 14.45 psia. This value compared well with the value of 0.013 obtained by Rohsenow at atmospheric and higher pressures. However, the present experimental results indicated a significant effect of vacuum pressure on this constant as shown in Table 1. Fig. 6 indicates the shifting of the correlation curves over the present pressure range. For example, for the same value of the dimensionless superheat temperature, say equal to 0.005, the dimensionless heat flux had a value of 0.08 at a pressure of 14.45 psia, whereas at a pressure of 0.92 psia it had a value of 0.3. This was almost a fourfold increase in the rate of heat transfer. These findings should be of interest to designers and researchers.

In summary, this experimental work showed that while the vacuum pressure has little influence on the exponent (r), it has a significant effect on the constant (C_{sf}) in the Rohsenow pool-boiling correlation.

References

1 Rohsenow, W. M., "A Method of Correlating Heat-Transfer Data for Surface Boiling of Liquids," TRANS. ASME, Vol. 74, No. 6, Aug. 1952, pp. 969–976.

2 Vachon, R. I., Nix, G. H., and Tanger, G. E., "Evaluation of Constants for the Rohsenow Pool-Boiling Correlation," JOURNAL OF HEAT TRANSFER, TRANS. ASME, Series C, Vol. 90, No. 2, May 1968, pp. 239–247.

Coefficients for Calculation of Freezing in a Semi-Infinite Region

S. W. CHURCHILL[1] and L. B. EVANS[2]

CONDUCTION to (or from) a surface at constant temperature, T_W, from (or to) a semi-infinite region at a uniform, initial temperature, T_0, with freezing at an intermediate temperature, T_F, can be described as follows:

$$\frac{\partial T}{\partial t} = K_S \frac{\partial^2 T}{\partial x^2} \qquad x_F > x > 0 \tag{1}$$

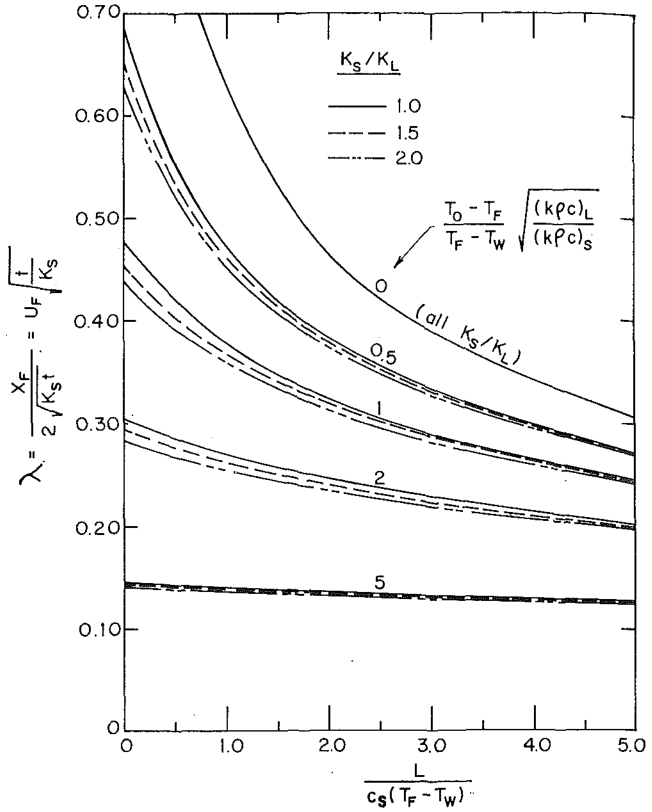

Fig. 1 Freezing front velocity and location as a function of $L/c_S(T_F - T_W)$

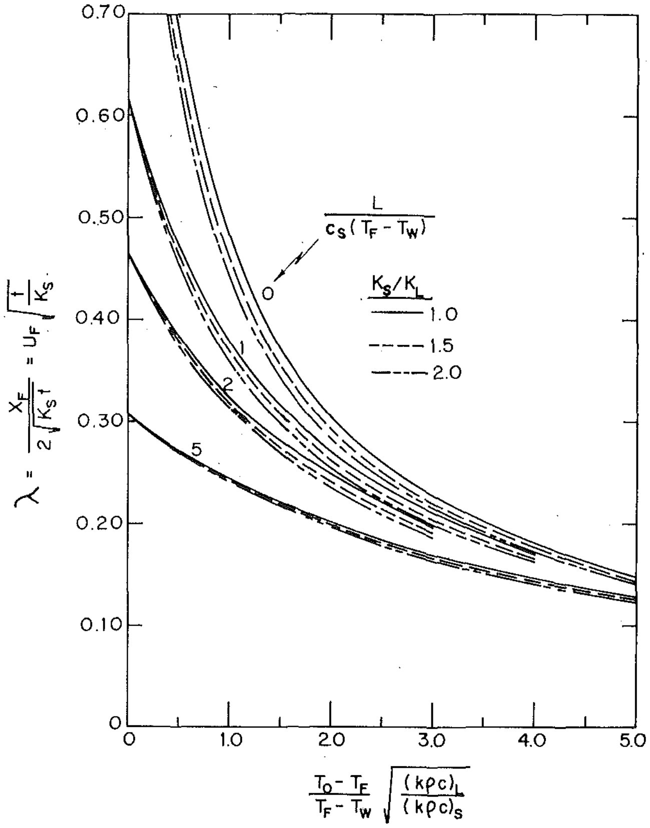

Fig. 2 Freezing front velocity and location as a function of $(T_0 - T_F)\sqrt{(k\rho c)_L}/(T_F - T_W)\sqrt{(k\rho c)_S}$

---

[1] Carl V. S. Patterson Professor of Chemical Engineering, University of Pennsylvania, Philadelphia, Pa.

[2] Associate Professor, Department of Chemical Engineering, Massachusetts Institute of Technology, Cambridge, Mass.

Contributed by the Heat Transfer Division of THE AMERICAN SOCIETY OF MECHANICAL ENGINEERS. Manuscript received by the Heat Transfer Division March 4, 1969; revised manuscript received July 13, 1970.

Table 1 Coefficients for analytical solution for freezing in a semi-infinite region

$\left(\frac{T_0-T_F}{T_F-T_W}\right)\left(\frac{(k\rho c)_L}{(k\rho c)_S}\right)^{1/2}$		0.5		1.0		1.5		2.0		3.0		5.0		10.0	
$\frac{L}{c_S(T_F-T_W)}$	$\frac{K_S}{K_L}$	λ	$\frac{1}{\mathrm{erf}\,\lambda}$	λ	$\frac{1}{\mathrm{erf}\,\lambda}$	λ	$\frac{1}{\mathrm{erf}\,\lambda}$	λ	$\frac{1}{\mathrm{erf}\,\lambda}$	λ	$\frac{1}{\mathrm{erf}\,\lambda}$	λ	$\frac{1}{\mathrm{erf}\,\lambda}$	λ	$\frac{1}{\mathrm{erf}\,\lambda}$
0.0	0.0	0.9451	1.222	0.6584	1.543	0.4991	1.924	0.3982	2.344	0.2803	3.245	0.1731	5.153		
0.0	0.5	0.7371	1.423	0.5137	1.878	0.3973	2.349	0.3245	2.827	0.2376	3.800	0.1547	5.773		
0.0	1.0	0.6841	1.500	0.4769	2.000	0.3708	2.500	0.3046	3.000	0.2253	4.000	0.1488	6.000		
0.0	1.5	0.6504	1.557	0.4536	2.088	0.3538	2.609	0.2917	3.125	0.2172	4.145	0.1447	6.167		
0.0	2.0	0.6256	1.603	0.4365	2.160	0.3413	2.698	0.2821	3.225	0.2110	4.263	0.1415	6.305		
0.5	0.5	0.56861	1.7281	0.44028	2.1437			0.30101	3.0333						
0.5	1.0	0.54564	1.7868	0.41794	2.2446	0.33924	2.7130	0.28552	3.1884	0.21675	4.1528	0.14606	6.1106	0.080264	11.065
0.5	1.5	0.52949	1.8314	0.40282	2.3196	0.32663	2.8101	0.27517	3.3021	0.20962	4.2898	0.14221	6.2739	0.078904	11.255
0.5	2.0	0.51681	1.8686	0.39122	2.3814	0.31702	2.8894	0.26728	3.3948	0.20415	4.4014	0.13921	6.4074	0.077816	11.412
0.5	3.0	0.49723	1.9303	0.37376	2.4820			0.25548	3.5445						
0.5	4.0	0.48221	1.9813	0.36067	2.5651			0.24669	3.6655						
0.5	5.0	0.46997	2.0254	0.35019	2.6345			0.23966	3.7687						
0.5	6.0	0.45963	2.0648	0.34145	2.6967			0.23382	3.8595						
1.0	0.5	0.48353	1.9766	0.39328	2.3702			0.28260	3.2197						
1.0	1.0	0.46985	2.0259	0.37776	2.4581	0.31524	2.9047	0.27005	3.3617	0.20924	4.2973	0.14351	6.2179	0.079798	11.130
1.0	1.5	0.45989	2.0637	0.36689	2.5243	0.30536	2.9927	0.26147	3.4668	0.20293	4.4271	0.13989	6.3765	0.078467	11.317
1.0	2.0	0.45185	2.0956	0.35835	2.5794	0.29768	3.0653	0.25483	3.5531	0.19805	4.5334	0.13706	6.5065	0.077401	11.473
1.0	3.0	0.43907	2.1489	0.34518	2.6698			0.24476	3.6933						
1.0	4.0	0.42897	2.1934	0.33505	2.7444			0.23713	3.8075						
1.0	5.0	0.42054	2.2322	0.32679	2.8088			0.23097	3.9053						
1.0	6.0	0.41329	2.2671	0.31980	2.8660			0.22580	3.9916						
1.5	1.0	0.41979	2.2358	0.34795	2.6501	0.29613	3.0804	0.25711	3.5230	0.20258	4.4346	0.14111	6.3222	0.079341	11.193
1.5	1.5	0.41286	2.2692	0.33964	2.7100	0.28809	3.1615	0.24984	3.6212	0.19694	4.5583	0.13770	6.4765	0.078038	11.379
1.5	2.0	0.40718	2.2974	0.33300	2.7600	0.28177	3.2287	0.24415	3.7021	0.19254	4.6599	0.13503	6.6031	0.076994	11.533
2.0	0.5	0.39033	2.3863	0.33377	2.7541			0.25498	3.5512						
2.0	1.0	0.38341	2.4252	0.32462	2.8262	0.28039	3.2438	0.24606	3.6745	0.19661	4.5658	0.13885	6.4237	0.078895	11.256
2.0	1.5	0.37822	2.4554	0.31799	2.8812	0.27368	3.3192	0.23978	3.7669	0.19152	4.6841	0.13563	6.5740	0.077619	11.441
2.0	2.0	0.37393	2.4809	0.31263	2.9274	0.26834	3.3821	0.23483	3.8434	0.18752	4.7815	0.13310	6.6976	0.076596	11.593
2.0	3.0	0.36124	2.5604	0.30413	3.0040	0.22714	3.9690								
2.0	4.0	0.36694	2.5240	0.29741	3.0680	0.22118	4.0722								
2.0	5.0	0.35637	2.5925	0.29179	3.1236	0.21630	4.1612								
2.0	6.0	0.35209	2.6214	0.28695	3.1735	0.21214	4.2403								
3.0	1.0	0.33285	2.7612	0.28988	3.1431	0.25570	3.5416	0.22802	3.9542	0.18629	4.8124	0.13470	6.6191	0.078029	11.381
3.0	1.5	0.32955	2.7869	0.28528	3.1911	0.25074	3.6086	0.22315	4.0375	0.18206	4.9217	0.13181	6.7624	0.076805	11.561
3.0	2.0	0.32679	2.8088	0.28151	3.2314	0.24674	3.6647	0.21925	4.1069	0.17870	5.0122	0.12953	6.8804	0.075821	11.711
5.0	1.0	0.27324	3.3243	0.24546	3.6831	0.22201	4.0575	0.20206	4.4457	0.17020	5.2573	0.12757	6.9846	0.076400	11.622
5.0	1.5	0.27147	3.3449	0.24277	3.7224	0.21889	4.1135	0.19880	4.5167	0.16709	5.3534	0.12519	7.1161	0.075268	11.797
5.0	2.0	0.26998	3.3625	0.24053	3.7556	0.21633	4.1607	0.19615	4.5762	0.16458	5.4335	0.12328	7.2249	0.074355	11.941
10.0	1.0	0.20372	4.4105	0.18914	4.7416	0.17606	5.0858	0.16431	5.4422	0.14421	6.1880	0.11428	7.7887	0.072823	12.191
10.0	1.5	0.20302	4.4253	0.18796	4.7705	0.17458	5.1279	0.16265	5.4966	0.14242	6.2645	0.11266	7.8999	0.071874	12.352
10.0	2.0	0.20242	4.4380	0.18698	4.7951	0.17335	5.1635	0.16128	5.5425	0.14096	6.3288	0.11134	7.9927	0.071104	12.485

$$\left(\frac{T_0-T_F}{T_F-T_W}\right)\left(\frac{(k\rho c)_L}{(k\rho c)_S}\right)^{1/2} = 0;\ \text{all}\ \frac{K_S}{K_L}$$

$L/c_S(T_F-T_W)$	0.5	1.0	1.5	2.0	3.0	5.0	10.0
λ	0.8006	0.6201	0.5256	0.4648	0.3881	0.3064	0.2200
1/erf λ	1.347	1.614	1.843	2.045	2.399	2.983	4.093

$$\frac{\partial T}{\partial t} = K_L\frac{\partial^2 T}{\partial x^2} \qquad x > x_F \tag{2}$$

$$k_S\left(\frac{\partial T}{\partial x}\right)_{x_F^-} - k_L\left(\frac{\partial T}{\partial x}\right)_{x_F^+} = \rho L\frac{dx_F}{dt} \tag{3}$$

$$T_{x_F^-} = T_{x_F^+} = T_F \tag{4}$$

$$T = T_W \qquad x = 0 \quad \text{and} \quad t > 0 \tag{5}$$

$$T = T_0 \qquad t = 0 \tag{6}$$

$$T \rightarrow T_0 \qquad \text{as} \quad x \rightarrow \infty \tag{7}$$

where T is temperature, t is time, x is distance from the constant-temperature surface, x_F is the location of the freezing front, k is the thermal conductivity, K is the thermal diffusivity, ρ is the density, and L is the latent heat of solidification. Subscripts S and L indicate the frozen and unfrozen regions, respectively.

This formulation postulates that the frozen and unfrozen regions are homogeneous and that the physical properties of the two regions are independent of temperature. The thermal conductivity and the thermal diffusivity are different but the density is the same for the two regions. No convection or diffusion of material occurs.

The solution for this problem can be written [1][3] as follows:

$$\frac{T - T_W}{T_F - T_W} = \frac{\mathrm{erf}\,(x_S/2\sqrt{K_S t})}{\mathrm{erf}\,(\lambda)} \tag{8}$$

$$\frac{T_0 - T}{T_0 - T_F} = \frac{\mathrm{erfc}\,(x_L/2\sqrt{K_L t})}{\mathrm{erfc}\,(\lambda\sqrt{K_S/K_L})} \tag{9}$$

$$\frac{j\sqrt{\pi K_S t}}{k_S(T_F - T_W)} = \frac{1}{\mathrm{erf}\,(\lambda)} \tag{10}$$

$$x_F/\sqrt{K_S t} = 2\lambda \tag{11}$$

and

$$U_F\sqrt{t/K_S} = \lambda \tag{12}$$

where j is the heat flux density at $x = 0$, U_F is the velocity of the freezing front, and λ is the root of the transcendental equation:

$$\frac{e^{-\lambda^2}}{\lambda\,\mathrm{erf}\,(\lambda)} - \left(\frac{T_0 - T_F}{T_F - T_W}\right)\left[\frac{(k\rho c)_L}{(k\rho c)_S}\right]^{1/2}\frac{e^{-\lambda^2 K_S/K_L}}{\lambda\,\mathrm{erfc}\,(\lambda\sqrt{K_S/K_L})} = \frac{L\sqrt{\pi}}{c_S(T_F - T_W)} \tag{13}$$

where c is the heat capacity.

Apparently only a few values of λ have been tabulated [1] although Horvay and Henzel [2] constructed nomograms from which λ can be read to perhaps two significant figures. Therefore equation (13) was solved on a digital computer for a wide spectrum of values of K_S/K_L, $L/c_S(T_F - T_W)$ and $(T_0 - T_F)\sqrt{(k\rho c)_L}/(T_F - T_W)\sqrt{(k\rho c)_S}$. The computed values of λ are given in Table 1 to four or five significant figures. These values are plotted in Figs. 1 and 2 for purposes of illustration. Thus the values of λ can be interpreted directly as the dimensionless location of the freezing front, $x_F/2\sqrt{K_S t}$, and also as the

---

[3] Numbers in brackets designate References at end of technical brief.

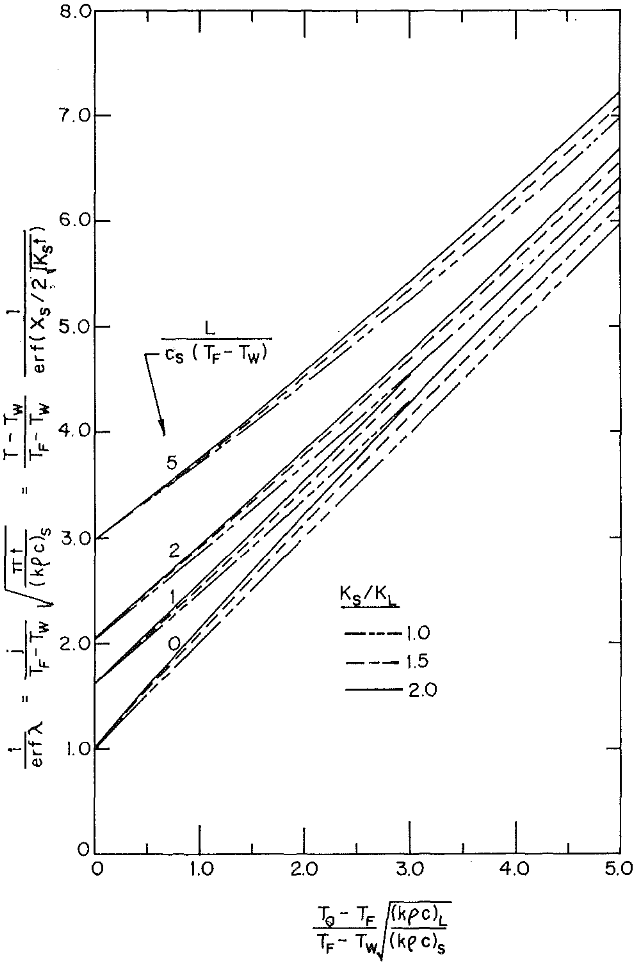

Fig. 3 Temperature distribution and heat flux density as a function of $L/c_S(T_F - T_W)$

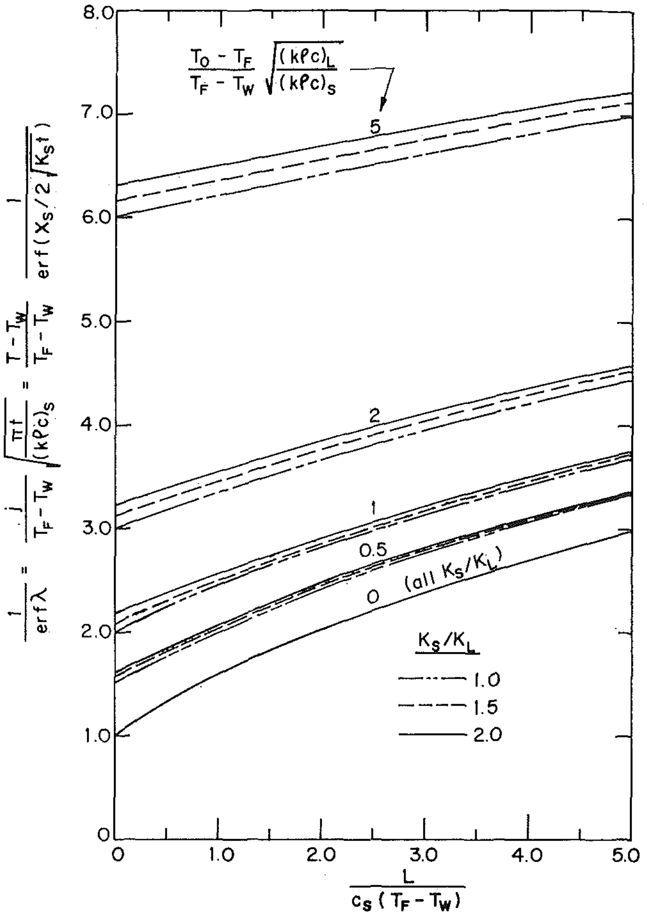

Fig. 4 Temperature distribution and heat flux density as a function of $(T_0 - T_F)\sqrt{(k\rho c)_L}/(T_F - T_W)\sqrt{(k\rho c)_S}$

dimensionless freezing front velocity $U_F\sqrt{t/K_S}$. The corresponding values of 1/erf (λ) are included in Table 1 and are plotted in Figs. 3 and 4. These values may be interpreted directly as the dimensionless heat flux $j\sqrt{\pi t}/(T_F - T_W)\sqrt{(k\rho c)_S}$, and also as the dimensionless temperature in the frozen region, $(T - T_W)/(T_F - T_W)$ erf $(x_S/2\sqrt{K_S t})$. The ordinate of Figs. 3 and 4 multiplied by $(T_F - T_W)\sqrt{(k\rho c)_S}/(T_0 - T_W)\sqrt{(k\rho c)_L}$, i.e., $(T_F - T_W)\sqrt{(k\rho c)_S}/(T_0 - T_W)\sqrt{(k\rho c)_L}$ erf λ, can be interpreted as the ratio of the heat flux at the surface with freezing to that without freezing ($L = 0$). Plots such as Figs. 1–4 can be constructed for particular regions to enhance the accuracy of interpolation between the tabulated values.

References

1 Carslaw, H. S., and Jaeger, J. C., *Conduction of Heat in Solids*, 2nd ed., Oxford University at the Clarendon Press, 1959, pp. 281–287.

2 Horvay, G., and Henzel, J. G., "Freezing of Liquid Metal in a Mold," *Trans. Metallurgical Soc. AIME*, Vol. 215, April 1959, p. 258.

Heat Transfer by Conduction and Radiation in Absorbing and Scattering Materials

J. B. BERGQUAM[1] and R. A. SEBAN[2]

Introduction

THE TWO-FLUX model is a classic differential approximation to the equations of transfer which is attractive because its simple form provides for analytical results in some cases and rather simple numerical ones in others. Hamaker [1][3] and Larkin and Churchill [2] have used the two-flux model to specify the radiative fluxes in semitransparent materials. The approach taken in reference [2] is to linearize the two-flux equations by assuming a linear variation in temperature across the medium. This simplification leads to a closed-form solution for the radiative fluxes but also requires that the net radiative flux be constant and therefore restricts the applicability of the solution.

Considering the situation of parallel walls separated by a distance L with a gray scattering and absorbing medium, with albedo ω_0 and extinction coefficient K_t, and assuming an index of refraction of unity, and defining q^+ and q^- as the fluxes, the transport equations, as given by Hottel and Sarofim [3], can be written

---

[1] Assistant Professor, Sacramento State College, Sacramento, Calif.; formerly, University of California, Berkeley, Calif.

[2] Professor and Chairman, Department of Mechanical Engineering, University of California, Berkeley, Calif.

Contributed by the Heat Transfer Division of THE AMERICAN SOCIETY OF MECHANICAL ENGINEERS. Manuscript received by the Heat Transfer Division March 23, 1970; revised manuscript received July 23, 1970.

[3] Numbers in brackets designate References at end of technical brief.

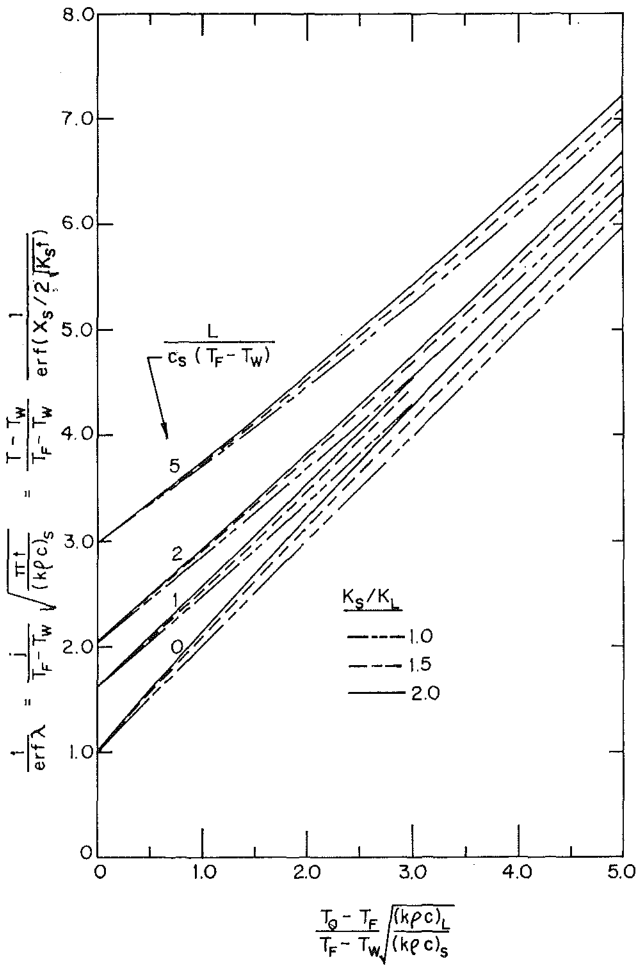

Fig. 3 Temperature distribution and heat flux density as a function of $L/c_S(T_F - T_W)$

dimensionless freezing front velocity $U_F\sqrt{t/K_S}$. The corresponding values of 1/erf (λ) are included in Table 1 and are plotted in Figs. 3 and 4. These values may be interpreted directly as the dimensionless heat flux $j\sqrt{\pi t}/(T_F - T_W)\sqrt{(k\rho c)_S}$, and also as the dimensionless temperature in the frozen region, $(T - T_W)/(T_F - T_W)$ erf $(x_S/2\sqrt{K_S t})$. The ordinate of Figs. 3 and 4 multiplied by $(T_F - T_W)\sqrt{(k\rho c)_S}/(T_0 - T_W)\sqrt{(k\rho c)_L}$, i.e., $(T_F - T_W)\sqrt{(k\rho c)_S}/(T_0 - T_W)\sqrt{(k\rho c)_L}$ erf λ, can be interpreted as the ratio of the heat flux at the surface with freezing to that without freezing ($L = 0$). Plots such as Figs. 1–4 can be constructed for particular regions to enhance the accuracy of interpolation between the tabulated values.

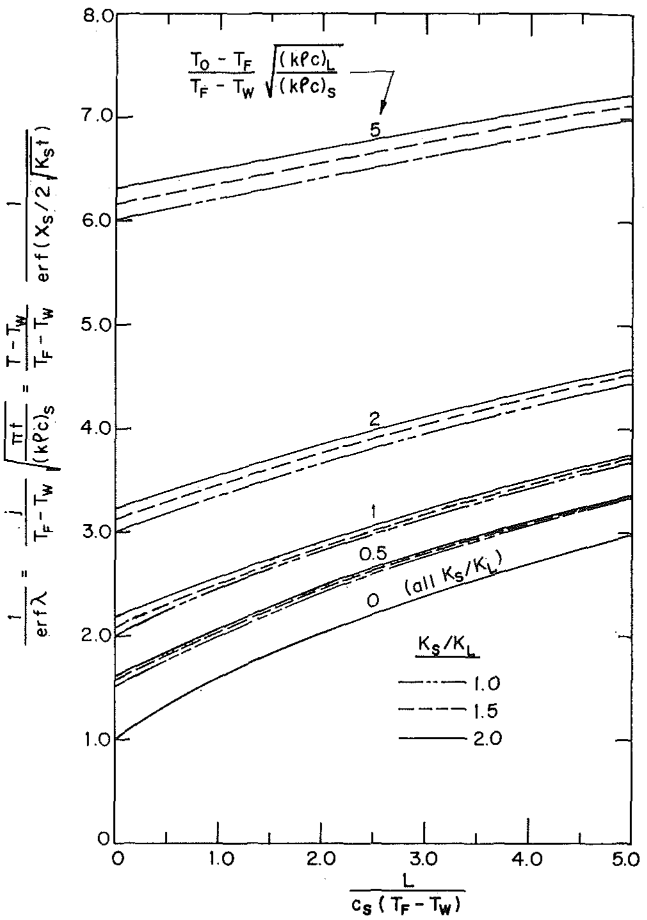

Fig. 4 Temperature distribution and heat flux density as a function of $(T_0 - T_F)\sqrt{(k\rho c)_L}/(T_F - T_W)\sqrt{(k\rho c)_S}$

References

1 Carslaw, H. S., and Jaeger, J. C., *Conduction of Heat in Solids*, 2nd ed., Oxford University at the Clarendon Press, 1959, pp. 281–287.

2 Horvay, G., and Henzel, J. G., "Freezing of Liquid Metal in a Mold," *Trans. Metallurgical Soc. AIME*, Vol. 215, April 1959, p. 258.

Heat Transfer by Conduction and Radiation in Absorbing and Scattering Materials

J. B. BERGQUAM[1] **and R. A. SEBAN**[2]

Introduction

THE TWO-FLUX model is a classic differential approximation to the equations of transfer which is attractive because its simple form provides for analytical results in some cases and rather simple numerical ones in others. Hamaker [1][3] and Larkin and Churchill [2] have used the two-flux model to specify the radiative fluxes in semitransparent materials. The approach taken in reference [2] is to linearize the two-flux equations by assuming a linear variation in temperature across the medium. This simplification leads to a closed-form solution for the radiative fluxes but also requires that the net radiative flux be constant and therefore restricts the applicability of the solution.

Considering the situation of parallel walls separated by a distance L with a gray scattering and absorbing medium, with albedo ω_0 and extinction coefficient K_t, and assuming an index of refraction of unity, and defining q^+ and q^- as the fluxes, the transport equations, as given by Hottel and Sarofim [3], can be written

---

[1] Assistant Professor, Sacramento State College, Sacramento, Calif.; formerly, University of California, Berkeley, Calif.

[2] Professor and Chairman, Department of Mechanical Engineering, University of California, Berkeley, Calif.

Contributed by the Heat Transfer Division of THE AMERICAN SOCIETY OF MECHANICAL ENGINEERS. Manuscript received by the Heat Transfer Division March 23, 1970; revised manuscript received July 23, 1970.

[3] Numbers in brackets designate References at end of technical brief.

$$\frac{dq^+}{d\tau} = -2(1-\omega_0 f)q^+ + 2\omega_0 b q^- + 2(1-\omega_0)\sigma T^4 \quad (1)$$

and

$$-\frac{dq^-}{d\tau} = -2(1-\omega_0 f)q^- + 2\omega_0 b q^+ + 2(1-\omega_0)\sigma T^4 \quad (2)$$

where $d\tau = K_t dx$ and f and b are factors which characterize the scattering and which are equal to 0.5 for isotropic scattering.

In the case of radiative equilibrium the net radiative flux $q^+ - q^-$ is constant depending only on the radiosities of the surfaces and the optical thickness, $\tau_0 = K_t L$, of the medium. For a nonscattering medium in radiative equilibrium, Adrianov and Polyak [4] have shown the flux, calculated from (1) and (2) with $\omega_0 = 0$, to be consistently lower than that given by an exact solution for values of optical thickness from 0 to 10; the maximum difference occurring for large values of τ_0 and being about 25 percent. Traugott and Wang [5] indicate that the prediction from the two-flux model for the nonscattering case can be substantially improved by changing the coefficient 2 in the first two terms on the right-hand side of equations (1) and (2) to $\sqrt{3}$.

For problems of combined conduction and radiation, the error in the total heat flux, with the net radiative flux specified by equations (1) and (2), might be expected to be less. This can be visualized by considering the case of pure scattering ($\omega_0 = 1$), in which there is no interaction between the conductive and radiative modes of transfer and the error, then arising out of the radiative mode, would be reduced in proportion to the relative contribution of the conductive mode. With an albedo of less than unity there is, of course, interaction with the conductive mode, and equations (1) and (2) must be solved in conjunction with the local energy balance

$$\frac{d}{d\tau}\left[-kK_t\frac{dT}{d\tau} + (q^+ - q^-)\right] = 0 \quad (3)$$

Evaluation of the two-flux model can then be made by solving equations (1), (2), and (3) and comparing the results with exact solutions as given by Viskanta [6]. Such an appraisal is important, for instance, with reference to the nongray problem in which the equations of transfer must be applied in wavelength increments, while the energy equation must be satisfied on a total basis and the two-flux model substantially reduces the complexity of these calculations.

For comparison with Viskanta's results, it is convenient to put equations (1), (2), and (3) in nondimensional form with: $\xi = \tau/\tau_0$, $\theta = T/T_1$, $\theta_2 = T_2/T_1$, $N = 4\sigma T_1^3/kK_t$, $\Phi^+ = q^+/\sigma T_1^4$, $\Phi^- = q^-/\sigma T_1^4$, $\Phi = \Phi^+ - \Phi^-$. With the above definitions equations (1), (2), and (3) become

$$\frac{d\Phi^+}{d\xi} = -2\tau_0(1-\omega_0 f)\Phi^+ + 2\tau_0\omega_0 b\Phi^- + 2\tau_0(1-\omega_0)\theta^4 \quad (1a)$$

$$-\frac{d\Phi^-}{d\xi} = -2\tau_0(1-\omega_0 f)\Phi^- + 2\tau_0\omega_0 b\Phi^+ + 2\tau_0(1-\omega_0)\theta^4 \quad (2a)$$

and

$$\frac{d}{d\xi}\left(-\frac{d\theta}{d\xi} + \frac{1}{4}\tau_0 N\Phi\right) = 0 \quad (3a)$$

with boundary conditions

$$\xi = 0:\quad \Phi^+ = \epsilon_1 + \rho_1\Phi^-,\quad \theta = 1$$

$$\xi = 1:\quad \Phi^- = \epsilon_2\theta_2^4 + \rho_2\Phi^+,\quad \theta = \theta_2$$

Note that the total heat flux, q'', is given by $q'' = -k\frac{dT}{dx} + (q^+ - q^-)$, or in dimensionless form

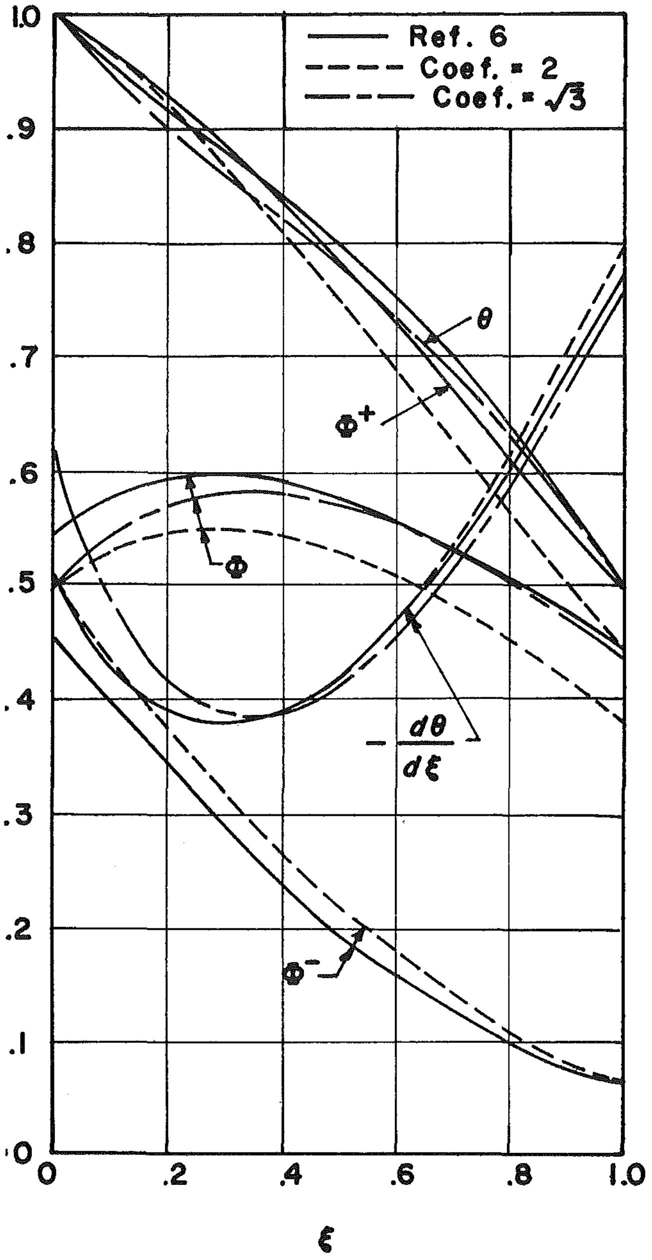

Fig. 1 Variation of θ, $d\theta/d\xi$, and radiant fluxes with optical depth for $N = 10$, $\omega_0 = 0.5$, $\tau_0 = \epsilon_1 = \epsilon_2 = 1$, $\theta_2 = 0.5$

$$\Psi = \frac{q''}{kK_t T_1} = -\frac{1}{\tau_0}\frac{d\theta}{d\xi} + \frac{N}{4}\Phi \quad (4)$$

This system is solved numerically, though to avoid convergence problems equations (1*a*) and (2*a*) are solved analytically for $\Phi^+ + \Phi^-$ and $\Phi^+ - \Phi^-$, reference [7]. The iterative method essentially involves the selection of a linear temperature profile, the solution of (1*a*) and (2*a*) to obtain Φ^+ and Φ^-, the solution of (3*a*) for a new $\theta = \theta(\xi)$ and repetition of the process. The temperatures and radiant fluxes were calculated for 41 values of ξ, i.e., values of ξ between 0 and 1 in increments of 0.025, and the iterations were terminated when two successive temperature distributions differed by less than 1 percent. It should be noted that, in almost all cases, this iterative solution requires less than 5 sec of computer time on a CDC 6400 computer.

A Typical Case

Fig. 1 illustrates the results obtained for the particular case of

Table 1

$N = 10,\ \tau_0 = \epsilon_1 = \epsilon_2 = 1,\ \omega_0 = 0.5$	θ_2	$d\theta/d\xi\vert_0$		$\Phi(0)$		Ψ	
		V	P	V	P	V	P
1	0.5	−0.5175	−0.5180	0.5428	0.4929	1.874	1.750
2*	0.5		−0.6171		0.4906		1.844
3	0.1	−0.7592	−0.7423	0.6412	0.5625	2.362	2.148
$N = 1,\ \tau_0 = \epsilon_1 = \epsilon_2 = 1,\ \theta_2 = 0.5$	ω_0						
4	0	−0.5019	−0.5024	0.5656	0.5178	0.6433	0.6318
5	0.5	−0.4967	−0.4965	0.5626	0.5146	0.6374	0.6251
6	1.0	−0.5000	−0.5000	0.5251	0.4688	0.6313	0.6172
$N = 10,\ \tau_0 = \epsilon_1 = \epsilon_2 = 1,\ \theta_2 = 0.5$	ω_0						
7	0.1		−0.6044		0.4729		1.787
8	0.5	−0.5175	−0.5180	0.5428	0.4929	1.874	1.750
9	1.0	−0.5000	−0.5000	0.5191	0.4688	1.798	1.672
$N = 10,\ \tau_0 = \epsilon_1 = \epsilon_2 = 1,\ \omega_0 = 0$	θ_2						
10	0.1	−0.8017	−0.8016	0.6488	0.5983	2.424	2.302
11*	0.1		−0.9423		0.5963		2.433
$N = 1,\ \tau_0 = 1,\ \theta_2 = 0.5,\ \omega_0 = 0.5$							
12	$\epsilon_1 = \epsilon_2 = 1.0$	−0.4967	−0.4965	0.5626	0.5146	0.6374	0.6251
13	$\epsilon_1 = 1.0;\ \epsilon_2 = 0$	−0.4727	−0.4737	0.4086	0.4070	0.5748	0.5754
14	$\epsilon_1 = 0;\ \epsilon_2 = 1.0$	−0.5517	−0.5524	0.0	0.0	0.5517	0.5524
15	$\epsilon_1 = \epsilon_2 = 0$	−0.5288	−0.5309	0.0	0.0	0.5288	0.5309

* Calculations made with coefficient changed from 2 to $\sqrt{3}$.

$\epsilon_1 = \epsilon_2 = \tau_0 = 1$, $\omega_0 = 0.5$, $\theta_2 = 0.5$, and $N = 10$, with isotropic scattering, i.e., $f = b = 0.5$. For this case the total flux Ψ is 1.750 compared to the exact value of 1.874 as given by Viskanta. The approximate temperature distribution corresponds almost exactly to the exact solution but the net radiation flux is less than the exact value and it is primarily this lower radiation flux that produces the disparity in the total flux. Further, the error in the total flux arises from the progressive under- and over-prediction of Φ^+ and Φ^-. Correction requires less attenuation of Φ^+, an effect which will also reduce the increase in Φ^-, and the Traugott suggestion of a change in coefficients from 2 to $\sqrt{3}$ produces this kind of effect. This prediction has been made by changing the 2 in the first two terms on the right-hand side of equations (1*a*) and (2*a*) to $\sqrt{3}$ and is included in Fig. 1. The result is that Φ is improved for $\xi > 0.3$ and $d\theta/d\xi$ is not much altered, so that the total flux Ψ is indeed increased, to 1.844. Near $\xi = 0$, however, Φ remains too small and the larger total flux is attained by a larger conductive flux. Thus the improved agreement in radiant and conductive fluxes for $\xi > 0.3$ is not accompanied by a similar improvement near $\xi = 0$.

Other Cases

Table 1 summarizes additional comparisons that can be made to Viskanta's results for $\tau_0 = 1$, where the temperature gradient $d\theta/d\xi|_{\xi=0}$ and the radiant flux $\Phi(0)$, at the high-temperature boundary, and the total heat flux are compared. The present results, P, are all for the coefficients in equations (1*a*) and (2*a*) being 2, as they appear in those equations, except for the previously discussed case of line 2 and the nonscattering case of line 11 where $\sqrt{3}$ was used with a consequent improvement in the distribution of Φ. The conclusions to be drawn for the nonscattering case are similar to those drawn for the case presented in Fig. 1. The comparisons for $\Phi(0)$ show the predicted radiation flux always to be low near $\xi = 0$. Although it is noted from lines 12, 13, 14, and 15 that as the emissivity of either one or both of the surfaces decreases, the correspondence between the exact and approximate solutions improves.

Note can also be taken of the effect of nonisotropy in the scattering to the extent permitted by the two-flux analysis in which, for completely forward scattering $f = 0.6$, $b = 0.4$ and for backward $f = 0.4$, $b = 0.6$. For this, exact results are not available, so that comparison can be made only to the isotropic result of the two-flux model. For $\tau_0 = 1$ and black walls, with $\omega_0 = 1$ the results are: with $f = 0.6$, $b = 0.4$, $\Phi = 0.5208$; with $f = 0.5$, $b = 0.5$, $\Phi = 0.4688$; and with $f = 0.4$, $b = 0.6$, $\Phi = 0.4261$. For the case corresponding to Fig. 1, or line 1 of Table 1, the fluxes Ψ are 1.821, 1.750, and 1.687 respectively, while the radiant fluxes $\Phi^+(1)$ are 0.4669, 0.4421, and 0.4207.

Conclusions

These limited results show that the two-flux model gives acceptable values of the total flux Ψ for $N < 10$ and $\tau_0 = 1$. For the system considered this flux is the primary engineering result. Should results associated with the radiant flux be desired, such as the prediction of the radiation which would emerge from a small hole pierced through the cold boundary at $\xi = 1$, the two-flux model will produce values substantially lower than the exact analysis, and for these cases there are indications that a change in the coefficients of the absorption and scattering terms will lead to improved results.

References

1 Hamaker, H. C., "Radiation and Heat Conduction in Light Scattering Material," *Philips Res. Reps.*, Vol. 2, 1947, pp. 55–67, pp. 103–111, 112–125, 420–425.

2 Larkin, B. K., and Churchill, S. W., "Heat Transfer by Radiation Through Porous Insulations," *AIChE Journal*, Vol. 5, 1959, pp. 467–474.

3 Hottel, H. C., and Sarofim, A. F., *Radiative Transfer*, McGraw-Hill, New York, 1967.

4 Adrianov, V. N., and Polyak, G. L., "Differential Methods for Studying Radiant Heat Transfer," *International Journal of Heat and Mass Transfer*, Vol. 6, 1963, pp. 355–362.

5 Traugott, S. C., and Wang, K. C., "On Differential Methods for Radiant Heat Transfer," *International Journal of Heat and Mass Transfer*, Vol. 7, 1964, pp. 269–273.

6 Viskanta, R., "Heat Transfer by Conduction and Radiation in Absorbing and Scattering Materials," JOURNAL OF HEAT TRANSFER, TRANS. ASME, Series C, Vol. 87, No. 1, Feb. 1965, pp. 143–150.

7 Bergquam, J. B., "Heat Transfer by Conduction and Radiation in Scattering, Absorbing, and Emitting Materials," PhD thesis, University of California, Berkeley, Calif., Dec. 1968.

Heat Transfer From an Oscillating Horizontal Wire

B. F. ARMALY[1] **and D. H. MADSEN**[2]

The effect of vibration on heat transfer by natural convection has been investigated experimentally using a thin wire, 0.010 in. in diameter, and air as a convection medium. Horizontal reciprocating motion of varying amplitudes, peak-to-peak values of 0–2.655 in., and frequencies, 0–20 cps, was applied to an electrically heated horizontal wire. The average wire velocity (frequency times total path length traveled per cycle by the wire) was used to correlate and predict the experimental results.

Introduction

IT HAS been well established that mechanical or acoustical vibrations of heated surfaces increase the transfer of heat. A detailed review of this effect was made by Richardson [1].[3] An increase in either amplitude or frequency increases the heat transfer coefficient. The range of frequencies and amplitudes which have been investigated in the literature can be separated into two categories. One deals with small amplitudes and high frequencies while the other deals with low frequencies and large amplitudes. The present study covers large amplitude vibrations with the intervening frequencies that have not been employed in previous investigations. The data fit in the regime of convection by time-average steady-flow equivalent as defined by Richardson [1].

Apparatus

The experimental apparatus consisted of a crank slider mechanism which supplied a reciprocating motion of various amplitudes, peak-to-peak values of 0–2.655 in., and frequencies, 0–20 cps, to the test section. The average velocity resulting from this horizontal reciprocating motion varied between 0 and 8.8 fps. The test section, from which the heat transfer was measured, consisted of a horizontal platinum wire 0.010 in. in diameter and 6.0625 in. in length. The wire was held horizontally by a U-shaped frame. The surrounding medium was air at approximately 80 deg F. Measurements of the voltage drop across the test section and the direct current flowing through it, at steady state, provided information to calculate the surface temperature and the convected heat transferred. The temperature difference between the heated surface and the surrounding air was varied between 160 and 500 deg F.

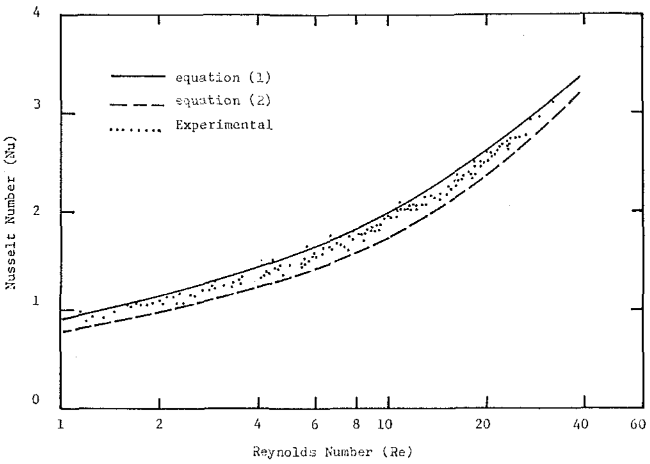

Fig. 1 Correlation of experimental results

Results

The experimental results are shown in Fig. 1 as a function of the Nusselt number, $\mathrm{Nu} = hD/K$, and the Reynolds number, $\mathrm{Re} = VD/\nu$, where h is the convective heat transfer coefficient, D is the wire diameter, V the average wire velocity due to the reciprocating motion (frequency times twice the peak-to-peak amplitude), K the thermal conductivity, and ν the kinematic viscosity. All physical properties refer to the convective medium (air in this experiment) and were evaluated at the film temperature $T_f = (T_s + T_\infty)/2$, where T_s and T_∞ are the temperatures of the heated wire and the surroundings respectively. As can be seen from Fig. 1, the experimental results could be predicted with an error of less than 10 percent by using the relations obtained by Hilpert [2] for forced convection from a wire in a uniform air stream. This relation is given by

$$\mathrm{Nu} = C\,\mathrm{Re}^n \tag{1}$$

where C and n are constants and dependent on the Reynolds number as follows:

	n	C
$1 < \mathrm{Re} < 4$	0.33	0.891
$4 < \mathrm{Re} < 40$	0.385	0.821

The experimental results were also compared, in Fig. 1, with the correlation of Penny and Deaver [3] for the forced-convection vibration region which is given by

$$\mathrm{Nu}/(\mathrm{Pr})^{0.3} = 0.35 + 0.48\,\mathrm{Re}^{0.52} \tag{2}$$

where $\mathrm{Pr} = \mu c_p/K$ is the Prandtl number, μ the dynamic viscosity, and c_p the constant-pressure specific heat. The Prandtl number can be considered as constant in the experimental range at a value of 0.705. The predicted values of the Nusselt number, using (2), differ by less than 17 percent from the experimental values. This appears to be mainly due to the differences in the region covered by the two experiments. The experimental Nusselt number for the case of no vibration, free convection only, was determined at various temperature levels. Its magnitude over the experimental range varied between 0.745 and 0.791 and was within 8 percent of the predicted ones [4]. An error analysis also confirmed this level of accuracy for the experimental results.

Conclusions

The results indicate that an increase in either the amplitude or the frequency of the vibration will increase the heat transferred. Also, in the region covered by this experiment, the effect of vibration could be predicted with reasonable accuracy by using the

---

[1] Assistant Professor, Department of Mechanical and Aerospace Engineering, University of Missouri–Rolla, Rolla, Mo. Assoc. Mem. ASME.

[2] Professor, Department of Mechanical Engineering, University of Iowa, Iowa City, Iowa. Mem. ASME.

[3] Numbers in brackets designate References at end of technical brief.

Contributed by the Heat Transfer Division of THE AMERICAN SOCIETY OF MECHANICAL ENGINEERS. Manuscript received by the Heat Transfer Division May 25, 1970; revised manuscript received July 23, 1970.

5 Traugott, S. C., and Wang, K. C., "On Differential Methods for Radiant Heat Transfer," *International Journal of Heat and Mass Transfer*, Vol. 7, 1964, pp. 269–273.

6 Viskanta, R., "Heat Transfer by Conduction and Radiation in Absorbing and Scattering Materials," JOURNAL OF HEAT TRANSFER, TRANS. ASME, Series C, Vol. 87, No. 1, Feb. 1965, pp. 143–150.

7 Bergquam, J. B., "Heat Transfer by Conduction and Radiation in Scattering, Absorbing, and Emitting Materials," PhD thesis, University of California, Berkeley, Calif., Dec. 1968.

Heat Transfer From an Oscillating Horizontal Wire

B. F. ARMALY[1] **and D. H. MADSEN**[2]

The effect of vibration on heat transfer by natural convection has been investigated experimentally using a thin wire, 0.010 in. in diameter, and air as a convection medium. Horizontal reciprocating motion of varying amplitudes, peak-to-peak values of 0–2.655 in., and frequencies, 0–20 cps, was applied to an electrically heated horizontal wire. The average wire velocity (frequency times total path length traveled per cycle by the wire) was used to correlate and predict the experimental results.

Introduction

IT HAS been well established that mechanical or acoustical vibrations of heated surfaces increase the transfer of heat. A detailed review of this effect was made by Richardson [1].[3] An increase in either amplitude or frequency increases the heat transfer coefficient. The range of frequencies and amplitudes which have been investigated in the literature can be separated into two categories. One deals with small amplitudes and high frequencies while the other deals with low frequencies and large amplitudes. The present study covers large amplitude vibrations with the intervening frequencies that have not been employed in previous investigations. The data fit in the regime of convection by time-average steady-flow equivalent as defined by Richardson [1].

Apparatus

The experimental apparatus consisted of a crank slider mechanism which supplied a reciprocating motion of various amplitudes, peak-to-peak values of 0–2.655 in., and frequencies, 0–20 cps, to the test section. The average velocity resulting from this horizontal reciprocating motion varied between 0 and 8.8 fps. The test section, from which the heat transfer was measured, consisted of a horizontal platinum wire 0.010 in. in diameter and 6.0625 in. in length. The wire was held horizontally by a U-shaped frame. The surrounding medium was air at approximately 80 deg F. Measurements of the voltage drop across the test section and the direct current flowing through it, at steady state, provided information to calculate the surface temperature and the convected heat transferred. The temperature difference between the heated surface and the surrounding air was varied between 160 and 500 deg F.

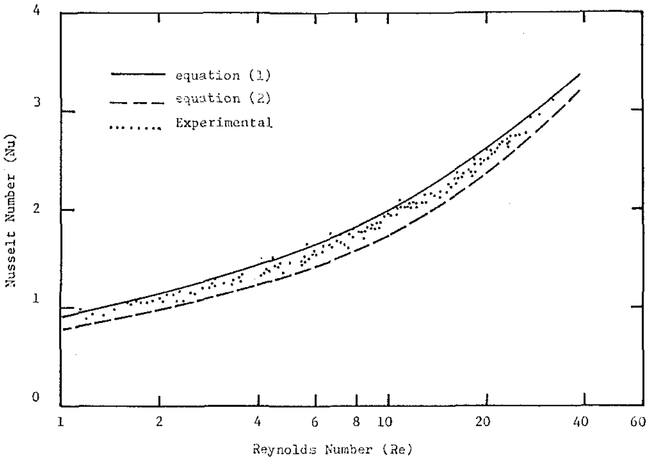

Fig. 1 Correlation of experimental results

Results

The experimental results are shown in Fig. 1 as a function of the Nusselt number, $\text{Nu} = hD/K$, and the Reynolds number, $\text{Re} = VD/\nu$, where h is the convective heat transfer coefficient, D is the wire diameter, V the average wire velocity due to the reciprocating motion (frequency times twice the peak-to-peak amplitude), K the thermal conductivity, and ν the kinematic viscosity. All physical properties refer to the convective medium (air in this experiment) and were evaluated at the film temperature $T_f = (T_s + T_\infty)/2$, where T_s and T_∞ are the temperatures of the heated wire and the surroundings respectively. As can be seen from Fig. 1, the experimental results could be predicted with an error of less than 10 percent by using the relations obtained by Hilpert [2] for forced convection from a wire in a uniform air stream. This relation is given by

$$\text{Nu} = C\,\text{Re}^n \tag{1}$$

where C and n are constants and dependent on the Reynolds number as follows:

	n	C
$1 < \text{Re} < 4$	0.33	0.891
$4 < \text{Re} < 40$	0.385	0.821

The experimental results were also compared, in Fig. 1, with the correlation of Penny and Deaver [3] for the forced-convection vibration region which is given by

$$\text{Nu}/(\text{Pr})^{0.3} = 0.35 + 0.48\,\text{Re}^{0.52} \tag{2}$$

where $\text{Pr} = \mu c_p/K$ is the Prandtl number, μ the dynamic viscosity, and c_p the constant-pressure specific heat. The Prandtl number can be considered as constant in the experimental range at a value of 0.705. The predicted values of the Nusselt number, using (2), differ by less than 17 percent from the experimental values. This appears to be mainly due to the differences in the region covered by the two experiments. The experimental Nusselt number for the case of no vibration, free convection only, was determined at various temperature levels. Its magnitude over the experimental range varied between 0.745 and 0.791 and was within 8 percent of the predicted ones [4]. An error analysis also confirmed this level of accuracy for the experimental results.

Conclusions

The results indicate that an increase in either the amplitude or the frequency of the vibration will increase the heat transferred. Also, in the region covered by this experiment, the effect of vibration could be predicted with reasonable accuracy by using the

---

[1] Assistant Professor, Department of Mechanical and Aerospace Engineering, University of Missouri–Rolla, Rolla, Mo. Assoc. Mem. ASME.

[2] Professor, Department of Mechanical Engineering, University of Iowa, Iowa City, Iowa. Mem. ASME.

[3] Numbers in brackets designate References at end of technical brief.

Contributed by the Heat Transfer Division of THE AMERICAN SOCIETY OF MECHANICAL ENGINEERS. Manuscript received by the Heat Transfer Division May 25, 1970; revised manuscript received July 23, 1970.

average wire velocity with an appropriate uniform forced convection relation.

References

1 Richardson, P. D., "Effects of Sound and Vibrations on Heat Transfer," *Applied Mechanics Reviews*, Vol. 20, No. 3, Mar. 1967.
2 Jacob, M., *Heat Transfer*, Vol. 1, Wiley, New York, 1958, p. 560.
3 Deaver, F. K., Penny, W. R., and Jefferson, T. B., "Heat Transfer From an Oscillating Horizontal Wire to Water," JOURNAL OF HEAT TRANSFER, TRANS. ASME, Series C, Vol. 84, No. 3, Aug. 1962, pp. 251–256.
4 Bosworth, R. C. L., *Heat Transfer Phenomena*, Wiley, New York 1952 p. 101.

The Effect of Flow Direction on Combined Convective Heat Transfer From Cylinders to Air

P. H. OOSTHUIZEN[1] **and S. MADAN**[2]

Introduction

IN COMBINED forced and free convective heat transfer from cylinders, the Nusselt number (N_d) depends on the Reynolds number (R_d), the Grashof number (G_d), the Prandtl number (P_r) and the angle (α) between the directions of the forced flow and the buoyancy force. The direction of the latter is, of course, vertically upward in the case of flow in the gravitational field. With air flow, the Prandtl number is essentially constant and in this case, therefore

$$N_d = f(R_d, G_d, \alpha) \qquad (1)$$

In most previous experimental studies of combined convective heat transfer from cylinders, e.g., references [1, 2],[3] α has been 90 deg. In an earlier study [3], the present authors reported measurements for $\alpha = 0$ deg and this note describes an extension of that work to investigate the effect of varying α, angles of 0, 90, 135, and 180 deg having been considered.

Apparatus

The apparatus used in the present study was essentially the same as that described in reference [3]. However, the 16-in. × 16-in., open-return wind tunnel was mounted in a vertical plane on a turntable which allowed its axis to be set at any angle to the vertical. The speed range of the tunnel was also extended and the accuracy of the speed measurement improved.

The heat-transfer measurements were again made with solid aluminum models, having diameters of $^3/_4$, 1, $1^1/_4$, and $1^1/_2$ in., using an unsteady technique which is described in reference [3]. Corrections for blockage were again applied.

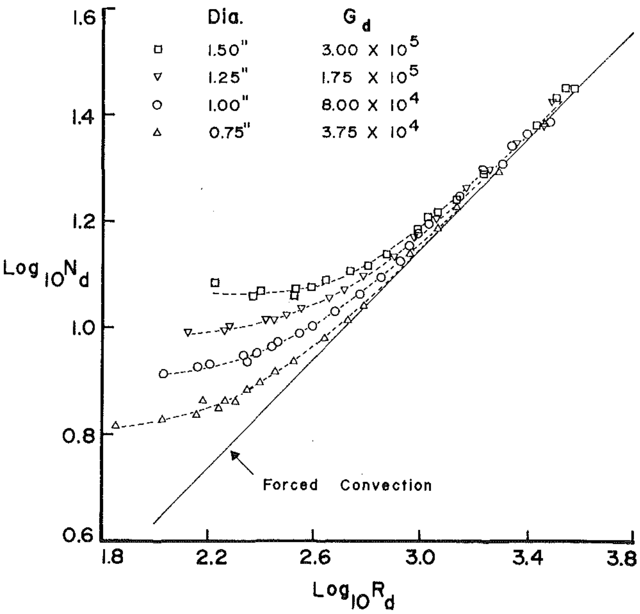

Fig. 1 Typical variations of measured Nusselt number with Reynolds number, corrected for blockage, at a fixed Grashof number for $\alpha = 0$ deg

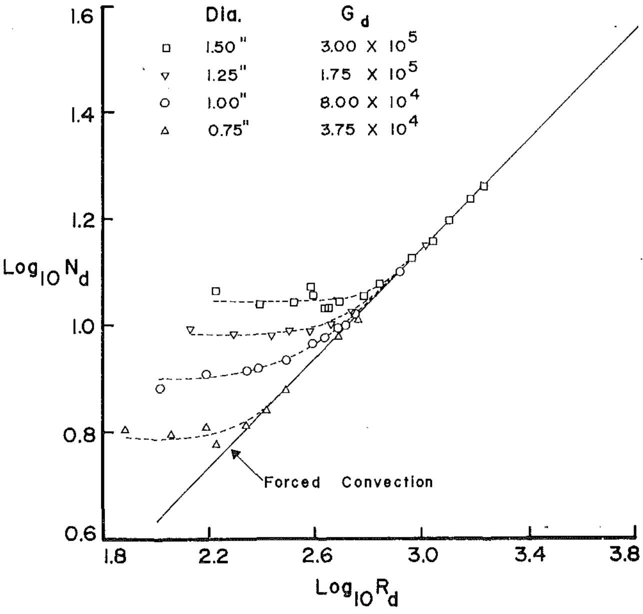

Fig. 2 Typical variations of measured Nusselt number with Reynolds number, corrected for blockage, at a fixed Grashof number for $\alpha = 90$ deg

Results

Typical measured mean heat-transfer rates in the four angular positions are shown in Figs. 1 to 4. The Grashof numbers indicated for the various models correspond to a model temperature of about 190 deg F above that of the air.

The $\alpha = 0$ deg (assisting-flow) results given in Fig. 1 are essentially identical to those given in reference [3]. The $\alpha = 90$ deg (normal-flow) results given in Fig. 2 have the same basic features as those given in reference [2] although the actual magnitudes are somewhat different due, probably, to the lower turbulence level existing in the tunnel used in the present study. In both the $\alpha = 0$ deg and $\alpha = 90$ deg cases, the buoyancy forces are seen to increase the heat-transfer rate above that which would exist at the same Reynolds number in purely forced convection.

The results for $\alpha = 135$ deg and $\alpha = 180$ deg (opposing flow), shown in Figs. 3 and 4 respectively, indicate that in these cases, the buoyancy forces initially decrease the heat-transfer rate below the corresponding forced-flow values. However, since at low velocity the heat-transfer rate must tend to its purely free convective value, it is seen that, with decreasing Reynolds number, the Nusselt numbers pass through a minimum and then rise above the forced-flow values. In their broad features, the present results are similar to those found for spheres in reference [4].

---

[1] Assistant Professor, Department of Mechanical Engineering, Queen's University, Kingston, Ontario, Canada.

[2] Research Assistant, Department of Mechanical Engineering, Queen's University, Kingston, Ontario, Canada.

[3] Numbers in brackets designate References at end of technical brief.

Contributed by the Heat Transfer Division of THE AMERICAN SOCIETY OF MECHANICAL ENGINEERS. Manuscript received by the Heat Transfer Division August 20, 1970.

average wire velocity with an appropriate uniform forced convection relation.

References

1 Richardson, P. D., "Effects of Sound and Vibrations on Heat Transfer," *Applied Mechanics Reviews*, Vol. 20, No. 3, Mar. 1967.

2 Jacob, M., *Heat Transfer*, Vol. 1, Wiley, New York, 1958, p. 560.

3 Deaver, F. K., Penny, W. R., and Jefferson, T. B., "Heat Transfer From an Oscillating Horizontal Wire to Water," JOURNAL OF HEAT TRANSFER, TRANS. ASME, Series C, Vol. 84, No. 3, Aug. 1962, pp. 251–256.

4 Bosworth, R. C. L., *Heat Transfer Phenomena*, Wiley, New York 1952 p. 101.

The Effect of Flow Direction on Combined Convective Heat Transfer From Cylinders to Air

P. H. OOSTHUIZEN[1] **and S. MADAN**[2]

Introduction

IN COMBINED forced and free convective heat transfer from cylinders, the Nusselt number (N_d) depends on the Reynolds number (R_d), the Grashof number (G_d), the Prandtl number (P_r) and the angle (α) between the directions of the forced flow and the buoyancy force. The direction of the latter is, of course, vertically upward in the case of flow in the gravitational field. With air flow, the Prandtl number is essentially constant and in this case, therefore

$$N_d = f(R_d, G_d, \alpha) \tag{1}$$

In most previous experimental studies of combined convective heat transfer from cylinders, e.g., references [1, 2],[3] α has been 90 deg. In an earlier study [3], the present authors reported measurements for $\alpha = 0$ deg and this note describes an extension of that work to investigate the effect of varying α, angles of 0, 90, 135, and 180 deg having been considered.

Apparatus

The apparatus used in the present study was essentially the same as that described in reference [3]. However, the 16-in. × 16-in., open-return wind tunnel was mounted in a vertical plane on a turntable which allowed its axis to be set at any angle to the vertical. The speed range of the tunnel was also extended and the accuracy of the speed measurement improved.

The heat-transfer measurements were again made with solid aluminum models, having diameters of $^3/_4$, 1, $1^1/_4$, and $1^1/_2$ in., using an unsteady technique which is described in reference [3]. Corrections for blockage were again applied.

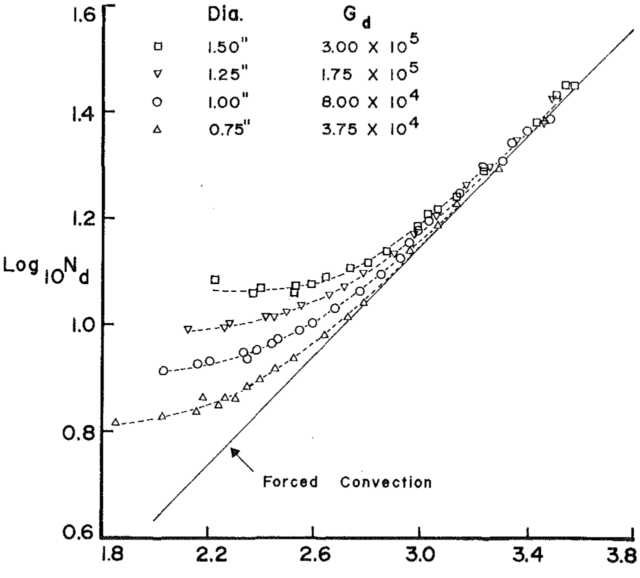

Fig. 1 Typical variations of measured Nusselt number with Reynolds number, corrected for blockage, at a fixed Grashof number for $\alpha = 0$ deg

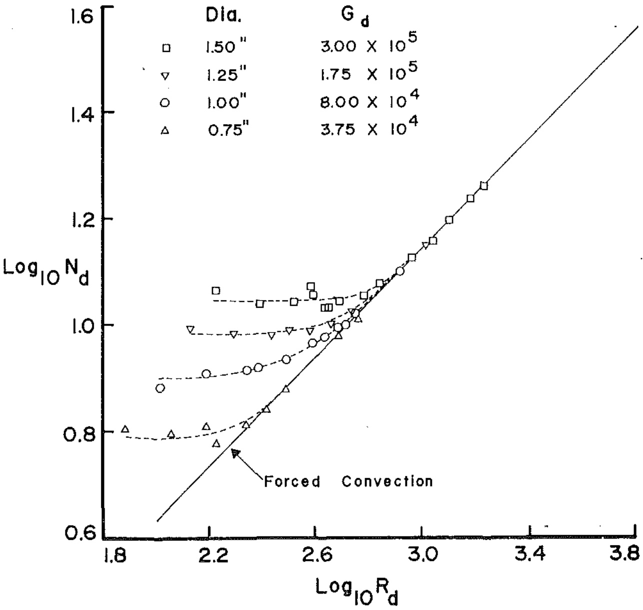

Fig. 2 Typical variations of measured Nusselt number with Reynolds number, corrected for blockage, at a fixed Grashof number for $\alpha = 90$ deg

Results

Typical measured mean heat-transfer rates in the four angular positions are shown in Figs. 1 to 4. The Grashof numbers indicated for the various models correspond to a model temperature of about 190 deg F above that of the air.

The $\alpha = 0$ deg (assisting-flow) results given in Fig. 1 are essentially identical to those given in reference [3]. The $\alpha = 90$ deg (normal-flow) results given in Fig. 2 have the same basic features as those given in reference [2] although the actual magnitudes are somewhat different due, probably, to the lower turbulence level existing in the tunnel used in the present study. In both the $\alpha = 0$ deg and $\alpha = 90$ deg cases, the buoyancy forces are seen to increase the heat-transfer rate above that which would exist at the same Reynolds number in purely forced convection.

The results for $\alpha = 135$ deg and $\alpha = 180$ deg (opposing flow), shown in Figs. 3 and 4 respectively, indicate that in these cases, the buoyancy forces initially decrease the heat-transfer rate below the corresponding forced-flow values. However, since at low velocity the heat-transfer rate must tend to its purely free convective value, it is seen that, with decreasing Reynolds number, the Nusselt numbers pass through a minimum and then rise above the forced-flow values. In their broad features, the present results are similar to those found for spheres in reference [4].

---

[1] Assistant Professor, Department of Mechanical Engineering, Queen's University, Kingston, Ontario, Canada.

[2] Research Assistant, Department of Mechanical Engineering, Queen's University, Kingston, Ontario, Canada.

[3] Numbers in brackets designate References at end of technical brief.

Contributed by the Heat Transfer Division of THE AMERICAN SOCIETY OF MECHANICAL ENGINEERS. Manuscript received by the Heat Transfer Division August 20, 1970.

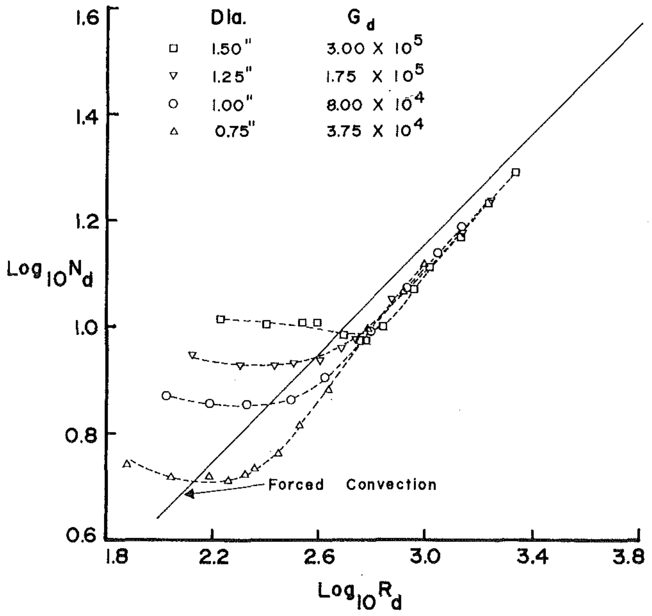

Fig. 3 Typical variations of measured Nusselt number with Reynolds number, corrected for blockage, at a fixed Grashof number for $\alpha = 135$ deg

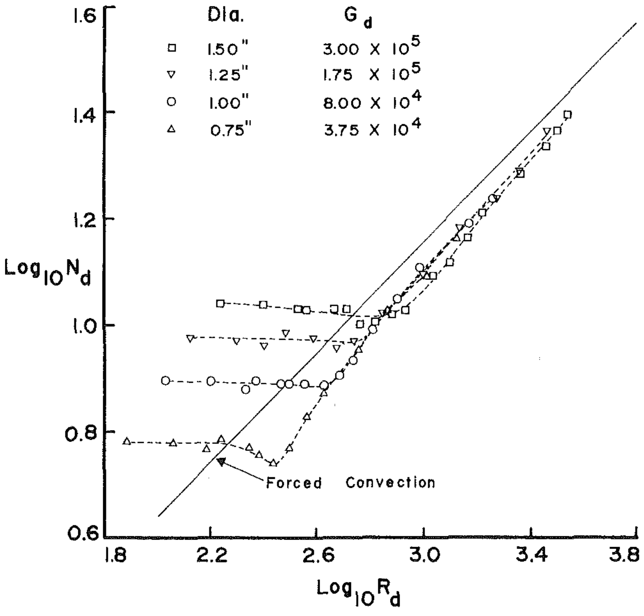

Fig. 4 Typical variations of measured Nusselt number with Reynolds number, corrected for blockage, at a fixed Grashof number for $\alpha = 180$ deg

In Fig. 5, an attempt to correlate the measured heat-transfer results at a given α in the form

$$N_d/N_{d\,\text{for}} = f(G_d/R_d^2) \tag{2}$$

is shown. $N_{d\,\text{for}}$ is the Nusselt number that would exist in purely forced convection at the same Reynolds number. From the mean lines drawn through these results it is concluded that if the combined convective region is assumed to end when the values of N_d are within 5 percent of the forced-flow values, then effectively purely forced flow exists approximately when

$$\begin{array}{llll} G_d/R_d^2 < 0.10 & \text{for} & \alpha = 0 & \text{deg} \\ \text{“} \quad \text{“} < 0.53 & \text{“} & \alpha = 90 & \text{“} \\ \text{“} \quad \text{“} < 0.04 & \text{“} & \alpha = 135 & \text{“} \\ \text{“} \quad \text{“} < 0.01 & \text{“} & \alpha = 180 & \text{“} \end{array} \tag{3}$$

Acknowledgments

The work described in the present note is part of a program sponsored by the National Research Council of Canada under Grant Number A5573.

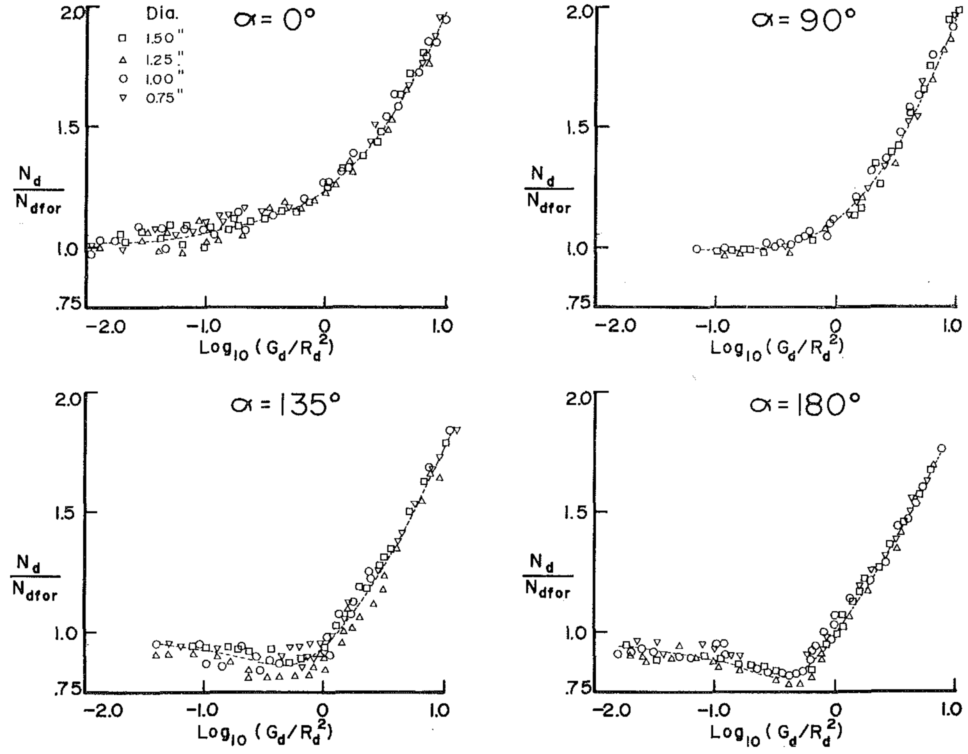

Fig. 5 Correlations of measured results in terms of the combined convection parameter G_d/R_d^2

References

1 Collis, D. C., and Williams, M. J., "Two-Dimensional Convection From Heated Wires at Low Reynolds Numbers," *Journal of Fluid Mechanics*, Vol. 6, 1959, pp. 357–384.

2 Sharma, G. K., and Sukhatme, S. P., "Combined Free and Forced Convection Heat Transfer From a Heated Tube to a Transverse Air Stream," JOURNAL OF HEAT TRANSFER, TRANS. ASME, Series C, Vol. 91, No. 3, Aug. 1969, pp. 457–459.

3 Oosthuizen, P. H., and Madan, S., "Combined Convective Heat Transfer From Horizontal Cylinders in Air," JOURNAL OF HEAT TRANSFER, TRANS. ASME, Series C, Vol. 92, No. 1, Feb. 1970, pp. 194–196.

4 Yuge, T., "Experiments on Heat Transfer From Spheres Including Combined Natural and Forced Convection," JOURNAL OF HEAT TRANSFER, TRANS. ASME, Series C, Vol. 82, No. 3, Aug. 1960, pp. 214–220.

Turbulent Flow in a Tube With Wall Suction

L. MERKINE,[1] A. SOLAN,[1] and Y. WINOGRAD[1]

The effect of wall suction on turbulent flow in a tube is analyzed, using a mixing-length model with an extended form of van Driest's damping factor. It is shown that an empirical damping factor similar to that proposed by Kays, Moffat, and Thielbahr, when incorporated in a method of solution developed by Kinney and Sparrow, predicts that the turbulence level in tube flow decreases with suction, and yields excellent correlation with the experiments of Weissberg and Berman.

Nomenclature

A^+ = parameter in damping factor, equations (10), (11)
DF = damping factor, equations (10), (11)
K = momentum flux variable, equation (8)
l^+ = dimensionless turbulent mixing length
p = pressure
Re = Reynolds number
r = radial coordinate
r_w = tube radius
U = mean axial velocity
u = axial velocity
u_* = friction velocity
v = radial velocity
v_w = suction velocity at wall
x = axial coordinate
y = transverse coordinate ($r - r_w$)
ρ = density
τ = shear stress
χ = variable defined in equation (12)
ν = kinematic viscosity

Superscript

$(\ )^+$ = dimensionless, equation (6)

Introduction

WITHDRAWAL of fluid at the boundary of a turbulent flow ("suction") has a marked effect on the turbulence level [1].[2] For external flows, this effect has been studied both analytically and experimentally quite thoroughly, and it is well known that suction has a laminarizing effect. For tube flow, much less work has been done. Weissberg and Berman [2, 3] measured the velocity field and pressure drop in tube flow with suction and observed that the turbulence levels were lowered by suction over the entire cross section. Kinney and Sparrow [4] approached the problem analytically and developed a model for the prediction of the flow field from basic equations. A crucial step in their treatment is the assumption of a relation between the turbulent mixing length and the local properties of the flow field. Here they assumed a usual mixing-length relation, with a van Driest damping factor modified for wall suction. In their derivation, a parameter A^+ appears, which for want of better data is assigned the constant value $A^+ = 26$, as in the case of a flat plate without suction. Thus, their analysis is compatible with the no-suction case. However, in general, one would expect A^+ itself to be a function of the suction rate. Indeed, in a series of experiments on turbulent boundary-layer flow with suction, Kays et al. [5] found that the parameter A^+ increases with suction. Rotta [6], in his analysis of the data of Favre et al. [7], arrives at a similar result.

Inspection of Kinney and Sparrow's model shows that the assumption of constant A^+ yields a turbulence level increasing with suction, which is contrary to the well-known experimental evidence for flat plates and to Weissberg and Berman's measurements in tubes.

It is the purpose of this paper to integrate Kinney and Sparrow's analysis with the damping-factor data of Kays et al. and Rotta. The results show the expected decrease of turbulence with increasing suction, and are in good agreement with the data of Weissberg and Berman.

Analysis

The governing equations for turbulent flow in a circular tube are, in the usual notation,

$$\frac{\partial(ru)}{\partial x} + \frac{\partial(rv)}{\partial r} = 0, \tag{1}$$

$$\rho\left[r\,\frac{\partial(u^2)}{\partial x} + \frac{\partial(ruv)}{\partial r}\right] = -r\,\frac{\partial p}{\partial x} - \frac{\partial(r\tau)}{\partial r}, \tag{2}$$

where τ is the shear stress, the specification of which will require the assumption of a turbulent transport model. The boundary conditions at the wall are

$$r = r_w{:}\quad u = 0,\quad v = v_w. \tag{3}$$

For low ratio of the suction velocity v_w to the mean axial velocity U, local similarity may be assumed, i.e.,

$$u/U = f(r/r_w). \tag{4}$$

According to the mixing-length theory, the local shear stress is given by

$$\frac{\tau}{\tau_w} = \left(1 + l^{+2}\,\frac{du^+}{dy^+}\right)\frac{du^+}{dy^+}, \tag{5}$$

where

$$u^+ = u/u_*,\quad y^+ = yu_*/\nu,\quad u_* = \sqrt{\tau_w/\rho},\quad y = r - r_w, \tag{6}$$

and l^+ is the dimensionless turbulent mixing length, to be discussed below.

Following Kinney and Sparrow, equations (1)–(6) can be reduced to an integro-differential equation

$$\begin{aligned}\frac{du^+}{dy^+} + l^{+2}\left(\frac{du^+}{dy^+}\right)^2 &= \frac{r^+}{r_w{}^+} - \left(\frac{v_w}{U}\right)\\ &\quad\times\left\{\frac{\mathrm{Re}}{2} - \frac{2}{r_w{}^+}\int_0^{y^+} u^+(r_w{}^+ - y^+)dy^+\right\}\frac{u^+}{r^+}\\ &\quad + 4\left(\frac{v_w}{U}\right)\frac{1}{r_w{}^+}\left\{\left[1 - \left(\frac{r^+}{r_w{}^+}\right)^2\right]\frac{\mathrm{Re}^2}{8}\,K\right.\\ &\quad\left. - \int_0^{y^+} u^{+2}(r_w{}^+ - y^+)dy^+\right\}\frac{1}{r^+},\end{aligned} \tag{7}$$

---

[1] Faculty of Mechanical Engineering, Technion—Israel Institute of Technology, Haifa, Israel.

[2] Numbers in brackets designate References at end of technical brief.

Contributed by the Heat Transfer Division of THE AMERICAN SOCIETY OF MECHANICAL ENGINEERS. Manuscript received by the Heat Transfer Division August 4, 1970.

References

1 Collis, D. C., and Williams, M. J., "Two-Dimensional Convention From Heated Wires at Low Reynolds Numbers," *Journal of Fluid Mechanics*, Vol. 6, 1959, pp. 357–384.

2 Sharma, G. K., and Sukhatme, S. P., "Combined Free and Forced Convection Heat Transfer From a Heated Tube to a Transverse Air Stream," JOURNAL OF HEAT TRANSFER, TRANS. ASME, Series C, Vol. 91, No. 3, Aug. 1969, pp. 457–459.

3 Oosthuizen, P. H., and Madan, S., "Combined Convective Heat Transfer From Horizontal Cylinders in Air," JOURNAL OF HEAT TRANSFER, TRANS. ASME, Series C, Vol. 92, No. 1, Feb. 1970, pp. 194–196.

4 Yuge, T., "Experiments on Heat Transfer From Spheres Including Combined Natural and Forced Convection," JOURNAL OF HEAT TRANSFER, TRANS. ASME, Series C, Vol. 82, No. 3, Aug. 1960, pp. 214–220.

Turbulent Flow in a Tube With Wall Suction

L. MERKINE,[1] A. SOLAN,[1] and Y. WINOGRAD[1]

The effect of wall suction on turbulent flow in a tube is analyzed, using a mixing-length model with an extended form of van Driest's damping factor. It is shown that an empirical damping factor similar to that proposed by Kays, Moffat, and Thielbahr, when incorporated in a method of solution developed by Kinney and Sparrow, predicts that the turbulence level in tube flow decreases with suction, and yields excellent correlation with the experiments of Weissberg and Berman.

Nomenclature

A^+ = parameter in damping factor, equations (10), (11)
DF = damping factor, equations (10), (11)
K = momentum flux variable, equation (8)
l^+ = dimensionless turbulent mixing length
p = pressure
Re = Reynolds number
r = radial coordinate
r_w = tube radius
U = mean axial velocity
u = axial velocity
u_* = friction velocity
v = radial velocity
v_w = suction velocity at wall
x = axial coordinate
y = transverse coordinate $(r - r_w)$
ρ = density
τ = shear stress
χ = variable defined in equation (12)
ν = kinematic viscosity

Superscript

$(\ )^+$ = dimensionless, equation (6)

Introduction

Withdrawal of fluid at the boundary of a turbulent flow ("suction") has a marked effect on the turbulence level [1].[2] For external flows, this effect has been studied both analytically and experimentally quite thoroughly, and it is well known that suction has a laminarizing effect. For tube flow, much less work has been done. Weissberg and Berman [2, 3] measured the velocity field and pressure drop in tube flow with suction and observed that the turbulence levels were lowered by suction over the entire cross section. Kinney and Sparrow [4] approached the problem analytically and developed a model for the prediction of the flow field from basic equations. A crucial step in their treatment is the assumption of a relation between the turbulent mixing length and the local properties of the flow field. Here they assumed a usual mixing-length relation, with a van Driest damping factor modified for wall suction. In their derivation, a parameter A^+ appears, which for want of better data is assigned the constant value $A^+ = 26$, as in the case of a flat plate without suction. Thus, their analysis is compatible with the no-suction case. However, in general, one would expect A^+ itself to be a function of the suction rate. Indeed, in a series of experiments on turbulent boundary-layer flow with suction, Kays et al. [5] found that the parameter A^+ increases with suction. Rotta [6], in his analysis of the data of Favre et al. [7], arrives at a similar result.

Inspection of Kinney and Sparrow's model shows that the assumption of constant A^+ yields a turbulence level increasing with suction, which is contrary to the well-known experimental evidence for flat plates and to Weissberg and Berman's measurements in tubes.

It is the purpose of this paper to integrate Kinney and Sparrow's analysis with the damping-factor data of Kays et al. and Rotta. The results show the expected decrease of turbulence with increasing suction, and are in good agreement with the data of Weissberg and Berman.

Analysis

The governing equations for turbulent flow in a circular tube are, in the usual notation,

$$\frac{\partial(ru)}{\partial x} + \frac{\partial(rv)}{\partial r} = 0, \tag{1}$$

$$\rho\left[r\frac{\partial(u^2)}{\partial x} + \frac{\partial(ruv)}{\partial r}\right] = -r\frac{\partial p}{\partial x} - \frac{\partial(r\tau)}{\partial r}, \tag{2}$$

where τ is the shear stress, the specification of which will require the assumption of a turbulent transport model. The boundary conditions at the wall are

$$r = r_w\colon\quad u = 0,\quad v = v_w. \tag{3}$$

For low ratio of the suction velocity v_w to the mean axial velocity U, local similarity may be assumed, i.e.,

$$u/U = f(r/r_w). \tag{4}$$

According to the mixing-length theory, the local shear stress is given by

$$\frac{\tau}{\tau_w} = \left(1 + l^{+2}\frac{du^+}{dy^+}\right)\frac{du^+}{dy^+}, \tag{5}$$

where

$$u^+ = u/u_*,\quad y^+ = yu_*/\nu,\quad u_* = \sqrt{\tau_w/\rho},\quad y = r - r_w, \tag{6}$$

and l^+ is the dimensionless turbulent mixing length, to be discussed below.

Following Kinney and Sparrow, equations (1)–(6) can be reduced to an integro-differential equation

$$\begin{aligned}\frac{du^+}{dy^+} + l^{+2}\left(\frac{du^+}{dy^+}\right)^2 = \frac{r^+}{r_w^+} - \left(\frac{v_w}{U}\right)\\ \times\left\{\frac{\mathrm{Re}}{2} - \frac{2}{r_w^+}\int_0^{y^+} u^+(r_w^+ - y^+)dy^+\right\}\frac{u^+}{r^+}\\ + 4\left(\frac{v_w}{U}\right)\frac{1}{r_w^+}\left\{\left[1 - \left(\frac{r^+}{r_w^+}\right)^2\right]\frac{\mathrm{Re}^2}{8}K\right.\\ \left. - \int_0^{y^+} u^{+2}(r_w^+ - y^+)dy^+\right\}\frac{1}{r^+},\end{aligned} \tag{7}$$

---

[1] Faculty of Mechanical Engineering, Technion—Israel Institute of Technology, Haifa, Israel.

[2] Numbers in brackets designate References at end of technical brief.

Contributed by the Heat Transfer Division of THE AMERICAN SOCIETY OF MECHANICAL ENGINEERS. Manuscript received by the Heat Transfer Division August 4, 1970.

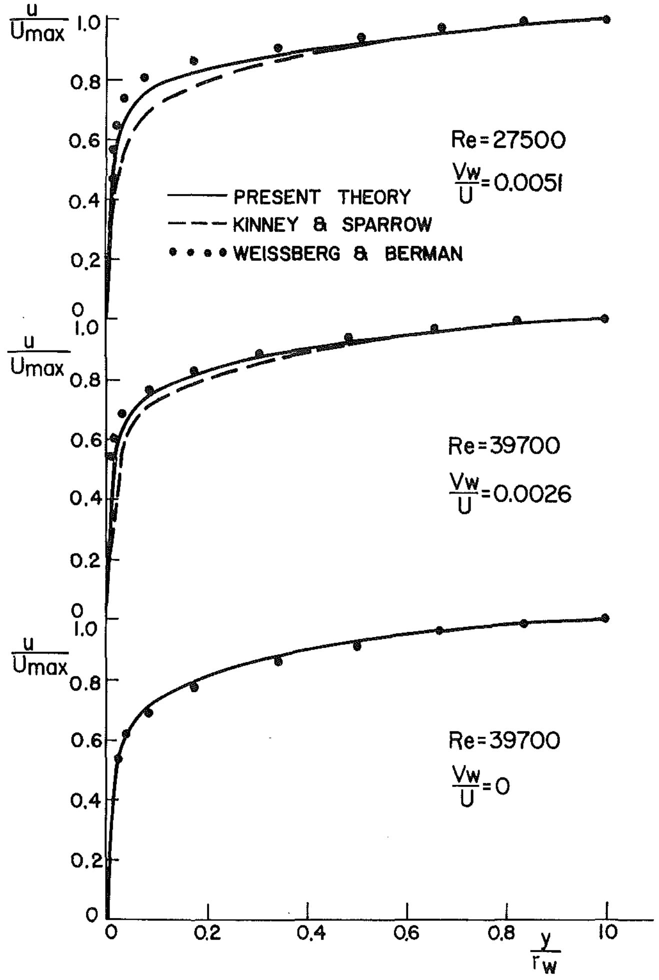

Fig. 1 Velocity profiles across tube

with the boundary condition $u^+ = 0$ at $y^+ = 0$. Here the Reynolds number Re and the parameter K are given by

$$\mathrm{Re} = \frac{2r_w U}{\nu} = \frac{4}{r_w^+}\int_0^{r_w^+} u^+(r_w^+ - y^+)dy^+,$$
$$K = \frac{8}{\mathrm{Re}^2}\int_0^{r_w^+} u^{+2}(r_w^+ - y^+)dy^+. \tag{8}$$

At this point, a model for l^+ must be chosen. The mixing-length relation for an impermeable round tube, with a van Driest damping factor, is

$$\frac{l^+}{r_w^+} = DF\left[0.4\,\frac{y^+}{r_w^+} - 0.44\left(\frac{y^+}{r_w^+}\right)^2 + 0.24\left(\frac{y^+}{r_w^+}\right)^3 - 0.06\left(\frac{y^+}{r_w^+}\right)^4\right], \tag{9}$$

where the damping factor,

$$DF = 1 - \exp\left(-y^+/A^+\right), \tag{10}$$

is based on the solution of the flow next to an oscillating impermeable plane. The assumption of a given A^+ is equivalent to assuming a representative frequency, and it is found that a constant value $A^+ = 26$ gives good correlation with experimental data.

Kinney and Sparrow generalized the damping factor by basing it on the solution of the flow next to an oscillating plane with suction. This yields

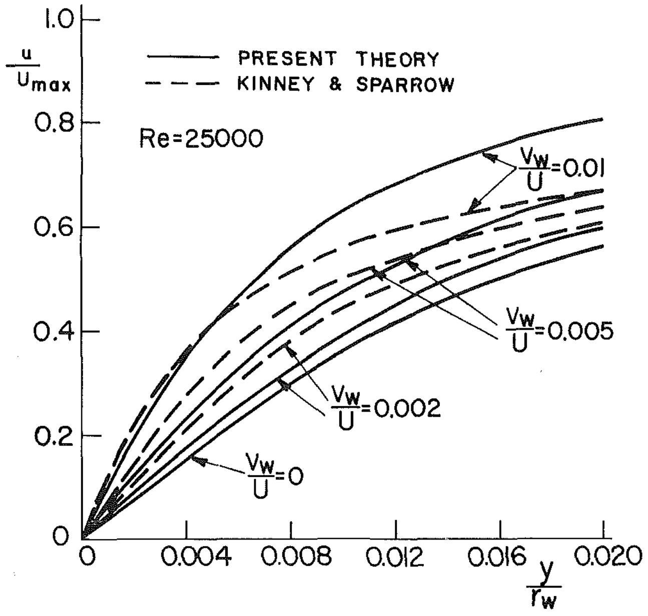

Fig. 2 Velocity profiles near tube wall

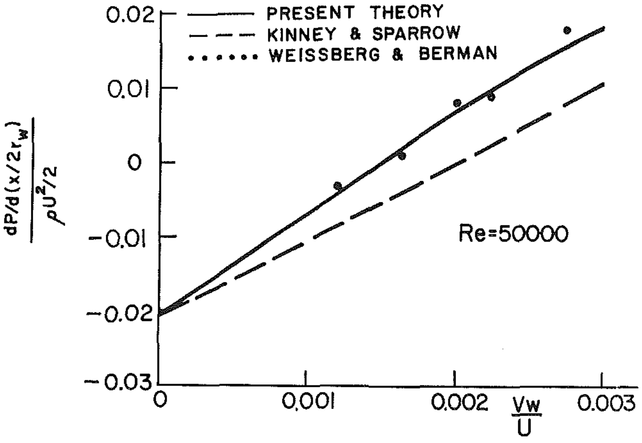

Fig. 3 Pressure gradient as a function of suction rate

$$DF = 1 - \exp\left\{-\chi - \frac{1}{\sqrt{2}}\left[\left(\chi^4 + 4\left(\frac{y^+}{A^+}\right)^4\right)^{1/2} + \chi^2\right]^{1/2}\right\}, \tag{11}$$

where

$$\chi = \frac{1}{2}\,v_w^+ y^+, \tag{12}$$

and A^+ is again unspecified. For compatibility with the no-suction case, they assumed $A^+ = 26$. This model predicts that the damping factor in equation (11) increases with suction, i.e., the turbulence level increases. This is contrary to well-established experimental evidence for flat plates and to Weissberg and Berman's measurements in tubes.

In principle, there is no reason to expect that A^+ will be independent of v_w. In fact, Kays et al. [5], in an analysis of their experimental data for flat plates, propose a damping factor as in equation (10), with an empirical relation for A^+ the dominant term of which is

$$A^+ = 4.42/(0.17 - v_w^+), \tag{13}$$

which reduces to $A^+ = 26$ for $v_w^+ = 0$. This is in good agreement with the curve of A^+ vs. v_w^+ in Rotta's [6] analysis of the data of Favre et al. [7] for flat plates. (Both Kays et al. and Rotta normalize the distance y^+ in (10) with respect to the local shear stress $\tau = \tau_w - v_w u$, rather than τ_w.) Note that equations (10) and (13) predict that the damping factor for a flat plate decreases with suction, i.e., the turbulence level decreases. Clearly, then, for tube flow one would also expect the expression for A^+ in terms of v_w^+ to exhibit the same property.

After consideration of the different approaches, it seems that the simplest model for the problem considered here would consist of the damping factor as in equations (10), (13), with y^+ normalized in the usual manner with respect to τ_w. This, together with the equations (7)–(9), provides an analytically well-posed model, which exhibits the expected and experimentally observed physical behavior.

As in [4], for given Re and v_w/U, equation (7) is solved by assuming trial values for r_w^+ and K. The equation is integrated numerically from $y^+ = 0$ to r_w^+, and the resulting velocity profile should then satisfy equations (8). In case of disagreement, the assumed values of r_w^+ and K are corrected and the integration is repeated until the process converges.

Results

The problem was solved for parameter values which admit comparison with the theory of [4] and the experimental data of [2] and the results are presented in Figs. 1–3.

Fig. 1 shows the velocity profiles for parameter values common to [2] and [4]. In considering this figure, one should note that in the dimensionless representation used, all curves converge at $y/r_w = 0$ and at $y/r_w = 1$. Therefore, the agreement between the curves near the end points is self-evident, and the theoretical curves should be judged solely by their agreement with experiment in the range near $y/r_w = 0.1$. It will be seen that the present theory yields much better agreement with experiment than [4].

Fig. 2 shows the effect of suction on the velocity profile for Re = 25,000, together with the curves from [4]. (No experimental data is available for these parameter values.)

In Fig. 3, the dimensionless pressure gradient is presented, together with the prediction [4] and points calculated from the experimental data of [2]. The agreement of the present theory with experiment is excellent.

On the basis of the limited amount of directly relevant experimental data available, it may be concluded that the present theory yields better results than [4]. Clearly, extensive experimental work is required before an exact empirical relation for A^+ in turbulent pipe flow with suction will be available. The main point is, however, that this relation must predict a *decrease* of the turbulent level with suction.

Acknowledgment

The authors are indebted to Prof. E. M. Sparrow for a thorough discussion of reference [4].

References

1 Schlichting, H., *Boundary Layer Theory,* 6th ed., McGraw-Hill, New York, 1968, p. 483.

2 Weissberg, H. L., and Berman, A. S., "Velocity and Pressure Distributions in Turbulent Pipe Flow with Uniform Wall Suction," *Proceedings of the Heat Transfer and Fluid Mechanics Institute,* Vol. 14, 1955, pp. 1–30.

3 Weissberg, H. L., "Velocity Profiles and Friction Factors for Turbulent Pipe Flow with Uniform Wall Suction," Report K-1264, Union Carbide Nuclear Co., Oak Ridge Gaseous Diffusion Plant, Oak Ridge, Tenn., 1956.

4 Kinney, R. B., and Sparrow, E. M., "Turbulent Flow, Heat Transfer, and Mass Transfer in a Tube With Surface Suction," Journal of Heat Transfer, Trans. ASME, Series C, Vol. 92, No. 1, Feb. 1970, pp. 117–125.

5 Kays, W. M., Moffat, R. J., and Thielbahr, W. H., "Heat Transfer to the Highly Accelerated Turbulent Boundary Layer With and Without Mass Addition," Journal of Heat Transfer, Trans. ASME, Series C, Vol. 92, No. 3, Aug. 1970, pp. 499–505.

6 Rotta, J. C., "Ueber die Geschwindigkeitsverteilung bei turbulenter Stroemung in der Naehe poroeser Waende," *Deutsche Luft- und Raumfahrt,* Forschungsbericht 66-45, Aerodynamische Versuchsanstalt, Goettingen, 1966.

7 Favre, A., Dumas, R., Verollet, E., and Coantic, M., "Couche limite turbulente sur paroi poreuse avec aspiration," *Journal de Mecanique,* Vol. 5, 1966, pp. 3–28.

A Solution for Radiation Heating of a Diathermanous Solid Subject to Convection Cooling

HAROLD J. BREAUX[1]

Nomenclature

c = specific heat

H = heat-transfer coefficient

h = $H/k\lambda$, dimensionless heat-transfer coefficient (Biot number)

k = thermal conductivity

$q(y, t)$ = $Q(Q_0,\ \lambda,\ y/\lambda,\ t)/Q_0\lambda$, dimensionless source function

$Q(Q_0, \lambda, x, \tau)$ = source function

Q_0 = maximum intensity of source function

x = distance from surface

y = λx, dimensionless distance from surface

t = $\lambda^2 \alpha \tau$, dimensionless time (Fourier number)

T = $(\theta - \theta_0)k\lambda/Q_0$, dimensionless temperature

α = $k/\rho c$, thermal diffusivity

θ = temperature

θ_0 = initial temperature, temperature of cooling medium

λ = parameter in source term, absorption coefficient in source term for Lambert-law absorption

ν = radiation frequency

ρ = density

τ = time

Introduction

Attention is focused on a class of problems characterized by the presence of a source term in the one-dimensional heat equation for a semi-infinite solid. A typical physical situation in which this type problem arises is the case of a diathermanous solid irradiated by a radiation source having an arbitrary spectral distribution and where the energy absorbed by the solid is governed by Lambert's exponential absorption law. The solid is assumed to be simultaneously losing heat at its surface in a manner governed by Newton's law of cooling. The problem is first solved in general form for an arbitrary source term with unspecified time dependence and spatial distribution. The solution is then specialized to those situations where the source term is time-independent. An exact solution in the form of tabulated functions is obtained for the case where the source arises from monochromatic radiation and the energy is deposited in the solid according to Lambert's law. The solution is then extended to the case of a radiation source having an arbitrary spectral distribution. The final result is given in terms of a definite integral which can easily be evaluated by means of numerical quadrature.

---

[1] Mathematician, Applied Mathematics Division, Ballistic Research Laboratories, Aberdeen Research and Development Center, Aberdeen Proving Ground, Md.

Contributed by the Heat Transfer Division of The American Society of Mechanical Engineers. Manuscript received by the Heat Transfer Division December 29, 1970.

ment with the curve of A^+ vs. v_w^+ in Rotta's [6] analysis of the data of Favre et al. [7] for flat plates. (Both Kays et al. and Rotta normalize the distance y^+ in (10) with respect to the local shear stress $\tau = \tau_w - v_w u$, rather than τ_w.) Note that equations (10) and (13) predict that the damping factor for a flat plate decreases with suction, i.e., the turbulence level decreases. Clearly, then, for tube flow one would also expect the expression for A^+ in terms of v_w^+ to exhibit the same property.

After consideration of the different approaches, it seems that the simplest model for the problem considered here would consist of the damping factor as in equations (10), (13), with y^+ normalized in the usual manner with respect to τ_w. This, together with the equations (7)–(9), provides an analytically well-posed model, which exhibits the expected and experimentally observed physical behavior.

As in [4], for given Re and v_w/U, equation (7) is solved by assuming trial values for r_w^+ and K. The equation is integrated numerically from $y^+ = 0$ to r_w^+, and the resulting velocity profile should then satisfy equations (8). In case of disagreement, the assumed values of r_w^+ and K are corrected and the integration is repeated until the process converges.

Results

The problem was solved for parameter values which admit comparison with the theory of [4] and the experimental data of [2] and the results are presented in Figs. 1–3.

Fig. 1 shows the velocity profiles for parameter values common to [2] and [4]. In considering this figure, one should note that in the dimensionless representation used, all curves converge at $y/r_w = 0$ and at $y/r_w = 1$. Therefore, the agreement between the curves near the end points is self-evident, and the theoretical curves should be judged solely by their agreement with experiment in the range near $y/r_w = 0.1$. It will be seen that the present theory yields much better agreement with experiment than [4].

Fig. 2 shows the effect of suction on the velocity profile for Re = 25,000, together with the curves from [4]. (No experimental data is available for these parameter values.)

In Fig. 3, the dimensionless pressure gradient is presented, together with the prediction [4] and points calculated from the experimental data of [2]. The agreement of the present theory with experiment is excellent.

On the basis of the limited amount of directly relevant experimental data available, it may be concluded that the present theory yields better results than [4]. Clearly, extensive experimental work is required before an exact empirical relation for A^+ in turbulent pipe flow with suction will be available. The main point is, however, that this relation must predict a *decrease* of the turbulent level with suction.

Acknowledgment

The authors are indebted to Prof. E. M. Sparrow for a thorough discussion of reference [4].

References

1 Schlichting, H., *Boundary Layer Theory,* 6th ed., McGraw-Hill, New York, 1968, p. 483.

2 Weissberg, H. L., and Berman, A. S., "Velocity and Pressure Distributions in Turbulent Pipe Flow with Uniform Wall Suction," *Proceedings of the Heat Transfer and Fluid Mechanics Institute,* Vol. 14, 1955, pp. 1–30.

3 Weissberg, H. L., "Velocity Profiles and Friction Factors for Turbulent Pipe Flow with Uniform Wall Suction," Report K-1264, Union Carbide Nuclear Co., Oak Ridge Gaseous Diffusion Plant, Oak Ridge, Tenn., 1956.

4 Kinney, R. B., and Sparrow, E. M., "Turbulent Flow, Heat Transfer, and Mass Transfer in a Tube With Surface Suction," JOURNAL OF HEAT TRANSFER, TRANS. ASME, Series C, Vol. 92, No. 1, Feb. 1970, pp. 117–125.

5 Kays, W. M., Moffat, R. J., and Thielbahr, W. H., "Heat Transfer to the Highly Accelerated Turbulent Boundary Layer With and Without Mass Addition," JOURNAL OF HEAT TRANSFER, TRANS. ASME, Series C, Vol. 92, No. 3, Aug. 1970, pp. 499–505.

6 Rotta, J. C., "Ueber die Geschwindigkeitsverteilung bei turbulenter Stroemung in der Naehe poroeser Waende," *Deutsche Luft- und Raumfahrt,* Forschungsbericht 66-45, Aerodynamische Versuchsanstalt, Goettingen, 1966.

7 Favre, A., Dumas, R., Verollet, E., and Coantic, M., "Couche limite turbulente sur paroi poreuse avec aspiration," *Journal de Mecanique,* Vol. 5, 1966, pp. 3–28.

A Solution for Radiation Heating of a Diathermanous Solid Subject to Convection Cooling

HAROLD J. BREAUX[1]

Nomenclature

c = specific heat
H = heat-transfer coefficient
h = $H/k\lambda$, dimensionless heat-transfer coefficient (Biot number)
k = thermal conductivity
$q(y, t)$ = $Q(Q_0, \lambda, y/\lambda, t)/Q_0\lambda$, dimensionless source function
$Q(Q_0, \lambda, x, \tau)$ = source function
Q_0 = maximum intensity of source function
x = distance from surface
y = λx, dimensionless distance from surface
t = $\lambda^2 \alpha \tau$, dimensionless time (Fourier number)
T = $(\theta - \theta_0)k\lambda/Q_0$, dimensionless temperature
α = $k/\rho c$, thermal diffusivity
θ = temperature
θ_0 = initial temperature, temperature of cooling medium
λ = parameter in source term, absorption coefficient in source term for Lambert-law absorption
ν = radiation frequency
ρ = density
τ = time

Introduction

ATTENTION is focused on a class of problems characterized by the presence of a source term in the one-dimensional heat equation for a semi-infinite solid. A typical physical situation in which this type problem arises is the case of a diathermanous solid irradiated by a radiation source having an arbitrary spectral distribution and where the energy absorbed by the solid is governed by Lambert's exponential absorption law. The solid is assumed to be simultaneously losing heat at its surface in a manner governed by Newton's law of cooling. The problem is first solved in general form for an arbitrary source term with unspecified time dependence and spatial distribution. The solution is then specialized to those situations where the source term is time-independent. An exact solution in the form of tabulated functions is obtained for the case where the source arises from monochromatic radiation and the energy is deposited in the solid according to Lambert's law. The solution is then extended to the case of a radiation source having an arbitrary spectral distribution. The final result is given in terms of a definite integral which can easily be evaluated by means of numerical quadrature.

---

[1] Mathematician, Applied Mathematics Division, Ballistic Research Laboratories, Aberdeen Research and Development Center, Aberdeen Proving Ground, Md.

Contributed by the Heat Transfer Division of THE AMERICAN SOCIETY OF MECHANICAL ENGINEERS. Manuscript received by the Heat Transfer Division December 29, 1970.

Integral Solution for Arbitrary Sources With Surface Cooling

The partial differential equation, initial and boundary conditions, governing the transient temperature behavior in a semi-infinite solid with an internal source term is given by

$$\rho c \frac{\partial \theta}{\partial \tau} = k \frac{\partial^2 \theta}{\partial x^2} + Q(Q_0, \lambda, x, \tau), \quad \tau > 0, \quad 0 < x < \infty \qquad (1)$$

$$k \frac{\partial \theta}{\partial x} = H(\theta - \theta_0), \qquad \tau > 0, \quad x = 0 \qquad (2)$$

$$\frac{\partial \theta}{\partial x} = 0, \qquad \tau \geqq 0, \quad x = \infty \qquad (3)$$

$$\theta = \theta_0, \qquad \tau = 0, \quad 0 \leqq x < \infty. \qquad (4)$$

Employing the dimensionless variables defined in the Nomenclature, the equations (1)–(4) become

$$\frac{\partial T}{\partial t} = \frac{\partial^2 T}{\partial y^2} + q(y, t), \quad t > 0, \quad 0 < y < \infty \qquad (5)$$

$$\frac{\partial T}{\partial y} = hT, \qquad t > 0, \quad y = 0 \qquad (6)$$

$$\frac{\partial T}{\partial y} = 0, \qquad t \geqq 0, \quad y = \infty \qquad (7)$$

$$T = 0, \qquad t = 0, \quad 0 \leqq y \leqq \infty. \qquad (8)$$

The solution was obtained by application of a generalized Fourier integral transform derived by Churchill [1].[2] The solution is given by

$$T(y, t) = \int_0^t \int_0^\infty K(y, s)\bar{q}(s, t_1)e^{-s^2(t-t_1)}ds dt_1, \qquad (9)$$

where $K(y, s)$ is the kernel of the generalized Fourier transform defined by

$$K(y, s) = (2/\pi)^{1/2}(h^2 + s^2)^{-1/2}[h \sin (sy) + s \cos (sy)], \qquad (10)$$

and $\bar{q}(s, t_1)$ is given by

$$\bar{q}(s, t_1) = \int_0^\infty K(y, s)q(y, t_1)dy. \qquad (11)$$

For time-independent sources $q(y)$ the solution reduces to

$$T(y, t) = \int_0^\infty K(y, s)\bar{q}(s)s^{-2}(1 - e^{-s^2 t})ds. \qquad (12)$$

Exact Solution for Lambert-Law Radiation Absorption

If the solid is irradiated by monochromatic radiation and the energy absorbed at the depth x can be represented by Lambert's exponential absorption law then the time-independent source term is given by

$$Q(Q_0, \lambda, x) = \lambda Q_0 e^{-\lambda x}, \qquad (13)$$

which in dimensionless form reduces to

$$q(y) = e^{-y}. \qquad (14)$$

By use of (1), p. 14, and (1), p. 72, of Erdelyi et al. [2] $\bar{q}(s)$ is given by

$$\bar{q}(s) = (2/\pi)^{1/2}(1 + h)s(h^2 + s^2)^{-1/2}(1 + s^2)^{-1}. \qquad (15)$$

The solution for the transient temperature is given by

$$T(y, t, h) = T_{ss}(y, h) - T_1(y, t, h) \qquad (16)$$

where the steady-state temperature $T_{ss}(y, h)$ is given by

$$T_{ss}(y, h) = (2/\pi)(1 + h) \int_0^\infty s^{-1}(s^2 + h^2)^{-1}(1 + s^2)^{-1} \times [h \sin (sy) + s \cos (sy)]ds \qquad (17)$$

and $T_1(y, t, h)$ is given by

$$T_1(y, t, h) = (2/\pi)(1 + h) \int_0^\infty s^{-1}(s^2 + h^2)^{-1}(1 + s^2)^{-1} \times [h \sin (sy) + s \cos (sy)]e^{-s^2 t}ds. \qquad (18)$$

By expanding the denominators of (17) and (18) into partial fractions and employing the Fourier sine and cosine transform pairs, (20), p. 15, (11), p. 8, (21), p. 73, (26), p. 74, and (15), p. 15, of Erdelyi et al. [2], the integral solutions (17) and (18) reduce to

$$T_{ss}(y, h) = h^{-1} + (1 - e^{-y}) \qquad (19)$$

and

$$\begin{aligned} T_1(y, t, h) = {} & (1 + h)h^{-1} \operatorname{erf} (\tfrac{1}{2}t^{-1/2}y) - \tfrac{1}{2}e^{t-y} \operatorname{erfc} (t^{1/2} - \tfrac{1}{2}t^{-1/2}y) \\ & + \tfrac{1}{2}(1 + h)(h - 1)^{-1}e^{t+y} \operatorname{erfc} (t^{1/2} + \tfrac{1}{2}t^{-1/2}y) \\ & - (h - 1)^{-1}h^{-1} \exp (h^2 t + hy) \operatorname{erfc} (t^{1/2}h + \tfrac{1}{2}t^{-1/2}y). \end{aligned} \qquad (20)$$

It should be noted that $T_{ss}(y, h)$ is unbounded for $h = 0$.

For $h = 0$ and $h = 1$ the transient solution $T(y, t, h)$ contains indeterminate forms of the type (0/0). By use of l'Hospital's rule the solution for $h = 0$ is found to be

$$\begin{aligned} T(y, t, 0) = {} & \tfrac{1}{2}[e^{t-y} \operatorname{erfc} (t^{1/2} - \tfrac{1}{2}t^{-1/2}y) \\ & + e^{t+y} \operatorname{erfc} (t^{1/2} + \tfrac{1}{2}t^{-1/2}y)] \\ & - e^{-y} - y \operatorname{erfc} (\tfrac{1}{2}t^{-1/2}y) + 2\pi^{-1/2}t^{1/2}e^{-y^2/(4t)} \end{aligned} \qquad (21)$$

which agrees with the special-case result obtained by Williams [3]. See also Carslaw and Jaeger [4]. For $h = 1$, again employing l'Hospital's rule we obtain

$$\begin{aligned} T(y, t, 1) = {} & 2 \operatorname{erfc} (\tfrac{1}{2}t^{-1/2}y) - e^{-y} \\ & - (\tfrac{3}{2} - 2t - y)e^{t+y} \operatorname{erfc} (t^{1/2} + \tfrac{1}{2}t^{-1/2}y) \\ & + \tfrac{1}{2}e^{t-y} \operatorname{erfc} (t^{1/2} - \tfrac{1}{2}t^{-1/2}y) - 2\pi^{-1/2}t^{1/2}e^{-y^2/(4t)}. \end{aligned} \qquad (22)$$

The solution given by (19), (20), (21), and (22) is a generalization of several specialized results given in the literature. In addition to the solution for $h = 0$, Williams [3] obtained an approximate solution for $y = 0$ and $h < 1$. For $h = \infty$, i.e., a constant surface temperature, the solution is given by Luikov [5]. Solutions in the form of multiple integrals for source terms that are time-, space-, and temperature-dependent were obtained by Paterson [6]. For an analysis of the applicability and validity of the no-heat-loss solution ($h = 0$) to the effects due to the absorption of laser radiation see Ready [7].

Solution for Radiation With Arbitrary Spectral Distribution

If the radiation source has its energy distributed across a band of frequencies and the absorption coefficient is frequency-dependent then the source term is given by

$$Q(x) = \int_a^b \lambda(\nu)Q_0(\nu)e^{-\lambda(\nu)x}d\nu \qquad (23)$$

which can be expressed by the limit

$$Q(x) = \lim_{\Delta\nu_i \to 0} \sum_{i=1}^{M} \lambda(\nu_i)Q_0(\nu_i)e^{-\lambda(\nu_i)x}\Delta\nu_i. \qquad (24)$$

If we consider one term of the sum in (24) as the source then the corresponding solution for the transient temperature is given by

$$k\lambda(\nu_i)[\theta_i(x, \tau, h) - \theta_0]/[Q_0(\nu_i)\Delta\nu_i] = T_i(y, t, h) \qquad (25)$$

where $T_i(y, t, h)$ is given by the solution obtained previously for monochromatic radiation. If the source is defined by a finite

---

[2] Numbers in brackets designate References at end of technical brief.

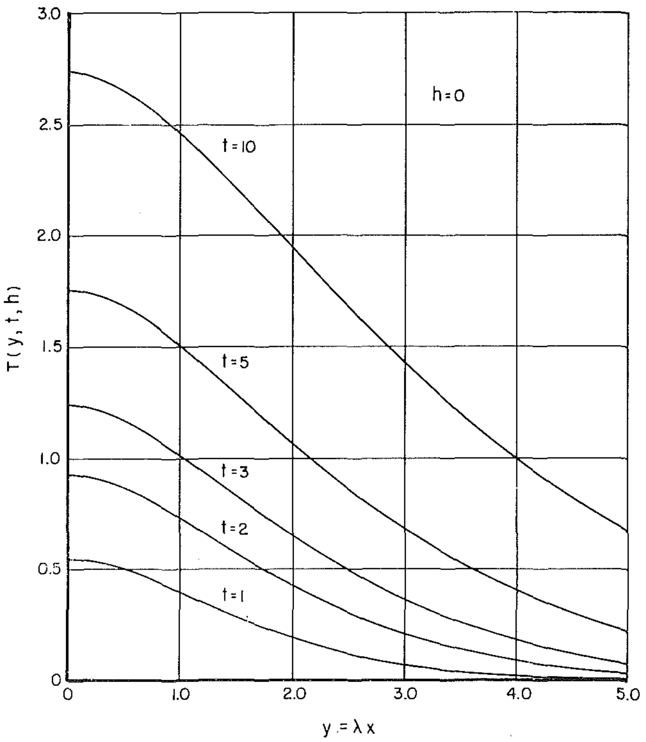

Fig. 1 Dimensionless transient temperature within the solid for no surface cooling ($h = 0$)

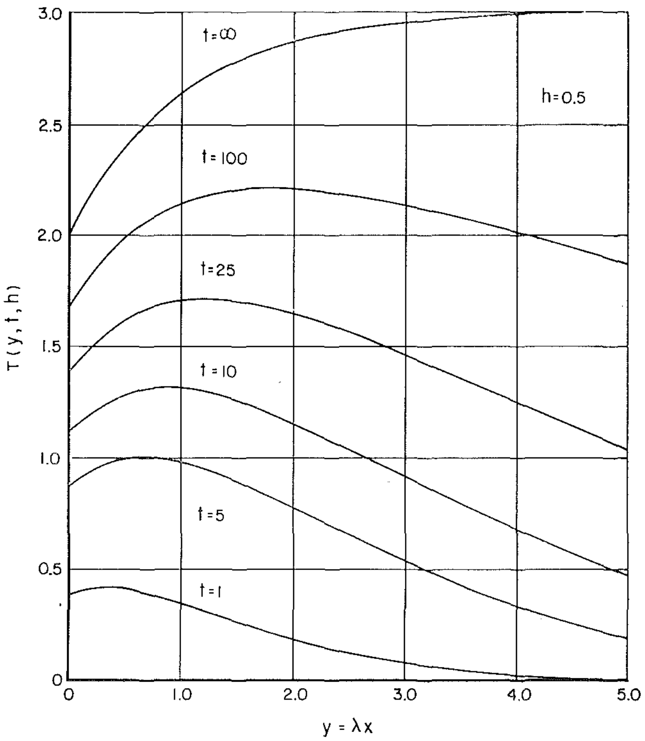

Fig. 2 Dimensionless transient temperature within the solid with surface cooling ($h = 0.5$)

sum of source components as in (24) then by use of the principle of superposition the temperature for the corresponding source is given by

$$\theta - \theta_0 = \sum_{i=1}^{M} (\theta_i - \theta_0) = \sum_{i=1}^{M} [Q_0(\nu_i)/k\lambda(\nu_i)]T_i(y, t, h)\Delta\nu_i. \quad (26)$$

By passing to the limit in (26) the transient temperature is then given by

$$\theta(x, \tau, h) = \theta_0 + k^{-1}\int_a^b [Q_0(\nu)/\lambda(\nu)]T(y, t, h)d\nu \quad (27)$$

where $T(y, t, h)$ is converted to the appropriate function of (x, τ, h, λ) through substitution of the dimensional variables for their dimensionless counterparts.

Numerical Evaluation of Transient Solution for Monochromatic Radiation

In the numerical evaluation of the transient solution for monochromatic radiation on a digital computer one may make use of highly accurate and efficient rational approximations for the error function. For large values of t as encountered in generating numerical data for Fig. 3 one experiences acute computational difficulty in the evaluation of the solution by straightforward means. This difficulty occurs in the evaluation of the function

$$f(a, b) = e^{a+b}\,\mathrm{erfc}\,(a^{1/2} + \tfrac{1}{2}a^{-1/2}b). \quad (28)$$

If $(a + b)$ is sufficiently large $(a + b > 100$, e.g.) then the number generated for exp $(a + b)$ will cause an overflow on most digital computers rendering ensuing computations useless. This can be avoided by the following procedure: By use of the asymptotic series

$$\mathrm{erfc}\,x = \pi^{-1/2}e^{-x^2}[x^{-1} - \tfrac{1}{2}x^{-3} + \tfrac{3}{4}x^{-5} - \tfrac{15}{8}x^{-7} + \ldots] \quad (29)$$

and letting

$$x = a^{1/2} + \tfrac{1}{2}a^{-1/2}b \quad (30)$$

one obtains for $f(a, b)$

$$f(a, b) = \pi^{-1/2}e^{-1/4a^{-1}b^2}[x^{-1} - \tfrac{1}{2}x^{-3} + \tfrac{3}{4}x^{-5} - \tfrac{15}{8}x^{-7} + \ldots]. \quad (31)$$

When employing the truncated series in (31) the exponential function of large argument need not be evaluated. The truncation of the series in (31) results in an error less than the magnitude of the first omitted term. Since resort to this series is required only for large values of x, the series yields high accuracy with only a few terms.

Graphical Results

Figs. 1 and 2 contrast the transient temperature distribution as a function of the dimensionless space coordinate y for the case of no cooling, Fig. 1, versus the case of cooling with $h = 0.5$, Fig. 2. Fig. 3 is a plot of the ratio of the transient surface temperature

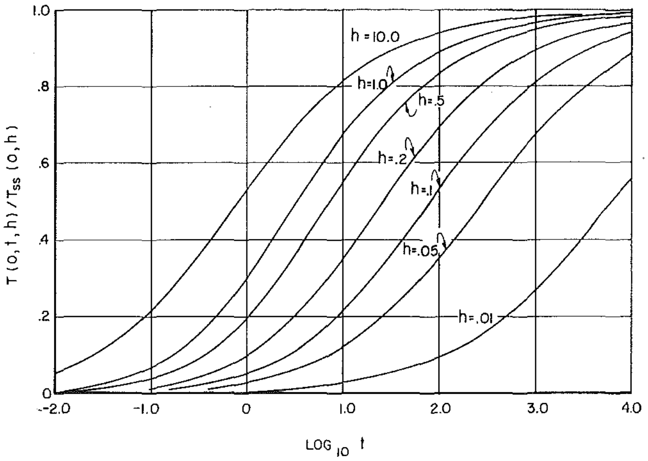

Fig. 3 Effect of Biot number, h, on ratio of transient surface temperature to steady-state surface temperature

to the steady-state value for various values of the Biot number, h. Note that the steady-state surface temperature is given by

$$T_{ss}(0, h) \doteq h^{-1}. \qquad (32)$$

References

1 Churchill, R. V., "Generalized Fourier Integral Formulas," *Mich. Math. Journ.*, Vol. 2, 1953–54, pp. 133–139.

2 Erdelyi, W., Magnus, W., Oberhettinger, F., and Tricomi, F. G., *Tables of Integral Transforms*, Vol. 1, McGraw-Hill, New York, 1954.

3 Williams, C. C., "Damage Initiation in Organic Materials Exposed to High Intensity Thermal Radiation," Sc.D. thesis, Department of Chemical Engineering, M.I.T., Cambridge, Mass., 1953.

4 Carlsaw, H. S., and Jaeger, J. C., *Conduction of Heat in Solids*, 2nd ed., Oxford University Press, London, 1959, p. 80.

5 Luikov, A. V., *Analytical Heat Diffusion Theory*, Academic, New York, 1968, p. 354.

6 Paterson, S., "The Conduction of Heat in a Medium Generating Heat," *Phil. Mag.*, Vol. 32, 1941, pp. 384–392.

7 Ready, J. F., "Effects Due to Absorption of Laser Radiation," *Journ. of Appl. Physics*, Vol. 36, No. 2, 1965, pp. 462–468.

Combining Forced and Free Convective Equations to Represent Combined Heat-Transfer Coefficients for a Horizontal Cylinder

THOMAS W. JACKSON[1] and HOWARD H. YEN[2]

An analytical correlation of superposed free and forced convection for air for a horizontal cylinder in which the forced convection and free convection forces act in the same direction is considered. A simplified method by which the ordinary formulas for forced convection and for free convection can be used together to give the Nusselt number is presented. The method proposed herein can easily be modified to work for other combinations of free and forced flow systems. The method, therefore, may have wide application because standard formulas for simple systems are easily combined to obtain formulas which are valid for complicated systems.

Introduction

Oosthuizen and Madan in a technical note [1][3] presented an empirical analysis for the combined convective heat transfer from horizontal cylinders to air. In their investigation the experimental apparatus was so arranged that the force flow and buoyancy forces were in the same direction. In other words the forced flow was vertically upward. In the test results given in reference [1], the Reynolds number was varied from approximately 100 to 3000 and the Grashof number was varied from 25,000 to 300,000.

The experimental data from reference [1] are shown in Fig. 1 together with Oosthuizen and Madan's correlation. The correlating equation is as follows:

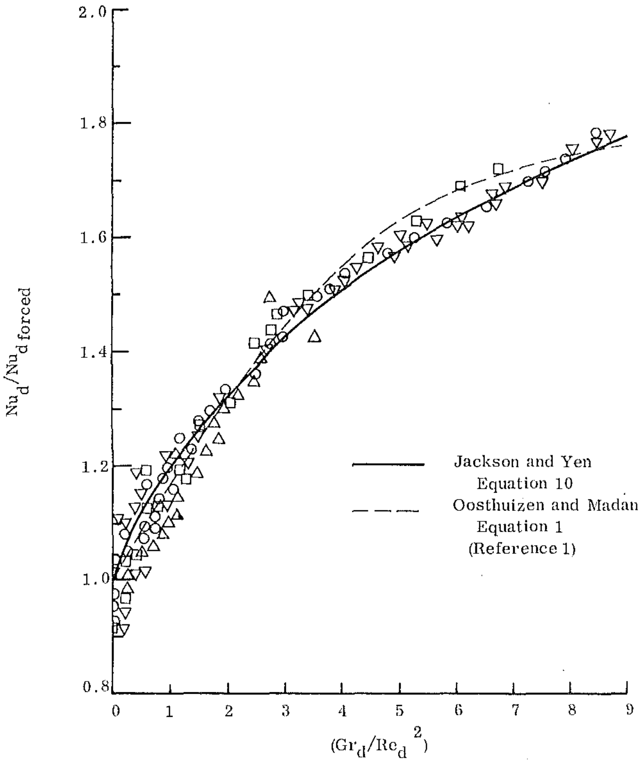

Fig. 1 Correlation of Nusselt numbers in terms of combined convection parameter

$$\frac{\mathrm{Nu}_d}{\mathrm{Nu}_{d_{\mathrm{forced}}}} = 1 + 0.18 \left\{ \mathrm{Gr}_d/\mathrm{Re}_d{}^2 \right\} - 0.011 \left\{ \mathrm{Gr}_d/\mathrm{Re}_d{}^2 \right\}^2 \qquad (1)$$

From the experimental data the forced convection equation chosen to use in equation (1) was:

$$\mathrm{Nu}_{d_{\mathrm{forced}}} = 0.464\ \mathrm{Re}_d{}^{0.5} + 0.0004\ \mathrm{Re}_d \qquad (2)$$

After consideration of reference [1] it appeared desirable to obtain a heat-transfer equation for the combined flow which was based on a combination of a simple forced convection equation and a simple free convection equation. An attempt to do this is given in the following analysis.

Analysis

Consider the flow situation shown schematically in Fig. 2. The heat-transfer equation for forced convection [2] is

$$\mathrm{Nu}_d = 0.615\ \mathrm{Re}^{0.466} \qquad (3)$$

and the equation for free convection [3] is

$$\mathrm{Nu}_d = 0.53\ (\mathrm{Gr\ Pr})^{0.25} \qquad (4)$$

Assuming the Prandtl number for air is 0.7, equation (4) reduces to

$$\mathrm{Nu}_d = 0.50\ \mathrm{Gr}^{0.25} \qquad (5)$$

It is interesting to note that equations (3) and (5) were not obtained from the experimental data of reference [1]. If the forced convection flow, equation (3), can be represented by

$$\mathrm{Nu}_{d_{\mathrm{forced}}} = 0.50\ \mathrm{Re}_{d_{\mathrm{forced}}}{}^{0.50} \qquad (6)$$

then the analysis is simplified appreciably. Equation (6) at a Reynolds number of 100 is 5 percent below equation (3) and at a Reynolds number of 3000 is 7 percent above equation (3).

Equating equation (6) for forced convection to equation (5) for free convection to determine an equivalent flow velocity for the free convection effects gives

---

[1] Professor, School of Mechanical Engineering, Georgia Institute of Technology, Atlanta, Ga. Currently on leave as Technical Director, National Industrial Pollution Control Council, U. S. Department of Commerce, Washington, D. C. Mem. ASME.

[2] Senior Research Engineer, Skidaway Institute of Oceanography, Savannah, Ga. Mem. ASME.

[3] Numbers in brackets designate References at end of technical brief.

Contributed by the Heat Transfer Division of THE AMERICAN SOCIETY OF MECHANICAL ENGINEERS. Manuscript received by the Heat Transfer Division August 17, 1970.

to the steady-state value for various values of the Biot number, h. Note that the steady-state surface temperature is given by

$$T_{ss}(0, h) \doteq h^{-1}. \qquad (32)$$

References

1 Churchill, R. V., "Generalized Fourier Integral Formulas," *Mich. Math. Journ.*, Vol. 2, 1953–54, pp. 133–139.

2 Erdelyi, W., Magnus, W., Oberhettinger, F., and Tricomi, F. G., *Tables of Integral Transforms*, Vol. 1, McGraw-Hill, New York, 1954.

3 Williams, C. C., "Damage Initiation in Organic Materials Exposed to High Intensity Thermal Radiation," Sc.D. thesis, Department of Chemical Engineering, M.I.T., Cambridge, Mass., 1953.

4 Carlsaw, H. S., and Jaeger, J. C., *Conduction of Heat in Solids*, 2nd ed., Oxford University Press, London, 1959, p. 80.

5 Luikov, A. V., *Analytical Heat Diffusion Theory*, Academic, New York, 1968, p. 354.

6 Paterson, S., "The Conduction of Heat in a Medium Generating Heat," *Phil. Mag.*, Vol. 32, 1941, pp. 384–392.

7 Ready, J. F., "Effects Due to Absorption of Laser Radiation," *Journ. of Appl. Physics*, Vol. 36, No. 2, 1965, pp. 462–468.

Combining Forced and Free Convective Equations to Represent Combined Heat-Transfer Coefficients for a Horizontal Cylinder

THOMAS W. JACKSON[1] **and HOWARD H. YEN**[2]

An analytical correlation of superposed free and forced convection for air for a horizontal cylinder in which the forced convection and free convection forces act in the same direction is considered. A simplified method by which the ordinary formulas for forced convection and for free convection can be used together to give the Nusselt number is presented. The method proposed herein can easily be modified to work for other combinations of free and forced flow systems. The method, therefore, may have wide application because standard formulas for simple systems are easily combined to obtain formulas which are valid for complicated systems.

Introduction

Oosthuizen and Madan in a technical note [1][3] presented an empirical analysis for the combined convective heat transfer from horizontal cylinders to air. In their investigation the experimental apparatus was so arranged that the force flow and buoyancy forces were in the same direction. In other words the forced flow was vertically upward. In the test results given in reference [1], the Reynolds number was varied from approximately 100 to 3000 and the Grashof number was varied from 25,000 to 300,000.

The experimental data from reference [1] are shown in Fig. 1 together with Oosthuizen and Madan's correlation. The correlating equation is as follows:

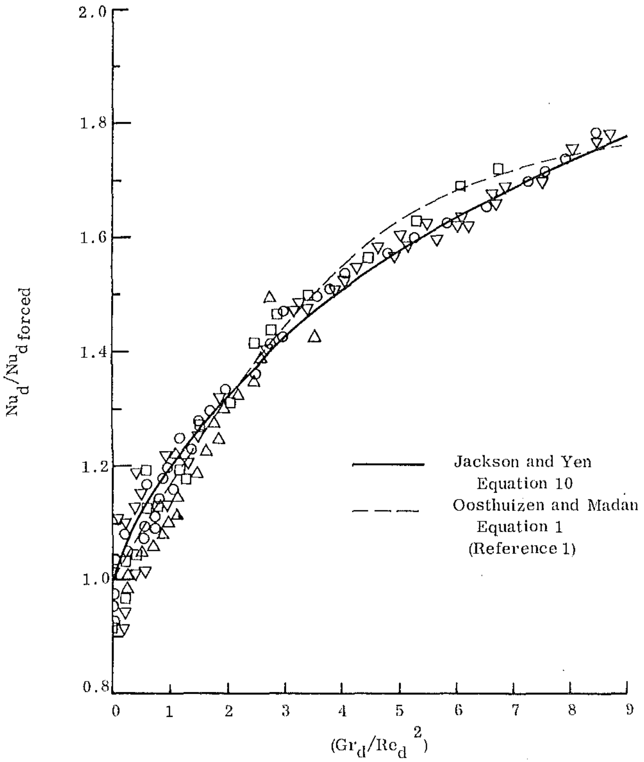

Fig. 1 Correlation of Nusselt numbers in terms of combined convection parameter

$$\frac{Nu_d}{Nu_{d_{forced}}} = 1 + 0.18 \left\{ Gr_d/Re_d^2 \right\} - 0.011 \left\{ Gr_d/Re_d^2 \right\}^2 \qquad (1)$$

From the experimental data the forced convection equation chosen to use in equation (1) was:

$$Nu_{d_{forced}} = 0.464\, Re_d^{0.5} + 0.0004\, Re_d \qquad (2)$$

After consideration of reference [1] it appeared desirable to obtain a heat-transfer equation for the combined flow which was based on a combination of a simple forced convection equation and a simple free convection equation. An attempt to do this is given in the following analysis.

Analysis

Consider the flow situation shown schematically in Fig. 2. The heat-transfer equation for forced convection [2] is

$$Nu_d = 0.615\, Re^{0.466} \qquad (3)$$

and the equation for free convection [3] is

$$Nu_d = 0.53\, (Gr\, Pr)^{0.25} \qquad (4)$$

Assuming the Prandtl number for air is 0.7, equation (4) reduces to

$$Nu_d = 0.50\, Gr^{0.25} \qquad (5)$$

It is interesting to note that equations (3) and (5) were not obtained from the experimental data of reference [1]. If the forced convection flow, equation (3), can be represented by

$$Nu_{d_{forced}} = 0.50\, Re_{d_{forced}}^{0.50} \qquad (6)$$

then the analysis is simplified appreciably. Equation (6) at a Reynolds number of 100 is 5 percent below equation (3) and at a Reynolds number of 3000 is 7 percent above equation (3).

Equating equation (6) for forced convection to equation (5) for free convection to determine an equivalent flow velocity for the free convection effects gives

---

[1] Professor, School of Mechanical Engineering, Georgia Institute of Technology, Atlanta, Ga. Currently on leave as Technical Director, National Industrial Pollution Control Council, U. S. Department of Commerce, Washington, D. C. Mem. ASME.

[2] Senior Research Engineer, Skidaway Institute of Oceanography, Savannah, Ga. Mem. ASME.

[3] Numbers in brackets designate References at end of technical brief.

Contributed by the Heat Transfer Division of THE AMERICAN SOCIETY OF MECHANICAL ENGINEERS. Manuscript received by the Heat Transfer Division August 17, 1970.

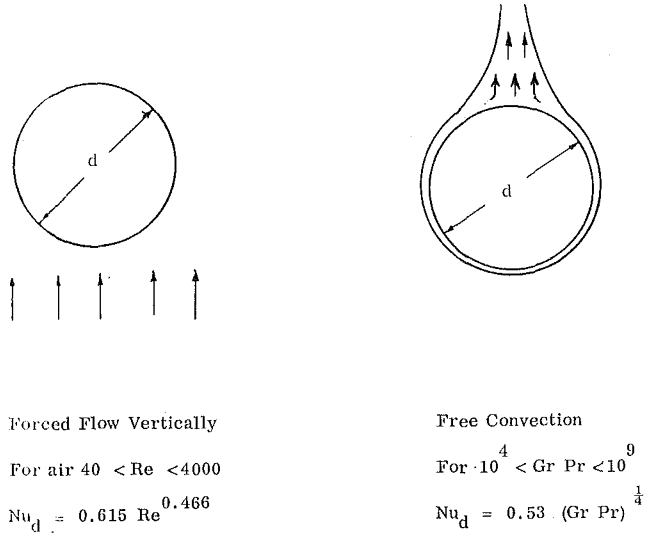

Fig. 2 Basic equations for forced and free convection, reference [2], pp. 147, 167.

$$\mathrm{Re}_{d_{\mathrm{free}}}{}^2 = \mathrm{Gr} \tag{7}$$

It can be shown by means of Reynolds analogy [4] that, at least for a confined flow, the heat-transfer coefficient is a function of the work performed on the system. Work on the system, however, involves a flow change of momentum, which in turn is proportional to the fluid velocity squared or $\mathrm{Re}_d{}^2$. Therefore using equation (6),

$$\mathrm{Nu}_d = 0.50\ \underbrace{[\mathrm{Re}_d{}^2]^{0.25}}_{\substack{\text{forced flow}\\ \text{work equiv.}}} = f(\text{work}) \tag{8}$$

Adding equation (7), which represents the work term for free convection, to the equivalent work term for forced convection as indicated in equation (8) gives

$$\begin{aligned}\mathrm{Nu}_d &= 0.50[\mathrm{Re}_{d_{\mathrm{forced}}}{}^2 + \mathrm{Re}_{d_{\mathrm{free}}}{}^2]^{0.25}\\ &= 0.50[\mathrm{Re}_{d_{\mathrm{forced}}}{}^2 + \mathrm{Gr}]^{0.25}\end{aligned} \tag{9}$$

To compare equation (9) to the experimental data it is necessary to divide it by equation (6). This gives

$$\frac{\mathrm{Nu}_d}{\mathrm{Nu}_{d_{\mathrm{forced}}}} = \left[1 + \frac{\mathrm{Gr}}{\mathrm{Re}^2}\right]^{0.25} \tag{10}$$

Equation (10) is also shown in Fig. 1. It is interesting to note that this very simple equation agrees well with the empirically determined equation by Oosthuizen and Madan [1] being less than 3 percent low over a $\mathrm{Gr}/\mathrm{Re}^2$ range of 1 to 9. It is also noted that a method similar to that proposed herein for a Reynolds-number range of from 0.01 to 45 and Gr Pr range from 0.0001 to 10 was utilized by Hatton et al. [5]. Their results complement the relationships given in this paper which are for a Reynolds-number range of 100 to 3000 and a Grashof range of from 25,000 to 300,000.

Discussion of Results

An equation, which is a combination of simplified forced and free convection equations, is presented which agrees quite well with the experimentally determined equation from reference [1]. The simplicity of the analysis indicates that it may have other applications where combined flows exist. To utilize the method outlined in the paper only the simple equations for each of the various types of flow need to be known.

References

1 Oosthuizen, P. H., and Madan, S., "Combined Convective Heat Transfer From Horizontal Cylinders in Air," JOURNAL OF HEAT TRANSFER, TRANS. ASME, Series C, Vol. 92, No. 1, Feb. 1970, pp. 194–196.

2 Holman, J. P., *Heat Transfer*, McGraw-Hill, New York, 1963, p. 147.

3 Ibid., p. 167.

4 Eckert, E. R. G., and Drake, R. M., Jr., *Heat and Mass Transfer*, McGraw-Hill, New York, 1959, pp. 203–204.

5 Hatton, A. P., Jones, D. D., and Swire, H. W., "Combined Forced and Natural Convection with Low-Speed Air Flow over Horizontal Cylinders," *Journal of Fluid Mechanics*, Vol. 42, Part 1, 1970, pp. 17–31.

Charts for Thermal Transients in Composite Cylinders

W. W. BOWLEY[1] and H. A. KOENIG[1]

Nomenclature

a = inner radius of composite cylinder, ft
b = interface radius at inner and outer cylinders, ft
c = outer radius of composite cylinder, ft
C_p = specific heat, Btu/lb-deg F
K = thermal conductivity, Btu/hr-ft-deg F
r = radius, ft
T = temperature, deg F
T_i = initial temperature of entire cylinder, deg F
T_0 = temperature to which inner radius of cylinder is stepped, deg F
κ = thermal diffusivity = $K/\rho C_p$, ft²/hr
κ' = $\sqrt{\kappa_1/\kappa_2}$
α = eigenvalue from appropriate frequency equation, ft^{-1}
β = $\kappa t/c^2$ = dimensionless time
ρ = density of material, lb/ft³
1 = subscript denoting inner cylinder $a \le r \le b$
2 = subscript denoting outer cylinder $b \le r \le c$

THERE ARE several problems of engineering interest which require a detailed knowledge of the transient temperatures in the interior of cylinders which are composed of two or more materials. Two examples of this type of problem are composite cylindrical rocket nozzles and insulated steam lines. In both of these cases the internal film coefficient is an extremely large number and the surface resistance to heat transfer is therefore low. Because of the low surface resistance, a sudden step in the surface temperature can be used as a good approximation for the boundary condition of the diffusion equation.

The labor involved in repeatedly solving the diffusion equation for this type of problem warrants the construction of a chart of the solution much in the manner of those constructed by Heisler [1].[2] This chart then allows the engineer to obtain a solution to the diffusion equation by merely substituting the properties and conditions involved in his problem into the dimensionless parameters used on the chart.

The solution to the diffusion equation for composite cylinders was obtained by means of the Laplace transform technique which was described in a paper by Jaeger [2].

---

[1] Associate Professor, Mechanical Engineering Department, University of Connecticut, Storrs, Conn. Assoc. Mem. ASME.

[2] Numbers in brackets designate References at end of technical brief.

Contributed by the Heat Transfer Division of THE AMERICAN SOCIETY OF MECHANICAL ENGINEERS. Manuscript received by the Heat Transfer Division November 4, 1970.

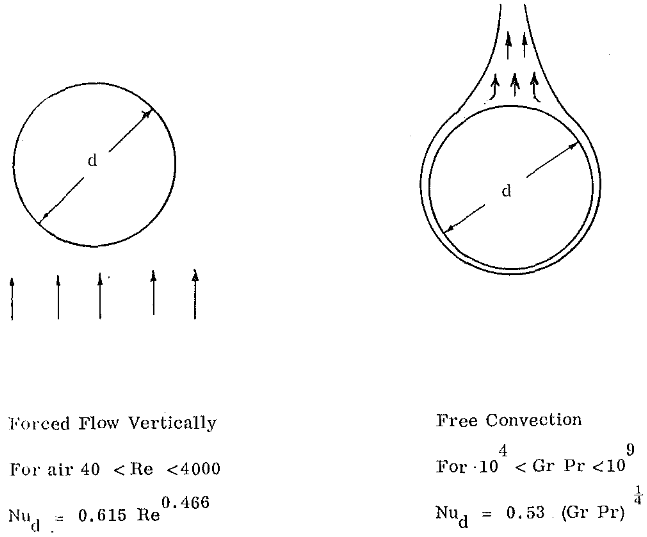

Fig. 2 Basic equations for forced and free convection, reference [2], pp. 147, 167.

$$\mathrm{Re}_{d_{\mathrm{free}}}{}^2 = \mathrm{Gr} \tag{7}$$

It can be shown by means of Reynolds analogy [4] that, at least for a confined flow, the heat-transfer coefficient is a function of the work performed on the system. Work on the system, however, involves a flow change of momentum, which in turn is proportional to the fluid velocity squared or $\mathrm{Re}_d{}^2$. Therefore using equation (6),

$$\mathrm{Nu}_d = 0.50\ \underset{\substack{\text{forced flow}\\ \text{work equiv.}}}{[\mathrm{Re}_d{}^2]^{0.25}} = f(\text{work}) \tag{8}$$

Adding equation (7), which represents the work term for free convection, to the equivalent work term for forced convection as indicated in equation (8) gives

$$\begin{aligned}\mathrm{Nu}_d &= 0.50[\mathrm{Re}_{d_{\mathrm{forced}}}{}^2 + \mathrm{Re}_{d_{\mathrm{free}}}{}^2]^{0.25}\\ &= 0.50[\mathrm{Re}_{d_{\mathrm{forced}}}{}^2 + \mathrm{Gr}]^{0.25}\end{aligned} \tag{9}$$

To compare equation (9) to the experimental data it is necessary to divide it by equation (6). This gives

$$\frac{\mathrm{Nu}_d}{\mathrm{Nu}_{d_{\mathrm{forced}}}} = \left[1 + \frac{\mathrm{Gr}}{\mathrm{Re}^2}\right]^{0.25} \tag{10}$$

Equation (10) is also shown in Fig. 1. It is interesting to note that this very simple equation agrees well with the empirically determined equation by Oosthuizen and Madan [1] being less than 3 percent low over a $\mathrm{Gr}/\mathrm{Re}^2$ range of 1 to 9. It is also noted that a method similar to that proposed herein for a Reynolds-number range of from 0.01 to 45 and Gr Pr range from 0.0001 to 10 was utilized by Hatton et al. [5]. Their results complement the relationships given in this paper which are for a Reynolds-number range of 100 to 3000 and a Grashof range of from 25,000 to 300,000.

Discussion of Results

An equation, which is a combination of simplified forced and free convection equations, is presented which agrees quite well with the experimentally determined equation from reference [1]. The simplicity of the analysis indicates that it may have other applications where combined flows exist. To utilize the method outlined in the paper only the simple equations for each of the various types of flow need to be known.

References

1 Oosthuizen, P. H., and Madan, S., "Combined Convective Heat Transfer From Horizontal Cylinders in Air," JOURNAL OF HEAT TRANSFER, TRANS. ASME, Series C, Vol. 92, No. 1, Feb. 1970, pp. 194–196.

2 Holman, J. P., *Heat Transfer*, McGraw-Hill, New York, 1963, p. 147.

3 Ibid., p. 167.

4 Eckert, E. R. G., and Drake, R. M., Jr., *Heat and Mass Transfer*, McGraw-Hill, New York, 1959, pp. 203–204.

5 Hatton, A. P., Jones, D. D., and Swire, H. W., "Combined Forced and Natural Convection with Low-Speed Air Flow over Horizontal Cylinders," *Journal of Fluid Mechanics*, Vol. 42, Part 1, 1970, pp. 17–31.

Charts for Thermal Transients in Composite Cylinders

W. W. BOWLEY[1] **and H. A. KOENIG**[1]

Nomenclature

a = inner radius of composite cylinder, ft
b = interface radius at inner and outer cylinders, ft
c = outer radius of composite cylinder, ft
C_p = specific heat, Btu/lb-deg F
K = thermal conductivity, Btu/hr-ft-deg F
r = radius, ft
T = temperature, deg F
T_i = initial temperature of entire cylinder, deg F
T_0 = temperature to which inner radius of cylinder is stepped, deg F
κ = thermal diffusivity $= K/\rho\, C_p$, ft²/hr
$\kappa' = \sqrt{\kappa_1/\kappa_2}$
α = eigenvalue from appropriate frequency equation, ft^{-1}
$\beta = \kappa t/c^2$ = dimensionless time
ρ = density of material, lb/ft³
1 = subscript denoting inner cylinder $a \leq r \leq b$
2 = subscript denoting outer cylinder $b \leq r \leq c$

THERE ARE several problems of engineering interest which require a detailed knowledge of the transient temperatures in the interior of cylinders which are composed of two or more materials. Two examples of this type of problem are composite cylindrical rocket nozzles and insulated steam lines. In both of these cases the internal film coefficient is an extremely large number and the surface resistance to heat transfer is therefore low. Because of the low surface resistance, a sudden step in the surface temperature can be used as a good approximation for the boundary condition of the diffusion equation.

The labor involved in repeatedly solving the diffusion equation for this type of problem warrants the construction of a chart of the solution much in the manner of those constructed by Heisler [1].[2] This chart then allows the engineer to obtain a solution to the diffusion equation by merely substituting the properties and conditions involved in his problem into the dimensionless parameters used on the chart.

The solution to the diffusion equation for composite cylinders was obtained by means of the Laplace transform technique which was described in a paper by Jaeger [2].

---

[1] Associate Professor, Mechanical Engineering Department, University of Connecticut, Storrs, Conn. Assoc. Mem. ASME.

[2] Numbers in brackets designate References at end of technical brief.

Contributed by the Heat Transfer Division of THE AMERICAN SOCIETY OF MECHANICAL ENGINEERS. Manuscript received by the Heat Transfer Division November 4, 1970.

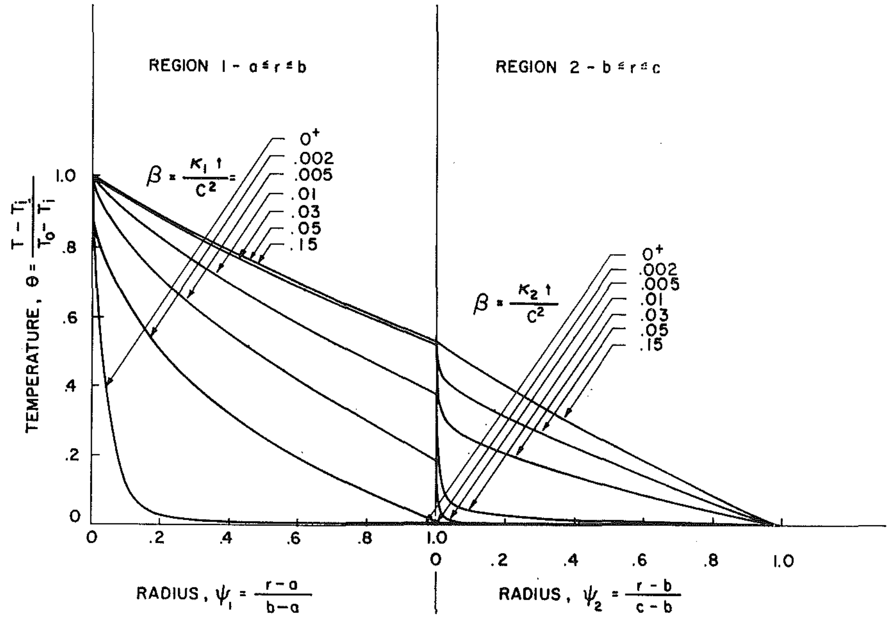

Fig. 1 Temperature charts for composite cylinders

$$T_2 = T_0 \frac{K_1 \log (r/c)}{K_1 \log (b/c) - K_2 \log (b/a)}$$

$$- \pi K_1 K_2 T_0 \sum_{s=1}^{\infty} e^{-\kappa_1 \alpha^2{}_s t} C(\kappa' r\alpha_s, \kappa' c\alpha_s) C(\kappa' b\alpha_s, \kappa' c\alpha_s)$$

$$\times C(b\alpha_s, a\alpha_s) F(\alpha_s) \quad (1)$$

$$T_1 = T_0 \frac{K_1 \log (b/c) - K_2 \log (b/r)}{K_1 \log (b/c) - K_2 \log (b/a)}$$

$$- \pi K_1 K_2 T_0 \sum_{s=1}^{\infty} e^{-\kappa_1 \alpha^2{}_s t} C(r\alpha_s, a\alpha_s) C^2(\kappa' b\alpha_s, \kappa' c\alpha_s) F(\alpha_s) \quad (2)$$

This solution is valid when the temperature at $r = c$ is held at its initial value. A computer program was written to obtain numerical values of the solution to equations (1) and (2) for the range of dimensionless parameters given in Fig. 1.

References

1 Heisler, M. P., "Temperature Charts for Induction and Constant Temperature Heating," TRANS. ASME, Vol. 69, 1947, pp. 227–236.

2 Jaeger, J. C., "Heat Conduction in Composite Circular Cylinders," *Philosophical Magazine*, Vol. 32, No. 7, 1941, p. 324.

Heat-Transfer and Flow-Friction Data for Two Fin–Tube Surfaces

F. C. McQUISTON[1] **and D. R. TREE**[2]

THE PURPOSE of this technical brief is to report the results of an experimental investigation to determine the heat-transfer and flow-friction performance of two continuous fin–tube surfaces. The objective was to obtain generalized correlations of Colburn factor, St $Pr^{2/3}$, and Fanning friction factor versus Reynolds number. The experiments were carried out in an open-loop steam-to-air test apparatus very similar to that used so successfully by Kays and London [1].[3] Complete details of the construction and operation of the test apparatus are given in reference [2]. The steady-state technique with the N_{tu}–Effectiveness method was used to obtain and reduce the raw data. This method is described by Shah [3] and the exact details for this investigation are given in reference [2].

The geometry of the surfaces tested is given in Fig. 1 and Table 1. The surfaces were of all-aluminum construction with a mechanical bond between fins and tubing. No undue thermal resistance was observed at this junction. Both surfaces were quite smooth with no sharp edges or burrs.

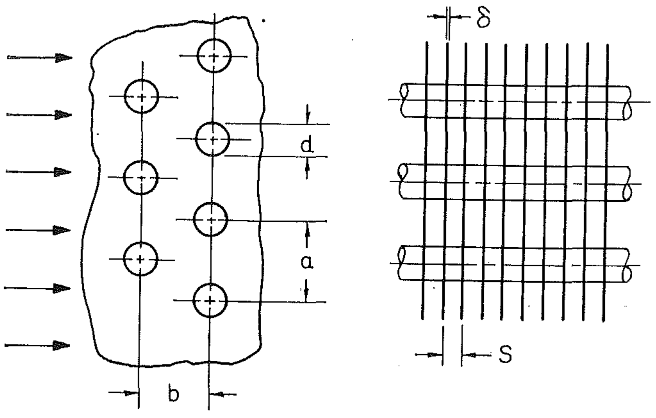

Fig. 1 Continuous fin–tube surface geometry

The results of the investigation are shown in Fig. 2 with the Colburn factor and the Fanning friction factor plotted versus the Reynolds number. It is estimated that the uncertainty in determination of the Reynolds number was ±2 percent while the Colburn and friction factors have a ±5 percent uncertainty. These accuracies are equal to those claimed by Kays and London [1, 4]. The correlations have been scaled to an infinite number of tube rows as described in reference [4].

One or two deviations require explanation. In Fig. 2, for surface number C-1314E the Colburn factor is observed to drop

---

[1] Associate Professor, School of Mechanical and Aerospace Engineering, Oklahoma State University, Stillwater, Okla.

[2] Associate Professor, School of Mechanical Engineering, Purdue University, Lafayette, Ind.

[3] Numbers in brackets designate References at end of technical brief.

Contributed by the Heat Transfer Division of THE AMERICAN SOCIETY OF MECHANICAL ENGINEERS. Manuscript received by the Heat Transfer Division November 30, 1970.

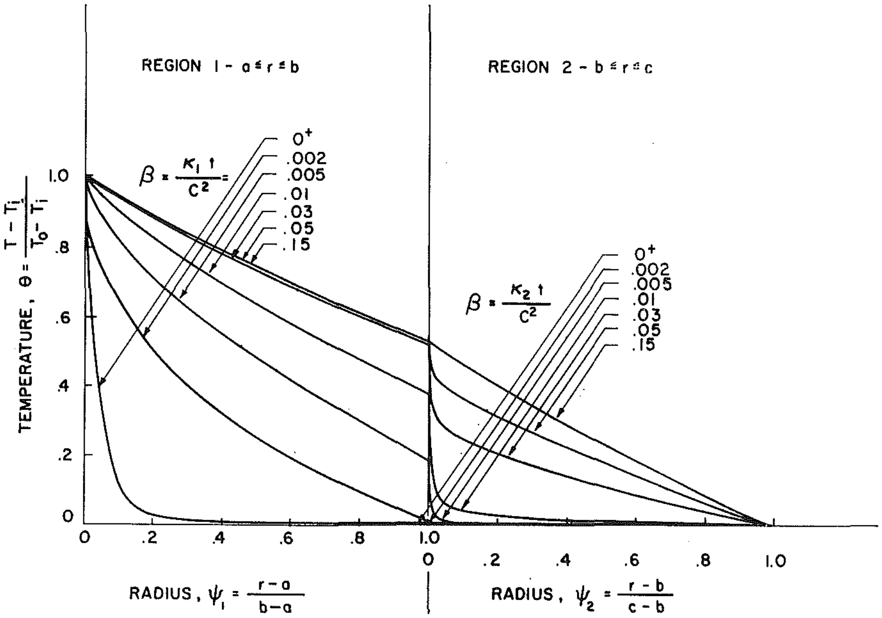

Fig. 1 Temperature charts for composite cylinders

$$T_2 = T_0 \frac{K_1 \log (r/c)}{K_1 \log (b/c) - K_2 \log (b/a)}$$

$$- \pi K_1 K_2 T_0 \sum_{s=1}^{\infty} e^{-\kappa_1 \alpha^2 s^t} C(\kappa' r\alpha_s, \kappa' c\alpha_s) C(\kappa' b\alpha_s, \kappa' c\alpha_s)$$

$$\times C(b\alpha_s, a\alpha_s) F(\alpha_s) \quad (1)$$

$$T_1 = T_0 \frac{K_1 \log (b/c) - K_2 \log (b/r)}{K_1 \log (b/c) - K_2 \log (b/a)}$$

$$- \pi K_1 K_2 T_0 \sum_{s=1}^{\infty} e^{-\kappa_1 \alpha^2 s^t} C(r\alpha_s, a\alpha_s) C^2(\kappa' b\alpha_s, \kappa' c\alpha_s) F(\alpha_s) \quad (2)$$

This solution is valid when the temperature at $r = c$ is held at its initial value. A computer program was written to obtain numerical values of the solution to equations (1) and (2) for the range of dimensionless parameters given in Fig. 1.

References

1 Heisler, M. P., "Temperature Charts for Induction and Constant Temperature Heating," Trans. ASME, Vol. 69, 1947, pp. 227–236.

2 Jaeger, J. C., "Heat Conduction in Composite Circular Cylinders," *Philosophical Magazine*, Vol. 32, No. 7, 1941, p. 324.

Heat-Transfer and Flow-Friction Data for Two Fin–Tube Surfaces

F. C. McQUISTON[1] **and D. R. TREE**[2]

The purpose of this technical brief is to report the results of an experimental investigation to determine the heat-transfer and flow-friction performance of two continuous fin–tube surfaces. The objective was to obtain generalized correlations of Colburn factor, St $Pr^{2/3}$, and Fanning friction factor versus Reynolds number. The experiments were carried out in an open-loop steam-to-air test apparatus very similar to that used so successfully by Kays and London [1].[3] Complete details of the construction and operation of the test apparatus are given in reference [2]. The steady-state technique with the N_{tu}–Effectiveness method was used to obtain and reduce the raw data. This method is described by Shah [3] and the exact details for this investigation are given in reference [2].

The geometry of the surfaces tested is given in Fig. 1 and Table 1. The surfaces were of all-aluminum construction with a mechanical bond between fins and tubing. No undue thermal resistance was observed at this junction. Both surfaces were quite smooth with no sharp edges or burrs.

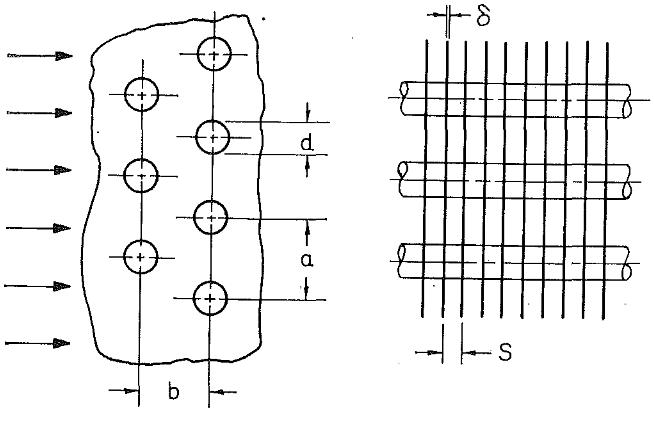

Fig. 1 Continuous fin–tube surface geometry

The results of the investigation are shown in Fig. 2 with the Colburn factor and the Fanning friction factor plotted versus the Reynolds number. It is estimated that the uncertainty in determination of the Reynolds number was ±2 percent while the Colburn and friction factors have a ±5 percent uncertainty. These accuracies are equal to those claimed by Kays and London [1, 4]. The correlations have been scaled to an infinite number of tube rows as described in reference [4].

One or two deviations require explanation. In Fig. 2, for surface number C-1314E the Colburn factor is observed to drop

---

[1] Associate Professor, School of Mechanical and Aerospace Engineering, Oklahoma State University, Stillwater, Okla.

[2] Associate Professor, School of Mechanical Engineering, Purdue University, Lafayette, Ind.

[3] Numbers in brackets designate References at end of technical brief.

Contributed by the Heat Transfer Division of The American Society of Mechanical Engineers. Manuscript received by the Heat Transfer Division November 30, 1970.

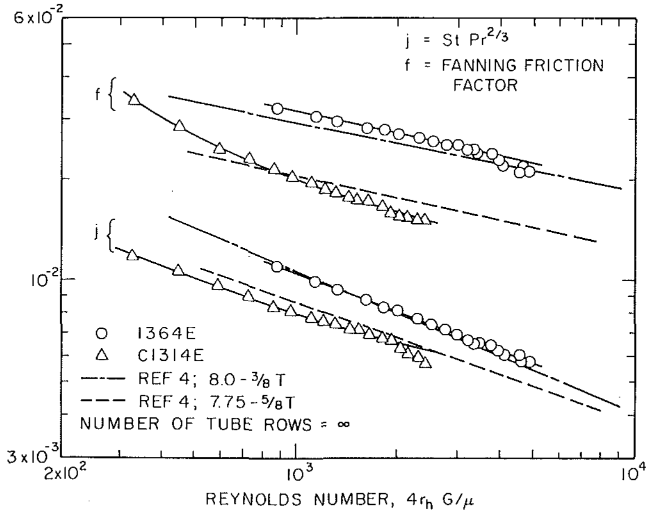

Fig. 2 Comparison of heat-transfer and flow-friction correlations

off sharply at high Reynolds numbers. This was due to a greater than normal buildup of condensate inside the tubes which introduced a large unknown thermal resistance. This condition could not be prevented. For surface number 1364E the friction factor drops off at large Reynolds numbers. This was believed due to slight fluctuations in the flow which caused a large uncertainty in the mass flow rate and finally in the friction factor. Smooth curves representing the best interpretation of the data have been drawn through the data points. Correlations for two surfaces of similar geometry, given by Kays and London [4], are shown in Fig. 2 for comparison. Table 2 contains an accurate listing of data based on the smooth curves.

Methods for using the above data for design purposes are outlined in reference [4]. It is not recommended that the data be extrapolated to higher or lower Reynolds numbers and scaling of the surface geometry is not recommended. The data should be equally valid for all common gases since the test fluid was air ($\Pr \approx 0.7$).

Table 1 Surface geometry

Surface characteristics	Surface number C-1314E	1364E
Tube arrangement	staggered	staggered
Fin type	plain	plain
Transverse tube spacing, a, in.	0.800	0.800
Longitudinal tube spacing, b, in.	0.692	0.692
Fins per inch, $1/S$	14.3	8.0
Fin thickness, δ, in.	0.0065	0.0065
Tube outside diameter, d, in.	0.407	0.407
Hydraulic diameter, $4r_h$, ft	0.0055	0.0101
Minimum free-flow/frontal area,* σ	0.398	0.439
Heat-transfer area/total volume, α, ft²/ft³	290.0	174.0
Fin area/total area	0.917	0.855

* Minimum free-flow area in spaces transverse to flow.

Table 2 Heat-transfer and friction data

Re	St $\Pr^{2/3}$ C-1314E	f	Re	St $\Pr^{2/3}$ 1364E	f
2500.	0.00626	0.0151	5000.	0.00575	0.0224
2000.	0.00665	0.0160	4000.	0.00628	0.0236
1500.	0.00719	0.0175	3000.	0.00699	0.0251
1200.	0.00764	0.0188	2000.	0.00815	0.0273
1000.	0.00801	0.0200	1500.	0.00908	0.0292
800.	0.00861	0.0218	1200.	0.00987	0.0307
600.	0.00947	0.0246	1000.	0.01061	0.0319
500.	0.01010	0.0269	900.	0.01110	0.0327
400.	0.01095	0.0302	800.	0.01155	0.0334
300.	0.01235	0.0363			

References

1 Kays, W. M., and London, A. L., "Heat-Transfer and Flow-Friction Characteristics of Some Compact Heat-Exchanger Surfaces, Part 1—Test System and Procedure," Trans. ASME, Vol. 72, 1950, pp. 1075–1085; also Stanford TR No. 2.

2 McQuiston, F. C., "Optimization of Fin-Tube and Plate-Fin Heat Transfer Surfaces Operating Under Conditions of Forced Convection," PhD thesis, Purdue University, Jan. 1970.

3 Shah, R. K., "Data Reduction Procedures for the Determination of Convective Surface Heat Transfer and Friction Flow Characteristics—Steam-to-Air Test Cores," TR No. 64, Department of Mechanical Engineering, Stanford University, 1967.

4 Kays, W. M., and London, A. L., *Compact Heat Exchangers*, 2nd ed., McGraw-Hill, New York, 1964.

Influence of Temperature Dependent Properties on a Step-Heated Semi-Infinite Solid

R. L. ASH[1] and G. R. CROSSMAN[2]

Nomenclature

$b = \dfrac{1}{k_0}\dfrac{dk}{dT}$, 1/deg C
c = specific heat, J/kg-deg C
$G_n(\eta)$ = nth similarity function
k = thermal conductivity, J/m-sec-deg C
k_0 = initial thermal conductivity
q_0 = step heat flux, J/m²-sec
T = temperature, deg C
t = time, sec
$t_{\max}$ = reference time
x = space coordinate, m
α = thermal diffusivity, m²/sec
α_0 = initial thermal diffusivity
$\beta = \dfrac{1}{\alpha_0}\dfrac{d\alpha}{d\phi}$, 1/deg C
$\eta = \xi/2\sqrt{\tau}$, dimensionless similarity variable
$\epsilon = \beta q_0(\alpha_0 t_{\max})^{1/2}/k_0$, perturbation parameter
$\epsilon_b = b q_0(\alpha_0 t_{\max})^{1/2}/k_0$, thermal conductivity parameter
$\theta = k_0\phi/q_0(\alpha_0 t_{\max})^{1/2}$, dimensionless Kirchhoff temperature
θ_n = nth perturbation term
$\xi = x/(\alpha_0 t_{\max})^{1/2}$, dimensionless space coordinate
ρ = density, kg/m³
$\tau = t/t_{\max}$, dimensionless time
ϕ = Kirchhoff temperature, deg C
$\psi = k_0 T/q_0(\alpha_0 t_{\max})^{1/2}$, dimensionless temperature

Introduction

ONE method for measuring the thermophysical properties of solids has been to monitor the surface temperature of a radiatively heated sample. If the sample thickness was large in comparison with a time and property dependent length parameter ($\sqrt{\alpha t_{\max}}$), the temperature history could be represented by a step-heated, semi-infinite solid.

---

[1] Associate Professor of Engineering, Old Dominion University, Norfolk, Va. Assoc. Mem. ASME.

[2] Assistant Professor of Engineering Technology, Old Dominion University, Norfolk, Va.

Contributed by the Heat Transfer Division of THE AMERICAN SOCIETY OF MECHANICAL ENGINEERS. Manuscript received by the Heat Transfer Division July 20, 1970.

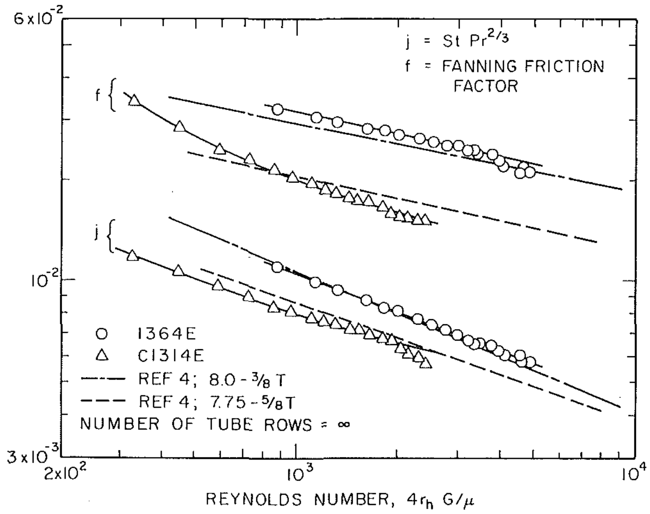

Fig. 2 Comparison of heat-transfer and flow-friction correlations

off sharply at high Reynolds numbers. This was due to a greater than normal buildup of condensate inside the tubes which introduced a large unknown thermal resistance. This condition could not be prevented. For surface number 1364E the friction factor drops off at large Reynolds numbers. This was believed due to slight fluctuations in the flow which caused a large uncertainty in the mass flow rate and finally in the friction factor. Smooth curves representing the best interpretation of the data have been drawn through the data points. Correlations for two surfaces of similar geometry, given by Kays and London [4], are shown in Fig. 2 for comparison. Table 2 contains an accurate listing of data based on the smooth curves.

Methods for using the above data for design purposes are outlined in reference [4]. It is not recommended that the data be extrapolated to higher or lower Reynolds numbers and scaling of the surface geometry is not recommended. The data should be equally valid for all common gases since the test fluid was air ($\mathrm{Pr} \approx 0.7$).

Table 1 Surface geometry

Surface characteristics	Surface number C-1314E	Surface number 1364E
Tube arrangement	staggered	staggered
Fin type	plain	plain
Transverse tube spacing, a, in.	0.800	0.800
Longitudinal tube spacing, b, in.	0.692	0.692
Fins per inch, $1/S$	14.3	8.0
Fin thickness, δ, in.	0.0065	0.0065
Tube outside diameter, d, in.	0.407	0.407
Hydraulic diameter, $4r_h$, ft	0.0055	0.0101
Minimum free-flow/frontal area,* σ	0.398	0.439
Heat-transfer area/total volume, α, ft²/ft³	290.0	174.0
Fin area/total area	0.917	0.855

* Minimum free-flow area in spaces transverse to flow.

Table 2 Heat-transfer and friction data

Re	$\mathrm{St\,Pr}^{2/3}$ C-1314E	f	Re	$\mathrm{St\,Pr}^{2/3}$ 1364E	f
2500.	0.00626	0.0151	5000.	0.00575	0.0224
2000.	0.00665	0.0160	4000.	0.00628	0.0236
1500.	0.00719	0.0175	3000.	0.00699	0.0251
1200.	0.00764	0.0188	2000.	0.00815	0.0273
1000.	0.00801	0.0200	1500.	0.00908	0.0292
800.	0.00861	0.0218	1200.	0.00987	0.0307
600.	0.00947	0.0246	1000.	0.01061	0.0319
500.	0.01010	0.0269	900.	0.01110	0.0327
400.	0.01095	0.0302	800.	0.01155	0.0334
300.	0.01235	0.0363			

References

1 Kays, W. M., and London, A. L., "Heat-Transfer and Flow-Friction Characteristics of Some Compact Heat-Exchanger Surfaces, Part 1—Test System and Procedure," Trans. ASME, Vol. 72, 1950, pp. 1075–1085; also Stanford TR No. 2.

2 McQuiston, F. C., "Optimization of Fin-Tube and Plate-Fin Heat Transfer Surfaces Operating Under Conditions of Forced Convection," PhD thesis, Purdue University, Jan. 1970.

3 Shah, R. K., "Data Reduction Procedures for the Determination of Convective Surface Heat Transfer and Friction Flow Characteristics—Steam-to-Air Test Cores," TR No. 64, Department of Mechanical Engineering, Stanford University, 1967.

4 Kays, W. M., and London, A. L., *Compact Heat Exchangers*, 2nd ed., McGraw-Hill, New York, 1964.

Influence of Temperature Dependent Properties on a Step-Heated Semi-Infinite Solid

R. L. ASH[1] and G. R. CROSSMAN[2]

Nomenclature

$b = \dfrac{1}{k_0}\dfrac{dk}{dT}$, 1/deg C
c = specific heat, J/kg-deg C
$G_n(\eta)$ = nth similarity function
k = thermal conductivity, J/m-sec-deg C
k_0 = initial thermal conductivity
q_0 = step heat flux, J/m²-sec
T = temperature, deg C
t = time, sec
$t_{\max}$ = reference time
x = space coordinate, m
α = thermal diffusivity, m²/sec
α_0 = initial thermal diffusivity
$\beta = \dfrac{1}{\alpha_0}\dfrac{d\alpha}{d\phi}$, 1/deg C
$\eta = \xi/2\sqrt{\tau}$, dimensionless similarity variable
$\epsilon = \beta q_0(\alpha_0 t_{\max})^{1/2}/k_0$, perturbation parameter
$\epsilon_b = b q_0(\alpha_0 t_{\max})^{1/2}/k_0$, thermal conductivity parameter
$\theta = k_0\phi/q_0(\alpha_0 t_{\max})^{1/2}$, dimensionless Kirchhoff temperature
θ_n = nth perturbation term
$\xi = x/(\alpha_0 t_{\max})^{1/2}$, dimensionless space coordinate
ρ = density, kg/m³
$\tau = t/t_{\max}$, dimensionless time
ϕ = Kirchhoff temperature, deg C
$\psi = k_0 T/q_0(\alpha_0 t_{\max})^{1/2}$, dimensionless temperature

Introduction

ONE method for measuring the thermophysical properties of solids has been to monitor the surface temperature of a radiatively heated sample. If the sample thickness was large in comparison with a time and property dependent length parameter ($\sqrt{\alpha t_{\max}}$), the temperature history could be represented by a step-heated, semi-infinite solid.

---

[1] Associate Professor of Engineering, Old Dominion University, Norfolk, Va. Assoc. Mem. ASME.

[2] Assistant Professor of Engineering Technology, Old Dominion University, Norfolk, Va.

Contributed by the Heat Transfer Division of THE AMERICAN SOCIETY OF MECHANICAL ENGINEERS. Manuscript received by the Heat Transfer Division July 20, 1970.

The constant property assumption is dangerous in view of the fact that the theory predicts an unbounded surface temperature rise. Since the thermophysical properties of all materials are temperature dependent to some degree and the front surface temperature may vary over a wide range of temperatures, any temperature dependence may alter significantly the shape of the temperature history curve and result in errors in property estimation. These errors could be quite large since property variations cannot be predicted in advance. A model has been developed here which incorporates variable property effects in the theoretical temperature history and simultaneously utilizes the experimentally justified upper time limit.

Recently, Cooper [1][3] has presented a solution for constant surface heating of a variable conductivity half-space. However, his model assumed that the thermal diffusivity was constant and that the thermal conductivity was an exponential function of temperature. The present work is neither restricted to constant thermal diffusivity nor to a particular functional form for the thermal conductivity.

Analysis

If all properties are referenced to the initial temperature of the solid and that temperature is arbitrarily taken as zero, Kirchhoff's temperature variable can be defined by

$$\phi(x, t) = \frac{1}{k_0}\int_0^T k(T)dT, \tag{1}$$

and the half-space temperature distribution is governed by

$$\frac{\partial \phi}{\partial t} = \alpha(\phi)\frac{\partial^2 \phi}{\partial x^2} \tag{2}$$

subject to the initial and boundary conditions

$$\frac{\partial \phi}{\partial x}(0, t) = -\frac{q_0}{k_0}$$

$$\lim_{x \to \infty} \phi(x, t) = 0 \tag{3}$$

and

$$\phi(x, 0) = 0.$$

In reality, the model which is presented here requires only that the thermal diffusivity be expressible as a polynomial function of the Kirchhoff temperature variable. However, that aspect of the problem is well discussed by Andre-Talamon [2] in his analysis of the complementary problem of a step change in surface temperature, and the present discussion will restrict consideration to the case when the thermal diffusivity can be expressed by:

$$\alpha = \alpha_0(1 + \beta\phi). \tag{4}$$

As was previously mentioned, attention will be restricted to finite time intervals and it is therefore appropriate to define the upper time limit as $t_{\max}$. This time value along with the initial specimen thermal conductivity (k_0) and thermal diffusivity (α_0) can be used to construct the dimensionless variables θ, τ, and ξ given by:

$$\tau = t/t_{\max}, \qquad \xi = x/(\alpha_0 t_{\max})^{1/2},$$

and (5)

$$\theta = \phi k_0/[q_0(\alpha_0 t_{\max})^{1/2}].$$

The resulting dimensionless governing equation is

$$\frac{\partial \theta}{\partial \tau} = (1 + \epsilon\theta)\frac{\partial^2 \theta}{\partial \xi^2}, \tag{6}$$

where

$$\epsilon = \beta q_0(\alpha_0 t_{\max})^{1/2}/k_0. \tag{7}$$

The new boundary conditions are

$$\frac{\partial \theta}{\partial \xi}(0, \tau) = -1, \qquad \lim_{\xi \to \infty} \theta(\xi, \tau) = 0,$$

and (8)

$$\theta(\xi, 0) = 0.$$

If ϵ is small, a perturbation solution can be employed. Consequently, $\theta(\xi, \tau)$ is assumed to take the form:

$$\theta(\xi, \tau) = \theta_0(\xi, \tau) + \epsilon\theta_1(\xi, \tau) + \epsilon^2\theta_2(\xi, \tau) + \ldots. \tag{9}$$

Substituting (9) into (6), and requiring that the solution be independent of the particular value of ϵ, yields the set of equations

$$\frac{\partial \theta_0}{\partial \tau} = \frac{\partial^2 \theta_0}{\partial \xi^2}, \tag{10}$$

$$\frac{\partial \theta_1}{\partial \tau} = \frac{\partial^2 \theta_1}{\partial \xi^2} + \theta_0\frac{\partial^2 \theta_0}{\partial \xi^2}, \tag{11}$$

$$\frac{\partial \theta_2}{\partial \tau} = \frac{\partial^2 \theta_2}{\partial \xi^2} + \theta_0\frac{\partial^2 \theta_1}{\partial \xi^2} + \theta_1\frac{\partial^2 \theta_0}{\partial \xi^2}, \text{ etc.} \tag{12}$$

Since the boundary conditions do not depend upon ϵ, $\theta_0(\xi, \tau)$ must satisfy the original boundary conditions, and is therefore the constant property solution. This solution has been known for some time [3] and can be written $\theta(\xi, \tau) = \tau^{1/2}G_0(\eta)$ where $\eta = \xi/2(\tau)^{1/2}$ and $G_0(\eta)$ is the solution to

$$G_0''(\eta) + 2G_0'(\eta) - 2G_0(\eta) = 0, \tag{13}$$

with boundary conditions

$$G_0''(0) = -2 \qquad \text{and} \qquad G_0(\infty) = 0. \tag{14}$$

The solution to $G_0(\eta)$ is

$$G_0(\eta) = \frac{2}{\sqrt{\pi}}e^{-\eta^2} - 2\eta \operatorname{erfc}(\eta). \tag{15}$$

Employing the solution for $\theta_0(\xi, \tau)$ in (11), it is found that $\theta_1(\xi, \tau)$ should take the form

$$\theta_1(\xi, \tau) = \tau G_1(\eta). \tag{16}$$

Then, $G_1(\eta)$ is governed by

$$G_1''(\eta) + 2\eta G_1'(\eta) - 4G_1(\eta) = 2[\eta G_0(\eta)G_0'(\eta) - G_0^2(\eta)], \tag{17}$$

and since the boundary conditions cannot depend on ϵ, the boundary conditions on $G_1(\eta)$ are:

$$G_1'(0) = 0, \qquad \text{and} \qquad G_1(\infty) = 0. \tag{18}$$

This equation has been integrated numerically using the Runge-Kutta method, and guessing $G_1(0)$ until the solution converged. A comparison with $G_0(\eta)$ is shown in Fig. 1. In addition, values for G_0, G_0', G_1, and G_1' are tabulated in Table 1. An analytic solution could be generated using Green functions, but still would require numerical integration.

Similarly, it was found that $\theta_2(\xi, \tau)$ should take the form

$$\theta_2(\xi, \tau) = \tau^{3/2}G_2(\eta), \tag{19}$$

where $G_2(\eta)$ is governed by

$$G_2'' + 2\eta G_2' - 6G_2 = 2G_0^3 + 2\eta[G_0G_1' + G_0'G_1 - G_0^2G_0'] - 6G_0G_1 \tag{20}$$

with boundary conditions

$$G_2'(0) = 0 \qquad \text{and} \qquad G_2(\infty) = 0. \tag{21}$$

This solution is also tabulated in Table 1.

---

[3] Numbers in brackets designate References at end of technical brief.

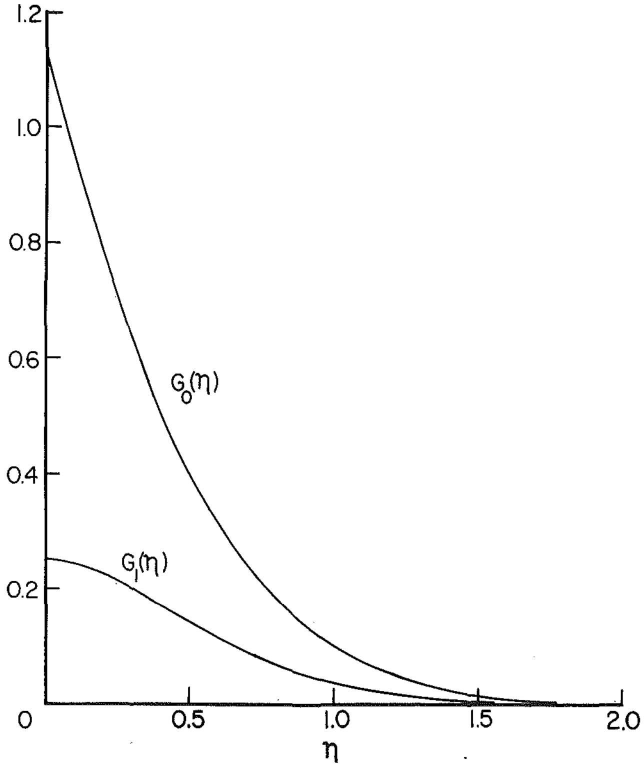

Fig. 1 Dimensionless similarity functions

At this point the solution for $\theta(\xi, \tau)$ is given by:

$$\theta(\xi, \tau) = \tau^{1/2}G_0(\eta) + \epsilon\tau G_1(\eta) + \epsilon^2\tau^{3/2}G_2(\eta) + \ldots \quad (22)$$

Further expansion was of questionable value, since it would require considerably smaller integration increments and because the relative importance of these terms will be small provided ϵ is less than one. However, these terms would have helped in determining how large ϵ could be without causing the series to diverge. From the magnitudes of $G_1(\eta)$ and $G_2(\eta)$, it would appear that ϵ can take on considerably larger values than expected and still be represented by the perturbation solution. Comparison of maximum values of $G_2(\eta)$ and $G_1(\eta)$ indicates that $G_2(\eta)$ is relatively insignificant even for $\epsilon = 1$. Unfortunately, because the succeeding terms are not generated here, no definite limits can be placed on the maximum values of ϵ.

Table 1 Similarity functions

η	G_0	G_0	G_1	G_1'	G_2	G_2'
0.0	1.128379	-2.000000	0.250000	0.000000	-0.024638	0.000000
0.1	0.939644	-1.755074	0.243017	-0.132227	-0.020720	0.067039
0.2	0.773216	-1.554595	0.224997	-0.221285	-0.013047	0.079441
0.3	0.628437	-1.342747	0.200048	-0.271772	-0.005857	0.060890
0.4	0.504255	-1.143215	0.171709	-0.290307	-0.001294	0.029369
0.5	0.399283	-0.976663	0.142798	-0.284500	-0.000002	
0.6	0.311871	-0.792288	0.115365	-0.261985		
0.7	0.240197	-0.644398	0.090727	-0.229654		
0.8	0.182347	-0.515798	0.069571	-0.193168		
0.9	0.136403	-0.406184	0.052090	-0.159274		
1.0	0.100509	-0.314599	0.038126	-0.123167		
1.1	0.072931	-0.239590	0.027308	-0.094001		
1.2	0.052098	-0.179372	0.019158	-0.069843		
1.3	0.036629	-0.131984	0.013175	-0.050613		
1.4	0.025340	-0.095429	0.008887	-0.035828		
1.5	0.017246	-0.067789	0.005884	-0.024807		
1.6	0.011544	-0.047303	0.003825	-0.016817		
1.7	0.007599	-0.032419	0.002442	-0.010712		
1.8	0.004917	-0.021819	0.001532	-0.007277		
1.9	0.003128	-0.014419	0.000945	-0.004651		
2.0	0.001956	-0.009356	0.000572	-0.002917		
2.1	0.001201	-0.005959	0.000341	-0.001796		
2.2	0.000725	-0.003726	0.000200	-0.001086		
2.3	0.000430	-0.002287	0.000115	-0.000645		
2.4	0.000250	-0.001377	0.000065	-0.000376		
2.5	0.000143	-0.000814	0.000036	-0.000215		
2.6	0.000080	-0.000472	0.000020	-0.000121		
2.7	0.000044	-0.000269	0.000011	-0.000067		
2.8	0.000024	-0.000150	0.000006	-0.000036		
2.9	0.000013	-0.000082	0.000003	-0.000019		
3.0	0.000007	-0.000044	0.000001	-0.000010		
3.1	0.000003	-0.000023	0.000001	-0.000005		
3.2	0.000002	-0.000012	0.000000	-0.000003		
3.3	0.000001	-0.000006				
3.4	0.000000	-0.000003				

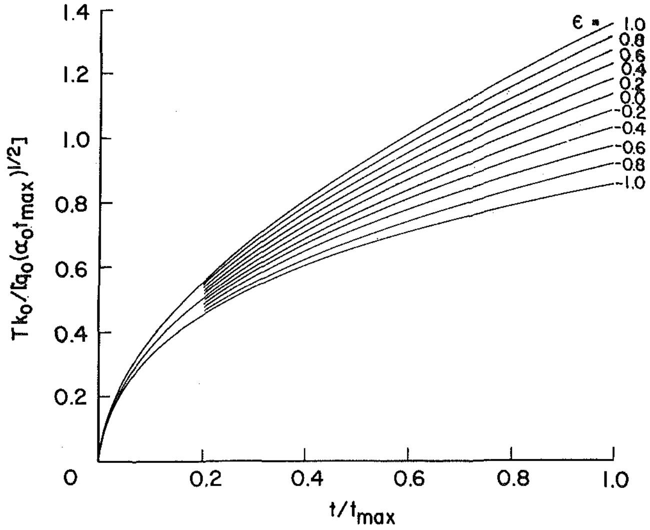

Fig. 2 Surface temperature history (constant thermal conductivity)

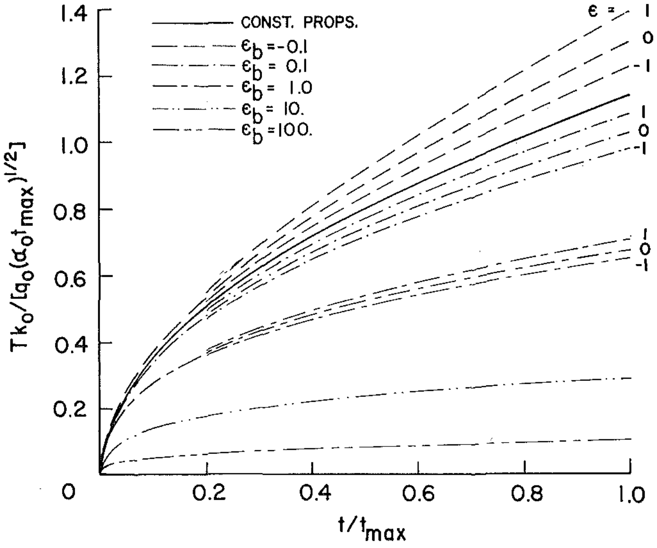

Fig. 3 Surface temperature history (thermal conductivity a linear function of temperature)

Consider the particular problem where the thermal conductivity is constant, but the thermal diffusivity is a linear function of temperature. This condition exists in some plastics used for model construction in wind tunnels, but is of interest here primarily because under these conditions the variable ϕ becomes the temperature, and $\theta(\xi, \tau)$ represents the dimensionless temperature history. From equation (22) the front surface temperature distribution is given by

$$\theta(0, \tau) = 1.1284\tau^{1/2} + 0.2500\epsilon\tau - 0.0246\epsilon^2\tau^{3/2}. \quad (23)$$

Variation of the front surface temperature with time for different values of ϵ is shown in Fig. 2.

As a second example, consider the case when the thermal conductivity is a linear function of temperature, say

$$k(T) = k_0(1 + bT). \quad (24)$$

Then, the Kirchhoff temperature is given by

$$\phi(x, t) = T + (1/2)bT^2. \quad (25)$$

Defining a dimensionless temperature variable ψ as

$$\psi(\xi, \tau) = k_0T/[q_0(\alpha_0 t_{max})^{1/2}], \quad (26)$$

it can be seen that

$$\psi(\xi, \tau) + \epsilon_b\psi^2(\xi, \tau) = \theta(\xi, \tau), \tag{27}$$

where $\theta(\xi, \tau)$ is given by equation (22) and ϵ_b is defined as

$$\epsilon_b = bq_0(\alpha_0 t_{\max})^{1/2}/2k_0. \tag{28}$$

Consequently,

$$\psi(\xi, \tau) = \frac{1}{2\epsilon_b}\left[(1 + 4\epsilon_b\theta)^{1/2} - 1\right]. \tag{29}$$

The front surface temperature history for different values of ϵ_b is shown in Fig. 3 for the limiting values $\epsilon = 1, -1$, and 0. It is interesting to note that for large values of ϵ_b, the variation in temperature due to diffusivity changes becomes negligibly small.

Conclusions

A perturbation solution for the temperature distribution in a step-heated semi-infinite medium has been presented which is time limited. From the definition of ϵ, equation (7), it can be seen that the time interval can be used to vary ϵ. As a consequence, *the solution presented can be used to represent any heating-thermophysical property combination* for some period of time, although a very small time interval may be required. Otherwise, the time interval will be imposed by the physical limitations of the particular experiment.

Examination of equations (23) and (29) along with Fig. 3 suggests how an experimental temperature history can be used to estimate ϵ and ϵ_b in order to best fit the theoretical curves and finally calculate $k_0\sqrt{\alpha_0}$. If these quantities are all known, β and b can be calculated and then one additional measurement is required to complete the linearized temperature dependent property calculations. An experimental investigation of this technique is currently in progress at NASA Langley Research Center.

Acknowledgment

The authors would like to thank Robert E. Wright, Jr. of NASA Langley Research Center for bringing this problem to their attention.

References

1 Cooper, L. Y., "Constant Surface Heating of a Variable Conductivity Half-Space," *Quarterly of Applied Mathematics*, Vol. 27, 1969, pp. 173–183.

2 Andre-Talamon, T., "Sur la diffusion non-lineaire de la Chaleur," *International Journal of Heat and Mass Transfer*, Vol. 11, 1968, pp. 1351–1357.

3 Carslaw, H. S., and Jaeger, J. C., *Conduction of Heat in Solids*, 2nd ed., Oxford University Press, London, 1959, pp. 75–77.

Prandtl Number Effects on Natural Convection in an Enclosed Vertical Layer

R. K. MacGREGOR[1] and A. F. EMERY[2]

Introduction

In an earlier paper [1][3] the authors presented data for free convection in enclosed vertical layers for fluids whose Prandtl numbers were from 5 to 20,000. Since that time, additional experiments have been completed with glycerin (Pr ~20,000–30,000), silicone oil (Pr ~3000), water (Pr ~5), and mercury (Pr ~0.02) and the results are reported herein. The experimental conditions were those of reference [1] and consisted of a two-dimensional fluid layer of height H, layer thickness W, heated by a spatially constant heat flux and cooled by an isothermal cold surface. The upper and lower cross-surfaces of the layer were insulated and fluid filled the enclosure such that no free liquid surface existed.

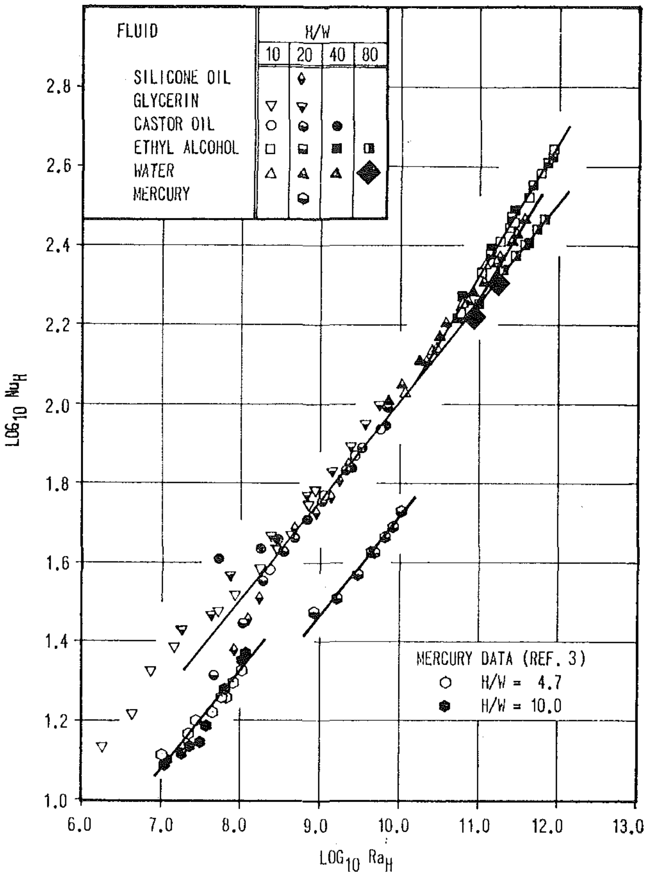

Fig. 1

Prandtl Number Effects

Fig. 1 is a compendium of the data of reference [1] and the additional data secured in this study. The data possess there primary characteristics:

1 Fluids whose Prandtl numbers were greater than 1 and whose properties were reasonably independent of temperature over the range of Ra used (i.e., less than a 2-to-1 change in Prandtl number) agglomerate about the solid lines, which is in good agreement with the correlations of reference [1].

2 The heat transfer of fluids whose properties vary strongly (changes in Pr of the order of 10 to 1) are extremely aspect-ratio dependent when the fluid nears the pure conduction mode of heat transfer. For larger values of Ra, for which the heat transfer mode is primarily convection, these fluids behave similarly to the fluids described in [1].

3 Low Prandtl number fluids (e.g., liquid metals), for which the heat is transferred mainly by conduction, have significantly reduced heat transfer coefficients and effectively represent the only situation for which the correlations do not hold. For the liquid metals, the high conductivities prevent the formation of a boundary layer flow and the resulting heat transfer is more geometry-dependent than normal fluids. However, for the range of layer temperature differences which are measurable with reasonable accuracy, the liquid metal data does aggregate about a $1/4$ power line.

---

[1] Specialist Engineer, The Boeing Co., Seattle, Wash. Assoc. Mem. ASME.

[2] Professor of Mechanical Engineering, University of Washington, Seattle, Wash. Mem. ASME.

[3] Numbers in brackets designate References at end of technical brief.

Contributed by the Heat Transfer Division of The American Society of Mechanical Engineers. Manuscript received by the Heat Transfer Division October 29, 1970.

it can be seen that

$$\psi(\xi, \tau) + \epsilon_b\psi^2(\xi, \tau) = \theta(\xi, \tau), \tag{27}$$

where $\theta(\xi, \tau)$ is given by equation (22) and ϵ_b is defined as

$$\epsilon_b = bq_0(\alpha_0 t_{\max})^{1/2}/2k_0. \tag{28}$$

Consequently,

$$\psi(\xi, \tau) = \frac{1}{2\epsilon_b}\left[(1 + 4\epsilon_b\theta)^{1/2} - 1\right]. \tag{29}$$

The front surface temperature history for different values of ϵ_b is shown in Fig. 3 for the limiting values $\epsilon = 1, -1$, and 0. It is interesting to note that for large values of ϵ_b, the variation in temperature due to diffusivity changes becomes negligibly small.

Conclusions

A perturbation solution for the temperature distribution in a step-heated semi-infinite medium has been presented which is time limited. From the definition of ϵ, equation (7), it can be seen that the time interval can be used to vary ϵ. As a consequence, *the solution presented can be used to represent any heating–thermophysical property combination* for some period of time, although a very small time interval may be required. Otherwise, the time interval will be imposed by the physical limitations of the particular experiment.

Examination of equations (23) and (29) along with Fig. 3 suggests how an experimental temperature history can be used to estimate ϵ and ϵ_b in order to best fit the theoretical curves and finally calculate $k_0\sqrt{\alpha_0}$. If these quantities are all known, β and b can be calculated and then one additional measurement is required to complete the linearized temperature dependent property calculations. An experimental investigation of this technique is currently in progress at NASA Langley Research Center.

Acknowledgment

The authors would like to thank Robert E. Wright, Jr. of NASA Langley Research Center for bringing this problem to their attention.

References

1 Cooper, L. Y., "Constant Surface Heating of a Variable Conductivity Half-Space," *Quarterly of Applied Mathematics*, Vol. 27, 1969, pp. 173–183.

2 Andre-Talamon, T., "Sur la diffusion non-lineaire de la Chaleur," *International Journal of Heat and Mass Transfer*, Vol. 11, 1968, pp. 1351–1357.

3 Carslaw, H. S., and Jaeger, J. C., *Conduction of Heat in Solids*, 2nd ed., Oxford University Press, London, 1959, pp. 75–77.

Prandtl Number Effects on Natural Convection in an Enclosed Vertical Layer

R. K. MacGREGOR[1] **and A. F. EMERY**[2]

Introduction

In an earlier paper [1][3] the authors presented data for free convection in enclosed vertical layers for fluids whose Prandtl numbers were from 5 to 20,000. Since that time, additional experiments have been completed with glycerin (Pr ~20,000–30,000), silicone oil (Pr ~3000), water (Pr ~5), and mercury (Pr ~0.02) and the results are reported herein. The experimental conditions were those of reference [1] and consisted of a two-dimensional fluid layer of height H, layer thickness W, heated by a spatially constant heat flux and cooled by an isothermal cold surface. The upper and lower cross-surfaces of the layer were insulated and fluid filled the enclosure such that no free liquid surface existed.

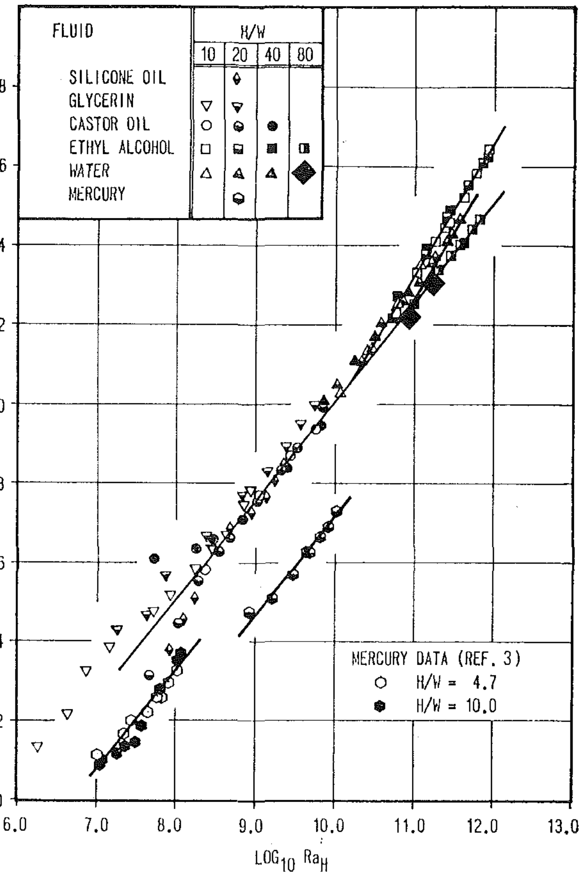

Fig. 1

Prandtl Number Effects

Fig. 1 is a compendium of the data of reference [1] and the additional data secured in this study. The data possess there primary characteristics:

1 Fluids whose Prandtl numbers were greater than 1 and whose properties were reasonably independent of temperature over the range of Ra used (i.e., less than a 2-to-1 change in Prandtl number) agglomerate about the solid lines, which is in good agreement with the correlations of reference [1].

2 The heat transfer of fluids whose properties vary strongly (changes in Pr of the order of 10 to 1) are extremely aspect-ratio dependent when the fluid nears the pure conduction mode of heat transfer. For larger values of Ra, for which the heat transfer mode is primarily convection, these fluids behave similarly to the fluids described in [1].

3 Low Prandtl number fluids (e.g., liquid metals), for which the heat is transferred mainly by conduction, have significantly reduced heat transfer coefficients and effectively represent the only situation for which the correlations do not hold. For the liquid metals, the high conductivities prevent the formation of a boundary layer flow and the resulting heat transfer is more geometry-dependent than normal fluids. However, for the range of layer temperature differences which are measurable with reasonable accuracy, the liquid metal data does aggregate about a $^1/_4$ power line.

---

[1] Specialist Engineer, The Boeing Co., Seattle, Wash. Assoc. Mem. ASME.

[2] Professor of Mechanical Engineering, University of Washington, Seattle, Wash. Mem. ASME.

[3] Numbers in brackets designate References at end of technical brief.

Contributed by the Heat Transfer Division of The American Society of Mechanical Engineers. Manuscript received by the Heat Transfer Division October 29, 1970.

Turbulent Transition

During these tests and those of reference [1], it was noted that narrow vertical layers seemed to delay the transition of the overall heat transfer data from a $^1/_4$ power law dependence to a $^1/_3$ power law. It was speculated that the turbulent fluctuations were restricted by the narrow layer. Consequently, the fluid could not complete the transition to fully turbulent flow until the Grashof number reached a higher value than normal. From Fig. 1, the water data for $H/W = 20$ are displaced to the right of the $H/W = 10$ data and the alcohol data for $H/W = 80$ does not appear to have become turbulent as has the alcohol for $H/W = 10$, 20, and 40; however, Landis [2] has noted that the overall heat transfer behavior of a vertical layer of fluid is a very poor indicator of the fluid motion within the layer.

Accordingly, the system was modified in order that the vertical layer could be mounted in a shadowgraph. Preliminary tests with water operating in a laminar mode and through to a highly turbulent mode indicated the transition from laminar to turbulent flow could be reasonably well observed in the shadowgraph. The layer was then filled with alcohol with $H/W = 80$ and observed. No turbulent effects were noted and the overall heat transfer (Fig. 1) was on the $^1/_4$ power correlation. Water was then used in an $H/W = 20$ layer and it was noted that the boundary layers were first laminar, then as the Grashof number increased transition set in. During the early phases the layers would trip about 2 in. from the leading edge, then revert to a low-frequency sinuous motion at about 4 in. and finally trip again at 18 in. (20-in. cell height). For sufficiently high Grashof numbers, the entire boundary layers were turbulent. When water was placed in the $H/W = 80$ layer and tested, no signs of turbulent motion were noted even at the maximum heating capacity of the system. The data points for these runs are shown in Fig. 1 and although they do not extend very far up the $^1/_4$ power line, they are a fairly definitive indication that the layer aspect ratio can have a strong effect on the turbulent transition. At the highest heat flux, the layer flow was beginning to become quite sinuous and it would not be too unlikely that the $H/W = 80$ data would soon lie on the $^1/_3$ power line if further increases in the Grashof number were made.

Conclusions

The data suggest that the heat transfer performance of fluids, other than liquid metals, can be correlated as a single line only in the limited range of Rayleigh numbers between the point of full boundary layer development and the transition to turbulent flows. Liquid metals and very viscous fluids at low Rayleigh numbers show decided layer size effects and point out that no comparative conclusions can be drawn between experiments unless the experimental setups are of equal dimensions or are conducted for ranges of parameters for which the cell width is not an influencing parameter.

Acknowledgments

The results reported herein were obtained under the sponsorship of the National Science Foundation (Grant GK-567) and the Department of Mechanical Engineering, University of Washington, Seattle, Wash.

References

1 MacGregor, R. K., and Emery, A. F., "Free Convection Through Vertical Plane Layers—Moderate and High Prandtl Number Fluids," JOURNAL OF HEAT TRANSFER, TRANS. ASME, Series C, Vol. 91, No. 3, Aug. 1969, pp. 391–403.

2 Landis, F., discussion of "Heat Transfer Across Vertical Layers," by Emery, A., and Chun, N. C., JOURNAL OF HEAT TRANSFER, TRANS. ASME, Series C, Vol. 87, No. 1, Feb. 1965, p. 114.

3 Emery, A. F., "The Effect of a Magnetic Field Upon the Free Convection of a Conducting Fluid," JOURNAL OF HEAT TRANSFER, TRANS. ASME, Series C, Vol. 85, No. 2, May 1963, pp. 119–124.

Predictions of Flow-Level Angles in Two-Phase, One-Component Stratified Flow

P. K. SARMA,[1] A. S. P. SARMA,[2] and K. VENKATA APPARAO[1]

An analytical method is proposed to predict the flow-level angles under two-phase, one-component stratified flow in a horizontal tube with and without mass transfer. The analysis is restricted to adiabatic flow phenomena. A comparison of the present analysis with the available experimental data has revealed excellent agreement.

Nomenclature

A = cross-sectional flow area, m^2
D = diameter of the tube, m
f = friction coefficient, dimensionless
G = mass rate of discharge, kgm/sec
g_c = conversion factor, kgm$_m$·m/kgm$_f$·sec^2
h_m = mean heat-transfer coefficient, kcal/m^2·sec·deg C
h_{fg} = latent heat of condensation, kcal/kgm$_m$
h_{fg}' = corrected latent heat of condensation taking subcooling enthalpy into consideration = $(h_{fg} + 0.68\, C_p\Delta t)$, kcal/kgm$_m$
P = pressure, kgm$_f$/m^2
p = wetted perimeter, m
U = fluid velocity, m/sec
x = fluid quality, dimensionless
Z = location along the tube, m
α = form factor, dimensionless
β = momentum correction factors, dimensionless
ρ = fluid density, kgm/m^3
μ = fluid viscosity, kgm/m·sec
ψ = half of flow-level angle, rad
Re = Reynolds number = $UD\rho/\mu$, dimensionless
τ_w = wall shear stress multiplied by g_c, kgm$_m$/m·sec^2

Subscripts

L = liquid
V = vapor
TP = two-phase

Introduction

OF THE many analytical solutions available in two-phase phenomena, the equations of Levy [1][3] or Zivi [2] are often used for predicting the voids ratio. While Levy developed his equation based on a "momentum exchange model," Zivi applied the principle of minimum entropy production in order to obtain an estimate of entrainment and wall friction. It is observed [3] that the application of these equations to stratified flow phenomena with simultaneous condensation of vapors has not been found successful. Rufer and Kezios [4] developed flow-level equations for two-phase, one-component stratified flow with and without condensation. The flow-level equation is arrived at by extending and making use of the similarity analysis of Wicks, Dukler, and Cleveland [5, 6]. For diabatic conditions a step-by-step procedure is made use of for evaluating the flow-level angles under variable system conditions. The flow-level equations for different flow regimes under adiabatic conditions are as follows:

---

[1] Department of Mechanical Engineering, Andhra University, Waltair, India.

[2] Probationary Officer, Hindustan Shipyard, Waltair, India; formerly Junior Research Fellow, C.S.I.R. Government of India, Department of Mechanical Engineering, Andhra University, Waltair, India.

[3] Numbers in brackets designate References at end of technical brief.

Contributed by the Heat Transfer Division of THE AMERICAN SOCIETY OF MECHANICAL ENGINEERS. Manuscript received by the Heat Transfer Division November 10, 1970.

Turbulent Transition

During these tests and those of reference [1], it was noted that narrow vertical layers seemed to delay the transition of the overall heat transfer data from a $^1/_4$ power law dependence to a $^1/_3$ power law. It was speculated that the turbulent fluctuations were restricted by the narrow layer. Consequently, the fluid could not complete the transition to fully turbulent flow until the Grashof number reached a higher value than normal. From Fig. 1, the water data for $H/W = 20$ are displaced to the right of the $H/W = 10$ data and the alcohol data for $H/W = 80$ does not appear to have become turbulent as has the alcohol for $H/W = 10$, 20, and 40; however, Landis [2] has noted that the overall heat transfer behavior of a vertical layer of fluid is a very poor indicator of the fluid motion within the layer.

Accordingly, the system was modified in order that the vertical layer could be mounted in a shadowgraph. Preliminary tests with water operating in a laminar mode and through to a highly turbulent mode indicated the transition from laminar to turbulent flow could be reasonably well observed in the shadowgraph. The layer was then filled with alcohol with $H/W = 80$ and observed. No turbulent effects were noted and the overall heat transfer (Fig. 1) was on the $^1/_4$ power correlation. Water was then used in an $H/W = 20$ layer and it was noted that the boundary layers were first laminar, then as the Grashof number increased transition set in. During the early phases the layers would trip about 2 in. from the leading edge, then revert to a low-frequency sinuous motion at about 4 in. and finally trip again at 18 in. (20-in. cell height). For sufficiently high Grashof numbers, the entire boundary layers were turbulent. When water was placed in the $H/W = 80$ layer and tested, no signs of turbulent motion were noted even at the maximum heating capacity of the system. The data points for these runs are shown in Fig. 1 and although they do not extend very far up the $^1/_4$ power line, they are a fairly definitive indication that the layer aspect ratio can have a strong effect on the turbulent transition. At the highest heat flux, the layer flow was beginning to become quite sinuous and it would not be too unlikely that the $H/W = 80$ data would soon lie on the $^1/_3$ power line if further increases in the Grashof number were made.

Conclusions

The data suggest that the heat transfer performance of fluids, other than liquid metals, can be correlated as a single line only in the limited range of Rayleigh numbers between the point of full boundary layer development and the transition to turbulent flows. Liquid metals and very viscous fluids at low Rayleigh numbers show decided layer size effects and point out that no comparative conclusions can be drawn between experiments unless the experimental setups are of equal dimensions or are conducted for ranges of parameters for which the cell width is not an influencing parameter.

Acknowledgments

The results reported herein were obtained under the sponsorship of the National Science Foundation (Grant GK-567) and the Department of Mechanical Engineering, University of Washington, Seattle, Wash.

References

1 MacGregor, R. K., and Emery, A. F., "Free Convection Through Vertical Plane Layers—Moderate and High Prandtl Number Fluids," JOURNAL OF HEAT TRANSFER, TRANS. ASME, Series C, Vol. 91, No. 3, Aug. 1969, pp. 391–403.

2 Landis, F., discussion of "Heat Transfer Across Vertical Layers," by Emery, A., and Chun, N. C., JOURNAL OF HEAT TRANSFER, TRANS. ASME, Series C, Vol. 87, No. 1, Feb. 1965, p. 114.

3 Emery, A. F., "The Effect of a Magnetic Field Upon the Free Convection of a Conducting Fluid," JOURNAL OF HEAT TRANSFER, TRANS. ASME, Series C, Vol. 85, No. 2, May 1963, pp. 119–124.

Predictions of Flow-Level Angles in Two-Phase, One-Component Stratified Flow

P. K. SARMA,[1] A. S. P. SARMA,[2] and K. VENKATA APPARAO[1]

An analytical method is proposed to predict the flow-level angles under two-phase, one-component stratified flow in a horizontal tube with and without mass transfer. The analysis is restricted to adiabatic flow phenomena. A comparison of the present analysis with the available experimental data has revealed excellent agreement.

Nomenclature

A = cross-sectional flow area, m^2
D = diameter of the tube, m
f = friction coefficient, dimensionless
G = mass rate of discharge, kgm/sec
g_c = conversion factor, kgm$_m\cdot$m/kgm$_f\cdot$sec^2
h_m = mean heat-transfer coefficient, kcal/m$^2\cdot$sec$\cdot$deg C
h_{fg} = latent heat of condensation, kcal/kgm$_m$
h_{fg}' = corrected latent heat of condensation taking subcooling enthalpy into consideration = $(h_{fg} + 0.68\ C_p\Delta t)$, kcal/kgm$_m$
P = pressure, kgm$_f$/m^2
p = wetted perimeter, m
U = fluid velocity, m/sec
x = fluid quality, dimensionless
Z = location along the tube, m
α = form factor, dimensionless
β = momentum correction factors, dimensionless
ρ = fluid density, kgm/m^3
μ = fluid viscosity, kgm/m$\cdot$sec
ψ = half of flow-level angle, rad
Re = Reynolds number = $UD\rho/\mu$, dimensionless
τ_w = wall shear stress multiplied by g_c, kgm$_m$/m$\cdot$sec^2

Subscripts

L = liquid
V = vapor
TP = two-phase

Introduction

OF THE many analytical solutions available in two-phase phenomena, the equations of Levy [1][3] or Zivi [2] are often used for predicting the voids ratio. While Levy developed his equation based on a "momentum exchange model," Zivi applied the principle of minimum entropy production in order to obtain an estimate of entrainment and wall friction. It is observed [3] that the application of these equations to stratified flow phenomena with simultaneous condensation of vapors has not been found successful. Rufer and Kezios [4] developed flow-level equations for two-phase, one-component stratified flow with and without condensation. The flow-level equation is arrived at by extending and making use of the similarity analysis of Wicks, Dukler, and Cleveland [5, 6]. For diabatic conditions a step-by-step procedure is made use of for evaluating the flow-level angles under variable system conditions. The flow-level equations for different flow regimes under adiabatic conditions are as follows:

---

[1] Department of Mechanical Engineering, Andhra University, Waltair, India.

[2] Probationary Officer, Hindustan Shipyard, Waltair, India; formerly Junior Research Fellow, C.S.I.R. Government of India, Department of Mechanical Engineering, Andhra University, Waltair, India.

[3] Numbers in brackets designate References at end of technical brief.

Contributed by the Heat Transfer Division of THE AMERICAN SOCIETY OF MECHANICAL ENGINEERS. Manuscript received by the Heat Transfer Division November 10, 1970.

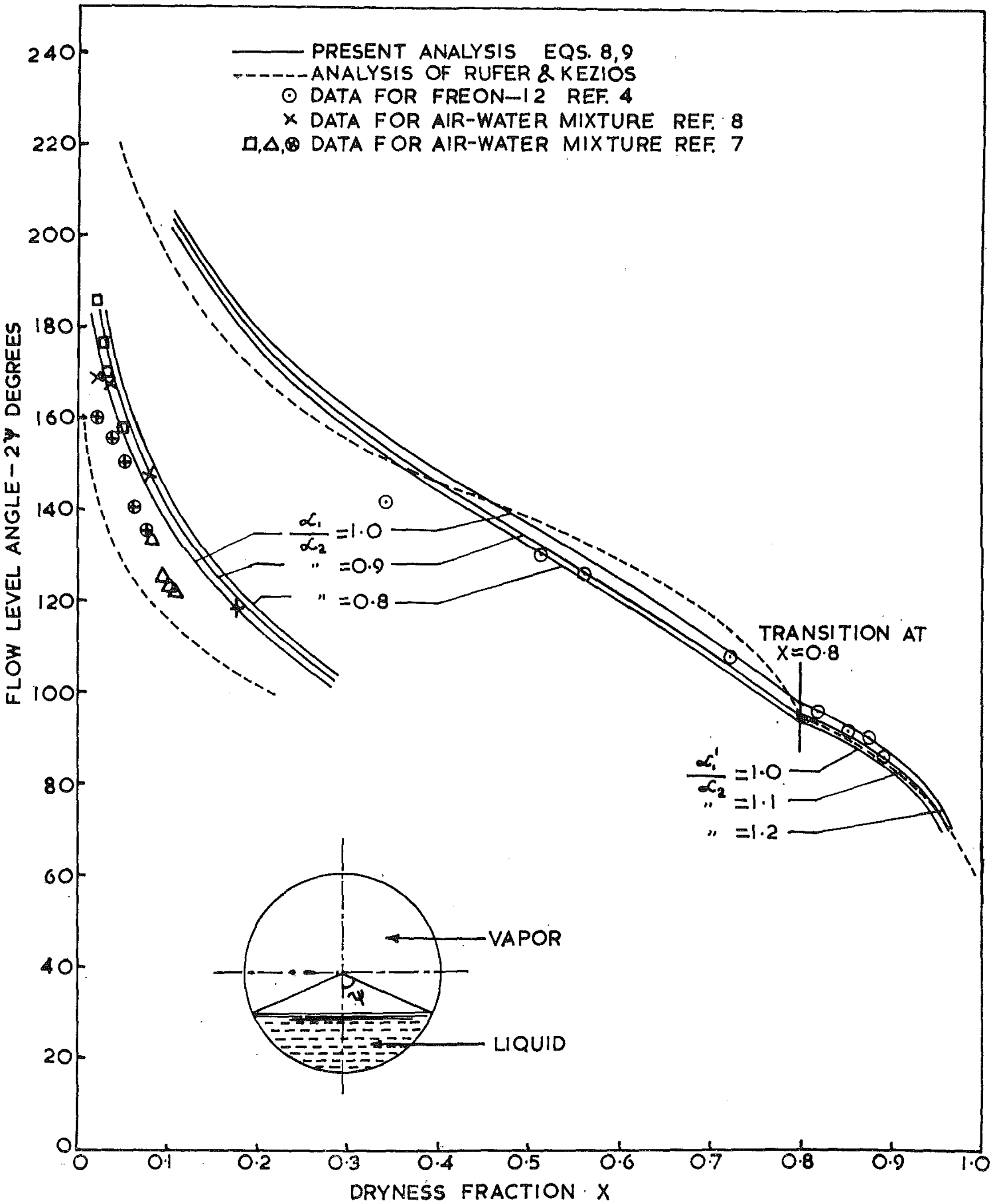

Fig. 1 Comparison of holdup correlations (horizontal flow)

$$\frac{(\psi - \frac{1}{2}\sin 2\psi)^3}{\psi} = \pi^2 \frac{\rho_{\mathrm{TP}}}{\rho_{\mathrm{L}}} \frac{f_{\mathrm{L}}}{f_{\mathrm{TP}}} (1 - x)^2$$

where
$$\frac{f_{\mathrm{L}}}{f_{\mathrm{TP}}} = \frac{\alpha_1}{\alpha_2} \left[\frac{\psi}{\pi} \frac{1}{(1 - x)} \left(\frac{\mu_{\mathrm{L}}}{\mu_{\mathrm{TP}}} \right) \right]^{1/4}$$

for liquid turbulent, vapor turbulent, and

$$\frac{f_{\mathrm{L}}}{f_{\mathrm{TP}}} = 120 \frac{\alpha_1'}{\alpha_2} \frac{\psi}{\pi^{1/4}} \frac{1}{(1 - x)} \left(\frac{D}{2G} \right)^{3/4} \frac{\mu_{\mathrm{L}}}{\mu_{\mathrm{TP}}^{0.25}}$$

for liquid laminar, vapor turbulent. Nevertheless, the above two equations can be rearranged to obtain the result $\left(\frac{dP}{dZ}\right)_{\mathrm{TP}} = \left(\frac{dP}{dZ}\right)_{\mathrm{L}}$ which may serve only as an assumed approximation.

The present note, abstracted from [3], attempts to propose an analytical method to obtain the flow-level equation for adiabatic flow treating it as a special case of diabatic (condensation) phenomena. A comparison of the present theory with relevant data obtained from [4, 7, 8] reveals excellent agreement.

Physical Model

In two-phase stratified flow with condensation, the condensate formed on the inner periphery of the tube rolls down and collects at the bottom of the tube under the action of gravity. The condensate collected at the bottom flows along the length of the tube with its height gradually increasing as more and more condensate joins the stream from the sides of the tube. Further, the flow of the condensate is assumed to be maintained by the static pressure gradient.